

Geophysical Methods

GEOS3104

Christian Heine, Simon Williams, Leonardo Quevedo
School of Geosciences, The University of Sydney, Australia

2011



THE UNIVERSITY OF
SYDNEY

Organisation

Lecturers

Dr. Christian Heine (course co-ordinator), Madsen Building, Rm. 418

✉ <mailto:Christian.Heine@sydney.edu.au>

☎ 02 9114 0997

Dr. Simon Williams, Madsen Building, Rm. 418

✉ <mailto:Simon.Williams@sydney.edu.au>

☎ 02 9114 0997

Dr. Leonardo Quevedo, Madsen Building, Rm. 416

✉ <mailto:Leonardo.Quevedo@sydney.edu.au>

☎ 02 9351 2442

Lectures and practicals

Lectures: Tuesdays 12.00 to 1.00 pm, and Thursdays 11.00 to 12.00 pm, Lab 336

Practicals: Thursdays 1.00 pm to 4.00 pm, Computer Lab 304

Course details

Course synopsis

The aim of this course is to introduce the geophysical methods used to investigate the Earth. The course is mainly based on the techniques used for minerals and hydrocarbon exploration and production, covering marine and terrestrial applications. Where appropriate, applications in global geophysics will also be described. The course is relevant for students with interests in land-based and marine resource exploration, as well as environmental applications. Students wishing to become professional geophysicists are strongly encouraged to expand their geophysics background through completion of an Honours degree.

Geophysical fieldwork

In 2011 the course will, for the first time, include a short field practicum at some location close to University. Course participants will go and measure gravity, topography and magnetism using the geophysical instruments. The collected data will be used in subsequent

pracs for further exercises. We will update you during the first lectures on when and how this will be done.

Assessment

The assessment for this course is based on 50% coursework and 50% exam. Late assignments will be penalized 10% per day (weekends count as 1 day). The examination will be 2 hours long and will be held during the examination period at the end of semester. To satisfactorily complete the course, you must pass both the coursework and the exam components.

Course program

| Week Cal | No. Sem | L | P | Lecture | Prac | Lecturer |
|-------------|----------------------------|----|----|-------------------------------------|--|----------|
| 30 | 1 | 1 | | Introduction to Geophysical Methods | | CH |
| | | 2 | 1 | Solid Earth: Overview | Matlab intro (not assessed) | CH,SW |
| 31 | 2 | 3 | | Petrophysics | | CH |
| | | 4 | 2 | Gravity 1: Intro, isostasy | Geophysical field work | CH,SW,LQ |
| 32 | 3 | 5 | | Gravity 2 | | SW |
| | | 6 | 3 | Gravity 3 | Gravity data analysis | SW |
| 33 | 4 | 7 | | Magnetics 1 | | SW |
| | | 8 | 4 | Magnetics 2 | Magnetics onshore: acquisition, case scenario | SW |
| 34 | 5 | 9 | | Electromagnetics | | SW |
| | | 10 | 5 | Radiometry | Magnetics offshore: acquisition, anomalies, MAGMOD | SW |
| 35 | 6 | 11 | | Seismics 1: Seismic waves | | CH |
| | | 12 | 6 | Seismics 2: acquisition | Earthquake exercise | CH |
| 36 | 7 | 13 | | Seismics 3: processing | | CH |
| | | 14 | 7 | Seismics 4: interpretation | Seismic processing/signal processing | CH |
| 37 | 8 | 15 | | Well logs | | CH |
| | | 16 | 8 | Well logs/sequence stratigraphy | Well log interpretation | CH |
| 38 | 9 | 17 | | Sequence stratigraphy | | CH |
| | | 18 | 9 | Global Tectonics | Seismic interpretation and stratigraphy | LQ,CH |
| 39 | Mid-semester recess | | | | | |
| 40 | 10 | 19 | | Geodynamics 1: Plate Driving Forces | | LQ |
| | | 20 | 10 | Geodynamics 2: Mantle convection | Mantle convection exercise | LQ |
| 41 | 11 | 21 | | Heatflow 1 | | LQ |
| | | 22 | 11 | Heatflow 2 | Heat Diffusion exercise | LQ |
| 42 | 12 | 23 | | Lithospheric Flexure | | LQ |
| | | 24 | 12 | Basin analysis intro | Subsidence analysis and backstripping | CH |
| 43 | 13 | 25 | | Basin analysis 1 | | CH |
| | | 26 | 13 | Basin analysis 2 | Integrated basin analysis | CH |

Bibliography

Keary, P., & Brooks, M., 1991. An Introduction to Geophysical Exploration. Blackwell Publishing, 254 pp. <http://books.google.com/books?id=yj7CMOMvxnMC&dq=isbn:0632049294>

This is quite a good (although slightly outdated) textbook on the main geophysical techniques used for hydrocarbon and mineral exploration. It is probably the best currently available resource on geophysical exploration at introductory level. It can be used as a supplementary text to the lectures.

Jones, E.J.W., 1999, Marine geophysics: Chichester; New York, Wiley, 466 p.

This volume on marine geophysics has two objectives: to provide a comprehensive review of techniques and to examine what geophysical observations can tell us about the structure and tectonics of the oceans. This book is of interest to marine scientists and advanced undergraduates and postgraduates following courses on, or undertaking research in, geophysics, marine geology, oceanography, physical sciences, remote sensing, marine surveying and offshore engineering.

Parasnis, D.S., 1986. Principles of Applied Geophysics. Chapman and Hall, 402 p.

A good introductory text book, especially for the geophysical methods used in minerals exploration.

Telford, W.M., Geldhart, L.P. and Sheriff, R.E., 1990, Applied Geophysics: Cambridge University Press, 770 p.

A very thorough description of most methods of geophysical exploration.

Sheriff, R.E., and Geldart, L.P., 1995, Exploration seismology: Cambridge; New York, Cambridge University Press, 592 p.

This book covers the theory and geometry of seismic waves, partitioning at an interface, seismic velocity, characteristics of seismic events, equipment, reflection field methods, data processing, geologic interpretation of reflection data and refraction methods.

Contents

| | |
|--|-------------|
| Organisation | i |
| Course details | i |
| Contents | v |
| List of Figures | x |
| List of Tables | xxii |
| 1 Introduction to Geophysics | 1 |
| 2 Petrophysics | 3 |
| 2.1 Density | 3 |
| 2.2 Elastictcity | 5 |
| 2.3 Magnetism | 6 |
| 2.4 Electrical properties | 7 |
| 2.5 Electromagnetism | 11 |
| 2.6 Radioactivity | 11 |
| 2.7 Thermal properties | 11 |
| 3 Seismic waves | 13 |
| 3.1 Seismic Body waves | 13 |
| 3.2 Surface waves | 18 |
| 4 Global Geophysics | 20 |
| 4.1 Introduction to the layering of the Earth | 20 |
| 4.2 Continental crust | 21 |
| 4.3 Oceanic crust | 24 |
| 4.4 Main differences between oceanic and continental crust | 25 |
| 4.5 The Mantle | 26 |
| 4.6 Core | 27 |

| | |
|---|------------|
| 4.7 Data on the Earth's Interior | 28 |
| 4.8 Mantle convection | 29 |
| 5 Data Attributes and Signal Processing | 56 |
| 5.1 Waves | 56 |
| 5.2 Digital representation of signals | 58 |
| 5.3 Numerical Transforms | 61 |
| 5.4 The Fourier series and finite Fourier series | 63 |
| 5.5 Autocorrelation, cross-correlation and convolution | 68 |
| 6 Lithosphere, Asthenosphere, and Plates: definitions | 76 |
| 6.1 Lithosphere | 76 |
| 6.2 Asthenosphere | 80 |
| 6.3 The Plate | 81 |
| 6.4 Plate boundaries | 84 |
| 6.5 Plate tectonic concepts | 84 |
| 7 Modelling Lithospheric Deformation and Mantle Convection Dynamically | 87 |
| 7.1 Dimensional analysis and mathematical framework | 87 |
| 7.2 Rayleigh Number | 88 |
| 7.3 Viscosity | 89 |
| 7.4 Brittle Failure | 89 |
| 7.5 Strain Weakening | 89 |
| 7.6 Mechanics of Deformation and Model Formulation | 90 |
| 8 Heat flow | 95 |
| 8.1 Introduction | 95 |
| 8.2 Heat flow measurements | 96 |
| 8.3 Character of the Earth's Heat Flow | 97 |
| 9 Conductive Heatflow | 102 |
| 9.1 Introduction | 102 |
| 9.2 Conductive heat flow in solids | 106 |
| 9.3 Geological applications | 110 |
| 9.4 Instantaneous heating or cooling | 112 |
| 9.5 Terrestrial heat flow | 116 |
| 9.6 Modelling Heat Flux Partitioning Between the Oceans and the Continents | 117 |
| 9.7 References | 135 |
| 10 Isostatic compensation | 144 |
| 10.1 Introduction | 144 |
| 10.2 Airy model | 144 |
| 10.3 Pratt model | 145 |
| 11 Driving forces of Plate Tectonics | 147 |

| | |
|---|------------|
| 11.1 Introduction | 147 |
| 11.2 Ridge Push | 147 |
| 11.3 Slab Pull | 148 |
| 11.4 Collisional Forces | 149 |
| 11.5 Basal Shear Traction | 151 |
| 11.6 Trench Suction | 151 |
| 11.7 What drives plate tectonics? | 151 |
| 12 Multibeam Bathymetry and side-scan | 158 |
| 12.1 Introduction | 158 |
| 12.2 Data Acquisition and the Physics of Multibeam Technology | 161 |
| 12.3 Image Enhancement Techniques | 163 |
| 13 The Magnetic Field | 165 |
| 13.1 Introduction | 165 |
| 13.2 Mapping the oceanic magnetic field | 165 |
| 13.3 Character of the magnetic field | 167 |
| 13.4 Geomagnetic field reversals | 169 |
| 13.5 Magnetic potential | 170 |
| 13.6 Magnetization of oceanic crust | 172 |
| 13.7 Forward modeling magnetic anomalies | 176 |
| 13.8 Interpreting observed oceanic magnetic anomalies | 189 |
| 13.9 Magnetic Maps - from data acquisition to interpretation | 190 |
| 14 The Gravity Field | 199 |
| 14.1 Overview | 199 |
| 14.2 Gravitational potential and acceleration | 200 |
| 14.3 The Earth's gravity field | 201 |
| 14.4 Relative gravity measurements | 209 |
| 14.5 Gravity anomaly reductions | 216 |
| 14.6 Gravity Modelling | 220 |
| 14.7 References | 235 |
| 15 Electrical and electromagnetic methods | 238 |
| 15.1 Electrical (resistivity) surveys | 239 |
| 15.2 The magnetotelluric method (MT) | 245 |
| 15.3 Self potential surveys | 245 |
| 15.4 Induced polarization surveys (IP) | 247 |
| 15.5 Electromagnetic Surveys | 249 |
| 15.6 Radar and the radio imaging method | 259 |
| 16 Radiometric Methods | 263 |
| 17 Seismic Reflection Method | 269 |

| | |
|---|------------|
| 17.1 Introduction | 269 |
| 17.2 Acquisition of marine seismic reflection data | 269 |
| 17.3 The reflection method | 272 |
| 17.4 Seismic data processing | 283 |
| 17.5 Wide-angle marine seismic data | 311 |
| 18 Seismic Refraction Method | 314 |
| 18.1 Seismic acquisition | 314 |
| 18.2 Shallow seismic refraction surveying | 316 |
| 18.3 Travel time curves | 317 |
| 18.4 Simple depth calculation | 318 |
| 18.5 Dipping layers | 321 |
| 18.6 Practical exercise: The reciprocal method | 322 |
| 19 Quantitative seismic interpretation | 323 |
| 19.1 Seismic Sections | 323 |
| 19.2 Synthetic Seismograms | 328 |
| 19.3 Synthetic Seismogram Construction | 328 |
| 19.4 Link between Lithology and Seismic Section | 329 |
| 19.5 Geology and Seismic Sections | 330 |
| 19.6 Recognising Lithology | 336 |
| 19.7 Reflections Associated with Hydrocarbon and Diagenetic Effects | 340 |
| 20 Borehole logging | 343 |
| 20.1 Introduction | 343 |
| 20.2 Radiometric tools | 347 |
| 20.3 Acoustic and optical scanners | 352 |
| 20.4 Self potential logging | 353 |
| 20.5 Logging methods for hard rock/mineral targets | 354 |
| 21 Sedimentary Basins and margins | 357 |
| 21.1 Introduction | 357 |
| 21.2 Extensional Basins | 360 |
| 21.3 References | 377 |
| 21.4 Flexural basins | 381 |
| 21.5 Inversion and basin uplift | 383 |
| 21.6 References | 385 |
| 21.7 Extensional basin modelling | 387 |
| A MATLAB manual | 404 |
| A.1 Introduction: What is MATLAB TM ? | 404 |
| A.2 Getting started | 404 |
| A.3 Getting help | 405 |
| A.4 Introductory tutorials | 405 |

| | |
|---|------------|
| A.5 Colons and brackets | 408 |
| A.6 Command line tricks | 410 |
| A.7 M-FILES | 410 |
| A.8 Conditionals and Loops | 410 |
| A.9 Plotting/Graphs | 412 |
| A.10 Formats, Saving and Loading files | 417 |
| A.11 Debugging | 419 |
| B SI Units and other useful tables | 420 |
| B.1 Basic Units for the SI System as Used in Geophysics | 420 |
| B.2 Greek alphabet | 420 |
| Bibliography | 422 |
| Index | 440 |

List of Figures

| | | |
|------|--|----|
| 3.1 | (a) P-Wave motion and (b) S-Wave motion (tranverse-wave motion). In both figures the wave travels from left to right. | 13 |
| 3.2 | Schematic depiction of wavefronts | 14 |
| 3.3 | Reflection and refraction of a seismic wave at a boundary between two layers with different material properties. | 15 |
| 3.4 | Seismic refraction | 16 |
| 3.5 | Scattering of a body wave at a non-planar boundary | 16 |
| 3.6 | Mode conversion of seismic waves at layer bondaries | 18 |
| 3.7 | Two types of surface waves | 19 |
| 4.1 | Earth's layering | 20 |
| 4.2 | Estimation of the size of the Earth's core | 21 |
| 4.3 | P- and S-wave paths through the Earth originating from the 1995 Kobe earthquake | 22 |
| 4.4 | 3D view of the Earth's interior | 23 |
| 4.5 | Continental crustal thickness (km), compiled by W. Mooney | 24 |
| 4.6 | This is an idealized section of oceanic crust reconstructed from observations of an ophiolite. A thin layer of sediment overlies pillow basalts and a thick pile of gabbro sills. Both the lavas and the sills are intruded by gabbro dikes. | 25 |
| 4.7 | Seismic Discontinuities | 26 |
| 4.8 | Regional variations in shear wave velocity at D'' | 28 |
| 4.9 | Cartoon of D'' region | 29 |
| 4.10 | The Preliminary Reference Earth Model (PREM) from Montagner and Anderson (1989). V_p = P-wave velocity. V_s = S-wave velocity. ρ = density . . . | 30 |
| 4.11 | Global distribution of rising plumes in the mantle, imaged by mantle tomography | 31 |
| 4.12 | Possible locations of mantle reservoirs and relationship to mantle dynamics | 32 |
| 4.13 | Effects of pressure and water on melting | 34 |
| 4.14 | Seismic shear velocity anomalies at three mantle depths | 35 |

| | |
|--|----|
| 4.15 Phase change from a Spinel-Perovskite structure above to Magnesiowustite | 36 |
| 4.16 Top-down tectonics? | 38 |
| 4.17 Comparison of 4 different seismic tomographic models by (Wen and Anderson (1995)) | 39 |
| 4.18 Clustering of hotspots relative to geoid highs | 41 |
| 4.19 Spherical harmonic expansion of topography of hotspot swells | 42 |
| 4.20 Top: Geoid (highs are red). Bottom: core-mantle boundary topography (400m contours). | 43 |
| 4.21 Observed characteristics of the Southeast Indian Ocean | 45 |
| 4.22 Reconstruction of Gondwanaland at 130 Ma | 46 |
| 4.23 Initial condition for a mantle convection model constrained by imposed plate motions through time | 47 |
| 4.24 Plate velocities and predicted dynamic topography for AUS-ANT | 48 |
| 4.25 Vertical cross sections of temperature for convection model | 49 |
| 4.26 Comparison of observed and predicted structures of the ocean south of Australia | 50 |
| 4.27 Eustatic (global) sea level vs Australian inundation | 51 |
| 4.28 Paleogeographic reconstructions of Australia during the Cretaceous | 52 |
| 4.29 Constant Viscosity Convection (above) with normalised geotherms (right) and surface velocity (top). Colour is temperature, red is hot. | 53 |
| 4.30 Stagnant Lid Convection with geotherms (right) and surface velocity (above). | 54 |
| 4.31 Mobile Lid Convection with geotherms (left) and surface velocities (above). Colour scale is temperature, red is hot; white represents strain. | 55 |
| 5.1 A wave based on a sine function | 57 |
| 5.2 Convolution of two time series | 61 |
| 5.3 Temperature distribution of the iron ring | 63 |
| 5.4 Spectral decomposition of a signal into sinusoids | 64 |
| 5.5 Some caption | 67 |
| 5.6 caption | 67 |
| 5.7 caption | 68 |
| 5.8 Sinusoids, Amplitude, and phase spectra | 69 |
| 5.9 Calculating cross correlation | 70 |
| 5.10 Frequency filtering of a signal. | 72 |
| 5.11 (a) First filtering result. (b) high pass filter | 73 |
| 5.12 Image f-k domain filtered | 74 |
| 5.13 F-k domain, now filtered | 75 |
| 5.14 Final result | 75 |
| 6.1 Oceanic lithospheric cross-section | 77 |
| 6.2 Definitions of boundaries within the oceanic lithosphere | 78 |

| | | |
|------|---|-----|
| 6.3 | Depth of isotherms of the oceanic thermal boundary layer as a function of oceanic crustal age, the depth of the seismic LID, the effective elastic plate thickness (open circles) and the depths of Earthquakes modified from Anderson (1995). | 79 |
| 6.4 | Global distribution of continental cratons, and their approximate thickness | 80 |
| 6.5 | Continental lithospheric sections showing relative abundances of different rock types in depth slices through continental lithosphere (Griffin et al., 1999). | 81 |
| 6.6 | Main tectonic plates | 82 |
| 6.7 | Rheology of young (rift) versus old (shield) tectonic plates. Young and old refers to the most recent “thermal event” in this case. Dot marks lower boundary of plate | 83 |
| 6.8 | Schematic cross-section of a subduction zone | 83 |
| 6.9 | Global plate boundaries, including broad, diffuse boundaries, and present day plate motion vectors | 85 |
| 7.1 | Oceanic and Continental Rheological Profiles (from Molnar, 1988). | 90 |
| 7.2 | Typical Stress Profiles for Stagnant Lid Convection. | 91 |
| 7.3 | Stagnant lid profiles against depth-dependant yield stress. | 92 |
| 7.4 | Typical Stress Profiles for placeMobile Lid Convection. | 93 |
| 8.1 | The probe needs 5-10 minutes to approach steady state after decay of frictional heating. The typical temperature difference over a 10 m depth interval is 0.5 deg. C. The accuracy of the measurement is about 1%, i.e. 0.005 C. | 96 |
| 8.2 | Example of screen print of 16-sensor heat flow probe output. | 97 |
| 8.3 | Distribution of measured heat flow values for Gulf of Mexico stations | 98 |
| 8.4 | Australian heat flow | 100 |
| 9.1 | Heat energy from the ground. Steam in rock fractures flows up a well to a power plant where it spins turbines, generating electricity without polluting the atmosphere. After use, waste water and any remaining steam are pumped back underground again. | 103 |
| 9.2 | Geothermal gradient | 104 |
| 9.3 | Radioactivity and time | 105 |
| 9.4 | default | 107 |
| 9.5 | Kelvin’s estimate of the solid earth’s age | 114 |
| 9.6 | Diamond Press | 117 |
| 9.7 | Isoviscous, bottom heated convection | 138 |
| 9.8 | Temperature fields (red-blue) for bottom heated isoviscous convection with a chemically distinct continent | 139 |
| 9.9 | Weak, deformable continent (low viscosity) being entrained into the convecting mantle despite its chemical buoyancy with respect to the mantle material. | 140 |
| 9.10 | Convective flow pattern with geotherms for continental extents | 140 |

| | |
|--|-----|
| 9.11 Depth-Age plot | 141 |
| 9.12 Here there is a clear deviation of the modal depths older than 80 Ma from the simple model (dashed line) as well, but for younger ages the fit is quite good. | 141 |
| 9.13 Isostatic compensation in the oceanic lithosphere | 142 |
| 9.14 3-D plot of temperature/depth with time for cooling oceanic lithosphere . . | 142 |
| 9.15 default | 143 |
| 10.1 default | 144 |
| 10.2 $\rho_m \cdot b = \rho_c \cdot (b + h)$ | 145 |
| 10.3 $\rho_1 \cdot H = \rho_2 \cdot (H + h)$ | 145 |
| 10.4 Isostasy: The average density of all crustal columns above a depth of compensation is the same. | 146 |
| 11.1 Trench length as a percentage of plate circumference | 150 |
| 11.2 Indo-Australian/Australian plate with plate boundary forces applied to contemporary (a), Miocene (b) and Eocene (c) plate configuration, with rheological provinces in Australia outlined in gray, projected onto a Lambert equal area map with its origin at 135°E, 20°S and standard parallels at 0° and 40°S. Oceanic (palaeo-) age is shown in color, and used to compute ridge push force. HYM = Himalayas (fixed boundary); SUM = Sumatra Trench; JAVA = Java Trench; BA = Banda Arc; PNG = Papua New Guinea; SOL = Solomon Trench; NH = New Hebrides; CT = Continental Topographic Force; TS = Tasman Sea; NZ = New Zealand; NZS = Southern New Zealand Alps; AAD = Australia Antarctic Discordance; SW-MOR & SE-MOR = South-West and South-East Mid Ocean Ridges respectively. Force arrows are not drawn to scale. | 153 |
| 11.3 Digital model of Australian geology, distinguishing cratons, fold belts, and basins in terms of their relative differences in mechanical stiffness. | 154 |
| 11.4 Modeled SHmax orientations with realistic material properties for the Australian continental and continental shelf | 155 |
| 11.5 Predicted maximum horizontal compressive paleo-stress regime of the Australian continent and continental margin for the early Miocene | 156 |
| 11.6 Predicted maximum horizontal compressive paleo-stress regime of the Australian continent and continental margin for the Eocene | 157 |
| 12.1 Multibeam bathymetry surveying | 159 |
| 12.2 Sinc function defining the distant wavefield of a echosounder beam | 160 |
| 12.3 Theoretical beam pattern for Sea Beam system (from de Moustier, 1988) . . | 160 |
| 12.4 Relationship between incidence angle, backscatter strength and seafloor character | 163 |
| 12.5 Backscatter affects | 164 |
| 13.1 Sources of anomalies in the crustal magnetic field (from Gernigon, 2007). . . | 166 |

| | |
|---|-----|
| 13.2 Proton precession and the spinning top analogy | 167 |
| 13.3 The Earth's dipole field | 168 |
| 13.4 The magnetic field vector | 169 |
| 13.5 Magnetic field inclination | 170 |
| 13.6 Magnetic inclination as a function of latitude | 171 |
| 13.7 A small section of the magnetic polarity timescale | 171 |
| 13.8 Global variation in the intensity and direction of the Earth's magnetic field . | 173 |
| 13.9 Total magnetic intensity | 174 |
| 13.10 Magnetization of oceanic crust | 174 |
| 13.11 Magnetic polarity reversals in oceanic crust | 175 |
| 13.12 Edge effects due to adjacent magnetic polarity reversal boundaries | 177 |
| 13.13 Galapagos Islands | 178 |
| 13.14 Bathymetric map of a guyot (flat-topped drowned seamount) | 178 |
| 13.15 Magnetization of seamounts | 179 |
| 13.16 Magnetization of seamounts, part 2 | 180 |
| 13.17 Cross-section through a thin tabular body, analogous to a magnetized stripe in ocean crust | 181 |
| 13.18 Magnetic field components | 181 |
| 13.19 The Earth Filter | 182 |
| 13.20 Relationship between profile direction and magnetic anomaly phase | 184 |
| 13.21 Relationship between profile direction and magnetic anomaly phase, part 2 . | 184 |
| 13.22 Relationship between profile direction and magnetic anomaly phase, part 3 . | 185 |
| 13.23 Position vectors and magnetization directions | 187 |
| 13.24 Cross product vectors | 188 |
| 13.25 Upward continuation of the magnetic field from the seafloor (0 m) to 1.5 km and 2.5 km above the seabed | 190 |
| 13.26 Observed and ship profiles across the Tasman Sea | 191 |
| 13.27 Total Magnetic Intensity Anomaly Map for Australia (source: Geoscience Australia) | 192 |
| 13.28 Synthetic anomalies are shown for different simple source geometries | 195 |
| 13.29 Magnetic data from Namibia, illustrating derivative maps and RTP for map data. (source: Salem et al. (2007)) | 196 |
| 13.30 Map showing depth to basement for a sedimentary basin in Tanzania based on seismic and well data (source: Salem et al. (2008)) | 197 |
| 13.31 Magnetic data over sedimentary basins in Tanzania | 198 |
| 14.1 gravitational acceleration | 201 |
| 14.2 Polar coordinates | 202 |
| 14.3 The spheroidal shape of the Earth | 203 |
| 14.4 Relationship between geocentric and geographic latitude | 204 |
| 14.5 The Geoid across North America | 205 |
| 14.6 How underwater masses affect the geoid (and therefore the observed sea surface) | 206 |

| | |
|---|-----|
| 14.7 Legendre polynomials | 208 |
| 14.8 Zonal, sectorial and tesseral harmonics | 209 |
| 14.9 Resolution of gravity data acquired from different acquisition methods, and the improvement over time | 210 |
| 14.10 Example of profile observations from a marine gravity survey | 212 |
| 14.11 Satellite altimetry measures the height of the sea surface, from which we can derive estimates of the geoid and gravity field | 214 |
| 14.12 Satellite track across the Tasman Sea | 215 |
| 14.13 Sea surface height, regional and residual geoid for satellite track across the Tasman Sea | 216 |
| 14.14 Free-air gravity anomalies of the Australian Plate | 217 |
| 14.15 Understanding the Bouguer slab formula - part 1 | 218 |
| 14.16 Understanding the Bouguer slab formula - part 2 | 218 |
| 14.17 Gravity anomaly due to a sphere | 220 |
| 14.18 Nonuniqueness of gravity anomalies - Gravity anomalies due to different density distributions cause an observed anomaly with the same shape | 221 |
| 14.19 Gravity field of a periodic mass distribution | 222 |
| 14.20 Gravity field measured over a topographic surface | 223 |
| 14.21 Isostatic compensation of surface loads | 224 |
| 14.22 The Airy model of isostatic compensation | 224 |
| 14.23 The Pratt model of isostatic compensation | 225 |
| 14.24 Isostasy: The average density of all crustal columns above a depth of com- pensation is the same. | 225 |
| 14.25 Isostasy: a simple two layer case | 226 |
| 14.26 Gravity anomalies associated with seamounts | 227 |
| 14.27 Gravity-topography transfer function (admittance) from Smith and Sandwell (1994) | 228 |
| 14.28 Admittance curves for different ratios of Moho load to surface load | 231 |
| 14.29 Admittance curve for the USA | 232 |
| 14.30 Basis of the coherence technique | 233 |
| 14.31 Coherence between gravity and topography for different values of elastic thickness | 234 |
| 14.32 Elastic Plate thickness of Australia from coherence | 234 |
| 14.33 Geological map of Australia. Note broad correlation of geological provinces with coherence results (previous figure). Rheologically strong areas corre- spond to Archean cratons, and weak areas to sedimentary basins. | 237 |
| 15.1 Resistivity Surveying | 240 |
| 15.2 Design of electrodes used for resistivity surveys | 240 |
| 15.3 Potential at two electrodes | 241 |
| 15.4 Electrode configuration in a Wenner array | 241 |
| 15.5 Resistivity Profile from a Wenner array | 242 |
| 15.6 Electrode configuration for a Schlumberger array | 242 |

| | |
|---|-----|
| 15.7 Resistivity sounding from a Schlumberger array | 243 |
| 15.8 Electrode configuration for a dipole-dipole array | 243 |
| 15.9 Methodology for generating a resistivity pseudo-section from a dipole-dipole array | 244 |
| 15.10 Example resistivity pseudo-section from a dipole-dipole array | 244 |
| 15.11 Example of geological section showing shape and resistivities of subsurface layering inferred from a resistivity survey. | 244 |
| 15.12 The magnetotelluric method | 245 |
| 15.13 SP survey locating a buried pipe | 246 |
| 15.14 SP results locating a change in groundwater flow due to the presence of an impermeable crushed zone | 246 |
| 15.15 Generation of self potential over a conductive mineral deposit. | 247 |
| 15.16 Induced polarization surveying - build-up of charge at the boundaries of electrical conductors | 248 |
| 15.17 Induced polarization surveying - potential difference after applied current is turned off | 248 |
| 15.18 Apparent resistivity and chargeability sections from an IP survey | 249 |
| 15.19 Electromagnetic surveying - relationship between transmitter coils, receiver coils and subsurface targets | 250 |
| 15.20 VLF surveying | 252 |
| 15.21 Conductivity surveying | 252 |
| 15.22 A Conductivity Map derived using a Geonics EM31 | 253 |
| 15.23 TDEM measurement principles, part 1 | 254 |
| 15.24 TDEM measurement principles, part 2 | 254 |
| 15.25 TDEM measurement principles - how stacking reduces noise | 255 |
| 15.26 TDEM measurement principles - decay curves from good conductors decay more slowly than those from poor conductors | 256 |
| 15.27 TDEM ground surveys | 257 |
| 15.28 Computer modelling of TDEM data | 257 |
| 15.29 A thick, conductive weathered layer can prevent data being obtained from a deeper metallic ore body | 258 |
| 15.30 TDEM sounding | 259 |
| 15.31 An example of TDEM results from a borehole | 260 |
| 15.32 Left. Source to receiver raypaths for a cross borehole RIM tomographic survey. Right. tomographic result highlighting areas of strong wave attenuation which coincide with mineralized zones. | 261 |
| 15.33 Electrical properties of different rocks and other materials in the subsurface | 262 |
| 15.34 An example GPR result | 262 |
| 16.1 The range of frequencies over which gamma radiation is emitted | 264 |
| 16.2 Multi Channel Gamma Ray Spectrum | 265 |
| 16.3 Example of processing to strip out the spectra for the different decay series | 266 |
| 16.4 Example radiometric survey data | 267 |

| | |
|--|-----|
| 16.5 Aerial Photograph | 268 |
| 16.6 Radiometric results (false colour image) | 268 |
| 17.1 Schematic drawing of a marine seismic acquisition. | 270 |
| 17.2 Tail buoys ready to be deployed for a marine seismic reflection survey. | 271 |
| 17.3 Bird (red) and pinger (green) attached to a streamer. | 271 |
| 17.4 Snell's Law. | 272 |
| 17.5 Travel-Time Curves. | 273 |
| 17.6 Reflection of spherical wave from a point source from a plane interface (from <i>Fowler, 1990</i>). | 274 |
| 17.7 A typical layout of marine multichannel acquisition system. From <i>McQuillin, Bacon, and Barclay, 1984</i> | 275 |
| 17.8 Bottom-simulating reflectors (BSRs) | 276 |
| 17.9 Common mid-point concepts | 277 |
| 17.10 Seismic acquisition vessel | 278 |
| 17.11 Far field wave shapes generated by marine seismic sources | 279 |
| 17.12 Air and Water guns | 281 |
| 17.13 Pre-processing steps for seismic reflection data using data from an offshore survey | 285 |
| 17.14 Schematic depiction of the recording geometry | 286 |
| 17.15 CMP gathers | 287 |
| 17.16 Velocity analysis of CDP gathers | 288 |
| 17.17 Normal moveout correction (NMO) | 289 |
| 17.18 CMP gathers after muting of stretched zones | 290 |
| 17.19 NMO-corrected CMP gathers from a land seismic line (a) before and (b) after residual statics corrections. Note that the distorted events (CMP 191, 216) have nearly been flattened. | 291 |
| 17.20 CMP stack. A time-variant filter (TVF) applied, followed by an rms gain correction. | 292 |
| 17.21 Migration effects | 293 |
| 17.22 The concept of migration. | 293 |
| 17.23 Focussing or defocussing effects after migration. Synclines appear narrower (b) than their true form (a) after frequency migration. | 295 |
| 17.24 Seismic reflection paths over a syncline. | 296 |
| 17.25 Bow tie effect | 296 |
| 17.26 (a) unmigrated version of a seismic line, two dipping reflections between 1.8 and 2.1s, below B, could be interpreted to have been overthrust by the flatter overlying reflections to the right. (b) cleaned up section after migration techniques had been applied. | 297 |
| 17.27 Migrated CMP stack | 297 |
| 17.28 Set of multiples within a seismic section | 299 |
| 17.29 Simple multiples | 300 |
| 17.30 Schematic depiction of multiples in dipping layers. | 300 |

| | |
|---|-----|
| 17.31 Multiples | 301 |
| 17.32 Multiples in a seismically quiet zone. | 301 |
| 17.33 Ghosts | 302 |
| 17.34 Diffraction of seismic waves at abrupt interface changes. | 302 |
| 17.35 reflected refraction | 303 |
| 17.36 Velocity effects when collecting seismic reflection data along dip (a) and strike (b) direction | 303 |
| 17.37 Apparent thinning downdip of the structure | 304 |
| 17.38 Apparent thinning related to faults | 304 |
| 17.39 Imaging issues related to salt structures: (a) Seismic line across a salt struc- ture; (b) Velocity artefacts related to a salt dome (schematic). | 305 |
| 17.40 Velocity push-down beneath shale diapirs. The seismic velocity of shales is lower than the surrounding rocks. | 306 |
| 17.41 Seismic velocity anomalies related to imaging of carbonates. | 307 |
| 17.42 Velocity artefacts related to (a) seafloor relief and (b) velocity pull-up be- neath an infilled channel | 308 |
| 17.43 Velocity artefacts - Reflections to the west of the reefoid mass in figure (a) dip to the east and there is no structural closure.(b) shows the line after depth conversion. | 308 |
| 17.44 Seismic imaging and the effects of geological structures. (a) Imaging of faults depending on seismic line orientation relative to the fault; (b) Velocity arte- facts through poor line orientation close to a major fault. | 309 |
| 17.45 Deep seismic reflection transect Geoscience Australia 120/1 | 310 |
| 17.46 OBS seismic acquisition | 311 |
| 17.47 Schematic cross section of an ocean bottom seismometer (OBS). Here: Scripps Institution of Oceanography OBS. | 312 |
| 17.48 Seismic record section from oceanic crust. Vertical channel | 312 |
| 17.49 Seismic record section with picked 'P' arrivals | 313 |
| 18.1 A Vibroseis truck in action during a seismic acquisition campaign | 315 |
| 18.2 Vibroseis sweep signal. | 315 |
| 18.3 Simple survey layout with a source and 12 recording geophones. Seismic wave paths are schematised, $V_1 < V_2$ | 317 |
| 18.4 Time vs. distance (travel time) plot. | 318 |
| 18.5 Intercept time and cross over distance for a 3-layer case. | 319 |
| 18.6 Geometric setup for calculation of layer thickness using seismic arrival times. | 319 |
| 18.7 Seismic wave paths in dipping layers and reciprocal time. | 321 |
| 19.1 Seismic section intersecting a well penetrating a turbiditic gas and oil field, offshore West Africa | 325 |
| 19.2 Schematic depth trends of sand and shale impedances. | 327 |
| 19.3 Ricker wavelet at 60 Hz centred on the central peak of the watergun wavelet | 329 |
| 19.4 Relationship between velocity, density, reflection coefficient, and synthetic seismogram for an ocean drilling site (Site 1137) on the Kerguelen Plateau . | 330 |

| | |
|---|-----|
| 19.5 Correlation of seismic reflection data from the Queensland Plateau, collected in 1987 by AGSO on the R.V. Rig Seismic, using a water gun source with synthetic seismograms for ODP Site 812 on the Queensland Plateau off north-east Australia. | 331 |
| 19.6 Continuity of seismic reflectors | 332 |
| 19.7 Interval velocities, here given in the handy kFt/sec unit, for major sedimentary rocks | 333 |
| 19.8 Distribution of sediment grain sizes in relation to water currents (a) and expected sequence stratigraphy (b) | 333 |
| 19.9 Onlap and downlap | 334 |
| 19.10 Lithologic sequences and seismic imaging | 334 |
| 19.11 Several periods of clastic deposition and their sequence stratigraphic expression. | 334 |
| 19.12 Differential compaction in clay sequences | 335 |
| 19.13 Amplitude and thickness changes of localised shallow water depositional units below seismic resolution. | 335 |
| 19.14 Reflection configuration criteria for recognizing carbonate buildup on seismic profiles | 336 |
| 19.15 Carbonate environments and their spatial configuration | 337 |
| 19.16 Seismic imaging patterns of salt structures and related salt-tectonics. | 337 |
| 19.17 Volcanics and igneous rocks on seismic | 338 |
| 19.18 Sills on seismic | 338 |
| 19.19 Recent volcanics on seismic (top) and interpretation (below) | 339 |
| 19.20 Acoustic impedance of a hydrocarbon reservoir | 340 |
| 19.21 Bright and dim spots in seismic data and polarity effects | 341 |
| 19.22 Gas chimneys on seismic data | 342 |
| 20.1 Schematic description of geophysical wireline logging. From Desbrandes (1985; Fig 9.2) | 344 |
| 20.2 Trade Names of Main Logging Tools | 346 |
| 20.3 Gamma ray log tool | 347 |
| 20.4 Radiometric log data (neutron, density and natural gamma) through a sequence of sandstones, shales and coal | 349 |
| 20.5 Sonic log tool (a) and annotated sonic log (b) | 350 |
| 20.6 Resistivity logging (schematic) | 352 |
| 20.7 Caliper, temperature, focused resistivity, velocity and natural gamma logs for the previous example. | 353 |
| 20.8 Acoustic scanner data. Left - changes in acoustic impedance indicates changes in rock type. Right – dipping fractures and breakout evident in detailed section of scanner log. Diagonal banding is due to tool being off the centre of the borehole. | 354 |
| 20.9 Conductivity Logging | 355 |
| 20.10 Example of geophysical log results in sphalerite (Zn) ore from Century Mine | 356 |

| | |
|--|-----|
| 21.1 Global distribution of sediment thickness > 2km from Sclater and Célérier (1989) | 358 |
| 21.2 Dipping reflector sequences (below thick black lines) consisting primarily of basalt flows on (top) the Kerguelen oceanic plateau and (bottom) the Norwegian volcanic passive margin. the dipping wedge of Norway was sampled at Ocean Drilling Project site 642; no dipping reflectors were drilled on Kerguelen. Taken from Coffin and Eldholm (1994) | 359 |
| 21.3 Conceptual evolution of a magma-poor margin | 361 |
| 21.4 Basement subsidence averaged from seventeen wells on the US East Coast margin (Sleep, 1971). | 362 |
| 21.5 Pure shear (top) and simple shear (bottom) extension model | 363 |
| 21.6 Analogue crustal extension model (Brun and Beslier, 1996) | 364 |
| 21.7 Schematic representation of the lithospheric stretching model | 365 |
| 21.8 Relationship between vertical and horizontal strain rate described by a physical model for time-dependent stretching | 366 |
| 21.9 Water-loaded basement subsidence as a function of time for various values of the extension factor | 367 |
| 21.10 Lithospheric thinning and total subsidence may vary significantly across a sedimentary basin | 368 |
| 21.11 Profile of lithospheric thinning across a typical continental margin | 369 |
| 21.12 From ?: the elevation plotted as $\log 10[e^t]$ versus time for different extension factors β . The curves are almost straight lines when $\beta < 4$ for all times. | 370 |
| 21.13 Observed and computed subsidence for a well on the Nova Scotia continental margin off eastern Canada | 371 |
| 21.14 Extensional models | 373 |
| 21.15 Total subsidence S_t for five different time intervals of extension for $\beta = 4.0$ and $h_c = 35$ km (Sclater et al., 1986). The numbers on the curves indicate the time interval of extension in m.y. | 374 |
| 21.16 Domino model of upper crustal brittle faulting under extension | 375 |
| 21.17 Classical example: Viking Graben in the North Sea where Triassic and Jurassic sedimentary strata have been rotated between subparallel high-angle listric faults. | 376 |
| 21.18 So-called "listric" faults form due to formation of several generations of faults. Once the initial fault has rotated substantially it becomes easier to form a new fault than continue | 377 |
| 21.19 The isostatic balance requires the mass of the mantle displaced to be the same as the mass of the surface load. Alternatively, we can model the lithosphere as a viscoelastic sheet, behaving elastically on a short time scale, and viscously on a long time scale(from Beaumont, 1981). | 383 |
| 21.20 Eocene-early Miocene obduction of the Austro-Alpine and Penninic nappes onto the margin of the North European craton | 383 |
| 21.21 Profile of the foreland basin in northern Alps, Austria. Kuhn, 1998. | 384 |

| | |
|--|-----|
| 21.22Interpreted seismic section showing movement on the Pinnacle Fault, Cann- | 386 |
| ning Basin | |
| 21.23Inputs and outputs of basin models. | 398 |
| 21.24Decomposition of a sediment column by backstripping. | 399 |
| 21.25Compaction decay of the porosity | 399 |
| 21.26Porosity-depth curves for 8 typical lithologies | 400 |
| 21.27Porosities (bold curve) are too low after backstripping the top 500 m of a sedimentary sequence. The original porosities (finer curve) must be restored to the section. | 401 |
| 21.28 $\frac{\phi}{1-\phi}$ plotted versus the porosity of the decompactured section | 401 |
| 21.29Diagram showing the procedure for iteratively backstripping a fully com- pacted sedimentary column | 402 |
| 21.30Paleo-waterdepth determination from a well based on micropaleontology . | 402 |
| 21.31Different scenarios for the presence of a hiatus. | 403 |
| A.1 Matlab workflow for generating 2D graphs. | 414 |
| A.2 Matlab workflow for generating 3D graphs. | 415 |
| A.3 Some important graph features | 416 |

List of Tables

| | | |
|------|---|-----|
| 21.1 | Lithologies and decompaction parameters of eight typical lithologies found in sedimentary basins | 390 |
| B.1 | Common prefixes for use with SI units | 420 |
| B.2 | The Greek Alphabet | 421 |

Chapter 1

Introduction to Geophysics

What is geophysics? Literally, it is the science of the physics of the earth. The earth possesses physical properties and geophysics is concerned with the determination of those properties through measurement and observation. Global geophysics is concerned with the physics of the entire earth, the core, the mantle, the crust, the tectonic plates. Applied geophysics is concerned with practical problems such as exploration for minerals and petroleum and in other near-surface investigations. In essence there is a difference in the scale of the investigations in global and applied geophysics but it is the same types of measurements that are taken.

What are the types of measurements that geophysicists take? Their measurements are of:

- 1.) The earth's gravity field
- 2.) The earth's magnetic field
- 3.) The earth's heat flow
- 4.) The emissions due to radioactive decay
- 5.) Seismic waves
- 6.) Electromagnetic fields.

These measurements could all be seen as passive measurements meaning that they are being made of naturally occurring phenomena. Geophysicists can also excite the earth in various ways and measure the responses. These are the active geophysical measurements and they can include the responses due to:

- 1.) Generation of artificial seismic waves
- 2.) Generation of artificial electromagnetic waves, including the passage of electric currents

3.) Exposure to radiation.

To a lay person, geophysical methods are the methods for seeing into the earth. You didn't know it but Superman with his X-ray vision could be called a geophysicist. However, we intuitively know there is something wrong with this thought. We know that our mobile phones don't work in the underground railway. We know that gold prospecting is not just about walking across the ground surface with a metal detector. We also know that buried land mines are sadly very difficult to detect. These are examples of the limitations of geophysics. In air, radar can track the approach of an aircraft from kilometres away. In the ground, the penetration of radar waves is measured in tens of metres at best.

We can be philosophical about this and say that the earth does not readily give up her secrets. Geophysics is concerned with taking the signals and responses that the earth does provide us and trying to gain an insight into the structures and processes within the earth that have created those signals.

In this course, it is our intention to provide you with a basic knowledge of the principal geophysical methods, their applications and their limitations. We will cover aspects of both global and applied geophysics. You will learn of the physical basis of the methods and the properties of rocks that allow the methods to be applied. For all the methods you will learn some basic interpretation techniques. It is our hope that by the end of this course, your understanding of the principals of geophysics will be adequate for you understand geophysical results when presented to you. If you wish to be a geophysicist, further study will almost certainly be required.

Chapter 2

Petrophysics

Geophysical methods exploit the contrasts in the physical properties of earth materials. If the earth were homogeneous there would be no contrasts and the geophysical responses would be somewhat bland. A homogeneous earth would also not contain geological variability and there would be no mineral deposits. So the existence of contrasts in rock properties is fundamental to geology and geophysics. Petrophysics is the name given to the study of the physical properties of the materials that make up the earth. There are 7 main properties that we are interested in:

- 1.) Density
- 2.) Elasticity
- 3.) Magnetism
- 4.) Electrical properties
- 5.) Electromagnetism
- 6.) Radioactivity
- 7.) Thermal properties

2.1 Density

The density of a rock is a function of the densities of its constituent minerals, the porosity and the density of the fluids filling the pores. Measurements of total density can be made by measuring the weight of a rock and its volume. If there is no porosity, then the density can also be determined directly from a knowledge of the proportions and densities of the constituent minerals.

When there is porosity present (e.g. in sedimentary rocks), the density is given by:

$$\rho = \rho_{ma}(1 - \phi) + \rho_f\phi\rho = \rho_{ma}(1 - \phi) + \rho_f\phi$$

where:

ρ is the overall density

ρ_{ma} is the average density of the grains

ϕ is the porosity expressed as a fraction of the total volume

ρ_f is the density of the fluid filling the pores.

The density of rocks affects the earth's gravity field and forms the basis of the gravity method. Notice that in general, the densities of igneous and metamorphic rocks are greater than the densities of sedimentary rocks. Unconsolidated sediments have the lowest densities.

The main reason for these differences is that sedimentary rocks and unconsolidated sediments are porous.

The density of rocks also affects the speed at which seismic waves travel.

| Mineral | Range (g/cm ³) | Average (g/cm ³) | Mineral | Range (g/cm ³) | Average (g/cm ³) |
|--------------------------|-------------------------------|---------------------------------|-----------------------|-------------------------------|---------------------------------|
| Metallic minerals | | | | | |
| Oxides, carbonates | | | Non-metallic minerals | | |
| Bauxite | 2.3 – 2.55 | 2.45 | Petroleum | 0.6 – 0.9 | — |
| Limonite | 3.5 – 4.0 | 3.78 | Ice | 0.88 – 0.92 | — |
| Siderite | 3.7 – 3.9 | 3.83 | Sea Water | 1.01 – 1.05 | — |
| Rutile | 4.18 – 4.3 | 4.25 | Lignite | 1.1 – 1.25 | 1.19 |
| Manganite | 4.2 – 4.4 | 4.32 | Soft coal | 1.2 – 1.5 | 1.32 |
| Chromite | 4.3 – 4.6 | 4.36 | Anthracite | 1.34 – 1.8 | 1.50 |
| Ilmenite | 4.3 – 5.0 | 4.67 | Chalk | 1.53 – 2.6 | 2.01 |
| Pyrolusite | 4.7 – 5.0 | 4.82 | Graphite | 1.9 – 2.3 | 2.15 |
| Magnetite | 4.9 – 5.2 | 5.12 | Rock salt | 2.1 – 2.6 | 2.22 |
| Franklinite | 5.0 – 5.22 | 5.12 | Gypsum | 2.2 – 2.6 | 2.35 |
| Hematite | 4.9 – 5.3 | 5.18 | Kaolinite | 2.2 – 2.63 | 2.53 |
| Cuprite | 5.7 – 6.15 | 5.92 | Orthoclase | 2.5 – 2.6 | — |
| Cassiterite | 6.8 – 7.1 | 6.92 | Quartz | 2.5 – 2.7 | 2.65 |
| Wolframite | 7.1 – 7.5 | 7.32 | Calcite | 2.6 – 2.7 | — |
| Sulfides, arsenides | | | Anhydrite | 2.29 – 3.0 | 2.93 |
| Sphalerite | 3.5 – 4.0 | 3.75 | Biotite | 2.7 – 3.2 | 2.92 |
| Malachite | 3.9 – 4.03 | 4.0 | Magnesite | 2.9 – 3.12 | 3.03 |
| Chalcopyrite | 4.1 – 4.3 | 4.2 | Fluorite | 3.01 – 3.25 | 3.14 |
| Stannite | 4.3 – 4.52 | 4.4 | Barite | 4.3 – 4.7 | 4.47 |
| Stibnite | 4.5 – 4.6 | 4.6 | | | |
| Pyrrhotite | 4.5 – 4.8 | 4.65 | | | |
| Molybdenite | 4.4 – 4.8 | 4.7 | | | |
| Marcasite | 4.7 – 4.9 | 4.85 | | | |
| Pyrite | 4.9 – 5.2 | 5.0 | | | |
| Bornite | 4.9 – 5.4 | 5.1 | | | |
| Chalcocite | 5.5 – 5.8 | 5.65 | | | |
| Cobaltite | 5.8 – 6.3 | 6.1 | | | |
| Arsenopyrite | 5.9 – 6.2 | 6.1 | | | |
| Bismuthinite | 6.5 – 6.7 | 6.57 | | | |
| Galena | 7.4 – 7.6 | 7.5 | | | |
| Cinnabar | 8.0 – 8.2 | 8.1 | | | |

| Rock type | Range (g/cm ³) | Average (g/cm ³) |
|--------------------------|-------------------------------|---------------------------------|
| Sediments (wet) | | |
| Overburden | | 1.92 |
| Soil | 1.2 – 2.4 | 1.92 |
| Clay | 1.63 – 2.6 | 2.21 |
| Gravel | 1.7 – 2.4 | 2.0 |
| Sand | 1.7 – 2.3 | 2.0 |
| Sandstone | 1.61 – 2.76 | 2.35 |
| Shale | 1.77 – 3.2 | 2.40 |
| Limestone | 1.93 – 2.90 | 2.55 |
| Dolomite | 2.28 – 2.90 | 2.70 |
| Sedimentary rocks (av.) | | 2.50 |
| Igneous rocks | | |
| Rhyolite | 2.35 – 2.70 | 2.52 |
| Andesite | 2.4 – 2.8 | 2.61 |
| Granite | 2.50 – 2.81 | 2.64 |
| Granodiorite | 2.67 – 2.79 | 2.73 |
| Porphyry | 2.60 – 2.89 | 2.74 |
| Quartz diorite | 2.62 – 2.96 | 2.79 |
| Diorite | 2.72 – 2.99 | 2.85 |
| Lavas | 2.80 – 3.00 | 2.90 |
| Diabase | 2.50 – 3.20 | 2.91 |
| Basalt | 2.70 – 3.30 | 2.99 |
| Gabbro | 2.70 – 3.50 | 3.03 |
| Peridotite | 2.78 – 3.37 | 3.15 |
| Acid igneous | 2.30 – 3.11 | 2.61 |
| Basic igneous | 2.09 – 3.17 | 2.79 |
| Metamorphic rocks | | |
| Quartzite | 2.5 – 2.70 | 2.60 |
| Schists | 2.39 – 2.9 | 2.64 |
| Graywacke | 2.6 – 2.7 | 2.65 |
| Marble | 2.6 – 2.9 | 2.75 |
| Serpentine | 2.4 – 3.10 | 2.78 |
| Slate | 2.7 – 2.9 | 2.79 |
| Gneiss | 2.59 – 3.0 | 2.80 |
| Amphibolite | 2.90 – 3.04 | 2.96 |
| Ectogite | 3.2 – 3.54 | 3.37 |
| Metamorphic | 2.4 – 3.1 | 2.74 |

2.2 Elasticity

At low strains, rocks are elastic and it is possible for elastic waves to pass through them in the form of seismic waves. Strain is defined by the deformation per unit length that occurs when pressure (stress) is applied to a rock. The strains that are associated with seismic wave propagation are of the order of 10^{-6} . (i.e. deformations of 1 micron per metre). Elastic material are defined by properties such as:

1.) Youngs modulus, E = axial strain/axial stress, which is also called the stiffness

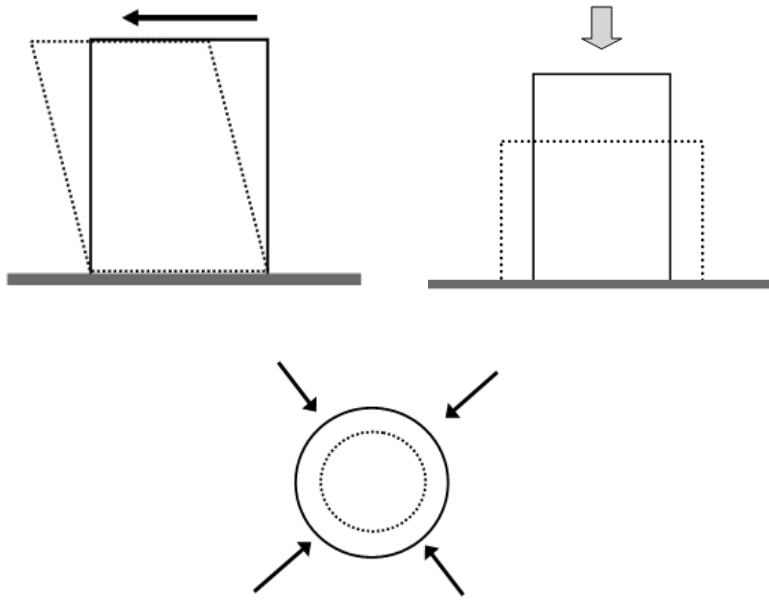
2.) Incompressibility or bulk modulus, K which is the resistance to compression:

$$K = \frac{\text{stress}_{vol}}{\text{strain}_{vol}}$$

3.) Shear modulus or rigidity, μ which is the resistance to shear:

$$\mu = \frac{\text{stress}_{shear}}{\text{strain}_{shear}}$$

- 4.) Poisson's ratio σ which is the ratio of lateral strain to axial strain when the applied stress is in the vertical direction.



In rock mechanics, the stresses required to deform rocks are in the MPa range and rock moduli are in the GPa range.

These properties of rocks can be established by laboratory measurements. Together with the density, they also define the speeds at which seismic waves propagate. Seismic surveying is one of the most important geophysical methods.

2.3 Magnetism

Local variations in the earth's magnetic field are observed mainly because of:

- 1.) variations in the magnetic susceptibility of rocks and
- 2.) the presence of remanent magnetisation present in certain minerals.

Magnetic susceptibility, κ , is a dimensionless quantity. Pyrrhotite (iron sulphide), ilmenite (FeTiO_3) and magnetite (Fe_3O_4) are the three minerals with exceptionally high susceptibilities. Maghemite, formed through the weathering of iron rich rocks has the same form as magnetite and also has high susceptibility. These four minerals may be present in many rock types but only as secondary minerals. They belong to a class of materials known as ferrimagnetic minerals.

In some minerals and rock types, the magnetic susceptibility is negative and the magnetic field is locally reduced.

In general terms, mafic rocks have higher susceptibility than silicic rocks (e.g. gabbros are more magnetic than granites), and igneous rocks tend to be more magnetic than sediments, but there is a very wide range of overlap. Direct measures of susceptibility are required to work within these huge ranges of variability.

Remanent magnetisation occurs when rocks containing ferrimagnetic minerals cool from a liquid melt and pass through the Currie temperature (approximately 580 degrees C). The minerals become permanently aligned in the direction of the earth's magnetic field at that time. If the rocks change their position (e.g. tectonic processes) or the earth's field changes, the rocks will still possess their remanent magnetisation and this will interact with the current magnetic field.

| Igneous | | | | |
|-----------------|-----------------------------------|------|-------|---------------|
| Lithology | Magnetic susc. X 10 ⁻⁵ | | | Remanence |
| | Average | Min. | Max | |
| Granite | 251 | 0 | 5027 | Weak |
| Rhyolite | - | 25 | 3770 | Weak - Strong |
| Dolerite | 1759 | 126 | 3770 | Weak |
| Augite-Syenite | - | 3393 | 4524 | Weak - Strong |
| Olivine-Diabase | 2513 | - | - | Weak |
| Diabase | 5655 | 101 | 16336 | Weak |
| Porphyry | 6283 | 25 | 20986 | Weak |
| Gabbro | 7540 | 101 | 9048 | Weak |
| Basalt | 7540 | 25 | 18221 | Weak - Strong |
| Diorite | 8797 | - | - | Weak |
| Pyroxenite | 13194 | - | - | Weak |
| Peridotite | 16336 | 9551 | 19604 | Weak |
| Andesite | 16964 | - | - | Weak - Strong |

2.4 Electrical properties

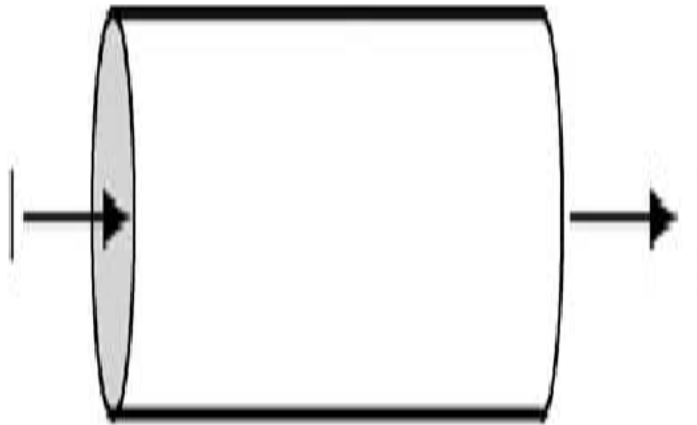
The electrical properties of a rock is given by its resistivity, ρ , or its inverse, its conductivity, σ . The SI unit of resistivity is the ohm metre (Ωm) and it is defined by the resistance, R, of a cylinder of material length, l, and cross sectional area, A.

$$\rho = \frac{RA}{l}$$

The resistivities of rocks minerals cover an enormous range of many orders of magnitudes. The metallic minerals and some clays are good conductors. Most other minerals are insulators. If rocks are porous and contain fluids, their resistivities are found to

| Minerals | | | | |
|------------------|---|-------------|------------|------------------|
| Lithology | Magnetic susc. X 10⁻⁵ | | | Remanence |
| | Average | Min. | Max | |
| Clays | 20 | 0 | 0 | Weak? |
| Chalcopyrite | 32 | 0 | 0 | Weak? |
| Sphalerite | 60 | 0 | 0 | Weak? |
| Siderite | 100 | 310 | 150 | Weak? |
| Pyrite | 130 | 4 | 420 | Weak? |
| Limonite | 220 | 0 | 0 | Weak? |
| Arsenopyrite | 240 | 0 | 0 | Weak? |
| Hematite | 550 | 40 | 3000 | Weak? |
| Chromite | 600 | 240 | 9400 | Weak? |
| Franklinite | 36000 | 0 | 0 | Weak? |
| Pyrrhotite | 125000 | 100 | 500000 | Strong |
| Ilmenite | 150000 | 25000 | 300000 | Strong |
| Magnetite | 500000 | 100000 | 1600000 | Weak - Strong |

| Lithology | Magnetic Susc. SI x 10⁻⁵ | | | Remanence |
|--------------------|--|------------|------------|------------------|
| | Average | Min | Max | |
| Sedimentary | | | | |
| Dolomite | 13 | 0 | 94 | Weak |
| Limestone | 31 | 3 | 352 | Weak |
| Sandstone | 38 | 0 | 2086 | Weak |
| Shale | 63 | 6 | 1860 | Weak |
| Metamorphic | | | | |
| Amphibolite | 75 | - | - | Weak |
| Schist | 151 | 31 | 302 | Weak |
| Phyllite | 163 | - | - | Weak |
| Gneiss | | 13 | 2513 | Weak |
| Quartzite | 440 | - | - | Weak |
| Serpentinite | 0 | 314 | 1759 | Weak |
| Slate | 628 | 0 | 3770 | Weak |



be largely a function of the porosity and the resistivity of the fluid. The electrical flow through the fluids will be electrolytic and involve dissolved ions present in the water

As a general rule, 'hard' rocks usually have greater resistivities than 'soft' rocks because of the differences in porosity.

Archies Law provides an empirical formula for calculating the resistivity of sedimentary rocks:

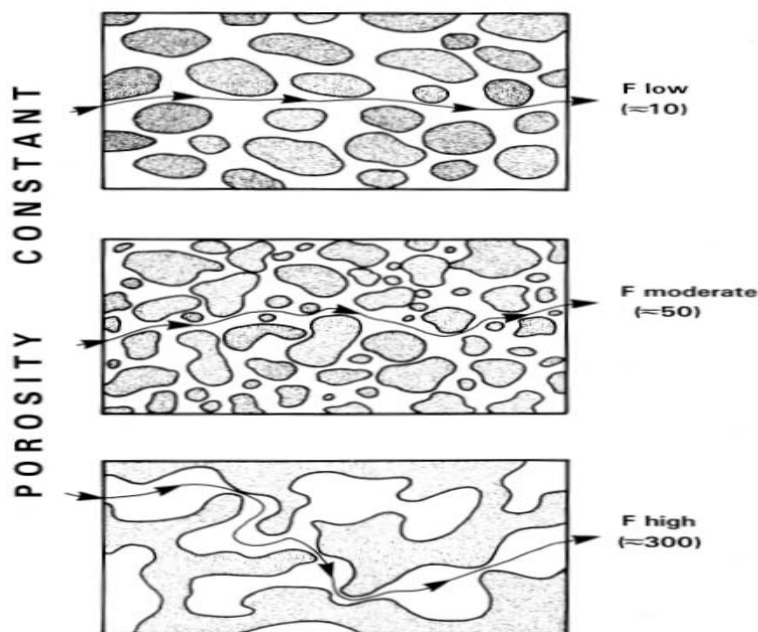
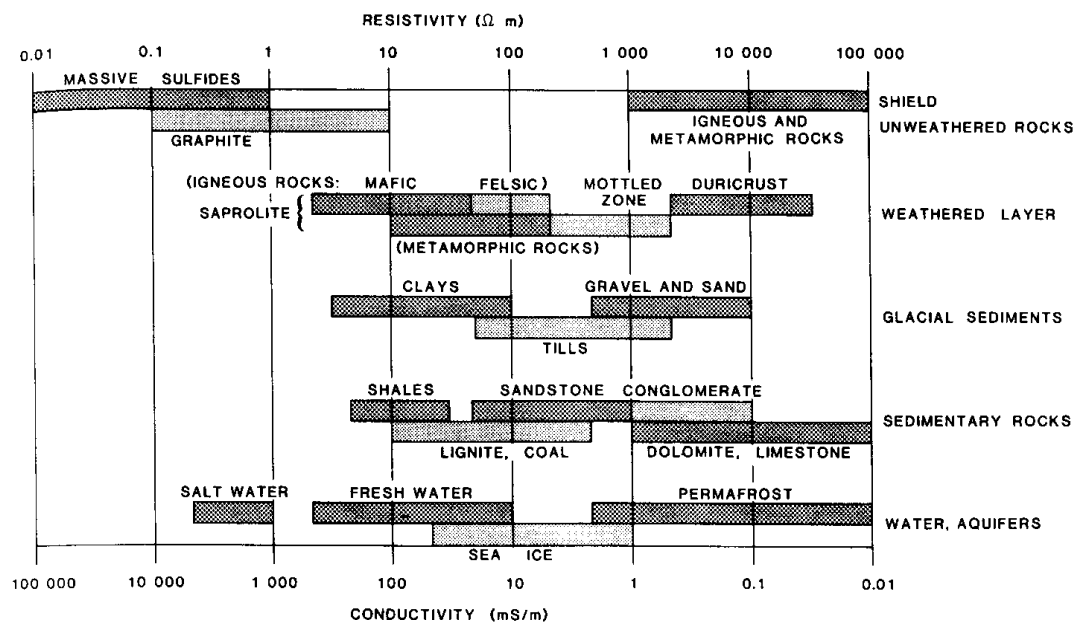
$$\rho = \rho_w a \phi^{-m}$$

Here, ρ_w is the resistivity of the pore water, a is the coefficient of saturation (the value in most sediments is between 0.6 and 1) and m is cementation factor. It has values of about 2 in well cemented formations and 1.5 or less in moderately to poorly cemented formations.

Another term used in describing the resistivities of porous rocks is the formation factor, F :

$$\rho = F \rho_w$$

The formation factor varies according to the tortuosity of the current flow through the pore spaces.



2.5 Electromagnetism

For most of the electromagnetic methods of geophysics, the ability of rocks to support an electrical current induced by a time varying magnetic field is of most concern. Rock resistivity is therefore of prime importance.

Geophysics also makes use of electromagnetic methods where waves propagate through the earth. As with all electromagnetic wave propagation, the propagation is affected by the dielectric properties of the medium, the conductivity and the magnetic permeability. For most cases, it can be assumed that rocks have little influence on magnetic permeability (except for magnetite, maghemite, ilmenite and pyrrhotite). The dielectric constant for most rocks is between 3 and 20. Water has a dielectric constant of 80 and is an exception because of the polar nature of water molecules.

2.6 Radioactivity

Radioactivity in rocks is due to the natural disintegration of atomic nuclei and the emission of:

- 1.) energy in the form of gamma radiation
- 2.) particles of mass in either the form of alpha particles (Helium nuclei) or beta particles (electrons).

There are about 50 natural and 800 artificial radioactive nuclei. The radioactive nuclei are mainly from four radiometric series – from neptunium (^{239}Np), Uranium (two series ^{238}U and ^{235}U) and Thorium (^{232}Th). The most significant series is from ^{238}U which has a half life of $4.51 \cdot 10^9$ years. In addition, there are other naturally occurring isotopes of these, ^{40}K which has a half life $4.5 \cdot 10^8$ years is the most important.

Radon (an inert gas) is a daughter product of the U and Th series and is soluble in water. Its presence can lead to environmental issues (cancers etc) when significant amounts of ^{238}U are present- e.g. with granitic bedrock.

2.7 Thermal properties

The source of the earth's temperature is:

- 1.) Cooling of original molten mass
- 2.) Heat generated by radioactive decay (especially in the continental crust due to the presence of granites)

The temperature gradient in the crust is typically $20 - 30\text{ C/km}$. The thermal conductivity, K , (units of W/mC) is a measure of how easily heat flows through rocks. Q is the heat conducted and is given by:

$$Q = A \times \frac{\Delta T}{L} \times K$$

Most rocks have low thermal conductivities, so the earth is cooling only slowly - approximately 0.2 C/million years. K is especially low in snow, soil/sand, coal ($K < 1$ W/mC)

Chapter 3

Seismic waves

In seismology, seismic energy travels in the form of waves. There are two types of body waves which travel through the earth medium and two types of surface waves. Purpose of this chapter is to introduce the general concepts of how seismic waves travel inside the Earth.

3.1 Seismic Body waves

Two types of body waves exist – P-waves (compressional waves; Fig. 3.1a) and S-waves (shear waves; Fig. 3.1b). The particle vibration for the P-waves is in the direction of the wave propagation. For the S-waves, the particle vibration is perpendicular to the direction of propagation. Sound waves are an example of P-waves. If no S-waves exist, the P-wave motion can be called an acoustic wave.

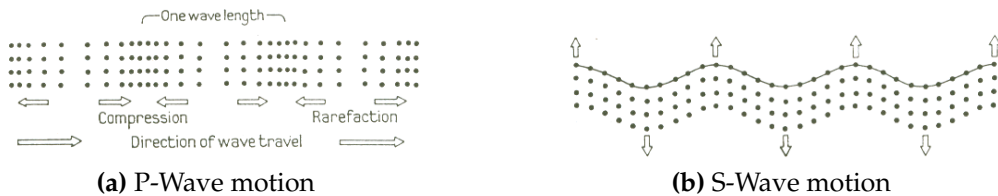


Figure 3.1: (a) P-Wave motion and (b) S-Wave motion (transverse-wave motion). In both figures the wave travels from left to right.

The velocities of P-waves (V_p) and S-waves (V_s) are given by the elastic constants for the material in question and its density.

$$V_p = \sqrt{\frac{K + 4/3\mu}{\rho}} \quad V_s = \sqrt{\frac{\mu}{\rho}}$$

It follows that the velocity of P-waves is greater than the velocity of S-waves. Note also that because the shear modulus in a liquid is zero, S-waves do not travel in liquids.

From a knowledge of V_p and V_s it is also possible to determine the elastic parameters. The equation for the determination of Poisson's ratio from V_p and V_s is as follows:

$$\sigma = \frac{0.5 - \left(\frac{V_s}{V_p}\right)^2}{1 - \left(\frac{V_s}{V_p}\right)^2}$$

3.1.1 Wavefronts and rays

Just as waves travel out from the point of impact when a stone is thrown in water, seismic body waves will spread out from the source of the energy. The drawing of wavefronts is a convenient way to convey the sense of the outwards propagation of the wave (Fig. 3.2).

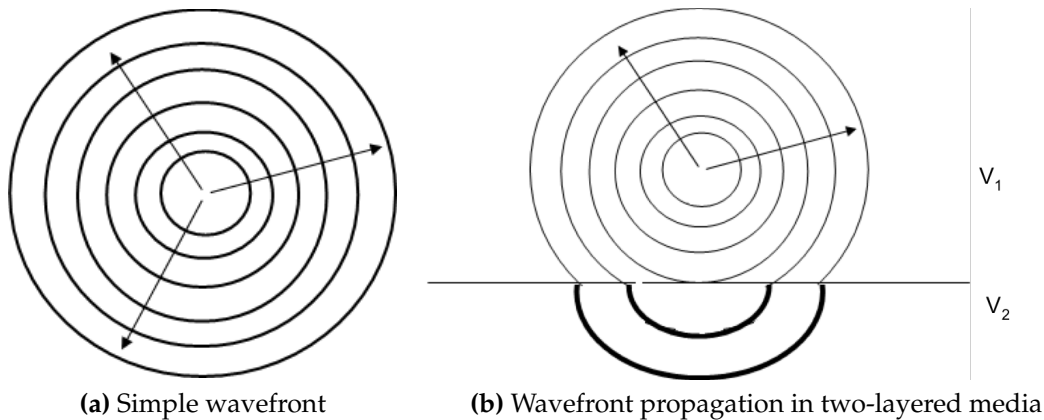


Figure 3.2: Schematic depiction of wavefronts. (a) The concentric cycles indicate where the wave has reached at any particular time. Lines drawn perpendicular to the wavefronts with an arrow indicating the direction of the motion are known as rays. The drawing of rays also provides a means of conveying where the seismic energy is travelling. (b) If two layers are present with the velocity V_2 in the lower layer being faster than in the upper layer, the wavefronts spread more rapidly in the lower layer.

3.1.2 Reflection, refraction and scattering

When a body wave meets a boundary, the incident wave is reflected back into the upper medium and refracted into the lower medium (Figure 3.3). The laws of physics state that the angle of incidence equals the angle of reflection, so the reflected ray leaves the interface at the same angle as the arriving incident ray.

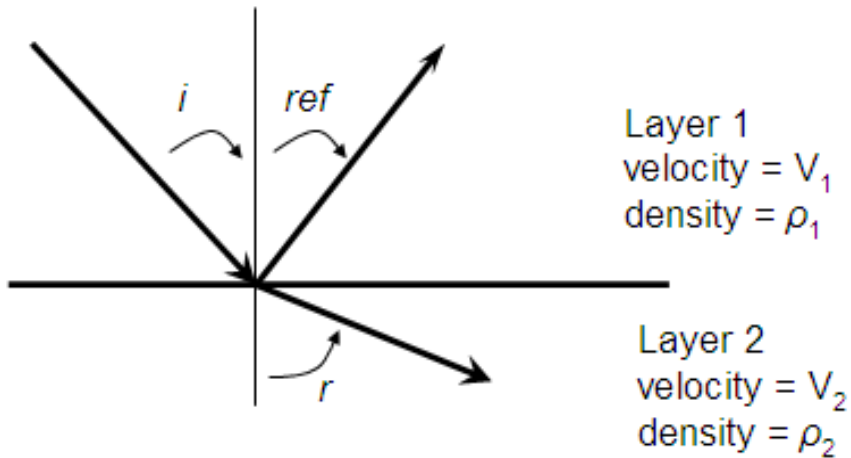


Figure 3.3: Reflection and refraction of a seismic wave at a boundary between two layers with different material properties.

In the case of normal incidence, the amplitude of the reflected wave (the reflection coefficient rc) is given by the equation:

$$rc = \frac{\rho_2 V_2 - \rho_1 V_1}{\rho_2 V_2 + \rho_1 V_1}$$

The equations defining the reflection coefficient for non-normal incidence are more complex and for most purposes the equation for normal incidence is adequate. Note that when the velocity and density contrasts are large, the reflected signal is strong. Strong reflections will limit the amount of energy available for transmission to deeper layers.

$$\frac{\sin i}{\sin r} = \frac{V_1}{V_2}$$

For the refraction of waves into the lower medium, the angle at which the refracted ray leaves is given by Snell's law. Provided V_2 is greater than V_1 , the refracted wave will always be "bent" towards the interface. A special case occurs when the angle of refraction is 90 degrees. In this case the refracted wave will travel along the interface between the two layers at the speed of the wave in the lower layer (Fig. 3.4). Energy will cross the boundary and depart at the appropriate angle of incidence. In this case, critical refraction is said to have occurred and the angle of incidence is given by:

$$\sin(i) = \frac{V_1}{V_2}$$

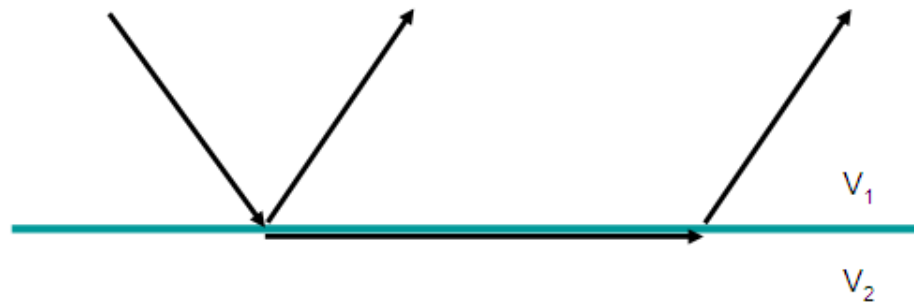


Figure 3.4: Refraction. A seismic wave encounters a boundary between two media with different seismic velocities V_1 and V_2 where $V_1 < V_2$. The refracted wave travels along the interface between the two layers at the speed of wave in the faster media.

Recall that $\sin(90) = 1$. When a body wave strikes a non planar boundary, scattering occurs (Fig. 3.5). Again we are familiar with this notion through observations of wave propagation in water. The concept is easily sketched by wavefronts and rays. Scattered energy can travel in all directions. In some ways, scattered energy can be viewed as if it came from a secondary source.

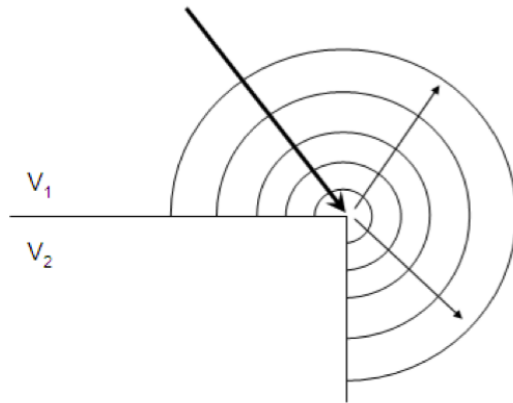


Figure 3.5: Scattering of a body wave at a non-planar boundary

3.1.3 Other aspects of body wave propagation

As suggested above, the generation of strong reflections is not necessarily desirable in exploration seismology because the energy is not available to travel to deeper levels representing the targets of the survey. Energy is also lost through a number of other mechanisms:

- Through geometrical spreading – the energy becomes distributed over broader and broader wavefronts. Given that the surface area of a sphere is proportional to the radius squared, the energy falls off in inverse proportion to the radius squared. (Because energy is proportional to the wave amplitude squared, the amplitude of the waves falls in inverse proportion to the radius.)
- Through absorption of energy by the ground. We should intuitively realise that seismic energy is ultimately absorbed by the earth (in the form of heat). If it did not, the earth would be a very noisy place. The energy loss is related to the frequency of the wave propagation. There is energy lost with each cycle of vibration, so the higher the frequency, the greater the energy loss. Signals with low frequency components travel further than those with high frequency components. This is why thunder sounds like crack (i.e. an impulse with a broad frequency range) when we are close by, but becomes a rumble (low frequencies only are present) when we are far away. Mathematically, the energy loss per cycle I is:

$$I = I_o e^{-\alpha r}$$

- Through mode conversions at the layer boundaries (Fig. 3.6). At each boundary, reflected P- and S-waves are formed, as are refracted P- and S-waves. If our seismic survey is looking at reflected P-wave behaviour, the strength of the P-waves is progressively lost through mode conversions.
- The strength of the wave energy and its amplitude is usually expressed in the decibel notation:

$$10 \log \frac{I}{I_0} \quad 20 \log \frac{A}{A_0}$$

where I_0 and A_0 are a chosen reference intensity and amplitude respectively.

- Wave propagation is also affected by the variability in the layers. A layer is said to be *homogeneous* if its elastic properties are equal everywhere and in all directions. A layer is *inhomogeneous* (heterogeneous) if it has unequal elastic properties but at any point they are constant with direction. A layer is *anisotropic* if its elastic properties at any point change with direction. Shales represent a good example of an anisotropic rock. P-wave velocities are faster in the direction of the bedding than in the direction across the bedding. The reason has to do with the direction of the particle vibration and it is interesting to note that the reverse is the situation for shear waves in shale.

3.1.4 Indicative body wave velocities

For P-waves:

- 1.) sound in air ≈ 330 m/s
- 2.) soils $\approx 330\text{-}1200$ m/s

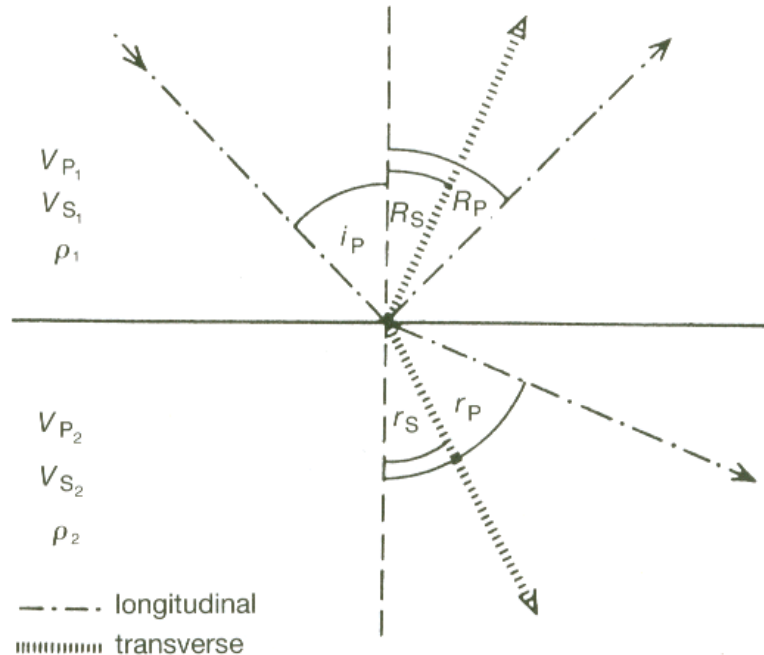


Figure 3.6: Mode conversion of seismic waves at layer boundaries

- 3.) sound in water ≈ 1500 m/s
- 4.) coal < 2500 m/s
- 5.) weathered rocks 1000-2500 m/s
- 6.) Sedimentary rocks, e.g. sandstones, shales: 2500–5000 m/s
- 7.) igneous rocks > 5000 m/s
- 8.) sulfides > 4000 m/s

For S-waves, the velocities will be less than the P-wave velocities. If the Poisson's ratio is 0.25, then the S-wave velocity will be less by a factor of $\sqrt{3}$.

3.2 Surface waves

Surface waves are a class of seismic waves that travel along the boundaries between layers. They are of nuisance value to seismic surveying and an annoying source of noise. In earthquake seismology they are extremely important because it is the surface waves travelling across the ground surface which cause the damage to buildings and other structures. Surface waves travel at velocities that are less than the shear wave

velocity in the faster of the two layers. The waves are said to be dispersive because they travel at different velocities, depending on their frequency. Fortunately this is a complication we do not have to deal with in exploration seismology using body waves. To a first approximation, body waves are non-dispersive. As shown in Fig. 3.7, there are two types of surface waves.

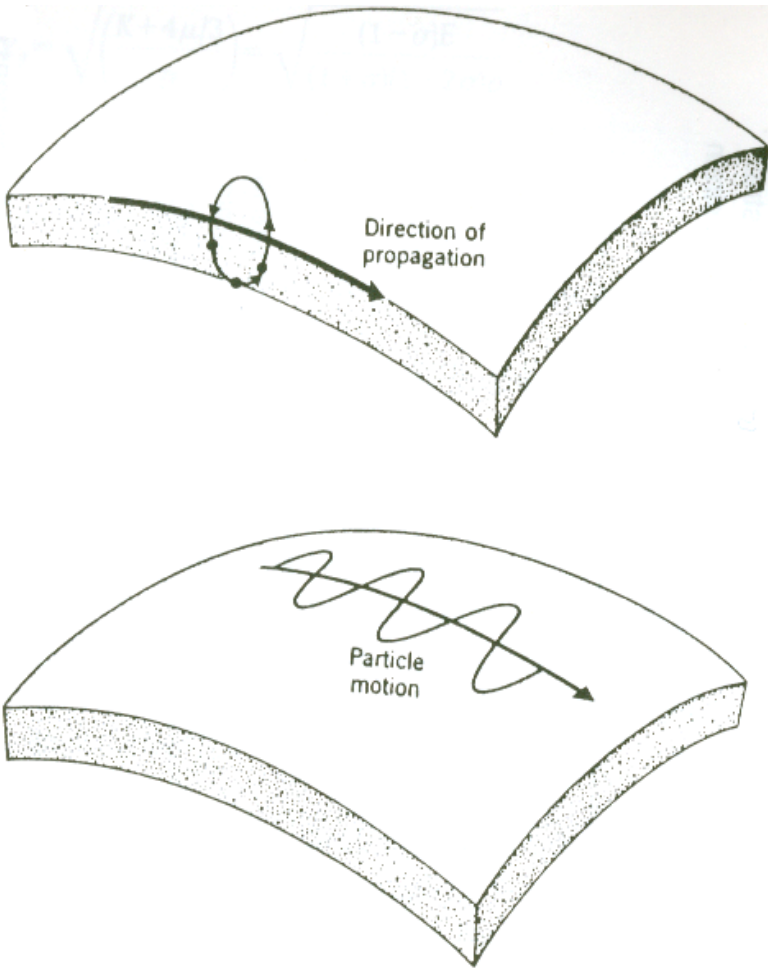


Figure 3.7: Two types of surface waves. The top image depicts a wave with its characteristic retrograde elliptical vibration which is called a Rayleigh wave. The second wave with its transverse particle motion is known as a Love wave.

Chapter 4

Global Geophysics

4.1 Introduction to the layering of the Earth

Compressional P waves will travel and refract through both fluid and solid materials. Shear S waves, however, cannot travel through fluids like air or water. Fluids cannot support the side-to-side particle motion that makes S waves.

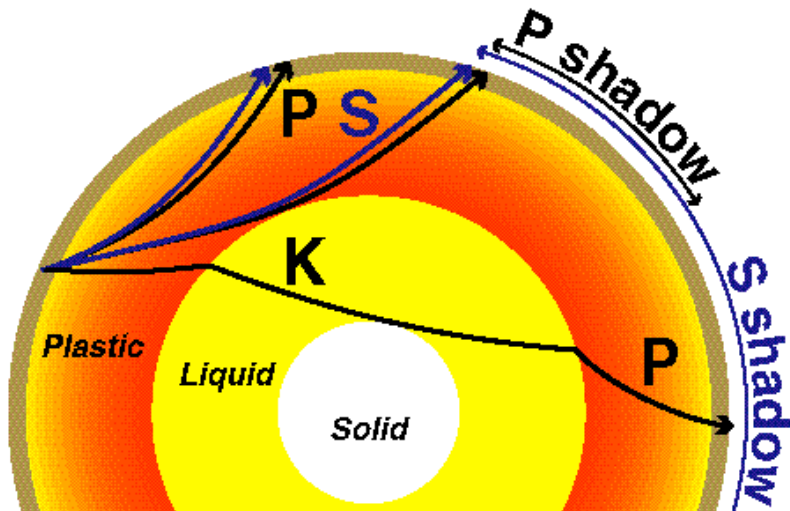


Figure 4.1: Earth's layering

Seismologists noticed that records from an earthquake made around the world changed radically once the event was more than a certain distance away, about 105 degrees in terms of the angle between the earthquake and the seismograph at the center of the earth. After 105 degrees the waves disappeared almost completely, at least until the slow surface waves would arrive from over the horizon. The area beyond 105 degrees distance forms a shadow zone. At larger distances, some P waves would arrive, but

still no S waves.

Conclusion: The Earth has to have a molten, fluid core to explain the lack of S waves in the shadow zone, and the bending of P waves.

You can get a rough estimate of the size of the Earth's core by simply assuming that the last S wave, before the shadow zone starts at 105 degrees, travels in a straight line. Knowing that the Earth has a radius of about 6350 km, you have a right triangle where the cosine of half of 105 degrees equals the radius of the core divided by the radius of the earth.

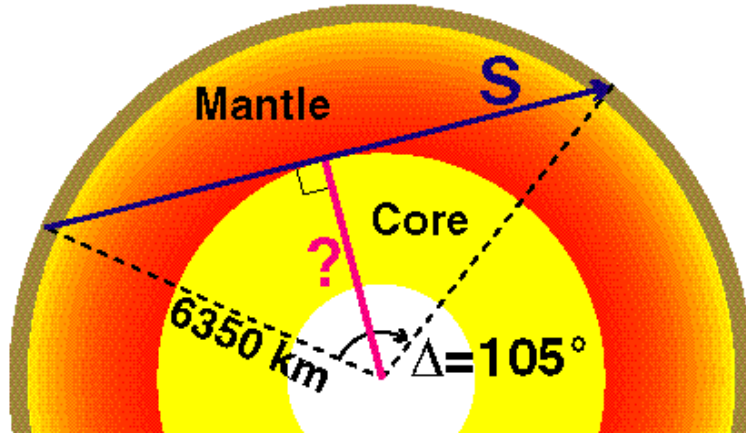


Figure 4.2: Estimation of the size of the Earth's core

4.2 Continental crust

4.2.1 Composition

The continental crust contains 0.554% of the mantle-crust mass. This is the outer part of the Earth composed essentially of crystalline rocks. These are low-density buoyant minerals dominated mostly by quartz (SiO_2) and feldspars (metal-poor silicates). The crust (both oceanic and continental) is the surface of the Earth and as such is the coldest part of our planet. Since cold rocks deform slowly, we refer to this rigid outer shell as the lithosphere (the rocky or strong layer).

4.2.2 Structure of continental crust

- 1.) average thickness: 35 km
- 2.) thins to less than 20km beneath some tectonically active areas
- 3.) thickens to up to 80 km beneath young mountain belts

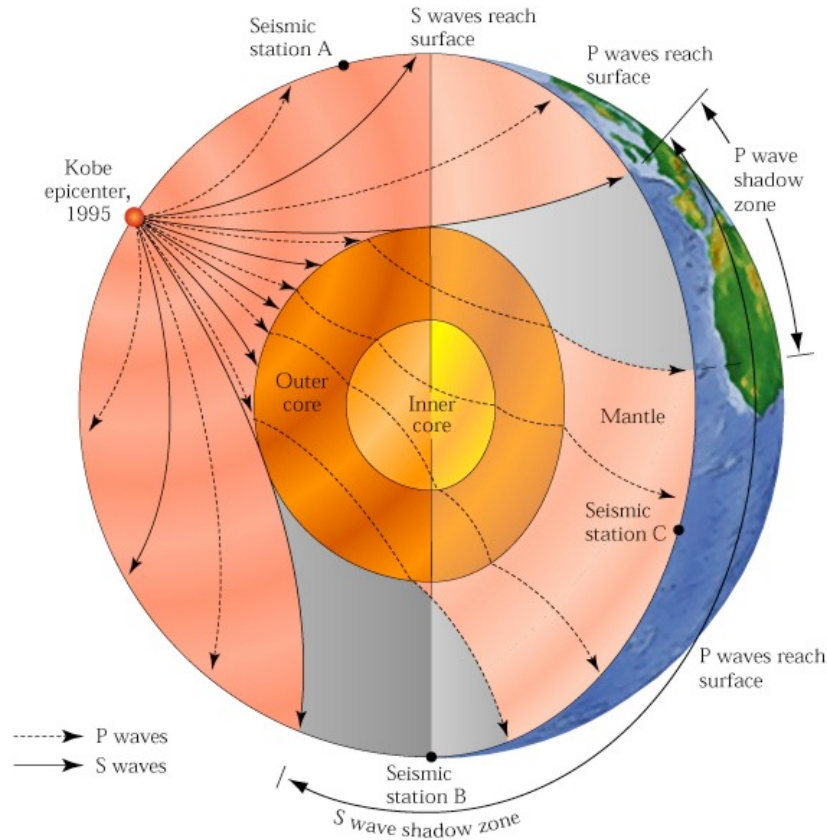


Figure 4.3: P- and S-wave paths through the Earth originating from the 1995 Kobe earthquake

The boundary between the crust and mantle is called the **Mohorovicic discontinuity** (or Moho); it is named in honor of the man who discovered it from studies of the seismic waves generated by the Croatia 1909 earthquake, the Croatian scientist Andrija Mohorovicic. It can be detected by a **sharp increase downward in the speed of earthquake waves** there.

The explanation for the increase in velocity at the Moho is a change in rock types from crustal to mantle rocks. Drill holes to penetrate the Moho have been proposed, and a Soviet hole on the Kola Peninsula has been drilled to a depth of 12 kilometers, but drilling expense increases enormously with depth, and Moho penetration is not likely very soon.

Another discontinuity was found by Conrad within the crust in 1925, which divides crust into upper and lower crust. Unlike the Moho the **Conrad discontinuity** is not always present. The composition of the upper crust is granodiorite and diorite. The composition of the lower crust is compositionally and structurally complex

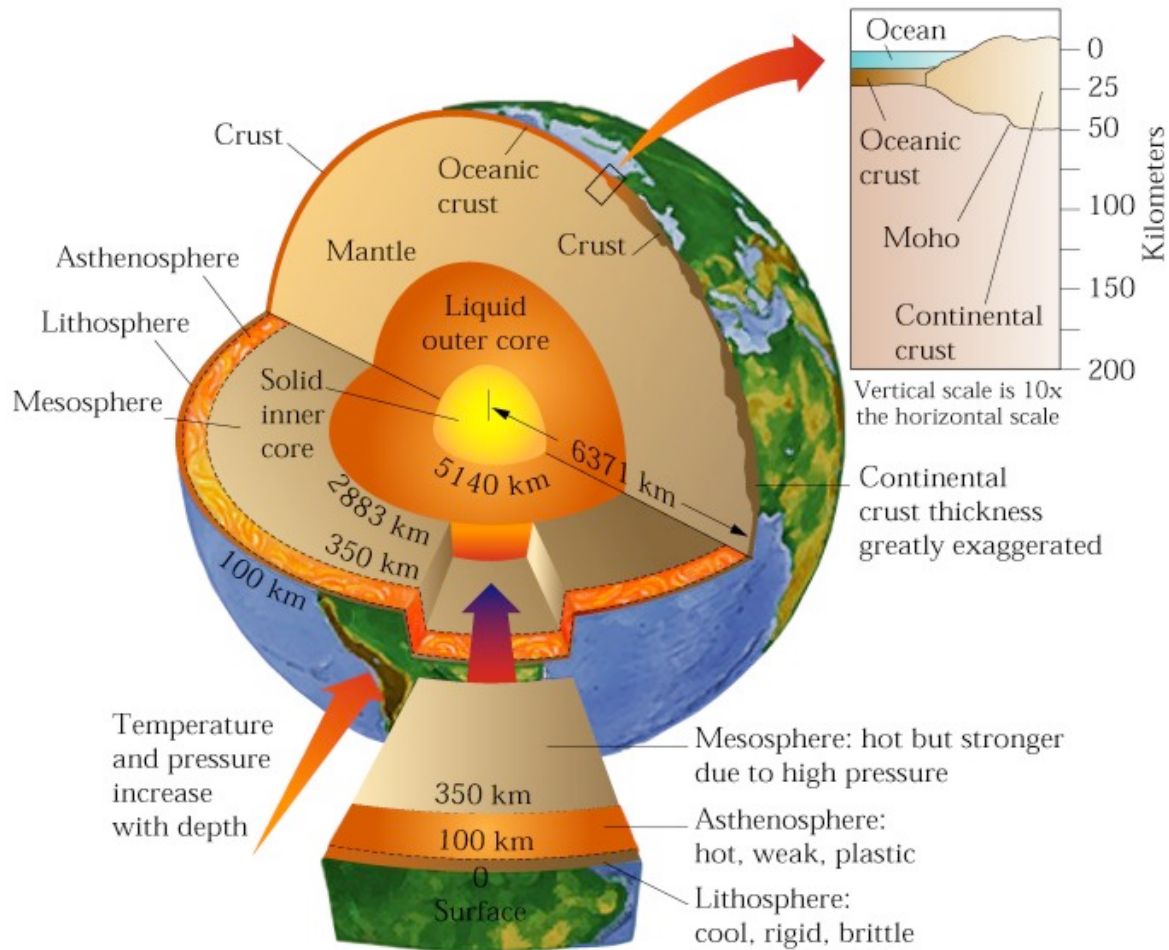
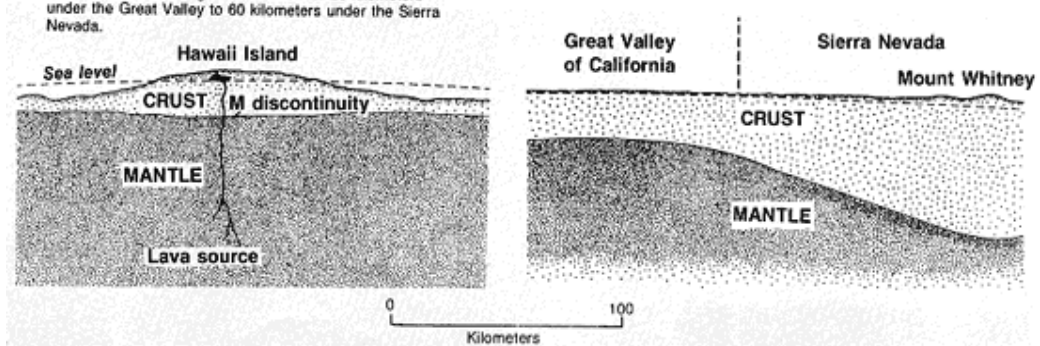


Figure 4.4: 3D view of the Earth's interior

The oceanic crust at Hawaii Island is about 5 kilometers thick. The thickness of the continental crust under eastern California ranges from a normal 25 kilometers under the Great Valley to 60 kilometers under the Sierra Nevada.



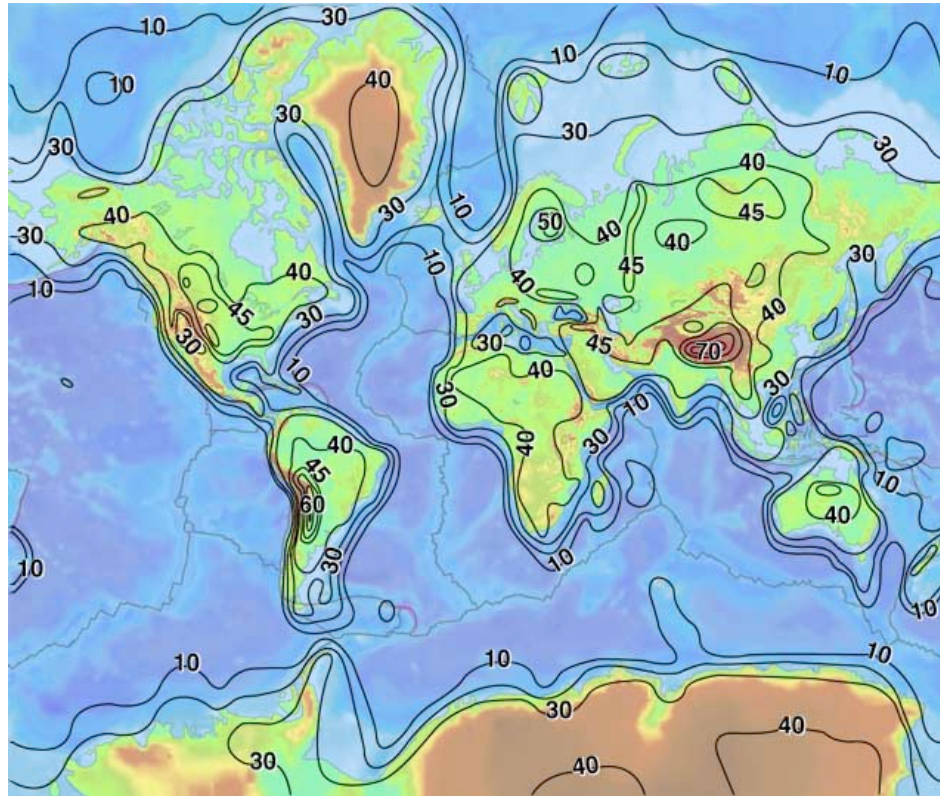


Figure 4.5: Continental crustal thickness (km), compiled by W. Mooney

4.3 Oceanic crust

4.3.1 Composition

The oceanic crust contains 0.147% of the mantle-crust mass. The majority of the Earth's crust was made through volcanic activity. The oceanic ridge system, a 40,000-km-long network of volcanoes, generates new oceanic crust at the rate of 17 km^3 per year, covering the ocean floor with basalt. Hawaii and Iceland are two examples of the accumulation of basalt piles.

4.3.2 Structure of oceanic crust

- 1.) average thickness: 6-7 km
- 2.) much more homogeneous than continental crust
- 3.) progressive velocity increase with depth

Layer 1: sediments (average thickness 0.4 km)

Layer 2: basalt (thickness 1-1.5 km)

a: fractured basalt

b: massive basalt with sheeted dykes

c: sheeted dykes with massive basalt

Layer 3: gabbros and metagabbros

4.3.3 Ophiolites

Pieces of ocean crust *obducted* onto continents (ophiolite = “snake rock”, greek origin). They are associated with deep sea sediments, basalts, gabbros, and ultrabasic rocks. Probably related to back-arc basin oceanic crust.

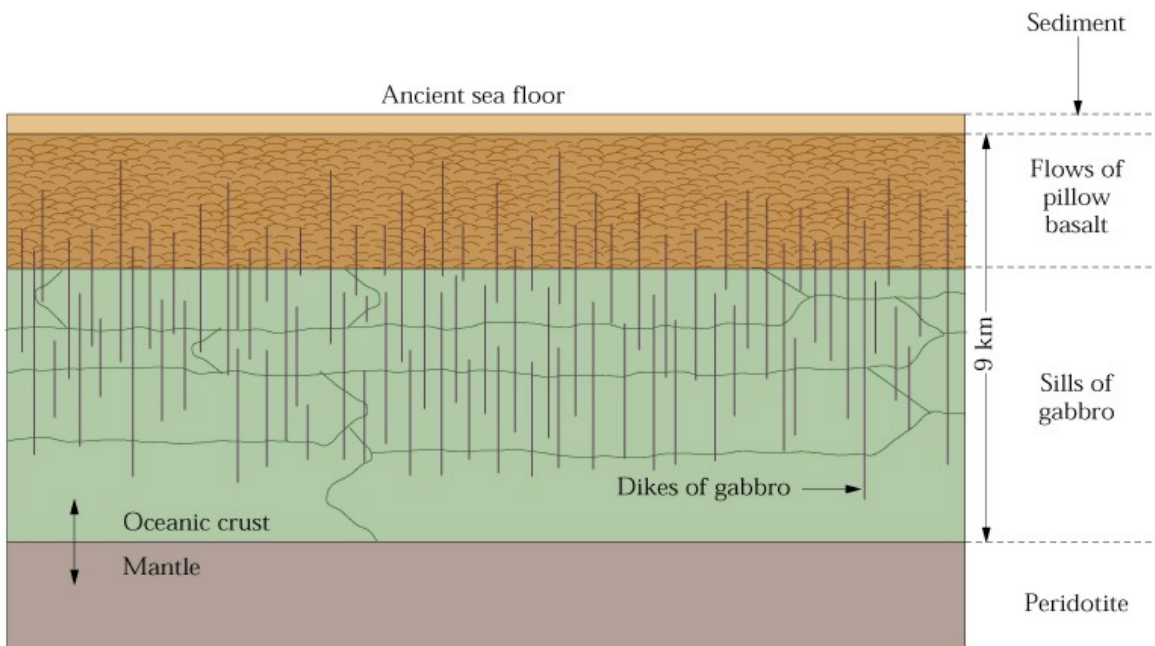


Figure 4.6: This is an idealized section of oceanic crust reconstructed from observations of an ophiolite. A thin layer of sediment overlies pillow basalts and a thick pile of gabbro sills. Both the lavas and the sills are intruded by gabbro dikes.

4.4 Main differences between oceanic and continental crust

- 1.) layering
- 2.) thickness

- 3.) age
- 4.) tectonic activity
- 5.) igneous activity

4.5 The Mantle

4.5.1 Overview

- 1.) seismic velocities generally increase with depth
- 2.) a low-velocity zone is present between 80 and 300km depth
- 3.) between 400 and 650 km velocity increases stepwise (due to mineral phase changes)
- 4.) 650 km: lower-upper mantle boundary
- 5.) Gutenberg discontinuity: core-mantle boundary at a depth of 2885 km
- 6.) composition: upper mantle: peridotite; lower mantle: perovskite

4.5.2 Seismic discontinuities

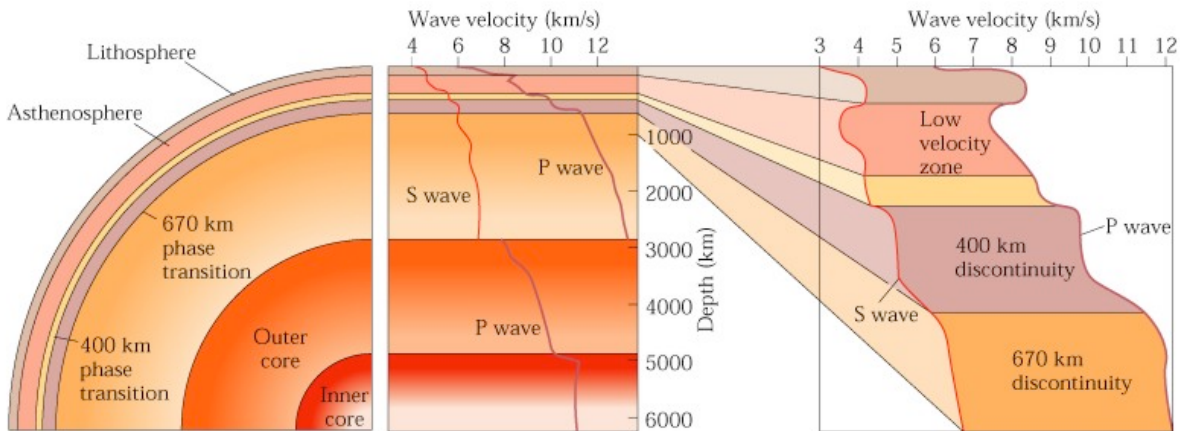


Figure 4.7: Seismic Discontinuities

4.5.2.1 Upper mantle: depth of 10-400 km

The upper mantle contains 15.3% of the mantle-crust mass. Fragments have been excavated for our observation by eroded mountain belts and volcanic eruptions. Olivine $(\text{Mg},\text{Fe})_2\text{SiO}_4$ and pyroxene $(\text{Mg},\text{Fe})\text{SiO}_3$ have been the primary minerals found in this way. These and other minerals are refractory and crystalline at high temperatures; therefore, most settle out of rising magma either forming new crustal material or never leaving the mantle. Part of the upper mantle called the asthenosphere may be partially molten.

4.5.2.2 Transition region: depth of 400-650 km

The transition region or mesosphere (for middle mantle), sometimes called the fertile layer, contains 11.1% of the mantle-crust mass and is the source of basaltic magmas. It also contains calcium, aluminum, and garnet, which is a complex aluminum-bearing silicate mineral. This layer is dense when cold because of the garnet and buoyant when hot because these minerals melt easily to form basalt which can then rise through the upper layers as magma.

4.5.2.3 Lower mantle: depth of 650-2,890 km

The lower mantle contains 72.9% of the mantle-crust mass and by deduction contains mainly silicon, magnesium, and oxygen. It probably also contains some iron, calcium, and aluminum. These deductions are made by assuming the Earth has a similar abundance of cosmic elements as found in the Sun and primitive meteorites (including by inference other planets) and according to the proportions found thereon. It is amazing what scientists can learn through deduction, inference, elimination and assumption.

4.6 Core

4.6.1 Outer core: depth of 2,890-5,150 km

The outer core is a hot electrically conducting liquid within which convective motion occurs. This combined with the Earth as a rotating body creates a dynamo effect which maintains the system of electrical currents known as Earth's magnetic field. It is also responsible for the subtle jerking of Earth's rotation. This layer is not as dense as pure molten iron which indicates the presence of lighter elements. Scientists suspect about 10% of sulfur and/or oxygen because of their abundance in the cosmos and due to the fact that they would dissolve readily in molten iron.

4.6.2 D": depth of 2,700-2,890

This layer is 200-300 km thick and represents about 4% of the mantle-crust mass. Although it is often identified as part of the lower mantle, seismic discontinuities suggest

the D'' layer may differ chemically from the lower mantle lying above it. Theories suggest the material either dissolved in the core at some point or because of its density, was able to sink through the mantle but not into the core.

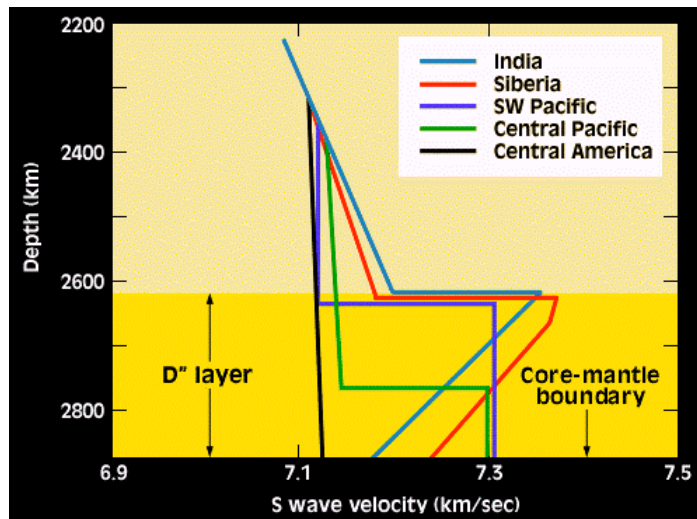


Figure 4.8: Regional variations in shear wave velocity at D''

4.6.3 Inner core: depth of 5,150-6,370 km

The inner core is solid and unattached to the mantle, suspended in the molten outer core. It is believed to have solidified as a result of pressure-freezing which occurs to most liquids when temperature decreases or pressure increases.

4.7 Data on the Earth's Interior

Crust Thickness: 30 km

Type of rock: Silicic rocks. Density: 2.2 g/cm³

Type of rock: Andesite, basalt at base. Density: 2.9 g/cm³

Upper mantle Thickness: 720 km

Type of rock: Peridotite, eclogite, olivine, spinel, garnet, pyroxene. Density: 3.4 g/cm³

Type of rock: Perovskite, oxides. Density: 4.4 g/cm³

Lower mantle Thickness: 2171 km

Type of rock: Magnesium. Density: 4.4 g/cm³

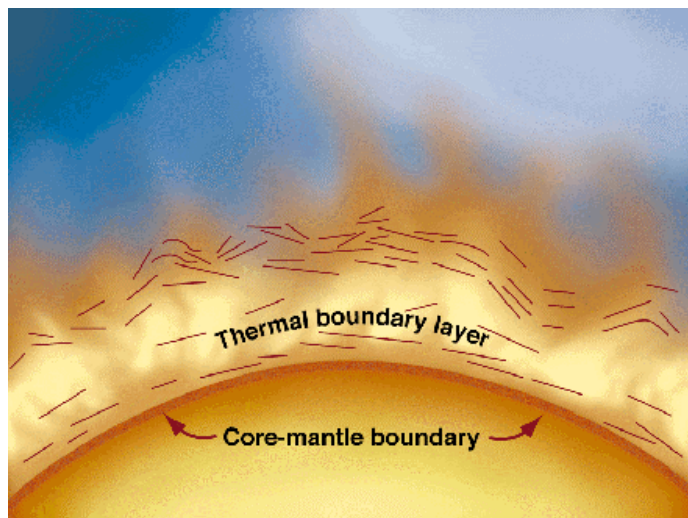


Figure 4.9: Cartoon of D'' region

Type of rock: Silicon oxides. Density: 5.6 g/cm³

Outer core Thickness: 2259 km

Type of rock: Iron, oxygen, sulfur. Density: 9.9 g/cm³

Type of rock: Nickel alloy. Density: 12.2 g/cm³

Inner core Thickness: 1221 km

Type of rock: Iron, oxygen, sulfur. Density: 12.8 g/cm³

Type of rock: Nickel alloy. Density: 13.1 g/cm³

4.8 Mantle convection

Mantle convection is related to plate tectonics and associated geological activity on the surface of our planet, including continental drift, earthquakes, volcanoes, and mountain building. Mantle convection and plate tectonics are one system, because oceanic plates are the cold upper thermal boundary layer^{*1} of the convection. The slow motion of plates and the mantle is powered by radiogenic heating and by the slow cooling of our planet over its 4.5-billion-year history. Mantle convection and plate tectonics provide the central framework linking the sub-disciplines of solid Earth science, including geochemistry, seismology, mineral physics, geodesy, tectonics, and geology.

¹ * In fluid mechanics, a thermal boundary layer is a layer in which heat is transferred by conduction.

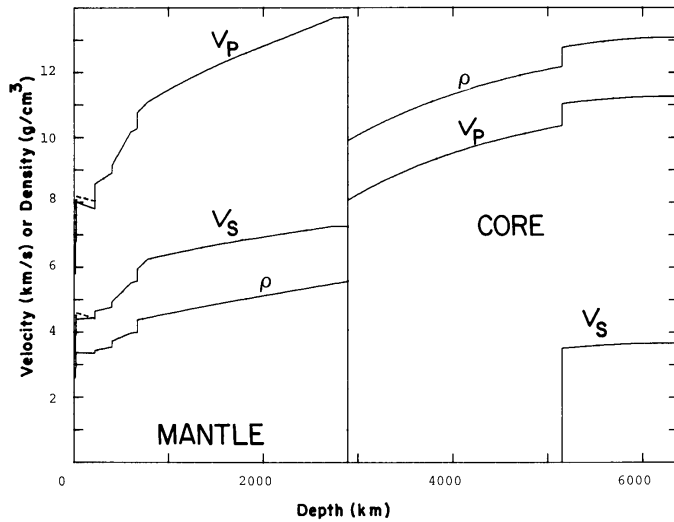


Figure 4.10: The Preliminary Reference Earth Model (PREM) from Montagner and Anderson (1989). V_p = P-wave velocity. V_s = S-wave velocity. ρ = density

4.8.1 Mantle convection: what do we know?

The advent of plate tectonics has resulted in the realisation that the Earth loses most of its heat by convection, and that mid-ocean ridges, subducting slabs, and hotspots must play a major role in the underlying convection mechanism. Unfortunately, the location of ridges today does not tell us much about mantle convection. Ridges are locations of passive upwelling of mantle material due to decompression melting. Their location is determined by the geometry of the plates, not by large-scale mantle convection, with upwelling limbs at ridges and downwelling limbs at subduction zones, as it is often illustrated in old textbooks.

Hotspots are localised thermal anomalies above which hot and buoyant mantle material is carried to the surface in mantle plumes. They originate at some boundary layer within the earth. It was suggested by Wilson (1963) and Morgan (1971) that hotspots are fixed in the mantle with respect to plate motions. Because of the apparent fixity of hotspots relative to plate motions, they have been postulated to have a deep origin, either at the core-mantle boundary or at the lower-upper mantle boundary (asthenosphere-mesosphere transition ca. 660 km below the surface). However, recent work has shown that hotspots are not actually fixed in the reference frame of the spin axis of the earth.

One of the characteristics of mantle convection on Earth is its apparent asymmetry, with upwellings represented by columnar swells, and downwellings by subducting slabs (e.g. McNutt and Judge, 1990). The down-going flow is represented by the subducting slabs, and thus is sheetlike. The up-going flow is accomplished by hotspots, which have cylinder-like shapes. Hotspot upwelling is not coincident with mid-ocean.

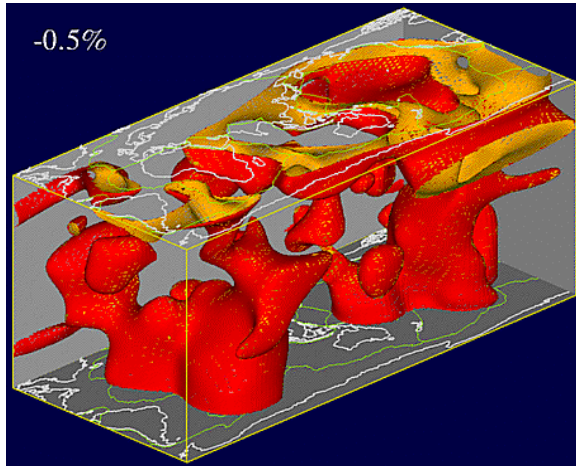


Figure 4.11: Global distribution of rising plumes in the mantle, imaged by mantle tomography

This picture has emerged both from mantle seismic tomography (e.g. Su et al., 1994b) as well as from 3-D modeling of mantle convection (e.g. Bercovici et al., 1989a).

The details of geometry of mantle convection are hotly debated. Seismic tomography reveals a domical shape of mantle plume with a broad base and smaller apex. This is at odd with mushroom shaped plumes generated by physical or numerical experiments. The viscosity contrast between the material in the plume and its surroundings is probably the key parameter controlling the geometry of plumes.

The three-dimensional topology of the flow is another area of uncertainties. One end-member shows a relative symmetry with hot material flowing up into mushroom shaped plume, while cold material flows into inverted mushroom-shaped anti-plumes. This type of convection is obtained by isoviscous (the viscosity in the mantle is constant) bottom heated top cooled system (the mantle is heating at the core/mantle boundary and cooled at the surface). When the mantle is heating form within, by decay of radiogenic isotopes, a very different style of mantle convection emerges. Cold fingers detach from the thermal boundary layer and drop down into the deeper mantle. As the mantle is incompressible, this down flow is compensated by a broadly distributed up flow. In this end-member mantle plumes do not exists.

Another major question is how the differing chemical compositions of erupted magmas, which require several chemically distinct reservoirs within the mantle, can be reconciled with other observational and dynamical constraints favoring whole-mantle convection, which should mix chemical heterogeneities. Essentially, one can divide existing models into two classes: those requiring whole mantle convection, and those based on a stratified mantle.

There are several arguments for stratified mantle convection. Pressure suppresses the effect of temperature on density, making it more difficult for the deep mantle to convect at deeper depths. It also suppresses the effect of temperature on seismic velocities,

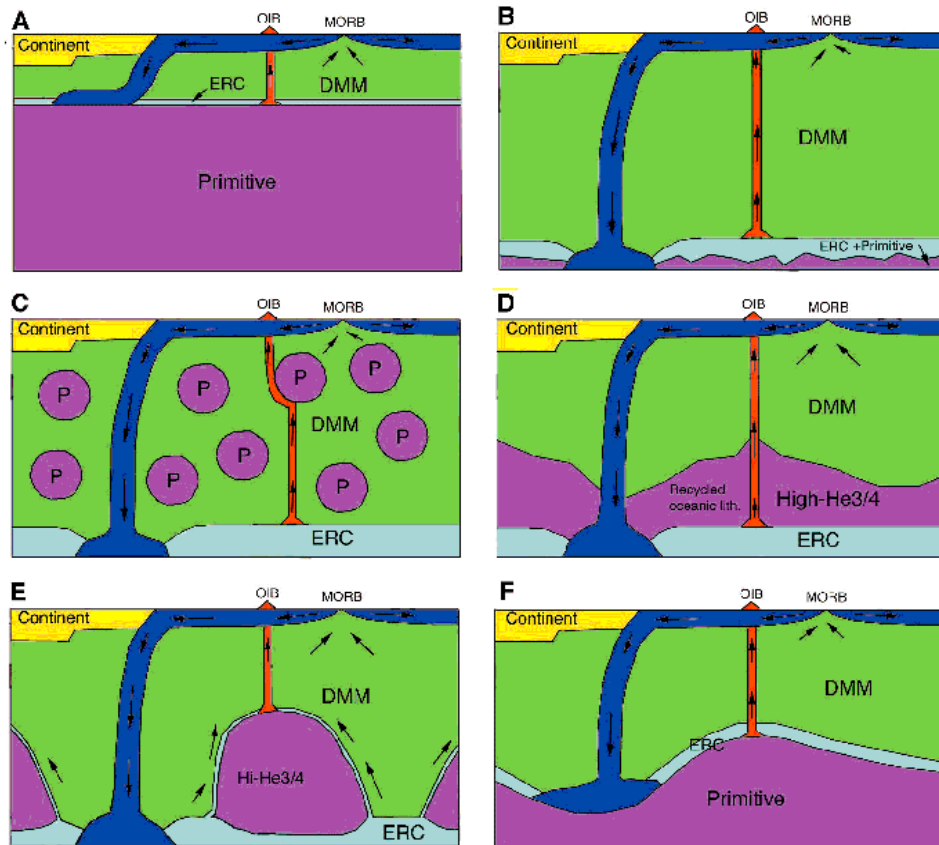


Figure 4.12: Some possible locations of mantle reservoirs and relationship to mantle dynamics. Convective features: blue, oceanic plates/slabs; red, hot plumes. Geochemical reservoirs: dark green, DMM; purple, high 3 He/ 4 He (“primitive mantle”); light green, enriched recycled crust (ERC). (A) Typical geochemical model layered at 660 km depth. (B) Typical geodynamical model: homogeneous except for some mixture of ERC and primitive material at the base. (C) Primitive blob model with added ERC layer. (D) Complete recycling model. (E) Primitive piles model. (F) Deep primitive layer (Tackley, 1998; from).

which are used by seismologists to map temperature variations.

Computer simulations of three-dimensional (3D) mantle convection with self-consistent thermal properties and variable heating (Tackley, 1998) show thermochemical convection involving deep dense layers, which help explain the spatial features of tomographic models derived from seismic data. In order to shed some light on mantle behavior, we will now have a look at some mantle physical properties.

4.8.2 Physical properties of the mantle

4.8.2.1 Viscosity of the Mantle

The mantle is made of olivine, pyroxene, either plagioclase (pressure $<1\text{GPa}$), or spinel (pressure $>1\text{ GPa}$), or garnet (pressure $>5\text{ GPa}$), and other trace elements including hydrogen. Pressure, temperature, hydrogen contents, and melt are key parameters controlling the viscosity of the mantle (Karato and Wu, 1993; Karato and Jung, 1998). However, many of the problems involved in the early modelling of plate tectonics arose from the immobility and stagnation of the upper boundary layer in a convecting system with an extremely temperature dependent viscosity (e.g. Tackley, 1998; Solomatov, 1995). As a result, the modelling of mantle convection with an extremely temperature dependent viscosity has become the focus of much recent modelling work (e.g. Moresi and Solomatov, 1998). In this type of modelling, researchers usually concentrate on the effects of a temperature dependent viscosity, and ignore the complexities presented by a pressure dependent viscosity. This inherently assumes two things:

Firstly, the pressure dependency of viscosity in the Earth's mantle has led to the suggestion that mantle convection could be segregated into two discrete layers, ie upper mantle and lower mantle convection. That this is the case is by no means certain (e.g. Van der Hilst et al., 1991; Albarede and van der Hilst, 1999). Much observational evidence has similarly been gathered to support the notion of whole mantle convection (Kincaid and Olson, 1987; Albarede and van der Hilst, 1999). However, it is presumptuous to present these models as representative of whole mantle convection without considering the complex mechanical interplay of a pressure dependent viscosity. Thus, these models can only rarely be presented as modelling upper mantle convection, where the effect of a pressure dependent viscosity is assumed minimal.

Similarly, the upper mantle on Earth is characterised by a strong lithosphere overlying a weak asthenospheric layer. It has been suggested that this asthenosphere arises from the approach of the deep geotherms, particularly in oceanic regions, to the peridotite solidus in PT space, resulting a degree of partial melting (Karato and Wu, 1993). The presence of hydrogen (water) in the upper mantle (Karato and Jung, 1998) has likewise been postulated to reduce the peridotite solidus and increasing the degree of partial melting in the asthenosphere (Karato and Jung, 1998). Such a phase change, involving a large viscosity variation, is difficult to model. However, on the earth, the presence of a weak asthenosphere may have a significant role in partially decoupling the plates from the motion of the deeper mantle.

4.8.2.2 Seismic velocities

Evidence for whole mantle convection comes primarily from seismic tomography, which works much like medical scanner both imaging material of different elastic properties hence different elastic-waves velocities. Seismic tomographic models of the mantle have developed significantly in the last 10 years, and have now reached a lateral resolution of about 3000 km. Seismology has provided important constraints on whether or not slabs penetrate the upper-lower mantle boundary.

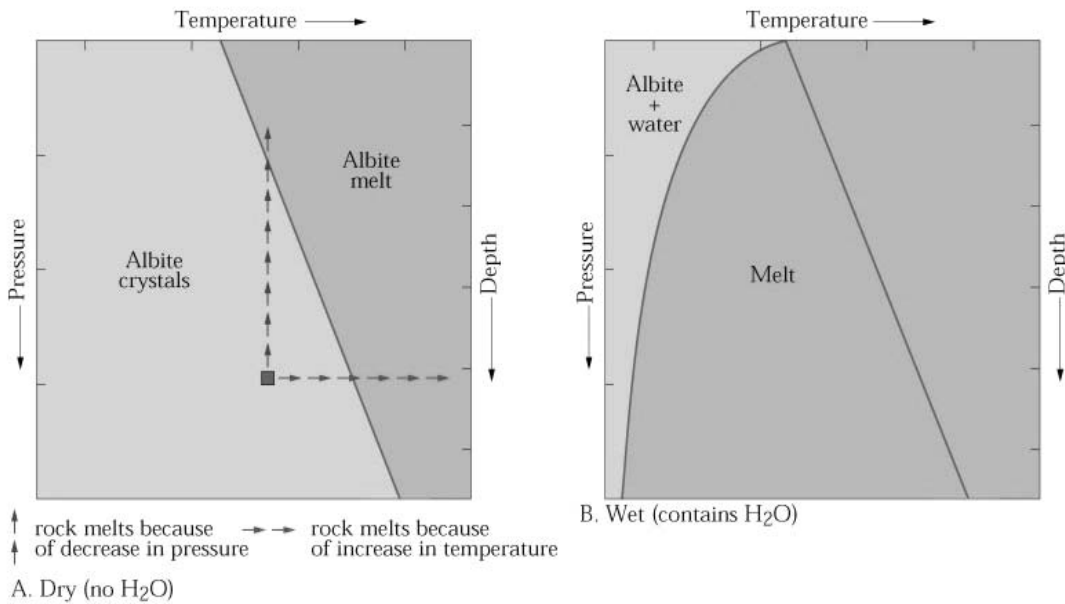


Figure 4.13: Effects of pressure and water on melting. A. The melting temperature of a dry mineral will increase if pressure is increased, as shown here for the mineral albite. If you increase the temperature of a mineral sufficiently at a given pressure, it will surpass its melting point. This is shown by the vertical arrows. Alternatively, if you decrease the pressure on a mineral sufficiently at a given temperature, it will surpass its melting point (decompression melting). This is shown by the horizontal arrows. B. The melting temperature of a wet mineral typically gets lower and lower as pressure increases. This is the opposite of what happens to dry minerals.

Some slabs clearly sink into the lower mantle, and others are deflected at the upper-lower mantle boundary (Van der Hilst et al., 1991). Fukao et al. (2001) found that subducted slabs tend to be sub-horizontally deflected or flattened in the upper and lower mantle transition region, the depth range of which corresponds roughly to the so-called Bullen transition region (400–1000 km). There is little indication for most of these slabs to continue “directly” to greater depths well beyond the transition region. The previous figure shows a good example for a subducted slab that has stagnated at the 670 km discontinuity south of Australia.

4.8.2.3 Elasticity

The viscoplastic rheology employed by these models does not take into account the elasticity of the Earth’s lithosphere and mantle. The result of this simplification is most apparent in the structure of subduction zones. The symmetry of these downwellings in computer models is quite unlike the asymmetric morphology of subduction zones

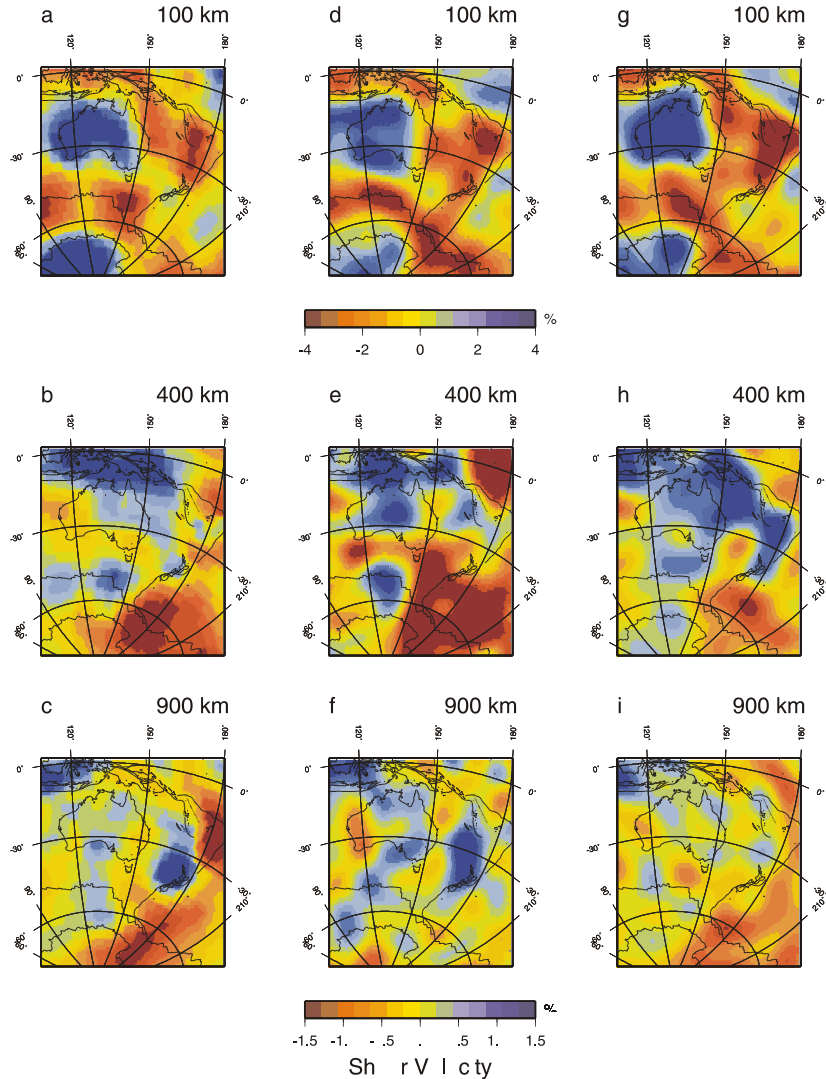


Figure 4.14: Seismic shear velocity anomalies at three mantle depths (100 km, 400 km, and 900 km) from three different global seismic inversions. Model SB4L18 (Masters et al., 2000) is shown on the left (a, b, and c). Model SAW24B16 (Mégnin and Romanowicz, 2000) is shown in the center (d, e, and f). Model S20RTS (Ritsema et al., 1999) is shown on the right (g, h, and i). The upper scale bar is only for 100 km depth while the lower scale bar is for both 400 km and 900 km depths (Gurnis and Müller, 2003; from)

on the Earth today. Conrad and Hager (1999) have argued that bending of the lithosphere at subduction zones is one of the major controlling factors on the evolution of the oceanic lithosphere.

Similarly, McKenzie (1978) argued that the flexure of oceanic plates at subduction zones is one of the principal opposing forces to subduction of oceanic lithosphere. Hence the inclusion of elasticity into the models is likely to inhibit subduction of oceanic lithosphere. Although there are significant unanswered questions pertaining to the subduction of oceanic lithosphere (e.g. Davies, 1993). However, since the dynamics of subduction, specifically the initiation of subduction, are inherently a three dimensional problem (e.g. Cloetingh et al., 1989), such modelling problems can only be adequately addressed by a three dimensional, computationally intensive code (not used in this class).

Three dimensional modelling (Tackley, 1998) has led to the suggestion than strain-rate weakening may be an important factor in allowing toroidal (strike-slip) motion and narrow, long-lived transform faults in three dimensional dynamic systems. However, recent investigations into the inclusion of elasticity into the models has led to the suggestion that this is superfluous, and that elasticity with simple strain-weakening can allow realistic shear-localisation in three dimensions (Poliakov and Herrmann, 1994; ?).

4.8.2.4 Phase transitions

Further, both the 400 km and the 670 km discontinuities represent mineral phase changes presents either an obstacle to subduction or helping to facilitate it.

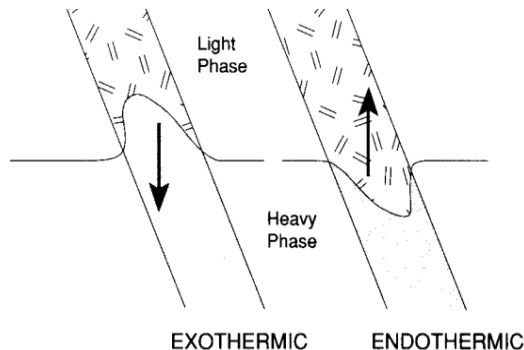


Figure 4.15: Phase change from a Spinel-Perovskite structure above to Magnesiowustite below the 670 km boundary (right). The nature of this transition is endothermic, i.e. it absorbs heat, where in contrast the phase transition at 400 km depth is exothermic, based on a phase transition from an olivine structure to a spinel crystal structure (left). For subduction, this means that the descent of a slab through the 400 km discontinuity is accelerated, as the phase transition occurs further up in the slab as compared to the surrounding mantle (left). In contrast, the phase transition at 670 km is delayed, representing an obstacle to subduction.

4.8.2.5 The vigour of convection: The Rayleigh number

An important measure of the vigor of convection and the distance from static equilibrium is the **Rayleigh number**, R . The smaller R is, the harder it is for convection to occur. In a spherical shell, convection occurs spontaneously when R is about 104. Whole mantle convection models usually assume $R > 10^7$, but Tackley (1998) derived a value of only about 4000 for the base of the mantle. If the lower 1000 km of the mantle is isolated, R may drop to 500.

These results have far-reaching implications. Small values of R imply that instabilities forming at the base of the mantle must be sluggish, long-lived, and immense. This is consistent with lower mantle tomography, which has shown that the deep mantle is characterised by two immense regions of low seismic velocity, and makes it more plausible than previously thought for the mantle to be chemically stratified.

4.8.3 The spatial pattern of mantle convection: driven by the plates or from below?

Rather than being driven by mantle plumes from below, plate tectonics itself may be the driving force of the large-scale thermal temperature structure of the mantle. Subducting slabs cool the mantle, and areas protected from subduction for a long time naturally become the loci of large-scale upwellings.

4.8.4 Tracking subduction through time: insights into mantle convection?

If we follow the idea that mantle convection may be driven by subduction, then we should be able to gain major insights by tracking subduction zone locations and the volume of subducted plates through time. Wen and Anderson (1995) modeled the subduction history for the last 130 m.y. by using published plate models for relative plate motion, the absolute plate motion model by Müller et al. (1993) and the global digital age map by Müller et al. (1997). They reconstructed both the volume and location of subducted slabs, and compared the results with seismic tomographic images. The figure below shows the area distribution of subducted slabs in 30 m.y. intervals in an Atlantic-Indian hotspot reference frame. The subducted area is proportional to the area of the square plotted, and normalized to the maximum within that time interval (Wen and Anderson, 1995; from):

4.8.5 Origin and fixity of hotspots

When we discussed absolute plate motions we showed that there is substantial evidence that Pacific hotspots do not represent the same reference frame as Atlantic/Indian hotspots. Recently, a geophysical survey of the Pitman Fracture Zone in the southwest Pacific allowed reconstruction of Pacific Antarctic plate motions much more accurately than previously possible (Cande et al., 1995). Pacific-Antarctic plate motions represent one of the major tectonic links between the Pacific and Atlantic/Indian oceans. The following figure shows the predicted track of the Hawaiian hotspot, by following the

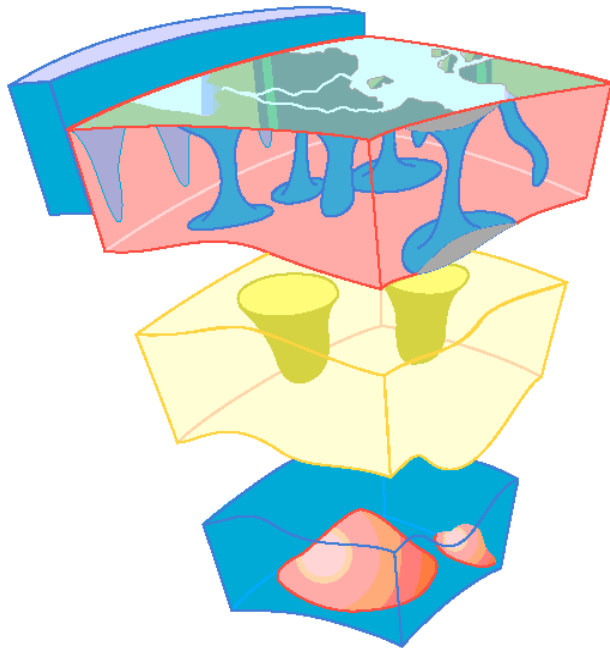


Figure 4.16: Top-down tectonics? The tectonic plates can be viewed as an open, far-from-equilibrium,dissipative and self-organizing system that takes matter and energy from the mantle and converts it to mechanical forces (ridge push,slab pull),which drive the plates. Subducting slabs and cratonic roots cool the mantle and create pressure and temperature gradients,which drive mantle convection. The plate system thus acts as a template to organize mantle convection. In contrast, in the conventional view the lithosphere is simply the surface boundary layer of mantle convection and the mantle is the self-organizing dissipative system ((Anderson, 2001; from)).

assumption that all hotspots are fixed, and using the Atlantic-Indian hotspot frame, rotated to the Pacific plate.

It is clear that there are large misfits, which are likely, at least in part, to be attributed to relative motion between the hotspots underlaying the Pacific and Atlantic/Indian oceans, respectively. In a coordinate system of placeAtlantic/ Indian hotspots fixed to the spin axis, the sub-Pacific mantle would have moved southward by about 1000 km from about 75 to 40 Ma, a conclusion supported by the paleomagnetic data shown above. In other words, it appears that both the mantle underlaying the placePacific ocean and the hotspots it includes would have moved at least temporarily fairly fast relative to the Atantic-Indian mantle.

There is also a good correlation between the global distribution of hotspots, seismic tomographic velocity anomalies in the upper mantle, and long wavelength observed geoid anomalies. The following figure shows the global hotspot distribution and the residual geoid obtained from subtracting the subduction geoid from the total GEM8

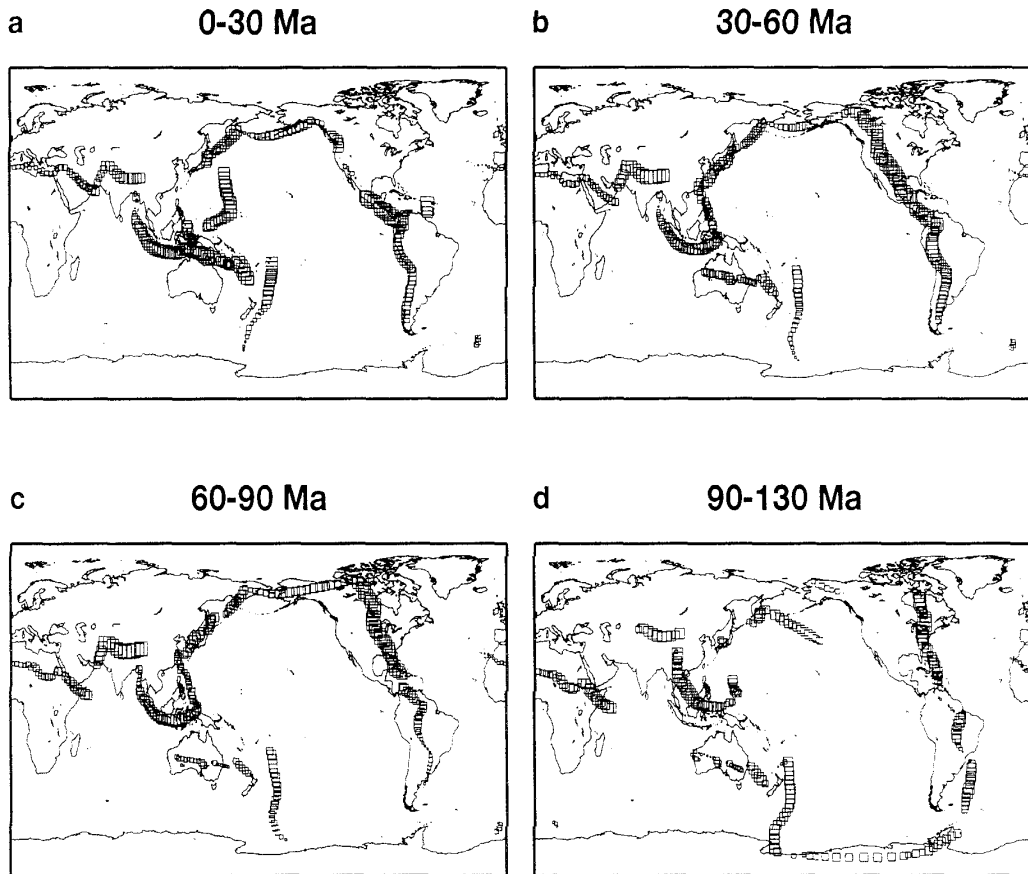
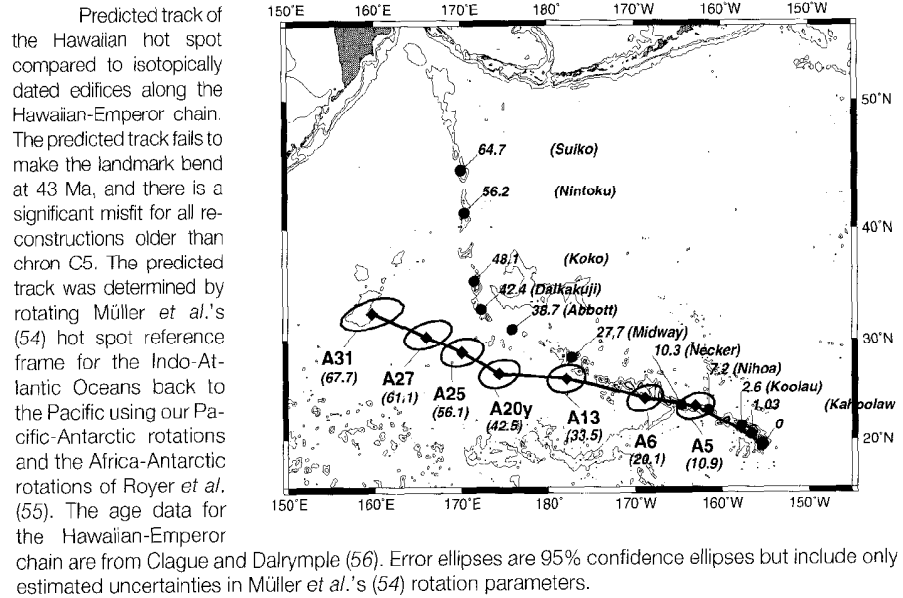


Figure 4.17: (Wen and Anderson (1995)) compared 4 different seismic tomographic models with their results and found that cold downwelling regions appear to be trapped in the middle mantle at depths between 800-1100 km, suggesting that there may be a significant boundary in the mantle in this depth range. They proposed that a mantle discontinuity at 920 km, recently mapped from seismic evidence ((Kawakatsu and Niu, 1994)) may play a role as a geodynamic barrier. This contradicts a commonly held point of view that the main discontinuity between the upper and lower mantle is located at about 650 km, and that subducted slabs would sink all the way to the core-mantle boundary, once subducted beyond 650 km depth.



geoid from Crough and Jurdy (1980). Black dots are locations of hotspots:

If the spherical harmonic expansion of the global hotspot distribution is calculated, power spectrum peaks are found at degrees 1,2 and 6 (Gegout and Cazenave, 1993), further confirming this observation. Gegout and Cazenave (1993) also computed the degree 6 pattern of the spherical harmonic expansion of the topography of hotspot swells and upper mantle velocity anomalies at 400 km:

The swell topographies were calculated by determining the spatial extent and height of hotspot swells, fitting Gaussian shapes to the swells and computing their Fourier expansion. The degree 6 pattern of velocity anomalies for the upper mantle (Gegout and Cazenave, 1993) was computed from seismic velocity anomalies from Woodhouse and Dziewonski (1984).

The figure above shows that the two major hotspot swells in the Pacific and over Africa correlate well with low upper mantle velocities, suggesting that the hotspot groups are related to large upwelling cells in the upper mantle which also cause the observed geoid highs over both groups. However, this is an area of ongoing research, and without new data and a proper error analysis it is hard to reach any definite conclusion.

The following figure demonstrates that core-mantle boundary topography correlates very nicely with geoid highs, suggesting that both phenomena are caused by large-scale hot upwellings that originate at the core-mantle boundary (CMB), probably in the form of previously subducted plates. However, this does not prove that ALL mantle plumes originate from the CMB.

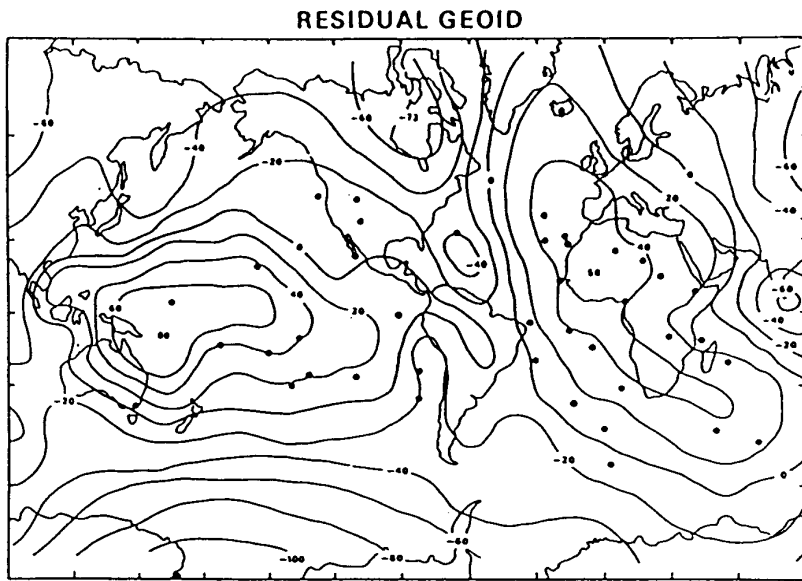


Figure 4.18: This figure demonstrates that hotspots are clustered within the two long-wavelength geoid highs that are observed over the Pacific Ocean and over Africa, the eastern South Atlantic and the southwestern placeIndian Ocean.

4.8.6 Plate- mantle interaction: mantle delamination and dynamic topography

The Earth's surface adjusts vertically in response to temporal changes in the forces applied at the base of the lithosphere, such as might be caused by changes in temperature, mineral phase, or pattern of convection. For most processes, the predicted vertical motions are too slow to be detected by GPS instrumentation at present, or even with likely improvements in the next 10 years, with two possible exceptions. The first is the possibility that broad continental plateaus, such as Tibet and the Altiplano, might experience rapid uplift as the result of delamination of the dense lower lithosphere that becomes convectively unstable on account of over-thickening of the lithosphere at continental convergence zones.

For example, it has been proposed that 8 million years ago the Tibet Plateau abruptly rose by 1 to 3 km within the span of a million years on account of delamination of its cold, thickened lithospheric root. The rise of this abrupt and massive continental feature had a major influence on climate in southern placeAsia by triggering the onset of the monsoons. At rates of a few millimetres per year, vertical uplift in response to convective destabilisation of the lower lithosphere could be measured and used to understand how the dynamics of the lower lithosphere affects continental tectonics.

The second example is the positive dynamic topography (uplift) of the Earth's sur-

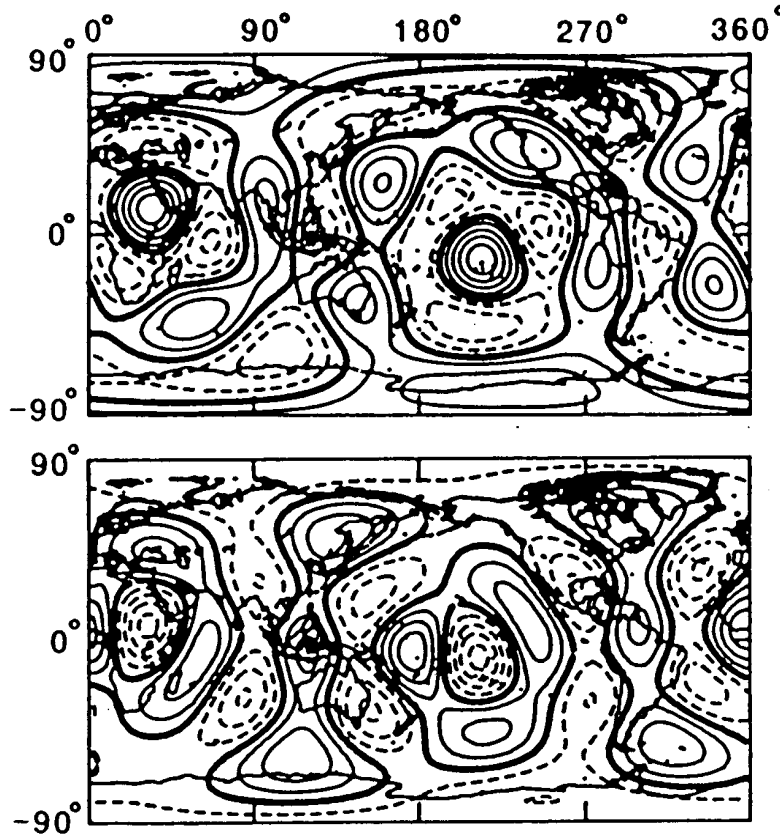


Figure 4.19: Top figure: Degree 6 pattern of spherical harmonic expansion of topography of hotspot swells (contours at 20m-intervals, solid (dashed) contours are positive (negative) anomalies. Bottom figure: Upper mantle velocity anomalies at 400 km (contours at 0.01 km/s intervals, solid (dashed) lines represent high (low) velocities ((Gegout and Cazenave, 1993; from)).

face as the lithosphere rides over mantle hot spots. From analysis of depth anomalies in the ocean basins, it is clear that the uplift is of the order of a kilometre or two, and it reaches its full height within a few million years. Investigation of the rate and pattern of uplift provides important information on the thermal and dynamic properties of hot spots and how they interact with the lower lithospheric boundary layer. Nothing is known about this process for hot spots underlying continental lithosphere, such as placeYellowstone and the many African hot spots, because we lack a vertical reference for measuring uplift associated with the passage of the lithosphere over these hot spots. GPS provides the only hope of recording this process of hot spot-continental lithosphere interaction, but detecting this small signal will require improvements in the

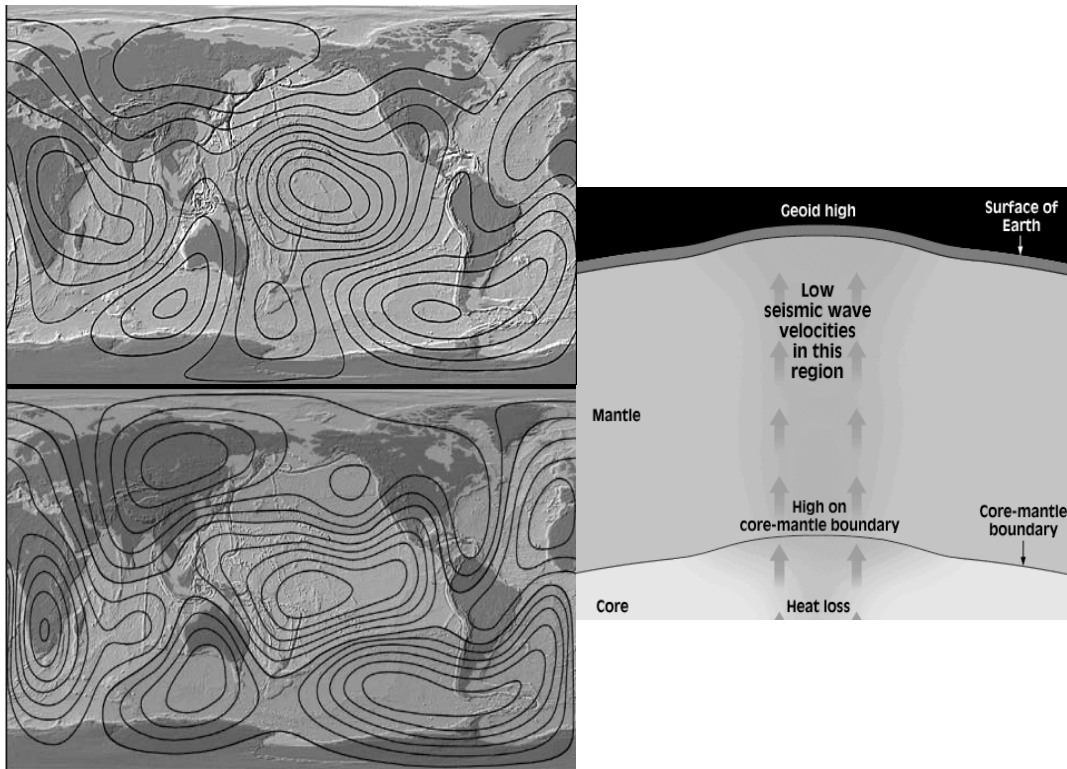


Figure 4.20: Top: Geoid (highs are red). Bottom: core-mantle boundary topography (400m contours).

vertical accuracy.

A third example is given by negative dynamic topography by surface plates moving over a sinking, subducting slab. This phenomenon is best expressed south of Australia, where the Southeast Indian Ridge in the area of the Australian Antarctic Discordance (AAD) is now spreading above a subducted slab, which dates back to subduction east of Gondwanaland in the Mesozoic.

4.8.7 Mantle convection modelling with imposed plate motions: an Australian example

The AAD, a 600 km long segment of the South East Indian Ridge (SEIR) south of Australia at 130E, is the deepest portion of the mid-ocean ridge system. Not only is the AAD anomalous in terms of bathymetry, but it is also characterised by unusual seafloor morphology, isotope geochemistry, petrology, and seismic structure. The Australian Antarctic Discordance is characterised by extremely rugged ridge flank morphology, axial depths 800 m deeper than normal, and a series of closely spaced, N-S trending

fracture zones (Fig. 1A). The clearest means by which to view the AAD is through residual depth anomalies – the topography which results when normal subsidence of the oceanic lithosphere is removed from observed bathymetry (Crough, 1983). When corrected for normal subsidence and loading from observed sediment thicknesses, the resulting residual depth is characterised by a prominent linear north-south trending depression from the Great Australian Bight through to the AAD (Cochran and Talwani, 1978) and down to nearly the Antarctic margin with values exceeding 1000 meters (Fig. 1B).

Mesozoic paleogeographic reconstructions showing subduction near the restored eastern Australian margin and the seismic detection of a slab-like structure within the lower mantle beneath the AAD, the approximate former position of subduction in a fixed hotspot reference frame (next figure), indicate that a subducted slab moved through the mantle over the last 130 Ma resulting in the anomalous cold zone centred at the AAD.

The initial model condition of the subduction zone consists of a slab with a dip, age, and position from the restored eastern margin of Australia. Having rotated the Lord Howe Rise back to its pre-rift position the model trench was located parallel to the continental margin. The plate motions change over the course of the model. First, there was a general motion toward the Pacific by three plates which were part of Gondwanaland (AUS, LHR, and ANT) with velocities exceeding 5 cm/yr with respect to the hot spot reference. Second, following a period of relative quiescence (during which time Australia rifts from Antarctica but moves only slowly northward), Australia moved away from Antarctica at about 45 Ma with nearly constant velocities between 7 and 8 cm/yr. While the plates change their positions, dynamic topography continuously evolves as the former slab changed its structure and depth distribution (Fig. 7A-D).

During the first phase of westward motion, the slab partially stalls above the phase transition at 670 km depth. From 60 Ma to the present, cold subducted material becomes drawn upward beneath the ridge. At the present, the position of the ridge is directly above the area where mantle, a few tens of a degree cooler than normal, is being drawn upward. The intense, circular topographic depression is caused by a linear source of negative buoyancy orthogonal to the upwelling flow.

This model explains two perplexing features which were previously not understood in terms of plate tectonics are associated with the Australian plate:

- 1.) The complete subaerial exposure of Australia during the Cretaceous global sea level maximum. Stratigraphic and paleogeographic evidence demonstrate that broad regions of Australia underwent vertical motion without substantial folding or faulting during the Mesozoic and Cenozoic.
- 2.) The existence of a cold spot, possibly a convective downwelling, beneath the Australian-Antarctic spreading center.

Our mantle convection shows that Australia overrode an ancient, long-lived subduction zone after 130 Ma. It predicts both the anomalous Cretaceous vertical mo-

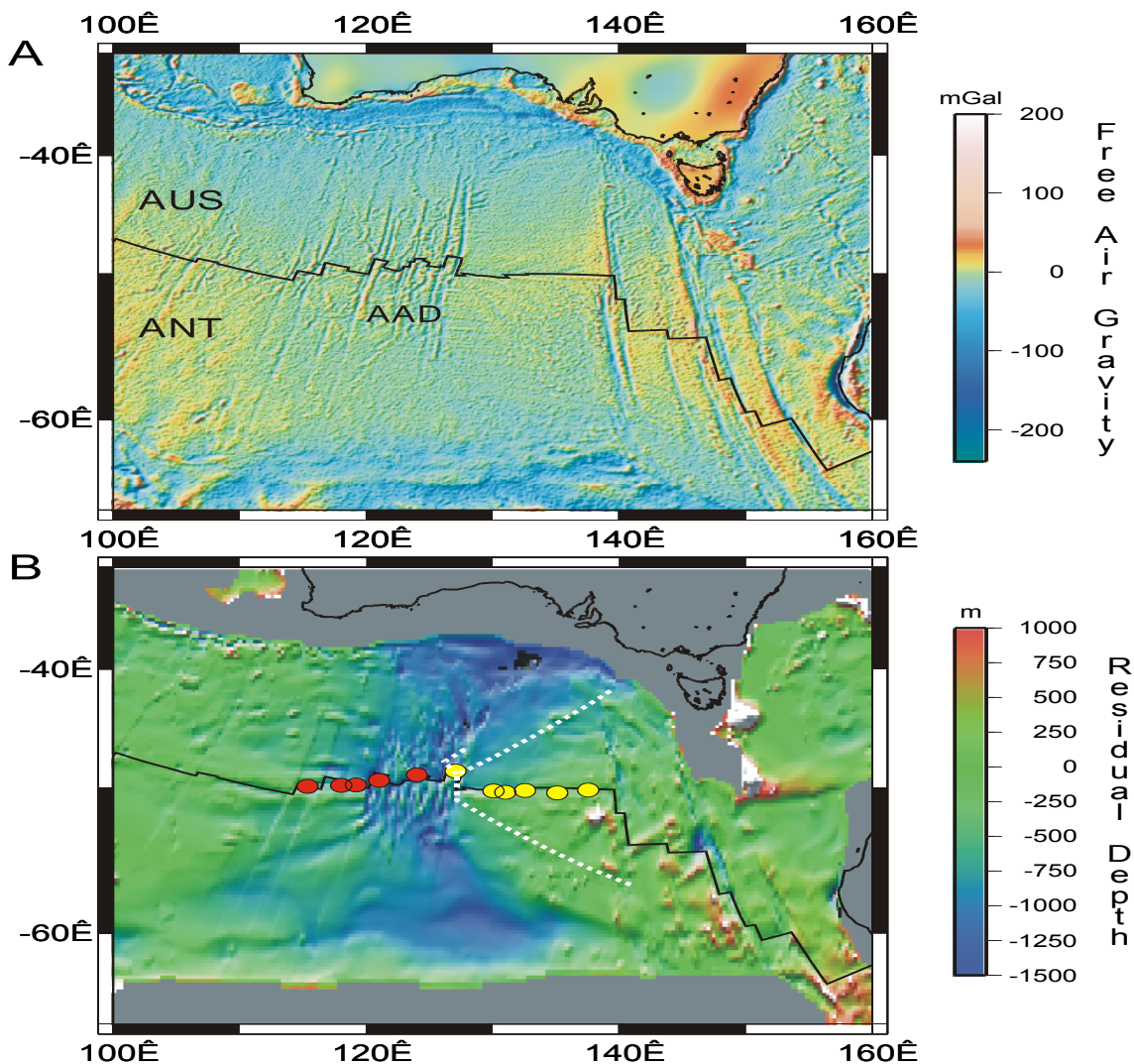


Figure 4.21: Observed characteristics of the Southeast Indian Ocean. A. Free gravity from (Sandwell and Smith (1997)) is used as a base map to illustrate the tectonic fabric (sun angle 60 W of N). B. Residual topography (anomalous topography which cannot be explained by the depth-age behaviour of oceanic lithosphere) with sun angle 20 W of N. Isotopic signature of the mid-ocean ridge basalts ((Klein and Langmuir, 1989)) with Pacific mantle composition in yellow and Indian mantle composition in red; dotted line is hypothesised trace of the isotopic boundary from (Pyle et al. (1995)).

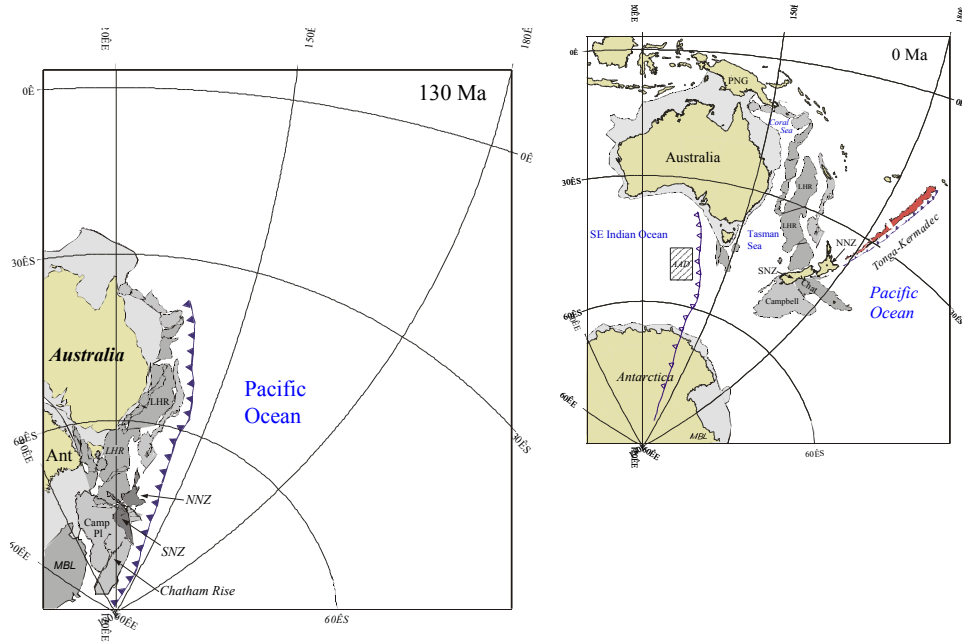


Figure 4.22: Reconstruction of Gondwanaland at 130 Ma. Before this time, a westward dipping subduction zone was located east of the Lord Howe Rise (LHR), which became extinct at about 130 Ma. The projection is general stereographic, with the projection centre at 120 E, 30 S. b. Present-day plate configuration in the southwest Pacific Ocean, with the 130 Ma location of the subduction zone superimposed, now situated just east of the AAD.

tion of Australia and the present day distinctive geochemistry and geophysics of the Australian-Antarctic Discordance. The dynamic models predict that a subducted slab associated with the long-lived Gondwanaland-Pacific converging margin passed beneath Australia during the Cretaceous, partially stagnated in the mantle transition zone, and is presently being drawn up by the South East Indian Ridge. The method demonstrates the predictive power of mantle convection models when they incorporate plate tectonics.

4.8.8 Modes of Mantle convection

In the previous example, we looked at mantle convection with plate motions being superimposed. Even though these models are extremely useful, we desire to develop “fully dynamic” models, where the motion of plates is an integral part of the system, and do not have to be specified separately. This requires to have a closer look at the physics behind mantle convection. Over geological time spans, the mantle acts as a fluid. Note that the use of the term fluid here does not imply that the material is a liquid - the term is more descriptive of the way in which a material will deform and is independent of its physical state. Although gases and most liquids will usually exhibit

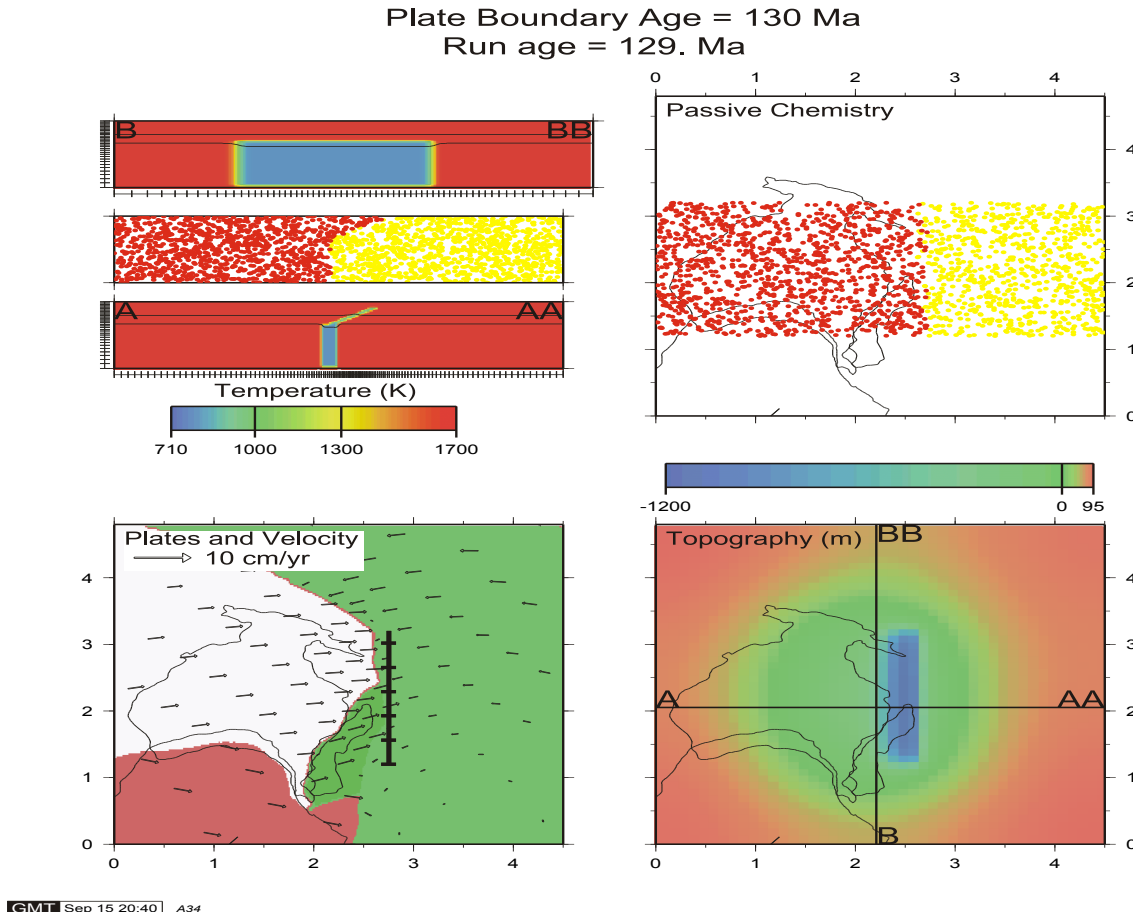


Figure 4.23: Initial condition for a mantle convection model constrained by imposed plate motions through time, with plate stencils (ANT for Antarctica, AUS for Australia, LHR Lord Howe Rise, and PAC for Pacific) and imposed velocity vectors shown on the lower left. The position of the trench is shown by the vertical line with the crossing tick marks such that the slab extends from $y=1.2$ to 3.2 . Major tick marks on the box edges have a 2000 km spacing. In the upper left, the initial configuration of the slab is shown by two intersecting cross-sections (a-a' and b-b'); the center of the slab delineates the boundary between “Gondwanaland” tracers shown as black dots and “Pacific” tracers shown as gray dots. In the upper right, the tracers are plotted for those depths less than 10^{-5} .

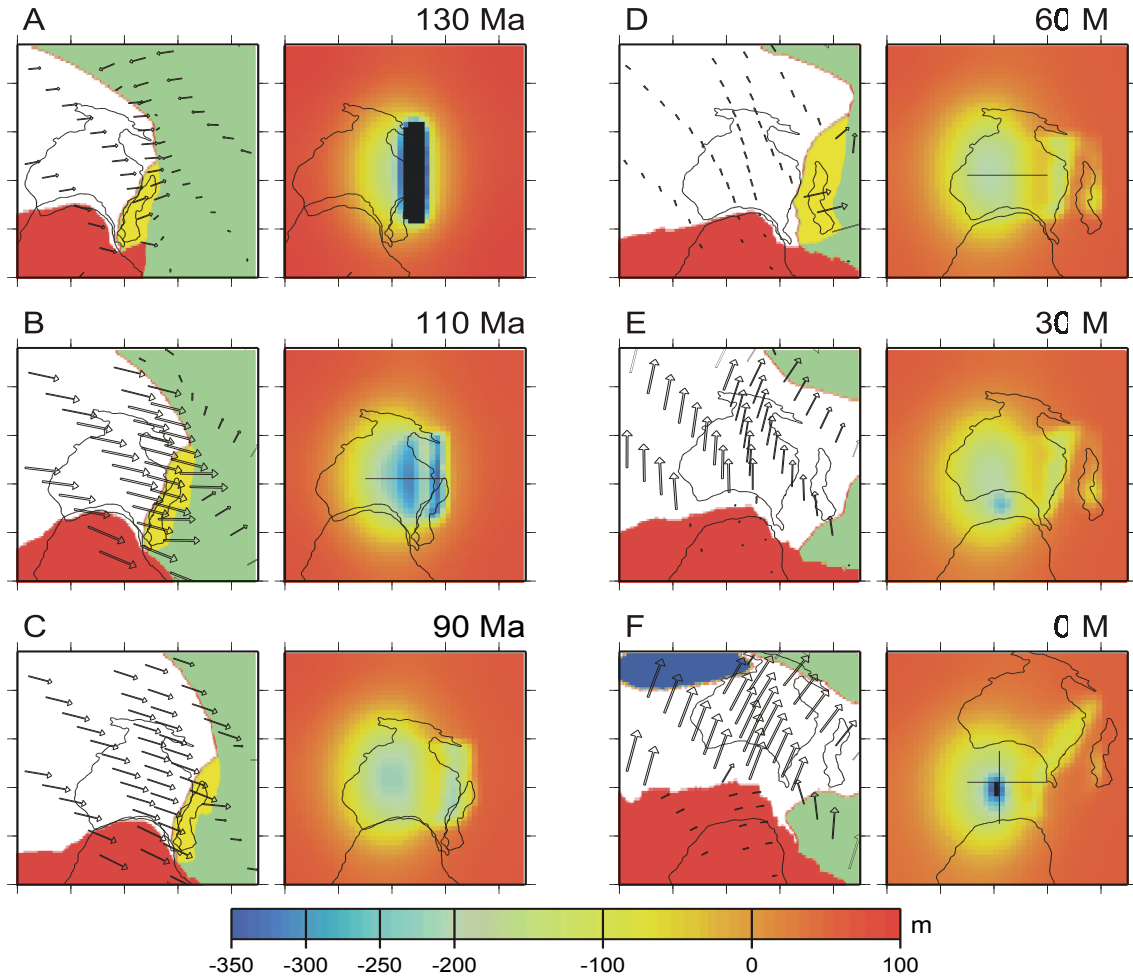


Figure 4.24: Plate stencils and imposed plate velocity (left) and predicted dynamic topography at six times for the nominal case with initial conditions shown in previous figure. The black lines on some of the topography plots denote the temperature cross sections shown in the following figure.

fluid flow under reasonable time scales, this is not necessarily always the case.

The best example of a liquid behaving like a solid is glass, which is actually a liquid and does ‘flow’ over a relatively long time scale (hundreds of years), but over shorter time scales can fracture and break easily enough (catastrophically at that). Like glass, solids can also flow like fluids over large time scales. Under stress, solids will deform in an elastic manner and also undergo a continuous creep process. Over a long time scale this may result in a completely new shape which can be viewed as a fluid-like property.

The key property of a liquid that determines how easily it will flow is its viscosity. Viscosity is the fluid analogue to friction between solids, and the higher the viscosity of

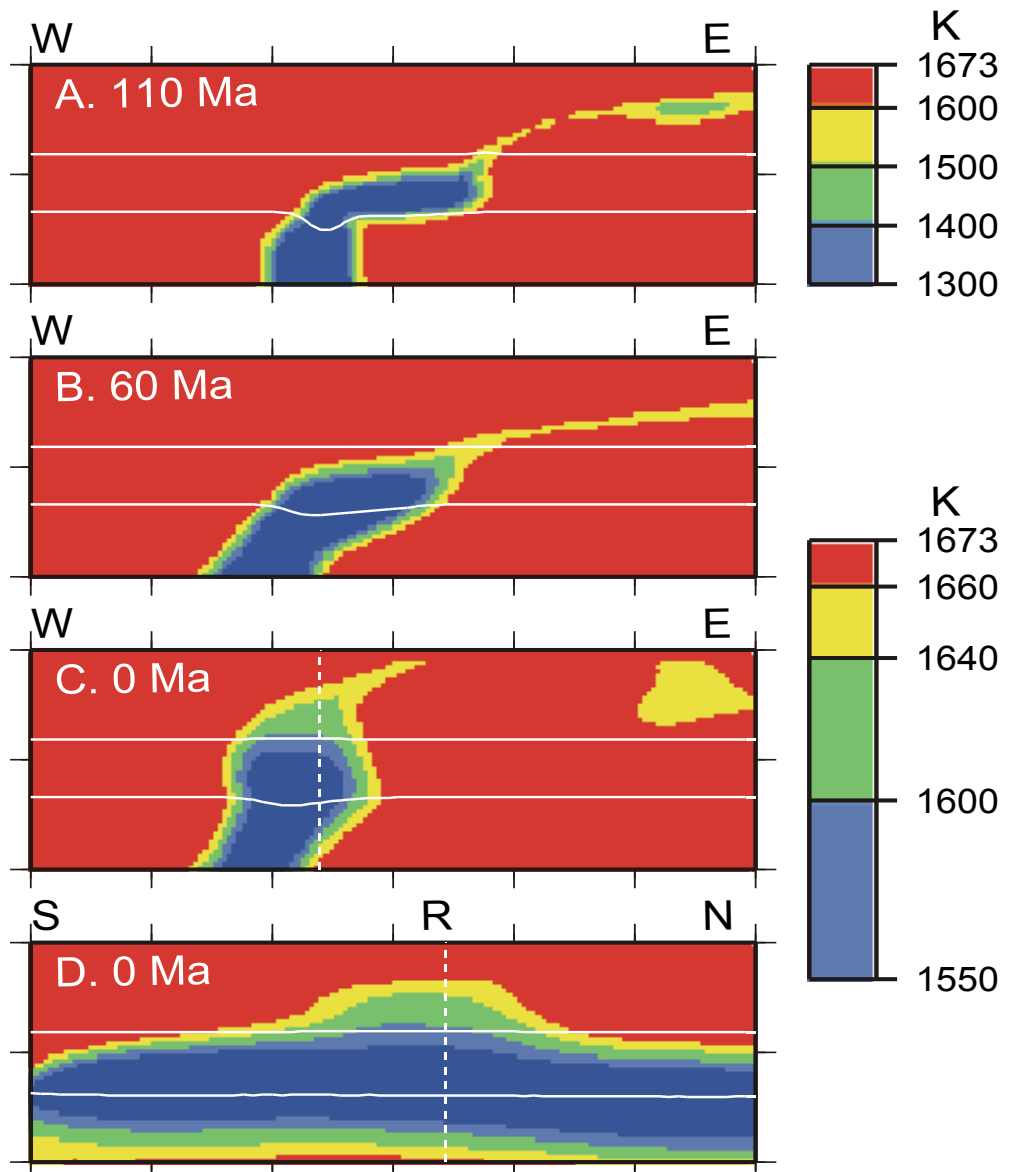


Figure 4.25: Vertical cross sections of temperature for convection model. A-C are nearly east-west profiles. D and C are two orthogonal sections with respective lines of intersection shown by white vertical dashed lines. In D the 'R' denotes the present position of the SEIR. Locations of cross sections are shown as white lines in previous figure. The upper scale is only for A (representing a large temperature span) while the lower scale is for B-D. The tick marks have a 500 km spacing. The horizontal white lines mark the positions of the 410 km and 670 km phase transitions.

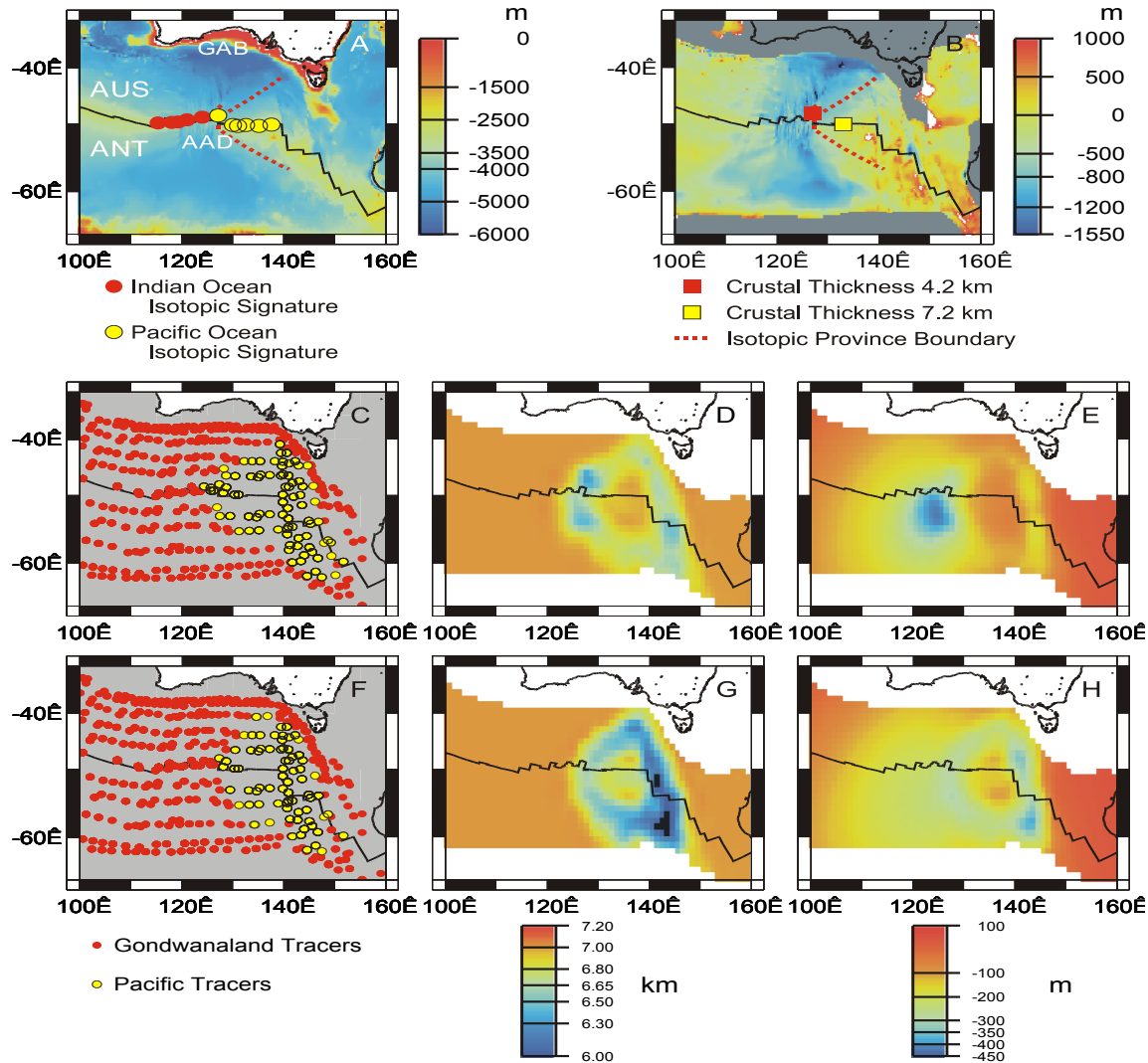


Figure 4.26: Comparison of observed and predicted structures of the ocean south of Australia. A. Observed isotopic signature and inferred motion of isotope boundary from (Pyle et al. (1995)). B. Inferred residual depth anomaly. Predicted isotope provinces (C), crustal thickness, and depth anomaly (E).

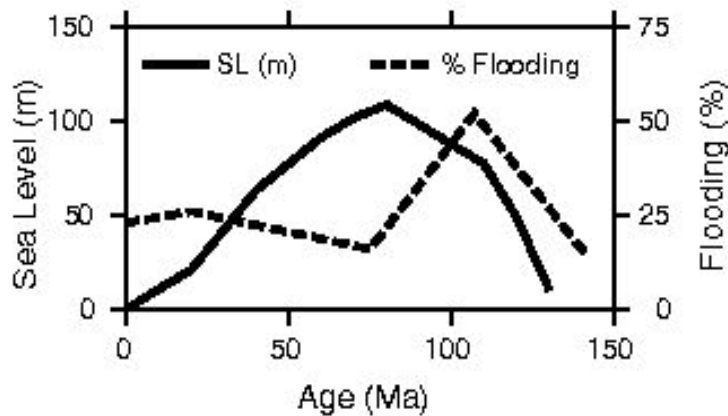


Figure 4.27: Eustatic (global) sea level (solid line) inferred from passive margins in the Atlantic ocean and the percent area of Australia above 200 m below present sea-level flooded. Note global sea level maximum at 80 Ma, and maximum flooding of eastern Australia before 100 Ma.

a fluid, the greater its resistance to flow by an applied force. Although the Earth's mantle is solid, with a sufficiently high viscosity it can be treated as a fluid over geological time scales. To give an impression of the relative magnitudes of the viscosities involved here, table 1 gives some typical values.

| Substance | Temperature (C) | Viscosity (Pa × s) |
|------------------|-----------------|----------------------|
| Water | 25 | $8.91 \cdot 10^{-4}$ |
| Glycerol | 25 | 0.85 |
| Andesitic basalt | 1, 150 | 8,000 |
| Motomura, Japan | 1, 200 | 3,120 |
| Motomura, Japan | 1, 400 | 12 |
| Lava, Vesuvius | 1, 100 | 2,830 |
| Lava, Vesuvius | 1, 200 | 276 |
| Lava, Vesuvius | 1, 400 | 26 |
| Mantle | | $10^{19} - 10^{22}$ |

Some viscosities with temperatures

As is evident from the above table, **viscosity is strongly temperature dependent - generally viscosity decreases exponentially with increasing temperature**. Also, the viscosities of the earth-like materials are very large, and this factor needs to be taken into consideration for the models to function efficiently.

Let's consider a fluid with temperature dependant viscosity and internal heating, much like the mantle. If the fluid is initially hot, its viscosity will be low, and it will rapidly convect away much of its excess heat. This will result in a temperature drop

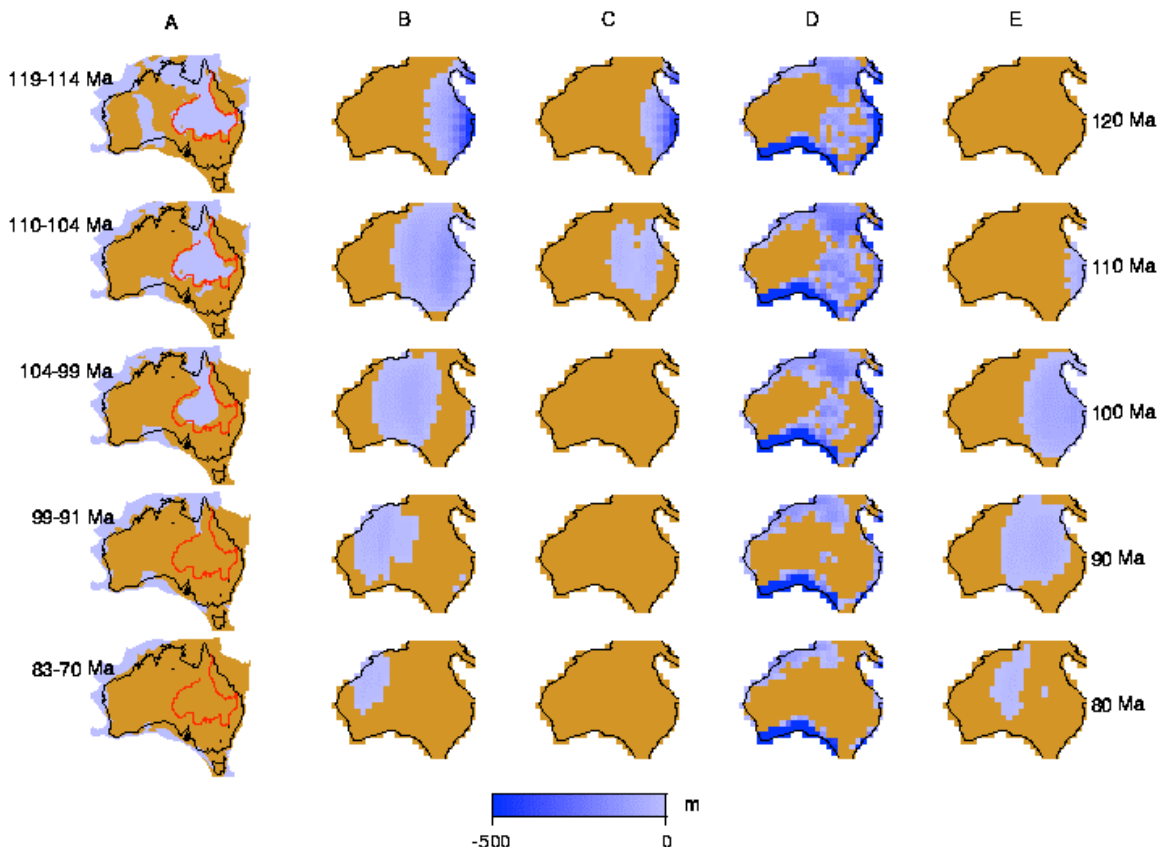


Figure 4.28: Paleogeographic reconstructions of Australia during the Cretaceous; light shading denotes marine inundation while medium shading denotes those parts of the continent that are subaerially exposed. The age ranges to the left only refer to the inferred paleogeographic reconstructions. B-E Predicted marine inundation of Australia from convection models. Ages to the right refer only to models. Areas with grey scale spanning from light to dark are those areas covered by shallow seas; medium shading denote those parts of the continent predicted to be exposed. A. Standard case with sedimentation rate of 5m/Myr; B. the same as A except 10M/Myr; C. model with a 90° dip angle, 5m/Myr; D. 30° dip angle and 2,400 km off the Australian margin with 5m/Myr.

in the fluid, which will subsequently reduce the viscosity. Thus the fluid will convect much more sluggishly, losing heat less efficiently, and will heat up due to its finite rate of internal heat production. Such a feedback mechanism complicates the behaviour of a system with temperature dependant viscosity. In order to understand planetary evolution and tectonics, we first need to investigate the primary features of different modes of convection, and investigate how analogies may be drawn between them and mantle convection in the Earth.

4.8.8.1 Isoviscous Convection

Shown below is a picture of simple isoviscous convection.

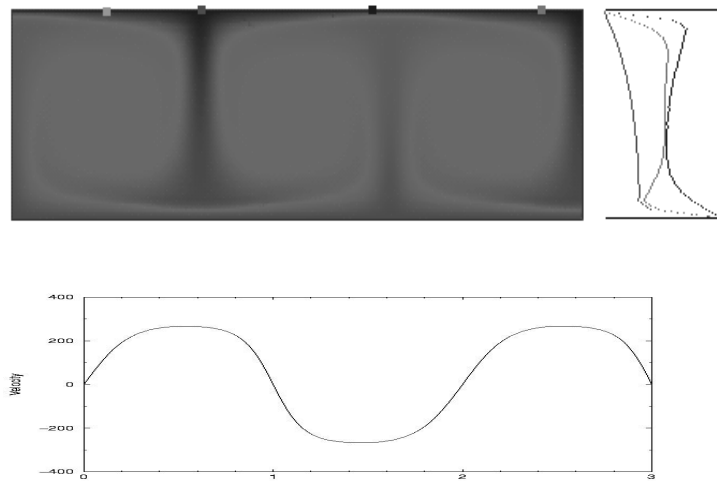


Figure 4.29: Constant Viscosity Convection (above) with normalised geotherms (right) and surface velocity (top). Colour is temperature, red is hot.

Constant viscosity convection constitutes the simplest form of convection. In this form it is essentially a form of free lid convection in that its upper thermal boundary layer participates in the convective overturn. This is a particularly efficient form of heat transport, and the mobilisation of its upper thermal boundary layer is an effect that dominates its heat flux behaviour. The surface velocity, however, is smoothly deforming. This is one point in which isoviscous convection differs from plate tectonics, where the surface moves as coherent units each with more or less uniform velocities.

A further difference is seen in the stress distribution. The uniform deformation of an isoviscous fluid in response to stress means that any applied stress is rapidly diffused away, and does not accumulate in the upper thermal boundary layer, whereas

rigid plates are able to indefinitely accommodate stresses below that required for plastic deformation.

4.8.8.2 Stagnant Lid Convection

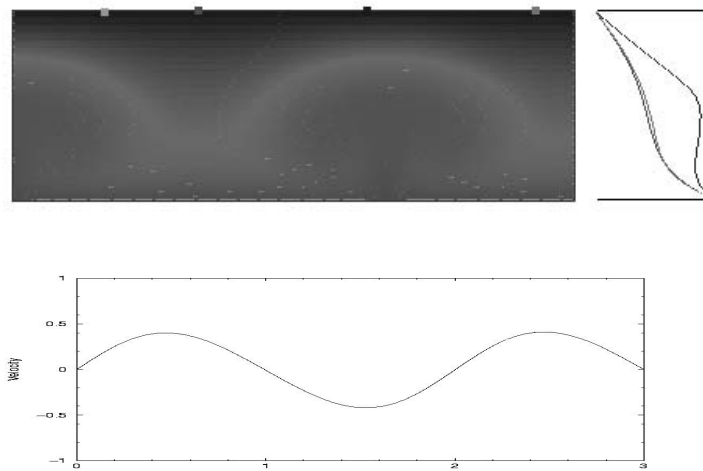


Figure 4.30: Stagnant Lid Convection with geotherms (right) and surface velocity (above).

Stagnant lid convection (Solomatov, 1995) is a form of convection commonly encountered in fluids with a strongly temperature dependant viscosity. Here the viscosity of the cool material near the surface is great enough that the upper thermal boundary can resist the convective stresses applied by the hotter, deeper convecting material. As a result it effectively becomes removed from the convection beneath, forming a rigid, stagnant lid. This mode of convection is shown below.

The stresses encountered in the stagnant lid are quite high, and its viscosity and strength must be substantial in order for the lid to remain immobile. Though incorporating a temperature dependant viscosity, stagnant lid convection is quite a poor model for mantle convection on Earth, as it essentially predicts no surface motion. However, it does seem to be **representative of mantle convection on the Moon, Mars and Mercury** (Solomatov and Moresi, 1997) Since its upper thermal boundary layer does not participate in the convective overturn, it is also quite an inefficient form of heat loss.

4.8.8.3 Mobile lid convection

Mobile lid convection is a term that effectively describes a form of convection consisting of a **temperature dependant viscosity**, and **yield stress** (Moresi and Solomatov, 1998).

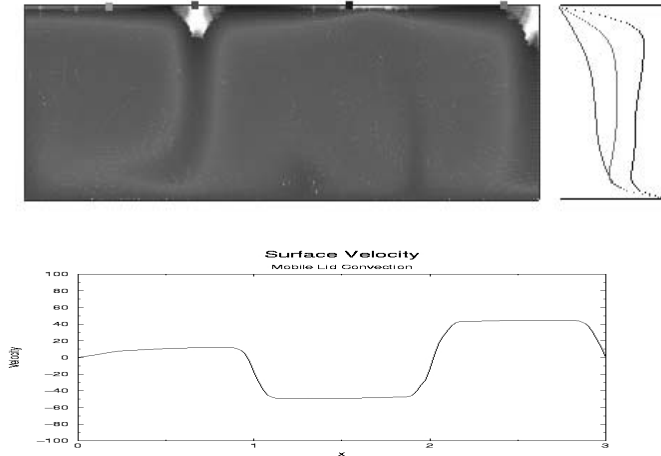


Figure 4.31: Mobile Lid Convection with geotherms (left) and surface velocities (above). Colour scale is temperature, red is hot; white represents strain.

In this way, the upper thermal boundary layer consists of a high viscosity, rigid layer, as in stagnant lid convection. However, the inclusion of plastic behaviour, in the form of a yield criterion, means that when high enough stresses are reached in the lid, it fails. This mobilises the lid, allowing it to participate in the convective overturn of the system. This is illustrated below.

The participation of the lid in convection results in heat flux behaviour quite similar to that encountered with isoviscous convection. The rigidity of the upper boundary layer means that large portions of it move as coherent units, with a velocity distribution essentially analogous to that expected for plate tectonics. The stress distributions seen in mobile lid convection are in principle analogous to that inferred for Earth's lithosphere, at least in the oceans. This combination of features makes mobile lid convection appealing as a model for plate tectonics on the Earth. Though it will always be impossible to encompass all the details in a computer simulation, in what are historically regarded as determinable features of plate tectonics, mobile lid convection is essentially accurate.

Chapter 5

Data Attributes and Signal Processing

Geophysical methods rely on the language of mathematics and physics to represent their data and results. The SI system is the international system of units that most geophysicists use. Depending on the magnitude of a particular value, prefixes are often attached to the SI units. Symbols from the Greek alphabet are frequently used.

5.1 Waves

Many geophysical methods involve the propagation of a wave through the earth. Seismic and electromagnetic waves are particularly important. Waves can take the form of a simple sine or cosine curve. Each wave has an amplitude which can vary with time.

Waves can also take the form of an impulse.

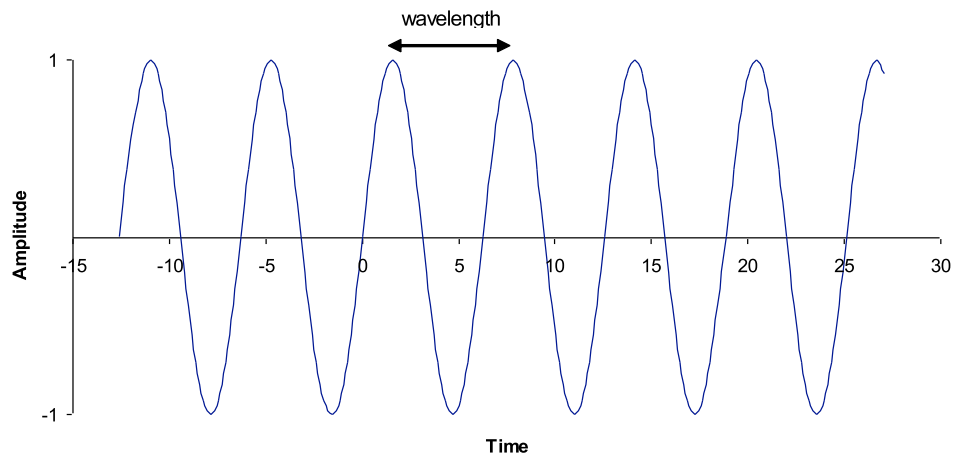
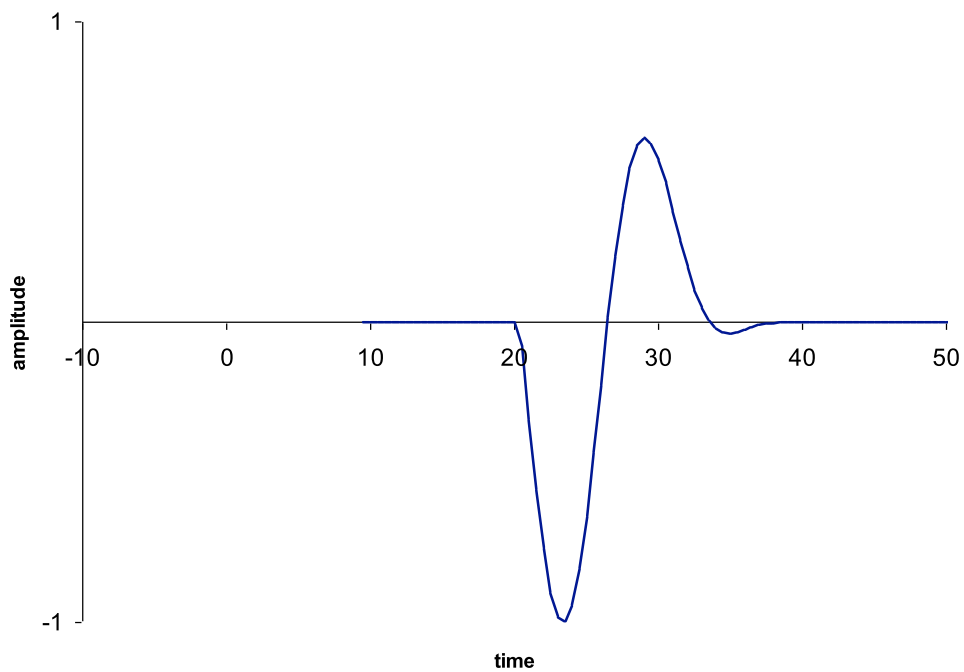


Figure 5.1: A wave based on a sine function



Basic science teaches the following key measures of wave properties:

- 1.) Velocity v , is the speed at which the wave travels.
- 2.) Wavelength λ , is the interval between peaks (cycles) in units of distance.

- 3.) Period τ , is the interval between peaks (cycles) in units of time.
- 4.) Frequency f , is the number of cycles per unit time.
- 5.) Phase, is a measure in degrees of how far the zero crossing is from the zero point in time (For example, a sine curve with a phase of -90 degrees is the same as a cosine curve.)

Equations:

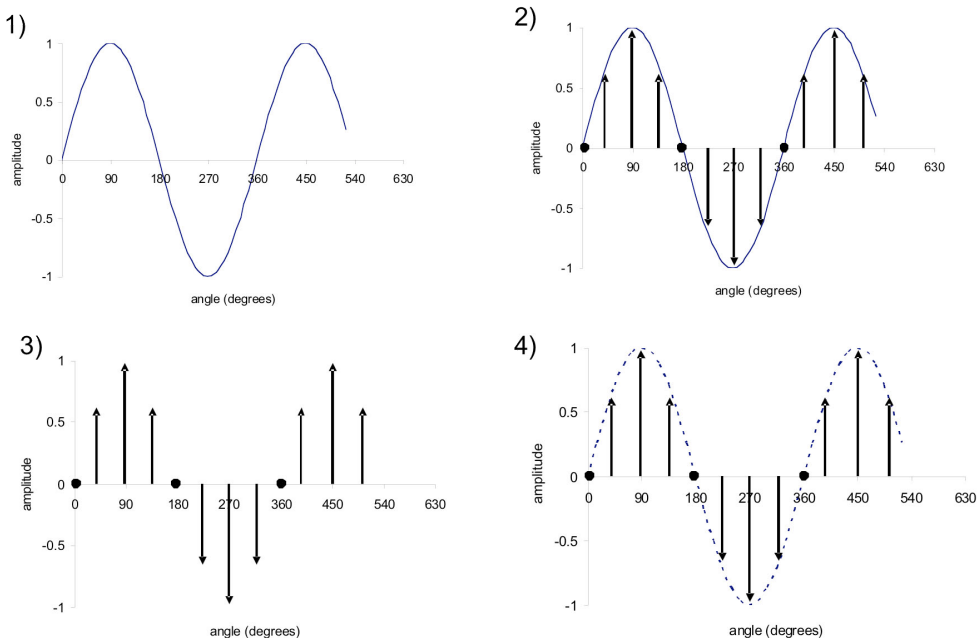
$$v = f\lambda \quad (5.1)$$

$$\tau = \frac{1}{f} \quad (5.2)$$

The concept that waves can travel through the earth is not difficult to appreciate and you will be learning about electromagnetic and seismic wave propagation in this course. However, the mathematical theory that is used to describe wave propagation is also useful for the general description and manipulation of any series of measurements we might choose to make. Terms such as signal, data series, waves and waveforms are often used interchangeably. Wave theory also underpins the mathematical representation of data for computing.

5.2 Digital representation of signals

From a simplistic point of view, a stream of data (a signal) that is stored on a computer is represented by a series of numbers representing the value of the signal at regular intervals.

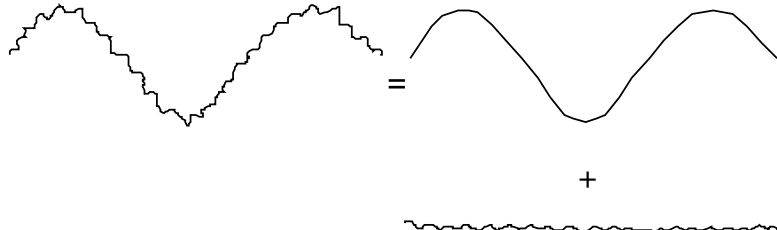


In this example, the continuous (or analogue) signal in representation 1 has been sampled at intervals of 45 degrees by measuring its amplitude at each point, representation 2. The computer stores the amplitudes and the sample intervals, representation 3. In the computer this stream of samples can be manipulated – for example multiplied by a constant. If we need to show the original analogue signal, it is a simple matter of drawing a line between the sample points, representation 4.

The question arises as to how many times an analogue signal needs to be sampled in order for the digital representation to properly express the true signal. One answer might be, “*as many as possible, given the storage capacity of our computer*”. Fortunately we can be more scientific in our approach to this question.

5.2.1 Convolution

Geophysical time series of data will typically contain both high-frequency, rapidly varying, and low-frequency, slowly varying components. Suppose the high frequency component is due to waves breaking at the surface or to engine noise from a ship, and the low frequency component is due to seismic waves being reflected from the deep Earth after being generated by an explosive source like an air gun. Then, conceptually, the observed data, consisting of a sequence of samples at equal time increments, is the sum of two time sequences which can be represented as the point by point sum of two graphs:



Here it seems reasonable to identify the high frequency component as noise, and the low frequency as signal, but the roles may be reversed. It is well known in geophysics that one person’s noise is another’s signal. To remove the high frequency portion, we can imagine a smoothing operation as appropriate. Smoothing can be done by taking local averages. We now introduce the idea of discrete transient convolution to perform the local averaging, which is a particular example of digital filtering.

To compute a local average of the data, one could take one third the sum of three values, one fifth the sum of five, one ninth the sum of nine, etc., and assign this average to be the middle time sample of the average. Various averaging sequences are shown, with the common trait that their sum is one.

Examples of averaging sequences:

$$\left(\frac{1}{4}, \frac{1}{2}, \frac{1}{4} \right); \left(\frac{1}{3}, \frac{1}{3}, \frac{1}{3} \right); \left(\frac{1}{5}, \frac{1}{5}, \frac{1}{5}, \frac{1}{5}, \frac{1}{5} \right)$$

Suppose we have a time series p_t , the subscript denoting discrete values of time at the sample intervals with uniform sampling in time. The result of the smoothing is a

new time series, say s_t (standing for smoothed). p_t and s_t are related by a digital filter equation such as:

$$s_t = p_t - \frac{p_{t-1}t}{3} + \frac{p_t}{3} + \frac{p_{t+1}}{3} \quad (5.3)$$

where it is understood that t takes on all integer values. The practical problem of a finite length series, and how to start the filter at the beginning of the series will be ignored for the moment. This result can be generated mechanically, by considering writing the filter as a set of numbers (whichever of the averaging filters is chosen) onto a strip of paper, cross-multiplying, adding, then sliding the strip of paper to the right by one sample (see below). This is discrete convolution which is written in a more compact form as

$$s_t = p_t * \left(\frac{1}{3}, \frac{1}{3}, \frac{1}{3}\right) \quad (5.4)$$

We may use either this convolution notation or the digital filter equation above. They mean exactly the same thing.

Discrete transient convolution is defined more generally for two time series of different lengths as

$$f_t * g_t = f_2, f_1, f_0 \rightarrow g_0, g_1, g_2 = f_0g_0, f_0g_1 + f_1g_0, \dots \quad (5.5)$$

Let f_t and g_t for $-\infty < t < \infty$ be two digital signals. Then their **convolution** is defined to be the digital signal

$$s_t = f_t * g_t = \sum_{k=-\infty}^{\infty} f_k g_{t-k} \quad (5.6)$$

Thus convolution is a sequence of three elementary operations. For fixed time-index t :

1.) time-reverse g_k :

$$g_{-k}$$

2.) delay g_{-k} by t -samples:

$$g_{-(k-t)} = g_{t-k}$$

3.) scalar product of f_k and g_{t-k} :

$$s_t = \sum_{k=-\infty}^{\infty} f_k g_{t-k}$$

In terms of the sliding strip of paper, the series which goes on the moving strip must be reversed. The reason for reversing one series is that the operation becomes commutative if this is done, so that either the filter or the time series could be written

on the moving strip, and we may then consider that the filter is being applied to the time series, or the time series is being applied to the filter, or in other words, the notion of which is data does not matter:

$$f_t * g_t = g_t * f_t$$

The effect of convolving two time sequences is to produce a new time sequence, of length $N + M - 1$, where N, M are the original series lengths (Fig. 5.2).

Example Let $x_t = (2, -1, 0, 1)$ and $y_t = (1, 2, 3)$.

| | | | | | | | | | | | | |
|---------|--|----|---|----|---|---|---|---|---|---|---|-------------------------|
| $t = 0$ | <table border="1" style="display: inline-table; vertical-align: middle;"> <tr><td></td><td>2</td><td>-1</td><td>0</td><td>1</td></tr> <tr><td>3</td><td>2</td><td>1</td><td></td><td></td></tr> </table> | | 2 | -1 | 0 | 1 | 3 | 2 | 1 | | | $c_0 = 2$ |
| | 2 | -1 | 0 | 1 | | | | | | | | |
| 3 | 2 | 1 | | | | | | | | | | |
| $t = 1$ | <table border="1" style="display: inline-table; vertical-align: middle;"> <tr><td></td><td>2</td><td>-1</td><td>0</td><td>1</td></tr> <tr><td>3</td><td>2</td><td>1</td><td></td><td></td></tr> </table> | | 2 | -1 | 0 | 1 | 3 | 2 | 1 | | | $c_1 = 4 - 1 = 3$ |
| | 2 | -1 | 0 | 1 | | | | | | | | |
| 3 | 2 | 1 | | | | | | | | | | |
| $t = 2$ | <table border="1" style="display: inline-table; vertical-align: middle;"> <tr><td></td><td>2</td><td>-1</td><td>0</td><td>1</td></tr> <tr><td>3</td><td>2</td><td>1</td><td></td><td></td></tr> </table> | | 2 | -1 | 0 | 1 | 3 | 2 | 1 | | | $c_2 = 6 - 2 + 0 = 4$ |
| | 2 | -1 | 0 | 1 | | | | | | | | |
| 3 | 2 | 1 | | | | | | | | | | |
| $t = 3$ | <table border="1" style="display: inline-table; vertical-align: middle;"> <tr><td></td><td>2</td><td>-1</td><td>0</td><td>1</td></tr> <tr><td>3</td><td>2</td><td>1</td><td></td><td></td></tr> </table> | | 2 | -1 | 0 | 1 | 3 | 2 | 1 | | | $c_3 = -3 + 0 + 1 = -2$ |
| | 2 | -1 | 0 | 1 | | | | | | | | |
| 3 | 2 | 1 | | | | | | | | | | |
| $t = 4$ | <table border="1" style="display: inline-table; vertical-align: middle;"> <tr><td></td><td>2</td><td>-1</td><td>0</td><td>1</td></tr> <tr><td></td><td>3</td><td>2</td><td>1</td><td></td></tr> </table> | | 2 | -1 | 0 | 1 | | 3 | 2 | 1 | | $c_4 = 0 + 2 = 2$ |
| | 2 | -1 | 0 | 1 | | | | | | | | |
| | 3 | 2 | 1 | | | | | | | | | |
| $t = 5$ | <table border="1" style="display: inline-table; vertical-align: middle;"> <tr><td></td><td>2</td><td>-1</td><td>0</td><td>1</td></tr> <tr><td></td><td></td><td>3</td><td>2</td><td>1</td></tr> </table> | | 2 | -1 | 0 | 1 | | | 3 | 2 | 1 | $c_5 = 3$ |
| | 2 | -1 | 0 | 1 | | | | | | | | |
| | | 3 | 2 | 1 | | | | | | | | |

Figure 5.2: Convolution of two time series

5.3 Numerical Transforms

5.3.1 The transform concept

Let's think of a function g_t , for example $e^{-\|t\|}$ on which some explicit operation \mathbf{F} is carried out, leading to another function $F\{g(t)\}$. We call the new function G , whereby G is a *transform* of the initial function g . The functional shape of G derives from the original shape of g and *not* from either value of the independent variable. This is an important difference from the concept of a "function of a function", e.g. the operation that converts

$$g(t) = e^{-\|t\|}$$

to

$$\sin(e^{-\|t\|})$$

Here each resulting value depends on only a single value of t , as opposed to the whole shape of g . With the Fourier transform, the operation \mathbf{F} is as follows:

Multiply the function $g(t)$ by $e^{2\pi ift}$ where f is the transform variable, and integrate with respect to t from $-\infty$ to ∞ .

Applying this operation to

$$g(t) = e^{-\|t\|}$$

we find that

$$F\{g(t)\} = 2/[1 + (2\pi f)^2]$$

, which is the Fourier transform of e^t . It is apparent that any particular value of $G(f)$, e.g. $G(2)$, which equals 0.0126, takes into account the whole range of t . In other words, **the value depends on the shape of g as a whole**, not on any single point, as it is the case in a “function of a function”.

For geophysical data processing, we will be mainly concerned with the Fourier transform. This mathematical representation underlies one of the most important developments in the theory of signal processing, and can be applied to acoustic data such as seismic data, potential field data such as gravity and magnetic data, as well as electrical data. In order to understand the Fourier transform, we will first have a look at the Fourier series.

This is because the transform variable f (frequency) of the Fourier transform has real physical meaning and allows us to represent signals from the time or space domain in the frequency domain. A famous result due to Fourier showed how any function of time (or space) could be represented as a sum of sines and cosines of different amplitudes and frequency.

Fourier analysed the temperature of a heated iron ring that had been thrust halfway into a fire. Figure 5.3 illustrates the problem.

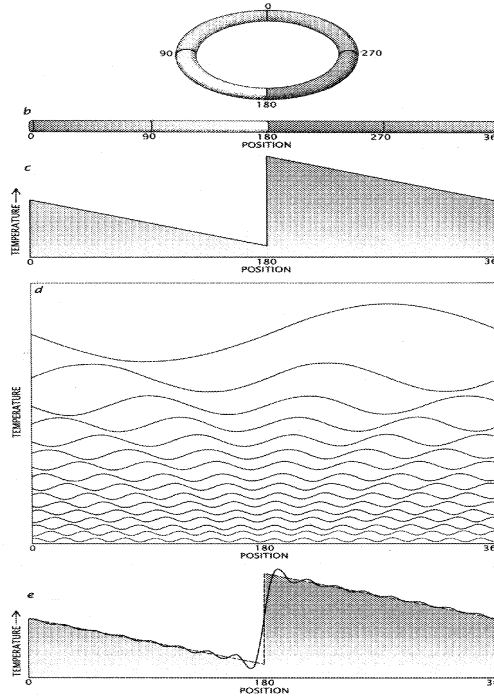


Figure 5.3: Temperature distribution of the iron ring (a), the temperature of the “uncoiled” ring (b), and plotted in a xy-diagram as temperature versus position (c). The temperature distribution is then decomposed into many sinusoidal curves having one, two, three or more cycles (d). When 16 of these curves are simply added together (solid line in (e)), they yield a good approximation of the original temperature distribution (broken line). From Bracewell (1999)

5.4 The Fourier series and finite Fourier series

Some good material on Fourier transforms can be found online, e.g. at Wolfram’s Mathworld: <http://mathworld.wolfram.com/FourierTransform.html>.

The Fourier series representation of a continuous function $g(t)$ defined on the interval $t \in [0, N]$ is:

$$g(t) = a_0 + \sum_{m=1}^{\infty} \left[a_m \cos\left(\frac{2\pi mt}{N}\right) + b_m \sin\left(\frac{2\pi mt}{N}\right) \right] \quad (5.7)$$

where

$$a_0 = \left(\frac{1}{N} \right) \int_0^N g(t) dt \quad (5.8)$$

$$a_m = \left(\frac{2}{N} \right) \int_0^N g(t) \cos \left(\frac{2\pi m t}{N} \right) dt \quad (5.9)$$

$$b_m = \left(\frac{2}{N} \right) \int_0^N g(t) \sin \left(\frac{2\pi m t}{N} \right) dt \quad (5.10)$$

The Fourier series represents a summation of sinusoids of different frequencies, as we introduced earlier under complex periodic functions. The subscript m is called the *harmonic number*. Each frequency is a harmonic (integer multiple) of the fundamental frequency, $\frac{1}{N}$, or one cycle per interval length, or, if N represents the length of a data record, then one cycle per record length. That is, an arbitrary function given on an interval of length N can be written as the summation of sinusoids at particular frequencies.

The implication of the summation to infinity is that an arbitrary continuous time function may contain infinitely high frequencies, corresponding to very rapid oscillations with respect to time. If $g(t)$ is the output of an instrument, or some experiment, then one usually finds that, if it magnified sufficiently, it is smooth, that is, it does not contain infinitely high frequencies, and is said to be *band limited*. This feature makes it possible to replace the continuous time function with discrete samples, as will be discussed later. For the moment, this band limited feature implies that representation in terms of a Fourier series does not require summation to infinity.

If only a finite number of terms in the summation are required, how do we find the exact number? In other words, how many terms are required to retain all of the information in the uniformly sampled data? The question may be answered by requiring that there be as many independent coefficients as there are data, since the number of data values is presumably the minimum number of independent quantities required

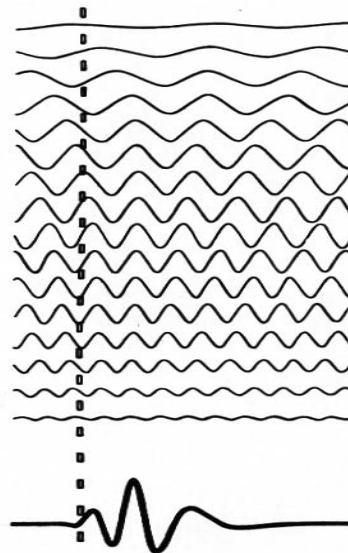


Figure 5.4: Spectral decomposition of a signal into sinusoids

to represent the continuous variation that was sampled. Thus for N samples of g , we have:

$$g_t = a_0 + \sum_{m=1}^{\frac{N}{2}} a_m \cos\left(\frac{2\pi mt}{N}\right) + b_m \sin\left(\frac{2\pi mt}{N}\right)$$

N must be an even number, and the last sine term (for $m = \frac{N}{2}$) is set to zero, i.e. $b_{\frac{N}{2}} = 0$. This leaves exactly N independent coefficients and is referred to as the *finite Fourier series*. In this series we can compute $\frac{N}{2}$ harmonics. The highest frequency in the sum corresponding to the limit $\frac{N}{2}$ is called the *Nyquist frequency*, equivalent to half the sampling frequency. Three data points, corresponding to twice the sampling period (or wavelength) is the minimum number of points to define a sine wave. The sampling interval h should equal half of the Nyquist period or wavelength, or in other words the sampling frequency should be twice the Nyquist frequency:

$$h = \frac{1}{2f_c}$$

and

$$f_s = 2f_c$$

where h is the sampling interval; f_s is the sampling frequency and f_c is the Nyquist (or critical) frequency.

Hence the wavelength of the Nyquist frequency is $2h$, where $2h$ is the distance between successive observations. If the data spacing is 1 (in arbitrary units), then the wavelength is $\frac{2}{N}$. The determination of the coefficients of the finite Fourier series can no longer be done with the integrals, since the data are discrete, but may be obtained by an analogous summation over the data:

$$a_0 = \left(\frac{1}{N}\right) \sum_{t=0}^{N-1} g_t \quad (5.11)$$

$$a_m = \left(\frac{2}{N}\right) \sum_{t=0}^{N-1} g_t \cos\left(\frac{2\pi mt}{N}\right) \quad (5.12)$$

$$b_m = \left(\frac{2}{N}\right) \sum_{t=0}^{N-1} g_t \sin\left(\frac{2\pi mt}{N}\right) \quad (5.13)$$

These equations are directly verifiable in the sense that one can show that for each t value, the coefficients will reproduce the data value g_t . It can be shown that this gives the coefficients of the sinusoid which are best in a least squares sense. That is, each sine

or cosine is the best fit function of that frequency that passes through the data points in the sense that the sum of the squared error is minimized:

$$\text{Squarederror} = \sum_{t=0}^{N-1} \left(g_t - a_m \cos \left(\frac{2\pi m t}{N} \right) \right)^2$$

5.4.1 Complex notation

We will now introduce the expression of Fourier series as complex sinusoids via the exponential function, instead of using real valued sinusoids. Complex quantities make operations easier and notation simpler. All the discussion could be handled with real valued quantities, but with the expense of cumbersome and extensive algebra.

The starting point for dealing with complex sinusoids is the *DeMoivre relationship*:

$$\exp(i2\pi ft) = \cos(2\pi ft) + i \sin(2\pi ft) \quad (5.14)$$

where i is the square root of -1, and $f = m/N$ is a (temporal) frequency in Hertz (Hz; cycles per second). Related quantities are the period $T = 1/f$ and the angular frequency $\omega = 2\pi f$. If we have the variable x instead of t , where x refers to spatial distance in meters, then the wavelength λ in the space domain substitutes the period T in the time domain. The frequency in the space domain is measured in units of cycles per meter, and is called the spatial frequency. The parallel quantity to the angular frequency is the wavenumber $k = \frac{1}{2\pi\lambda}$.

The complex sinusoid $\cos(2\pi ft) + i \sin(2\pi ft)$ are now numbers in the complex plane and correspond to a rotating unit vector pointing in the direction corresponding to the angle in the exponent, measured counterclockwise with respect to the real axis. The familiar real valued cosine function is the horizontal component, or projection onto the x-axis of the rotating unit vector; the sin function is the projection onto the y-axis.

It is often convenient to think of complex sinusoids as vectors since there is a one-to-one correspondence between vectors and points in the complex plane, and addition of complex numbers may be performed as with vector summation. The use of complex sinusoids is also natural in describing certain geophysical processes that involve motion in a plane. One example is the description of 2-dimensional particle motion, especially surface waves, like Rayleigh waves, where the motion tends to be retrograde near the surface, turning to prograde at depth. Another example is the motion of the Earth's rotation axis (wobble), which is a rotation in one direction. In each physical example there is a one to one correspondence between the data plane and the complex plane, and that there is a clear distinction between positive frequency (counter clockwise) and negative frequency (clockwise) motion, making it convenient to use complex exponentials.

5.4.2 Amplitude and phase

The Fourier transform yields pairs of imaginary and complex numbers, whose amplitude we can plot separately:

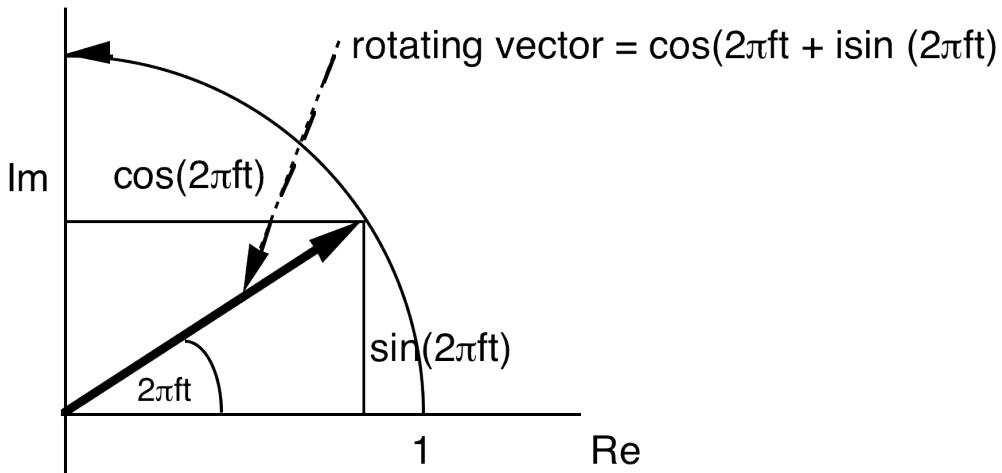


Figure 5.5: Some caption

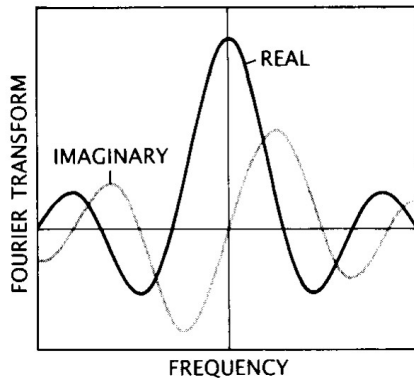


Figure 5.6: caption

From the imaginary and real parts of the signal, the Fourier amplitude and the phase can be calculated and plotted:

The Fourier amplitude is the square root of the sum of the squares of the real and imaginary parts (see above)

$$\text{Modulus} = \sqrt{\text{real}^2 + \text{imag}^2}$$

The Fourier phase angle is the arc tangent of the imaginary part divided by the real part:

$$\text{Phase} = \tan^{-1} \left(\frac{\text{imag}}{\text{real}} \right)$$

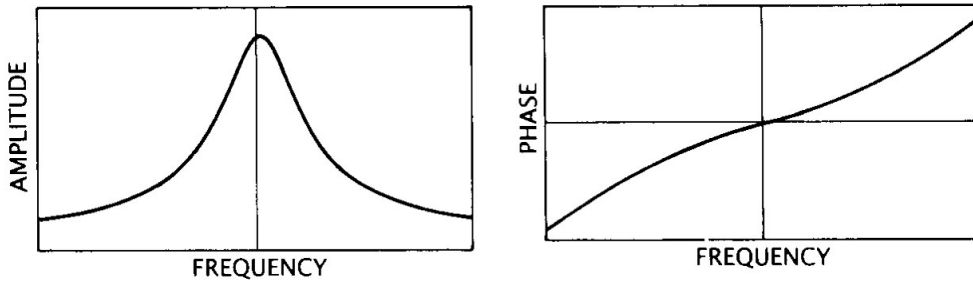


Figure 5.7: caption

To emphasise the concept of phase, consider the motion of a spring, yielding a sinusoidal curve (figure below is from Yilmaz (1987)). The peak amplitude represents the maximum displacement of the weight at the end of the spring (positive motion plotted upwards). The time between the two consecutive peaks is the period of the sinusoid, the inverse of which is the frequency. The time delay of the onset of one spring relative to another is defined as a phase-lag. In the figure below, sinusoids 1) and 3) are distinguished only by their difference in phase (their modulus is identical).

5.5 Autocorrelation, cross-correlation and convolution

These three operations are similar. The cross-correlation of two signals $f(t)$ and $g(t)$ is defined as:

$$\phi_{xy}(t) = \sum_k f_k g_{k+t}$$

The following example shows how to calculate the cross-correlation:

The cross-correlation therefore is the series (2, 3, 4, -2, 2, 3)

Think about what is happening here, of the two signals have some common elements, at the times, t , when those elements match, the process of the multiplication and addition will be constructive and the cross-correlation at that time will have a relatively large value. Elsewhere, there will be positive and negative products adding together and these will tend to cancel each other out. Cross-correlation, therefore, is a process that allows a measure of the degree of similarity or correlation between two signals.

The autocorrelation is the same as the cross correlation except that the signal is cross-correlated against itself.

$$\phi_{xx}(t) = \sum_k f_k f_{k+t}$$

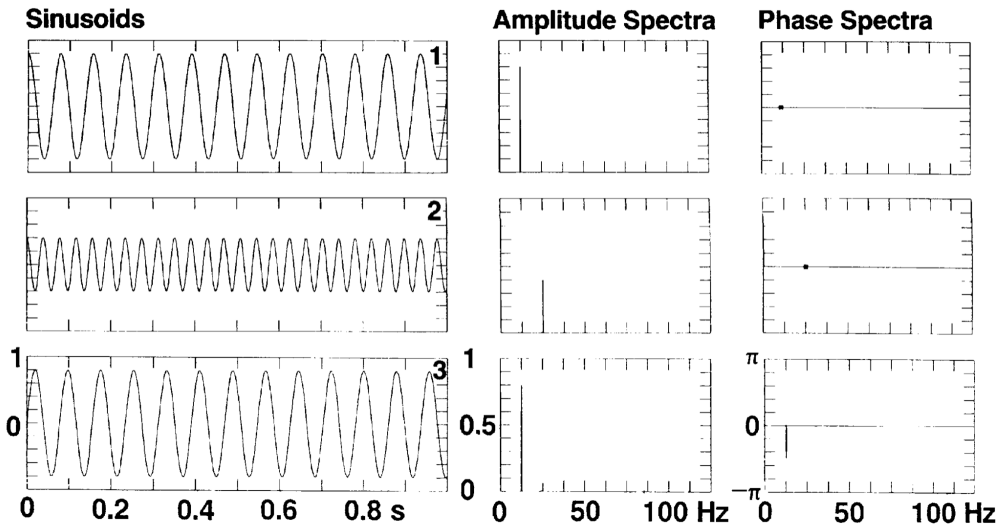


Figure 5.8: The peak amplitude represents the maximum displacement of the weight at the end of the spring (positive motion plotted upwards). The time between the two consecutive peaks is the period of the sinusoid, the inverse of which is the frequency. The time delay of the onset of one spring relative to another is defined as a phase-lag. Here, sinusoids 1) and 3) are distinguished only by their difference in phase (their modulus is identical). From Yilmaz (1987)

By undertaking an autocorrelation, it is possible to determine whether a signal contains repetitions of certain components. At the times that these line up during the multiplication and adding, the autocorrelation function will be larger.

Convolution is similar to the cross-correlation except that the second series goes through the multiplication and adding phase in the reverse direction.

$$s_t = f_t * g_t = \sum_k f_k g_{t-k}$$

The symbol $*$ is used to indicate convolution.

In the above example of cross-correlation, the convolution of these two signals would follow the same steps except the function $g(t)$ would be passed through in the reverse order i.e. as (the series (1, 2, 3)). Alternatively the example can be seen as the convolution of two signals:

(2, -1, 0, 1) and (1, 2, 3)

It turns out that the convolution of two signals has important physical meaning. If two signals are multiplied together in one domain e.g. the frequency domain, they can be convolved in another e.g. the time domain. Look at the example of the high pass filtering we discussed above. The filtering is being undertaken as a multiplication in the frequency domain (the amplitude spectrum of the filter multiplied by the frequency filter). If we wanted to perform this filtering operation in the original time domain, then

Example Let $x_t = (2, -1, 0, 1)$ and $y_t = (3, 2, 1)$

| | | |
|---------|--|-------------------------|
| $t = 0$ | $\begin{array}{ c c c c } \hline & 2 & -1 & 0 & 1 \\ \hline 3 & 2 & 1 & & \\ \hline \end{array}$ | $c_0 = 2$ |
| $t = 1$ | $\begin{array}{ c c c c } \hline & 2 & -1 & 0 & 1 \\ \hline & 3 & 2 & 1 & \\ \hline \end{array}$ | $c_1 = 4 - 1 = 3$ |
| $t = 2$ | $\begin{array}{ c c c c } \hline & 2 & -1 & 0 & 1 \\ \hline 3 & 2 & 1 & & \\ \hline \end{array}$ | $c_2 = 6 - 2 + 0 = 4$ |
| $t = 3$ | $\begin{array}{ c c c c } \hline & 2 & -1 & 0 & 1 \\ \hline & 3 & 2 & 1 & \\ \hline \end{array}$ | $c_3 = -3 + 0 + 1 = -2$ |
| $t = 4$ | $\begin{array}{ c c c c } \hline & 2 & -1 & 0 & 1 \\ \hline & 3 & 2 & 1 & \\ \hline \end{array}$ | $c_4 = 0 + 2 = 2$ |
| $t = 5$ | $\begin{array}{ c c c c } \hline & 2 & -1 & 0 & 1 \\ \hline & 3 & 2 & 1 & \\ \hline \end{array}$ | $c_5 = 3$ |

Figure 5.9: Calculating cross correlation

we would have to convolve the original signal with the transform of the frequency filter into the time domain.

Herein lies one of the very important aspects of signal processing. Some mathematical operations are much easier to achieve after they have been transformed into an alternate domain. In the case of frequency filtering which is a component of most geophysical data analysis, it is best to transform the original data into the frequency domain and perform the operation there. The data is then transformed back into its original domain. One of the breakthroughs in early computing was the development of a computationally efficient algorithm known as the *Fast Fourier Transform* (FFT). Prior to the development of the FFT it was almost a toss-up as to whether it was better to do frequency filtering by laborious convolution rather than go through a length process of converting the signal into and back from the frequency domain.

5.5.1 Frequency filtering

Through our discussion of the issues in digital sampling, we have introduced the Fourier transform and the idea that a signal in the time (or space) domain can also be represented in the frequency domain where the amplitude spectrum represents the amplitudes of the various sinusoids which are summed together to produce the original signal and the phase spectrum represents the phases of the sinusoids.

One of the advantages of representing a signal in the frequency domain is that it is possible to perform filtering tasks that can reduce the amount of noise present in our signal.

In making geophysical measurements, noise is the enemy. Through our everyday experiences, we all know about noise and how it is hard to identify and analyse a signal when the level of background noise is high. For example, it is hard to hear a quietly spoke friend in a noisy coffee shop. In the parlance of the geophysicist, the signal to noise ratio is very poor. In geophysical measurement and analysis we are always looking for ways to improve the signal to noise ratio. One way of achieving this is through frequency filtering.

Consider the case of an orchestral piece. Overall, the music has sounds which are low in frequency (from the base instruments) and sounds which are high in frequency (from violins, flutes etc.). If we wanted just to hear the high frequency parts of the piece, a frequency filter which chops out the low frequency parts of the overall signal would do the trick.

In geophysics, we can do the same. Figure 5.10 shows a signal transformed into the frequency domain. Its low frequency components are then removed by (set to zero) by multiplying the amplitude spectrum by a high pass filter. The signal is then transformed back to the time domain. Notice now how the signal appears to have much higher frequency (shorter period) behaviour.

There are various types of frequency filters that we can construct – high pass filters, low pass filters, band pass filters (filters which remove both high and low components outside of the required frequency bands) and notch filters (filters designed to remove a narrow band of frequencies – e.g. 50 Hz signals induced by nearby power lines)

When applying filters, it is necessary to taper the cut-offs of the filters. If the cut-off is too steep, undesirable ringing is introduced into the signal. Notice also that in our example we didn't have to do anything to the phase spectrum. The filtering can achieve its objective by acting on the amplitude spectrum alone.

5.5.2 Two-dimensional Fourier transform

To this point, we have been discussing the use of the Fourier transform to transform a single data series into the frequency domain and to undertake frequency filtering in that domain. What can we do if we have multiple data series as might be the case in the following example which shows a radar image formed by radar signals reflecting off subsurface boundaries as the radar measurement system is moved across the ground surface. In the vertical direction, reflections off various features in the subsurface are evident. These features change laterally along the ground surface. The radar image varies in two-dimensions.

One thing we can do with this image is to apply a frequency filter to the signals recorded at each position on the ground surface. The effect of a high pass filter cutting out all signals with frequencies below 10 MHz and tapering down from 40 MHz is illustrated below.

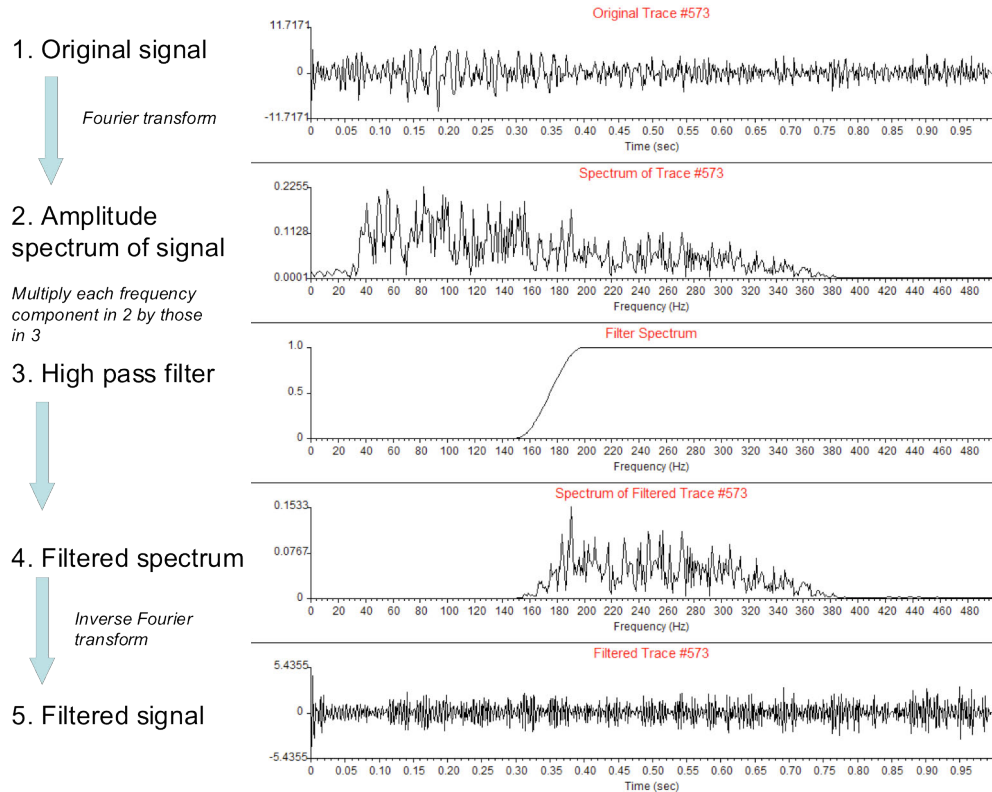


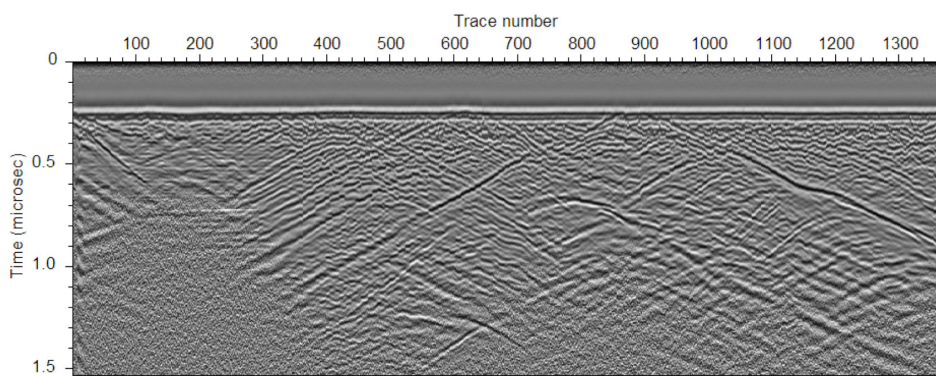
Figure 5.10: Frequency filtering of a signal.

With a two-dimensional Fourier transform the radar image is simultaneously transformed from the time and spatial domain. The result is given in the f-k domain (where k is wavenumber ($1/\lambda$) which is the spatial equivalent to the frequency domain).

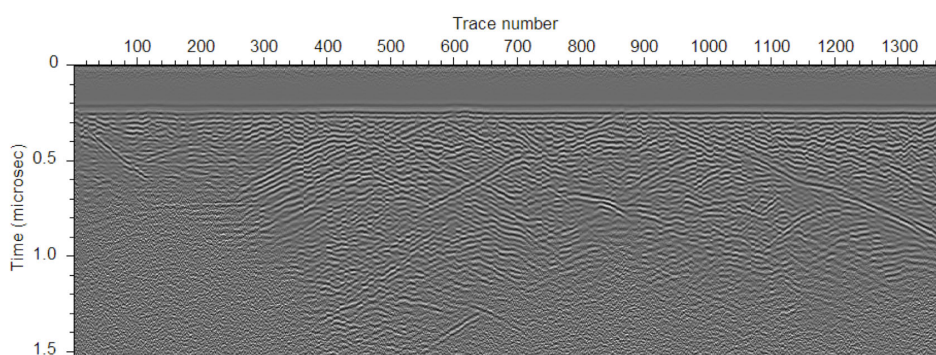
An important property of the results shown in the f-k domain is that the dip of features away from the origin indicates the slope of events in the original 2D data set. Horizontal events are dipping at 90 degrees, while vertical events are horizontal (no dip). Filtering in the f-k domain by zeroing out an appropriate section of the data has the effect of removing dipping components of the original 2D signal.

The filtering undertaken here is designed to remove horizontal events and negatively dipping events from the original radar result.

With 2D Fourier transforms and 2D filtering, the sampling of the signal across the ground surface is an issue. Just as samples are required every at half period of the highest frequency component present, spatial sampling (measurements) are required at intervals closer than every half wavelength of the spatial components present.



(a) Original data



(b) Transformed data

Figure 5.11: (a) First filtering result. (b) high pass filter

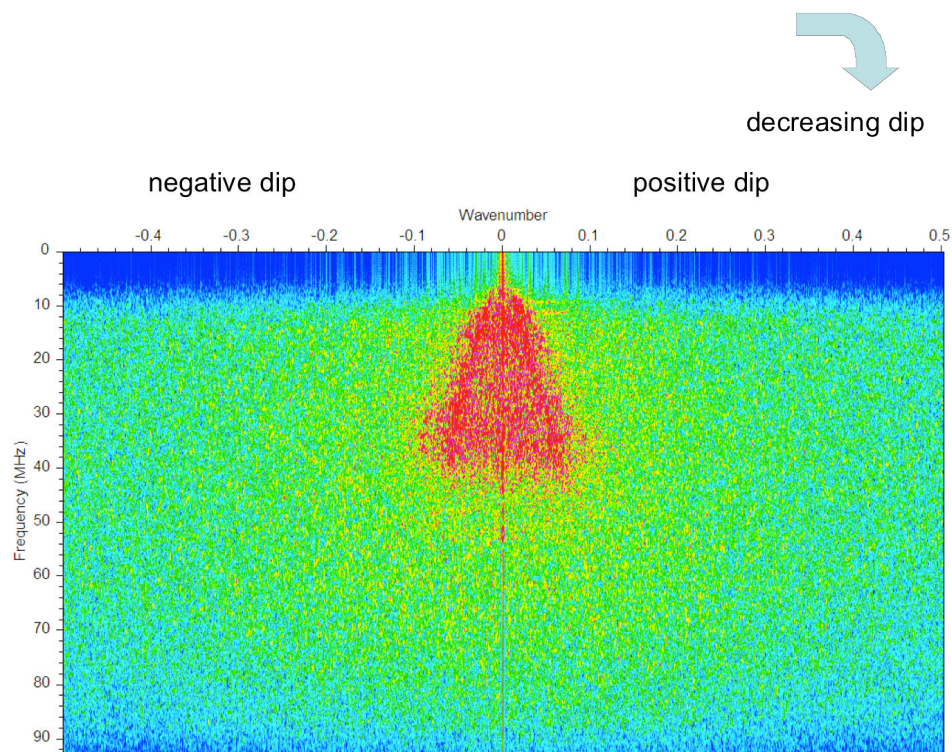


Figure 5.12: Image f-k domain filtered

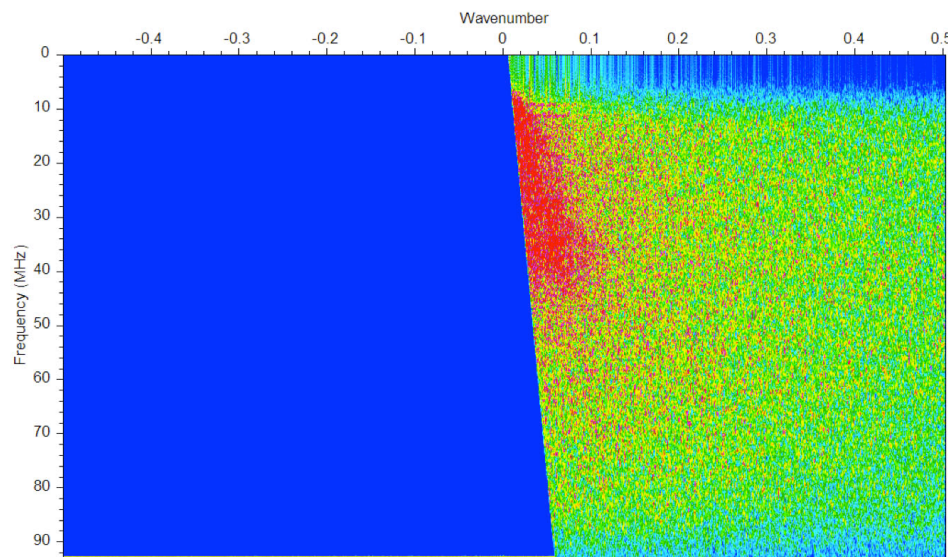


Figure 5.13: F-k domain, now filtered

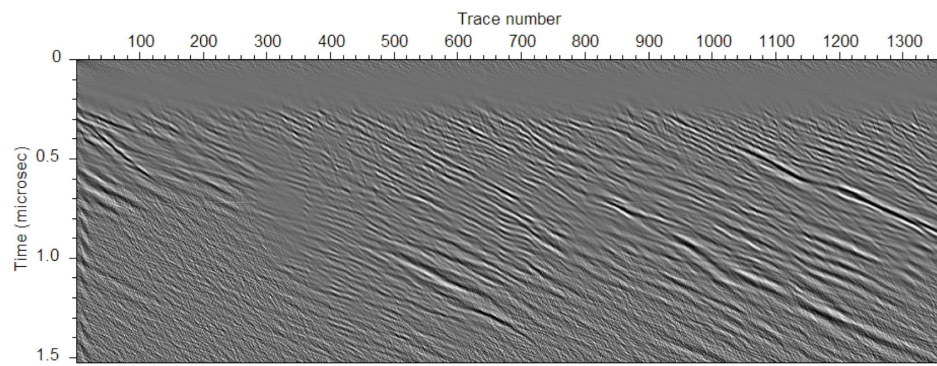


Figure 5.14: Final result

Chapter 6

Lithosphere, Asthenosphere, and Plates: definitions

Before we start discussing the geodynamics of the outer shell of the Earth, we first have to introduce some terms related to the layering of the Earth, to minimise the confusion that might arise otherwise.

6.1 Lithosphere

The idea of a lithosphere, representing a strong, outer layer of the Earth, overlying a weak asthenosphere, was first introduced by Barrell (1914), long before the realisation that the outer shell of the Earth forms a thermal boundary layer of a convecting system.

The rise of plate kinematic theory led to the view that mid-ocean ridges may be associated with a cold, strong boundary layer, and that trenches were sites where boundary layers became detached from the surface, being recycled back into the Earth's mantle (McKenzie, 1970). This approach led to some of the first successful attempts to create relatively simplistic, linear models for mantle convection (e.g. McKenzie et al., 1973), which agreed remarkably well with observations of bathymetry and heat flow from the ocean basins (Sclater and Francheteau, 1970; Sclater et al., 1971).

The realisation of how plate tectonics works has led to a natural definition of the lithosphere as a thermal boundary layer:

The oceanic lithosphere is the outer shell of the Earth where there is a conductive temperature gradient, overlying the well mixed adiabatic interior.

In other words, the bottom boundary of the oceanic lithosphere is the depth to a constant isotherm (McKenzie and Bickle, 1988), which is usually modelled to be in the range between 1250°C and 1350°C. These temperatures corresponds to a depth of about 10-125 km for ocean floor, depending on its age. The oceanic lithosphere is thinnest at the mid-ocean ridges, where new mid-ocean ridge basalts (MORB) are created by rising asthenosphere, which chills and solidifies upon contact with seawater.

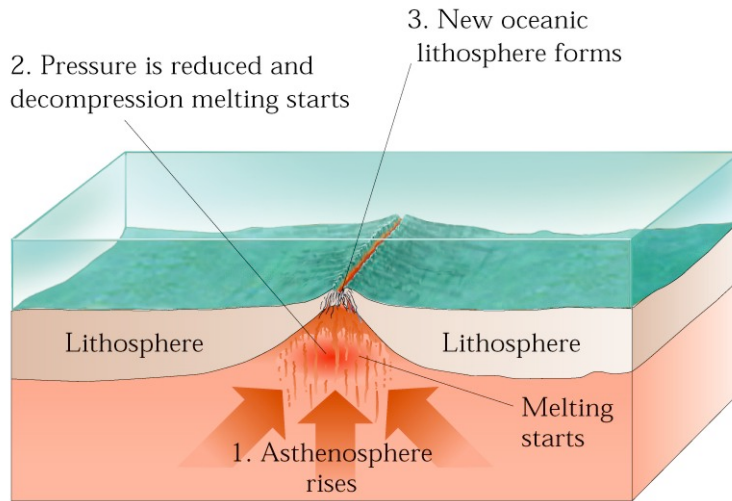


Figure 6.1: Oceanic lithospheric cross-section. At a spreading center, where two tectonic plates are moving apart, the asthenosphere rises into the fracture; pressure is reduced and melting begins; and the emerging lava chills and solidifies to form new oceanic crust

The oceanic lithosphere as defined above corresponds to the **thermal lithosphere**. The thermal lithosphere includes the crust, as well as a portion of the upper mantle. Opinions among Earth scientists diverge as to whether the thermal lithosphere should represent the lithosphere or not, since the lower part of the thermal lithosphere may deform in a ductile fashion over geological time periods, thus lacking the mechanical "strength" in Barrell (1914) definition of the lithosphere. The boundary between lithosphere and asthenosphere (see below) is characterised by a transition zone referred to as the **lower thermal boundary layer**. This layer is regarded as part of the lithosphere, but may be partly recycled over long time spans by small scale convection. Hence the lowermost part of the thermal lithosphere is not part of the "plate" which moves coherently as a mechanical unit (see Figure below).

Estimates of the thickness and basal temperature of the lithosphere have been determined from studies of the variation in heat flow and bathymetry with age in ocean basins. Oceanic subsidence curves do not continue to decay asymptotically, but flatten due to the addition of heat at the base of the lithosphere. Parsons and Sclater (1977) developed a model, which describes this additional heat. For oceanic lithosphere, they calculated a thickness of 125 km, and a basal temperature of 1333°C. Although oceanic lithosphere shows a direct relationship between age, heatflow and bathymetry (subsidence), continental lithosphere is much more variable and no close correlation between these parameters is observed.

Seismic velocities as a function of depth

The above definition of the lithosphere based on thermal arguments is not equal to the **seismic lithosphere** (usually referred to as LID). The LID is a seismic high-velocity

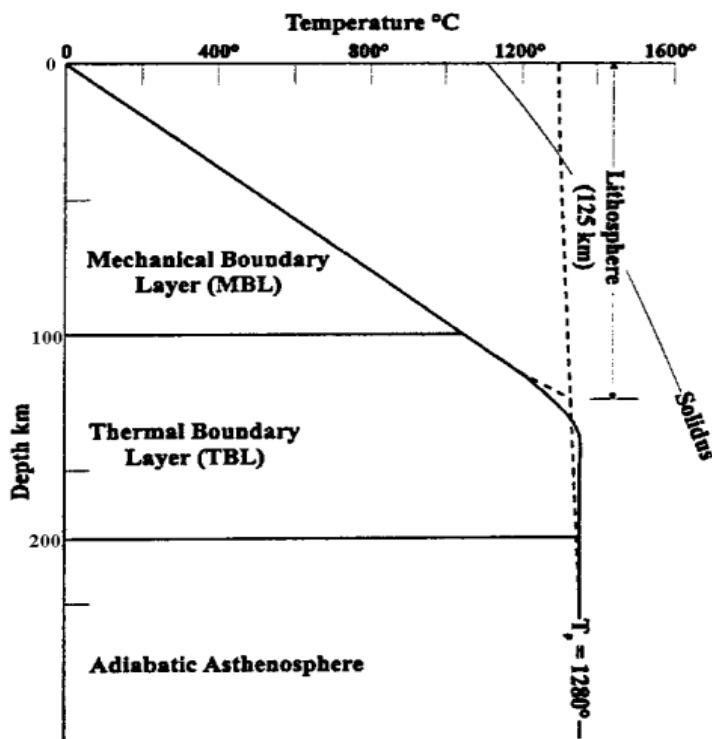


Figure 6.2: Definitions of boundaries within the oceanic lithosphere (after McKenzie and Bickle, 1988). The solid line shows a geotherm of old ocean crust for a potential temperature in the mantle of 1280°, a thickness of the mechanical boundary layer of 100 km and a viscosity of $2 \times 10^{17} \text{ m}^2\text{s}^{-1}$. The corresponding adiabatic upwelling curve (for the mid-ocean ridge) is shown dashed. The elevation of the ridge axis above the surface of the old plate is controlled by the area between the geotherm and the dashed line. The lithospheric thickness is obtained by calculating a depth on the adiabatic geotherm with the same area. The lower boundary of the lithosphere defined this way is within the convecting region, which episodically becomes unstable and is replaced by hotter mantle material. The term “potential temperature” refers to the temperature a fluid mass would have if it were compressed or expanded to some constant reference pressure (usually the pressure at the Earth’s surface).

region at the top of the mantle, which overlies a low-velocity zone (LVZ). The bottom of the LID is characterised by an abrupt decrease in shear-wave velocities, typically at depths between 150-200 km under the continents and at depths of about 10-50 km under the ocean floor, depending on its age (Regan and Anderson, 1984). It corresponds roughly to the 600° isotherm in the oceans, which approximates the **effective elastic plate thickness**, i.e. the core of the lithosphere which reacts to loads and deformation as an elastic sheet.

For continents lithospheric thickness typically ranges from 100-200 km. Old, cratonic lithosphere may possess a lithospheric thickness of up to 400 km (Jordan, 1975). This is

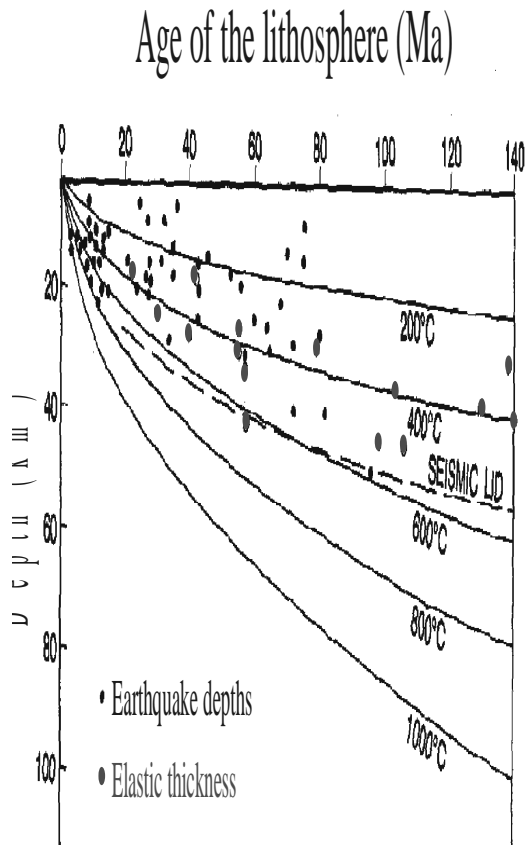


Figure 6.3: Depth of isotherms of the oceanic thermal boundary layer as a function of oceanic crustal age, the depth of the seismic LID, the effective elastic plate thickness (open circles) and the depths of Earthquakes modified from Anderson (1995).

because they form a **chemical lithosphere**.

The chemical lithosphere forms, because there is a secular evolution from Mg-rich low-density Archean mantle to denser Phanerozoic mantle; the most significant differences are between the Archean and Proterozoic mantle. The compositional variations produce differences in the density and elastic properties of lithospheric mantle of different age. Archean and Proterozoic mantle roots are highly buoyant; they cannot be delaminated back into the mantle, but require mechanical disaggregation (lithospheric thinning and/or rifting) and infiltration of upwelling fertile material to be destroyed or transformed. If such disaggregation does not occur, the chemically stabilized lithosphere can survive for long times (forever?). In contrast, Phanerozoic subcontinental

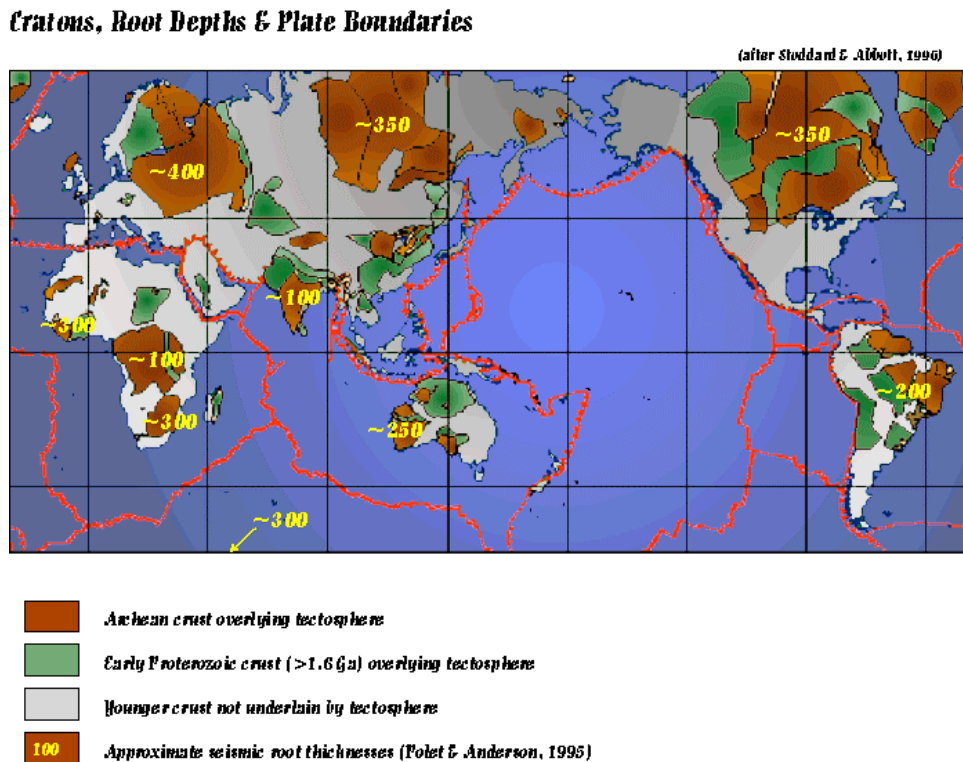


Figure 6.4: Global distribution of continental cratons, and their approximate thickness

lithospheric mantle is denser than the asthenosphere for observed thicknesses (100 km) and can “delaminate” under stress. (O'Reilly, 2001).

6.2 Asthenosphere

In the Earth density and seismic velocities increase with pressure and decrease with temperature. Within the outer shell of the Earth density and velocity decreases with depth due to the large temperature gradient, until the gradual increase in pressure starts to outweigh the increase in temperatures, thus causing an increase in velocity and density. Before pressure starts to dominate, mantle material becomes weak, partially molten, forming the asthenosphere. The asthenosphere contains a few percent partial melt because the geotherm in this depth interval intersects the melting curve, but the geotherm is at lower temperatures than the melting curve at deeper and shallower depths.

The asthenosphere is a weak zone in the upper mantle, underlying the lithosphere. It is often equated with the seismic LVZ, which is characterized by a high velocity gradient, but varies substantially laterally. It is assumed that mid-ocean ridge basalts originate in the asthenosphere. Processes that may contribute to the weakness of the as-

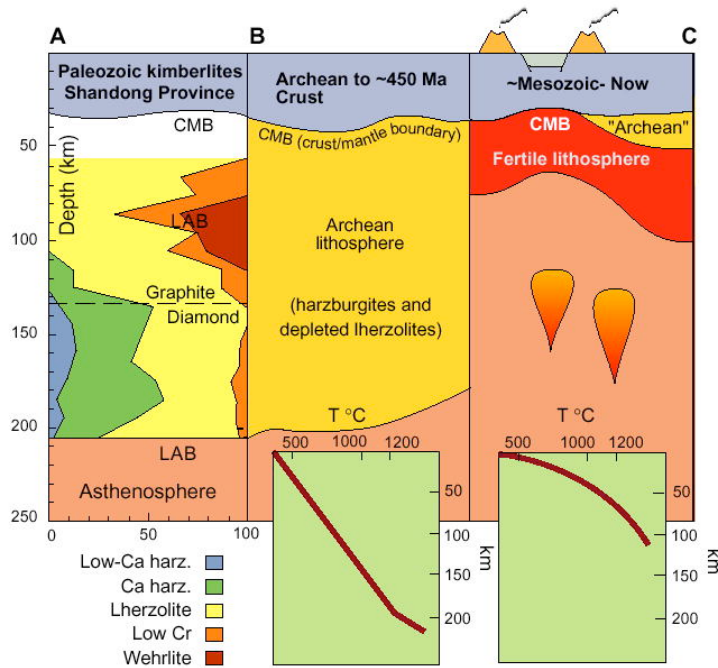


Figure 6.5: Continental lithospheric sections showing relative abundances of different rock types in depth slices through continental lithosphere (Griffin et al., 1999).

thenosphere include a phase change, such as dehydration or partial melting, a change in composition of mineralogy, an increase in stress or dislocation density, and a very rapid increase of the temperature gradient (Anderson, 1995).

6.3 The Plate

The plate is defined based on mechanical and rheological arguments:

The plate is that part of the outer shell of the Earth which moves coherently as a rigid body without significant internal deformation over geological timescales.

Plates correspond to the **mechanical (or rheological) lithosphere**. The elastic plate thickness is usually smaller than the mechanical plate thickness. The rotation of plates can be described by **Euler poles** (discussed later). The lower part of the plate may deform anelastically in a ductile manner on geological time scales due to high stresses or temperature gradients, but nevertheless remain attached to a tectonic plate without large scale relative horizontal motions.

The plate is not equal to the thermal lithosphere. The main difference is that the thermal lithosphere includes a lower thermal boundary layer, whereas the plate excludes this layer, since it is not a permanent part of the tectonic plate. The lower boundary of the plate is a mechanical boundary layer. The coupling between the asthenosphere and

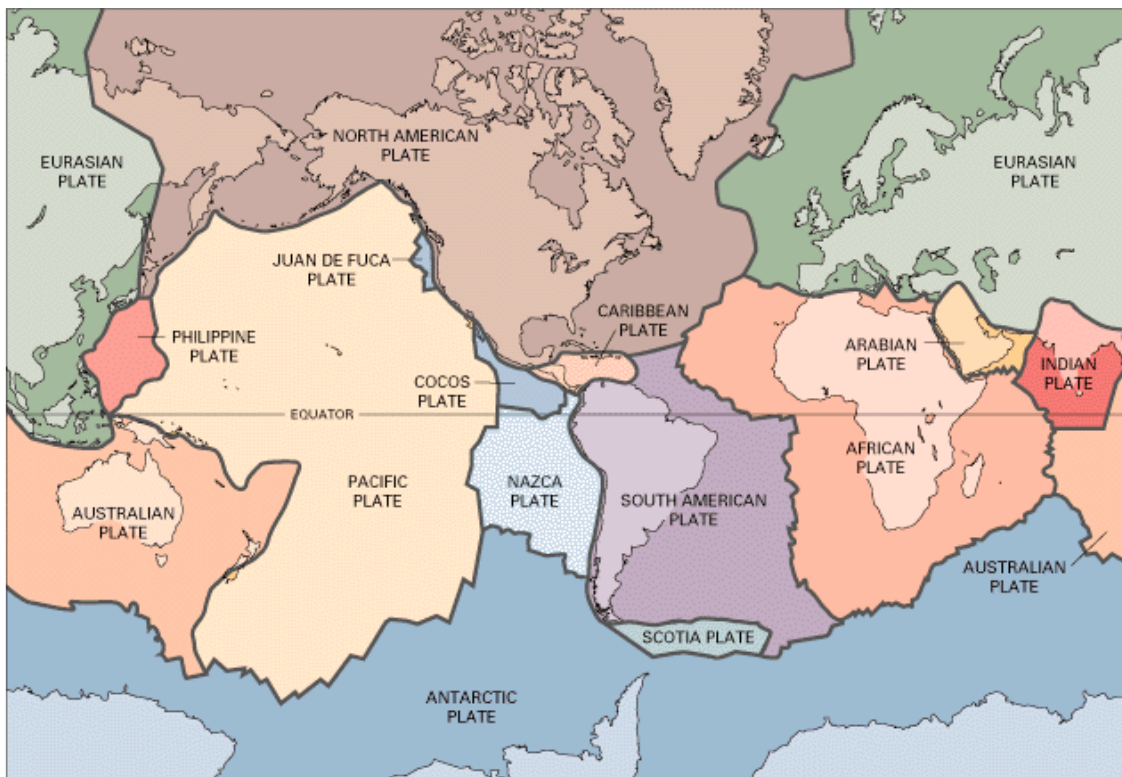


Figure 6.6: Main tectonic plates

the plate is probably weak, but some shear coupling may occur, whereby the moving plates would induce horizontal motion in the asthenosphere.

The **plate tectonic hypothesis** suggests that the surface of the Earth is composed of an interlocking set of internally rigid plates in constant motion. These plates are rigid except at plate boundaries which are lines between contiguous plates. The relative motion between plates gives rise to Earthquakes. These Earthquakes define plate boundaries.

In subduction zones, earthquake foci vary from shallow, near the trench, to deep, farther away from the trench in the direction of plate subduction. This sketch (below) shows earthquakes that occurred beneath the Tonga Trench in the placePacific Ocean, over a period of several months. Earthquakes in this region are generated by the downward movement of the Pacific Plate. Zones of shallow-to-deep earthquakes like this one, called Benioff zones, first alerted scientists to the existence of subduction zones. Most of the deep earthquakes form by phase transitions within the subducting slab, likely by a mechanism termed “anticrack failure” (see below), whereas shallow quakes form by brittle failure of rocks.

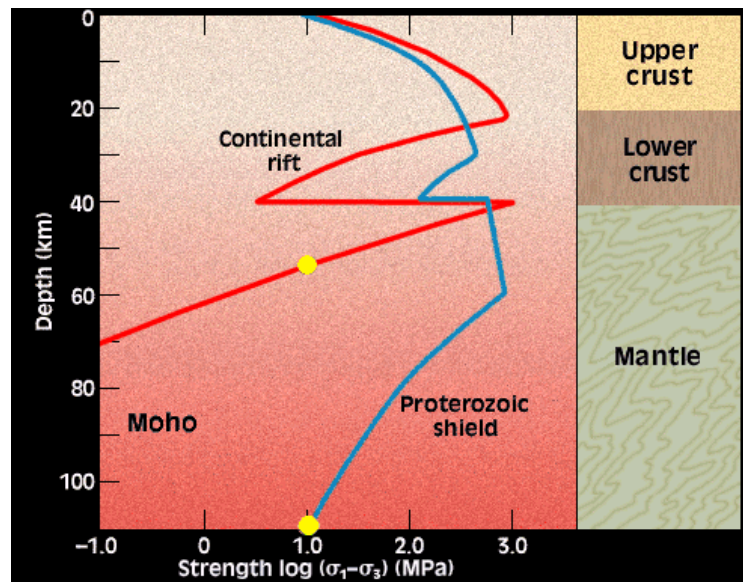


Figure 6.7: Rheology of young (rift) versus old (shield) tectonic plates. Young and old refers to the most recent “thermal event” in this case. Dot marks lower boundary of plate

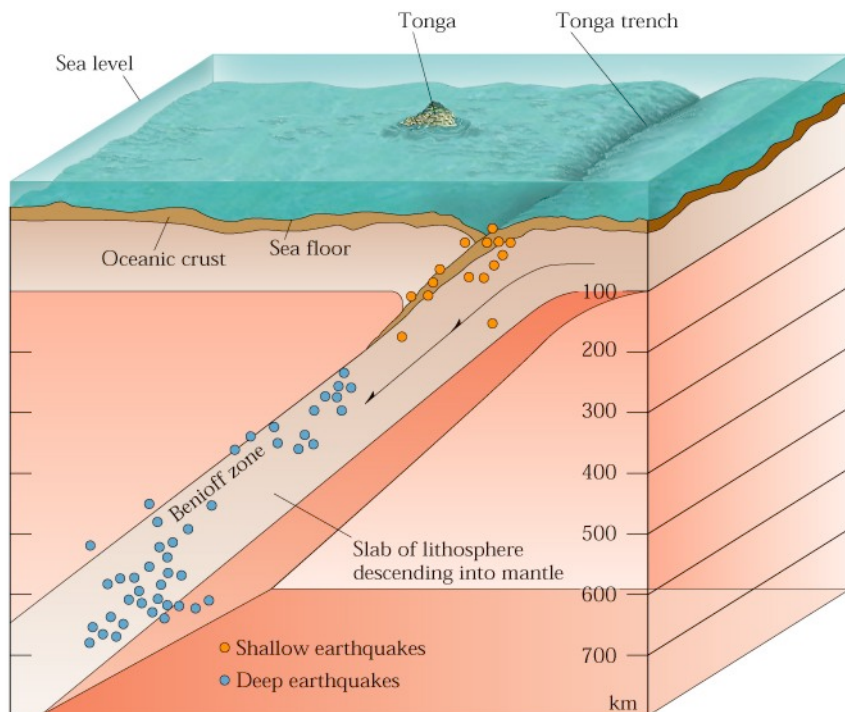


Figure 6.8: Schematic cross-section of a subduction zone

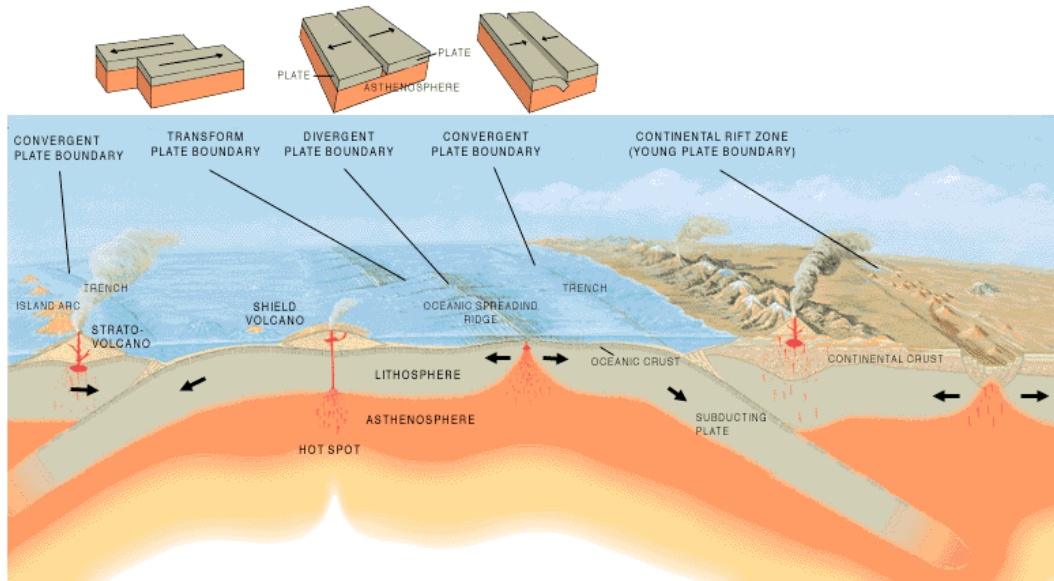
6.4 Plate boundaries

There are three types of plate boundaries:

Divergent boundaries – where new crust is generated as the plates diverge.

Convergent boundaries – where crust is destroyed as one plate dives under another.

Transform boundaries – where crust is neither produced nor destroyed as the plates slide horizontally past each other.



6.5 Plate tectonic concepts

Plate tectonic theory is based on three assumptions:

Continuity of plate boundaries

All plate boundaries are continuous and interconnected. Morgan (1968) separated the world into 10 plates. Today, we know that the actual number of plates is much larger. All major plates are surrounded by spreading centers, subduction zones, and transform faults. However, some plate boundaries are diffuse, i.e. they are broad rather than distinct, resulting in a breakdown of the classical plate tectonic concept. Most diffuse plate boundaries form in continental lithosphere, as it is much weaker than oceanic lithosphere.

Relative motion

All plates can be viewed as rigid caps on the surface of a sphere: the motion of a plate can be described by a rotation about a virtual axis which passes through the center of the sphere (Euler's Theorem). In terms of the Earth this implies that motions of plates can be described by an **angular velocity vector** originating at the center of the globe. The most widespread parametrization of such a vector is using latitude, longitude, describing the location where the rotation axis cuts the surface of the Earth,

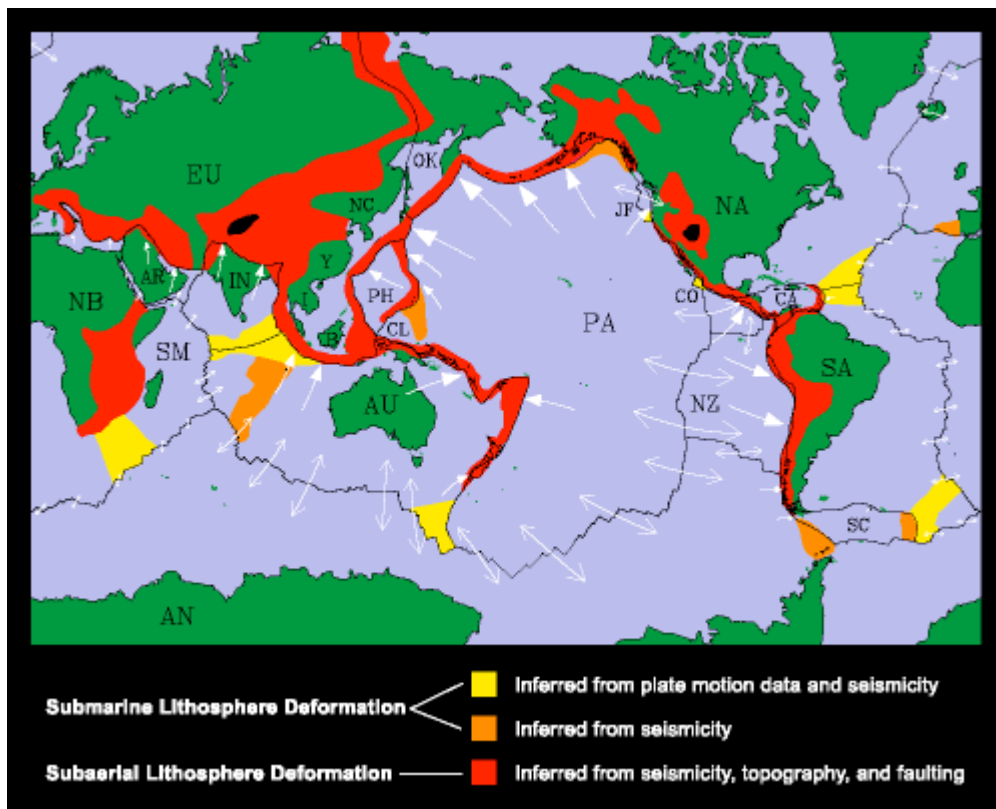


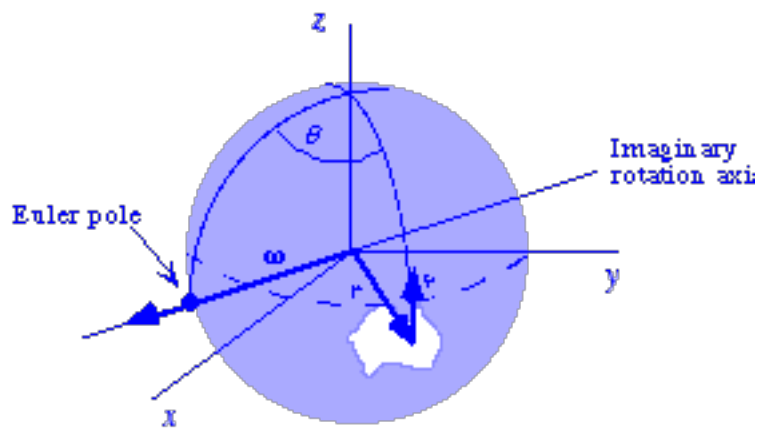
Figure 6.9: Global plate boundaries, including broad, diffuse boundaries, and present day plate motion vectors

and a rotation rate that corresponds to the magnitude of the angular velocity (degrees per m.y. or microradians per year). The latitude and longitude of the angular velocity vector are called the **“Euler pole”**.

Because angular velocities behave as vectors, the motion of a plate can be expressed as a rotation $\mathbf{w} = w \mathbf{k}$, where \mathbf{w} is the angular velocity, \mathbf{k} is a unit vector along the rotation axis, w the rotation rate. The motion of individual plates can be described by an **absolute motion angular velocity**. The motion between two plates, which have different absolute motion poles, can be expressed by an **angular velocity of relative motion**. Plate tectonic theory was developed by determining relative motion between plates, which - in general - is easier to measure than their absolute motions.

Rigidity

The concept of internal rigidity of tectonic plates together with Euler’s Theorem allows us to model the relative motion of plates quantitatively.



Chapter 7

Modelling Lithospheric Deformation and Mantle Convection Dynamically

In order to understand the characteristics of a convecting fluid, it is first necessary to briefly outline the relevant descriptive equations that govern its behaviour. The following provides a framework for the physical processes fundamental to modeling plate tectonics.

7.1 Dimensional analysis and mathematical framework

Most numerical approaches used for modeling geodynamics adopt several assumptions in order to simplify the flow equations to solve. Among them, the effects of elasticity and compressibility are at a first order neglected, eventually added later as a perturbation of the fluid-dynamic solution. Material properties are assumed to be embedded in an effective viscosity $\mu_{\text{eff}}(T, C)$ function of temperature, composition, etc., which defines the relationship between the gradient of velocity and σ , the viscous stress tensor

$$\sigma = -ptI + \mu_{\text{eff}}(T, C) (\nabla u + \nabla^t u) = -ptI + \mu_{\text{eff}}(T, C)\dot{\epsilon} \quad (7.1)$$

The Stokes equations comprise the momentum conservation and incompressibility condition

$$\nabla \cdot \sigma + \rho b = 0 \quad (7.2)$$

$$\nabla \cdot u = 0 \quad (7.3)$$

where b are the body forces. These two equations are coupled to the energy equation

$$\rho C_p \dot{T} = \nabla(\kappa(T, C) \nabla T) + \psi \sigma : \dot{\epsilon} + r + q \quad (7.4)$$

where $\kappa(T, C)$ is the diffusion coefficient, ψ is the fraction of shear heating transformed in heat, r represents inner sources, as radioactivity or sinks, and q surface heat effects.

Therefore the homogenous problem is often employed for extracting general informations, e.g. upper and lower bounds for the system to understand, but a detailed full solution of every realistic model of geophysical fluid-dynamics systems (mantle convection, magma migration, etc) requires the intense use of numerical methods.

7.2 Rayleigh Number

Among the number that expresses the quality of an iso-viscous geo-fluid-dynamic system, the Rayleigh number is probably the most employed, as it indicates whether a fluid layer, either heated from below or from inside, will convect or less and which form the convection will take. It is however very important to keep in mind that this number only denote the behaviour of a system where viscosity doesn't change from one point to the other in the system, i.e. where material properties are homogenous, which is normally not the case in geodynamics. So it must be taken only as a general indicator.

For a system heated from inside (radiogenic heating, in general), the Rayleigh number is:

$$Ra = \frac{g\rho^2\beta HD^5}{\mu\alpha\kappa}$$

Where β is the thermal expansion, α is thermal diffusivity and κ is the thermal conductivity and H the heat rate emission per volume. Notice the 5th power of D , the thickness of the layer. For a system heated from below, instead, the Rayleigh number is:

$$Ra = \frac{g\rho\beta\Delta TD^3}{\mu\kappa}$$

Where ΔT is the temperature difference between the upper and lower plate boundaries of the layer. Notice now the 3th power of the thickness of the layer D . One of the first considerations is the extreme dependency of the Ra number from the thickness of the system. For the mantle, for example, keeping constant all the other variables, the Ra for the entire mantle would be proportional to $(3000 \text{ km})^3$ or $(3000 \text{ km})^5$, depending on which heating system is predominant, while for the upper mantle only it is proportional to $(650 \text{ km})^3$ $(650 \text{ km})^5$. So the ratio between the Ra of the two systems is $(3000/650)^3 \approx 100$ up to $(3000/650)^5 \approx 2000$. Because the critical Ra for the onset of convection is around 1000 and the convective behaviour of a layered systems

is entirely different for Ra of 1-2 orders of magnitude higher, it is clear that the understanding whether the mantle convection is separated in layers or less is of fundamental importance for predicting its dynamic behaviour.

7.3 Viscosity

The viscosity of the mantle is a complicated function of temperature, pressure, strain, strain rate and grain size, of which few are independent parameters. Thus the mechanisms of deformation at depth in the earth are still poorly constrained (Karato and Wu, 1993). Nonetheless, it is generally accepted that the temperature dependence of viscosity is probably the dominant factor controlling mantle flow within the Earth (Christensen, 1984; Moresi and Solomatov, 1998). The temperature dependence of viscosity is of an Arrhenius form, which for diffusion creep can be written as

$$\mu = b \cdot e^{Q/RT}$$

For the large viscosity contrasts inferred for planetary interiors, the above relationship can be decomposed into an exponential function, known as the Frank-Kamenetskii approximation (Frank-Kamene "etiskiæi, 1969). This is of the form

$$\mu = \mu_i e^{-g(T-T_i)}$$

where $\mu_i = b \exp(Q/RT_i)$ is the viscosity of the interior, and $g = Q/RT_i^2$. Since here the total viscosity contrast of the system is of primary interest, it is sensible to express the viscosity as

$$\mu = \mu_o e^{-gT}$$

where $\mu_o = \mu_i e^{gT_i}$ is the surface viscosity.

7.4 Brittle Failure

To simulate brittle lithospheric failure, a non-linear viscosity is employed to model plastic deformation. The yield criterion are defined by Byerlee's frictional law (Byerlee and Brace, 1968):

$$\tau S_0 + \mu(\sigma_n - P_f)$$

where τ_{yield} is the yield stress, μ is the coefficient of friction, and P is the pressure.

7.5 Strain Weakening

The longevity of faults as zones of weakness in the Earth's lithosphere suggests that the application of strain weakening in addition to the above brittle failure is essential to

modelling large-scale lithospheric dynamics. In this way, pre-existing zones of weakness are preferentially utilised and reactivated during deformation as opposed to the fracturing of competent rock and the creation of a new zone of weakness.

The inclusion of strain weakening in a model can be achieved by employing a modified yield stress of the form

$$\tau_y = (\tau_0 + \tau_1 \cdot z) \cdot f$$

where $f(\epsilon) = 1 - (1 - E_a)(\epsilon/\epsilon_0)^n$ for $(\epsilon < \epsilon_0)$, where ϵ_0 is a critical strain and $E_a = \tau_y(\epsilon = \inf)/\tau_y(\epsilon = 0)$. At strains greater than or equal to ϵ_0 , the yield stress is given by: $\tau_y = (\tau_0 + \tau_1 \cdot z) \cdot E_a$.

7.6 Mechanics of Deformation and Model Formulation

7.6.1 Rheology of Oceanic and Continental Lithosphere

The rheology of oceanic lithosphere is fairly well understood. Though it is dependent on both temperature and pressure, its reasonably uniform lithology and structural simplicity mean that an oceanic lithospheric strength profile, like that shown below.

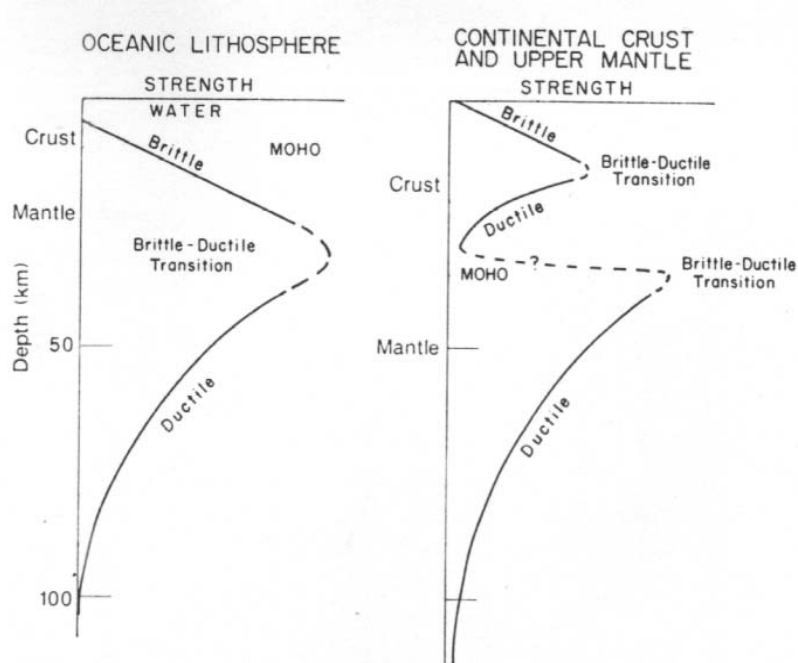


Figure 7.1: Oceanic and Continental Rheological Profiles (from Molnar, 1988).

The continents, on the other hand, are generally both lithologically and structurally complex. This inherent non-linearity in continental rheological profiles means that any

rheological model will inevitably simplify reality. Nonetheless, the broad features of continental rheology can be understood in terms of a stratified model, incorporating a reasonably strong, brittle upper crust above a weaker, ductile lower crust, and an underlying strong lithospheric mantle.

Despite their differences, one of the most important mechanisms of deformation for both oceanic and continental lithosphere is brittle failure. One way of simulating brittle effects is by plastic flow, where the lithosphere will accommodate stresses until a yield stress is reached. Once this yield stress is exceeded, the lithosphere will deform plastically.

7.6.2 Stresses in the Lithosphere

In order to assess the magnitude of stresses reached in the lithosphere, and subsequently to estimate the yield stress required to mobilise it, it is first necessary to explore the stresses encountered in the stagnant lid regime. In this case, a temperature-dependant viscosity without yield behaviour was used. The Figure below demonstrates the typically large near-surface stresses encountered in the stagnant lid regime for a variety of Rayleigh numbers.



Figure 7.2: Typical Stress Profiles for Stagnant Lid Convection.

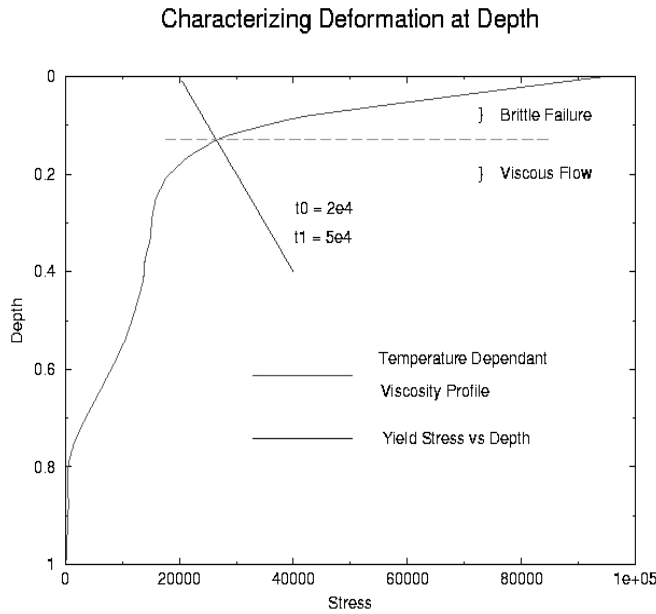


Figure 7.3: Stagnant lid profiles against depth-dependant yield stress.

To mobilise the lithosphere requires the employment of a yield stress to simulate the strength envelopes. This yield stress can be expressed as a non-dimensional function of depth. .

Another complexity is that due to the appreciably higher surface stresses encountered in the stagnant lid regime, the yield stresses required to mobilise a stagnant lid can be quite large. However, a comparable mobile-lid regime will exhibit much lower surface stresses, and requires, at a given depth, a much lower yield stress to keep maintain mobility relative to the stagnant lid model. As a result, there exists a transitional regime between mobile lid convection and stagnant lid convection descriptively labelled episodic overturn (Moresi and Solomatov, 1998). In this regime, as a stagnant lid develops, the surface stresses increase until they surpass the yield stress. At this point, there is a catastrophic failure of the lithosphere which is recycled into the mantle in a pulse of mobile-lid convection. However, as the surface stresses produced by this mobile mode are much smaller than the yield stress, the large viscosities at the surface result again in the development of a stagnant lid.

7.6.3 Mobilisation of the Lithosphere

At low values of yield stress, it is possible to mobilise indefinitely the upper boundary layer of a convecting system with temperature dependant viscosity. An example of idealized stress profiles associated with mobile lid convection is shown in the Figure below. In this stylised example, designed to elucidate the mechanisms of failure with depth in the mobile-lid regime, the observed stresses approach the yield stress throughout the depth of the thermal boundary layer. The zones of failure typically produced by this mode of deformation define the boundaries of coherent, rigid “plates” which move with more or less uniform velocities.

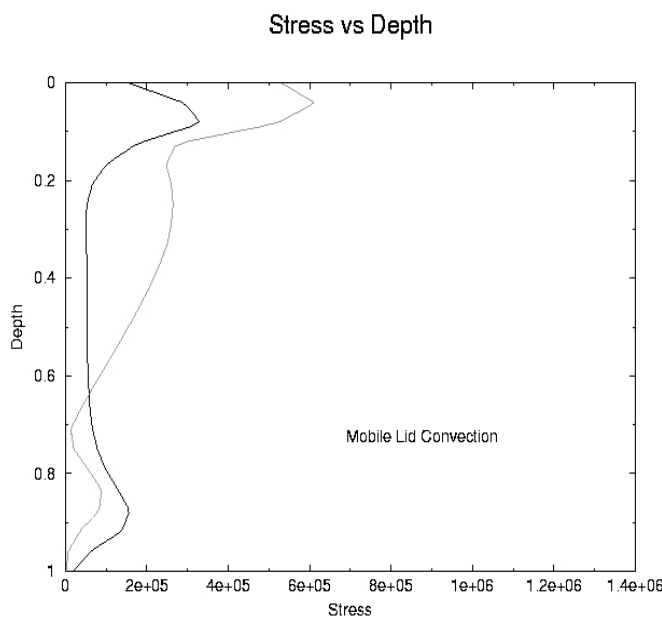


Figure 7.4: Typical Stress Profiles for placeMobile Lid Convection.

The longevity of major lithospheric faults and their preferential reactivation as zones of continuing strain lead to the concept of faults as distinct planes of weakness in the Earth’s lithosphere. Indeed, motion along well-established fault systems is often accompanied by a relatively small stress drop (Kikuchi and Kanamori, 1994). These observations are consistent with the accumulation of damage by zones of high strain, and can be simulated by incorporating a mechanism for strain weakening into the definition of the yield stress. The effect of this is to localize further the zones of strain and enhance their longevity.

7.6.4 Model formulation

The constitutive mathematics and mechanics outlined in the last two chapters are incorporated into software such as *Ellipsis* by a variant of the finite element formulation and solved numerically. Briefly, it involves expressing the equations in matrix form, then employing selected numerical schemes to solve them through time.

In this way it is possible to track the temperature, composition and stress fields (for example) of the modelled convecting system as it evolves through time. Among the outputs of *Ellipsis* are files containing surface observables such as heat flux and surface velocity, and files containing depth information for pre-selected points, such as geotherms and stress profiles. These are processed using perl scripts. Results are displayed using standard plotting tools, such as the free software *XMGrae*.

Chapter 8

Heat flow

8.1 Introduction

A heat flow measurement is the product of the temperature gradient and the thermal conductivity of any material, a rock, or sediments. When talking about heat flow, geoscientists usually refer to measurements of the outward flow of heat through the surface of the Earth. Heat flow at the surface of the Earth is a fundamental measurement that enables us to predict the temperature as a function of depth, if the thermal conductivity is known.

The heat flux per unit area q is measured in units of watts per square meter ($W m^{-2}$), and the thermal conductivity k is measured in Watts per meter and degree centigrade ($W m^{-1} \text{ } ^\circ C^{-1}$). Thermal conductivities of near-surface rocks are typically in the range of 2 to 3 $W m^{-1} \text{ } ^\circ C^{-1}$, and the temperature gradient is typically between 20 and 30 $^\circ C km^{-1}$ in the Earth's crust. These numbers yield an average heat flow between 40 and 90 $mW m^{-2}$. It is standard practice to take the upward surface heat flow to be a positive quantity, even though it has a negative value.

Heat flow measurements are used to monitor volcanic activity, for example at mid-ocean ridges or associated with subduction zones, as well as for petroleum exploration. The measured background or equilibrium heat flow, and measured sediment thermal conductivity provide strict constraints to geochemical models that determine regional scale maturation of basins with respect to oil and gas. In addition, area-wide heat flow surveys provide geological information on fluid flow from faults, lineaments, and around structures. Heat flow measurements in conjunction with seismic and sea floor geochemical studies provide a mechanism to assess fault and structural seals and contribute to a better understanding of regional hydrodynamics and hydrocarbon occurrence.

8.2 Heat flow measurements

At sea heat flow is measured with shallow probes. The most commonly used probe is the so-called “Lister-type” probe (after Clive Lister) that measures temperature gradients and in-situ thermal conductivity of sediments both in lakes and coastal areas (water depth in 100’s of meters) and in the deep ocean (water depths to 6,000m). The probe is capable of making multiple measurements over a single deployment of 12-24 hours and data acquisition, timing, and heat pulse firing are computer controlled.

Temperatures and temperature gradients within the sediment are measured by thermistors, which are located at a known (30 cm) spacing within a small-diameter tube held in tension parallel to a solid steel strength member. Measurement of the thermal conductivity of the sediment is accomplished by allowing the probe to remain at rest in the sediment to allow dissipation of the frictional heating generated by the penetration of the probe, and then heating the probe and surrounding sediment by application of a fixed amount of energy to a heater wire that parallels the thermistors within the sensor tube. Analysis of the temperature decay following this period of energy input (or “heat pulse”) yields the conductivity of the sediment.

The Heat Probe consists of instrumentation, consisting of 1-cm diameter sensor string tube, electronics data logger, heat pulse system, batteries, and pingers all contained within cylindrical pressure housings, mechanical components, including weight stand and 6cm solid steel bar which extends continuously from wire termination at the top to the sensor tube support fin at the bottom, and software with modules for communication, data analysis and graphic display.

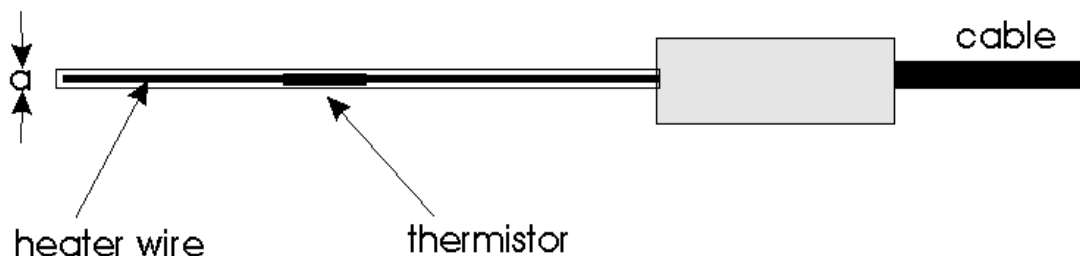


Figure 8.1: The probe needs 5-10 minutes to approach steady state after decay of frictional heating. The typical temperature difference over a 10 m depth interval is 0.5 deg. C. The accuracy of the measurement is about 1%, i.e. 0.005 C.

Limitations and corrections of heat flow measurements include:

- difficulties in extrapolation to background values
- correction for tilt of probe
- need to measure conductivity k

- simplest: use sediment water content and an empirical relationship between k and wt % water

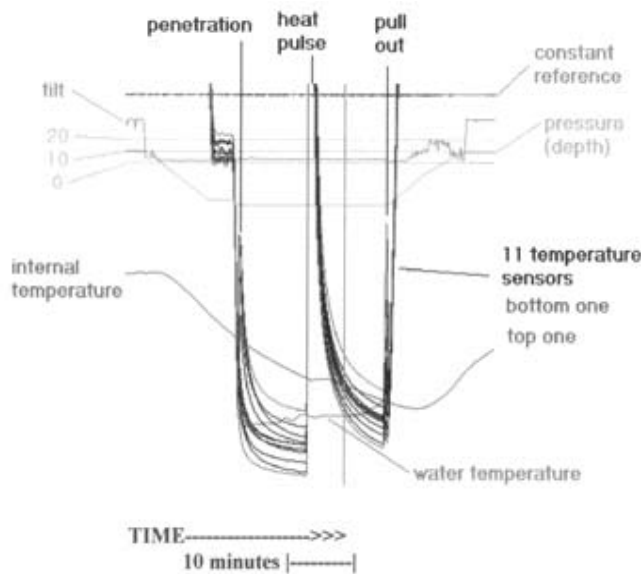


Figure 8.2: Example of screen print of 16-sensor heat flow probe output.

In the figure below, a set of Gulf of Mexico stations' measured heat flows are plotted as a frequency bar chart. A generally well-behaved (Gaussian-like) distribution is typically observed in such a set, with a few outliers that are considered anomalies.

8.3 Character of the Earth's Heat Flow

A heat flow measurement is the product of the temperature gradient and the thermal conductivity of any material, a rock, or sediments. When talking about heat flow, geoscientists usually refer to measurements of the outward flow of heat through the surface of the Earth. Heat flow at the surface of the Earth is a fundamental measurement that enables us to predict the temperature as a function of depth, if the thermal conductivity is known.

The motion of tectonic plates is driven by form of thermal convection. It was originally thought that measuring the outward flow of heat would lead directly to a knowledge of the scale of convection cells driving the plates. Unfortunately this is not the case, because heat flow is highly variable spatially, and most of the heat loss of the Earth occurs by creating new ocean crust at the mid-ocean ridges, and not by heat conduction through the plate.

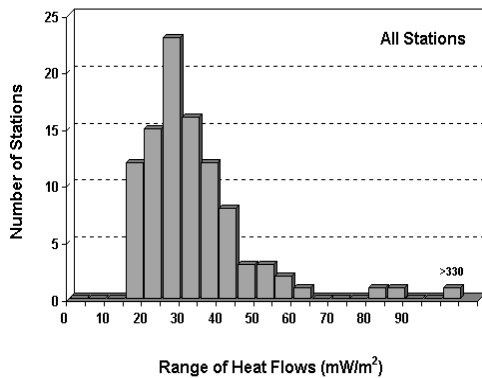


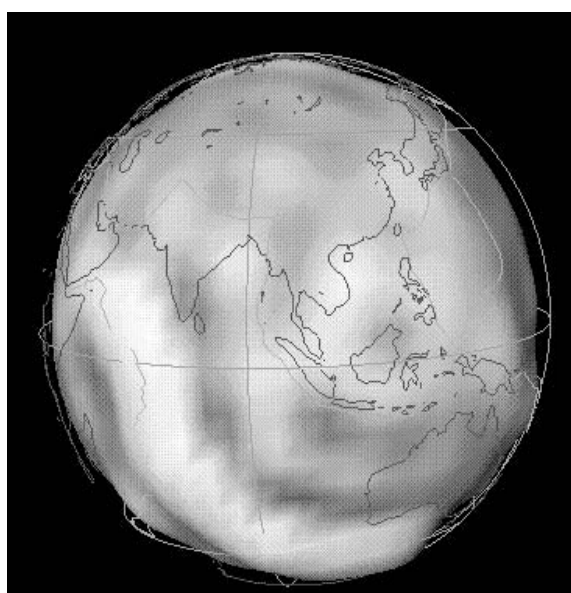
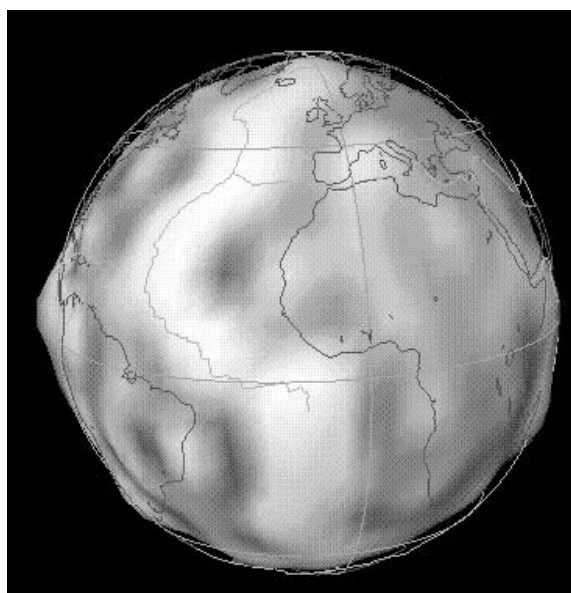
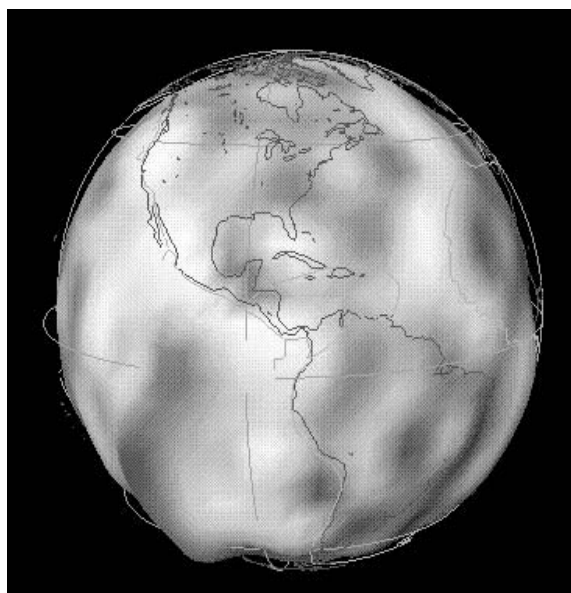
Figure 8.3: Distribution of measured heat flow values for Gulf of Mexico stations

The first scientist to concern himself with the outward flow of heat was *Boyle* in the late 17th century. He pointed out that the temperature within the Earth must increase with depth as mine shafts were warmer at the bottom than at the top. In addition, he observed that by placing beer or wine in deep cellars they could be kept at a relatively constant temperature although there was a large difference between winter and summer surface temperatures. Also, he noticed that these cellars had to be deeper in Moscow than in London, as the surface temperature variations were larger in Russia than in England. He correctly pointed out that these observations could only be explained if the temperature increased with depth in the Earth.

Fourier was the first to develop the theory of heat conduction in the beginning of the 19th century. He introduced the concept of conductivity and the original use of Fourier series was to solve problems in heat transfer between two flat plates. After his work it was recognized that the theory of heat conduction had practical applications in physics, engineering and geology.

Kelvin used Fourier's theory in the middle of the 19th century to estimate the age of the Earth. His estimate was around 50 m.y. This was in strong conflict with the estimate of geologists who argued for a much greater age to account for erosional changes and evolution. This started a major disagreement between geologists and geophysicists that was not resolved until after the discovery of radioactivity by *Becquerel*. Kelvin did not know about radioactivity, and thus he did not account for the heat associated with the decay of radioactive elements in the heat conduction equation. Once radioactivity had been discovered, *Rutherford* and others quickly pointed out Kelvin's error. In addition radioactive techniques started to be used to date rocks. The first reliable radioactive time scale was produced by *Holmes* in 1917. Also at the same time *Holmes and Jeffreys* showed that a crustal layer of 40 km of granite could explain two thirds of the heat flow through the Earth.

Holmes was the first major geologist/geophysicist to be convinced by *Wegener's* arguments for continental drift and set about finding a mechanism to explain the obser-



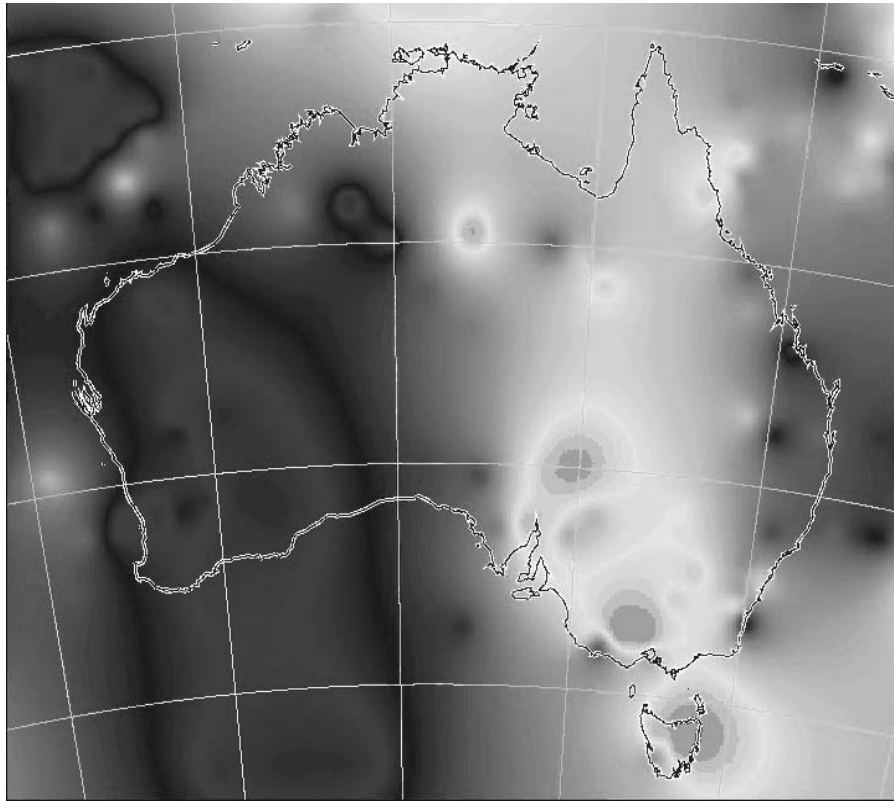


Figure 8.4: Australian heat flow

vations. In 1926, he suggested that there might be enough radioactivity in the upper mantle for maintaining a high enough temperature that the whole of the whole of the upper mantle was close to melting and might in fact be partially molten. He argued that any excess heat would result in thermal mantle convection, and that this convection would move the continents. It is interesting to note that at this time (1926) Holmes had already realized the connection between drifting continents and thermal convection, as well as mountain belts being regions where continents collide.

However, *Jeffreys* argued that the viscosity necessary to maintain the hydrostatic bulge of the Earth was too high to permit convection. For along period of time, this reasoning was accepted by most geophysicists. Finally, only overwhelming evidence for the motion of the plates led to the rejection of Jeffrey's argument.

Bullard at Cambridge pioneered world wide heat flow measurements both on land and in the oceans (e.g Bullard, 1956, 1947). He believed that only measurements would lead to a determination whether or not convection actually took place. He was looking for belts of high measurements indicating upwelling convection and low measurements indicating downwelling convection. Continental measurements were started in

the 1930s; oceanic measurements were started in the 1950s. *Hess* used the high heat flow at the mid-ocean ridge axes as evidence for recent intrusions, and *Hess* and *Dietz* developed the theory of sea floor spreading on the basis of these measurements and the occurrence of active Earthquakes at the ridge axis.

Heat flow measurements have shown:

- Much variability, especially on the ocean floor.
- Very high and very low values near the crest of the mid-ocean ridges.
- An apparent equality between the mean on oceans and continents

Analysis of the data has resulted in the following conclusions:

- The variability in oceanic measurements is due to water circulation.
- The variability on continents is due to variations in radioactivity of surface
- In ocean basins there is a relation between heat flow and age and depth and age.
- On continents there is a relation between heat flow and surface radioactivity.
- The Earth loses 2/3 of its heat by creating oceanic plates and the heat loss

Chapter 9

Conductive Heatflow

9.1 Introduction

Heat flow is one of the most essential subjects in terms of understanding dynamic Earth processes, both in terms of what drives plate tectonics, mantle evolution and plate boundary deformation, as well as from a green energy perspective.

A heat flow measurement is the product of the temperature gradient and the thermal conductivity of any material, a rock, or sediments. When talking about heat flow, geoscientists usually refer to measurements of the outward flow of heat through the surface of the Earth. Heat flow at the surface of the Earth is a fundamental measurement that enables us to predict the temperature as a function of depth, if the thermal conductivity is known.

The motion of tectonic plates is driven by form of thermal convection. It was originally thought that measuring the outward flow of heat would lead directly to a knowledge of the scale of convection cells driving the plates. Unfortunately this is not the case, because heat flow is highly variable spatially, and most of the heat loss of the Earth occurs by creating new ocean crust at the mid-ocean ridges, and not by heat conduction through the plate.

The first scientist to concern himself with the outward flow of heat was *Boyle* in the late 17th century. He pointed out that the temperature within the Earth must increase with depth as mine shafts were warmer at the bottom than at the top. In addition, he observed that by placing beer or wine in deep cellars they could be kept at a relatively constant temperature although there was a large difference between winter and summer surface temperatures. Also, he noticed that these cellars had to be deeper in CityMoscow than in CityLondon, as the surface temperature variations were larger in country-regionRussia than in England. He correctly pointed out that these observations could only be explained if the temperature increased with depth in the Earth.

Fourier was the first to develop the theory of heat conduction in the beginning of the 19th century. He introduced the concept of conductivity and the original use of Fourier series was to solve problems in heat transfer between two flat plates. After his

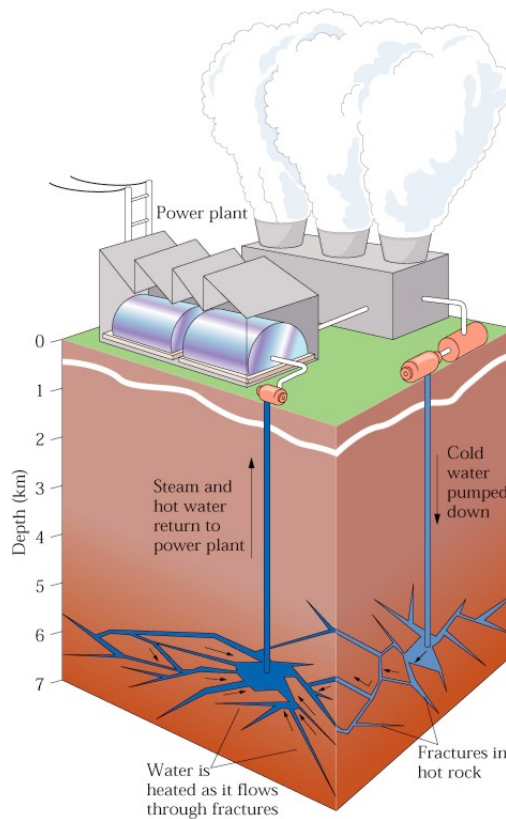


Figure 9.1: Heat energy from the ground. Steam in rock fractures flows up a well to a power plant where it spins turbines, generating electricity without polluting the atmosphere. After use, waste water and any remaining steam are pumped back underground again.

work it was recognised that the theory of heat conduction had practical applications in physics, engineering and geology.

Kelvin used Fourier's theory in the middle of the 19th century to estimate the age of the Earth. His estimate was around 50 m.y. This was in strong conflict with the estimate of geologists who argued for a much greater age to account for erosional changes and evolution. This started a major disagreement between geologists and geophysicists that was not resolved until after the discovery of radioactivity by *Becquerel*. Kelvin did not know about radioactivity, and thus he did not account for the heat associated with the decay of radioactive elements in the heat conduction equation. Once radioactivity had been discovered, *Rutherford* and others quickly pointed out Kelvin's error. In addition radioactive techniques started to be used to date rocks. The first reliable radioactive time scale was produced by *Holmes* in 1917. Also at the same time *Holmes and Jeffreys* showed that a crustal layer of 40 km of granite could explain two thirds of the heat flow through the Earth.

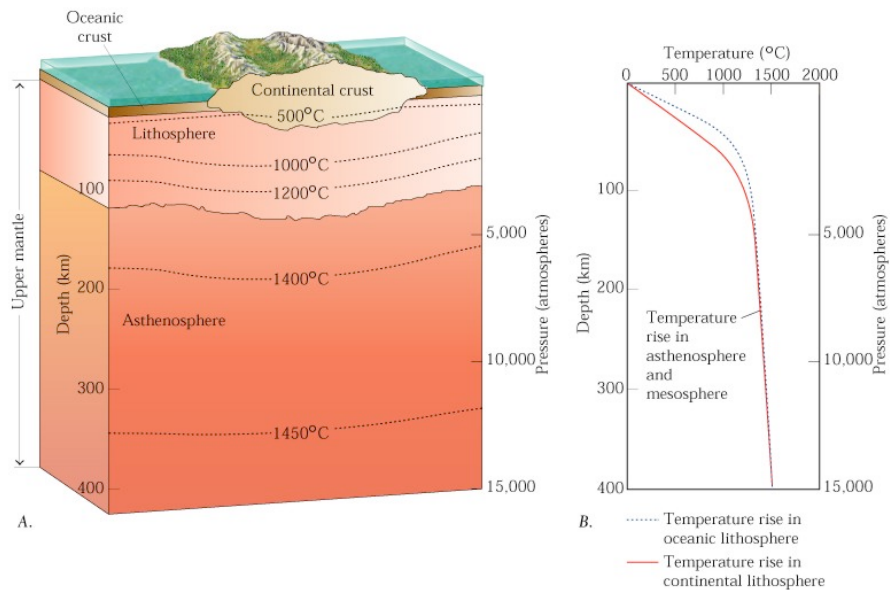


Figure 9.2: Geothermal gradient. Temperature increases with depth in the Earth, as shown here. The dashed lines are isotherms lines of equal temperature. Note that temperature increases more slowly with depth under the continents than under the oceans, where it gets quite hot at a shallow depth

Holmes was the first major geologist/geophysicist to be convinced by Wegener's arguments for continental drift and set about finding a mechanism to explain the observations. In 1926, he suggested that there might be enough radioactivity in the upper mantle for maintaining a high enough temperature that the whole of the whole of the upper mantle was close to melting and might in fact be partially molten. He argued that any excess heat would result in thermal mantle convection, and that this convection would move the continents. It is interesting to note that at this time (1926) Holmes had already realised the connection between drifting continents and thermal convection, as well as mountain belts being regions where continents collide.

However, Jeffreys argued that the viscosity necessary to maintain the hydrostatic bulge of the Earth was too high to permit convection. For a long period of time, this reasoning was accepted by most geophysicists. Finally, only overwhelming evidence for the motion of the plates led to the rejection of Jeffrey's argument.

Bullard at Cambridge pioneered world wide heat flow measurements both on land and in the oceans (e.g. Bullard *et al.*, 1956, Bullard, 1960). He believed that only measurements would lead to a determination whether or not convection actually took place. He was looking for belts of high measurements indicating upwelling convection and low measurements indicating downwelling convection. Continental measurements were started in the 1930s; oceanic measurements were started in the 1950s. Hess used the high heat flow at the mid-ocean ridge axes as evidence for recent intrusions, and Hess

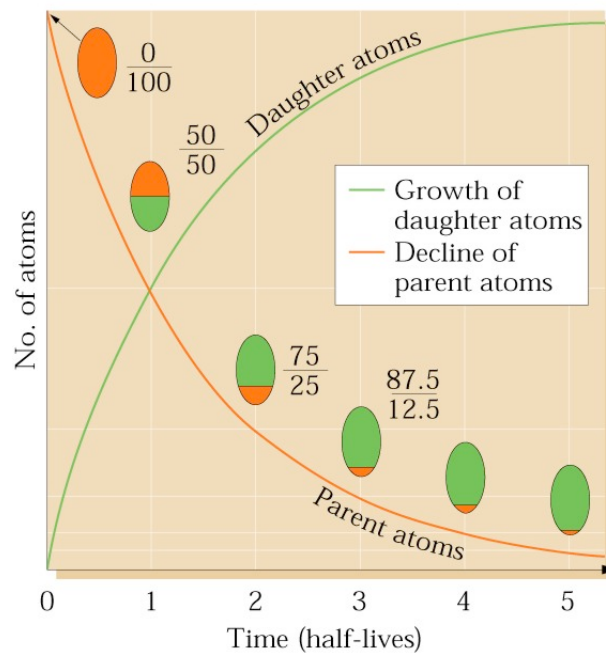


Figure 9.3: Radioactivity and time. These graphs illustrate the basic decay law of radioactivity. At time zero, a sample consists of 100 percent radioactive parent atoms. After one time unit, corresponding to the half-life of the material, 50 percent of the parent atoms will have decayed to daughter atoms. After two time units, 75 percent will have decayed. At any given time, the total number of daughter atoms plus remaining parent atoms equals the original number of parent atoms.

and Dietz developed the theory of sea floor spreading on the basis of these measurements and the occurrence of active Earthquakes at the ridge axis.

Heat flow measurements have shown:

- 1.) Much variability, especially on the ocean floor.
- 2.) Very high and very low values near the crest of the mid-ocean ridges.
- 3.) An apparent equality between the mean on oceans and continents

Analysis of the data has resulted in the following conclusions:

- 1.) The variability in oceanic measurements is due to water circulation.
- 2.) The variability on continents is due to variations in radioactivity of surface rocks, erosion and water circulation.
- 3.) In ocean basins there is a relation between heat flow and age and depth and age.

- 4.) On continents there is a relation between heat flow and surface radioactivity.
- 5.) The Earth loses 2/3 of its heat by creating oceanic plates and the heat loss through the oceans is 2.5 times that through the continents.

9.2 Conductive heat flow in solids

9.2.1 Introduction

When different parts of a body are at different temperatures then heat flows from the hotter to the colder part.

There are 3 distinct mechanisms for the transfer of heat:

- 1.) **Conduction** - heat is transferred through a medium via the net effect of molecular collision
- 2.) **Convection** - heat is transferred by the motion of the medium
- 3.) **Radiation** - heat is transferred by electromagnetic radiation

Advection is a special form of convection. If a hot region is uplifted by tectonic events or by erosion and isostatic rebound, heat is physically lifted up with the rocks.

In liquids and glasses convection and radiation are the most important mechanisms of heat transfer. In solids convection is absent. At the surface of the Earth, radiative heat transfer is negligible.

9.2.2 Fourier law of heat conduction

Consider an infinitely long and wide plate of thickness d , with its upper surface maintained at temperature T_1 and the lower surface maintained at T_2 , with $T_2 > T_1$.

The **heat flux q** , **the heat flow q per unit area and per unit time** up through the plate is

$$q = -k \frac{T(z + \delta z) - T(z)}{\delta z}$$

k is the constant of proportionality and is called the **thermal conductivity**, which is a physical property of a material. It is a measure of its physical ability to conduct heat. The minus sign appears since heat flows in the direction of decreasing temperature. The heat flux per unit area q is measured in units of watts per square meter (Wm^{-2}), and the thermal conductivity k is measured in Watts per meter and degree centigrade ($\text{Wm}^{-1}\text{°C}^{-1}$). A table of the thermal conductivities of different rocks can be found in *Turcotte and Schubert (1982)*.

To express heat flow using a differential equation, we will assume that the temperature at the upper surface z is T and that the temperature at the lower surface at $z + dz$ is $T + dT$ (see figure above). This yields

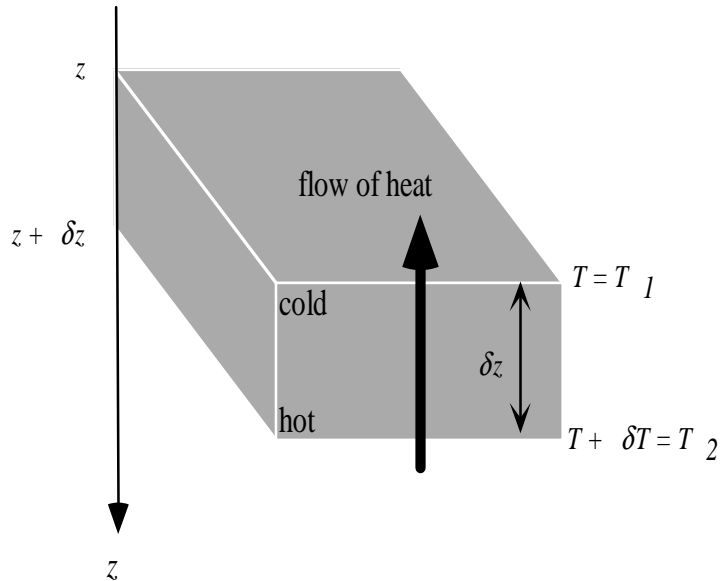


Figure 9.4: default

$$q(z) = -k \frac{T + \delta T - T}{\delta z} = -k \frac{\delta T}{\delta z}$$

In the limit as δz tends to 0, we obtain

$$q(z) = -k \frac{dT}{dz}$$

This is **Fourier's law** in one-dimension. The coordinate system in the figure above is chosen so that z represents depth beneath the surface, increasing downwards, and a positive temperature gradient upwards to represent heat flow at the surface of the Earth.

9.2.3 The Earth's surface heat flux

Thermal conductivities of near-surface rocks are typically in the range of 2 to 3 $Wm^{-1}^{\circ}C^{-1}$, and the **temperature gradient is typically between 20 and 30 $^{\circ}Ckm^{-1}$** in the Earth's crust. These numbers yield an average heat flow between 40 and 90 mWm^{-2} . It is standard practice to take the upward surface heat flow to be a positive quantity, even though it has a negative value as discussed above.

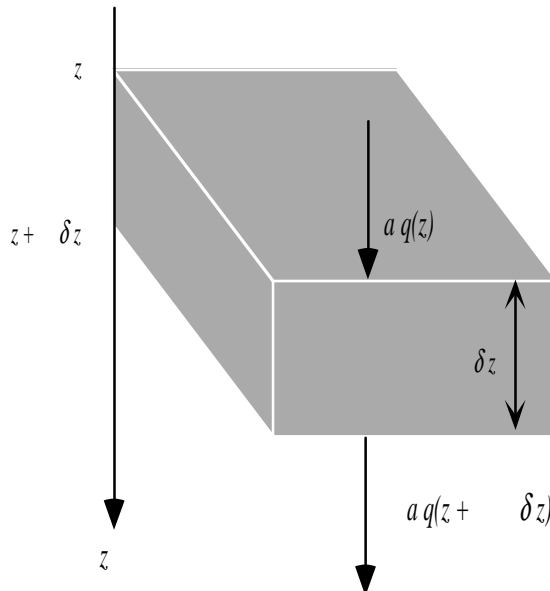
Temperature measurements in caves and mines give approximate values for the near-surface geothermal gradient, accurate measurements of the thermal gradient in continental areas require deep drillholes. Climatic variations of the Earth's surface temperatures have a considerable effect on the surface geothermal gradient. In order to reach steady-state thermal structures, holes must be drilled at least as deep as 300 m.

From Fourier's law it is apparent that besides knowing the temperature gradient, we also need to know the thermal conductivity of the rock. For drilled samples, this is usually done in the laboratory by subjecting the samples to known heat fluxes and measuring the temperature drops across them.

On the ocean floor needle probes of about 3 m length which carry a number of thermistors are dropped from a ship and penetrate the sediments. The near-surface heat flow in the oceans is almost constant because climatic variations do not affect the temperature of oceanic bottom water. Here the thermal conductivity of the sediments is determined using a heater in the heat-flow probe. The record of the increase in probe temperature with time after the heater is turned on can be interpreted to give thermal conductivity of the sediments.

9.2.4 The heat conduction equation

We will start looking at heat conduction in one dimension first, and then expand the solution to three dimensions. Consider a parallelepiped of height δz and cross-sectional area a .



Heat is conducted into and out of the element across the upper and lower faces only. We assume for the moment that heat transfer is only in the z -direction. Any change in temperature of the volume of this parallelepiped with time depends on:

1 - Flow of heat across the two faces (net flow in or out)

2 - Heat generated in the element

3 - Thermal capacity (specific heat) of the material

Specific heat c_p is defined as the amount of heat necessary to raise 1kg of material by $1^\circ C$. Specific heat is measured in $Wkg^{-1}^\circ C^{-1}$.

How much temperature the material of which the parallelepiped is made of will gain depends on its specific heat c_p . If the material has density ρ and specific heat c_p ,

and experiences a temperature increase δT in time δt , the rate at which heat is gained is

$$\dot{q} = c_p a \delta z \rho \frac{\delta T}{\delta t}$$

In order to obtain the rate in which heat is gained by the volume element we equate the heat gained in time by a volume of element with the heat flux given by the gradient of heat q

$$c_p \rho \frac{\partial T}{\partial t} a \delta z = \frac{\partial q}{\partial z} a \delta z$$

or, simpler:

$$c_p \rho \frac{\partial T}{\partial t} = \frac{\partial q}{\partial z}$$

and knowing that $q(z) = -k \frac{\partial T}{\partial z}$, one finds the evolution law of the temperature:

$$c_p \rho \frac{\partial T}{\partial t} = k \frac{\partial^2 q}{\partial z^2} + A$$

where the A is an additive constant due to the arbitrarily of the initial conditions and/or boundary conditions.

We can easily expand this equation from one into three dimensions, if temperature is assumed to be a function of (x, y, z) , and t :

$$\rho c_p \frac{\partial T}{\partial t} = k \nabla^2 T + A$$

where ∇^2 is sometimes referred to as the Laplacian, i.e. the divergence of a gradient and indicated with Δ . If k is not a constant throughout the medium, we obtain the **general heat conduction equation**:

$$\rho c_p \frac{\partial T}{\partial t} = \nabla (k \nabla T) + A$$

Often it is useful to use write this equation in the following form:

$$\frac{\partial T}{\partial t} = \nabla (k \nabla T) + \frac{A}{\rho c_p}$$

The term $K = k / \rho c_p$ is known as **thermal diffusivity**. Thermal diffusivity expresses the ability of a material to lose heat by conduction. K is measured in $m^2 s^{-1}$. If temperature changes occur with a characteristic time interval t , they will propagate a distance of \sqrt{Kt} .

In most cases the equation above cannot be solved analytically and has to be solved numerically. The major problems involved are that there are six variables involved, some of which have large ranges. In most cases it is necessary to reduce the problem to simple geometries in a homogeneous medium. This is how we are able to tackle geological problems.

9.2.5 Simplified conduction equations used in thermal studies

9.2.5.1 A homogenous isotropic solid without internal heat source

In this case, the thermal conductivity k is independent of position and there is no heat production. Thus we obtain:

$$\frac{\partial T}{\partial t} = \nabla (k \nabla T)$$

This is known as the **diffusion equation**.

9.2.6 A homogenous isotropic solid without internal heat source and steady state conditions

Under steady state conditions , the last equation reduces to

$$0 = \nabla (k \nabla T)$$

This is known as **Laplace's equation**.

9.2.7 A homogenous isotropic solid with internal heat source

In this case k is a constant and the three-dimensional heat conduction equation applies:

$$\frac{\partial T}{\partial t} = k \nabla^2 T + \frac{A}{\rho c_p}$$

However, this equation is difficult to solve analytically.

9.2.8 A homogenous isotropic solid with internal heat source in steady state

In this case k is constant and $\partial T / \partial t = 0$. Thus, the last equation reduces to

$$0 = k \nabla^2 T + \frac{A}{\rho c_p}$$

This is known as **Poisson's equation**. It is also found in gravity and magnetic problems.

9.3 Geological applications

9.3.1 Introduction

There are standard techniques for solving the heat conduction equation, but most are very cumbersome. As a consequence, many solutions are found by inspection, proceeding as follows:

- 1- The problem is posed.
- 2- The physical problem is reduced to a simple model.

- 3- The appropriate heat conduction equation is selected.
- 4- The boundary conditions are used to determine what type of solution will be tried.
- 5- A type of solution is chosen for the differential equation and the constants are determined using boundary conditions.

9.3.2 Calculation of geotherms

One of the main applications of the heat conduction equation in geology and geo-physics is the calculation **temperature-depth profiles in the Earth**. These are called **geotherms**. Imagine a one-dimensional column in the Earth's crust with no erosion and no deposition, and a constant heatflux. In this case, the column will eventually reach a state of thermal equilibrium and temperature-depth profile is called an equilibrium geotherm. The Poisson equation applies to tackle the problem:

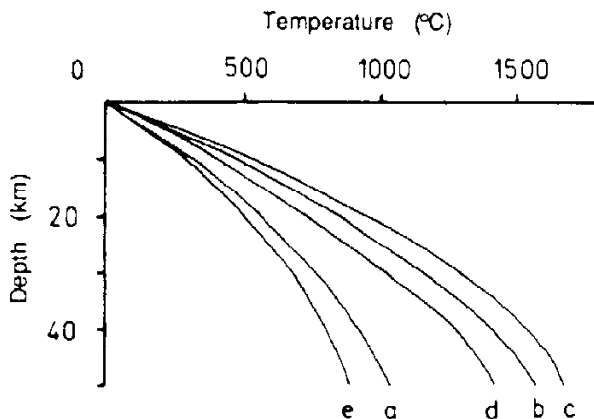
$$0 = k\nabla^2 T + \frac{A}{\rho c_p}$$

This is a second order differential equation, and we need to integrate twice to solve it. Hence we need two boundary conditions. We assume that the surface is at $z=0$ and that z is positive downwards. We obtain two boundary conditions by assuming that the temperature at the surface is $0^\circ C$, and that we have measured and know the heat flow q_0 at the surface.

Integration of Poisson's equation as a function of depth:

$$T = -\frac{A}{2k}z^2 + \frac{q_0}{k}z + c$$

The following figure from *Nisbet and Fowler (1982)* shows equilibrium geotherms calculated from the last equation for a 50 km thick crust and different values for conductivity, radioactive heat generation in the crust, and basal heat flow.



- (a) standard model: $k = 2.5 \text{ Wm}^{-1}\text{°C}^{-1}$, $A = 1.25 \text{ mWm}^{-3}$, and $qd = 21 \times 10^{-3} \text{ Wm}^{-2}$
- (b) standard model, but $k = 1.7 \text{ Wm}^{-1}\text{°C}^{-1}$

- (c) standard model, but $A = 1.7 \text{ mWm}^{-3}$
- (d) standard model, but $qd = 21 \times 10^{-3} \text{ Wm}^{-2}$
- (e) standard model, but $qd = 10.5 \times 10^{-3} \text{ Wm}^{-2}$

However, in the real world radioactive elements are usually concentrated at the top of the crust (e.g. in igneous bodies). In order to take this into account, we have to use a two-layer model for the crust, and calculate the geotherm for each layer separately with matching temperature gradients across the boundary (see *Fowler*, 1990, for details).

9.4 Instantaneous heating or cooling

Instantaneous heating or cooling is a concept that applies to geological situations such as:

- 1- rocks/sediments suddenly heated by a magmatic intrusion,
- 2- formation of new ocean crust at mid-ocean ridges.

9.4.1 The Age of the Earth

This is also the approach Lord Kelvin used in the 19th century to find out the age of the Earth. Kelvin made the assumption that the Earth had formed as a molten body at the temperature at which basalt melts and that it had cooled by conduction to its present temperature gradient. He considered the Earth to be spherically symmetric, and assumed that all heat was lost at the surface by conduction, and ignored the curvature of the Earth. Thus the problem is reduced to that of finding the temperature within a cooling half-space of infinite extent as a function of time after the half space is set at a specific temperature.

Mathematically the problem reduces to that of solving for the temperature structure within a halfspace bounded by the plane $z = 0$. In the case of instantaneous cooling, a semi-infinite halfspace has a homogeneous temperature of T_0 , whose surface is suddenly cooled to temperature T_s . In the case of seafloor spreading, the temperature T_0 is the mantle temperature T_m at great depths (1300°C), and the surface temperature is kept at $T_s = 0^\circ\text{C}$. Here a hot body of mantle material with temperature T_m throughout upwells at the mid-ocean ridge axis, comes into contact with sea water at temperature T_s , and is quenched. Subsequently the mantle column cools slowly from the top, until a linear gradient is established between the surface and the depth at which a constant isotherm is maintained. Kelvin's cooling Earth problem is equivalent.

In the case of a magmatic intrusion heating sediments or hard rocks, we have instantaneous heating. A cold body at temperature T_0 , whose surface is suddenly heated to temperature T_s . The mathematics of both cases is identical. In the following, let's investigate the case of instantaneous cooling of a semi-infinite half-space, as illustrated below:

Here T_m is the temperature of hot upwelling asthenospheric, and the surface temperature is set at $T_s = 0$. The one-dimensional heat conduction equation without any radioactive heat source applies to this model.

In the case of an intrusion at a mid-ocean ridge, which is chilled by seawater at the surface, $T_s = 0$, and we can obtain the temperature structure and the thickness of the lithospheric boundary layer (i.e. the depth to a particular isotherm) as a function of time by:

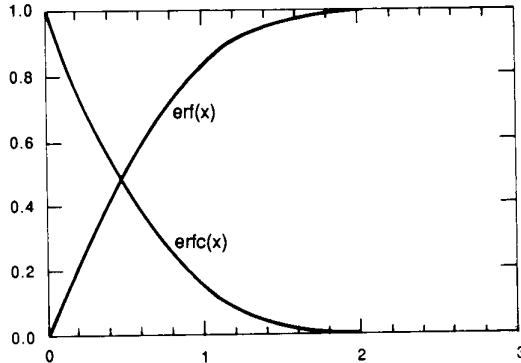
$$T = T_m \operatorname{erf} \left(\frac{z}{2\sqrt{Kt}} \right)$$

The error function was first tabulated during the mid-1800's during the development of probability theory. Its properties are

$$\begin{aligned}\operatorname{erf}(0) &= 0 \\ \operatorname{erf}(inf) &= 1 \\ \operatorname{erf}(-z) &= -\operatorname{erf}(z).\end{aligned}$$

The complementary error function $\operatorname{erfc}(z)$ is defined as

$$\operatorname{erfc}(z) = 1 - \operatorname{erf}(z)$$



Values for the error function are tabulated in tables [e.g. in *Fowler*, 1990, who also lists a programmable approximation].

The temperature gradient for the general solution can be found by differentiation. In the case of cooling of a mid-ocean ridge, $T_s = 0$; hence:

$$\frac{\partial T}{\partial z} = \frac{T_m}{\sqrt{\pi K t}}$$

We now go back to Kelvin's problem. He used exactly these equations to estimate the age of the Earth. In his original solution, he used the following values: $\frac{\partial T}{\partial z}$ at $z = 0$ $T = 30^\circ\text{C}/\text{km}$, $T_m = 2000^\circ\text{K}$, and $K = 0.01\text{cm}^2/\text{s}$.

He concluded that the age of the earth t_0 was given by

$$t_0 = \frac{T_s^2}{\pi K (\partial T / \partial z)}$$

and these values give an age of the Earth of 50 m.y.

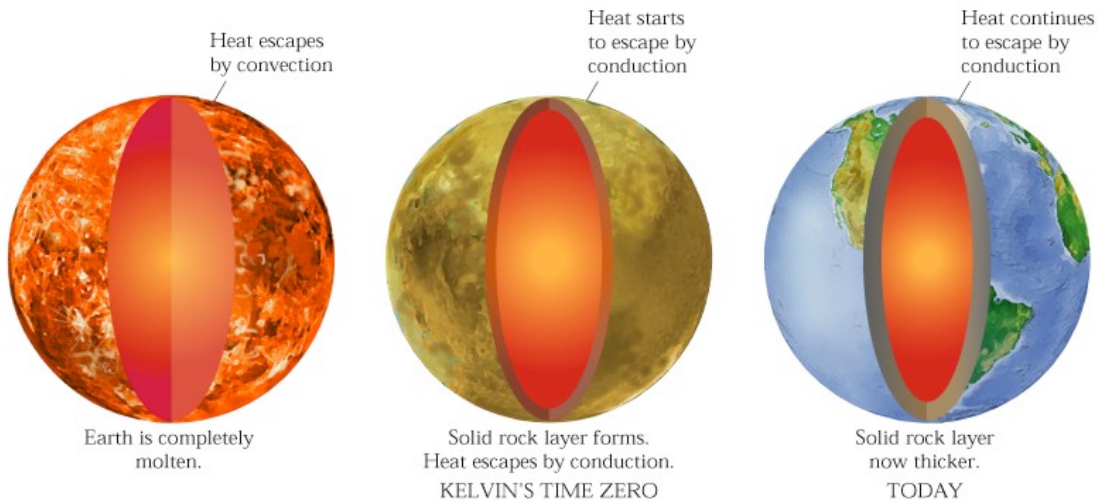
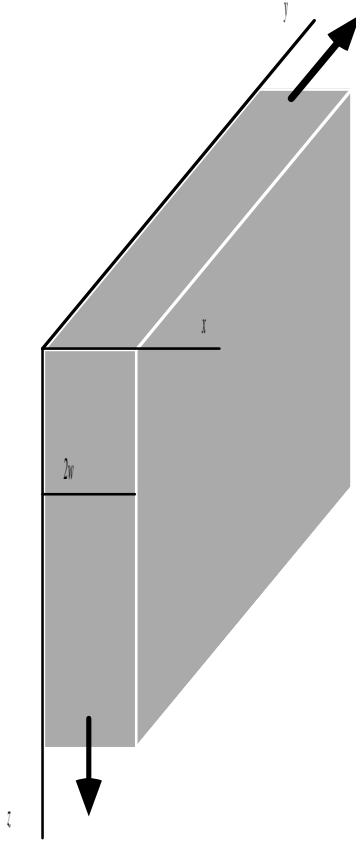


Figure 9.5: Kelvin's estimate of the solid earth's age. Lord Kelvin made two assumptions: that the Earth was once a completely molten small star and that no heat was added once it formed. Once a solid rocky outer layer had formed, the Earth cooled by conduction. By measuring today's rate of heat loss, and knowing the heat conduction properties of rocks, Kelvin calculated how long ago the Earth first cooled sufficiently for solid rocks to form. Even though his calculations were mathematically correct, and self-consistent, the age he obtained was completely wrong, because his assumption of no heat being added to the earth after its formation was incorrect.

9.4.2 Cooling of a dike

Another example from geology is the **cooling of a dike**. Consider a dike of width $2w$ and of infinite extent in the y and z directions.



We assume that there is no internal heat generation, and that the dike has an initial temperature of T_s . We ignore latent heat of solidification for the moment. Then we have to solve the familiar one-dimensional heat conduction equation

$$\frac{\partial T}{\partial t} = K \frac{\partial^2 q}{\partial z^2}$$

for the boundary conditions

$T = T_s$ at $t = 0$ for $-w < x < w$

$T = 0$ at $t = 0$ for $\text{abs}(x) > w$

The solution of this equation which satisfies the initial conditions is

$$T(x, t) = \frac{T_s}{2} \left[\text{erf} \left(\frac{w-x}{2\sqrt{Kt}} \right) + \text{erf} \left(\frac{w+x}{2\sqrt{Kt}} \right) \right]$$

A full derivation of this expression can be found in *Turcotte and Schubert [1982]*. If the dike has a width of 2m, i.e. $w = 1m$, and its initial temperature was $T_s = 1000^\circ C$, and $K = 10^{-6} m^2 s^{-1}$, then the temperature at the center of the dike would be about $640^\circ C$ after one week, $340^\circ C$ after one month, and only $100^\circ C$ after one year. At a distance w from the edge of the dike, the highest temperature is only about $T_s/4$, in this case $250^\circ C$

9.5 Terrestrial heat flow

After the discovery that Uranium and Thorium are radioactive at the turn of the century, it was believed that the earth's heat originates from the decay of Uranium, Thorium, and Potassium. The radioactive elements were assumed to originate from the stony portion of the earth which presumably accreted from chondritic meteorites. However, *Ringwood* (1979) pointed out that the actual heat loss of the earth which had been calculated by *Birch* (1958, 1965) based on the above assumption, is too small by a factor of 3.2 compared with the actual heat loss. Ringwood suggested that the discrepancy is related to the heat loss due to convection associated with plate tectonics, but that the present day heat flow is over three times greater than in the geological past.

McKenzie and Richter (1981) suggested that the meteoritic material may have been depleted of a portion of volatile elements during the consolidation of the earth, thereby increasing the relative abundance of radiogenic elements. This theory reduced the discrepancy between observed and modeled radiogenic heat flow to a factor of two. *Richter* (1984, 1985) accounted for the remaining discrepancy by secular cooling of the earth.

Unfortunately, a global survey of Helium in the oceans found only 5% of the helium that should have been there in the case of radiogenic heat production (*Oxburgh and O'Nions*, 1987). When radionucleides decay, they produce both heat and helium. *Oxburgh and O'Nions* (1987) argued that the implication is that helium has been stored in a convecting mantle, but also conceded most of the heat may come from a non-radiogenic source. In fact, *Dubrovsky and Pankov* (1972) had advocated earlier the theory that secular cooling and the release of gravitational potential energy by the absorption of FeO into the core.

It has become clear in the meantime due to progress in experimental high temperature and pressure work using laser heated diamond-anvil cells that at the core-mantle boundary molten iron in the core reacts with silicate perovskite $(\text{Fe}, \text{Mg})\text{SiO}_2$ in the lower mantle to form lighter, iron-free silicate perovskite and stishovite (*Knittle and Jeanloz*, 1989).

Vacquier (1991, 1992) estimated the radiogenic and non-radiogenic heat loss. The total global observed heat loss is $4.2 \times 10^{13} \text{ W/yr}$, the radiogenic heat loss is $1.14 \times 10^{13} \text{ W}$, and the non-radiogenic heat loss is $3.06 \times 10^{13} \text{ W/yr}$ at the present. Subsequently *Pollack et al.* (1993) published a global synthesis of 24,744 heat flow measurements and constrained the global heat loss to be $4.42 \times 10^{13} \text{ W/yr}$, slightly higher than the value assumed by *Vacquier* (1991).

Vacquier (1991, 1992) showed that due to **gradual absorption of iron from the mantle into the core, the core's surface has grown by about 7% relative to its original size**, that the non-radiogenic heat production was 2.4 times greater on average in the past than it is at present, and that up to three quarters of the original iron content of the mantle may have been lost to the core. This implies that on average a non-radiogenic heat loss of $7.34 \times 10^{13} \text{ W/yr}$ would have occurred in the geological past, and about 85% of the total heat loss were non-radiogenic.

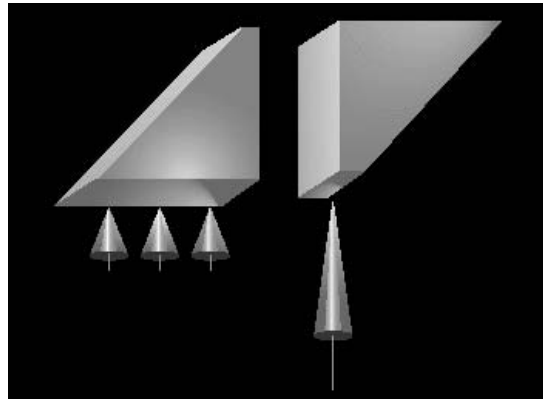


Figure 9.6: Diamond Press

About 2/3 of the earth's total heat loss occurs by means of convection through creation of new ocean crust at mid-ocean ridges (*Sclater et al.*, 1980). However, 87% of the radiogenic heat loss occurs through the continents. This is because U and Th are incompatible elements with regard to silicates. When melts form in the mantle incompatible elements escape first and accumulate in continental rocks. Recent work by *Chapman and Furlong* (1992) has established steady state geotherms for the continental crust that satisfy both heat flow data and are based on thermal parameters appropriate for crustal chemical compositions.

9.6 Modelling Heat Flux Partitioning Between the Oceans and the Continents

9.6.1 Background and Theoretical Considerations

A simple convecting system. Simple Convecting System. Here h is the thickness of the boundary material, d is the thickness of the thermal boundary layer, T_0 the surface temperature, T_i the temperature at a depth of h , k_s the thermal diffusivity of the bounding material, and k_1 the thermal diffusivity of the convecting material (adapted from Lenardic, 1998). **The way in which a convecting fluid loses heat to its surroundings can be described by a Biot number. It is defined by**

$$Bi = \kappa_s \delta / \kappa_1 h$$

Since the entire lithosphere participates in mantle convection in oceanic regions, the boundary condition seen by the convecting mantle is water. Since the relative thermal diffusivity of water with respect to the mantle is extremely large, the situation exists where $\kappa_s \gg \kappa_1$. In this limit, the Biot number tends toward infinity, ie $Bi \rightarrow \infty$.

In contrast, the continental thermal diffusivity is comparably close to the mantle, and thus their ratio is reasonably close to zero. This is an imperfect thermal couple, but for illustrative purposes it can be assumed that $\kappa_s/\kappa_1 \rightarrow 0$. This means that

$$\partial Q_i / \partial T_i \rightarrow 0$$

or, in other words, that $\partial Q = 0$. This is a constant heat flux condition. Here the Biot number approaches the limit

$$Bi \approx 0$$

In reality the condition is not one of completely constant heat flux. However, when compared to the oceanic regions, the imperfect thermal couple between the continents and the mantle is one of near constant heat flux.

9.6.2 Thermal Boundary Layer Models

Early numerical models consistently modelled the lithosphere as a thermal boundary layer, defined basally by a constant temperature condition. This is, essentially, a good first-order description of the oceanic lithosphere, and is supported by petrological, bathymetry, gravity and heat-flow data (Carlson and Johnson, 1994; Nagihara *et al.*, 1996). At first glance it also seems a good description for a temperature dependant continental rheology (e.g. Chapman and Pollack, 1977). An example of a simple convecting system with an upper thermal boundary layer is shown in the figure below.

As expected, this plot demonstrates that as the overall convective vigour of the system increases, the total heat flux out of the system also increases. However, the heat flux ratio remains essentially constant for a range of Rayleigh numbers. This result is consistent with that found by Lenardic (1998). In terms of the Earth, this implies that as we go back through time, and the convective vigour of the mantle increases, the oceans and the continents will both be forced to carry comparable increases in heat flux. The corollary to this is that given a hotter and more vigorously convecting mantle during the early evolution of the Earth (Archean), the ancient continents would have been forced to carry a proportionately larger heat flux leading to higher geothermal gradients and large-scale continental melting. However, an extensive body of evidence contradicting this rather universal conclusion suggests that the definition of the continents as a purely thermal boundary layer is inadequate.

9.6.3 Thermal Chemical Boundary Layer Models

In a geological context, the chemical distinction between continental crust and both the mantle and the oceanic lithosphere is fairly obvious. As a result it has been suggested (e.g. Jordan, 1981) that the continents may, in fact, act as a chemical boundary layer to mantle convection. This means that the convecting mantle sees a laterally heterogeneous surface boundary condition (Lenardic and Kaula, 1998). A simple isoviscous convecting system with a chemically distinct continent is shown in the figure below.

In these simulations the tendency is towards constant heat flux in the continental regions, which is consistent with the imperfect thermal couple between continents and

the mantle. Moreover, the geotherms are milder in continental regions compared to oceanic regions at similar depths. The heat flux ratio here is defined as the average oceanic heat flux divided by the average continental heat flux. In order to calculate the time-averaged heat flux and heat flux ratio, it is necessary to first let the system achieve a thermal steady state.

The surface heat flow in the internally heated case tends toward a greater equilibrium value than that for the basally heated case. Nonetheless, the heat flux ratios in both cases tend toward a similar value. This illustrates the inefficiency of internally heated convection as a mechanism for heat transport compared to basally heated convection (Christensen, 1984). In this case, regardless of the advective timescale for heat transport out from under a continent, the internal heat production of the mantle material results in higher temperatures beneath the continent, and the partitioning of heat between oceans and continents is less effective than in basally heated cases.

9.6.4 The Effect of Continents on Mantle Flow

It is reasonably well established that the thermal constraint imposed by continental crust causes the mantle to experience a heterogeneous surface boundary condition, which is significant enough to affect the structure of the mantle flow itself (Lenardic and Kaula, 1995). It is important to assess the effect that continents can have on the above results, and how the characteristics of the modelled continents can affect the conclusions.

Firstly, one of the most significant constraints is the rigidity of the continental blocks. It is widely accepted that the strength of the continental crust is, on the whole, much less than that inferred for oceanic crust (eg. Harry, *et al.*, 1995). This is a problem because regardless of its chemical buoyancy, weak crust will simply be entrained into the mantle due to the large surface stresses encountered in this mode of strongly temperature dependent viscosity convection. This is illustrated below.

That this occurs on the Earth for timescales of hundreds of millions of years is quite possible (Lenardic and Moresi, 1999). However, without a mechanism for continental regeneration (as is the case with these models), the destruction of continents is unrealistic.

The behaviour of weak, deformable, chemically buoyant continents in an isoviscous or weakly temperature dependent regime has been further explored by Lenardic (1998). In these cases, continents were found to accrete around downwellings, and to rift and split in the proximity of mantle upwellings. The partitioning of heat between oceans and continents was found to behave in a similar fashion to that previously outlined. Hence the effects of the rigidity of the continental crust are minor relative to more general heat flux issues.

However, the relative surface area of the continent is an issue of importance. At a certain point, the continent becomes sufficiently extensive that heat at the base of the continent can no longer be advected out from under it faster than it can be diffused through it. At this stage the heat lost through the oceans ceases to be efficient enough

to carry the larger proportion of any increase in the total surface heat flux, and the heat flux ratio no longer increases with Rayleigh number.

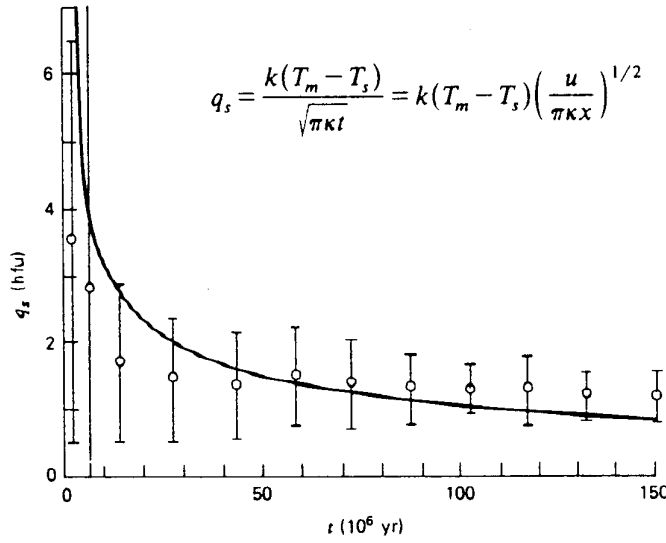
9.6.5 Heat flow and oceanic lithosphere

9.6.5.1 Oceanic heat-flow versus age

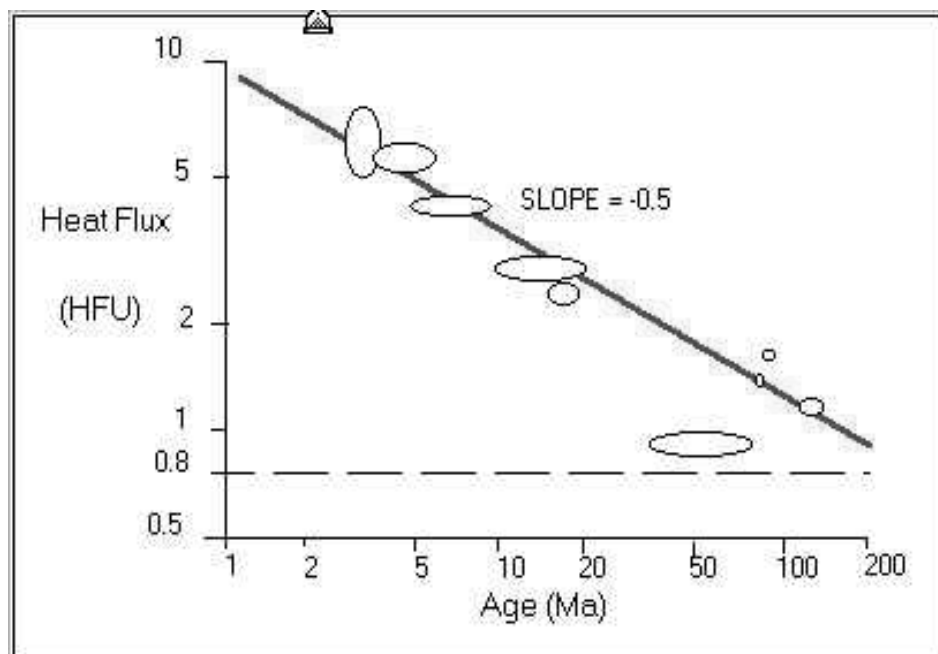
Oceanic heat flow can be used as a constraint on the thermal structure of the oceanic lithosphere. Oceanic heat flow measurements are made with an instrument which measures the temperature gradient along its length. The instrument also sends out an additional source temperature pulse to measure the thermal conductivity of the sediments that are penetrated. With the assumption that there is no hydrothermal convection in the sediment layer then

$$q = -K_{sed} \frac{\partial T_{sed}}{\partial z} = K_{lith} \frac{\partial T_{lith}}{\partial z}$$

This allows us to measure the near-surface lithospheric temperature gradient. If the oceanic crust is covered by an impermeable layer of sediment, there is no convective loss of heat at the sediment/water interface, even though there is hydrothermal circulation in the basement. The wavelength of this circulation is thought to be on the order of 5-10 km horizontally. Thus reliable heat flow measurements can be made only where the sediment cover is more extensive than about 20x20 km and the sediment thickness is greater than 200 m. The mean values and standard deviations of ocean floor heat flow measurements as functions of age are shown in the next figure [from Sclater *et al.*, 1980].

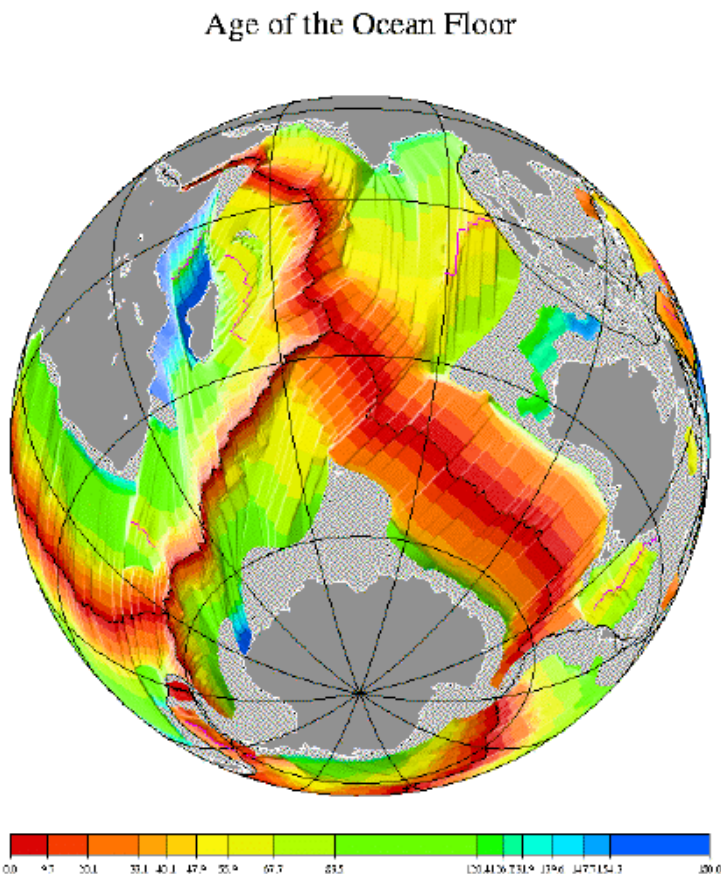


There is reasonable agreement between the model and the observations, except for near the ridge. Here the sediment cover is thinnest, or absent, and heat is lost by hydrothermal circulation, not just by conduction.



9.6.5.2 Ocean depth versus age

The Earth has a strongly bimodal topographic distribution. A hypsometric curve plots the cumulative area of the Earth's surface at a given elevation level (see Chapter 1).



However, the magnetic polarity time-scale gives us the information to investigate a far more profound relation – the relationship between seafloor depth and the age of the crust. Seafloor spreading implies that all seafloor is created at the ridge axis by the intrusion of hot molten magma, which cools, contracts, and subsides as it moves away from the spreading center. Hence mid-ocean ridges are shallower than older ocean basins. In fact, simple thermal subsidence models successfully predict that seafloor depth should be proportional to the square root of the seafloor age. Before investigating these models, let's have a look what observed depth-age profiles look like.

The western North Atlantic shows a depth/age distribution which might be considered "typical" or representative (from *Sclater and Wixon*, 1986):

The next figure shows a similar data set for the North Pacific from *Renkin and Sclater* (1988).

If only one process, thermal subsidence, shaped seafloor topography, then depth versus age plots would be a smoothly varying curve. In the real world depth/age plots reflect many topographic signals in addition to thermal subsidence away from a ridge. These include:

Fracture zones, associated with topography of troughs and ridges of magnitude of 1-3km and widths of 10-30 km.

Abyssal hill topography created near the ridge axis, which can have $\approx 500\text{m}$ relief at a slow-spreading ridge and $\approx 150\text{m}$ relief at a fast-spreading ridge.

Sediments, whose thickness is a function of seafloor age and of location – sedimentation rates are highest in areas in equatorial areas of high productivity near continental margins due to upwelling and/or input of clastic sediments from rivers. In order to determine seafloor depth in the absence of sedimentation, we have to map and remove the sediment cover, and account for the isostatic adjustment due to the sediments. Uncertainties in sediment density and thickness can introduce significant errors in analyses of the subsidence of ocean floor.

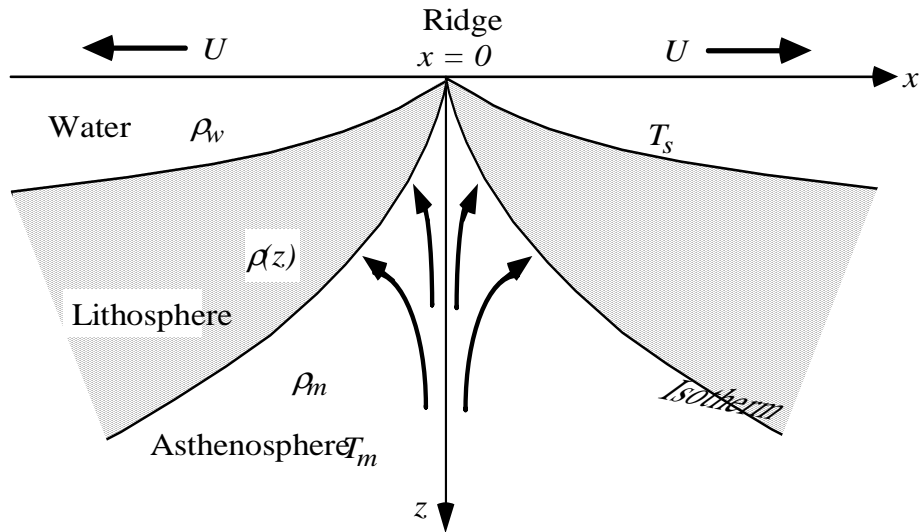
Volcanism such as off-axis seamounts and volcanic islands modify original seafloor topography

Further, the observed depth-age relationship is subject to errors in identification of magnetic anomaly identifications (or the lack of magnetic anomalies in the Cretaceous and Jurassic quiet zones), and errors in the magnetic polarity time scale. However, the observation that the modeled depth from the simple square root of age model fits the data very well for ages from 0-80 Ma has been taken as evidence that the underlying physical process may be relatively simple.

9.6.6 Models of plate formation and cooling at mid-ocean ridges

9.6.7 Half-space cooling model

The thermal boundary layer model for seafloor topography was first proposed by *Turcotte and Oxburgh (1967)*. In this model seafloor is created at the ridge axis, and while it moves away from the spreading centre it cools, contracts, and subsides:

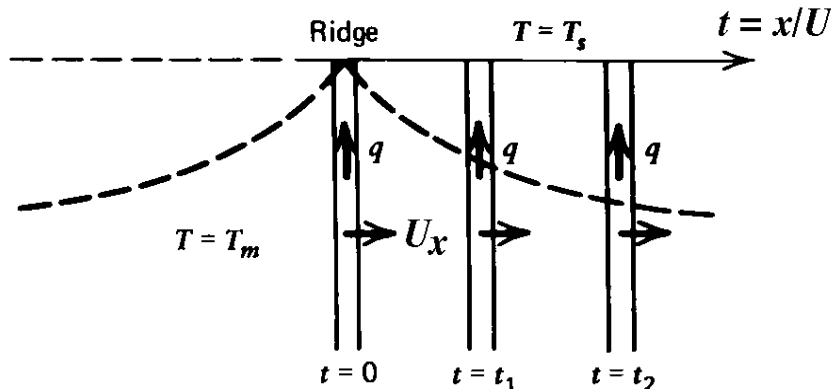


Two surface plates move horizontally on either side of the ridge with a velocity U . The plates are created from hot mantle that is upwelling beneath the ridge. The oceanic lithosphere can be thought of as the surface plate that moves rigidly over the deeper mantle (keep in mind that the oceanic crust is only about 7 km thick, i.e. this is the

depth of the Moho, the crust-mantle transition, but not the lithosphere boundary). The thermal lithosphere is equivalent to that part of the upper mantle whose temperature is less than some value below which mantle and crustal rocks do not readily deform (by ductile flow) over geological time. High-temperature laboratory experiments with rocks indicate that this temperature is about 1300°C. This implies that the lithosphere is the region between the surface and the 1300° isotherm, as shown in the above figure. The depth to this isotherm increases with the age of the lithosphere as it cools and increases in thickness.

We have seen before while discussing heat flow that the problem of instantaneous cooling applies to formation of new ocean crust at mid-ocean ridges. The problem is basically to find the temperature within a cooling half-space of infinite extent as a function of time after the half space is set at a specific temperature, using specific boundary conditions. This is the simplest model to understand the formation of new ocean crust at mid-ocean ridges and its subsidence, and we have derived the mathematical solution for the heat flow as a function of time for a dike of ocean crust in a fixed reference frame. In order to model the evolution of the oceanic lithosphere, we have to work in two dimensions (z and x), and consider that the lithosphere is *moving*, i.e. we cannot use a fixed reference frame. Since the ocean crust is moving we have to consider heat transport by advection and conduction.

Consider a column of lithosphere moving away from the ridge axis at a constant velocity U , as shown below (figure modified from Turcotte and Schubert, 1982):



The temperature at the ridge crest at $x=0$ beneath the plate is T_m . The sea water cools the surface rocks suddenly to the temperature T_s . As the column moves away from the ridge crest, its surface temperature is maintained at T_s , and it gradually cools. Fourier's law prescribes that the **conductive heat flux** q_{cond} across a region linearly proportional to the applied temperature gradient ∇T is

$$q^{cond} = -k\nabla T$$

where k is the thermal conductivity of the material. The advective heat flux q_{ad} across a region is linearly proportional to the velocity U and temperature T within the

region:

$$q^{ad} = \rho c_p U T$$

where ρ is the density, and c_p the specific heat of the material. Lithosphere moving at a uniform velocity U will have:

Horizontal heat transport by advection: $q_x^{ad} = \rho c_p U T$ Horizontal heat transport by conduction: $q_x^{cond} = -k \frac{\partial T}{\partial x}$

Vertical heat transport by advection: $q_x^{ad} = 0$ ($U_z = 0$) Vertical heat transport by conduction: $q_x^{cond} = -k \frac{\partial T}{\partial z}$

Conservation of energy implies: $\nabla q = \left(\frac{dq_x}{dx} + \frac{dq_z}{dz} \right) = 0$

$$\nabla q \left(\frac{dq_x}{dx} + \frac{dq_z}{dz} \right) = 0$$

i.e. there is no net heat transported into or out of the region (e.g. no heat production by radioactive decay, phase changes, etc.). Before we go any further, let's simplify our model scenario even more. Above we have listed two heat conduction terms and one heat advection term. But how important is horizontal conductive heat transport compared with horizontal advective heat transport?

$$q_x = \rho c_p U_x T - k \frac{\partial T}{\partial x}$$

$$\rho = 3300 \text{ kg/m}^3$$

$$c_p = 1000 \text{ Joule/kg/K}$$

$$k = 3 \text{ W/m/K}$$

$$U_x = 30 \text{ mm/yr} = 10^{-9} \text{ m/sec}$$

$$T = 1600 \text{ K} \approx 1300^\circ \text{C}$$

Using these values, the advective heat transport is:

$$q_x^{ad} = \rho c_p U_x T - k \frac{\partial T}{\partial x} \approx 5 \text{ Watts/m}^2$$

To conductively transport a comparable amount of heat implies a horizontal temperature gradient

$$\frac{\partial T}{\partial x} = 2000 \text{ K/km}$$

Since typical lithospheric horizontal temperature gradients are $< 1 \text{ K/km}$ we can safely ignore the effects of horizontal conductive heat transport with respect to advective heat transport within the lithosphere. Also vertical temperature gradients are much larger than horizontal temperature gradients. So we have reduced the problem to a **boundary layer approximation** for the thermal structure of the lithosphere involving two terms:

Horizontal heat transport by advection: $q_x^{ad} = \rho c_p U T$

Vertical heat transport by conduction: $q_x^{cond} = -k \frac{\partial T}{\partial z}$

Conservation of energy requires: $0 = \nabla q = \rho c_p U_x \frac{\partial T}{\partial x} - k \frac{\partial^2 T}{\partial z^2}$

or

$$U_x \frac{\partial T}{\partial x} = K \frac{\partial^2 T}{\partial z^2}$$

where K is the thermal diffusivity of the mantle, and $K = k/\rho c_p [m^2/sec]$.

Boundary conditions for the evolution of the lithosphere are:

(1) The temperature T is the mantle temperature T_m at great depths: $T = T_m$ at $x = 0, z > 0$

(2) the surface temperature is T_s : $T = T_s$ at $z = 0$

(3) at the ridge axis material is emplaced at the mantle temperature T_m : $T = T_m$ at $z \rightarrow \infty$

This problem is posed in a reference frame that is fixed to the ridge axis. It is slightly more convenient to use a reference frame tied to the plate, i.e. moving with a velocity U_x , so that the distance x covered in a time t is $x = U_x t$ (i.e. $dx = U_x dt$).

The boundary conditions are now:

$$T(z, 0) = T_m \text{ for } z > 0$$

$$T(0, t) = T_s$$

$$T = T_m \text{ as } z \rightarrow \infty$$

In the moving reference frame, the temperature becomes:

$$\frac{\partial T}{\partial t} = K \frac{\partial^2 T}{\partial z^2}$$

This is in fact the **one-dimensional heat conduction equation** without any radioactive heat source that we have encountered before while looking at the problem of instantaneous cooling or heating and Kelvin's problem of the age of the Earth, and we derived the solution there.

Now we assume local isostasy to solve for the **thermal subsidence** due to cooling as the lithosphere ages. Local isostatic compensation implies that the mass within each lithospheric column stays constant as it spreads away from the axis. We know that this assumption is incorrect, because its elastic thickness increases away from the ridge. However, as a first approximation we will neglect elastic properties of the lithosphere to calculate ocean depth versus age. As the lithosphere cools, its density increases due to thermal contraction and so the sea floor subsides to a greater water depth:

The mass per unit area in a column of any age is:

$$\int_0^{w+h} \rho(z) dz = \int_w^{w+h} \rho(z) dz + w\rho_w$$

At the ridge axis, the lithosphere has zero thickness, and the mass of the column at the ridge is

$$\rho_m(w + h)$$

where ρ_m is the density of the asthenospheric mantle. Isostatically balancing the column at the ridge with the off-ridge column (see figure above) results in:

$$\rho_m(w + h) = \int_w^{w+h} \rho(z) dz + w\rho_w$$

Substituting $y = z - w$ yields

$$(\rho_m - \rho_w)w = \int_0^h \rho(y) dy - h\rho_m = \int_0^h (\rho(y) - \rho_m) dy$$

whi, introducing the volume coefficient thermal expansion α_v :

$$\rho(y) - \rho_m = -\rho_m \alpha_v (T - T_m)$$

gives:

$$(\rho_m - \rho_w)w = -\rho_m \alpha_v \int_0^h (T(y) - T_m) dy$$

We substitute the temperature profile of the lithosphere derived earlier

$$T(z, t) = T_m \operatorname{erf} \left(\frac{z}{2\sqrt{Kt}} \right)$$

to obtain:

$$(\rho_m - \rho_w)w = \rho_m \alpha_v T_m \int_0^h \operatorname{erfc} \left(\frac{y}{2\sqrt{Kt}} \right) dy$$

where erfc is the complementary error function. Taking $h \rightarrow \infty$, and knowing that $\int_0^\infty \operatorname{erfc}(ax) = \frac{1}{a\sqrt{\pi}}$, one gets:

$$(\rho_m - \rho_w)w = 2\rho_m \alpha_v T_m \sqrt{\frac{Kt}{\pi}}$$

from which we can obtain the ocean depth relative to the ridge crest:

$$w = \frac{2\rho_m \alpha_v T_m}{\rho_m - rho_w} \sqrt{\frac{Kt}{\pi}}$$

which needs the depth of the crest in order to obtain the real ocean floor depth:

$$w = w_0 + \frac{2\rho_m \alpha_v T_m}{\rho_m - rho_w} \sqrt{\frac{Kt}{\pi}}$$

By using the following values,

$$\rho_w = 1000 \text{ kg m}^{-3}$$

$$\rho_m = 3300 \text{ kg m}^{-3}$$

$$\alpha = 3 \times 10^{-5} \text{ }^\circ\text{C}^{-1}$$

$$K = 10^{-6} \text{ m}^2 \text{ s}^{-1}$$

$$T_m = 1300 \text{ }^\circ\text{C}$$

$$w_0 = 2500 \text{ m}$$

we can obtain a simplified formula as given by (Parson and Sclater, 1977):

$$w = 2500 + 350\sqrt{t}$$

This formula satisfies observational constraints quite well for ocean crust younger than 80 m.y. as we have seen before.

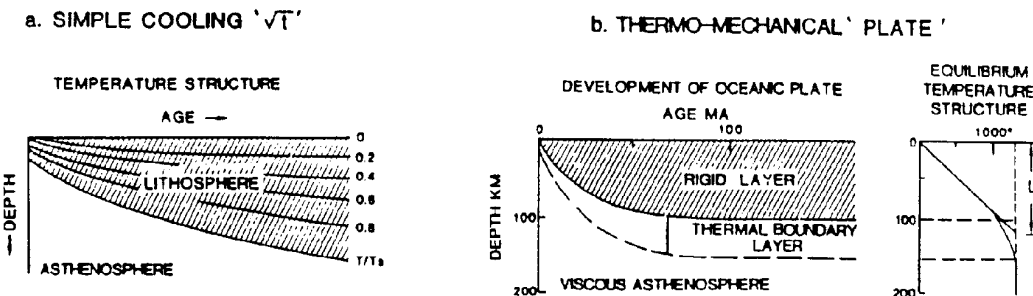
The following figure shows a 3-D plot of temperature/depth profiles in 2 m.y. intervals for temperatures from 0-1350°C and depths from 0-125 km, illustrating the evolution of the lithospheric temperature while it ages and cools.

9.6.7.1 Plate model

The ocean floor subsidence with age “flattens” for ages older than 80-100 m.y., i.e. the observed subsidence is smaller than expected from the above half-space cooling model. One possibility to explain the observed “flattening” is that by some means there is more heat beneath old lithosphere than predicted by the half-space cooling model. Possible mechanisms include small scale convection, radioactive heat decay, phase changes, and mantle plumes.

A popular alternative to the half-space cooling model is the so-called plate model proposed by Mckenzie and Parker (1967) and assessed by Parsons and Sclater (1977):

BOUNDARY LAYER MODELS OF OCEANIC LITHOSPHERE



For the plate model it is assumed that below some depth L the mantle temperature is maintained at T_m , and the proposed mechanism for the required supply of heat is small-scale convection in a lower thermal boundary layer. The boundary conditions are:

$$\begin{aligned} T(L, t) &= T_m \\ T(0, t) &= 0 \\ T(z, 0) &= T_m \end{aligned}$$

The solution for the two-dimensional heat conduction equation (without neglecting horizontal heat conduction), concludes that a w_{final} depth exists that is the asymptotic oceanic depth for ages greater than 80 Myrs.

The plate model fits observed ocean depths for ages greater than 80 m.y. much better than the cooling boundary layer model. The model was evaluated by Parsons and Sclater (1977) whose best fitting parameters to match observed depth and heat flow data are a plate thickness of 125 km and a ridge crest temperature of 1350°C.

Until now, the plate model has remained an empirical qualitative model whose predictions fit the observations, but there is no conclusive evidence, whether or not the mechanisms implied by the plate model work in the real world. Stein and Stein (1992) have presented a plate model with different parameters from the ones used by Parsons and Sclater (1977), i.e. a thinner and hotter plate, but in a subsequent study (Stein and Stein, 1992) they conceded that the best fitting parameters vary considerably between different ocean basins. The best fitting plate thickness varies from 90-150 km, and the ridge crest temperatures from 1325–1440°C. These differences are inconsistent with observed oceanic crustal thicknesses, which are quite constant at about 7 km for normal ocean crust (White *et al.*, 1992). An analysis of plate bending at trenches also showed that Stein and Stein (1992) plate model (named GDH1) is not consistent with bending moments observed at outer rises seaward of old trenches (Levitt and Sandwell, 1995). Another recent study (Carlson and Johnson, 1994) concluded that all plate models fail to explain the variation in subsidence and heat flow data for the entire oceanic age range of 0-160 m.y.

Also, it is not clear, by which physical mechanism heat would be supplied to the bottom of the lithosphere to maintain a constant lithospheric thickness, and provide a physical meaning for the “plate”. One suggestion has been, that the **plate consists of two parts: an upper mechanical boundary layer, and a lower viscous thermal boundary layer**. This thermal boundary layer may become unstable when ocean crust is about 60 m.y. old, and **small-scale convection** may develop (Parsons and McKenzie, 1978), as observed in laboratory experiments, resulting in increased heat flow to the base of the rigid layer, and a thermal structure as that predicted by the plate model.

Unfortunately, O’Connel and Hager (1981) showed that the stirring action of small scale convection acts to more rapidly cool the upper mantle, leading to increased rates subsidence, rather than delaying subsidence. Another piece of evidence in the favor of small scale convection are medium-wavelength (several 100s km) lineations in the gravity field over the ocean basins. However, a recent geophysical survey of a seamount chain in the central Pacific, which had been thought to reflect volcanism due to small scale convection over upwelling limbs of two convection cells, turned out to located in a gravity anomaly trough (presumably the downwelling limb) (Sandwell *et al.*, 1995).

The global observations of bathymetry and heat flow data have not been conclusive to discriminate between different plate models, or even between the plate models and the half-space cooling model, because

- 1) The quality of heat flow data varies substantially
- 2) The sediment thickness is often not known well enough to be corrected for
- 3) The oceanic crustal thickness is not known well enough in areas where it deviates from normal ocean crust (i.e. oceanic plateaus)
- 4) different ocean basins may have subsided from different ridge elevations at zero age,
- 5) the thermal effects of hotspots are difficult to constrain, varying both in time and space (*von Herzen et al.*, 1989), and
- 6) it is complicated to model the effect of asthenospheric flow on lithospheric subsi-

dence.

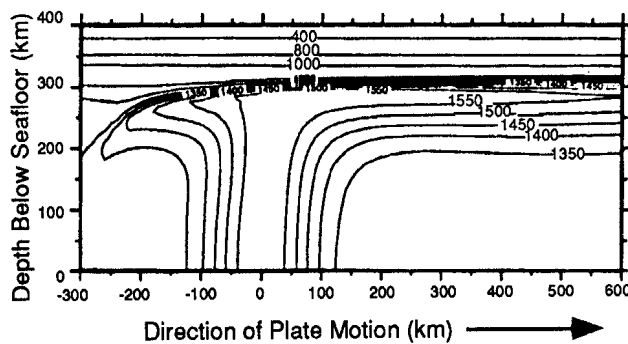
Given the unsatisfactory fit of different plate models to much of the data, and the lack of evidence for small-scale convection in a lower boundary layer of the plate, other models have been investigated. They fall in three categories:

- 1) **Thermal** – extra heat is added to the plate via hot spots: **Hotspot rejuvenation**
- 2) **Dynamic** – increasing pressure in the asthenosphere prevents seafloor from subsiding: **Asthenospheric flow**
- 3) **Chemical** – upper mantle mineralogy altered to low-density phases in the process of hot spot volcanism:

In the following we will briefly review these three model categories.

Hotspot rejuvenation Perhaps the simplest scenario to explain the addition of heat to older lithosphere is **hotspot rejuvenation**. When oceanic lithosphere passes over a hotspot of focused mantle upwelling, associated with volcanism, it may be thermally rejuvenated to a thermal structure like that of relatively young lithosphere of an age of 25m.y. This implies that the lithosphere would be both thinned and uplifted. The best known examples for such hotspot activity are StateHawaii and Iceland. It subsequently subsides like 25m.y. old lithosphere, unless it passes over yet another hotspot. In this scenario the apparent >80m.y. flattening trend of ocean floor might be explained from a significant fraction of older lithosphere passing over a hotspot at least once by the time it is ~100m.y. old. These ideas were explored by *Crough [1978]* and *Heestand and Crough [1981]*.

Recent numerical experiments modelling the effect of a hot, upwelling mantle plume on the lithosphere have shown that a low viscosity plume is very inefficient in thinning the overlying plate (*Ribe and Christensen, 1994; Sleep, 1994*).



Above a cross-section through the upper 400 km of the earth shows the interaction of a plume with a plate moving to the right. The vertical flux of the plume was adjusted to produce the observed amount of uplift for the Hawaiian swell. Note that the plume produces little thinning of the lithosphere, as measured by the shoaling of the 1200°C isotherm (from *Ribe and Christensen, 1994*). It has also been shown that there is insufficient time for conductive thinning of the lithosphere by a mantle plume, except for when the absolute plate motion speed is very low (*Liu and Chase, 1991*).

Much of the evidence for the “flattening” of the depth-age profile of old ocean crust has come from the western Pacific ocean basin. However, recent studies have indicated that the shallow depths in this area might be a residual effect of a Cretaceous “superplume” which created the great Pacific plateaus and created anomalously hot and thick asthenosphere, which might explain the geoid low over the superswell (Larsen, 1991; McNutt and Judge, 1990). In conclusion, it is likely that hotspots contribute to anomalous subsidence, but exactly how is not clear.

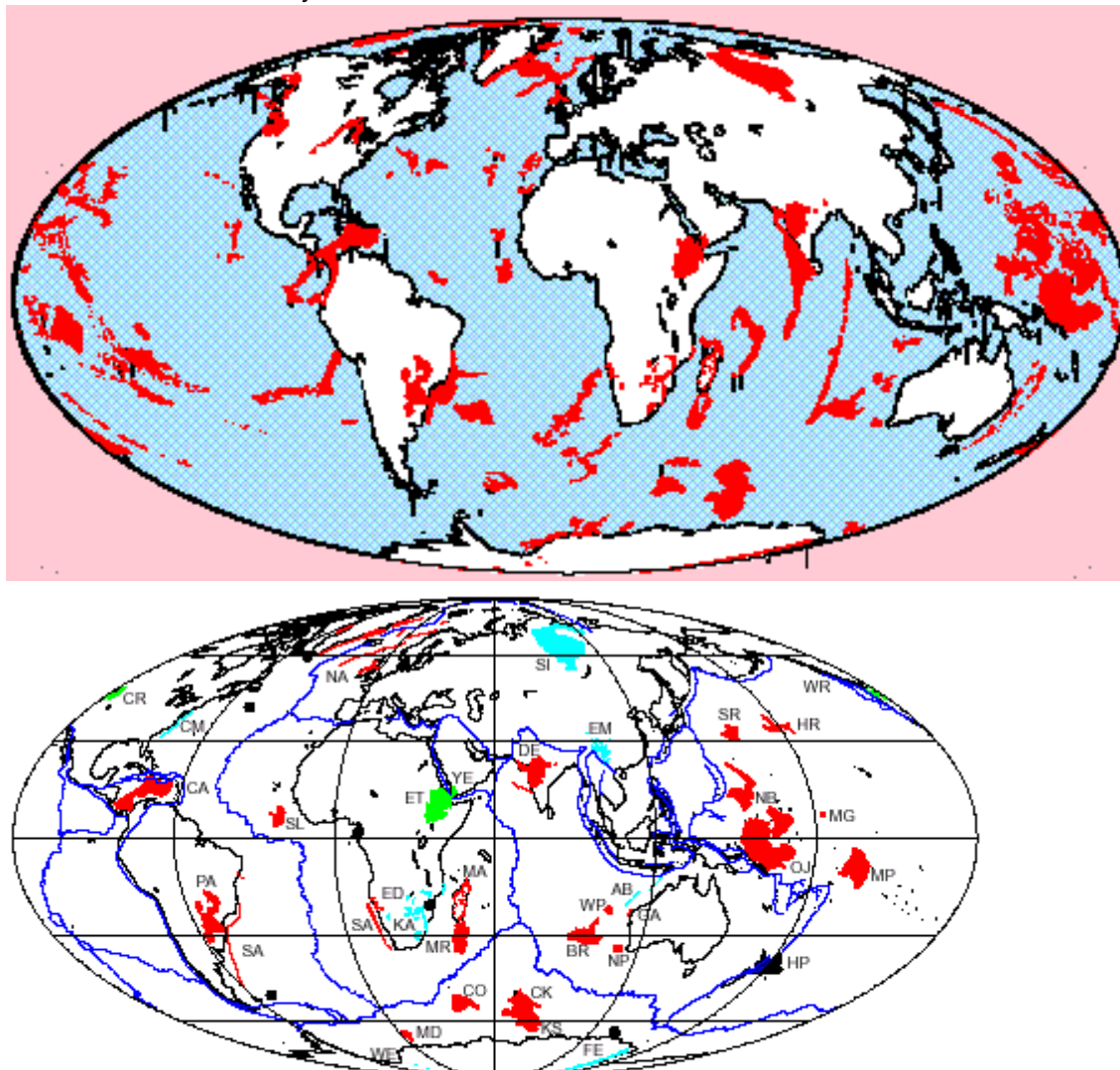


Figure 30. Distribution of major Mesozoic and Cenozoic transient LIPs, including oceanic plateaus, volcanic rifted margins, continental flood basalt provinces, submarine ridges and seamount chains. Light blue >150 Ma, red 150–50 Ma, green 50–0 Ma, black undated. Volcanic margin LIPs (lineations and circles) are mainly based on occurrences of seaward-dipping reflectors in seismic profiles. Current plate boundaries appear in dark blue. (Figure from Eichholz and Coffin, American Geophysical Union Monograph 121, 2000.)

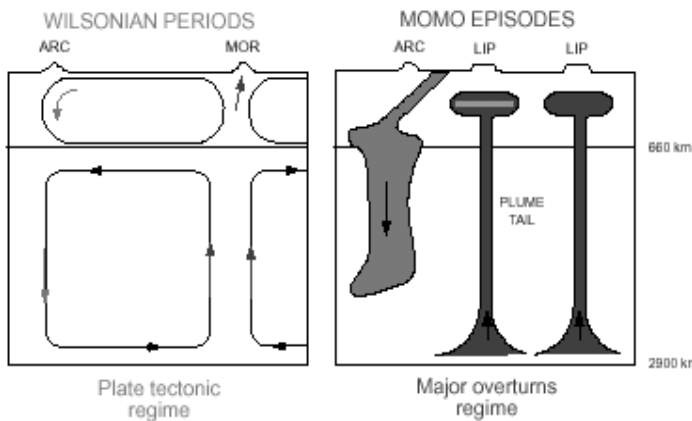


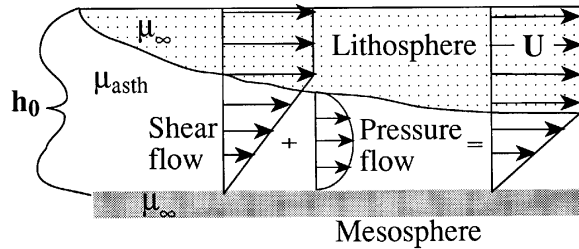
Figure 32: Model of Wilsonian periods and MOMO (Mantle Overturn, Major Orogeny) episodes. During Wilsonian periods (left), the normal mode of plate tectonics prevails, with opening and closing of oceans and mantle convection with isolated upper and lower mantle plumes originate predominantly from the base of the upper layer, and continental growth is dominated by arc accretion. During MOMO episodes (right), accumulated cold material descends from the 660-km boundary layer into the lower mantle, and multiple major plumes rise from the core-mantle boundary to form Large Igneous Provinces (LIPs) at the surface, thus creating a major overturn. (Figure from Stein and Hofman, *Nature*, 1994)

Asthenospheric flow Asthenospheric flow is a promising mechanism for modeling plate subsidence because as opposed to simple thermal cooling models or the plate model, it might be able to explain why the subsidence of conjugate ridge flanks is often asymmetric, i.e. one ridge flank subsides faster than the opposite one. Sub-axial asthenosphere flow from a near-ridge hotspot source as a mechanism to inducing asthenospheric flow was first suggested by *Vogt and Johnson* (1975). Recently, *Phipps Morgan and Smith* (1992) have developed an extended model for asthenospheric shear flow, which we will briefly discuss in the following.

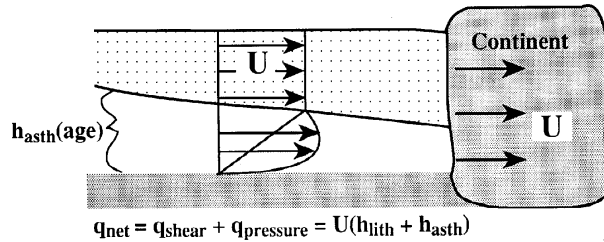
All thermal models discussed so far share one assumption, namely that the deeper mantle beneath the lithosphere is moving away from the ridge at the same speed as the sea floor. While it seems intuitively plausible that the cold, strong lithosphere should move as a rigid unit, the assumption that the asthenosphere is moving at the same uniform velocity as the overlying lithosphere is actually a very strong constraint on mantle flow patterns. If the asthenosphere is a weak decoupling zone between tectonic plates and the underlying deeper mantle, we might expect this region to be a zone of large-scale horizontal shear flow.

Shear flow boundary layer analysis suggests that a spatially uniform pattern of asthenospheric shear flow will produce detectable $(age)^{1/3}$ perturbations to the overall $(age)^{1/2}$ subsidence trend. *Phipps Morgan and Smith* (1992) have evaluated the mechanism for a model for asthenosphere flow which is fed by hotspots and consumed by plate accretion.

1a) Origin of Dynamic Flow Component



1b) Continental Flux B.C.



1c) Subduction Flux B.C.

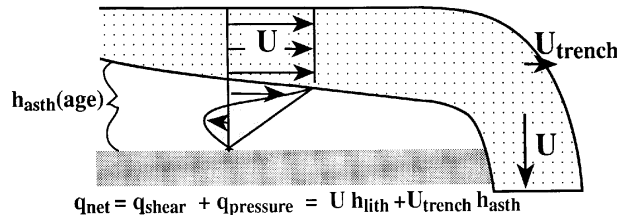


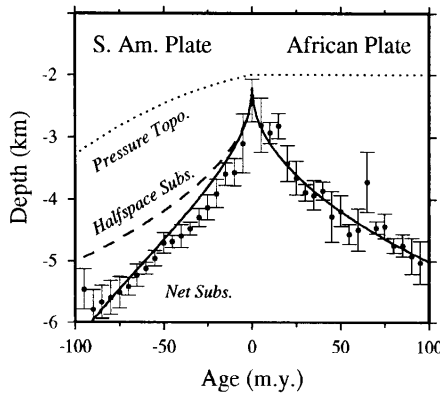
Figure 1a shows a sketch of a 2-D approximation for computing asthenospheric flow. The asthenosphere is bounded by an isotherm above, since the viscosity in the lithosphere-asthenosphere system is temperature dependent, and by an isobar below, since the viscosity at the boundary between asthenosphere and mesosphere is pressure dependent. While the plate cools and thickens, asthenospheric material is incorporated into the lithosphere. The net horizontal asthenosphere and lithosphere flux is constant. Thus the incorporation of asthenosphere into a cooling, accreting lithosphere produces a dynamic pressure gradient to drive a pressure-induced flow component to replenish this lithospheric sink.

Figure 1b illustrates the outflow boundary condition on asthenospheric flow for an oceanic-continental margin. Here the net asthenosphere and lithosphere flux is equal to the absolute plate motion times the total thickness of continental lithosphere and asthenosphere.

Figure 1c shows the outflow boundary condition for an oceanic subduction zone where only the lithosphere subducts. Also shown is an additional flow component if the trench is also migrating with respect to the mesosphere, e.g. towards the mid-ocean

ridge (trench roll-back).

This model has been tested to explain the asymmetric subsidence of a single South Atlantic tectonic corridor, and it appears to be a promising mechanism for the origin of asymmetric plate subsidence about a common ridge origin. In the South Atlantic the South American plate (which is moving westward w.r.t. the hotspot frame) is subsiding more rapidly with age than the conjugate (almost stationary w.r.t. hotspot frame) African plate on the other side of the Mid-Atlantic Ridge.



This asymmetric subsidence results in a roughly 1-km-depth anomaly of 100 Ma South American plate seafloor with respect to similar age African plate seafloor. We have discussed earlier that the relationship between a depth anomaly and the corresponding geoid anomaly allows one to infer the depth of the mass anomaly which ultimately compensates a dynamic surface depression.

From the ratio of dynamic depth anomaly to dynamic geoid anomaly we can infer the depth of the mass anomaly which is compensating the dynamic depression of the South American plate. This exercise yields a geoid compensation depth of only ~200 km, which may be the depth of the base of a hotter, and thus both lower viscosity and lower density asthenosphere channel – the same dynamic pressure effect which pulls down the seafloor will tend to pull up the base of this channel.

Chemical effects on seafloor depths Hotspot volcanism might increase the buoyancy of the lithosphere by augmenting crustal thickness and altering mantle mineralogy. Recent studies have shown that the amount of melt produced by hotspots might have been underestimated by a factor of 10 by overlooking the massive amount of volcanoclastic debris shed into the archipelagic aprons from mass wasting of the volcanoes (Filmer *et al.*, 1994; Wolfe *et al.*, 1994) and thick mafic bodies underplating the crust beneath the surface edifices (Caress *et al.*, 1995). Jordan (1979) originally proposed that melt extraction from the mantle would leave a less dense mantle residuum, which may form continental roots. Phipps Morgan *et al.* (1995) suggested that this residuum would form a high-viscosity, low density body at depths of about 60 km beneath a hotspot swell. Its subsequent lateral flow and spreading might be able to explain some departures of lithospheric subsidence from half-space cooling.

9.7 References

- Birch, F., 1958, Differentiation of the mantle, *Bull. geol. Soc. Am.*, 69, 483-486.
- Birch, F., 1965, Energetics of core formation, *J. Geophys. Res.*, 70, 6217-6221.
- Bullard, E.C., 1947, The time necessary for a borehole to attain temperature equilibrium, *Mon. Not. R.A.S., Geophys. Suppl.*, 5, 127.
- Bullard E.C., A.E. Maxwell, and R. Revelle, 1956, Heat flow through the deep sea floor, *Adv. Geophys.*, 3, 153.
- Carlson, R.L., and H.P. Johnson, 1994, On modeling the thermal evolution of the oceanic upper mantle: An assessment of the cooling plate model, *J. Geophys. Res.*, 99, 3201-3214.
- Chapman, D.S., and K.P. Furlong, 1992, Thermal state of the continental crust, in *Continental Lower Crust, Dev. Geotecton.*, 23, ed. by D.M. Fountain, R.J. Arculus, and R.W. Kay, Elsevier, New York, 179-199.
- Dubrovsky, V.A. and V.L. Par'kov, 1972, On the composition of the Earth's core, Acad. Sci., USSR, *Phys. Solid Earth*, No. 7, 452-455 (translation).
- Knittle, E. and R. Jeanloz, 1989, Simulating the core-mantle boundary – an experimental study of high-pressure reactions between silicates and liquid iron, *Geophys. Res. Lett.*, 16, 609-612.
- Jordan, T.H., 1979, Continents as a chemical boundary layer, *Philos. Trans. R. Soc. London A*, 301, 359-373.
- Larsen, R.L., 1991, Latest pulse in the earth: Evidence for a mid-Cretaceous super plume, *Geology*, 19, 547-550.
- Liu, M. and C.G. Chase, 1991, Evolution of the Hawaiian basalts: a hot spot melting model, *Earth Planet. Sci. Lett.*, 104, 151-165.
- McNutt, M.K. and A.V. Judge, 1990, The superswell and mantle dynamics beneath the South Pacific, *Science*, 248, 969-975.
- McKenzie, D.P., 1967, Some remarks on heat flow and gravity anomalies, *J. Geophys. Res.*, 72, 6261-6273.
- McKenzie, D.P. and F.M. Richter, 1981, Parameterized thermal convection in a layered region and the thermal history of the Earth, *J. Geophys. Res.*, 86, 11667-11680.
- O'Connell, R.J. and B.H. Hager, 1981, On the thermal state of the earth, in *Physics of the Earth's Interior, Proc. Enrico Fermi Int. Sch. Phys.*, ed. by A Dziewonski and E. Boschi, 78, 270-317.
- Oxburgh, E.R. and R.K. O'Nions, 1987, Helium loss, tectonics, and the terrestrial heat budget, *Science*, 237, 1583-1588.
- Parsons, B. and D.P. McKenzie, 1978, Mantle convection and the thermal structure of the plates, *J. Geophys. Res.*, 83, 4485-4496.
- Parsons, B. and J.G. Sclater, 1977, An analysis of the variation of ocean floor bathymetry and heat flow with age, *J. Geophys. Res.*, 82, 803-827.
- Phipps Morgan, J. and W.H.F.S. Smith., 1992, Flattening of the seafloor depth-age curve as a response to asthenospheric flow, *Nature*, 359, 524-527.

- Phipps Morgan, J., W.J. Morgan and E. Price, 1995, Hotspot melting generates both hot spot volcanism and a hot spot swell? *J. Geophys. Res.*, 1995.
- Pollack, H.N., S.J. Hunter, and J.R. Johnston, 1993, Heat flow from the earth's interior: Analysis of the global data set, *Rev. Geophys.*, 31, 267-280.
- Renkin, M.L. and J.G. Sclater, 1988, Depth and age in the north Pacific, *J. Geophys. Res.*, 93, 2919-2935.
- Ribe, N. and U.R. Christensen, 1994, Three-dimensional modeling of plume-lithosphere interactions, *J. Geophys. Res.*, 99, 669-682.
- Ringwood, A.E., 1979, *Origin of the Earth and Moon*, p. 34, Springer Verlag, New York.
- Richter, F.M., 1984, Regionalized models for the thermal evolution of the earth, *Earth Planet. Sci. Lett.*, 68, 471-484.
- Richter, F.M., 1985, Models for the Archean thermal regime, *Earth Planet. Sci. Lett.*, 73, 350-360.
- Sandwell D.T., E.L. Winterer, J. Mammerickx, R.A. Duncan, M.A. Lynch, D.A. Levitt, and C.L. Johnson, 1995, Evidence for diffuse extension of the Pacific plate from the Pukapuka ridges and crossgrain gravity lineations, *J. Geophys. Res.*, 1995.
- Sclater, J.G., C. Jaupart, and D. Galson, 1980, The heat flow through oceanic and continental crust and the heat loss of the earth, *Rev. Geophys. Space Phys.*, 18, 269.
- Sclater, J.G., C. Jaupart, D. Galson, 1980, The heat flow through oceanic through oceanic and continental crust and the heat loss of the Earth, *Rev. Geophys. Space Phys.*, 18, 269-311.
- Sclater, J.G. and L. Wixon, 1986, The relationship between depth and age and heat flow and age in the western North Atlantic, : in Vogt, R., and Tucholke, B. E., eds., *The Geology of North America, Vol. M, The Western North Atlantic Region*: Geol. Soc. Am.,
- Sleep, N.H., 1994, Lithospheric thinning by midplate mantle plumes and the thermal history of hot plume material ponded at sublithospheric depths, *J. Geophys. Res.*, 99, 9327-9343.
- Stein, C.A. and Stein S., 1992, A model for the global variation in oceanic depth and heat flow with lithospheric age, *Nature*, 359, 123-129.
- Stein, C.A. and Stein S., 1994, Comparison of plate and asthenospheric flow models for the thermal evolution of the lithosphere from global heat flow, *Geophys. Res. Lett.*, 21, 709-712.
- Turcotte, D.L., and Schubert, G., 1982, *Geodynamics: Applications of Continuum Physics to Geological Problems*, John Wiley & Sons, New York, 450 pp.
- Turcotte, D.L. and E.R. Oxburgh, 1967, Finite amplitude convection cells and continental drift, *J. Fluid Mech.*, 28, 29-42.
- Turcotte, D.L., and G. Schubert, 1982, *Geodynamics: Applications of Continuum Physics to Geological Problems*, John Wiley & Sons, New York, 450 pp.
- Vaquier, V., 1991, The origin of terrestrial heat flow, *Geophys. J. Int.*, 106, 199-202.
- Vaquier, V., 1992, Corrigendum to 'The origin of terrestrial heat flow', *Geophys. J. Int.*, 111, 637-638.
- Vogt, P.R. and G.L. Johnson, 1975, *J. Geophys. Res.*, 80, 1399-1428.

Von Herzen, R.P., M.J. Cordery, C. Fang, and R.S. Detrick, 1989, Heat flow and the thermal origin of hot spot swells revisited, *J. Geophys. Res.*, 94, 13783-13800.

White, R.S., McKenzie, D.P., and R.K. O'Nions, 1992, Oceanic crustal thicknesses from seismic measurements and rare earth element inversions, *J. Geophys. Res.*, 97, 19683-19715.

Wolfe, C.J., M.K. McNutt, and R.S. Detrick, The Marquesas archipelagic apron: Seismic stratigraphy and implications for volcano growth, mass wasting, and crustal underplating, *J. Geophys. Res.*, 99, 13591-13608.

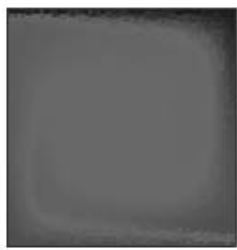
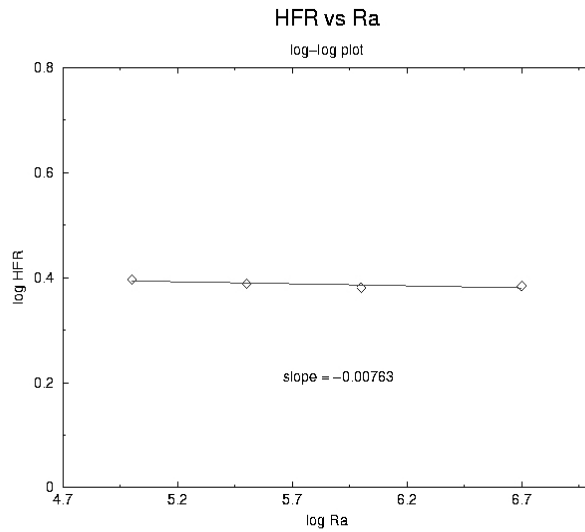


Figure 9.7: Isoviscous, bottom heated convection (left); and a log-log plot demonstrating the dependence the heat flux ratio on Rayleigh number (right). The heat flux ratio here is defined as the heat flux through the surface of the left tenth of the domain divided by the heat flux through the right tenth.

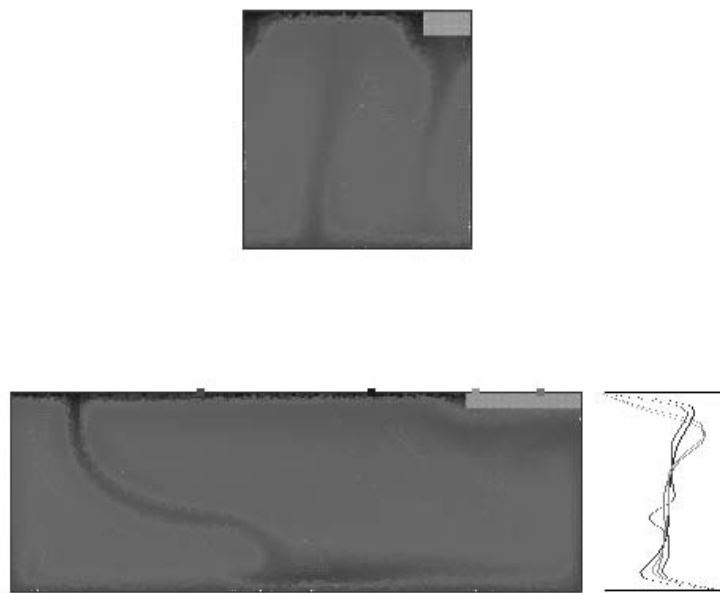


Figure 9.8: Temperature fields (red-blue) for bottom heated isoviscous convection with a chemically distinct continent (green) for a one by one cell (left) with periodic boundary conditions, and for a three by one cell with reflecting boundary conditions (right).

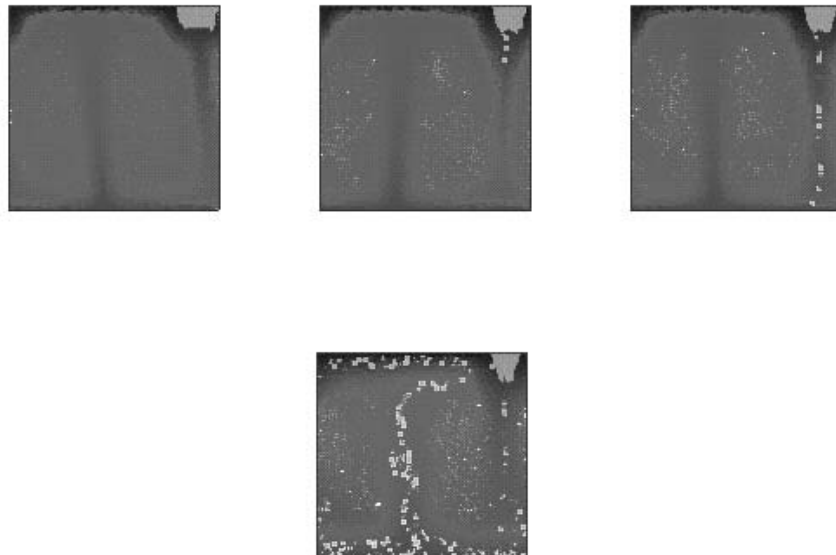


Figure 9.9: Weak, deformable continent (low viscosity) being entrained into the convecting mantle despite its chemical buoyancy with respect to the mantle material.

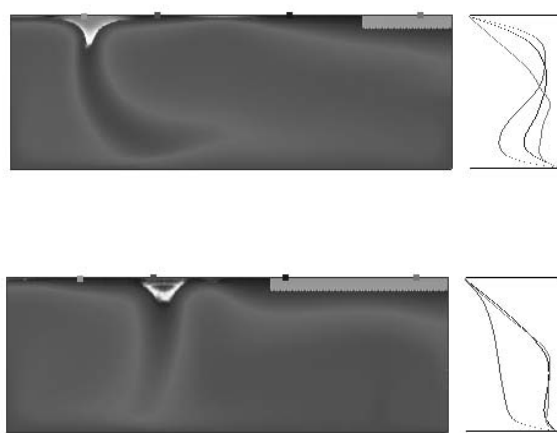


Figure 9.10: Convective flow pattern with geotherms for continental extents of 20% (top, left), 40% (top, right) and 60% (bottom, left) of the surface area. The cells are three by one with reflecting boundary conditions.

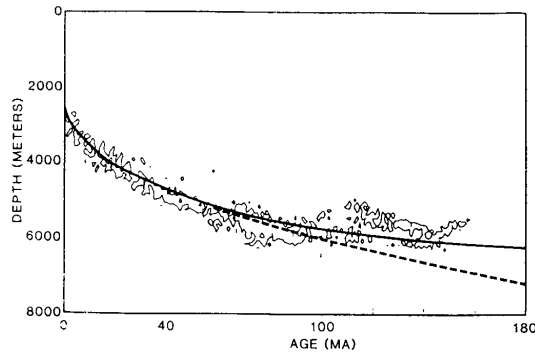


Figure 9.11: The above plot shows the **most frequent depths at a given age**, called the **mode**, versus age. The dashed line represents the predicted subsidence from a simple square root of age model based on a modeling a cooling boundary layer (*Parsons and Sclater, 1977*). It is obvious that the data fit this model very well for ages from 0 to ~80 Ma. For older ages the ocean crust is shallower than predicted by this model (we will explore the possible reasons for this later). The solid line represents the predicted subsidence from the so called “plate model” which was constructed in an attempt to account for the discrepancy between observations and the cooling boundary layer model.

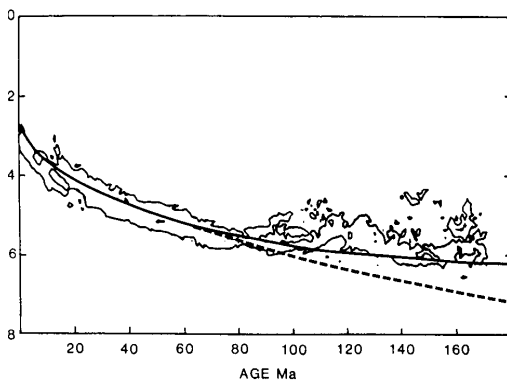


Figure 9.12: Here there is a clear deviation of the modal depths older than 80 Ma from the simple model (dashed line) as well, but for younger ages the fit is quite good.

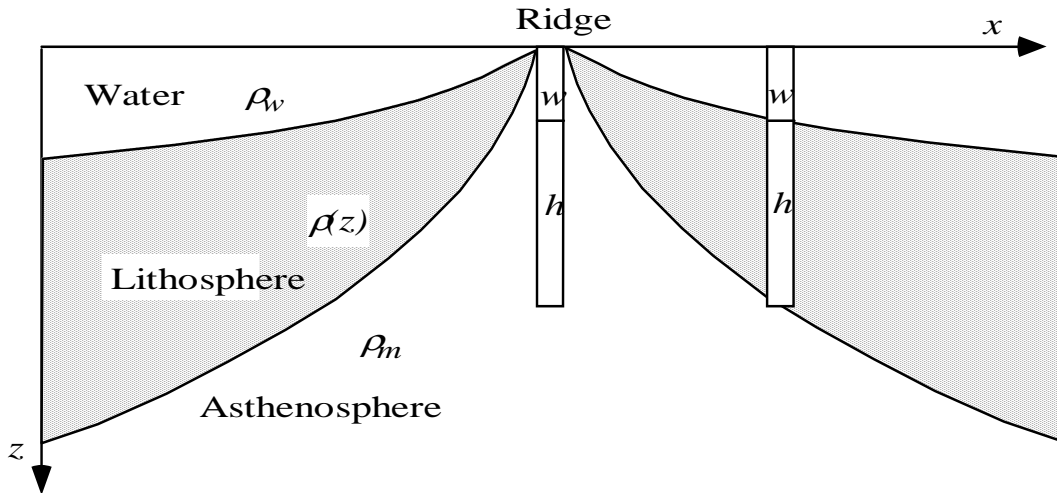


Figure 9.13: The two isostatically compensated columns shown above, one at the ridge, and one on the right ridge flank, extend from the surface to the depth of isostatic compensation at the lithosphere. They have the same mass per unit area, because the older column contains water to offset the added weight of dense lithospheric rock. Isostatic compensation is due to the ability of the mantle to act as a fluid on geological time scales. We can now use isostatic balancing and calculate the masses per unit area in these two columns to derive a formula for the depth of the ocean floor w as a function of age t or distance from the ridge x . The solution will be applicable to columns of all ages.

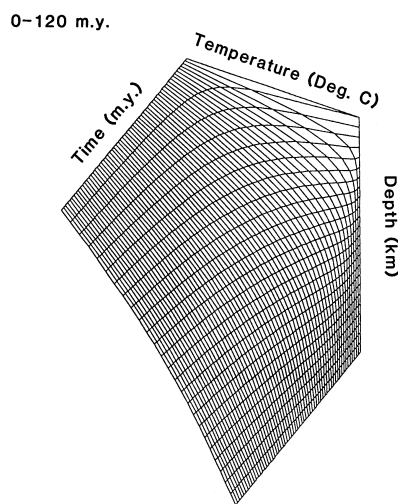
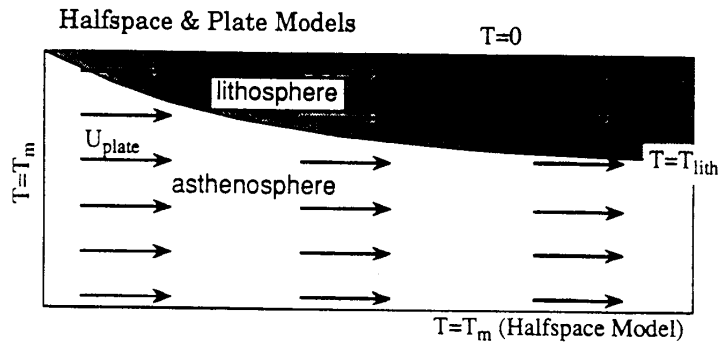
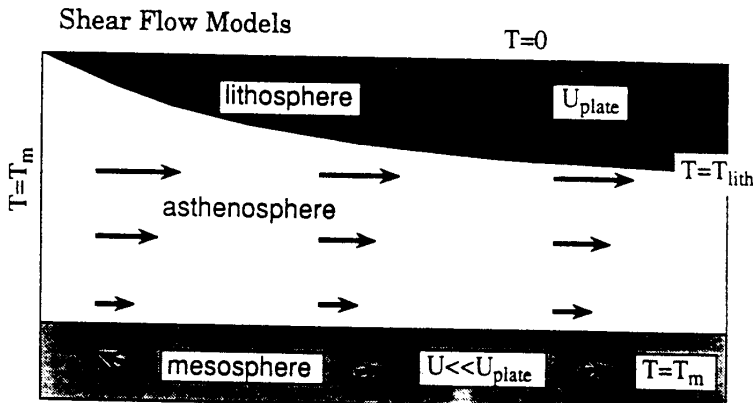


Figure 9.14: 3-D plot of temperature/depth with time for cooling oceanic lithosphere

Boundary layer flow patterns -- thermal implications



- Uniform flow of plate and underlying convecting mantle
- Implies strong coupling between plate and mantle
- Implies similar characteristic mantle and plate velocities
- These assumptions clash with many mantle flow paradigms



- Extensive asthenosphere separates lithospheric and mesospheric flow (except at subduction zones)

Figure 9.15: default

Chapter 10

Isostatic compensation

10.1 Introduction

A mass anomaly (such as a mountain) is said to be isostatically compensated if it is supported by the buoyancy of a mass anomaly of opposite sign rather than by elastic stresses. The observation that long-wavelength free-air gravity anomalies are small implies that large-scale topography must be isostatically compensated.

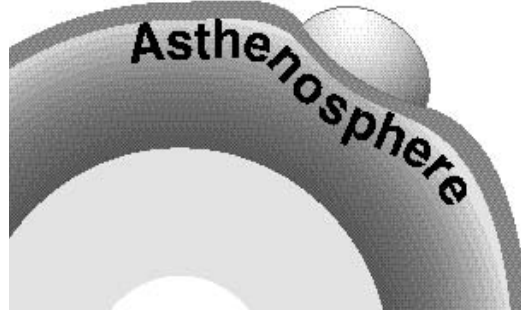


Figure 10.1: default

10.2 Airy model

There are two models for isostatic compensation. The first one is called the Airy model. It assumes hydrostatic equilibrium (i.e. floating iceberg model) which implies that regions with high elevation have a low-density root, whose depth depends on the density and the thickness of the body (e.g. thickness of the crust), as shown by the following sketch

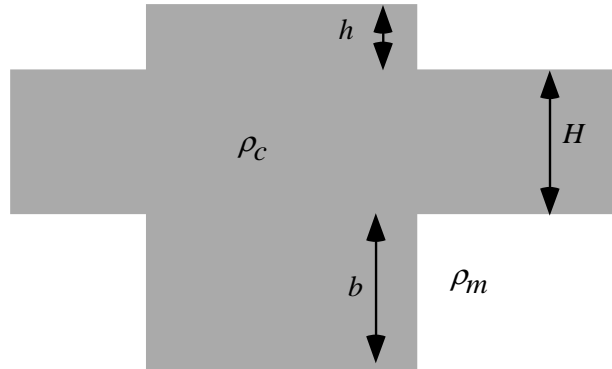


Figure 10.2: $\rho_m \cdot b = \rho_c \cdot (b + h)$

10.3 Pratt model

This model assumes that topography is compensated at the same depth for regions with different elevations. Isostatic compensation is achieved by varying densities in the layer.

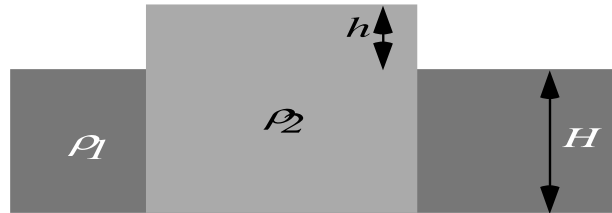


Figure 10.3: $\rho_1 \cdot H = \rho_2 \cdot (H + h)$

Although the Airy model is close to reality, in nature compensation is achieved at the regional scale rather than the local scale. In other terms the depth profile of base of the crustal root does not match peak for peak the mountain's topographic profile. Instead, the mountain belt is sustained by a crustal root with a smooth crust-mantle interface.

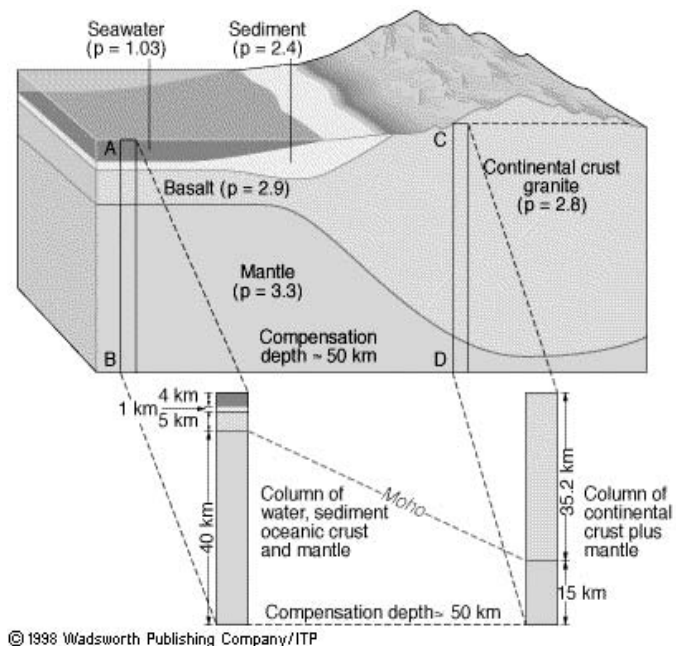


Figure 10.4: Isostasy: The average density of all crustal columns above a depth of compensation is the same.

Chapter 11

Driving forces of Plate Tectonics

11.1 Introduction

Even though it has been shown that surface tectonic plates can be self-consistently generated through 3D mantle convection (Tackley, 1998), the relative importance of driving forces of the time-dependent plate geometries and velocities of plates are still controversial. The question of what drives plate motion is indeed regarded as one of the most important scientific problems yet to be solved (Maddox, 1998). Identifying the main set of forces is relatively straightforward, but resolving the relative importance of individual forces for driving plate breakup and motion is more difficult. Ziegler (1993) argues for the dominance of basal shear traction (the convection drag) for causing plate motion. Others argue that basal shear only plays a small role due to weak coupling between the lithosphere and asthenosphere (even though the magnitude and lateral variability of this coupling is still unknown). Forsyth and Uyeda (1975), Richardson (1992) and Carlson (1983) argue that plate boundary forces are the main driving mechanisms of plate motion. Exactly which boundary forces play the most important role, however, is still an area of hot debate. Forces acting along the boundaries of plates that presumably drive plate motions are mainly caused by the upwelling of hot, buoyant asthenosphere at the mid ocean ridge and the subduction of cold, dense lithosphere at trenches.

11.2 Ridge Push

The ridge push force is often regarded as the primary plate driving mechanism (Coblentz et al., 1995; Meijer and Wortel, 1992; Richardson, 1992), although other authors regard it as secondary to other forces (Carlson, 1983; Forsyth and Uyeda, 1975). The ridge push force originates from a distributed pressure gradient (i.e., a body force) that acts on the entire plate normal to the strike of a mid ocean ridge. It arises from the isostatic sinking of the oceanic lithosphere away from the Mid Ocean Ridge as it cools and densifies

(Wilson, 1993).

The contribution of this topographic force can be calculated in two ways (Richardson, 1992). Firstly, it can be calculated as a line force acting along the length of the ridge normal to the strike of the ridge. Secondly, it can be calculated as a pressure gradient integrated over a profile perpendicular to the strike of the mid-ocean ridge crossing an entire ridge flank. The second method provides a more accurate result. The ridge push force F_{rp} can be calculated at a given location by the following equation based on a thermal boundary layer model (e.g. Turcotte and Schubert, 1982);

$$F_{rp} = g\rho_m\alpha_v(T_m - T_0) \left[1 + \frac{2}{\pi} \frac{\rho_m\alpha_v(T_m - T_0)}{(\rho_m - \rho_0)} \right] \kappa t$$

where $g = 10ms^{-2}$, $\rho_m = 3300kgm^{-3}$, $\rho_0 = 1000kgm^{-3}$, $\kappa = 1mm^2$, $(T_m - T_0) = 1200^\circ K$, $\alpha_v = 3 \times 10^{-5}^\circ K^{-1}$ and t is the age of the lithosphere.

If the plate model (McKenzie and Parker, 1967) is applied instead of a thermal boundary layer model then it follows that mainly oceanic crust younger than 80 m.y. contributes to the ridge push force as oceanic lithosphere older than this age does not cool considerably, resulting in the cessation of isostatic sinking of oceanic lithosphere older than 80 m.y.

Some authors have also found it advantageous to consider the ridge push force as a torque acting on the plate. Richardson (1992) used the equation above, integrated over the plate for lithosphere younger than 80 Ma, to give

$$T_{rp} = \int^A(r) \times F_{rp} dA$$

where T_{rp} is the torque from the R_{PF} , and A is the area of the plate younger than 80 Ma. Richardson (1992) demonstrated a good correlation between the azimuth of the ridge torque pole and the pole of absolute plate velocity. The T_{rp} has also been shown to correlate well with the direction of the first-order intraplate stress field of the Indo-Australian Plate (Coblentz et al., 1995).

11.3 Slab Pull

The slab pull force originates from the negative buoyancy of the downgoing dense oceanic lithosphere at subduction zones, and is proportional to the excess mass of the cold slab in relation to the mass of the warmer displaced mantle (Spence et al., 1987). This density contrast, and therefore energy contribution of the downgoing slab, can also be enhanced by the phase change from olivine to the more dense spinel, which occurs in the downgoing slab earlier than the surrounding mantle (Bott, 1982; Spence et al., 1987). Negatively buoyant slabs also induce mantle convection as they penetrate the mantle, in turn driving lithospheric plates through shear traction at the base of plates (Conrad and Lithgow-Bertelloni, 2004; Lithgow-Bertelloni and Richards, 1998). Because subduction induces mantle flow toward the downwelling material, these tractions cause

nearby plates to move toward subduction zones (Conrad and Lithgow-Bertelloni, 2004; Lithgow-Bertelloni and Richards, 1998).

Energy transmitted to the plate from the downgoing slab must be proportional to the excess mass M_e of the plate (Carlson, 1983). The excess mass is given by

$$M_e = 1/2(\rho_L - \rho_m) \frac{LE}{\sin \psi}$$

where ρ_L is the density of the lithosphere, ρ_m is the density of the mantle, L is the thickness of the lithosphere, E is the depth at which the excess density vanishes and ψ is the dip of the slab (Carlson, 1983). The force on the lithospheric plate F_{sp} can then be calculated using

$$F_{sp} = M_e g$$

where g is gravitational acceleration.

Forsyth and Uyeda (1975) regard slab pull as the main constraint on the velocity of plates (Figure 28). They consider the down-going slab as having a “terminal velocity” and that the potential energy stored in the down-going slab is an order of magnitude greater than any other force acting on the plate. The exact magnitude of the energy contained in the down-going slab has been disputed, with Spence et al. (1987) suggesting it may only be 3 times the size of other forces acting on the plate. Carlson (1983) suggested that the absolute plate speed is determined by the slab pull force, as a function of the age of the oceanic lithosphere being subducted at trenches, with older subducted lithosphere resulting in higher absolute plate velocities.

The “terminal velocity” of the plate, as discussed by Forsyth and Uyeda (1975), is due to high viscous drag forces acting on the down-going slab, that impede its entry into the mantle. Some authors have suggested that these viscous drag forces acting on the slab may actually be large enough to almost entirely balance out the negative buoyancy of the down-going slab (Coblentz et al., 1995; Sandiford et al., 1995). In this case, the net force experienced by the plate from the subducting slab may be of the same magnitude or less than other forces driving the plate. In contrast, Schellart (2004)’s recent dynamical lab experiments suggest that the net slab pull force may be up to twice as large as the ridge push force, and Conrad and Lithgow-Bertelloni (2004)’s models imply that slab suction and slab pull presently account for about 40 and 60% of the forces on plates, with ridge push globally playing a minor role.

11.4 Collisional Forces

Collisional forces do not act to drive the plate motions, but rather impede them. Collisional forces act along the boundary of plates and arise as a result of the frictional forces between the two colliding plates. At well-coupled subduction zones there is a build-up of frictional strain energy between the subducting plate and the overriding plate. This energy is then released through earthquakes and crustal deformation. Where the collision of a continental landmass is also involved, loss of energy from plate momentum

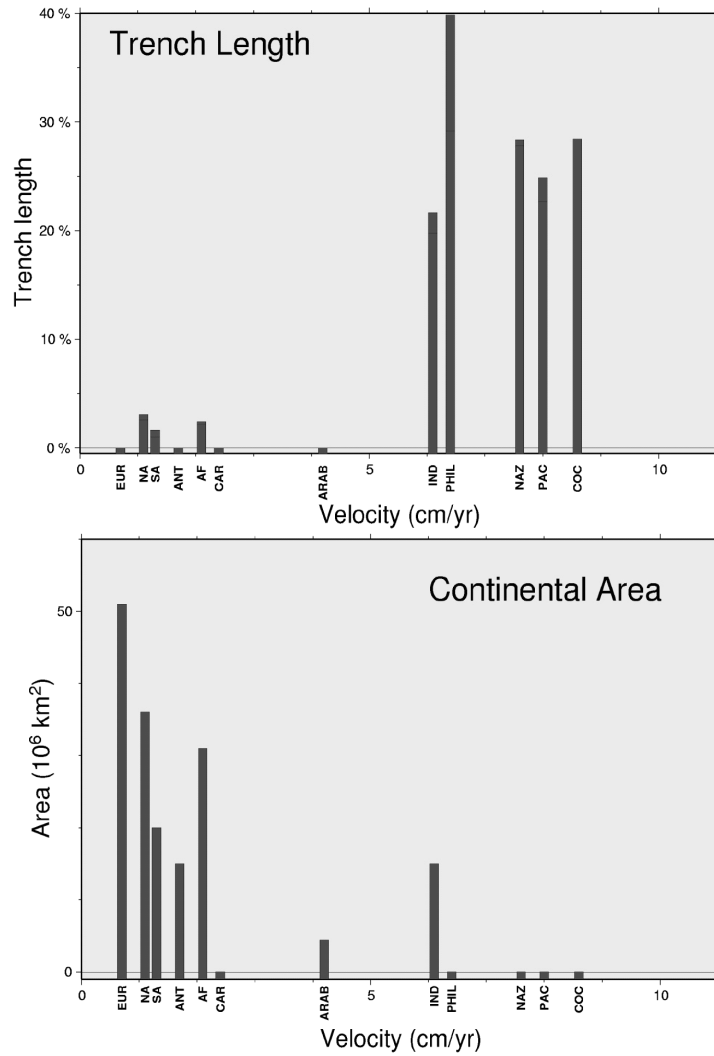


Figure 11.1: Trench length as a percentage of plate circumference, plotted versus the plates velocity (top). There is a clear correlation between high velocities and high percentage of trench length, suggesting trench pull is one of the more significant plate driving forces. Area of continental crust associated with a plate plotted versus plate velocity (bottom). It is seen that predominantly oceanic plates have significantly higher velocity than continental plates. Redrawn from Forsyth and Uyeda (1975).

is converted into excess gravitational potential energy stored as thickened crust (Bott, 1982). For instance, in the case of the collision between India and Asia responsible for the Himalayan orogen, the amount of energy converted into crustal thickening is of the same order as the plate driving forces, as the velocity of the plate slowed upon collision (Sandiford et al., 1995).

11.5 Basal Shear Traction

The notion of shear forces acting at the base of the plates with the convecting mantle acting as a “conveyor belt” driving the plates, while popular in the past, has fallen out of favour in preference to other plate driving mechanisms. While the relative importance of basal shear forces may be dominant under Pangea-style megacontinents (Ziegler, 1993), they probably play only a minor role in the kinematics of dispersed plates (for discussion see Wilson (1993)). Stoddard and Abbott (1996) argue that the crustal roots under cratons act like keels, and penetrate a rapidly convecting mantle. This interaction with the rapidly convecting mantle then acts to drive the motion of the plate. However, given our lacking knowledge of the extent of coupling of the lithosphere to the mantle (Coblentz et al., 1995), it is difficult to quantify the relative importance of basal shear relative to other forces.

11.6 Trench Suction

Trench suction is regarded as a lifting pressure or suction on the upper surface of the downgoing plate caused by an asthenospheric corner flow that is induced by the motion of the descending plate. This force is balanced by the negative buoyancy of the descending lithospheric plate that acts to pull it vertically down. by the motion of the descending plate. The balance of these two forces is thought to keep the plate at a finite descent angle (Stevenson and Turner, 1977).

11.7 What drives plate tectonics?

A major debate concerns a “top-down” versus mantle-driven mechanism for driving the organisation of plates (Anderson, 2001). Abundant plume-driven continental breakup examples and hypotheses associated with magmatic provinces (Coffin and Eldholm, 1992; Dalziel et al., 2000; Ebinger and Sleep, 1998; Storey, 1995) emphasize mantle driven tectonics. However, the good agreement between long-wavelength features of the intraplate stress field (Zoback, 1992) with the stress orientations predicted by ridge-push forces and large-scale absolute plate motions led to the view that plate motions and intraplate deformation result mainly from the balance between ridge push and collisional forces, emphasising a “top-down” mechanism, but without a significant role for slab pull (Richardson, 1992). Alternatively, slab-pull and slab-suction forces have been advocated as the most important driving forces of current plate motions (Con-

rad and Lithgow-Bertelloni, 2004, 2002; Forsyth and Uyeda, 1975; Schellart, 2004) in a “top-down” context.

Most analyses of plate driving forces and intraplate stresses are focused on the Earth’s present dispersed plate geometry (e.g. Cloetingh and Wortel, 1986; Richardson, 1992; Sandiford et al., 1995), where ridge-push is a major contributor to plate motions, most continents are under gravity-controlled compression, and the most prominent intra-continental rift, the Afar triangle in Africa, is driven by the excess gravitational potential produced by plume-driven uplift (Ebinger and Sleep, 1998). In contrast, the post-Devonian history of the Tethyan ocean between Gondwanaland and Laurasia is characterized by a history of at least 12 continental blocks or plates of varying sizes that were rifted off the northern passive margin of Gondwanaland without much evidence for associated magmatism, and accreted to Eurasia after crossing the Tethys (Audley-Charles et al., 1988; Metcalfe, 1999; Ricou, 1995). The absence of magmatism along the northeastern Gondwanaland passive margin during most of these continental breakup events precludes mantle upwelling as a dominating driving force and are difficult to understand if slab-pull plays no significant role in driving continental breakup. Slab retreat was suggested by Collins (2003) as the main mechanism causing breakup of Pangaea, and based on a mantle convection model Conrad and Lithgow-Bertelloni (2004) suggested that the importance slab pull has been increasing steadily through the Cenozoic because the mass and length of upper mantle slabs has been increasing, causing subducting plates to double their speed relative to nonsubducting plates during this time period.

Recently, a model approach has been developed to include rheologically heterogeneous plates in a finite element model with time-dependent plate geometries and plate driving forces (Dyksterhuis et al., 2005b,a; Dyksterhuis and Müller, 2004).

In the figures above, the Eocene plate driving regime is governed ridge push forces by a mid-ocean ridges to the east, south and west (the Tasman Sea ridge, a young south-east Indian Ocean ridge and the Wharton Basin ridge). After the Eocene, the Wharton Basin Ridge between the Indian and Australian plates became extinct, forming the Indo-Australian Plate and the “soft” collision between India and Eurasia started. At 52 Ma spreading in the Tasman Sea ceased. These changes helped establish a stress regime in the Miocene, which was dominated by ridge push south of Australia and the resisting force of the India-Eurasia collision. Between the Miocene and the present the main change in Australian plate driving forces is represented by the onset of collision along Papua New Guinea and the hard collision between India and Eurasia, paired with subduction plate boundary segments between the Java Trench and the Banda Arc that exert slab pull on Australia.

In these models reconstructions of plate boundaries and the age-area distribution of ocean basins around Australia are combined with a computer finite-element implementation of the geological make-up of the continent (see below) to which changing plate boundary forces are applied through time.

The digital model of the Australian geology distinguishes cratons, fold belts, and basins in terms of their relative differences in mechanical stiffness (Figure 30). These

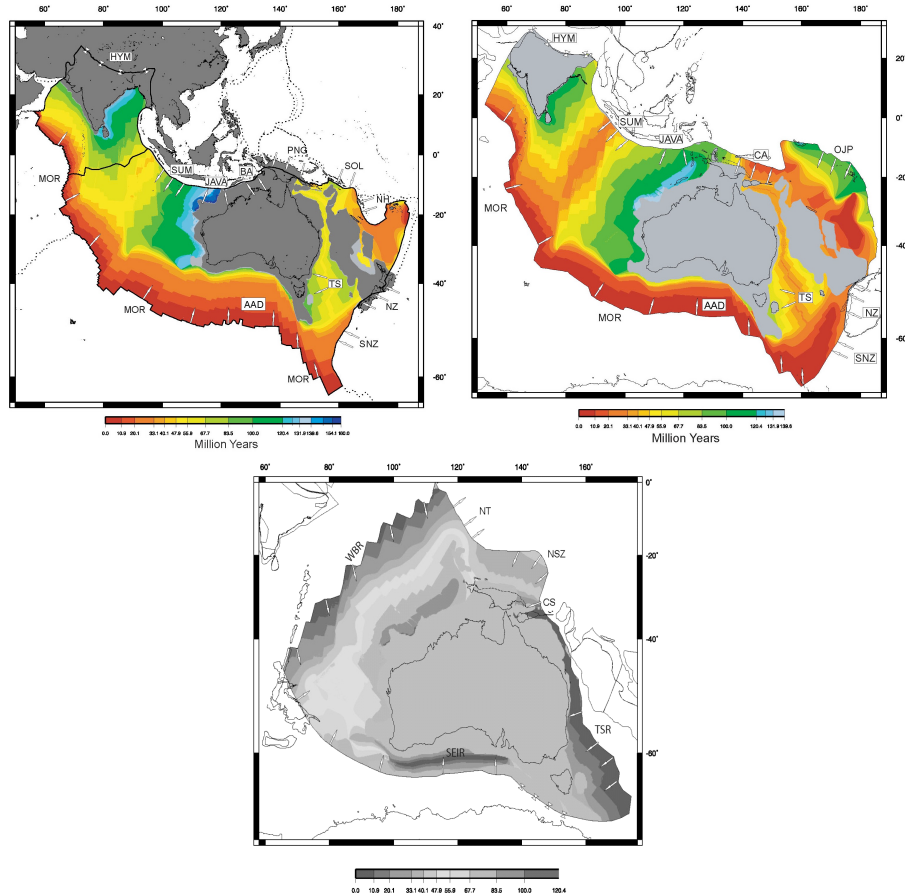


Figure 11.2: Indo-Australian/Australian plate with plate boundary forces applied to contemporary (a), Miocene (b) and Eocene (c) plate configuration, with rheological provinces in Australia outlined in gray, projected onto a Lambert equal area map with its origin at 135°E, 20°S and standard parallels at 0° and 40°S. Oceanic (palaeo-) age is shown in color, and used to compute ridge push force. HYM = Himalayas (fixed boundary); SUM = Sumatra Trench; JAVA = Java Trench; BA = Banda Arc; PNG = Papua New Guinea; SOL = Solomon Trench; NH = New Hebrides; CT = Continental Topographic Force; TS = Tasman Sea; NZ = New Zealand; NZS = Southern New Zealand Alps; AAD = Australia Antarctic Discordance; SW-MOR & SE-MOR = South-West and South-East Mid Ocean Ridges respectively. Force arrows are not drawn to scale.

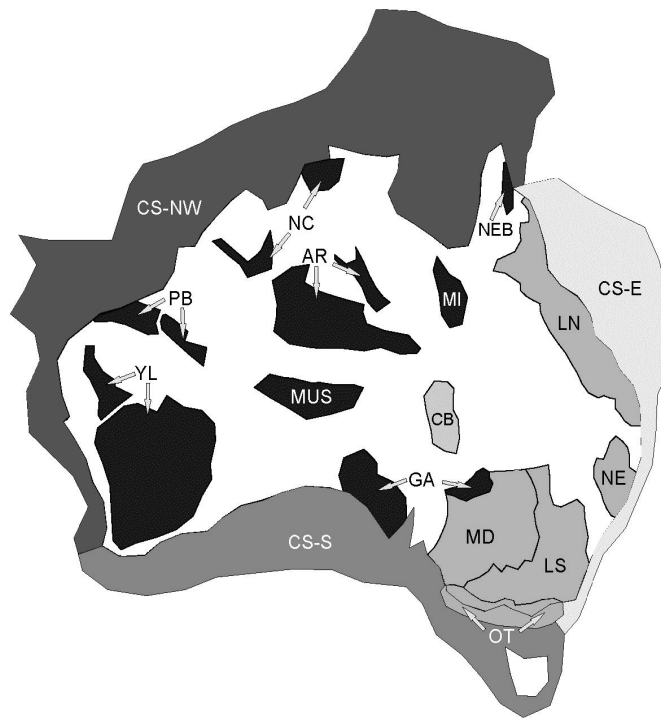


Figure 11.3: Digital model of Australian geology, distinguishing cratons, fold belts, and basins in terms of their relative differences in mechanical stiffness. These stiffness differences are implemented based on effective elastic plate thickness estimates from coherence analysis of gravity and topographic data as well as shear wave analysis and the known surface geology (Dyksterhuis et al., 2005b). Mechanical provinces implemented in models. YL = Yilgarn Craton; PB = Pilbara Craton; AR = Arunta Block; MUS = Musgrave Block; NC = Northern Cratons; MI = Mt Isa Block; GA = Gawler Block; NEB = North East Block; CB = Central Block; MD = Murray-Darling Basin; OT = Otway Basin; LN = Northern Lachlan Fold Belt; LS = Southern Lachlan Fold Belt; NE = New England Fold Belt; CS-NW = North-West Continental Shelf; CS-E = Eastern Continental Shelf; CS-S = Southern Continental Shelf.

stiffness differences are implemented based on effective elastic plate thickness estimates from coherence analysis of gravity and topographic data as well as shear wave analysis and the known surface geology (Dyksterhuis et al., 2005a). The current and paleostress models (Figures 31a-c, modified from Dyksterhuis et al. (2005b)) emphasize that the heterogeneous nature of continental rheology plays an important additional role in determining intraplate stress regimes.

Far-field intraplate stress regimes are sensitive to relatively small changes in plate boundary force magnitudes and material properties. The models show that magnitudes and orientations of the maximum horizontal compressive stress over the Australian continent has changed dramatically between the present, Miocene and Eocene. Eocene extension in the eastern Great Australian Bight is mainly due to slab pull north of Aus-

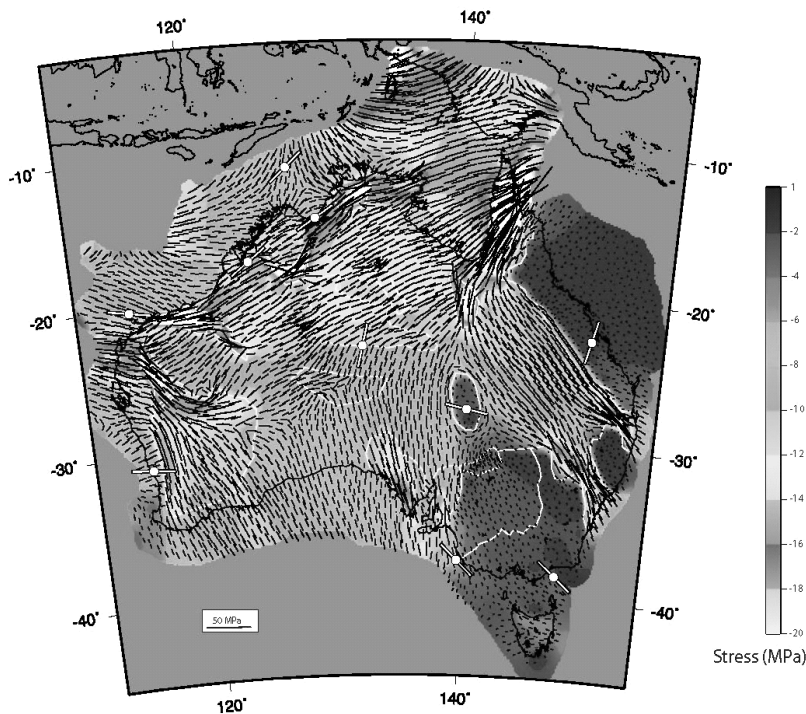


Figure 11.4: Modeled SHmax orientations with realistic material properties for the Australian continental and continental shelf. Filled black lines indicate compressional stress while red black lines indicate tensional stress. Filled white lines marked with a circle show average measured stress orientations taken from the Australian Stress Map database while colour contours show the magnitude of the maximum horizontal compressive stress.

tralia in this model, confirming that continental lithosphere with a realistic strength can support slab pull forces that are focussed along zones of weakness to induce rifting.

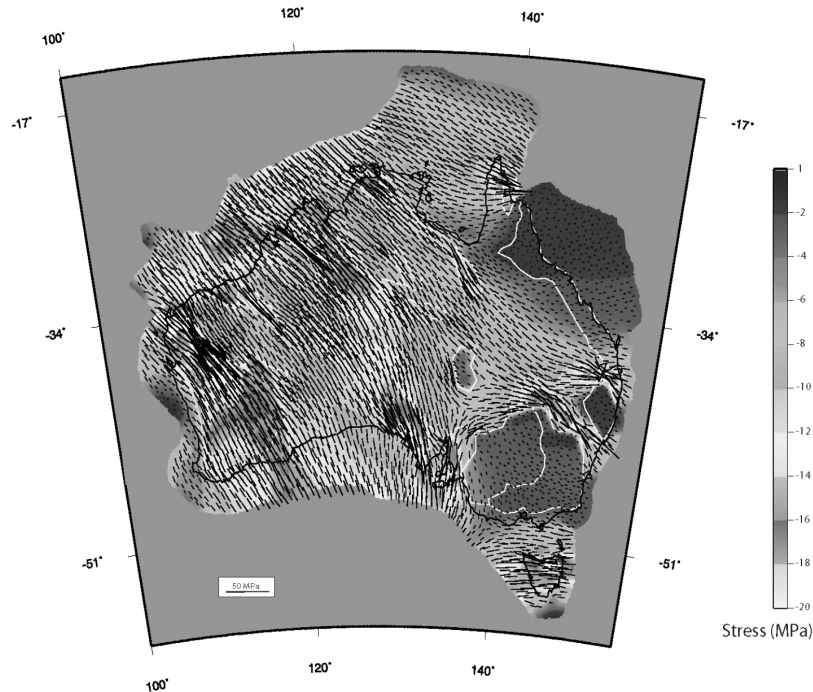


Figure 11.5: Predicted maximum horizontal compressive paleo-stress regime of the Australian continent and continental margin for the early Miocene. Filled black lines indicate compressional stress while red black lines indicate tensional stress. Colour contours show the magnitude of the maximum horizontal compressive stress. Overall, the Miocene stress field from southern to northern Australia is simplified compared with the present, with dominating NE-SW directions in most basins, and no stark stress rotations between cratons and basins. This illustrates that whether or not a rheologically heterogeneous plate model results in severe local/regional rotations of the stress field depends on the complex interplay between the geometry and rheology of juxtaposed geological elements as well as the applied forces.

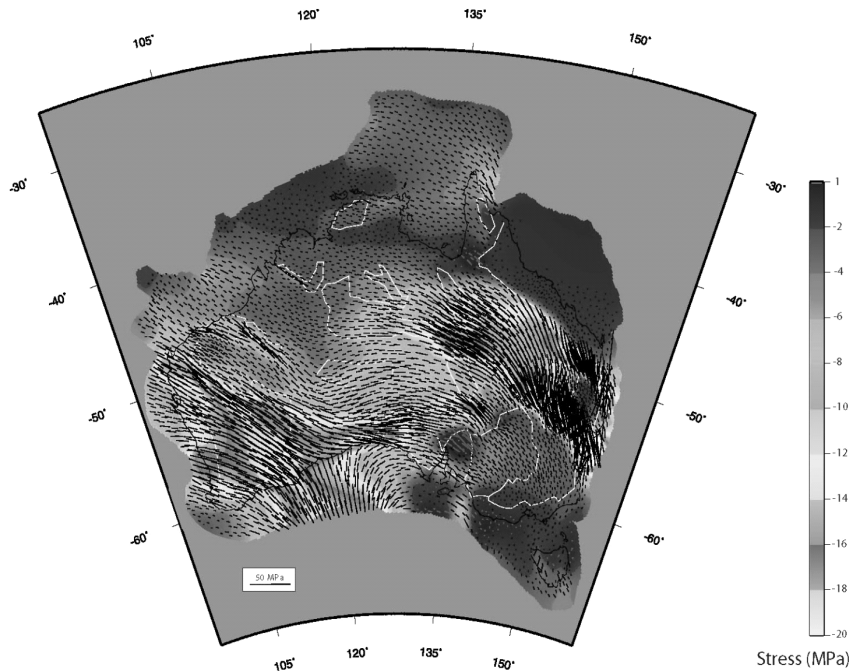


Figure 11.6: Predicted maximum horizontal compressive paleo-stress regime of the Australian continent and continental margin for the Eocene. Filled black lines indicate compressional stress while red black lines indicate tensional stress. Colour contours show the magnitude of the maximum horizontal compressive stress. The Eocene central Australian stress field is largely east-west oriented. The model predicts a 90° rotation in SHmax from the Eucla basin south onto the southern margin. This is because central Australia is wedged in between ridge push forces from the Wharton Basin to the west and the Tasman Sea to the east, whereas along the southern Australian margin the effect of the relatively small ridge push force originating from the young Southeast Indian Ocean ridge is felt.

Chapter 12

Multibeam Bathymetry and side-scan

12.1 Introduction

A fundamental measurement in marine geophysics concerns the bathymetric depth. Traditionally depth was measured from a ship using single-beam echosounders to collect a profile of water depth along the ship's track. The development of multibeam sonar systems has resulted in a number of fairly sophisticated systems which map a swath of seafloor underneath a ship's track, typically at least as wide as two times the water depth. Multibeam systems are manufactured by various companies such as SEA BEAM (USA), SIMRAD, e.g. "EM12" (Norway), and Krupp Atlas, "Hydrosweep" (Germany). A sketch of the Norwegian EM12 system, as used on the French N.O. *L'Atalante*, is shown below:

The principle of imaging is based on the fact that for a rectangular transducer window of width b , the aperture is $q = l/b$, and the angular spectrum of the distant wavefield is defined by a **sinc function**:

In modern interferometric multibeam systems, arrays of many transducers aligned along the ship's keel are driven in parallel to send out a single beam. Sound energy is backscattered from the ocean floor, and returns from different directions across-track are distinguished by using two reception arrays a vertical distance d apart. The difference of arrival times at the two arrays is then related to the angle of arrival. This operation is called **beamforming**.

A currently widely used multibeam system is the SEA BEAM 2000. It operates at a frequency of 12 kHz at depths from 10-11000 m with a swath width of 90°, in the presence of up to ±10° of roll and ±7.5° of pitch. A 120° swath width can be achieved down to intermediate depths up to 6000 m depending on sea conditions and backscatter coefficient. One transmit beam is sent out every 0.5 sec. at minimum. In intermediate and deep water the ping period increases in 1 sec. intervals to 22 sec. The pulse width is determined by the gate recording the deepest depth. It is 3 ms in shallow mode, 7 ms

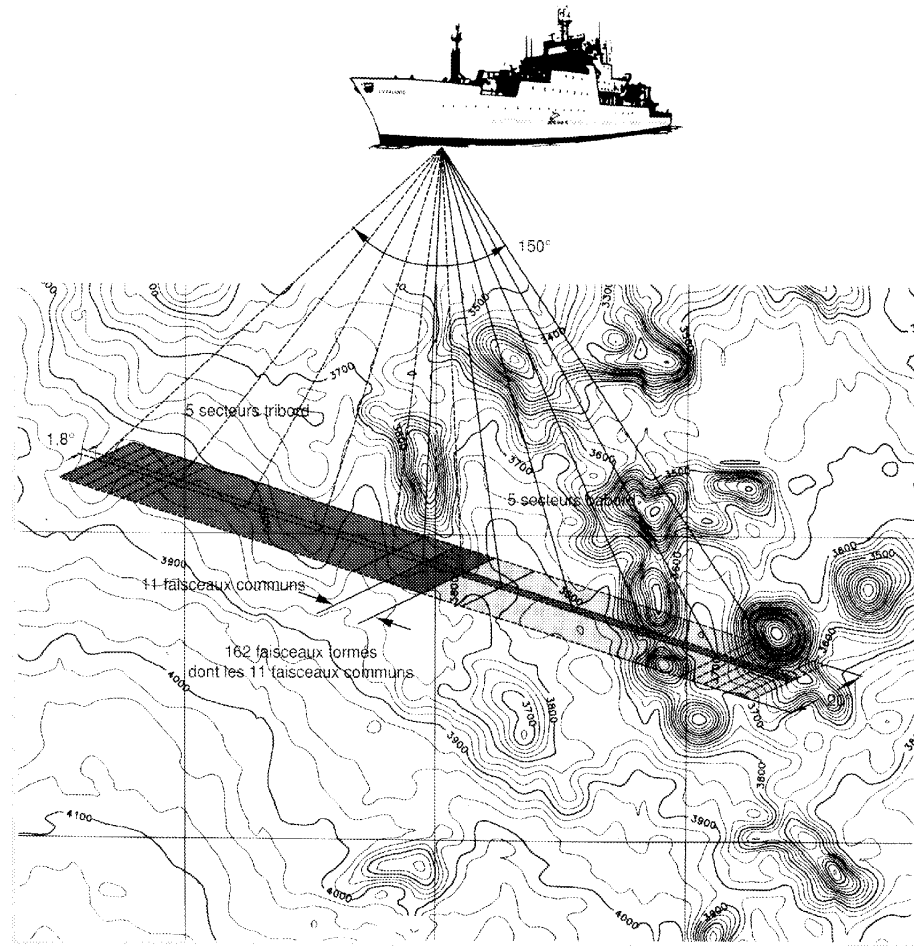


Figure 12.1: Multibeam bathymetry surveying

in deep mode with depths <5000 m, and 20 ms at depths >5000 m.

Figure 12.3 shows the theoretical beam pattern of the Sea Beam system for (a) transmission and (b) receiving. The cross-fan beam geometry is shown on the right (c) (from *de Moustier, 1988*).

The projector array is mounted along the keel of the ship, and contains 28 units with a total length of 4.3 m. The receiving hydrophone array consists of 84 wide band ceramic line elements, mounted in a V-shaped pattern across the hull of the ship, centered on the keel, with a length of 5.3 m. In 120° deep mode, a total of 121 received beams are computed by the array processor for each ping. For each of these processed beams, information from all 84 receiving elements is used. The gate for each of the 121 beams is centered on the average depth for that beam, and the gate width is determined by the observed depth variation plus allowance for the signal duration as determined by

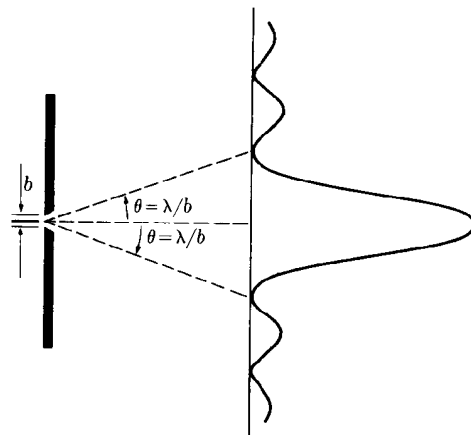


Figure 12.2: Sinc function defining the distant wavefield of an echosounder beam

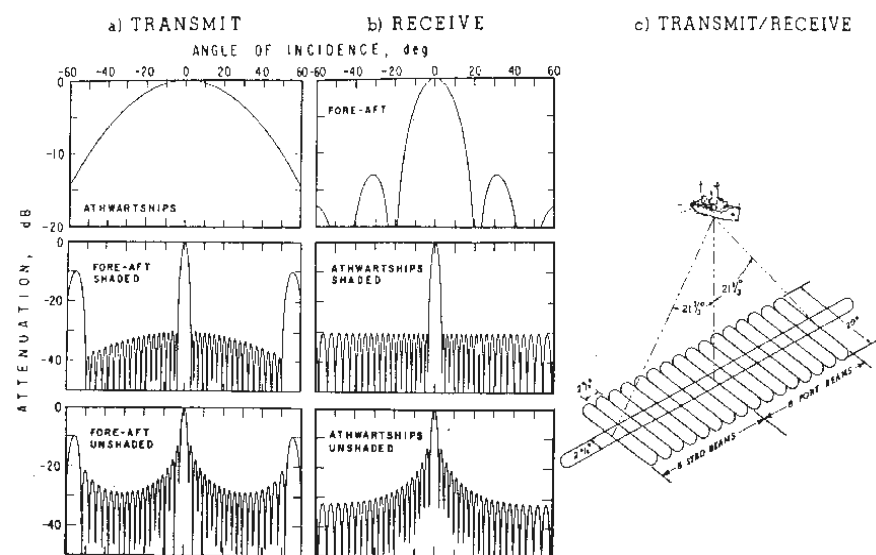


Figure 12.3: Theoretical beam pattern for Sea Beam system (from de Moustier, 1988)

depth, beam width, and beam angle. The average depth is the depth averaged over the last 5 pings, weighted towards more recent pings.

A digital filter tracks the doppler shift, originating from the motion of the ship between transmission and reception of the beam, and centers the received signal around the center of the transmitted frequency band. The system automatically drops outer beams as depth increases beyond that for which 120° operation is possible.

A parallel array processor carries out the tasks of:

- roll stabilized receiving beam formation,
- detection of range-to-target for each beam,
- noise rejection,
- side-scan (i.e. measuring backscattered amplitudes), and
- adjusting the beamforming algorithm in response to changes in sound velocity detected by the hull mounted sound velocimeter.

In order to form the 121 beams per ping, a weighted mean time of arrival technique is used. The time sequenced data recorded by the 84 hydrophones are converted to a spatial image for beam forming by Fourier transforms.

After beam formation, a number of corrections have to be applied. Sound waves travel through water along curved lines due to varying speed of sound in water as a function of depth, mainly dependent on the temperature profile. With increasing depth rays bend away from the ship, reducing the apparent depth, and increasing the cross-track distance at the sea bottom. In order to correct for ray bending, the sound velocity profile (SVP) of the water must be known accurately. For this purpose, the temperature profile of the upper 1800 m water depth (max.) is measured by eXpendable Bathymeters (XBT's), usually once a day during surveying. For deeper depths, the temperature profile for a given area is taken from so-called "Carter tables". Ray bending is then performed using a number of layers defined by depth boundaries which are given by depths of the SVP. Subsequently the depth is corrected for heave, pitch, and draft of the ship.

12.2 Data Acquisition and the Physics of Multibeam Technology

Interest in the field of remote characterization of the seafloor has significantly increased with the introduction of multibeam technology. Multibeam sonar is a popular tool because of its flexibility. It collects acoustic imagery (backscatter) data at the same time as the multibeam soundings, and they are therefore positioned with the same accuracy. The SIMRAD EM12-D multibeam sonar emits a signal every 10ms at a frequency of approximately 13kHz. The transmit beam generates a footprint on the seafloor with a

width of 150° in the across-track direction and 1.8° in the along-track direction. A total of 162 overlapping beams at a spacing of 1° receive the return signal. The widths of these beams are 3.5° across-track and 20° along-track, which allows a certain stability for pitch and roll. With this configuration of 3.5° across-track and a spacing of 1° , the beams overlap by about 2.5° , which is more than adequate to compensate for pitch and roll. The acoustic beams transmitted by the sonar interact with the seafloor and most of their energy is reflected specularly. This causes a zone along the ship track where the received signal is dominated by reflectance rather than backscatter. The distance travelled between the sonar and the seafloor, subtended by the elevation angle, is called the 'slant range'. This forms the angle of incidence with the seafloor. The grazing angle, which will be referred to further when considering geometric corrections, is 90° minus the angle of incidence.

The signal is received with three important pieces of information: the depth, which is calculated from the elapsed time, the angle from which it is received, and the backscatter data, which is a function of the intensity of the signal. For the purposes of seafloor classification, the remainder of this chapter will focus on the amplitude of the received signal. The backscatter intensity is related to the hardness and roughness of the seafloor, however, there are many complications. The echo sounder receives signals from every interface that is illuminated by the emitted signal. The signal obtained is therefore a combination of the source level, the insonified area of the seafloor, the backscattering strength of the seafloor and the transmission loss.

Transmission loss refers to the nature of the received signal being decreased in intensity, due to the diffusion of the emitted energy on a growing surface. The insonified area of the seafloor is dependent on the incidence angle. The greatest area is achieved at low angles of incidence and decreases rapidly with increased incidence angle. Backscattering strength (BS) is a convenient ratio of the intensity of the backscattered wave to the intensity of the incident wave. The scattered wave is a function of the insonified area and is therefore referred to in terms of dBm-2. It is because the BS value is reliant on the insonified area that the energy of waves reflected at high incidence angles is far less than those at low angles of incidence. Geometric effects and propagation losses are systematically corrected for by the sonar system, which makes assumptions on spherical spreading and a flat horizontal seafloor (Lambert's Law). The backscattering strength measurement takes into consideration the transmission loss and the insonified areas and can therefore be considered as 'reflectivity' data.

This information is then a useful indicator of surface character due to the consideration of the acoustic impedance and roughness. This value needs careful consideration, however, because it involves a complex relationship with the seafloor nature and structure, the incident angle and the emitted frequency and can become misleading. This data is more complicated than is initially apparent, because the received signal is not reflected as a single wave, but as numerous waves reflected off different surfaces. For example part of the incident acoustic energy is scattered at the water-bottom interface, due to a change in density and roughness. The remaining energy will continue to penetrate subsurface layers and will be backscattered by buried inhomogeneities. At

a frequency of 13kHz the wavelength would be approximately 12cm into water and would penetrate several wavelengths into soft sediment ($\sim 0.5\text{m}$), however, there would be very little penetration in rocks.

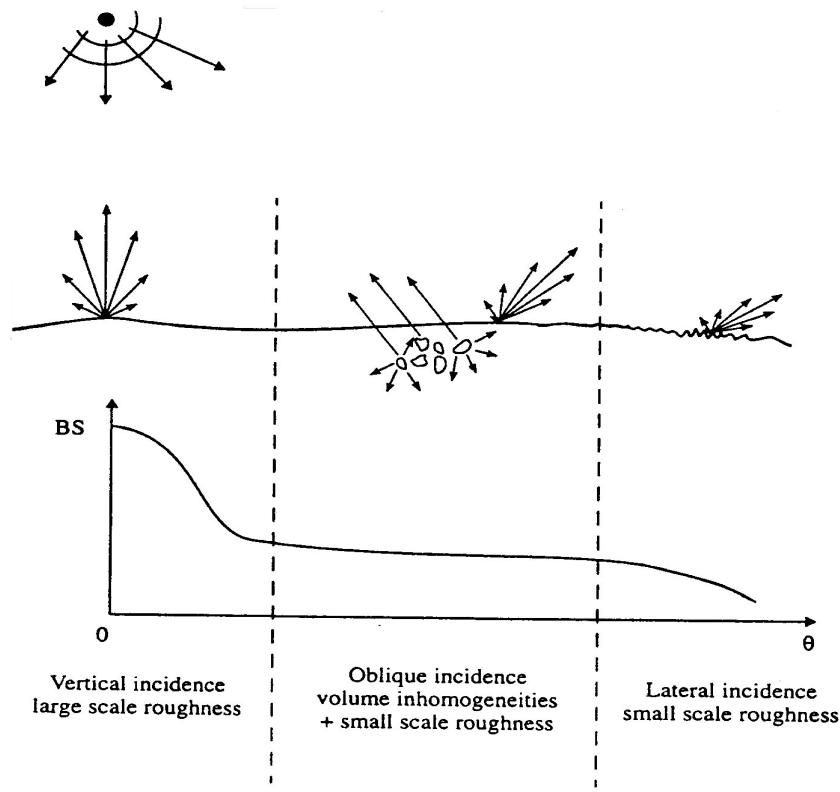


Figure 12.4: Relationship between incidence angle, backscatter strength and seafloor character

It is apparent that, for near vertical incidence, the intensity is higher due mainly to specular reflection. At this point the backscatter value is contributed to by a number of locally reflecting planes that relate to the slope roughness and not the seafloor character. At greater incidence angles sediment volume becomes a prominent contributor. Part of the incident energy is transmitted into the sediment where it is scattered by inhomogeneities from various origins or by sedimentary layer interfaces.

12.3 Image Enhancement Techniques

With the aim of developing computer assisted interpretation algorithms, image enhancement is a vital stage in the procedure. If a contaminated, noisy, region is used as a training set for a neural net then the results may not be as accurate. The three main

enhancement processes that have been carried out as standard methodology by Stewart *et al* (1994) and Müller *et al* (1997) are:

- 1.) Correction of backscattering strength values for incidence angle.
- 2.) Interpolation of missing data, and
- 3.) The filtering of high frequency speckle noise.

Numerous geometrical artefacts inherent to the system also need correction. The main being the occurrence of high reflectivity along ship-track, near nadir, and the reduction of backscatter intensity distal to the ship track, due to the invalidity of Lambert's law. At this stage, the problem of high reflectivity along track can only be suppressed, not solved. It is common for the purposes of computer assisted interpretation to discard the high reflectivity zone of backscatter data and set their values to represent no data. This effect gives the backscatter image the appearance of a seafloor illuminated by an artificial sun, with the use of bathymetry data to compensate for the variability of the backscatter strength values depending on the seafloor type and the incident angle.

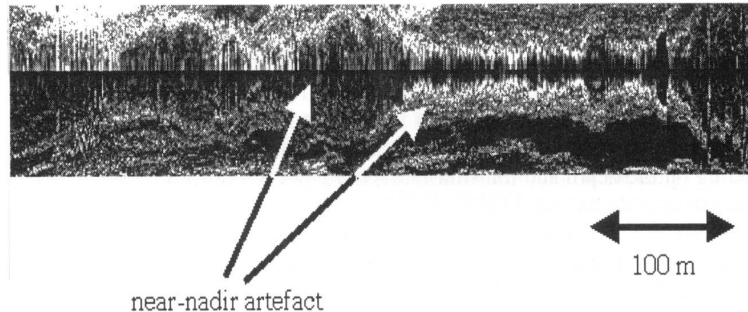


*Figure 8.3: High backscatter values near-nadir along the ships track. (Blondel *et al* 1997)*

Figure 12.5: Backscatter affects

Chapter 13

The Magnetic Field

13.1 Introduction

In common with the Earth's gravity field discussed in the previous chapter, the magnetic field that we observe at the surface of the Earth also varies spatially. The majority of the Earth's field is believed to be due to convection within the Earth's molten core (composed of liquid iron). At the Earth's surface, the core field varies smoothly (hence our ability to use the field as the basis for navigation with magnetic compasses). Additional, smaller-scale variations in the observed magnetic field are due to the crustal magnetic field - due to variations in the magnetization of material in the Earth's crust. Broadly speaking, the sources of the crustal field are located anywhere within the Earth's crust where the temperature is below the 'Curie temperature' (about 580°C), since rocks above this temperature lose their ability to retain magnetism. Typically this means the upper 20-30 km of the Earth, though the value varies across the Earth due to variations in the thermal structure of the crust.

This chapter focuses on the study of the crustal magnetic field - in particular, what it can tell us about geodynamics and crustal structure. The first section of this chapter describes the study of magnetic data over the oceans. Studying the variations in the crustal magnetic field over the oceans has played a fundamental role in the development of plate tectonic theory. The second section discusses the generation and interpretation of magnetic data over both land and sea to map out geological structures, and define the extent of sedimentary basins and igneous provinces that have little or no surface expression.

13.2 Mapping the oceanic magnetic field

We map the oceanic magnetic field by using a **proton precession magnetometer**. It was invented by Packard and Varian, and is the most commonly used magnetometer today. It is based on the fact that nuclear magnetic moments possess a spin, which will precess

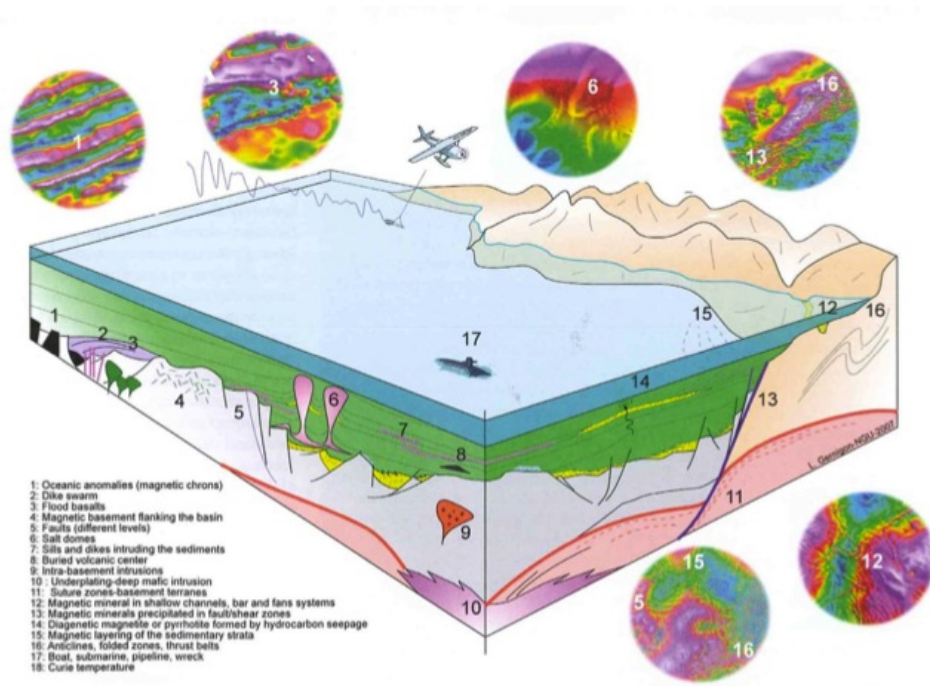


Figure 13.1: Sources of anomalies in the crustal magnetic field (from Gernigon, 2007).

about the earth's magnetic field. In the magnetometer the free-precession of hydrogen nuclei (= protons) is measured. In the absence of a magnetic field the dipole moments of protons in water are randomly oriented. In the presence of a strong magnetic field the dipoles become polarized in the direction of the field.

When the field is removed the protons spin oriented around the direction of the Earth's magnetic field for a short time, until they return to their random state. After the polarizing field has been switched off, the frequency of the spinning protons is counted. The precession frequency is proportional to the field strength. As a consequence the proton precession magnetometer produces a number of discrete measurements of the absolute field strength by means of the proton precession frequency. The advantage of this type of magnetometer is that the orientation of the instrument is not critical.

We measure the **total magnetic field** with a magnetometer (NOT its directional components)

The total magnetic field B that we measure with a magnetometer, either over continental or ocean crust, is always the sum of the ambient field B_a and the field originating from magnetized rocks B_r :

$$B = B_a + B_r \quad (13.1)$$

In general, the ambient field, B_a , is much stronger than the field generated by mag-

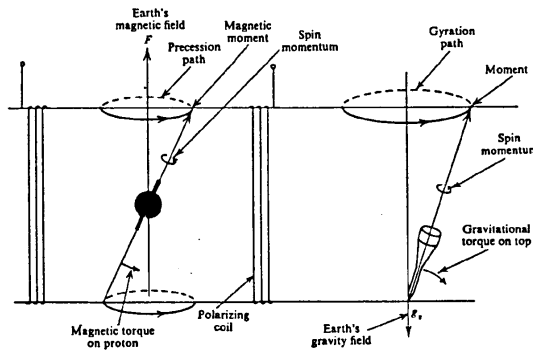


Figure 13.2: Proton precession and the spinning top analogy.

netized rocks, B_r ,

$$\parallel B_a \parallel >> \parallel B_r \parallel \quad (13.2)$$

13.3 Character of the magnetic field

The Earth's Magnetic Field is primarily a dipole field, exhibiting some small non-dipole components. It has both space and time variations consistent with an origin due to convection in a conducting, fluid outer core.

Note: field lines are the directions of magnetic force, a compass needle orients itself parallel to the local field line. Field lines are perpendicular surfaces of constant potential.

The parameters conventionally used are intensity B , declination D , and inclination I . I and D are measured in degrees. The figure below gives the reference frame for describing the magnetic field.

B_h is the projection of the field vector onto the horizontal plane and B_z is the projection onto the vertical axis

N_g denotes geographic north, and N_m magnetic north, E geographic east, and Z down.

- *inclination I*: angle between the field vector \mathbf{B} and the horizontal, measured positive down, i.e. it goes from +90 to -90.

It follows that the inclination is related to B_h and B_z by:

$$\tan I = B_z / B_h \quad (13.3)$$

- *declination D*: angle in the horizontal (N-E plane) between the field vector and the direction to the geographic north pole. Positive angles are clockwise with respect

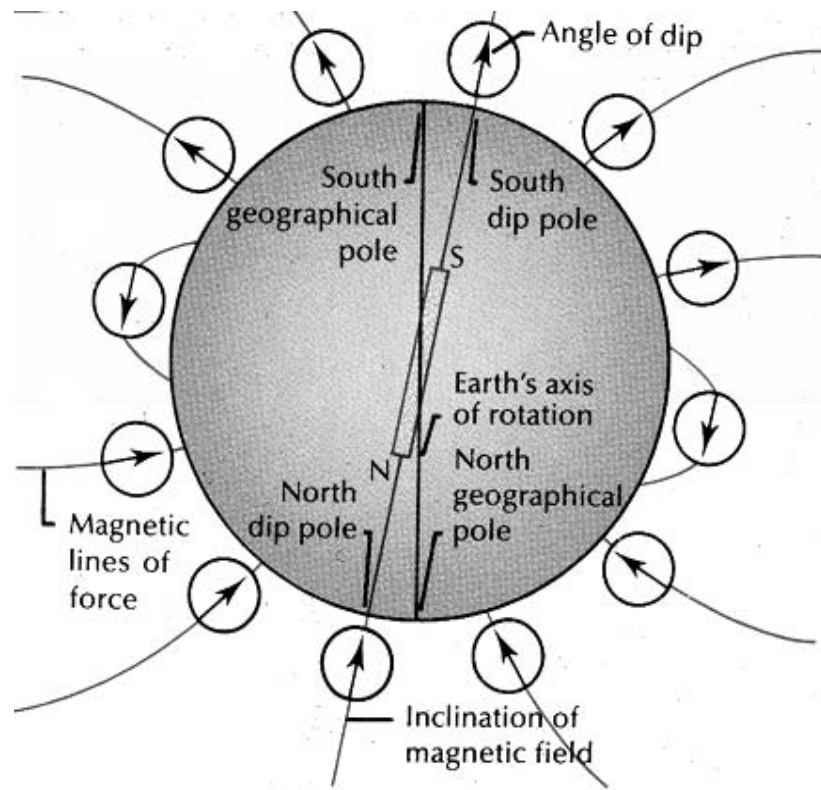


Figure 13.3: The Earth's dipole field

to the geographic north pole (from 0-360°). The horizontal projection of the field vector BH can also be projected onto the North and East axes:

In the horizontal (N-E plane) the declination D is the angle between the field vector and the direction to the geographic north pole. Positive angles are counterclockwise with respect to the geographic north pole (from 0-360°). The horizontal projection of the field vector BH can also be projected onto the North and East axes. D is measured positive in a clockwise direction from 0-360°.

The intensity of the magnetic field B is measured in nannoTeslas (nT) (SI-unit). Some useful conversions are: $1\text{nT} = 10^{-5}\text{ G}$ (Gauss), and, $1\text{nT}=1\text{g}$ (gamma). The following figure illustrates the orientation of the magnetic field vector and the corresponding angle of inclination as a function of latitude (λ) in a cross section through the Earth:

Colatitude and inclination are related by the **dipole formula**:

$$\tan I = 2 \cot(\theta) \quad (13.4)$$

$$\theta = 90 - \lambda \quad (13.5)$$

It follows that

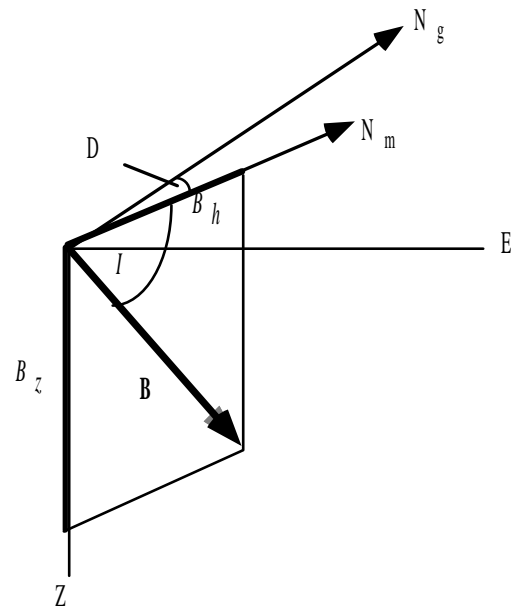


Figure 13.4: The magnetic field vector

$$\tan I = 2\tan(\lambda) \quad (13.6)$$

$$\tan(\lambda) = \tan I / 2. \quad (13.7)$$

Hence there is a straightforward relationship between the inclination of the magnetic field and the magnetic latitude, from which the distance from the magnetic pole can be computed. This is essential for reconstructing tectonic plates.

$$\begin{aligned} B_H &= B\cos(I) \\ B_N &= B\cos(I)\cos(D) \\ B_E &= B\cos(I)\sin D. \end{aligned} \quad (13.8)$$

The geomagnetic poles are presently at 79°N, 71°W and 79°S, 109°E.

13.4 Geomagnetic field reversals

- the Earth's dipole field flips polarity at irregular intervals
- the polarity is said to be "normal" when it is oriented the same as today
- on average, the field spends about half its time in each state

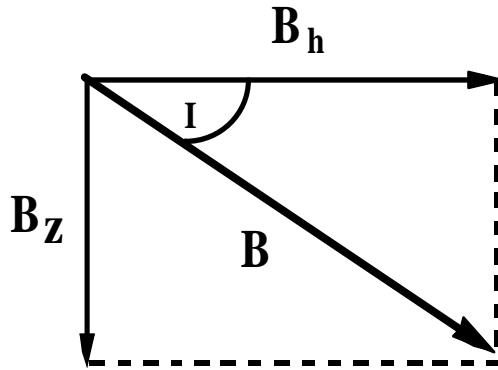


Figure 13.5: Magnetic field inclination

- reversals are observed from Precambrian times to the present although the frequency of reversals has changed considerably through time
- during a reversal, the intensity usually decreases by about an order of magnitude for several thousand years, while the field maintains its direction.
- the field then undergoes complicated directional changes over a period of 1000-4000 years and finally intensity grows with the field having reversed polarity
- the total time span of a reversal is up to 10.000 years
- the reversal sequence has been calibrated for the last 5 million years by dating basalts of known polarity.
- portions of the time scale which are of one dominant polarity are called *chrons*, and the most recent four chronos are named after scientists who contributed significantly to our understanding of the geomagnetic field (Brunhes, Matuyama, Gauss, Gilbert).
- Portions of the time scale which are of one dominant polarity are called **chrons**.

13.5 Magnetic potential

The Earth's magnetic potential can be expressed as an infinite series of spherical harmonic functions. The first term in this series is the term due to a dipole located at the center of the Earth with respect to a fixed origin at the center of the Earth. The magnetic potential V due to a dipole at a point specified by the vector \mathbf{r} is given by

$$V(r) = \frac{1}{4\pi r^3} mr \quad (13.9)$$

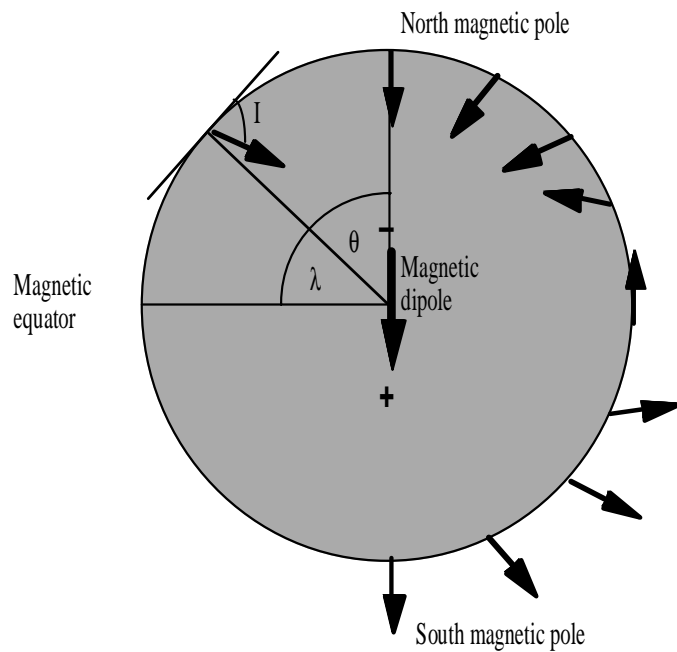


Figure 13.6: Magnetic inclination as a function of latitude

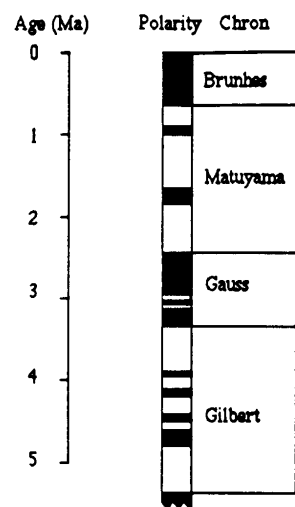


Figure 13.7: A small section of the magnetic polarity timescale

\mathbf{m} is the dipole moment (a vector aligned along the dipole axis). For the Earth $|\mathbf{m}| = 7.94 \cdot 10^{22} \text{ Am}^2$ (A = Ampere). The magnetic field $\mathbf{B}(\mathbf{r})$ at any position \mathbf{r} can be determined by differentiating the magnetic potential

$$B(r) = -\mu_0 \nabla V(r) \quad (13.10)$$

where μ_0 is the magnetic permeability of free space ($\mu_0 = 4\pi \cdot 10^{-7} \text{ kg m A}^{-2} \text{ s}^{-2}$). To apply this formula to the earth, we use spherical coordinates (r, f, q) . The magnetic field $\mathbf{B}(\mathbf{r})$ is written as $\mathbf{B}(\mathbf{r}) = (Br, Bf, Bq)$ (three scalar components) in this coordinate system.

In a scenario where a dipole magnet is aligned along the negative z axis (see figure above), the potential field is

$$V(r) = -\frac{1}{4\pi r^3} \mathbf{m} \cdot \mathbf{r} = -\frac{mcos(\theta)}{4\pi r^2} \quad (13.11)$$

Substitution of this equation into the expression for $\mathbf{B}(\mathbf{r})$ gives the three scalar components of \mathbf{B} with respect to r, f , and q , (radius, longitude, and colatitude).

$$Br = -\mu_0 \frac{\delta V}{\delta r} = \frac{\mu_0 m \cos(\theta)}{4\pi} \frac{\delta}{\delta r} \frac{1}{r^2} = -\frac{2\mu_0 m \cos(\theta)}{4\pi r^3} \quad (13.12)$$

$$B_\phi = -\mu_0 \frac{1}{rsin\theta} \frac{\delta V}{\delta \phi} = 0 \quad (13.13)$$

$$B_\theta = -\mu_0 \frac{\delta V}{\delta \theta} = \frac{\mu_0 m}{4\pi r^3} \frac{\delta}{\delta \theta} (\cos(\theta)) = -\frac{\mu_0 m \sin(\theta)}{4\pi r^3} \quad (13.14)$$

Because of the radial symmetry of the magnetic dipole field, there is no longitudinal component. As mentioned above, a spherical harmonic expansion is used to represent the mapped magnetic field of the Earth. Coefficients of this expansion are updated regularly to fit data from magnetic observatories or satellite data. The internationally agreed values are published every five years as the **International Geomagnetic Reference Field** (IGRF). To a first approximation the field is a dipole field, but there are non-dipole components as well. The geomagnetic poles are presently at 79°N, 71°W and 79°S, 109°E. The following figure shows mapped contours of the present field components:

13.6 Magnetization of oceanic crust

The process of sea floor spreading produces new oceanic basalt from molten lava. When the rocks cool to the Curie temperature, they “lock” in the Earth’s current magnetic field by gaining Thermal Remanent Magnetism (TRM) and the direction of magnetization depends upon the polarity of the Earth’s magnetic field:

The **total magnetic field** \mathbf{B} that we measure with a magnetometer, either over continental or ocean crust, is always the sum of the ambient field \mathbf{B}_a and the field originating from magnetized rocks \mathbf{B}_r , as shown in equation 13.1.

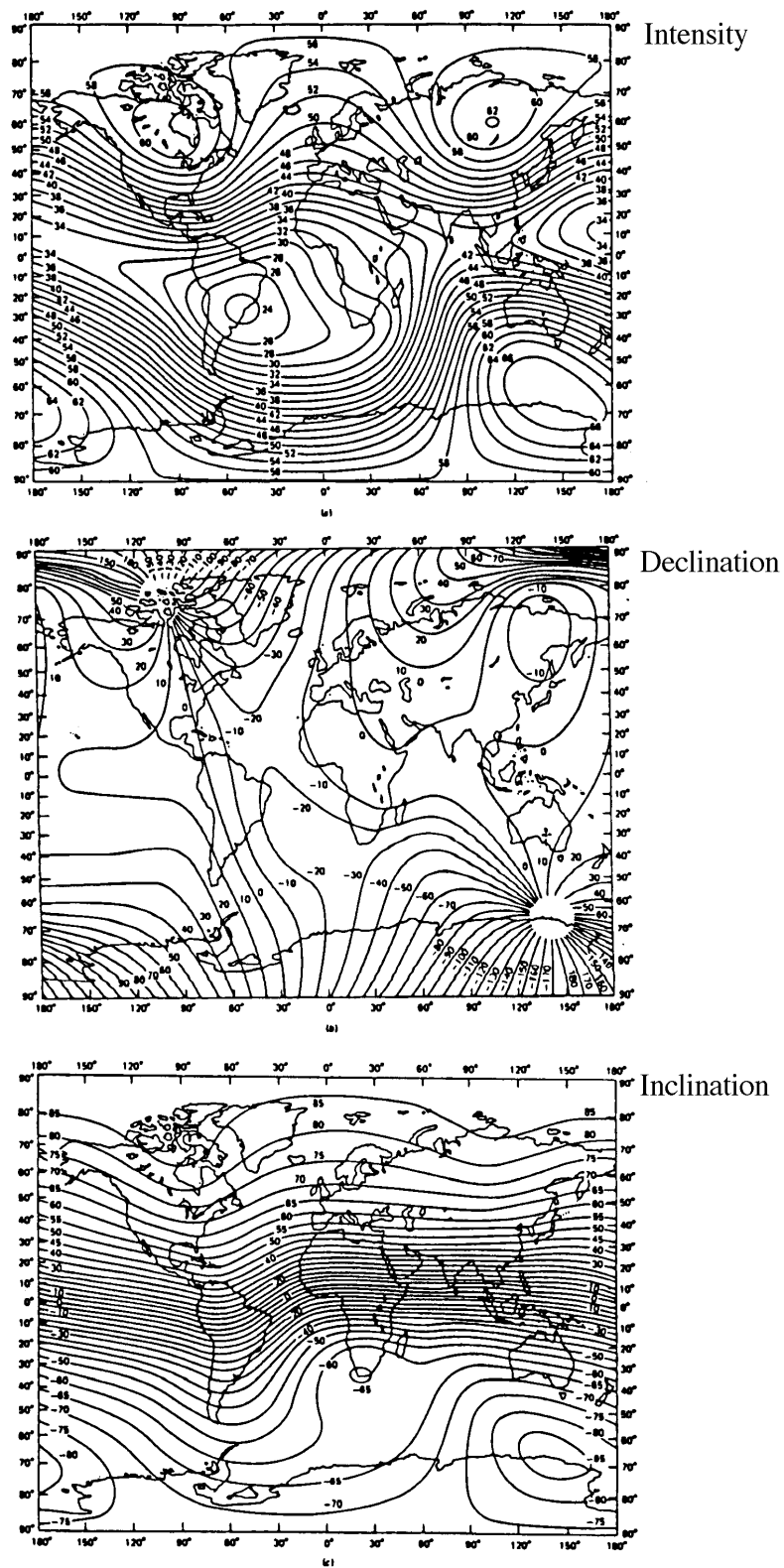


Figure 13.8: Global variation in the intensity and direction of the Earth's magnetic field

The anomalous magnetic field, caused by magnetized ocean crust, is derived from the total magnetic field which is measured by towing a proton precession magnetometer behind a ship. In general, the ambient field, \mathbf{B}_a , is much stronger than the field generated by magnetized rocks, \mathbf{B}_r (Fig. 13.9).

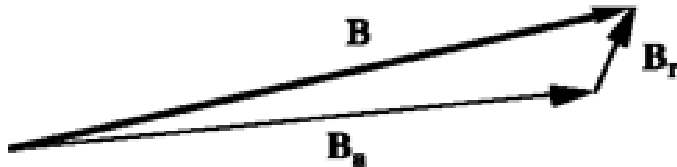


Figure 13.9: Total magnetic intensity

In order to reduce the field to that originating from the rocks, we remove the IGRF. The following figure shows a block of ocean floor with a remanent magnetization in the same direction of the earth's present magnetic field. We measure the total magnetic field at the sea surface, i.e. the sum of the ambient field and the field caused by the remanent magnetization of the ocean floor basalt (Fig. 13.10).

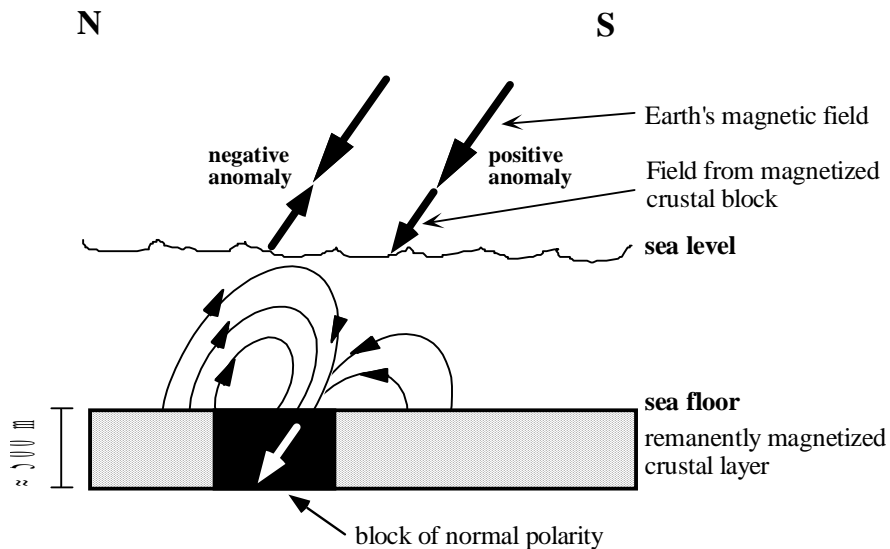


Figure 13.10: Magnetization of oceanic crust

From the figure above we can infer that the block of ocean floor was formed during a period of normal polarity in the northern hemisphere and has a magnetization parallel to the Earth's magnetic field. To the south (right), the field generated by the ocean floor adds to the Earth's magnetic field, and a positive magnetic anomaly is observed. To

the north (left) it opposes the Earth's magnetic field, and a negative anomaly is created. We first measure the total field, and then subtract the IGRF to compute the anomaly. The amplitude of the measured anomalies is usually of the order of a few hundred nannoTeslas, or about 1% of the dipole field.

The average thickness of the main magnetized layer in the upper ocean crust is about 500 m. Even though there are likely to be contributions from crustal magnetized rocks at depths larger than 500 m below the seafloor basement, the intensity of magnetization in the upper 500 m is largest because of the more rapid cooling, forming small magnetite grains ("single domain crystals"). The slower cooling at greater depths causes larger magnetite crystals to grow, whose intensity of magnetization is smaller.

Remanently magnetized blocks of ocean floor ridge segments cause linear magnetic anomalies. Magnetic anomalies due to seafloor spreading (i.e. without seamounts), arise from magnetized blocks parallel to the midocean ridge. It is important to point out that magnetic anomalies produced by normally magnetized blocks vary in character as a function of the paleolatitude at the time of magnetization.

The shape and intensity of seafloor magnetic anomalies is dependent on

- (1) **the segmentation of the mid-ocean ridge** by fracture zones (i.e. length of magnetized blocks along-axis),
- (2) **spreading velocity** (length of blocks across-axis). Fast spreading causes relatively longer blocks to form than slow spreading,
- (3) **frequency of polarity reversals** (length of blocks across-axis), and
- (4) **the direction of magnetization** in a given block.

When both the crustal magnetization and geomagnetic field vectors are steep (i.e. in the vicinity of the magnetic pole), the normal blocks cause positive anomalies. However, near the equator, east-west striking blocks magnetized in the same direction as the geomagnetic field produce negative anomalies.

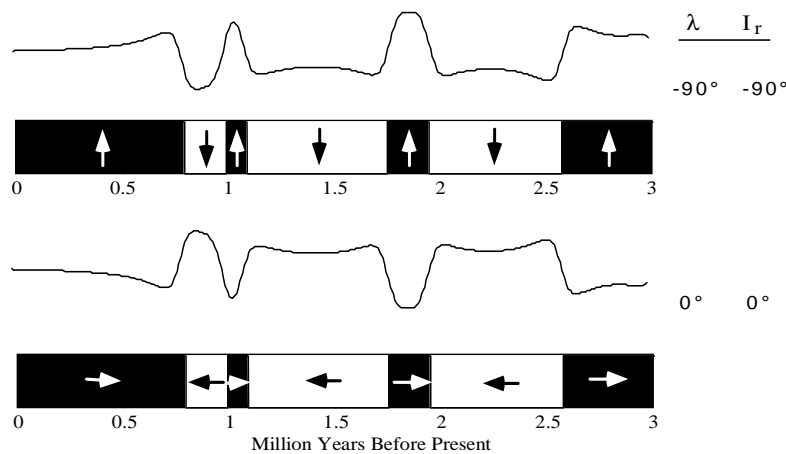


Figure 13.11: Magnetic polarity reversals in oceanic crust

The top profile is produced by a model of an east-west oriented spreading ridge, equivalent to north-south spreading, at the magnetic south pole, and the bottom profile shows the same ridge at the equator. Here l is the latitude, and I_r the remanent inclination. The profile at the equator is a mirror image of the profile at the pole. Note that north-south oriented magnetic blocks at the equator, produced by east-west spreading, cause no magnetic anomaly at all.

A **magnetic anomaly is caused by an edge effect** between two bodies with different magnetization. A series of magnetic lineations on the ocean floor will cause the magnetic anomalies caused by the individual edge effects to be superimposed on each other to give an observed anomaly. If two edges are far apart from each other, they will cause individual anomalies which are separated by an area where no anomaly is measured. The closer the two edge effects are the more the two individual anomalies will interfere with each other. If the distance is very small only one anomaly will be caused by two edge effects. This is illustrated in the following figure. Here we show first one edge effect alone, and then two edge effects 50, 25, and 10 km apart from each other, caused by normally and reversely magnetized blocks of ocean crust in a water depth of 2500 m.

The observed magnetic field in the ocean basins is complicated by seamounts, volcanic constructs which often possess a different magnetization vector from that of the underlying ocean floor, controlled by the latitude and polarity at the time of formation.

The shape of the magnetic anomaly caused by a magnetized seamount depends on the direction of the remanent magnetization.

The following example shows, how the shape of the magnetic anomaly caused by a magnetized seamount depends on the direction of the remanent magnetization.

13.7 Forward modeling magnetic anomalies

13.7.1 Model for marine magnetic anomalies

The theoretical foundations for modeling marine magnetic anomalies were established by Bott (1967), Schouten (1971), and Schouten and McCamy (1972). The principles outlined below are still used today in the exact same form.

Assumptions for modeling marine magnetic anomalies:

1) Magnetized bodies in the ocean floor can be approximated as two-dimensional structures confined by horizontal planes, because the anomaly patterns are fairly continuous parallel to the spreading axis, sometimes for distances over hundreds of kilometers.

2) The magnetic sources are near the surface. The oceanic depth defines the top horizontal plane, and the shallow Curie point isotherm within the crust the lower plane. Both depths are of the same order of magnitude. In the following examples we will assume that the top of the layer is at 3.5 km and the bottom at 4 km depth.

3) The direction of the magnetization is parallel or anti-parallel with the central axial dipole field of the Earth.

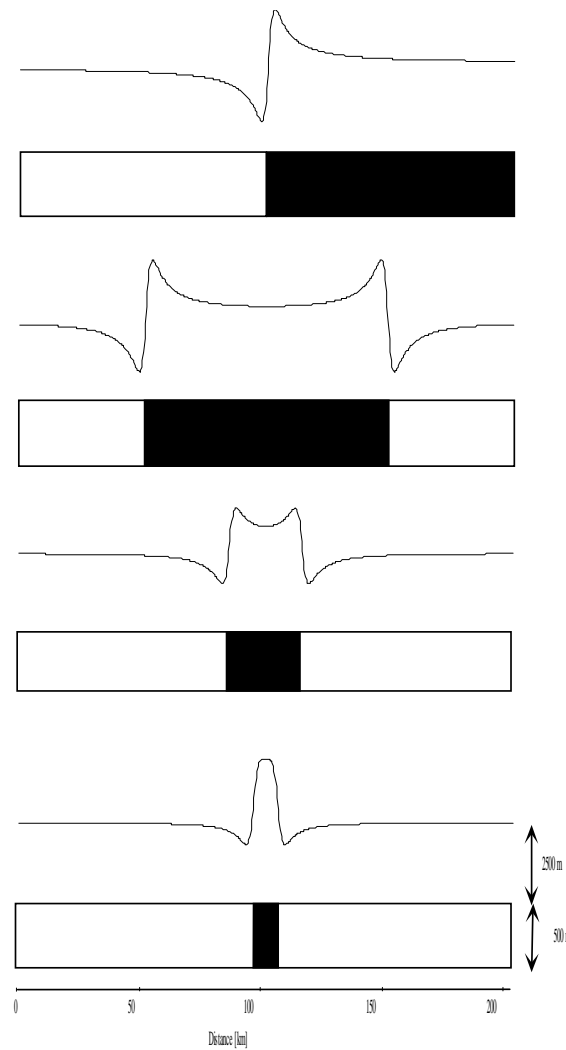


Figure 13.12: Edge effects due to adjacent magnetic polarity reversal boundaries

Consider a cross-section of a thin vertical tabular body of unit thickness in the ocean crust, bounded by two layers at depth $a = 3.5$ km and $b = 4$ km. This is equivalent to a cross-section across a mid-ocean ridge with only one magnetized stripe of unit width. The distribution is assumed to be a function of x and z , independent of y .

Here the magnetization direction is constant and arbitrary. We observe a magnetic field anomaly $m(x)$ at point $(x, 0)$. The intensity of magnetization $j(x)$ is assumed to be a function of x within the body and zero outside the body.

The observed magnetic anomaly $m(x)$ is the convolution of $j(x)$ and $g(x)$, which is written as:

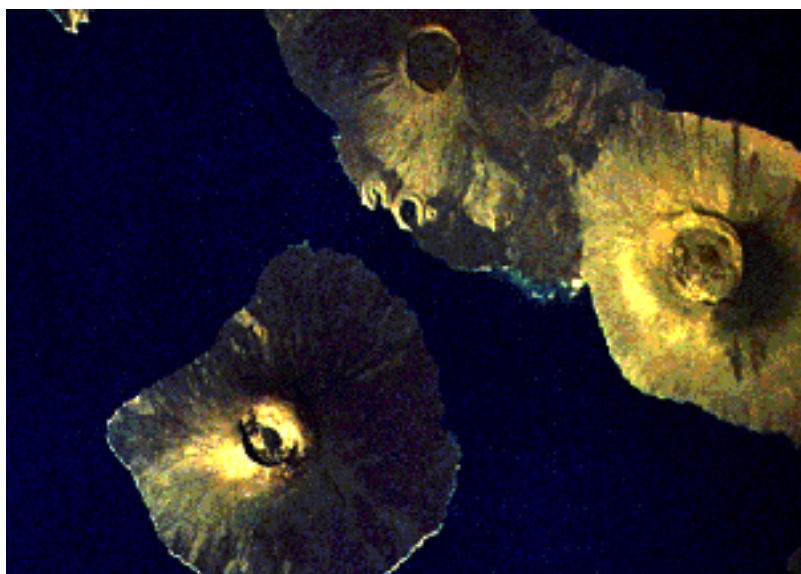


Figure 13.13: Galapagos Islands

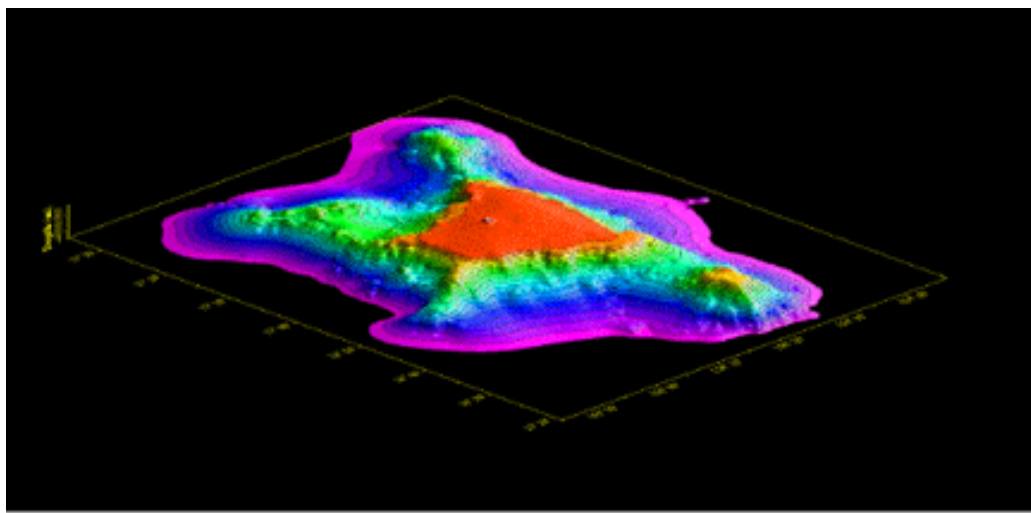


Figure 13.14: Bathymetric map of a guyot (flat-topped drowned seamount)

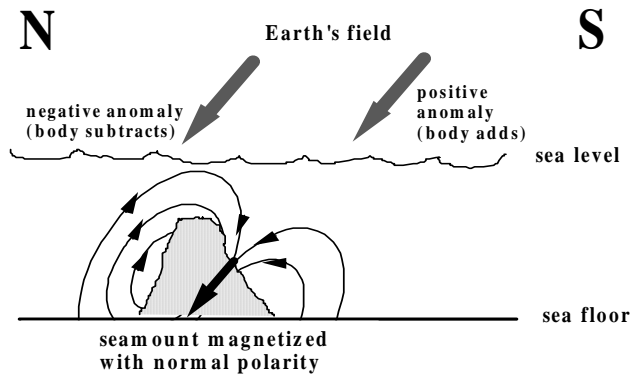


Figure 13.15: Magnetization of seamounts

$$m(x) = j(x) * g(x) \quad (13.15)$$

g is a function depending on a and b , the orientation of the magnetization vector, and the strike of the two-dimensional distribution, which is along the y -axis. Functions such as g are called **Green's functions**. $j(x)$ is the intensity of magnetization.

The magnetic anomalies observed at the sea surface are the convolution (in the time domain) between $j(x)$, any particular block-model for seafloor magnetization, and $g(x)$, the Green's function that determines the amplitude of the magnetic field at any point (z,x) resulting from tabular magnetized bodies. In the Fourier domain, this operation is equivalent to simple multiplication. The Fourier transform of $m(x)$ is

$$M(k) = J(k) G(k) \quad (13.16)$$

where $J(k)$ is the Fourier transform of the source magnetization, and $G(k)$ is the Fourier transform of the Green's function.

Substituting for x , the Green's function g can be expressed as follows:

$$g = \frac{1}{\pi} c \left\{ \left(\frac{a}{a^2 + t^2} - \frac{b}{b^2 + t^2} \right) \cos \theta_p + \left(\frac{t}{a^2 + t^2} - \frac{t}{b^2 + t^2} \right) \sin \theta_p \right\} \quad (13.17)$$

c = Constant which scales the amplitude of the anomaly, $c = (\sin I_r / \sin I_r')^2$

I_r = Inclination of magnetization vector in magnetized body

I_r' = Effective inclination defined by $\tan I_r' = \tan I_r / \sin \alpha$

α = Strike of vertical tabular body with respect to magnetic meridian

θ_p = Index parameter for vertical tabular body, here $\theta_p = 2I_r' - 180^\circ$

Inclination and effective inclination in a magnetized block of ocean crust:

The Fourier transform of $g(t)$ is

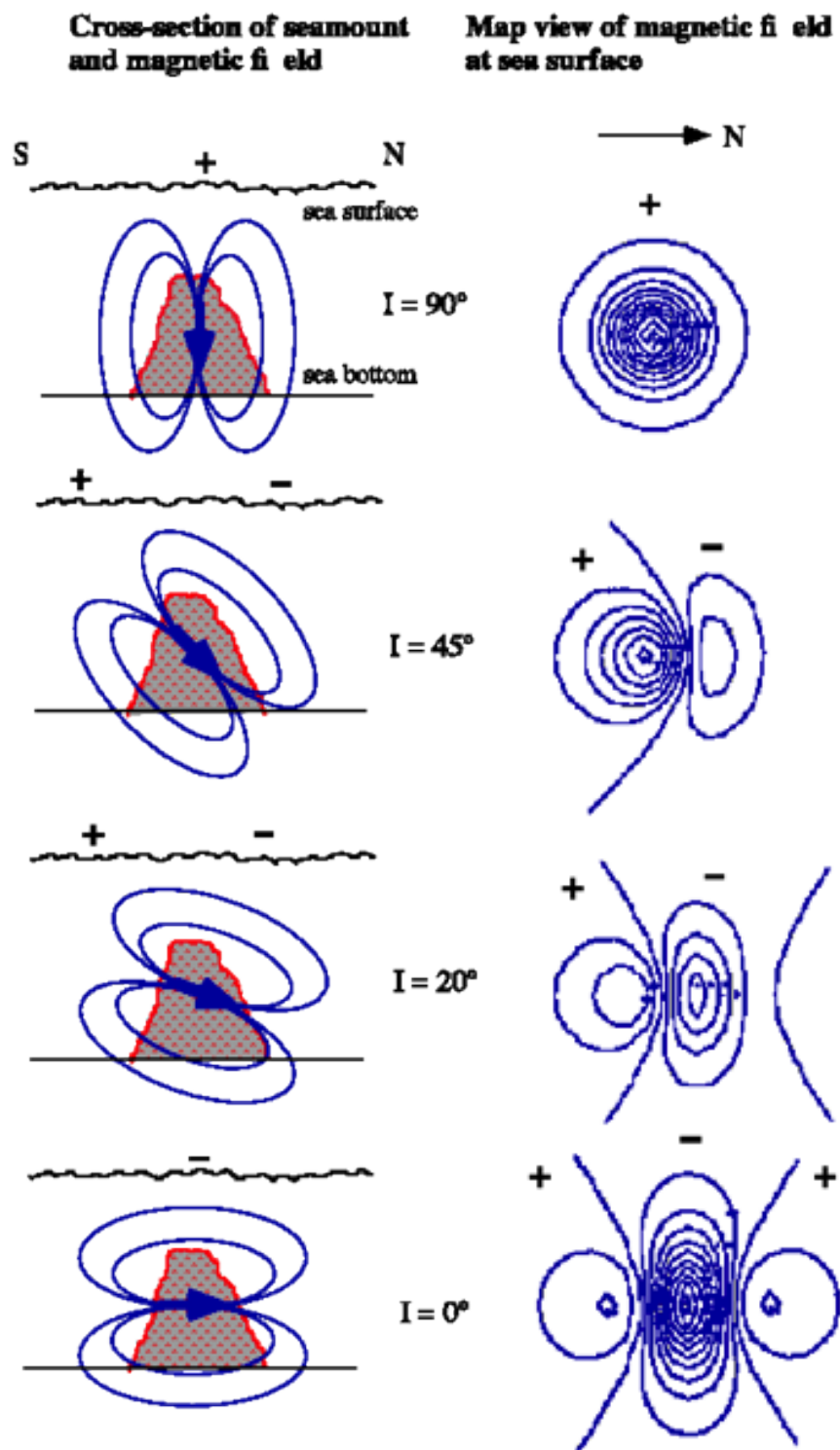


Figure 13.16: Magnetization of seamounts, part 2

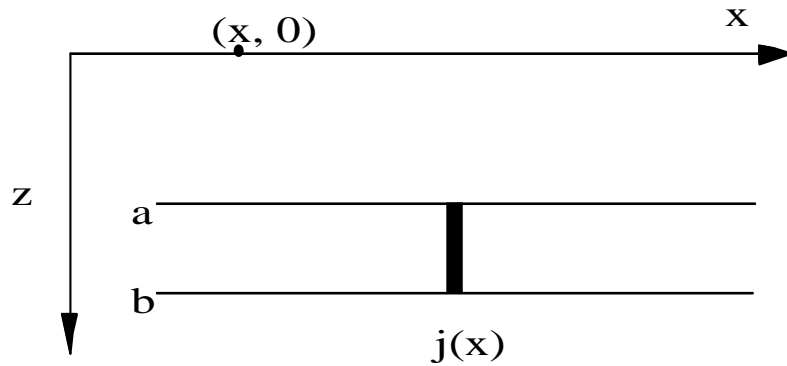
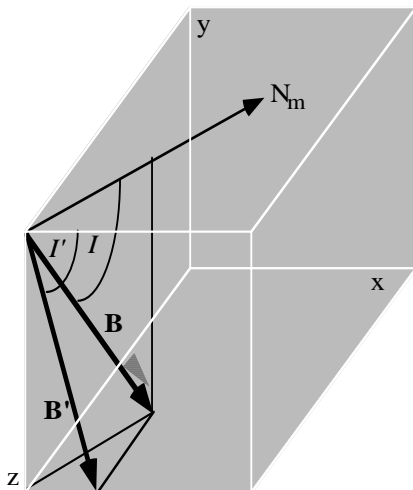


Figure 13.17: Cross-section through a thin tabular body, analogous to a magnetized stripe in ocean crust



x = Spreading direction
y = Strike of mid-ocean ridge

B = Magnetic field vector
B' = Magnetic field vector projected on the vertical xz-plane

I = Inclination
I' = Effective inclination

N_m = Magnetic North

Note that the magnetic field component in y-direction parallel to the mid-ocean ridge causes no magnetic anomaly. For this reason a N-S oriented mid-ocean ridge at the equator causes no magnetic anomaly (in this case there is no vertical component).

Figure 13.18: Magnetic field components

$$G(k) = c(e^{-a|k|} - e^{-b|k|}) \cdot (\cos\theta_p - i\operatorname{sign}(k)\sin\theta_p) \quad (13.18)$$

The real part of the complex spectrum $G(k)$ corresponds to the even or symmetrical part of the anomaly $g(t)$, and the imaginary part to the odd or antisymmetrical part of the anomaly.

The Fourier transform $G(k)$ can be simplified as follows (by using the **DeMoivre relationship**):

$$\exp(i2\pi f)t = \cos(2\pi f)t + i\sin(2\pi f)t \quad (13.19)$$

$$G(k) = c(e^{-|k|} - e^{-b|k|})(e^{-i\theta \text{sign}(k)}) \quad (13.20)$$

The amplitude spectrum of $g(t)$ is

$$|G(k)| = c(e^{-|k|} - e^{-b|k|}) \quad (13.21)$$

and its phase spectrum is

$$\theta(k) = -\text{sign}(k)\theta_p \quad (13.22)$$

Schouten and McCamy (1972) coined the term **Earth Filter** for the expression $(e^{-|k|} - e^{-b|k|})$, and **phase filter** for $e^{-i\theta_p \text{sign}(k)}$.

13.7.2 The Earth Filter

The Earth Filter, a purely real filter, sums the contributions of the lower and upper boundaries of the magnetized layer to the magnetic anomaly, and thus determines its amplitude. The square wave $j(x)$ represents the normal and reversed magnetization intensity recorded in the layer between depths a and b . The Earth Filter acts as a band-pass filter, which removes both short and long-wavelength components. The figure below shows the amplitude spectrum of the magnetic anomaly caused by the upper and lower boundary of the magnetized layer (left), and the amplitude spectrum of the magnetic anomaly of both layers subtracted from each other (right), constituting the Earth Filter.

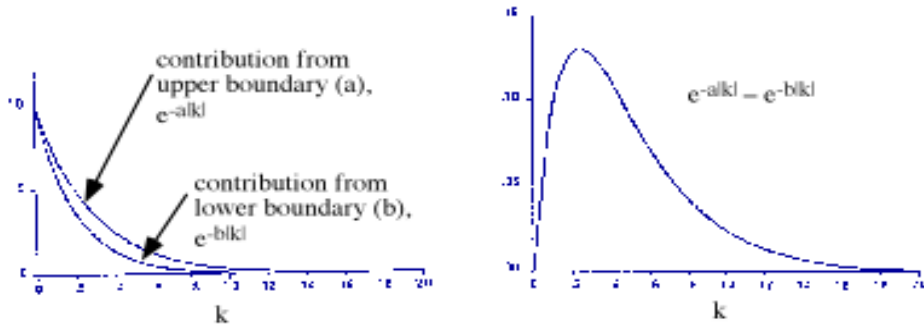


Figure 13.19: The Earth Filter

If we substitute the expression for $G(k)$ into the Fourier transform of $m(x)$ as outlined above we obtain

$$M(k) = J(k)c(e^{-|k|} - e^{-b|k|})(e^{-i\theta \text{sign}(k)}) \quad (13.23)$$

When the magnetic vectors are not vertical (they are vertical only at the magnetic poles), the Fourier transform of $G(k)$ becomes the product of the Earth Filter and the phase filter.

13.7.3 The phase filter

The phase filter is a complex all-pass filter, whose value is a function of the inclination and declination of the remanent magnetization, the inclination and declination of the Earth's magnetic field, and the azimuth of the two-dimensional magnetic structure. Unlike the earth filter, the phase filter is independent of the plane layer assumption, since θ_p depends only on the magnetic vectors and the azimuth of the two-dimensional object.

In order to calculate a synthetic magnetic anomaly, we need to know the phase shift index parameter θ_p which depends on the effective inclination of the ambient (present day) field I' and the inclination of the remanently magnetized body I_r

$$\theta_p = I' + I'_r - 180^\circ. \quad (13.24)$$

If we take the example of an active mid-ocean ridge, the value of θ depends on the effective inclination of the ambient (present day) field I' only, since in this case $I' = I'_r$.

$$\theta_p = 2I'_r - 180^\circ. \quad (13.25)$$

Example 1: Phase shift at an active mid-ocean ridge

Given a location along a mid-ocean ridge, and its strike, how do we determine the expected phase-shift of magnetic anomalies near the ridge? In this case, $I = I_r$. This case is more straightforward than looking at older magnetic anomalies.

(1) Compute the magnetic inclination I from the latitude l :

$$I = \tan^{-1}(2 \tan \lambda). \quad (13.26)$$

(2) Use the value for the angle α to compute the effective inclination I' (recall that I' is the angle between the horizontal and the projection of the magnetic vector into a vertical plane perpendicular to the magnetic lineation, as seen in the diagram of page 30).

$$I' = \tan^{-1}(\tan I / \sin \alpha). \quad (13.27)$$

Here α is the strike of the magnetic lineation with respect to the magnetic meridian. The angle α takes on a value between 0 and 360° . It is measured **90° clockwise from the direction into which the magnetic profile is projected perpendicular to a mid-ocean ridge**, as it is shown on the following figure:

(3) Given I' calculate the phase shift index parameter $qp = 2I' - 180^\circ$.

The next figure illustrates the phase shift at four different latitudes for north-south oriented profiles across an east-west oriented magnetized tabular body in the ocean crust at an active mid-ocean ridge. In this case the remanent magnetization of the magnetized body has the same direction as the present magnetic field, and the observed phase shift as a function of latitude/inclination is only a function of I .

λ = geographic latitude, I = magnetic inclination, θ = phaseshift, A = amplitude.

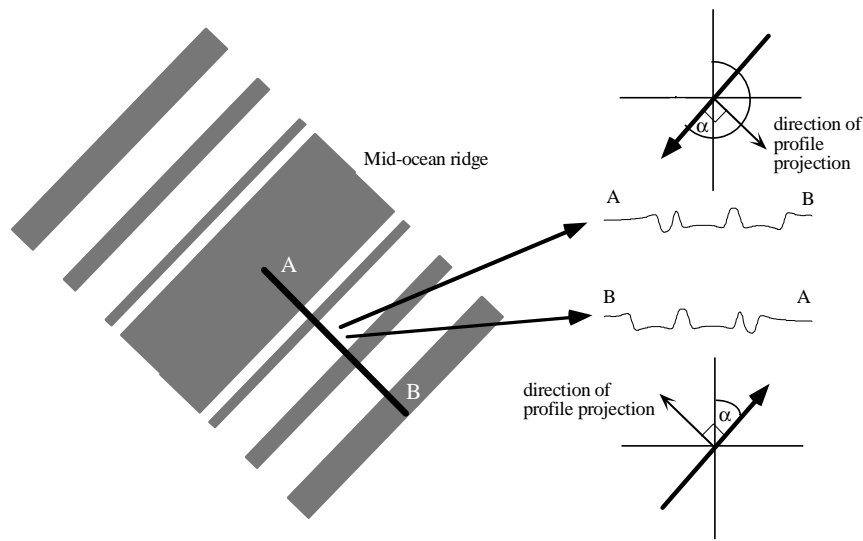


Figure 13.20: Relationship between profile direction and magnetic anomaly phase

N-S oriented magnetic profile across a magnetized crustal block at an E-W oriented mid-ocean ridge in the southern hemisphere at different latitudes

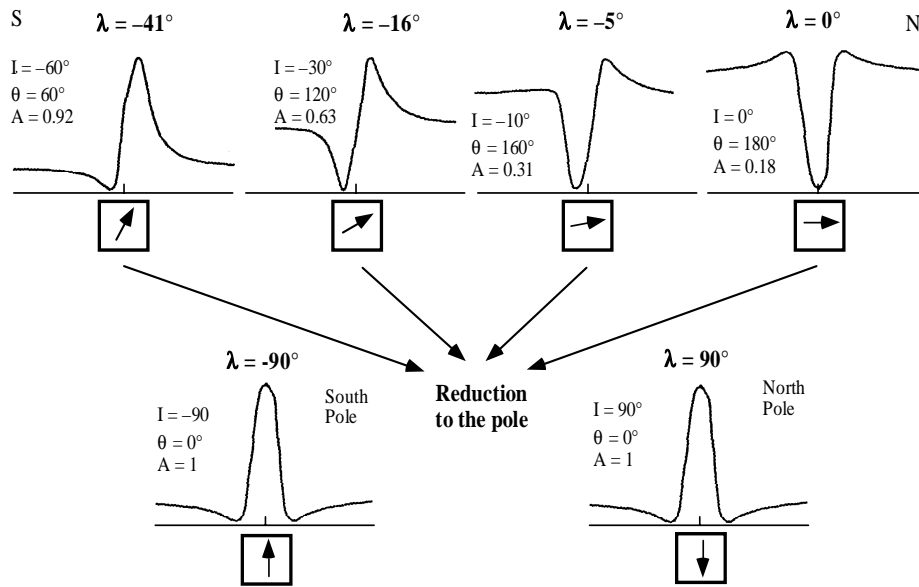


Figure 13.21: Relationship between profile direction and magnetic anomaly phase, part 2

Only an inclination of 90° (i.e. at the North Pole or South Pole) or 0° (at the equator) results in a symmetric magnetic anomaly. All inclinations other than 90° cause a phase shift ("skewness"), and a reduction in amplitude with respect to the corresponding anomaly at the pole.

Note that reduction to the north pole or the south pole yields identical results, since in both cases the remanent magnetic field adds to the earth's magnetic field, and thus creates a positive magnetic anomaly. If the inclination of a magnetized body is known, **reduction to the pole** may be applied to **deskew** the anomalies, i.e. remove the phase-shift resulting from an inclination other than 90° . Reduction to the pole creates symmetric magnetic anomalies over the center of the magnetized bodies.

The next figure illustrates **the effect of the strike of the mid-ocean ridge α at a constant latitude** (i.e. inclination) **on the phase shift index parameter θ_p** . Four synthetic profiles are plotted for magnetic anomalies 25-29, perpendicular to a mid-ocean ridge at 30°N , in 4000 m water depth, formed at a spreading half-rate of 30mm/y, using ridge strikes of 0, 15, 45, and 90 degrees.

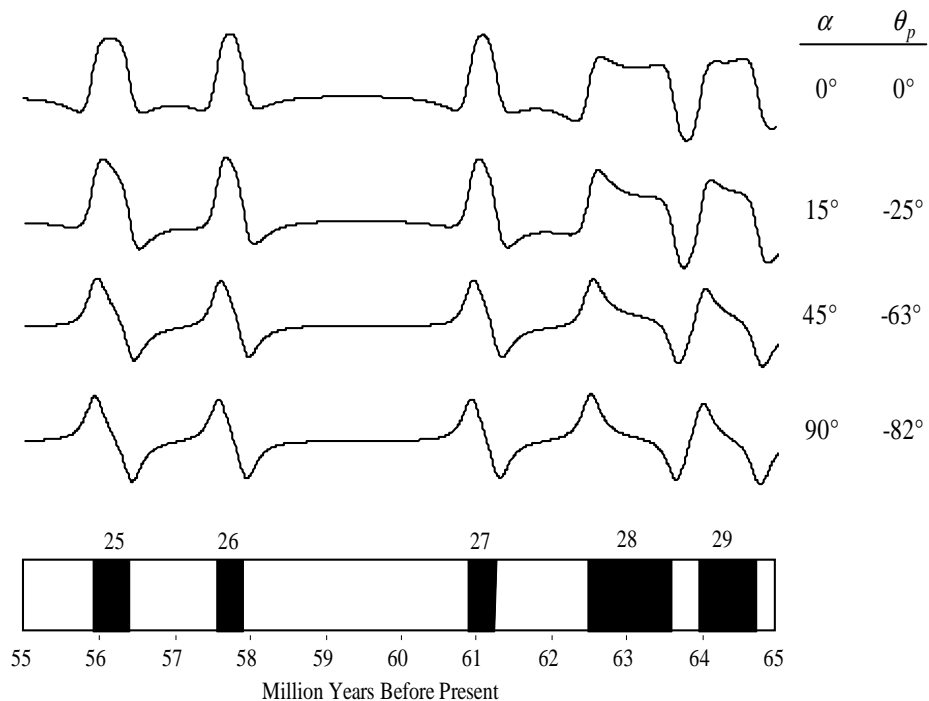


Figure 13.22: Relationship between profile direction and magnetic anomaly phase, part 3

A north-south oriented profile always results in a phase-shift of zero, independently of the latitude. An exception is given by the magnetic equator, where a north-south oriented tabular magnetic body does not produce any magnetic anomaly (hence the concept of phase shift is irrelevant here). An increasing phase shift is observed with

increasing angle between magnetic north and the strike of the ridge. An E-W oriented ridge at the equator reaches the maximum phase shift of 180° (as shown in the previous figure). At 30° north, the maximum phase shift caused by the strike of an E-W trending ridge is -82° .

Example 2: Phase-shift over old ocean crust

The nature of seafloor spreading implies that old crust is at some distance from the ridge where it was created and acquired its magnetization. As a result, the shape of an observed magnetic anomaly is dependent upon the paleolatitude and strike of the ridge where the ocean crust formed, giving I_r , as well as the inclination of the ambient field at the location, where ocean crust of interest is located now, giving I :

$$I' = \tan^{-1}(\tan I / \sin(\alpha - D)) \quad (13.28)$$

$$I'_r = \tan^{-1}(\tan I_r / \sin(\alpha - D_r)) \quad (13.29)$$

where I' , I'_r are the effective inclination of the present field and of the remanent magnetization field, respectively. D , D_r are the present day declination and the remanent declination. I and D can be calculated from the spherical harmonic coefficients of the present day field, α is the strike of the magnetized body.

The inclination depends on the latitude and the paleolatitude, as follows:

$I = \tan^{-1}(2 \tan \lambda)$; where λ is the latitude of the actual position

$I_r = \tan^{-1}(2 \tan \lambda_r)$; where λ_r is the paleolatitude.

In order to calculate the magnetized body's remanent inclination and declination, it is necessary to know

- 1.) The **site coordinate** λ_s, ϕ_s (on a seafloor isochron),
- 2.) the **paleomagnetic pole position** λ_p, ϕ_p with respect to the plate of interest,
- 3.) the **colatitude of the site** θ_r with respect to the paleomagnetic pole, and
- 4.) the **subtending angle** D_{rr} between the great circle passing through the paleomagnetic pole and the site, and the great circle between the geographic pole and the site (this is the remanent declination):

When discussing instantaneous plate motions, we saw that the angular distance between two points on a sphere can be expressed by the **scalar product of two unit vectors** in Cartesian coordinates. The following discussion is based on working with **unit vectors** on a **unit sphere**, i.e. **bold letters indicate unit vectors**.

The angular distance θ_r between the site and the paleomagnetic pole is given by

$$\theta_r = \cos^{-1}(\mathbf{s} \cdot \mathbf{p}) = \cos^{-1}(s_x p_x + s_y p_y + s_z p_z) \quad (13.30)$$

where \mathbf{s} and \mathbf{p} are unit vectors, and s_x, s_y, s_z are given by

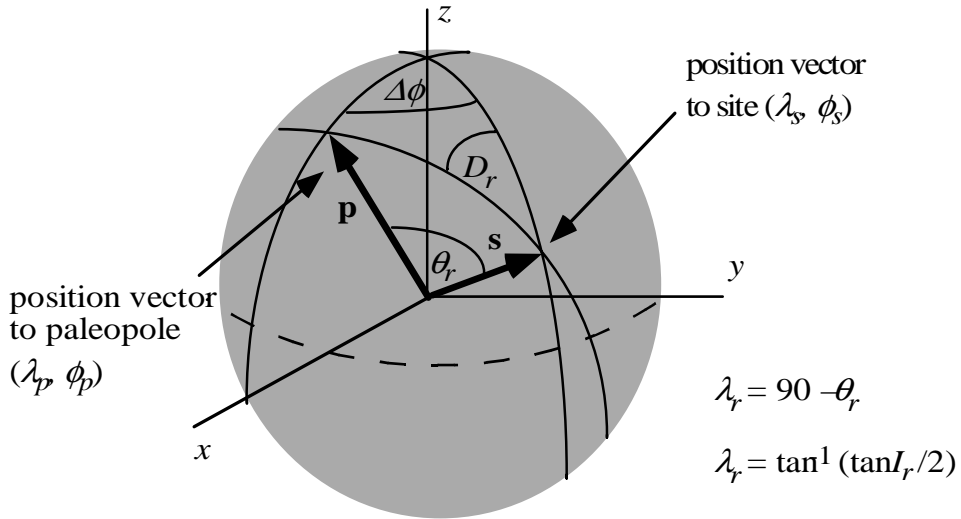


Figure 13.23: Position vectors and magnetization directions

$$\begin{aligned}
 s_x &= s \cos \lambda_s \cos \phi_s \\
 s_y &= s \cos \lambda_s \sin \phi_s \\
 s_z &= s \sin \lambda_s
 \end{aligned} \tag{13.31}$$

The Cartesian components of \mathbf{p} are similarly defined.

After finding the remanent colatitude θ_r , we can determine the remanent latitude, λ_r , and the remanent inclination I_r using the relations noted. The remanent declination, D_r , is given by the angle between the two great circles containing vectors \mathbf{s} and \mathbf{p} , and \mathbf{s} and \mathbf{z} , respectively (see below). In order to determine this angle, we first calculate the poles of the two great circles. These poles are equal to the **cross product** of the two pairs of vectors, $\mathbf{P}_1 = \mathbf{p} \times \mathbf{s}$, and $\mathbf{P}_2 = \mathbf{z} \times \mathbf{s}$.

The cross product is defined as a vector perpendicular to the plane defined by two vectors. Its direction is given by the right-hand rule, and can also be understood using the example of a screw. If \mathbf{p} and \mathbf{s} are both perpendicular to the axis of a right-handed screw, and the screw is rotated in the direction going from \mathbf{p} to \mathbf{s} , then the screw will advance in the direction of the vector defined by $\mathbf{p} \times \mathbf{s}$. The scalar length of the cross product vectors is given by

$$\begin{aligned}
 |P_1| &= \sin \delta_1 \\
 |P_2| &= \sin \delta_2
 \end{aligned}$$

The cross product is always positive, since the angular distances between two locations on the surface on the sphere is always less than 180° , and it is not a unit vector

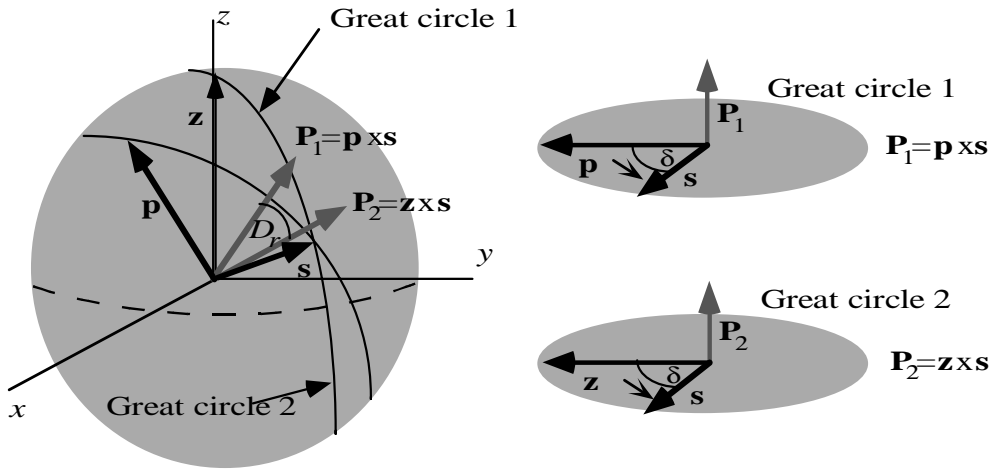


Figure 13.24: Cross product vectors

unless $\delta = 90^\circ$. We can convert it to a unit vector by dividing each component by their scalar length, e.g. $P_1 = \sin \delta$. The Cartesian components of the cross product are:

$$\begin{aligned} P_x &= p_x s_z - p_z s_y \\ P_y &= p_z s_x - p_x s_z \\ P_z &= p_x s_y - p_y s_x \end{aligned} \quad (13.32)$$

In our case the cross product of vectors $\mathbf{P}_1 = \mathbf{p} \times \mathbf{s}$ and $\mathbf{P}_2 = \mathbf{z} \times \mathbf{s}$ yield the **poles of the two great circles** shown above. The angular distance between the two great circle poles \mathbf{P}_1 and \mathbf{P}_2 is equal to the angle D_r between the two great circles, i.e. the remanent declination. We can find this angle by taking the dot product of \mathbf{P}_1 and \mathbf{P}_2 , as described earlier:

$$D_r = \cos^{-1}(P_1 \cdot P_2) \quad (13.33)$$

with $0^\circ \leq D_r \leq 90^\circ$.

We now have all necessary components to calculate the phase shift angle θ_p : I , D , I_r , D_r , and α , the strike of the ridge:

$$\theta_p = I + I_p - 180^\circ \quad (13.34)$$

$$\theta_p = \tan^{-1}\left(\frac{\tan I}{\sin(\alpha - D)}\right) + \tan^{-1}\left(\frac{\tan I_r}{\sin(\alpha - D)}\right) - 180^\circ \quad (13.35)$$

The position of paleopoles (their paleolatitudes and paleolongitudes) are usually determined from the remanent inclination and declination of continental rocks, but one can also invert the measured “skewness” or phase shift of oceanic magnetic anomalies

for obtaining paleomagnetic poles. This is particularly useful for plates like the Pacific plate which are almost entirely oceanic but for which there are essentially no reliable continental paleomagnetic poles.

13.7.3.1 Upward and downward continuation

The two elements of the forward Earth Filter are both **upward continuation** filters of the general form e^{-hk} , and give the observed anomaly at different observation levels. The filter parameter h indicates the change in observation level, and k is the wavenumber. **Upward continuation smoothes a signal due to attenuation of short wavelengths and reduction in amplitude** due to distance from the source.

The inverse Earth Filter represents the sum of two **downward continuation** filters of the general form e^{hk} . **Downward continuation amplifies high wave numbers**, and thus short wavelengths contained in the signal. It improves the resolution of the signal, but also amplifies noise.

The next figure illustrates the effect of upward continuing a sequence of magnetic anomalies. We show a magnetic profile over a flank of a mid-ocean ridge with ages ranging from 0-10 m.y. (An 1-5), spreading at 30 mm/y. The first profile plotted above the magnetic block model represents magnetic anomalies as measured directly at the seafloor. The two other profiles are upward continued to 1250 m and 2500 m, respectively. A depth of 2500 m corresponds to the average water depth at a mid-ocean ridge, i.e. the elevation at which we would normally measure these anomalies. Note the exponential attenuation of both amplitudes and short wavelengths in the upward continued signals.

13.8 Interpreting observed oceanic magnetic anomalies

- 1.) Take a particular polarity timescale, and create a block magnetization model for the time period of interest.
- 2.) Calculate the expected “skewness” of the magnetic anomalies.
- 3.) Apply the Earth filter to the magnetization model to compute synthetic anomalies.
- 4.) Plot these anomalies using an approximate seafloor spreading rate.
- 5.) Plot the observed data at the same scale.
- 6.) Take the polarity timescale used to create the block model to identify the sequence of magnetic anomalies of the observed profile.

Problems that are often encountered in interpreting magnetic anomalies are “anomalous” skewness, i.e. a larger phase-shift in the observed data than predicted, propagation and jumps of spreading ridges take place, leaving discontinuous sequences of magnetic anomalies on both sides of the ridge, and general noise in the data, just to name

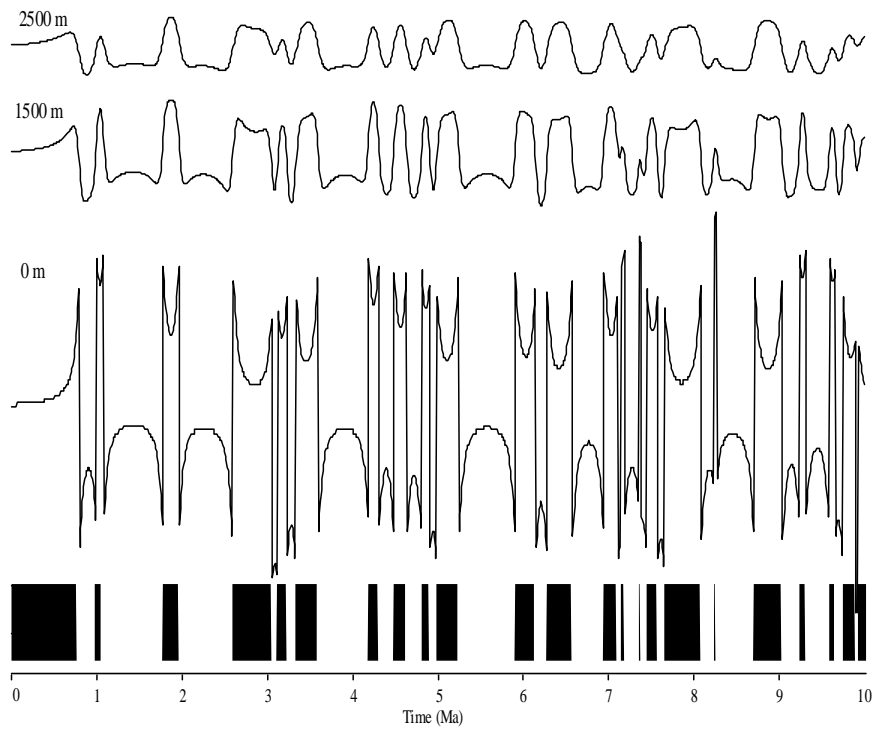


Figure 13.25: Upward continuation of the magnetic field from the seafloor (0 m) to 1.5 km and 2.5 km above the seabed

a few. The synthetic anomalies are phaseshifted by about -10° to match the observed data. Note the noise in the observed anomalies compared to the synthetic profile. The quality of this profile is fairly representative for magnetic anomalies in slowly spreading oceans. The faster the seafloor spreading, the better magnetic anomalies can be resolved, and the larger the signal to noise ratio.

13.9 Magnetic Maps - from data acquisition to interpretation

13.9.1 Overview

Large-scale magnetic surveys over land are typically acquired using instruments fixed to aircraft. Magnetic maps over the oceans can be derived by a combination of airborne data and shiptrack data (as described above). The book 'Aeromagnetic Surveys' by Colin Reeves provides a detailed description of all aspects of aeromagnetic data acquisition and processing. The following text briefly describes the various steps involved.

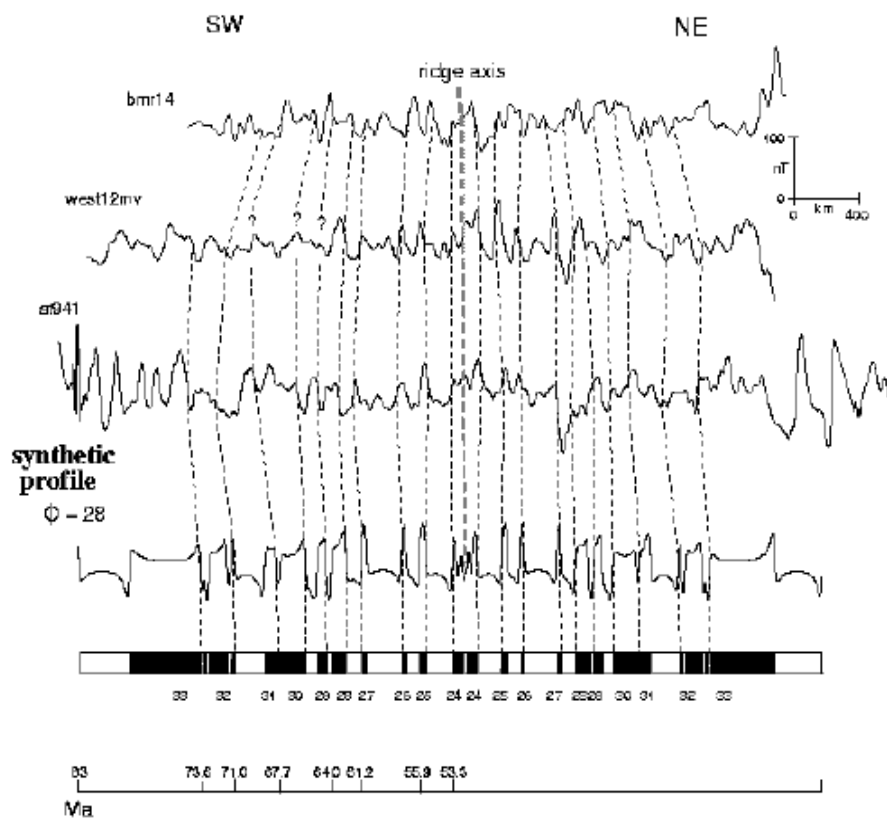


Figure 13.26: Observed and ship profiles across the Tasman Sea

13.9.2 Survey design

The design of the surveys need to take several factors into account.

- The path of the survey tracks. Surveys are often acquired systematically along a series of parallel flightlines or shiptracks. The direction of these lines should typically be perpendicular to the strike-direction of the geological structures in the survey areas. The ideal spacing between adjacent lines depends on the level of geological detail we want to image. In practical terms, the line spacing is a trade-off between achieving a dense data coverage and the resources (time, money) available to carry out the acquisition.
- The flying height for airborne surveys – a lower flying height yields higher resolution data, but in areas of severe terrain, flying too close to the ground may be dangerous.

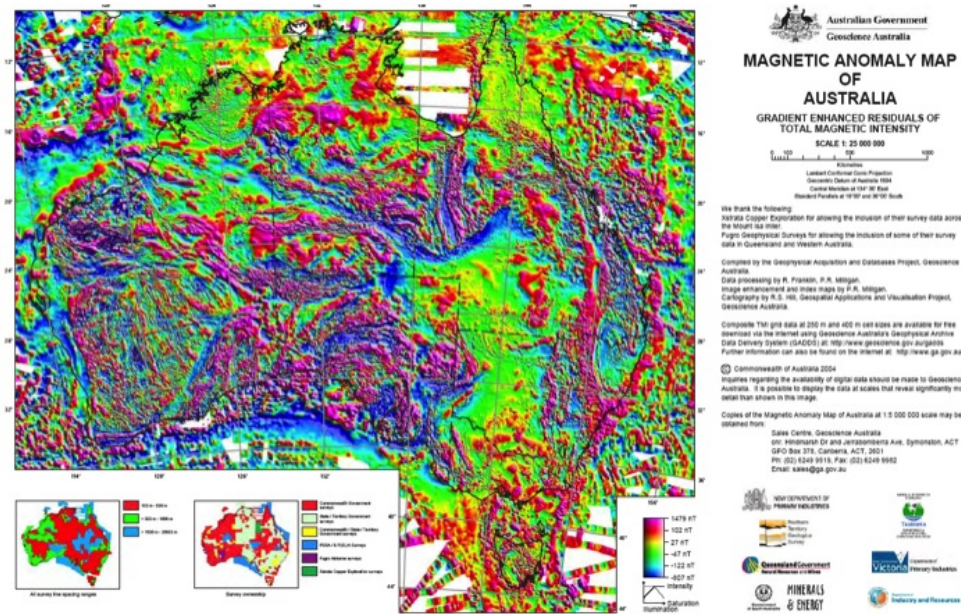


Figure 13.27: Total Magnetic Intensity Anomaly Map for Australia (source: Geoscience Australia)

- Avoiding where possible 'cultural' (man-made) sources of magnetic anomalies → for example pipelines, oil rigs, railway lines.

The Australian magnetic map is an example of how data from many individual airborne surveys are processed then compiled together to produce a large-scale magnetic map for the entire Australian continent. The processing steps required to generate this map are described in the next section.

13.9.3 Data Processing Steps

Refs: Reeves (2005), Quesnel et al (2009).

- *Quality Control* checking the data as it is acquired for obvious problems
- *Base station corrections* This is an attempt to correct for external time-varying fields such as micropulsations, diurnal variations and magnetic storms.
- *IGRF correction* The International Geomagnetic Reference Field (IGRF) is a model that describes the spatial variation of the core field, and how it has gradually changed with time. Most survey cover a small enough area that the core field is a relatively simple long wavelength trend, which can be removed by subtracting the IGRF model, calculated for the time of the survey.

- *Line Levelling and microlevelling* After the preceding processing steps, mismatches may still exist between the magnetic anomaly values on neighbouring survey lines or at the intersections between crossing survey lines. The line levelling stage involves systematically examining these mismatches to derive shifts that reduce the crossover errors.
- *Deculturing* Where the data contain anomalies from man-made objects, these data can be manually edited or carefully designed filters applied that remove the cultural anomalies without distorting the magnetic signal of geological sources.
- *Gridding* The gridding stage involves interpolating the data from the observation locations along the shiptracks or flightlines, onto a regular grid. As with gravity data, minimum curvature interpolation is the most common method.
- *Compilation of continental-scale surveys:* Magnetic maps covering entire countries or continents are generally compiled by piecing together maps derived from many smaller-scale surveys. In order to link these grids to produce a single self-consistent map from many input data sets, the data sets need to be reprocessed to common parameters. This can include regridding to a common grid spacing, and using continuation filters to adjust datasets acquired at different altitudes to a common level. The long wavelengths are likely to be poorly constrained in surveys that cover a small area, so the long wavelength component of the linked grid can be replaced with a better constrained estimate of the long wavelength crustal field derived from satellite data (Maus et al., 2008)

13.9.4 Interpretation

The goal of the processing steps described above is to produce a map of Total Magnetic Intensity (TMI). This data are represented on a regular grid of points. Data in grid format can be displayed using software such as GMT, matlab or GIS software. We can also apply simple filters to the magnetic grids to make them easier to interpret, or to enhance signals in specific wavelength ranges

13.9.4.1 Basic Filtering

Many of the basic filtering of magnetic maps are equally applicable to gravity maps and indeed any grid data (e.g. bathymetry, topography). Derivative-based filters, upward and downward continuation, and wavelength filters have already been described in the gravity chapter - some examples are shown in figures 13.28 and 13.29 for profile and map data respectively.

13.9.4.2 Reduction to Pole

An important type of filter which is specific to the interpretation of magnetic data is the so-called 'Reduction to Pole' (RTP). Unlike gravity anomalies, the shape of magnetic

anomalies is a function of the local inclination and declination of the Earth's field as well as the shape of the body causing the anomaly. Put another way, a the magnetic anomaly due to a simple source like an igneous intrusion or a basement fault will have a different shape depending on its geographic location on the Earth. This adds an extra layer of complexity to the interpretation of magnetic data. At the North and South magnetic poles anomalies are relatively simple to interpret since the Earth's field is vertical, hence anomalies for simple bodies are not asymmetric and are centred over the causative sources. Hence, in order to reduce the complexity of data from other magnetic latitudes, we can apply a filter that attempts to remove the influence of the local direction of the Earth's field and make anomalies from any latitude appear as if the magnetization is vertical.

$$F(T_p) = w^2 F(T)/[(G \cdot \hat{B})(G \cdot \hat{M})]. \quad (13.36)$$

In this equation, $F(T)$ is the Fourier transform of the observed TMI anomaly while $F(T_p)$ is the Fourier transform of same field at the pole (the RTP anomaly). \hat{B} is the geomagnetic field unit vector, \hat{M} is the magnetization unit vector, G is the wavenumber vector (iu, iv, w) and $w = (u^2 + v^2)$ (Swain, 2000). Note that we need to know the direction of magnetization. For data over continental crust, we generally assume that the rocks are magnetized in the direction of the Earth's field - that magnetization is mainly induced rather than remanent.

13.9.5 Depth Estimation

An important application of magnetic data is for mapping sedimentary basins, and generating regional maps of depth to basement. Sedimentary rocks typically (though not always) have much lower magnetic susceptibilities than the rocks in the underlying crystalline basement - so when we analyse magnetic data over sedimentary basins we can assume that the sediments are effectively 'invisible', and that the variations in the magnetic anomaly field are telling us about the basement below, and in particular how the depth to the basement is varying. Where short wavelength, shallow-sourced anomalies are observed, the basement is likely to be shallow, whereas in areas where the basement is deep, short wavelength anomalies are less prevalent. The figure below shows an example from Tanzania, where there is indeed a strong correlation between the wavelength of the anomalies and the basement depth. It is important to realise, however, that such simple assumptions are often flawed - for example, basement rocks may sometimes be weakly magnetized, while rocks within the sedimentary section (the sediments themselves, or more likely igneous intrusions within the sediments) can give rise to significant magnetic anomalies. In both these cases, care must be taken not to misinterpret the basement as being much shallower or deeper than it really is.

The Tanzania example shows how, just by looking at the magnetic map, we can get a qualitative idea of the extent of sedimentary basins. The aim of magnetic depth estimation is to provide quantitative estimates of the basement depth. We do this by making simple assumptions about the shape of the geological structures that are causing the

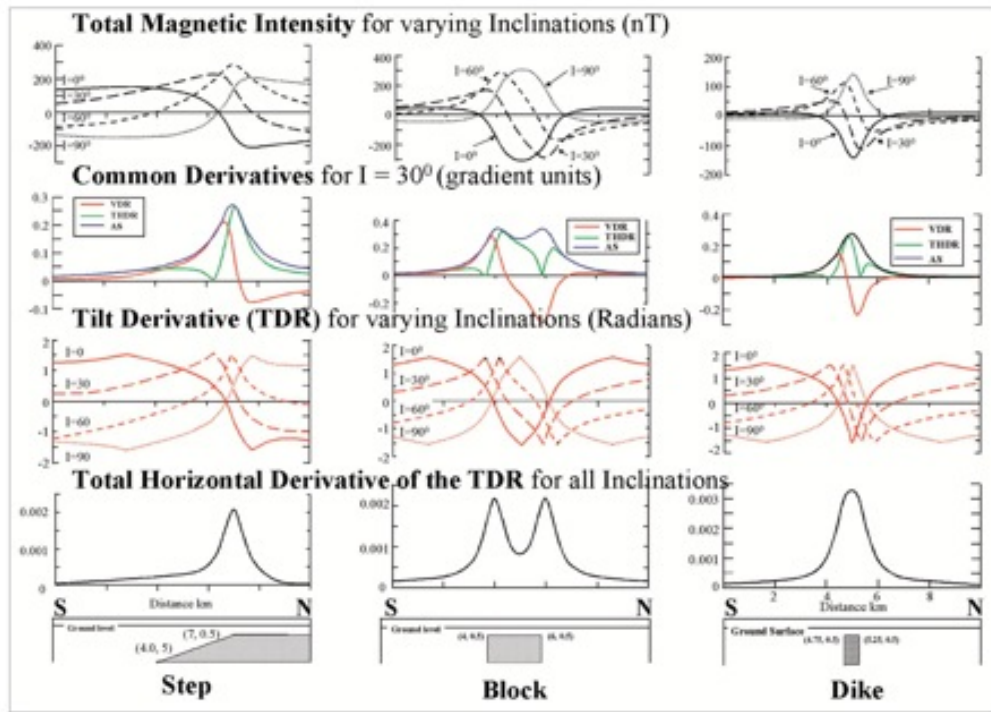


Figure 13.28: Synthetic anomalies are shown for different simple source geometries (bottom), at different magnetic latitudes. Note that the anomaly for $I=90^\circ$ (i.e. for a source located at the magnetic pole) the anomalies are centred over the source. For other magnetic latitudes, the anomalies are asymmetric even for symmetric source bodies. The different derivatives are used to provide sharper representations of source edges (which in geological terms will correspond to e.g. faults, edges of intrusions). Source: Verduzco et al. (2004)

magnetic anomalies. Based on mathematical descriptions of the magnetic field due to such simple source geometries, we can make simple inferences about the relationship between the shape of the observed anomalies and the depth to the sources.

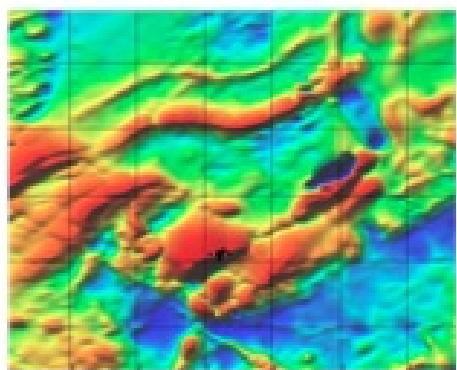


Figure 1. TMI magnetic anomaly grid

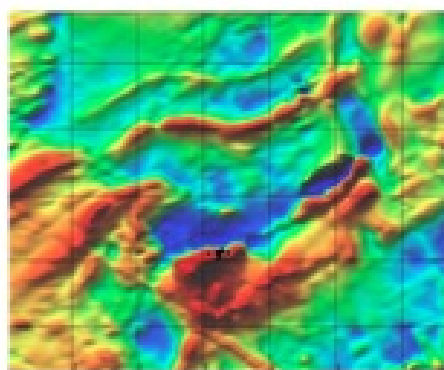


Figure 2. RTP magnetic anomaly Grid

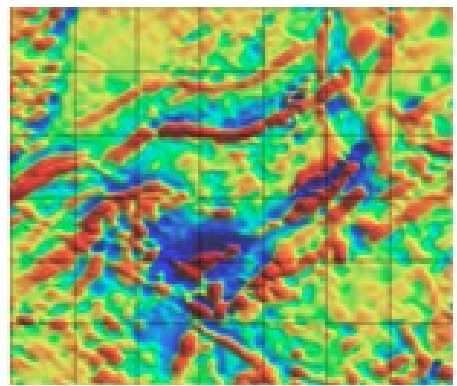


Figure 3. First Vertical Derivative

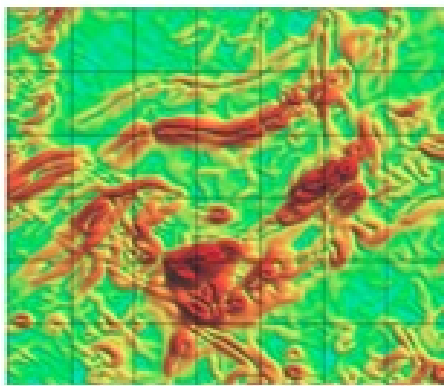


Figure 4. Total Horizontal Derivative

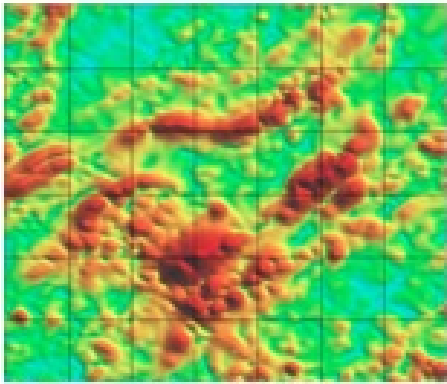


Figure 5. Analytic Signal

Figure 13.29: Magnetic data from Namibia, illustrating derivative maps and RTP for map data.
(source: Salem et al. (2007))

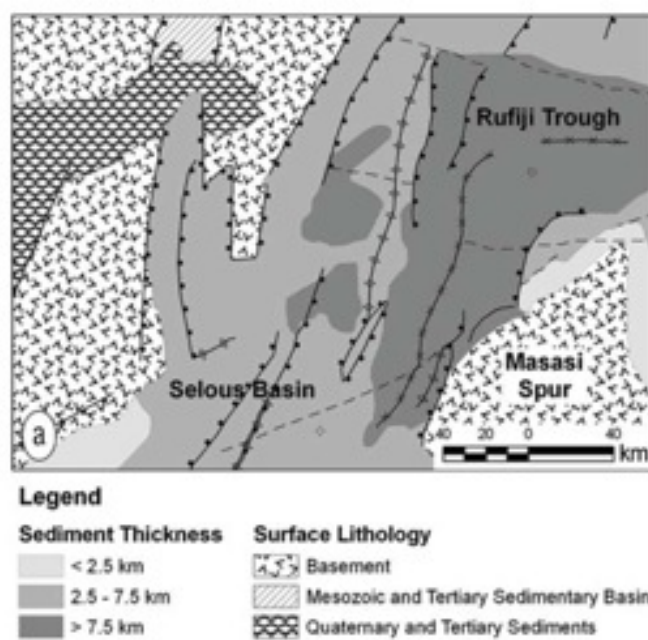


Figure 13.30: Map showing depth to basement for a sedimentary basin in Tanzania based on seismic and well data (source: Salem et al. (2008))

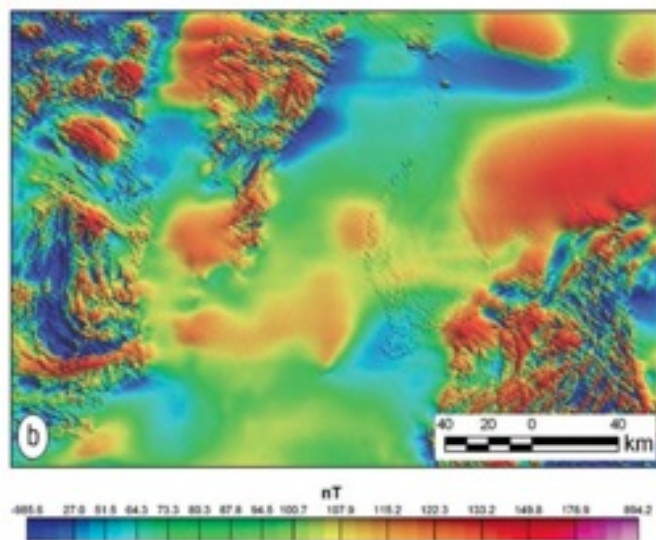


Figure 13.31: Magnetic data over sedimentary basins in Tanzania. Note the way that areas of intense short wavelength variations correspond to areas of shallow/exposed crystalline basement. By contrast, the magnetic anomaly field over areas of deep basement (in some places exceeding 7km) is dominated by smooth, long wavelength anomalies. (source: Salem et al. (2008))

Chapter 14

The Gravity Field

14.1 Overview

The strength of the Earth's gravity field varies spatially. The variations are small compared to the magnitude of the field itself - hence, we don't feel any difference in the strength of the gravity field between different parts of the globe. However, by taking measurements of the Earth's field with sufficiently sensitive equipment, we can map out the detailed variations in the gravity field. These maps are interesting to people working in various fields of study, including geodesy, oceanography and climate science. In this course we will focus on those related to geophysics, in other words what the Earth's gravity field tells us about the subsurface of the Earth. Variations in the Earth's gravity field are often related to variations in the physical properties of the material in the subsurface - specifically, their density. We know that the Earth's crust comprises many different lithological types (oceanic crust, ancient continental cratons, sedimentary basins, igneous intrusions). These different rock types have different densities - so spatial variations in the geology of the subsurface give rise to variations in the strength of the gravity field that we observe over them (a relatively low density rock unit causes anomalously low gravity readings, and vice versa). The gravity field is also influenced by other factors including variations in the thickness of the crust, mantle temperature/composition, and crustal strength. Studying the spatial variations of gravity anomalies across the Earth helps us to understand all of these phenomena. This chapter covers the study of gravity fields beginning with some basic theory of gravity fields and their representation. We then discuss the methodologies used to measure these fields, and how these measurements are processed to isolate the most interesting aspects of the gravity field. Finally we describe how the processed data (e.g. gravity anomaly maps) are interpreted to say something meaningful about subsurface geological structures and the geodynamic processes that created them.

14.2 Gravitational potential and acceleration

The force, F , between two point masses m_1 and m_2 at a distance r apart is attractive, and acts along the line joining the particles, with magnitude given by **Newton's law of universal attraction**.

$$F = \frac{m_1 m_2}{r^2} \quad (14.1)$$

G is the gravitational or Newtonian constant. In SI units G has a value of $6.67 \times 10^{-11} m^3 kg^{-1} s^{-2}$. This inverse square relationship of the distance relative to the force was a result of observing planetary motion, and it was established by Sir Isaac Newton in 1666. The acceleration of mass m_1 due to the presence of mass m_2 is Gm_2/r^2 .

The **gravitational potential energy** of a mass m_2 at a distance r from the mass m_1 is:

$$U(r) = \int_r^{r'} F(r) dr = -G \frac{m_1 m_2}{r} \quad (14.2)$$

If mass m_2 is moved from position r to the new position r' (with respect to mass m_2), the gravitational potential energy which is needed ($r > r'$) or released ($r < r'$) is the potential difference

$$= -G \frac{m_1 m_2}{r} + G \frac{m_1 m_2}{r'} \quad (14.3)$$

The gravitational potential U due to a mass m is

$$U = -\frac{Gm}{r} \quad (14.4)$$

The **gravitational acceleration** g towards m can be written in terms of the gravitational potential:

$$\begin{aligned} g &= -\frac{Gm}{r^2} \\ &= -\frac{\delta}{\delta r} \left(-\frac{Gm_1}{r} \right) \\ &= -\frac{\delta U}{\delta r} \end{aligned} \quad (14.5)$$

We generalize this equation to three dimensions by writing

$$g = -\nabla U. \quad (14.6)$$

A good example for visualizing this equation is the **sea surface**, which approximates an **equipotential surface**.

A good example for visualizing this equation is the **sea surface**, which approximates an **equipotential surface** (figure 14.6). \mathbf{g} is a vector function in three dimensions, since

$-\nabla U$, i.e. the gradient of U , is a vector function perpendicular to the potential surface defined by U . The divergence of the gravity field \mathbf{g} , however, is zero. In other words, the net flux of a gravity field across a closed surface surrounding no attracting matter is zero.

If we consider the radial pattern of lines of force around a point mass, and imagine an arbitrary box, the same number of lines that go into the box also come out of the box. This simple consideration leads us to **Laplace's equation**:

$$\nabla^2 U = \frac{\delta^2 U}{\delta x^2} + \frac{\delta^2 U}{\delta y^2} + \frac{\delta^2 U}{\delta z^2} \quad (14.7)$$

If we approximate the Earth's shape with a sphere, we find that at any point within a sphere the gravitational acceleration is due to all the material between the point and the center of the sphere. The contribution of all the material outside the point is zero.

Imagine a sphere that consists of a series of thin uniform spherical shells. None of the shells of radius greater than r make any contribution to the acceleration (see figure below).

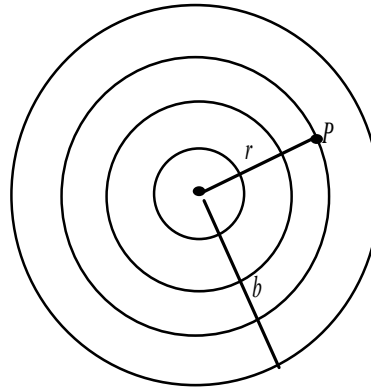


Figure 14.1: gravitational acceleration

The gravitational acceleration g at a distance r from the sphere of radius b ($b < r$) and density ρ is

$$g = -\frac{G \frac{4}{3}\pi b^3 \rho}{r^2} = -\frac{GM_e}{r^2} \quad (14.8)$$

14.3 The Earth's gravity field

14.3.1 The Earth's spheroid and its gravity field

We could apply the last formula to the Earth, if it were a perfect sphere. Then the gravitational acceleration towards the Earth would be given by:

$$g = -\frac{GM_e}{R_e^2} \quad (14.9)$$

where M_e is the mass of the Earth, and R_e its radius:

$$M_e = 5.98 \times 10^{24} \text{ kg}$$

$$R_e = 6.371 \times 10^6 \text{ m}$$

The **average value of the gravitational acceleration** at the surface of the Earth is

$$\bar{g} = -\frac{\delta U}{\delta r} = -\frac{GM_e}{R_e^2} = -9.82 \text{ ms}^{-2} \quad (14.10)$$

The **vertical gravity gradient of the Earth** is

$$\frac{\delta g}{\delta r} = -\frac{2GM_e}{R_e^3} = -\frac{2\bar{g}}{R_e} = 3.086 \text{ gu/m} = -0.3086 \text{ mgal/m} \quad (14.11)$$

This is in fact the so called **free-air correction** which is applied to gravity measurements from different altitudes, as we will see later.

The **units** used in gravity measurements are:

$$1 \text{ gal} = 1 \text{ cm/s}^2 = 10^{-2} \text{ m/s}^2 \text{ (cgs unit)}$$

$$1 \text{ mgal} = 10^{-3} \text{ cm/s}^2 = 10^{-5} \text{ m/s}^2 \text{ (cgs unit)}$$

$$1 \text{ gu} = 10^{-6} \text{ m/s}^2 \text{ (SI unit (gu = gravity unit))}$$

In order to consider the gravity field of the Earth, we need to use whole Earth coordinates in terms of r (radius), θ (colatitude), λ (geocentric latitude), and ϕ (longitude):

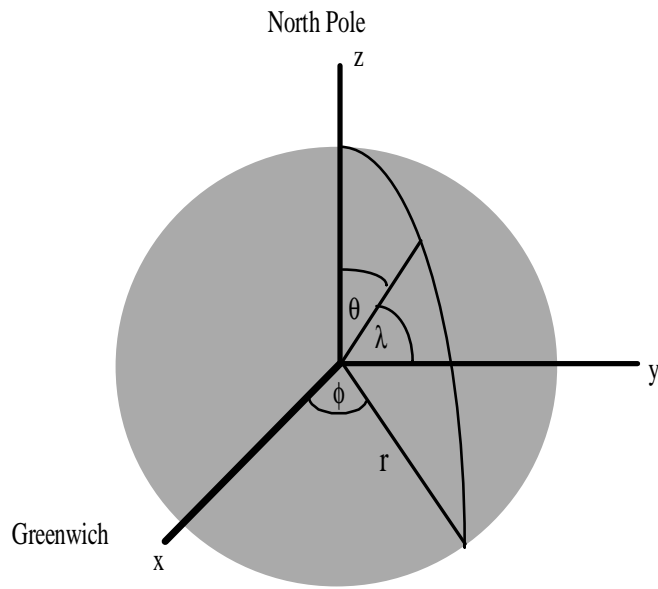


Figure 14.2: Polar coordinates

If the Earth were perfectly spherical and not rotating, the gravitational acceleration g would have the same value at every point. However, the Earth bulges at the equator and is flattened at the poles due to the centrifugal force caused by the rotation of the Earth (Fig. 14.3).

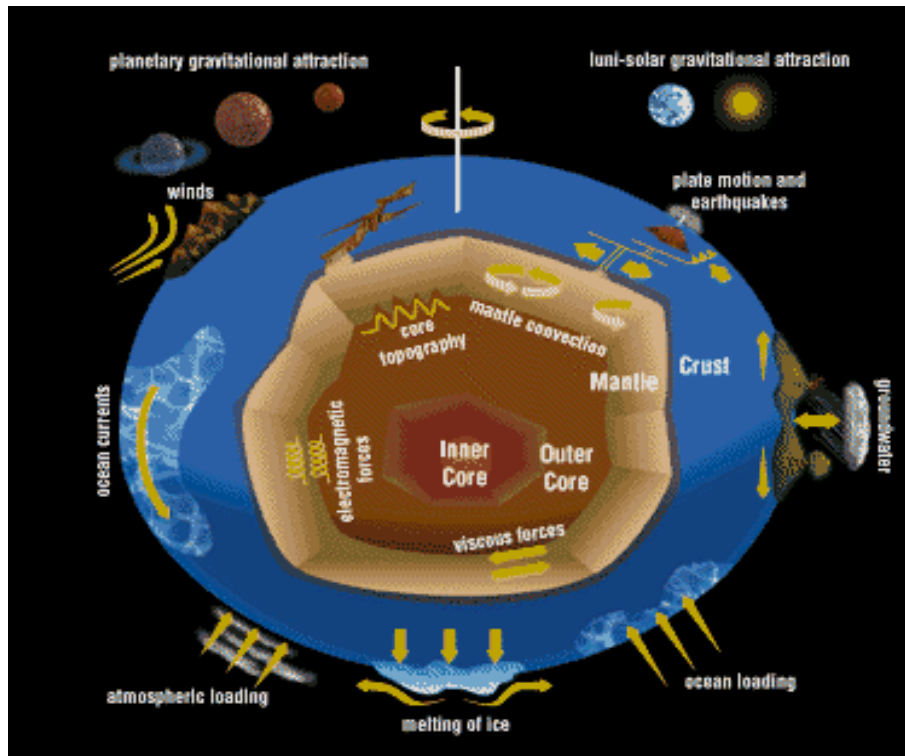


Figure 14.3: The spheroidal shape of the Earth

Hence the Earth's shape can be approximated by an **oblate spheroid**, i.e. the surface that is generated by rotating an ellipse about its minor (shorter) axis (a) (Fig. 14.4).

$a (=b)$ is the equatorial radius of the spheroid, and c is the polar radius.

λ = geocentric latitude

λ_g = geographic latitude

A relationship between geocentric and geographic latitude is given by:

$$\tan \lambda = \frac{c^2}{a^2} \tan \lambda_g \quad (14.12)$$

To first approximation the axes a , b , and c defining the ellipsoid have lengths as follows:

$$a = b = 6378139 \text{ m}$$

$$c = 6356754 \text{ m}$$

$$a - c = 21 \text{ km}$$

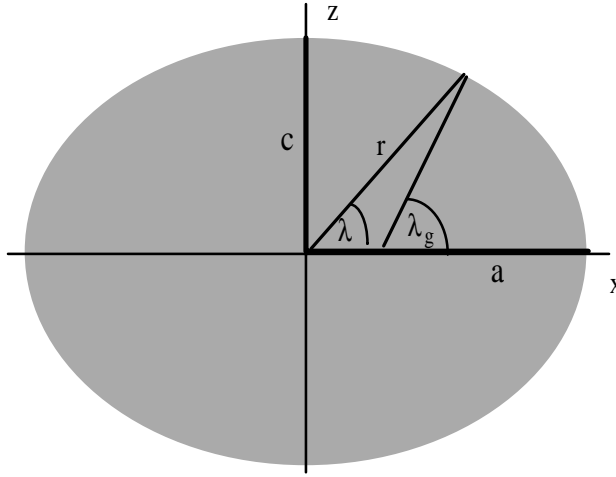


Figure 14.4: Relationship between geocentric and geographic latitude

The **flattening** f is defined as $f = (a - c) / a = 1/298.357$. The **radius of the spheroid as a function of latitude** is

$$r \cong a(1 - f \sin^2 \lambda) \quad (14.13)$$

The constant f is subject to change while the ellipsoid that best fits the Earth becomes better and better known, mostly due to satellite data. The **precession of the equinoxes**, which has a cyclicity of about 20000 years (one of the well known **Milankovitch cycles**), is a direct consequence of the elliptical shape of the Earth.

As a result of the equatorial bulge, the gravity field at the equator is significantly reduced with respect to the pole, since the surface at the equator is farther away from the center of the Earth. However, this effect accounts only for about 40% of the variation of gravity with latitude. The remaining 60% is a result of the centrifugal acceleration, which also has a reducing effect on g at the equator. This can be seen from the following formula which expresses g_{rot} , the gravitational acceleration of a rotating sphere, in relation to g of a non-rotating sphere as a function of latitude:

$$g_{rot} = g - \omega^2 R_e \cos^2 \lambda. \quad (14.14)$$

Here ω is the angular rotation velocity of the sphere. The gravitational acceleration of the Earth's reference ellipsoid as a function of latitude is expressed by the reference gravity formula:

$$g_0(\lambda) = g_e(1 + \alpha \sin^2 \lambda + \beta \sin^4 \lambda) \quad (14.15)$$

Here $g_e = 9.7803185$ is the gravitational acceleration at the equator, $\alpha = 5.278895 \times 10^{-3}$, $\beta = 2.3462 \times 10^{-5}$. After collecting gravity data, the **latitudinal correction** is one of

the reductions that needs to be applied routinely to correct for the variation of g with latitude.

A **gravity anomaly** is defined as the deviation of the gravitational acceleration from that predicted by the reference formula for any given latitude:

$$\Delta g = g - g_0(\lambda) \quad (14.16)$$

14.3.2 The geoid

Even though the Earth's shape can be approximated roughly by an oblate spheroid, its real shape is of course much more complicated (Fig. 14.5).

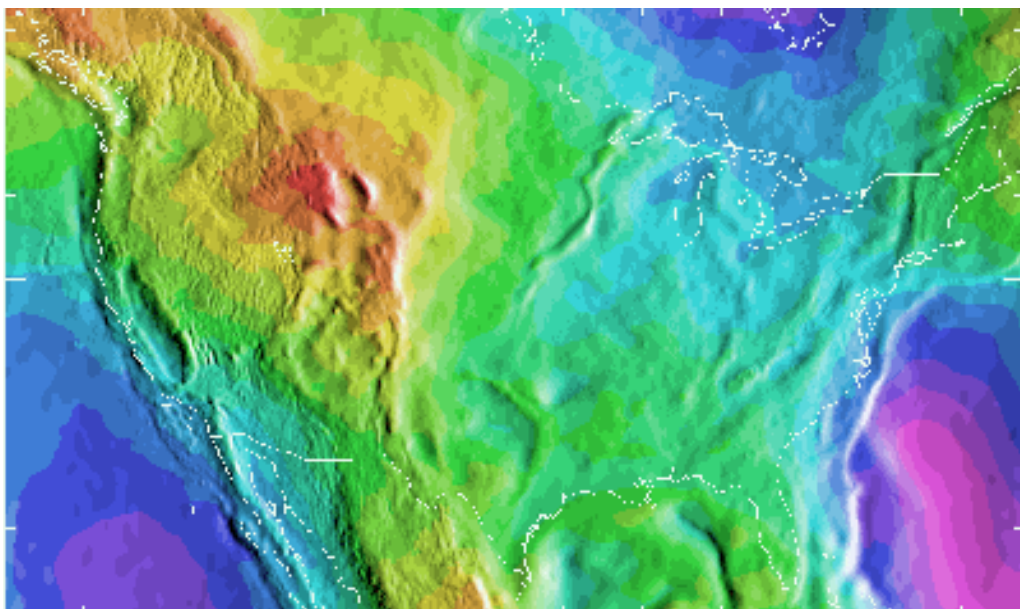


Figure 14.5: The Geoid across North America

Geodesists use the oceans as the reference surface, because a liquid surface is necessarily an equipotential surface. The equipotential is defined as a surface over which the potential has a constant value, i.e. the gradient of the potential is normal to this surface everywhere. Hence the gradient of the Earth's gravity field is normal to the mean sea level surface. This reference surface is called the **geoid**, which is defined by its height ΔN relative to the reference spheroid.

Over the continents, the geoid can be imagined by the level at which water would be if deep enough trenches were dug. A local mass excess causes both an outward warp of the geoid, i.e. a positive ΔN , and an addition to the potential, i.e. ΔU , while a mass deficiency causes ΔN and ΔU to be negative. This is expressed by **Brunhes formula**:

$$\Delta U = -g_0 \Delta N \quad (14.17)$$

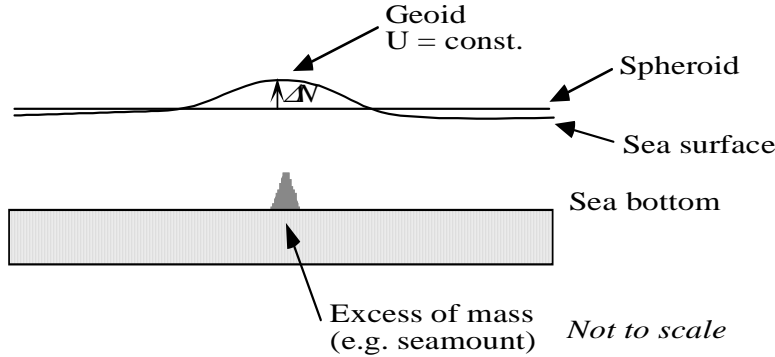


Figure 14.6: How underwater masses affect the geoid (and therefore the observed sea surface)

The relation between the **anomaly in the potential of the gravity field** ΔU , given as a measured value U_{obs} with respect to the potential at the **reference spheroid** U_0 , and the geoid anomaly ΔN can be derived as follows:

$$\Delta U = U_{obs} - U_0 \quad (14.18)$$

The radial derivative (gradient) of the potential is

$$\frac{\delta U}{\delta r} = -g_0 \quad (14.19)$$

Combining the last two equations we obtain

$$U_0 = U_{obs} + \left(\frac{\delta U}{\delta r}\right) \Delta N = U_{obs} + g_0 \Delta N \quad (14.20)$$

Hence a local **mass excess** produces an **outwarp of gravity equipotentials**, a **positive geoid anomaly** ΔN , and a **negative anomaly in the potential of the gravity field** ΔU .

How do we express the gravity anomaly measured on the geoid? The gravity anomaly Dg at sea level has its origin in two sources: one is the attraction of the anomalous mass, which can be expressed as the gradient of the anomalous observed potential:

$$\frac{\delta U_{obs}}{\delta r} = -g_{obs} \quad (14.21)$$

The second effect is the geoid height ΔN , as g_{obs} is observed on the geoid, whereas g_0 measures the anomalous gravitational acceleration on the reference spheroid. In other words, we have to express the effect of the geoid height ΔN on Δg . The effect of distance from the center of a spherical Earth on gravitational acceleration can be written as:

$$-g = \frac{GM_e}{r^2} \quad (14.22)$$

(see beginning of gravity chapter for comparison). It follows that

$$\frac{\delta g}{\delta r} = \frac{2GM_e}{r^3} = -\frac{2g}{r} \quad (14.23)$$

This is also called the free-air gravity effect, and describes the gravity gradient with height. If we combine this result with Brunhes formula, we can express the effect of the height as

$$-\frac{2g_0}{r}N = \frac{2U}{r}. \quad (14.24)$$

Now we can write the gravity anomaly Δg as a function of (1) the gradient of the anomalous potential and (2) the effect of elevation ΔN above the reference spheroid:

$$\Delta g = -\frac{\delta U}{\delta r} - \frac{2U}{r} = \frac{\delta U}{\delta r} - \frac{2g_0}{r}\Delta N \quad (14.25)$$

Note that geoid anomalies drop off with $1/r$ with increasing distance from a disturbing potential, while gravity anomalies drop off with $1/r^2$. This is because the gravity anomalies are defined by the gradient of the potential field. In other words, gravity anomalies enhance short wavelengths with respect to geoid anomalies (like any difference filter), but their amplitudes will diminish more quickly with increasing radius.

14.3.3 Spherical harmonics of the Earth's gravity field

It is convenient to be able to express the actual shape of the geoid in a concise way (as opposed to storing a vast array of numbers on the computer which define the height of a model geoid). This is done by using a **spherical harmonic expansion** of the geoid.

The solution of Laplace's equation

$$\nabla^2 U = \frac{\delta^2 U}{\delta x^2} + \frac{\delta^2 U}{\delta y^2} + \frac{\delta^2 U}{\delta z^2} = 0 \quad (14.26)$$

for a 3-dimensional function of the potential field of the Earth is achieved by using a large number of summed up sine and cosine components to describe the variations of the global gravity field (similar to Fourier transform representation of any time series in x-y coordinates). The sine and cosine components are of the form of

$$ce^{i(k_x x + k_y y + k_z z)} \quad (14.27)$$

where

$$k_x^2 + k_y^2 + k_z^2 = 0 \quad (14.28)$$

k_x , k_y , and k_z are spatial frequencies (or wave numbers), i.e. $2\pi/\text{wavelength}$.

If we write Laplace's equation in spherical polar coordinates, we obtain:

$$\frac{1}{r^2} \frac{\delta}{\delta r} (r^2 \frac{\delta U}{\delta r}) + \frac{1}{r^2 \sin \theta} \frac{\delta}{\delta \theta} (\sin \theta \frac{\delta U}{\delta \theta}) + \frac{1}{r^2 \sin^2 \phi} \frac{\delta^2 U}{\delta \phi^2} = 0 \quad (14.29)$$

Here θ and ϕ are the colatitude and the longitude, respectively, and r is the radius of the Earth. In order to express a particular function using spherical surface harmonics (again conceptually similar to expressing a time series by using Fourier harmonic coefficients of sinusoids), we can write:

$$f(\theta, \phi) = \sum_{l=0}^{\infty} [A_l P_{l,0}(\theta) + \sum_{m=1}^l (A_l^m \cos m\phi + B_l^m \sin m\phi) P_l^m(\theta)] \quad (14.30)$$

A and B are constants which are usually evaluated by computer; l, m are integers which denote the **degree** and **order** of a particular part of the model, and P_l^m are **associated Legendre functions**, which are related to Legendre polynomials.

Figure 14.7 shows Legendre's polynomials as functions of $t = \cos \theta$. In the top figure, $n=\text{even}$, in the bottom figure $n=\text{odd}$.

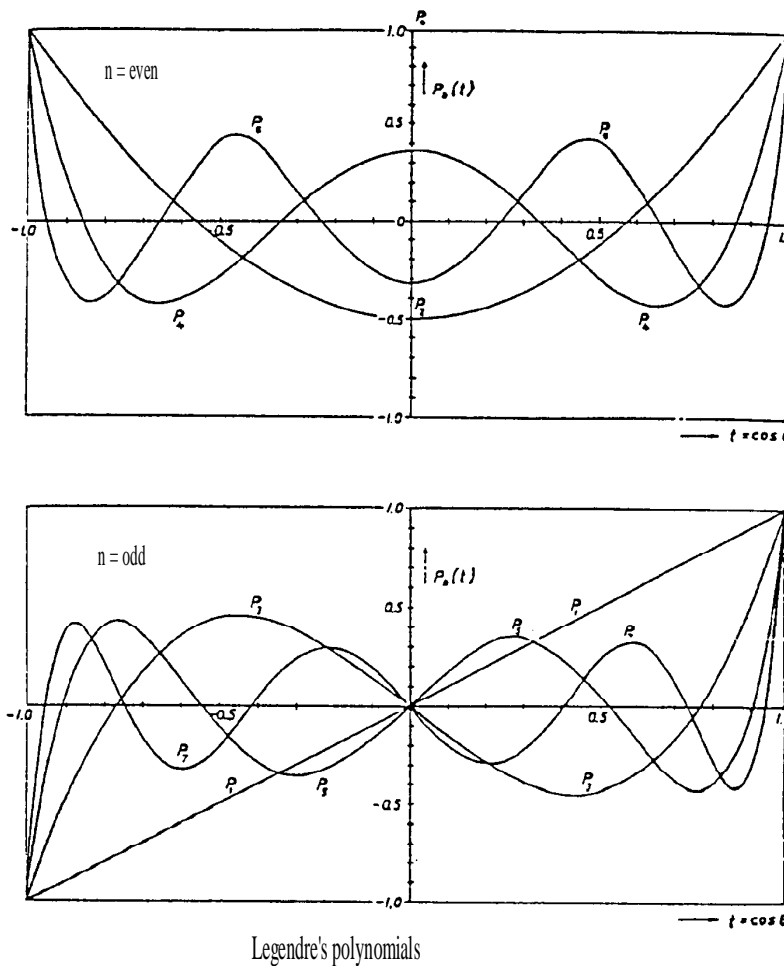


Figure 14.7: Legendre polynomials

The maximum degree of surface spherical harmonics is about 40. Degree 0 describes the longest wavelength component, i.e. 40,000 km, the circumference of the Earth. The order ranges from $0-l$. If $m = 0$, there is no dependence on longitude, and the dependence on latitude is given by the Legendre polynomials and called a **zonal harmonic**. If $l = m$, it depends only on longitude, and is called a **sectorial harmonic**. If $0 < m < l$, the harmonics depend both on latitude and on longitude and called a **tesseral harmonic**. Tessera means a square or a rectangle, or also a tile. Figure 14.8 illustrates examples for zonal, sectorial, and tesseral harmonics.

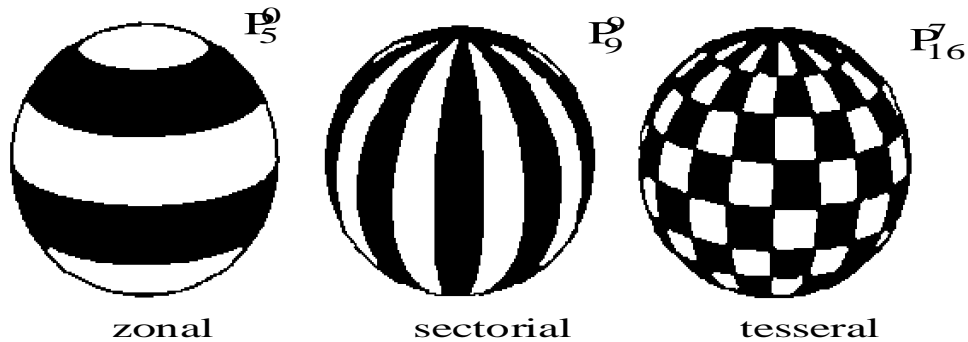


Figure 14.8: Zonal, sectorial and tesseral harmonics

14.4 Relative gravity measurements

(Refs: Nabighian et al, 2005; Fairhead and Odegard, 2002) Geophysicists are predominantly interested in relative gravity measurements, as opposed to the absolute value of the Earth's gravity field. Instruments to measure relative changes in the gravity field from one place to another are simpler, smaller, cheaper and quicker to use than instruments to measure the absolute value precisely. The various types of gravity meter are described by Nabighian et al (2005) - widely used types throughout the 20th Century were the pendulum, the free-fall gravimeter, the torsion-balance gravity gradiometer, the spring gravimeter, the vibrating-string gravimeter, and the rotating-disk gravity gradiometer.

The **units** used in gravity measurements are:

$$1 \text{ gal} = 1 \text{ cm/s}^2 = 10^{-2} \text{ m/s}^2 \text{ (cgs unit)}$$

$$1 \text{ mgal} = 10^{-3} \text{ cm/s}^2 = 10^{-5} \text{ m/s}^2 \text{ (cgs unit)}$$

$$1 \text{ gu} = 10^{-6} \text{ m/s}^2 \text{ (SI unit (gu = gravity unit))}$$

14.4.1 Typical processing flow

Processing of gravity observations at a station requires knowledge of the measurement time, the meter constant, the drift rate and characteristics, the absolute gravity value at a

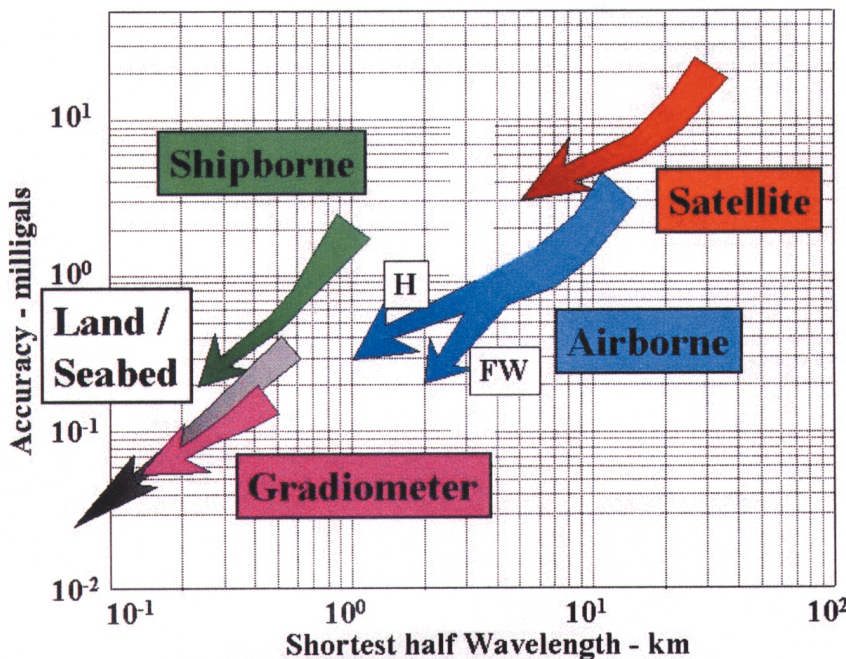


Figure 1. Time-trend log-log plot of gravity “best possible” resolution of survey systems (arrow points represent current claims). FW = fixed wing. H = helicopter.

Figure 14.9: Resolution of gravity data acquired from different acquisition methods, and the improvement over time

base station when relative gravimeters are used, and precise measurement of the station location (longitude, latitude and height) (Nabighian et al, 2005). Corrections need to be made to account for instrument drift, and the small but measurable (0.2 mGal) effect of Tidal variations (caused by the gravitational attraction of the moon). Relative gravity variations need to be tied to existing base stations where the absolute gravity is known, so that the data can be integrated with existing data sets. Depending on the type of survey, corrections may need to be applied for the motion of the measurement platform, or for the effect of terrain around the measurement points.

14.4.2 Ship gravity measurements

Vening Meinesz (1929) first introduced gravity measurements from sea vessels. Most of his work was on submarines, utilizing a modified pendulum instrument that he designed himself. When measuring gravity from a moving vehicle, the observer is moving relative to the Earth, and experiences a centripetal acceleration different from a

stationary position on the Earth. Hence there is a difference in gravitational acceleration g as well. The change in the observer's angular velocity due to an east-west velocity component v with respect to the angular velocity of the Earth ω can be written as $d\omega$. Then the change in acceleration is

$$da = 2r\omega d\omega = 2\omega v \quad (14.31)$$

Here r is the distance from the axis. At geocentric latitude l , the effect on the gravitational acceleration is:

$$dg = da \cos \lambda \quad (14.32)$$

This is known as the **Eötvös effect**. In middle latitudes, an east-west velocity of about 1.5 km/h corresponds to a change in g of 5 mgals. When collecting gravity data on a ship, the course and velocity of the ship is used to correct for this effect. This correction has become more straightforward since the onset of navigation by means of the **Global Positioning System** (GPS), which allows the determination of the course and speed of a ship more accurately than before.

The Global Positioning System consists of a group of satellites that were put into orbit around the Earth by the USA for military purposes. By addition of a sinusoidal signal the GPS quality is degraded for civilian usage. This sinusoidal signal varies in period and amplitude. The period is less than 20 minutes, and the amplitudes tend to vary over 24 hours and the sea state condition. This degrading results in an uncertainty of about 200 m in real-time navigation and may introduce errors of 4-6 mGals in the Eötvös correction (*Bill Robinson, pers. com., 1996*). As this problem varies in its intensity depending on the sea state and GPS data quality itself, several methods of smoothing are applied depending on the quality of the raw GPS navigation data, e.g. 4 min. – 20 min. smoothing. However, after GPS navigation data smoothing, turns in the ship's heading become "smeared out", which also results in an error in the Eötvös correction. Consequently 40-60 minutes of data centered on a ship's turning point are edited out of the gravity data. The final, corrected free-air anomaly is accurate to about 1 mGal.

The measurements by ship gravity meters also display instrument drift, which has to be corrected for (e.g. *Wessel and Watts, 1988*). This is done by tying the gravity measurements to base stations on land in the ports of call, and comparing these readings with the ship's gravity meter. If instrument drift is observed, linear drift between two gravity stations is assumed to correct the data. Collecting gravity data by ship has lost some of its significance, since satellite altimetry has been used very successfully to map the marine geoid, which in turn has been utilized to compute marine gravity anomalies down to wavelengths of about 20 km.

Below we show an example of gravity data collected in 1996 on the R.V. Maurice Ewing in the Tasman Sea. The profile shown is about 300 km long, and extends from the southeastern South Tasman Rise down the continental slope to Australian-Antarctic ocean crust. The figure shows (1) the east- and north- velocity components of the ship's velocity from the navigation data based on GPS, (2) the Eötvös correction based on

(1), (3) the observed gravity anomalies, (4) the free-air gravity anomalies obtained by applying the Eötvös correction to the observed field, (5) the observed bathymetry.

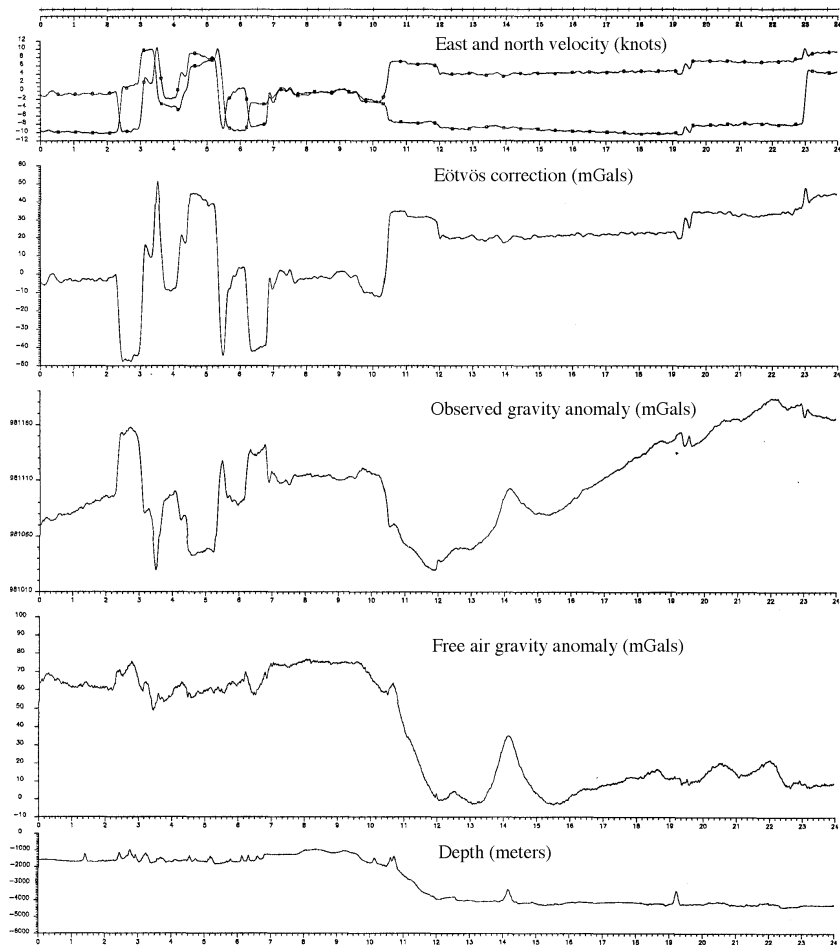


Figure 14.10: Example of profile observations from a marine gravity survey

14.4.3 Land measurements

The majority of the Earth's landmasses are now well covered by land-based gravity measurements. In easily accessible areas, gravity measurements can be acquired on regular grids. In less accessible areas, gravity stations are often located along existing roads or rivers. Acquisition of gravity data on land faces different challenges to the marine environment. The measurements are not typically taken on a moving platform, so the Eotvos correction described for seaborne measurement can be ignored. On the other hand, for measurements taken in areas of rugged terrain we need to introduce a

‘terrain correction’. Consider a gravity station located on a steep hillside - the excess of mass located above the gravity meter towards the hilltop tends to pull up on the meter and decrease the observed gravity; likewise, the ‘missing’ mass to the downslope side will also contribute to a decrease in the observed gravity. Hence, terrain corrections on land are always positive, and can have magnitudes exceeding 30 mGal. Corrections for the terrain effect can be made using detailed observations of the topography around the station, and using digital terrain models.

14.4.4 Airborne Gravity Measurements and Gravity gradiometry

Airborne gravity acquisition is similar in many ways to marine acquisition, facing the same issues of making gravity measurements on a moving platform. Eotvos corrections are much larger for instruments carried on fixed-wing aircraft, since the velocity of the platform is higher. In the same way that rough seas degrade the quality of marine gravity data, one of the limiting factors on the resolution of airborne gravity measurements is turbulence. Flying higher above the ground helps to avoid turbulent air, but the trade-off is a reduction in the level of detail in the measured data. A growth area within hydrocarbon and minerals exploration in the last two decades is the acquisition of airborne gravity gradiometry. The idea of a gradiometer is to measure the rate of change of the gravity field in the horizontal and vertical directions rather than just the strength of the field itself. Gradiometry systems have some important advantages over more conventional gravity instruments - in particular, they are less sensitive to turbulence on moving platforms, and yield data with higher signal to noise ratio at short spatial wavelengths. A noteworthy example from an Australian perspective is the Falcon system developed by BHP (REF).

14.4.5 Satellite force models

The path of a satellite is governed by motion in the presence of the gravity field of the Earth. Hence the position of a satellite can be expressed as an integral of all applied forces. The first use of artificial Earth satellites for determining the Earth’s gravity field started soon after the first vehicles were launched in the 1950s. The greatest improvements in the determination of the gross features of the Earth’s shape came from observations of perturbations to the orbit of the satellites due to the asymmetries of the Earth’s gravity field. The first geodetic parameters to benefit were the shape of anomalies which are symmetric about the rotational axis. The flattening of the Earth produces a force on the satellite in the direction of the equatorial plane. This force causes a slow precession of the satellite’s orbit.

The effect on the orbit of the satellite is cumulative, and observation of the precession over many orbits allows very accurate determination of the long-wavelength **zonal spherical harmonics** of the gravity field. In the 1960s spherical harmonic expansion solutions for the gravity field down to resolutions of 5° (≈ 550 km) were made using both surface gravity and orbital data, because orbital data alone did not resolve short wavelengths to that wavelength.

14.4.6 Sea surface altimetry

A local perturbation or “bump” in the gravity field causes the satellite to speed up as it enters the area of the bump and to slow down as it leaves it. These types of bumps correspond to **tesseral harmonics**, which we have encountered above. They do not result in drift of the satellite’s orbit. Mapping of this type of anomalies requires very accurate tracking of the satellites and errors increase as the size of the feature becomes smaller.

More recently, quite detailed satellite observations have been obtained from **radar altimetry**. Radar altimeters measure the distance between themselves and the sea surface, thus mapping the geoid (after correction for noise due to temporal changes of the sea surface). Figure 14.11 shows a schematic relation between observed height h_0 , geoid height N , sea-surface height Δh_s , and the satellite height H above the reference ellipsoid.

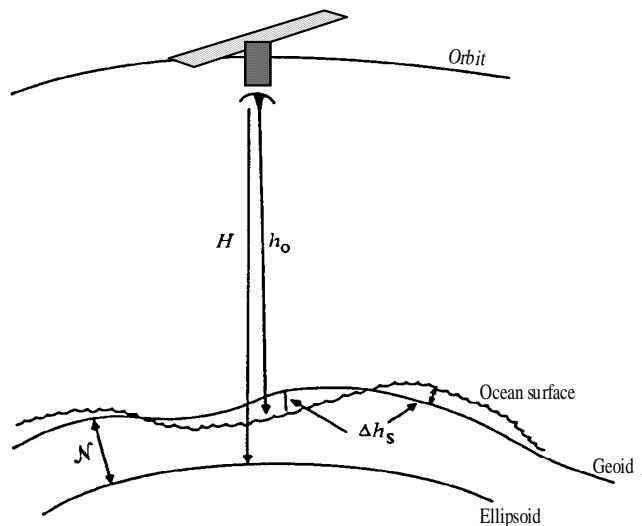


Figure 14.11: Satellite altimetry measures the height of the sea surface, from which we can derive estimates of the geoid and gravity field

The ellipsoid is the reference surface. The measurement of highest geodetic interest in N , the geoid height. The sea surface departs from this by the sea surface dynamic height, Δh_s . Over the Earth, N ranges up to about 200 meters, while Δh_s is 1-2 meters.

The first satellites which provided extensive data sets were the GEOS3 (launched in 1975) and SEASAT (1987) vehicles. The GEOSAT (1985) has operated in two different modes. The Exact Repeat mode duplicates its orbit path to look for variations in sea surface height and does not produce closely spaced tracks. The data from this mission is mostly useful for physical oceanographers, who are interested in investigating the variation in sea level function through time.

During the following Geodetic Repeat Mission the satellite was put into a drifting orbit. Hence a closely spaced net of tracks was produced. All the data from this mission were released in 1995, and have provided a detailed picture of ocean floor short-wavelength gravity anomalies (Smith and Sandwell, 1995).

The radar in these satellites operates at a frequency of about 15 Ghz and has a beamwidth of about 1° . The satellite orbit is about 100 km above the Earth's surface so that the "footprint" is 1-2 km. Uncertainties in time and along-track averaging increase the footprint size to about 5×7 km. The following two figures show a GEOS3 profile over the Tasman Sea to the New Hebrides Trench.

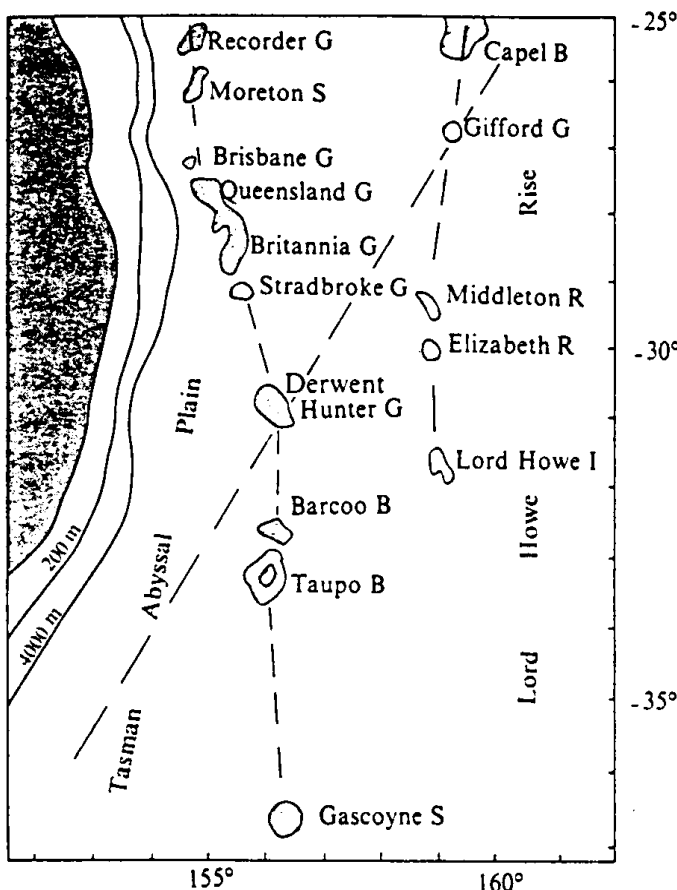


Figure 14.12: Satellite track across the Tasman Sea

This schematic map (Fig. 14.12) of the Tasman Sea south of 25°S shows a ground track of a GEOS-3 altimeter pass (SW-NE trending dashed line). The along-track profile is shown on figure 14.13. (G=guyot, S=seamount, B=bank, R=reef, I=island).

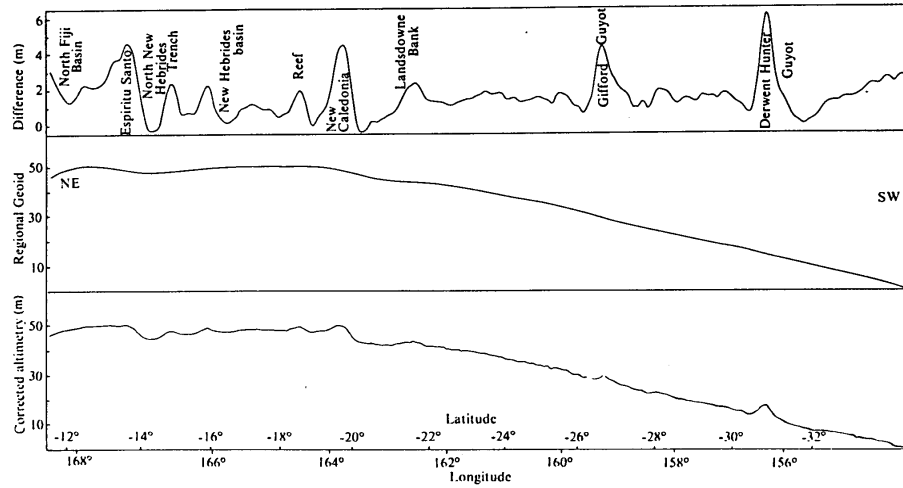


Figure 14.13: Sea surface height, regional and residual geoid for satellite track across the Tasman Sea

In figure 14.13, the lowermost curve is the observed variation in satellite height, and the middle curve is the regional geoid anomaly computed from all GEOS3 and SEASAT data for the region. The upper curve is the residual geoid anomaly.

14.5 Gravity anomaly reductions

14.5.1 Free-air correction

After measuring gravity anomalies, a number of corrections need to be applied. The free-air correction includes a correction for the change of gravity with latitude, and with elevation (both formulas given above). The term “free-air” derives from the assumption that the material between sea level and the measurement point is air. The free-air correction involves calculating the change in g with altitude above sea level. The free-air anomaly g_{FA} can be written as the observed gravity anomaly g_{obs} with the latitude and the free-air corrections applied

$$g_{FA} = g_{obs} - g_o(\lambda) + \Delta g \quad (14.33)$$

where

$$\Delta g_{FA} = g_e - g(h) = \frac{2h}{R} = g \quad (14.34)$$

and h is the elevation of the measuring point. The correction with elevation is about -0.3 mgal/m.

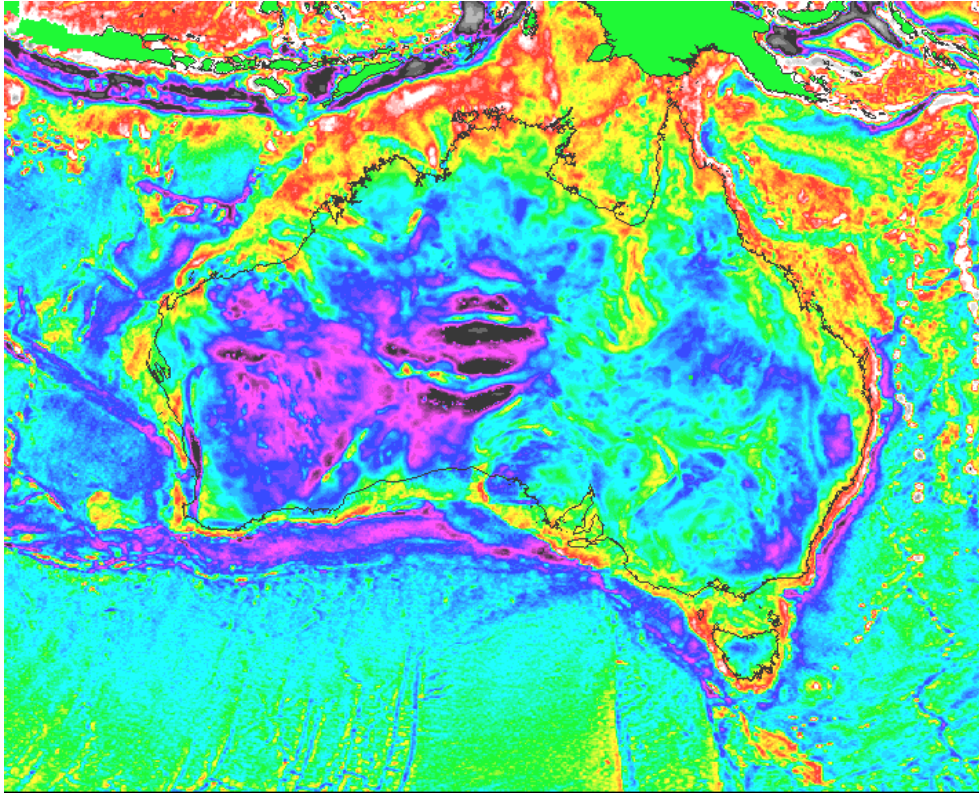


Figure 14.14: Free-air gravity anomalies of the Australian Plate

14.5.2 Bouguer correction

The Bouguer gravity correction relates the surface gravity anomaly at a point to the mass excess or deficiency beneath that point, i.e. the gravity anomaly due to topography, assuming that it is of infinite horizontal extent. In order to understand this correction, let's first look at the gravitational attraction of a sheet, whose height is small relative to its horizontal extent so that we approximate it by a flat sheet of mass with excess density $\Delta\rho$ as shown below:

Here α is the solid angle subtended by the sheet. In this case the gravitational attraction due to the sheet is given by

$$\Delta g = G\Delta\rho\alpha \quad (14.35)$$

If the horizontal extent of the sheet is very large, then

$$\Delta g = 2\pi G\Delta\rho \quad (14.36)$$

independent of the distance of the observer from the sheet, since the solid angle α approaches 2π in this case:

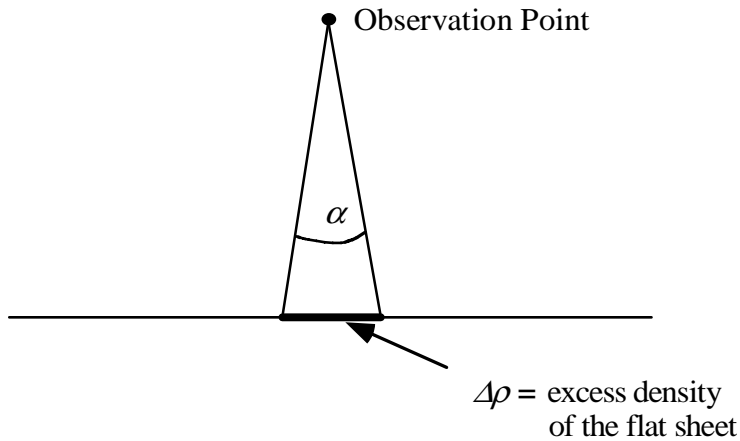


Figure 14.15: Understanding the Bouguer slab formula - part 1



Figure 14.16: Understanding the Bouguer slab formula - part 2

Bouguer (1749) suggested that an infinite horizontal slab of thickness h and excess volume density $\Delta\rho$ may therefore be replaced by a number of sheets of excess surface density $\Delta\rho\Delta h$, so that the gravitational attraction of the infinite sheet can be written as

$$\Delta g_B = 2\pi G \Delta\rho \quad (14.37)$$

which is the **Bouguer** formula, whose application results in a **simple Bouguer anomaly**. We use this method to remove the gravitational attraction of a layer of topography, if the assumption is warranted that the extent of the layer is large with respect to its thickness, and that there are no large gradients in topography. Since the slab of topography is assumed to be infinite, the measured g is the same no matter how far away from the slab it is measured.

Assuming a crustal density of $\rho_c = 2670 \text{ kg/m}^{-3}$, the gravity anomaly for each kilometre of elevation is $\Delta g = 1.12 \text{ mm s}^{-2}$. After removing the effect of the topography, the Bouguer anomaly of large scale topography (i.e. mountain ranges) essentially mirrors the topography with a negative sign, reflecting low-density roots due to isostatic compensation.

The attraction of three-dimensional anomalous bodies can be computed by dividing the bodies into plane sheets, and approximating each sheet by polygons (Talwani and Ewing, 1960). If gravity is measured in rough terrain with large elevation changes

nearby (i.e. mountainous terrain), another correction has to be made for the gravitational attraction of the topography near each gravity station. This is called the **terrain correction**. Application of the terrain correction results in a **complete Bouguer anomaly**.

Today digital elevation models are often used to calculate the gravitational attraction of the topography, both on land and at sea. In the oceans this is only straightforward in the absence of a thick sediment layer (i.e. near mid-ocean ridges) and if the bathymetry has been mapped in two dimensions by a multibeam system. Where sediments are present, the thickness and density of the sediments must be known to remove the effect of the sediment blanket and of the oceanic crustal basement separately.

Both for oceanic and continental crust, topographic features of very short wavelengths (tens of km) are always supported by the crust and cannot be locally compensated. Hence such features always have Bouguer anomalies that are zero, because these features have no crustal roots. For very long wavelength topography, the opposite is the case, i.e. the free-air anomalies go to zero (because of isostatic equilibrium), and if we subtract the gravity effect of the topography to compute the Bouguer anomaly, we end up with a negative image of the topography as Bouguer anomaly, which reflects the crustal roots of the topography.

14.5.3 Isostatic anomaly

This correction removes the gravity anomaly associated with a model for a low-density root of an isostatically compensated crustal body. In other words, this correction removes a negative Bouguer anomaly. The result is called an isostatic residual anomaly, i.e. the Bouguer anomaly minus the expected gravity anomaly of a 'root'. The result of the isostatic correction depends on which model we assume for isostatic compensation. We will examine isostatic gravity anomalies later.

isostatic compensation is local, where in reality we have to treat the lithosphere as an elastic sheet, i.e. local mass anomalies are compensated regionally. The area affected by plate flexure given a particular load depends on the elastic plate thickness. How do we model this added complexity?

14.5.4 Contouring and Gridding of Point Data

Gravity measurements are acquired at discrete points, often with an irregular distribution (e.g. along marine/airborne survey lines, roads, rivers). To produce a continuous map of the anomalous gravity field, we need to interpolate the data onto a regular grid. A commonly used method for interpolating potential field data is the minimum curvature method (Briggs, 1974), which estimates the smoothest possible surface that passes through all the available data points. Li and Gotze (1999) provide a comparison between this and other gridding techniques.

14.6 Gravity Modelling

14.6.1 Gravity anomaly of a sphere

The modeling of gravity anomalies given a density structure for a body falls in the category of **forward modeling**. Inverse modeling is referred to as the opposite case, i.e. given a gravity anomaly, calculate the source structure. The inverse problem is always non-unique, because there are an infinite number of density distributions which produce may result in the same gravity anomaly. Before we investigate the possibilities of inverse modeling, we will first look at some basic cases of forward modeling.

First we will look briefly at the calculation of the gravity anomaly due to a sphere.

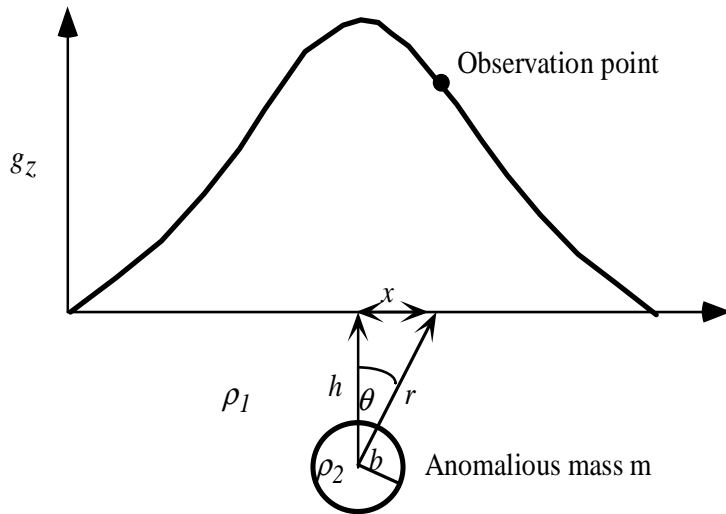


Figure 14.17: Gravity anomaly due to a sphere

The density contrast between the sphere and the surrounding mass is

$$\Delta\rho = \rho_1 - \rho_2 \quad (14.38)$$

The radial gravitational acceleration g caused by a sphere of mass m is

$$-g = Gm/r^2 \quad (14.39)$$

In order to compute the gravity anomaly at a particular height above the source, we must calculate the vertical component of g :

$$-g_z = g \cos\theta = \frac{Gm}{r^2} \cos\theta = \frac{Gm}{r^2} \frac{h}{r} = \frac{Gmh}{(x^2 + h^2)^{3/2}} \quad (14.40)$$

As a result, the gravity anomaly Δg_z is

$$\Delta g_z = -\frac{G \Delta \rho \frac{4}{3} \pi b^3 h}{(x^2 + h^2)^{3/2}} \quad (14.41)$$

The function given by g_z is a type of Green's function to compute the gravity anomaly from a mass anomaly at depth h . For mass anomalies of different shapes, different Green's functions can be derived.

Equivalently we can calculate the gravity anomaly resulting from an anomalous mass of other shapes. The next figure shows an example for a gravity anomaly of a diamond shaped body, as well as equivalent bodies of different aspect ratios which result in the same gravity anomaly. This example demonstrates well the non-uniqueness of gravity modelling. Without additional data it is not straightforward to distinguish between a smaller, deeper anomalous mass versus a broader, shallower body.

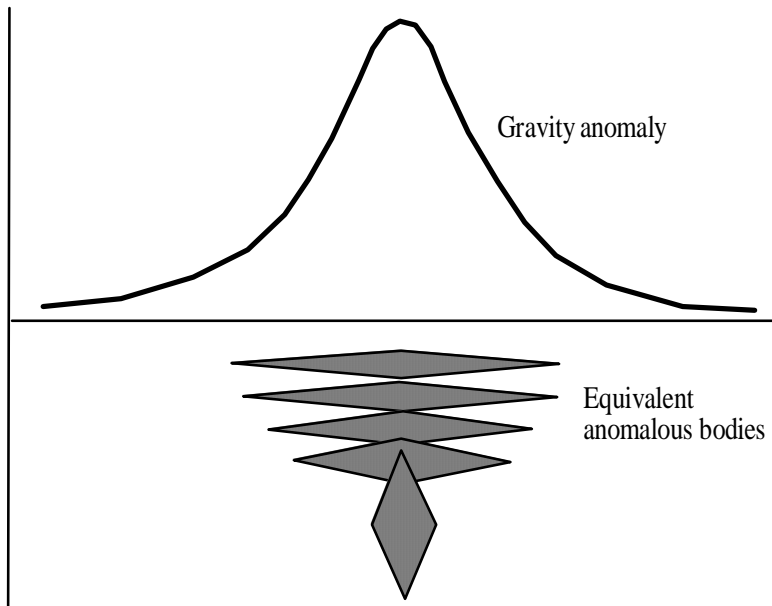


Figure 14.18: Nonuniqueness of gravity anomalies - Gravity anomalies due to different density distributions cause an observed anomaly with the same shape

14.6.2 Gravity anomaly of a periodic mass distribution

The Bouguer correction discussed earlier is only valid if the topographic layer extends to infinity, or in other words, if the observer's height above the mass layer is small compared with the layer thickness and its horizontal variation. Eventually, we will discuss how we can calculate the Bouguer anomaly of any layer with arbitrary horizontal variations in thickness (complete Bouguer correction). In order to understand how this is accomplished, we will first consider the gravity field of an infinitely wide and long

layer (in x and z directions), whose thickness in the y -direction is negligible, and whose surface density and mass varies periodically and is bounded in the x -direction by a topographic surface with height

$$h = h_0 \sin \frac{2\pi x}{\lambda} \quad (14.42)$$

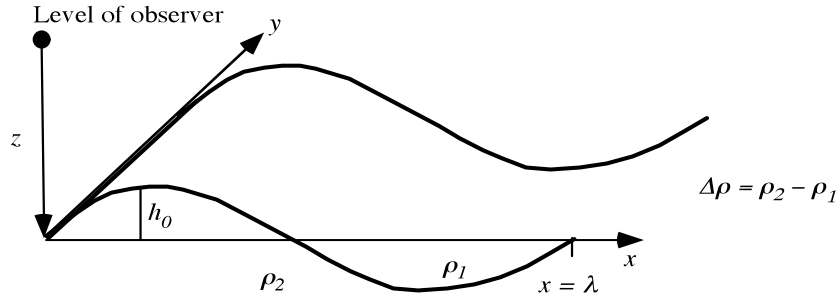


Figure 14.19: Gravity field of a periodic mass distribution

h_0 = the amplitude of the periodic topographic surface variation

λ = wavelength

$\Delta\rho$ = density contrast

Just above the surface layer, at $z = 0+$, the vertical component of g is given by the Bouguer formula

$$g_z = 2\pi\Delta\rho G h_0 \sin \frac{2\pi x}{\lambda} \quad (14.43)$$

The question we would like to answer is: How does g_z depend on z , or what is the gravity anomaly at different heights above this undulating surface? It can be shown (see Turcotte and Schubert, 1982) that the solution is

$$g_z = 2\pi\Delta\rho G h_0 \sin \frac{2\pi x}{\lambda} e^{-2\pi z} \quad (14.44)$$

The gravity anomaly decays exponentially with distance from the mass layer. The length scale for the decay is $\lambda/2\pi$. This equation provides the fundamentals for the upward or downward continuation of gravity anomalies measured at any level above a mass anomaly.

Any function can be Fourier-decomposed into periodic contributions of different wavelengths. Hence the equation above for g_z provides the basics for computing gravity anomalies due to an anomalous layer of arbitrary shape. This problem was solved by Parker (1972).

14.6.3 The gravity anomaly of a layer of arbitrary topography

Parker (1972) derived an expression in the Fourier domain for the gravity effect of a density contrast $\Delta\rho$ with a varying elevation $h(x)$:

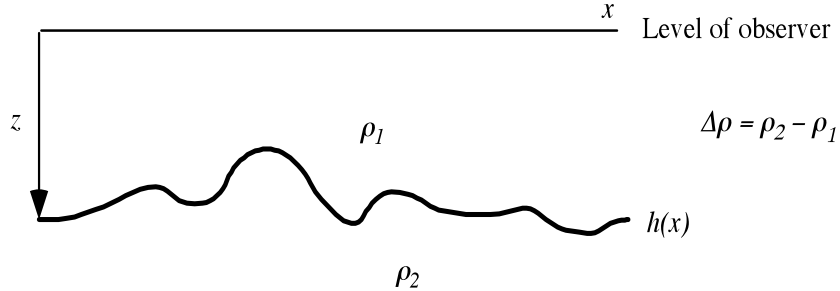


Figure 14.20: Gravity field measured over a topographic surface

The Fourier transform of the gravitational attraction $g(x)$ of the surface $h(x)$ defining a density contrast can be expressed as:

$$G(k) = 2\pi G \Delta\rho e^{-|k|z} \sum_{n=1}^{\infty} \frac{|k|^{n-1}}{n!} F[(h(x))^n] \quad (14.45)$$

Here $G(k)$ is the Fourier transform of the gravity anomaly $g(x)$, G is Newton's gravitational constant, k is the wavenumber $2\pi/\lambda$, where λ is a wavelength, $F()$ indicates a Fourier transform, and z is the mean depth to the density contrast (positive downward). It is usually sufficient to take four terms in the series.

14.6.3.1 Isostatic compensation

A mass anomaly (such as a mountain) is said to be isostatically compensated if it is supported by the buoyancy of a mass anomaly of opposite sign rather than by elastic stresses. The observation that long-wavelength free-air gravity anomalies are small implies that large-scale topography must be isostatically compensated.

14.6.4 Airy model

There are two models for isostatic compensation. The first one is called the Airy model. It assumes hydrostatic equilibrium (i.e. floating iceberg model) which implies that regions with high elevation have a low-density root, whose depth depends on the density and the thickness of the body (e.g. thickness of the crust), as shown by the following sketch

$$\rho_m b = \rho_c b + \rho_c h \quad (14.46)$$

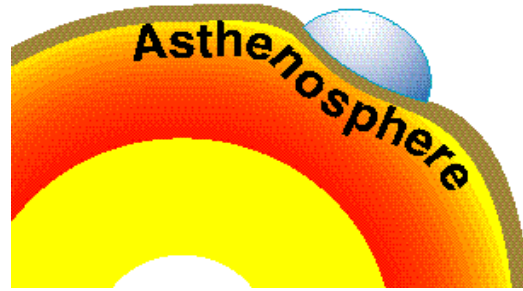


Figure 14.21: Isostatic compensation of surface loads

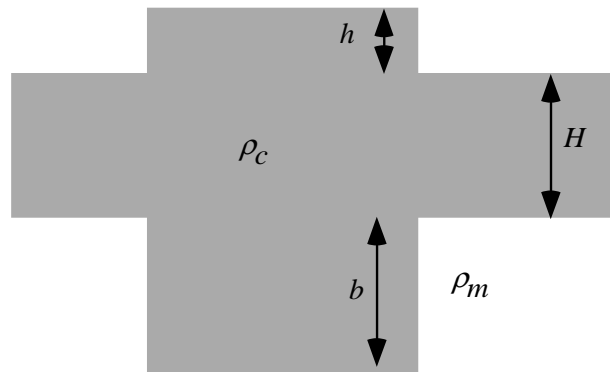


Figure 14.22: The Airy model of isostatic compensation

14.6.5 Pratt model

This model assumes that topography is compensated at the same depth for regions with different elevations. Isostatic compensation is achieved by varying densities in the layer.

$$\rho_2(H + h) = \rho_1 h \quad (14.47)$$

14.6.6 Isostatic gravity anomalies

What do gravity anomalies over isostatically compensated regions look like? Isostasy implies that the average density of all crustal columns is the same.

Does that mean that the free-air gravity anomaly is zero? Well, it doesn't, and we can actually use the gravity anomaly to obtain an estimate for the depth of compensation. Consider the simplified model in figure 14.25 of two layers representing the top and the bottom of an isostatically compensated crustal column:

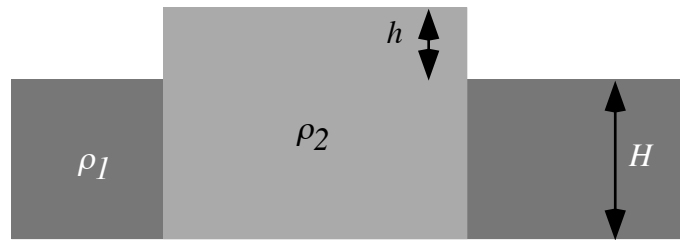


Figure 14.23: The Pratt model of isostatic compensation

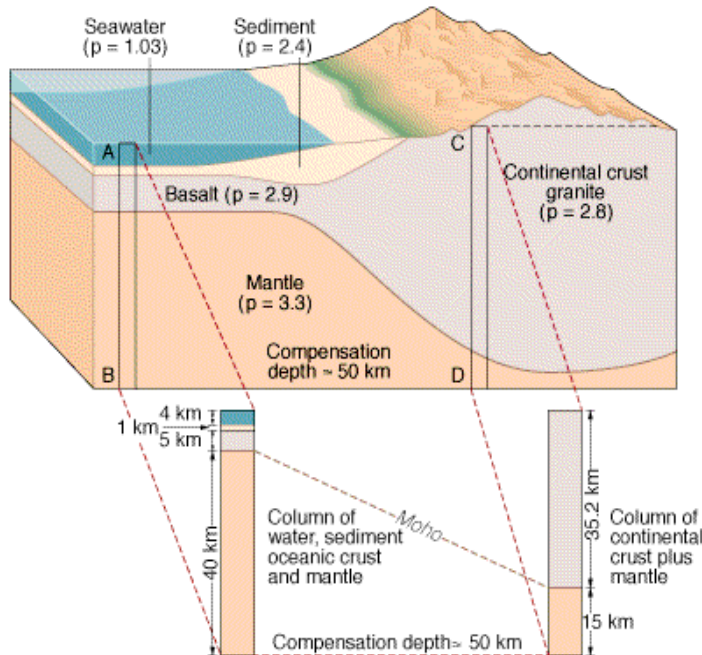


Figure 14.24: Isostasy: The average density of all crustal columns above a depth of compensation is the same.

Here we have made the assumption of local isostatic compensation, where the compensating mass is forced to be a negative image of the topography. Reality does not conform to this model, since the density contrasts at the upper and lower bounding surfaces of a given layer are usually not the same. For example, continental crust with a density of $\rho_c = 2600 \text{ kgm}^{-3}$ is overlain by air with a density close to zero, and underlain by mantle with a density of 3300 kgm^{-3} . Hence the density difference (the quantity which determines the amplitude of the gravity anomaly due to a layer surface) is $\Delta\rho = 2600 \text{ kgm}^{-3}$ for the upper bounding surface of the topography, and $\Delta\rho = 900 \text{ kgm}^{-3}$ for the lower bounding crustal surface (i.e. the Moho). This is the reason why Airy isostatically compensated mass has a much larger amplitude bottom topography

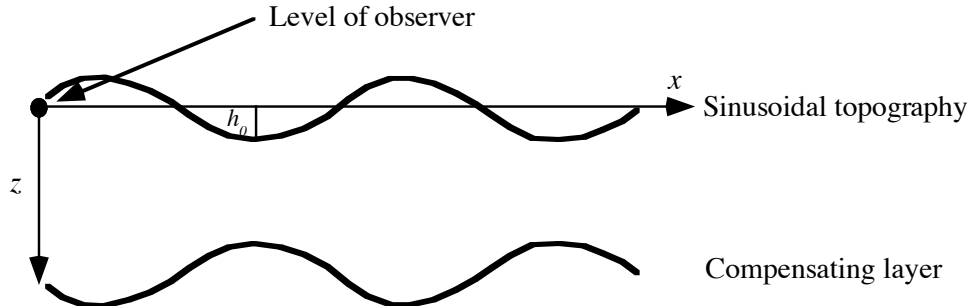


Figure 14.25: Isostasy: a simple two layer case

than surface topography (mountain chains have roots several times deeper than their surface topography).

To understand the concept of isostatic gravity anomalies, it is convenient to follow the simple model of sinusoidal topography pictured above, whose root is a negative image of the surface topography (implying that the density contrast $\Delta\rho$ is identical at both surfaces). We consider the one-dimensional harmonic components one at a time, i.e. sinusoidal topography with spatial wavelength $\lambda_1 = 2\pi/k_1$.

$$h(x) = h_0 e^{ik_1 x} \quad (14.48)$$

Following our analysis of the gravity field of sinusoidal topography above, the gravitational attraction of the sinusoidal topography can be expressed as

$$g_{topo}(x) = 2\pi\Delta\rho G h_0 e^{ik_1 x} \quad (14.49)$$

The gravitational attraction of the compensating surface at depth z , observed at the level of the topography is

$$g_{comp}(x) = -2\pi\Delta\rho G h_0 e^{ik_1 x} e^{-|k|z} \quad (14.50)$$

The free-air gravity anomaly g_{fa} , observed at the level of the topography, is $g_{topo} + g_{comp}$, which can be expressed as

$$g_{fa}(x) = 2\pi\Delta\rho G h_0 e^{ik_1 x} (1 - e^{-|k|z}) \quad (14.51)$$

The Bouguer anomaly is obtained by removing the effect of the topography, i.e.

$$g_{boug} = g_{fa} - g_{topo} = g_{topo} + g_{comp} - g_{topo} \quad (14.52)$$

This illustrates that the Bouguer anomaly is simply the anomaly caused by the compensating surface at depth z . Note that the expressions for g_{comp} and for g_{fa} both contain expressions that look like the field from the topography g_{topo} , but are modified (filtered) by wavelength-dependent filters. The free-air filter acts as a high-pass filter

for spatial frequencies, while the Bouguer anomaly filter is a low-pass function, due to exponentially upward continuing the gravity anomaly from depth z to the observer's level. This filter is an **upward continuation filter**, identical to the **Earth filter** which we have encountered for modeling the magnetic field.

We have just shown that the amplitude of the free-air anomaly depends on topography and the depth of the compensating layer. If we know both topography and free-air gravity, we should be able to design a filter which gives us some information about the depth at which the compensating mass resides. If we follow our simple model from above and divide g_{comp} by g_{topo} , we can write:

$$Q(|k|) = \frac{g_{comp}}{g_{topo}} = \frac{-2\pi\Delta\rho G h_0 e^{ik_1 x} e^{-|k|z}}{2\pi\Delta\rho G h_0 e^{ik_1 x}} = -e^{-|k|z} \quad (14.53)$$

Q is a type of transfer function which is called **isostatic response function** or **admittance**. Plotting the logarithm of $-Q(k)$ versus k produces a line with slope $-z$, i.e. the compensation depth.

In reality we have topography with more than one wavelength. For this case we can compute the transfer function $Q(|k|)$ as a function of the Fourier transformed topography $H(k)$ instead of using topography of one wavelength alone (h_0 , as above):

$$Q(|k|) = \frac{-2\pi\Delta\rho_2 G \cdot H(k) \cdot e^{-|k|z}}{2\pi\Delta\rho_1 G \cdot H(k)} = -\frac{\Delta\rho_2}{\Delta\rho_1} e^{-|k|z} \quad (14.54)$$

In all cases discussed so far we have assumed that isostatic compensation is local, where in reality we have to treat the lithosphere as an elastic sheet, i.e. local mass anomalies are compensated regionally. The area affected by plate flexure given a particular load depends on the elastic plate thickness. How do we model this added complexity?

Figure 14.26: Gravity anomalies associated with seamounts

Figure 14.26 consists of two vertically aligned plots. The top plot shows gravity anomalies in mGal on the y-axis (ranging from -25 to 100) against distance in km on the x-axis (ranging from -200 to 200). It contains three curves: a dashed curve representing the effect of topography only, a dotted curve representing the effect of compensation only, and a solid curve representing the combined effect. The solid curve shows a sharp positive peak centered at approximately 0 km, reaching about 80 mGal, and a smaller negative trough at approximately ±100 km, reaching about -15 mGal. The bottom plot shows a cross-section of the ocean crust with depth in km on the y-axis (ranging from -14 to 0) and distance in km on the x-axis (ranging from -200 to 200). It features several layers labeled with their densities: ρ_w (water, ~1025 kg/m³), ρ_c (upper crust, ~2700 kg/m³), m (middle crust, ~2700 kg/m³), ρ_m (lower crust, ~3000 kg/m³), and ρ_m (Moho, ~3000 kg/m³). A dashed curve labeled h represents a conical seamount, and a dotted curve labeled m represents the Moho deflection. A vertical double-headed arrow labeled d indicates the compensation depth, which is the depth at which the Moho deflection equals the topographic height of the seamount.

14.6.7 Isostatic response functions

14.6.7.1 Bouguer vs. free-air gravity anomalies

In the oceans we usually use the free-air gravity for computing an isostatic response function, because it is not as straightforward to calculate Bouguer anomalies as it is on continental crust, where we observe the gravity anomalies on the topographic surface.

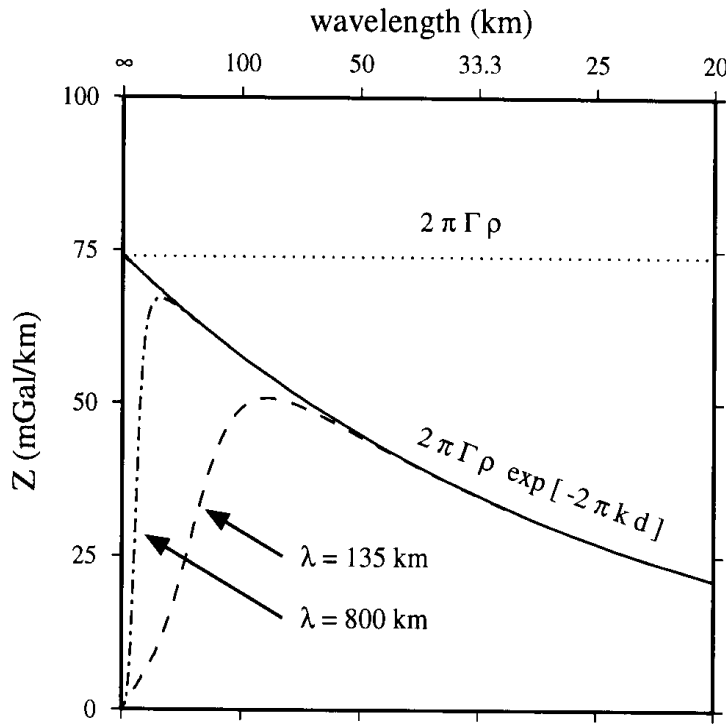


Figure 14.27: Gravity-topography transfer function (admittance) from Smith and Sandwell (1994)

The transfer function Q is more stable if we calculate it by using the Bouguer anomaly and the topography, rather than the free-air anomaly. Hence, for the continental case

$$Q(k) = \frac{G_{boug}(k)}{H(k)} \quad (14.55)$$

where $G_{boug}(k)$ is the Fourier transform of the Bouguer gravity anomaly, and $H(k)$ is the Fourier transform of the topography, and

$$Q(k) = 2\pi\rho_c G e^{2\pi kz_m} \left(1 + \frac{(2\pi k)^4 D}{(\rho_m + \rho_c)g}\right)^{-1} \quad (14.56)$$

where z_m is the depth of the Moho.

14.6.7.2 Experimental admittance

The procedure to compute the admittance from observed data involves the following steps:

- 1.) Take free-air or Bouguer gravity anomaly
- 2.) Calculate Fourier transforms G_{fa} and G_{boug}
- 3.) Calculate admittance Q . We mentioned before that an isostatic response function of the form $Q(k) = G_{fa}(k)/H(k)$ is very unstable. To gain stability (at the cost of systematic bias) we can calculate

$$Q = \frac{\langle G_{fa} \cdot H^* \rangle}{\langle H \cdot H^* \rangle} = \frac{\text{crosscorrelation}}{\text{normedtopography}} \quad (14.57)$$

The angle brackets indicate that we average around discrete wavenumber bands or over a number of individual profiles. Ideally this averaging would not be necessary. The asterisk indicates a complex conjugate.

- 4.) Plot $Q(k)$
- 5.) Compare the result with predictions from simple isostatic models

Limitations:

- 1.) The area we look at must have uniform properties (e.g. a fractured plate adds azimuthal asymmetry)
- 2.) The area must have consistent loading properties (e.g. all surface loads must be volcanic, or we may have a fixed fraction of loading by intrusions at Moho, etc.)
- 3.) Compensation mechanism must be the same over entire area (we need to sample long and short wavelengths to determine admittance)
- 4.) Variations in lithology (i.e. density ρ) must be uncorrelated with variations in topography $h(x)$.

14.6.7.3 Consequences of sub-surface loading distributions

It is important to recognize that the form of the loading distribution can strongly shape the resulting admittance relation between topography and gravity. Most model inversions of the admittance for the flexural rigidity of the lithosphere make the same assumptions: initially the lithosphere is a laterally homogeneous density structure which is deformed by surface loading. However, many tectonic processes involve density changes which act as internal or bottom loads in the lithosphere, e.g.:

- Metamorphism
- Plutonic intrusions
- Phase changes

- Crustal underplating
- Lithospheric reheating

This means that interpreting admittance as a straightforward response to surface loading may be misleading. Sometimes, the admittance for internal- or bottom loading of a strong plate may mimic the admittance expected for a weak plate that is loaded on top. This phenomenon may explain the discrepancy between relatively high estimates (10^{23} - 10^{24} Nm) for flexural rigidity of continents obtained from the study of the compensation of individual features and the low estimates (10^{19} - 10^{22} Nm) for the flexural rigidity of continents deduced from standard admittance studies. An extreme example is an admittance study by *McNutt and Parker* (1978), in which they found the elastic thickness of Australia to be ~1 km, a value which is fairly far on the low side for continental crust, especially a craton, which is expected to have an elastic thickness of the order of tens of km.

It is also important to recognize that the standard technique for averaging to improve the stability of the admittance determination results in the preferential weighting of the admittance in regions of the greatest topographic relief, e.g. if we solve

$$Q = \frac{\langle G_{fa} \cdot H^* \rangle}{\langle H \cdot H^* \rangle} \quad (14.58)$$

to determine the isostatic response function

$$Q(k) = \frac{G_{fa}(k)}{H(k)} \quad (14.59)$$

we are really solving $Q(k) = (\langle Q \cdot H \cdot H^* \rangle, \langle H \cdot H^* \rangle)$. Hence, if we are doing a regional study where we are averaging the isostatic response function from different regions or different types of loading, we are effectively weighting these functions by the square of the amplitude of the topography. Since young mountain belts are often regions of relatively low rigidity, this generally will bias elastic plate thickness estimates to the low side.

Below we show some examples of the theoretical isostatic response functions:

$$T_e = \sqrt[3]{\frac{12(1 - \mu^2)D}{E}} \text{ in km} \quad (14.60)$$

Isostatic response functions for top-loading are shown as dashed lines and loading at the Moho is indicated by solid lines. Numbers show the effective elastic thickness.

Note that for Airy compensation ($D = 0$) the response for Moho-loading is exactly the same as for top loading. For short wavelength loads where the strength of the plate damps the local response to loading, Q becomes large, because the gravitational signal of the load is much larger than the surface response. For long wavelength loads Q approaches Airy compensation.

Figure 14.28 shows an example of the isostatic response functions due to several top and Moho loading distributions on an elastic plate with plate thickness $T = 40$ km, and

a Moho depth $z_m = 35$ km. The different curves are shown for different ratios f of the amplitude of the Moho load to the surface load (shown are cases for $f = 0-5$). Note that the response functions for $f < 2$ are not much different from surface loading ($f = 0$) of a weaker plate with thinner crust, as shown in figure 14.28 (dashed line, 10 km elastic plate thickness).

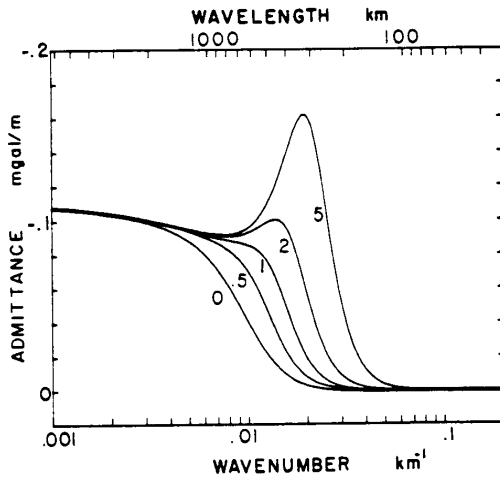


Figure 14.28: Admittance curves for different ratios of Moho load to surface load

Figure 14.29 is an example of the observed admittance over the USA (*Lewis and Dorman, 1970*):

Two fundamentally different isostatic models can explain the above linear transfer function (as explained in *Isostatic response function for oceanic crust*) for the United States:

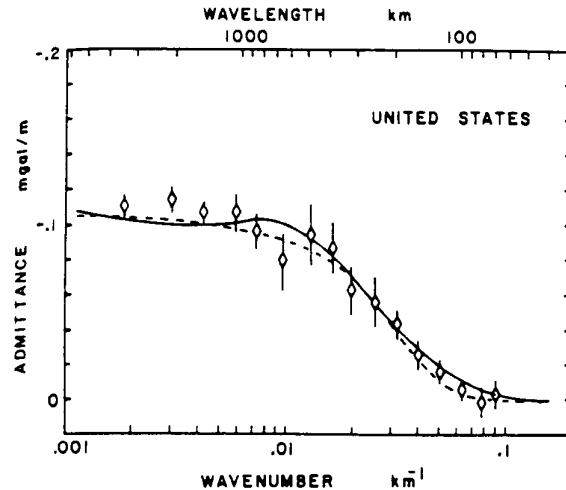
(1) Topography is created by emplacement of surface topographic loading on a weak plate with elastic thickness of a few km (dashed line), or

(2) Topography is created in response to sub-surface loads emplaced within or beneath the plate in a variety of tectonic provinces of varying flexural rigidity with an average elastic plate thickness of tens of km (solid line).

Both models fit the admittance data equally well. How can we distinguish between them? There is another independent way to estimate the elastic strength of a plate using gravity and topography data, given by *Forsyth (1985)*, who examined the **coherence** between gravity and topography signals.

14.6.7.4 Coherence

While admittance is a measure of the amplitude ratio of topographic and gravity signals at a given wavelength, the coherence is a measure of the relative phase between gravity and topography signals, as shown in figure 14.30 from *McNutt (1990)*.



Observed admittance (diamonds) for the continental United States determined by Lewis and Dorman [1970]. Error bars indicate one standard deviation. Dashed line represents the isostatic response function for an elastic plate with loading on top, using the best fitting model of Banks *et al.* [1977]. Solid line represents the weighted average isostatic response function for loading from below in a uniform population of provinces ranging in effective elastic thickness from zero to 100 km.

Figure 14.29: Admittance curve for the USA

For simple top loading, or a single mechanism of loading at depth, a coherence of -1 will be generated. However, when there are multiple types of loading within the plate of finite elastic strength, the coherence will be high at wavelengths that are large with respect to the flexural length of the plate and low at wavelengths that are smaller than the flexural length of the plate.

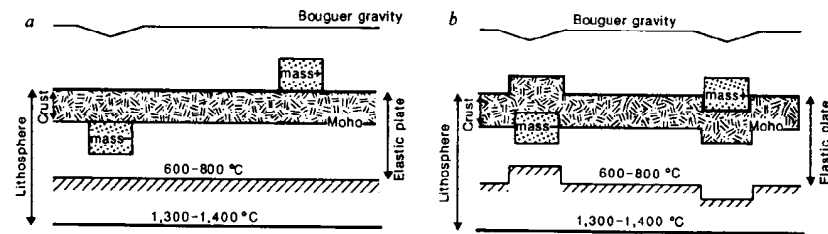
Consider the following end-member scenarios shown above:

(a) **A perfectly rigid plate with random loading at both the surface (topography) and Moho.** Because of the plate rigidity there is no topographic expression of the Moho loading. In this case, we can exactly solve for the surface load (just the topography). Then by downward continuing the Bouguer anomaly to the Moho, we could exactly determine the loading at the Moho (apart from the low-pass filter of downward continuation). In this rigid plate scenario, the relief on the surface and relief on the Moho are two independent processes that are decoupled by the rigid plate, and the expected coherence is 0.

(b) **Perfectly weak plate (Airy compensation).** Any surface load will deflect plate and Moho, producing a Bouguer anomaly showing the compensation of the load. Similarly, any load at the Moho (or at any depth that is small compared with the wavelength in question) will also deflect the surface of the plate thus compensating the load. The

Basis of the coherence technique

Imagine loads randomly placed on the Earth's surface and at the crust–mantle boundary (the 'Moho'). If the plate is infinitely rigid, *a*, neither surface nor subsurface loads can flex the plate. The topography then measures the magnitude of surface loading, the Bouguer gravity measures the magnitude of subsurface loading, and the lack of correlation between Bouguer gravity and topography at all wavelengths indicates that the plate is perfectly rigid.



If the plate is infinitely weak, *b*, every surface mass will warp the plate to produce a subsurface density anomaly, and every Moho load will lead to surface topography. The correlation between Bouguer gravity and topography will be perfect (and negative) at all wavelengths except very short ones where it approaches zero owing to upward attenuation of the gravity from the Moho loading.

Any realistic case will fall somewhere in between these two extremes, and the particular wavelength at which the correlation changes from -1 at long wavelengths to 0 at short wavelengths is a measure of the stiffness of the plate.

Figure 14.30: Basis of the coherence technique

two types of loading are indistinguishable in the case of a perfectly weak plate, and the expected coherence is 1 .

From these considerations we can expect that the coherence between gravity and topography signals will approach -1 at wavelengths that are long with respect to the flexural wavelength of the plate ('Airy compensation') and will approach 0 at wavelengths that are small with respect to the flexural length of the plate ('elastic "rigid" compensation').

The figure below shows coherence as a function of wavelength for equal loading at the surface of the plate and at the Moho at 30 km depth. Numbers indicate effective elastic plate thickness in kilometers. The wavelength of the transition between coherent and incoherent gravity and topography should provide a direct indication of the flexural rigidity.

Thus the coherence allows us to distinguish between different models that match the observed admittance equally well. It also provides another tool to estimate the relative importance of surface and subsurface loading, provided the isostatic response functions for the processes are different. The method for calculating coherence and loading from observed data is outlined by Forsyth (1985).

Caveats:

- (1) Estimates of the elastic thickness from coherence are not very sensitive to uncertainties in ratio of top to sub-surface loading.

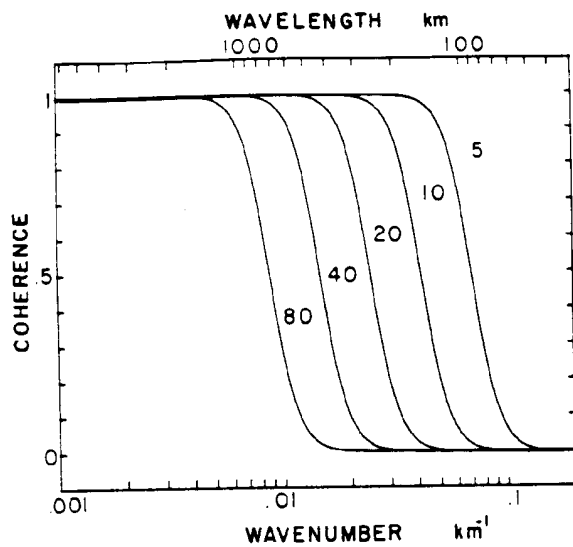


Figure 14.31: Coherence between gravity and topography for different values of elastic thickness

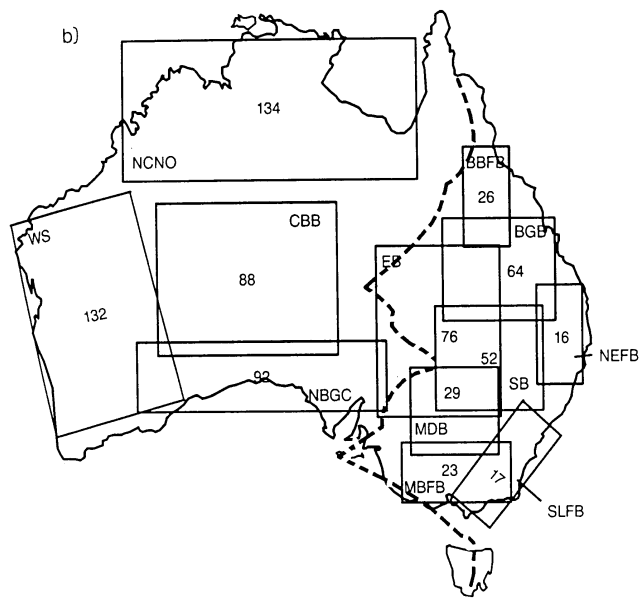


Figure 14.32: Elastic Plate thickness of Australia from coherence

(2) The basic assumption used in interpreting coherence to infer flexural rigidity is that surface and sub-surface loading are statistically independent. For many tectonic processes (e.g. volcanism) this is not true, at least not locally. Erosion may be an important factor in randomizing the relationships between surface and sub-surface loading: sub-surface loads are preserved while their corresponding tectonic surface complement is removed by erosional processes.

It is also important to note that we can obtain another bound on Q from

$$Q^{-1} = \frac{\langle H \cdot G^* \rangle}{\langle G \cdot G^* \rangle} \quad (14.61)$$

which provides a weighting that is proportional to the square of the Bouguer anomaly, i.e.

$$Q^{-1} = \frac{\langle Q^1 \cdot G \cdot G^* \rangle}{\langle G \cdot G^* \rangle} \quad (14.62)$$

If topography and gravity are due to loading a laterally uniform plate by surface loads then estimates of Q and Q^{-1} should agree. If top and bottom loads are present these two different approaches to weighting the data will not be equivalent. This can be used as a check on the internal consistency of the standard top-loading scenario.

14.7 References

- Bouguer, P., 1749, *La figure de la terre*. Paris
- Forsyth, D.W., 1985, Subsurface loading and estimates of the flexural rigidity of continental lithosphere, *J. Geophys. Res.*, 90, 12623-12632.
- Fowler, S. and D. McKenzie, 1989, Gravity studies of the Rockall and Exmouth Plateaux using Seasat altimetry, *Basin Res.*, 2, 27-34.
- Haxby, W.F. and Turcotte, D.L., 1978, On isostatic geoid anomalies, *J. Geophys. Res.*, 83, 5473-5478.
- Lewis, B.T.R. and L.M. Dorman, 1970, Experimental isostasy, 2, An isostatic model for the United States derived from gravity and topography data, *J. Geophys. Res.*, 75, 3367-3386.
- Liu, Ch.-Sh., Sandwell, D.T., and Curray, J.R., 1982, The negative gravity field over the 85°E Ridge, *J. Geophys. Res.*, 87, 7673-7686.
- McNutt, M., 1990, Flexure reveals great depth, *Nature*, 343, 596-597.
- McNutt, M.K. and R.L. Parker, 1978, Isostasy in Australia and the evolution of the compensation mechanism, *Science*, 199, 773-775.
- Parker, R. L., The rapid calculation of potential anomalies, *Geophys. J. R. Astron. Soc.*, 31, 447-455, 1972.
- Phipps Morgan, J., Morgan, W.J., Zhang, Y.-S., and Smith, W.H.F.S., 1995, Observational hints for a plume-fed, suboceanic asthenosphere and its role in mantle convection, *J. Geophys. Res.*, 1995, 12753-12767.

- Smith, W.H.F. and D.T. Sandwell, 1995, Marine gravity field from declassified Geosat and ERS-1 altimetry, *EOS transactions Am. Geophys. Union*, 76, 156.
- Talwani, M., and Ewing, M., 1960, Rapid computation of gravitational attraction of three-dimensional bodies of arbitrary shape, *Geophysics*, 25, 203.
- Turcotte, D.L., and Schubert, G., 1982, *Geodynamics: Applications of Continuum Physics to Geological Problems*, John Wiley & Sons, New York, 450 pp.
- Vening Meinesz, F.A., 1929, Theory and practice of gravity measurements at sea. Delft.
- Wessel, P., and A. B. Watts, On the accuracy of marine gravity measurements, *J. Geophys. Res.*, 93, 393–413, 1988.
- Watts, A.B., 1992, The effective elastic thickness of the lithosphere and the evolution of foreland basins, *Basin Research*, 4, 169-178.

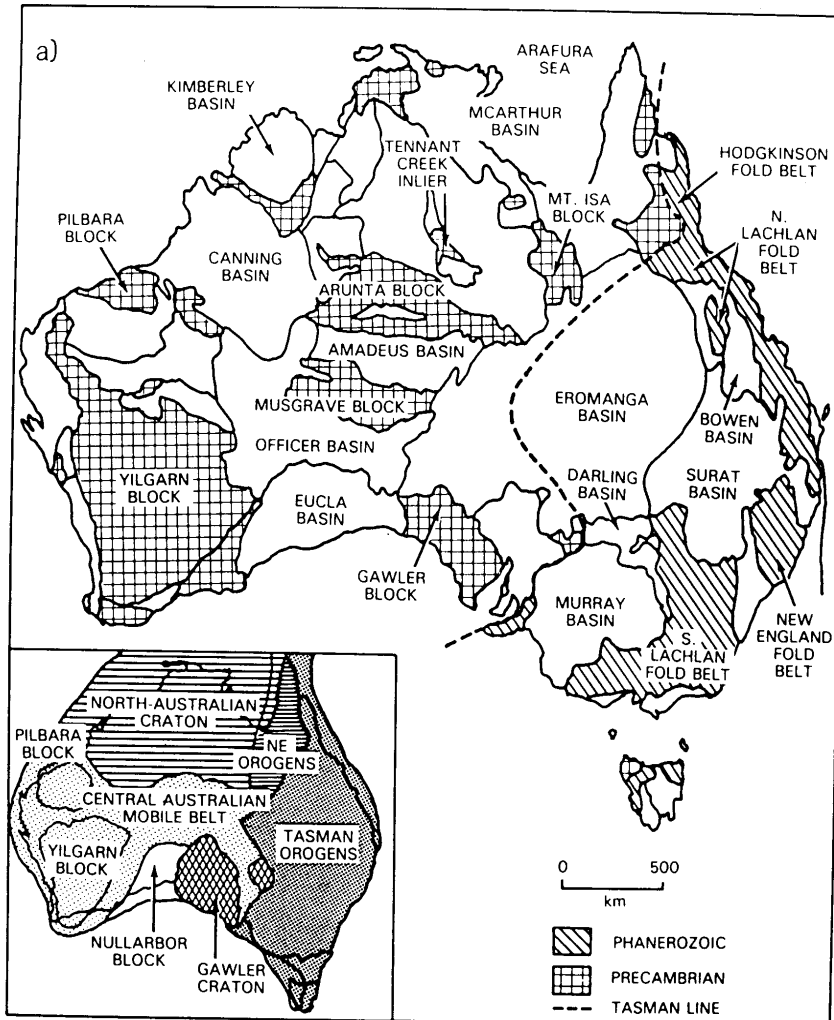


Figure 14.33: Geological map of Australia. Note broad correlation of geological provinces with coherence results (previous figure). Rheologically strong areas correspond to Archean cratons, and weak areas to sedimentary basins.

Chapter 15

Electrical and electromagnetic methods

For convenience, we are now going to discuss the electrical and electromagnetic methods of geophysics under the one heading. The electrical methods relate to the introduction of a DC electrical current into the ground. For the electromagnetic methods, AC currents are employed to generate a magnetic field which is transmitted into the ground.

The electrical and electromagnetic methods offer a considerable range geophysical techniques for exploration of the subsurface. Like the seismic methods, they are active methods which require the introduction of energy to the ground. They are also similar to the seismic methods in that the electromagnetic energy that they utilise propagates as waves within the earth. However, apart from radar surveying, there the similarity ends. Electromagnetic waves can be introduced into the earth over a huge range of frequencies – from DC electrical flow through to frequencies approaching 1 GHz. The choice of survey frequency and method depends on the resistivity of the target and the other relevant rock units. Just as with seismic surveying, the general rule is that the higher the frequency, the greater the resolution but the poorer the penetration. As we have also previously learnt, the range of resistivities encountered in the earth covers at least 7 orders of magnitude. It is for these reasons that there are so many different types of electromagnetic methods.

The results from electrical and electromagnetic surveys also tend to look different to seismic results. The resistivities of most rocks is a function of their porosity and the conductivity of the pore waters. Porosities need not change at rock boundaries, and other geological features – e.g. fractures and weathering crossing rock boundaries, can also cause large changes in resistivity. Similarly, when metallic ores are present in rocks and currents are able to flow, the distribution of the conductive mineralization can be quite complex and again across rock boundaries.

Electrical and electromagnetic methods, when used for minerals exploration, also need to be effective in complex 3-dimensional geological situations. Seismic reflection

surveying, even with 3D seismic surveying, relies on having reflecting targets that are largely sub-horizontal to the ground surface – i.e. they are relying on a basic 2D geometry. This allows the use of the powerful stacking procedures to enhance reflection signals. Producing equivalent 3D electromagnetic images of the subsurface is not trivial. Just as with gravity and magnetic surveying, modeling is often undertaken to explore the range of candidate geological interpretations.

In conducting electrical and electromagnetic surveys, a major difference between the two types of surveys is that in order to introduce a DC current into the ground and to measure the ground response, pairs of current and potential electrodes must be used. The electrical methods must therefore be conducted on the ground surface. For the introduction of an electromagnetic field into the ground and to measure the response, the need for direct ground contact is removed. Electromagnetic surveys can therefore be undertaken from moving platforms – aircraft and vehicles as well as from the ground surface.

The resistivity of the surface layers provides another important point of distinction. If the resistivities are high (e.g. desert sand and ice), then current flow is very difficult to achieve but electromagnetic penetration is possible. Conductive surface layers, on the other hand, may be useful for electrical surveys but problematic for electromagnetic surveys if deeper targets are being sought.

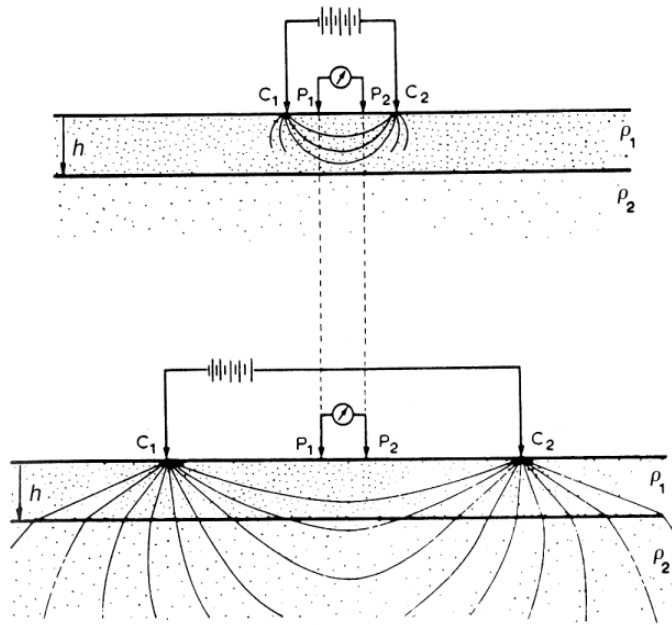
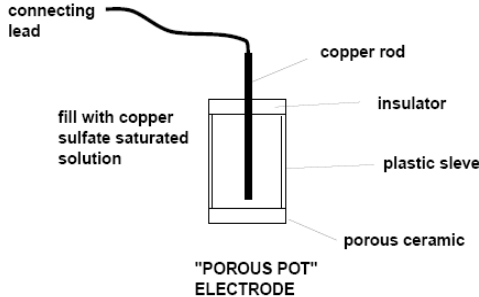
15.1 Electrical (resistivity) surveys

Geophysical surveys utilising direct current are usually termed resistivity surveys. A pair of current electrodes, usually simple metal stakes are used to introduce the electric current into the ground. The resistivity surveys then measure the variations in the potential differences at the ground surface that are due to that current. These are analysed to reveal the resistivities of the various layers beneath the ground surface. The general idea is that the further apart the current electrodes, the deeper will be the current flow. In other words for closely spaced current electrodes, the observed potential differences will be indicative of the resistivity of the surface layers. For widely spaced current electrodes, the potential differences will be indicative of the resistivities of deeper layers.

For the potential electrodes, consideration needs to be made of the possibility of an ionic build-up at the potential electrodes - as with the self potential effect utilised in the SP logging that we have already discussed, and the SP ground surveys we have yet to discuss. One way of avoiding SP effects is to utilise a low frequency AC source. At low frequencies, DC behaviour will be displayed. Another approach is to use porous pots as the potential electrodes.

The idea with a porous pot is that the porous ceramic container allows ionic flow from the ground into the copper sulfate solution but without any ionic build up at the copper electrode.

The main applications for resistivity surveys concerns the investigation of the near surface layering of the earth (to depths of about 100 m or so). Because of the role of pore

**Figure 15.1:** Resistivity Surveying**Figure 15.2:** Design of electrodes used for resistivity surveys

water in the governing the resistivity of a rock layer, there are important applications for these surveys in groundwater investigations.

15.1.1 Derivation of apparent resistivity

Between a pair of electrodes, by Ohm's law, the potential difference ΔV due to a current I and resistivity ρ is given by:

$$\Delta V = I\rho \quad (15.1)$$

The resistivity for a cylinder length l , cross sectional area A is defined as:

$$\rho = \frac{RA}{l} \quad (15.2)$$

So

$$\Delta V = \frac{I\rho l}{A} \quad (15.3)$$

and for a sphere radius r ,

$$\Delta V = -\frac{I\rho\Delta r}{2\pi r^2} \quad (15.4)$$

Integrating this,

$$V(r) = \frac{I\rho}{2\pi r} + Const \quad (15.5)$$

When $r = \infty$, $V = 0$ so the constant is zero.

Therefore we can define the voltage potential due to current electrode as:

$$V(r) = \frac{I\rho}{2\pi r} \quad (15.6)$$

And with two electrodes passing current at distances r and r' from point P,

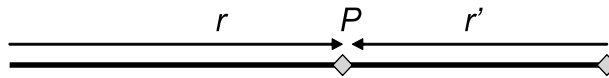


Figure 15.3: Potential at two electrodes

$$V(r) = \frac{I\rho}{2\pi} \left(\frac{1}{r} - \frac{1}{r'} \right) \quad (15.7)$$

From this equation it is possible to express measured potential differences (differences in $V(r)$ from the two current electrodes) for different electrode configurations. Further manipulation then allows apparent resistivities, ρ_a to be determined.

For example, the Wenner array is a linear electrode array used for conducting resistivity profiles across the ground surface with current electrodes at A and B, and potential electrodes at M and N, all spaced distance a .



Figure 15.4: Electrode configuration in a Wenner array

$$\Delta V = \frac{I\rho}{2\pi} \left(\frac{1}{AM} - \frac{1}{BM} - \frac{1}{AN} + \frac{1}{BN} \right) \quad (15.8)$$

Or

$$\rho = 2\pi a \frac{\Delta V}{I} = \rho_a \quad (15.9)$$

For a resistivity profiling survey using a Wenner array, the spacings between the electrodes is chosen so that the current flow will be sampling the region of interest in the subsurface. Changes in apparent resistivity will occur when the resistivity of the subsurface layers change.

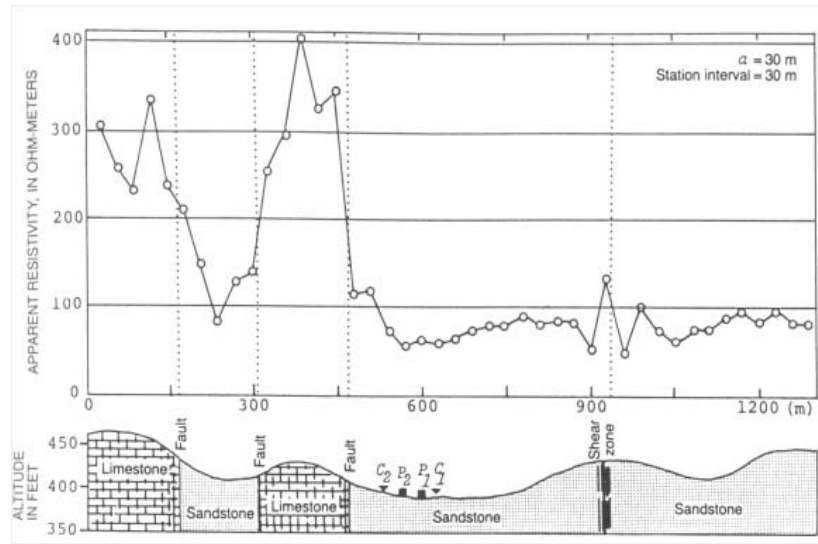


Figure 15.5: Resistivity Profile from a Wenner array

Another frequently used array is the Schlumberger array. Here the spacing between the potential electrodes at M and N ($2l$) is much less than the spacing between the current electrodes at A and B ($2L$).

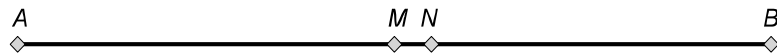


Figure 15.6: Electrode configuration for a Schlumberger array

$$\rho_a = \frac{\pi L^2}{2l} \frac{\Delta V}{I} \quad (15.10)$$

For surveys using the Schlumberger array, the spacing between A and B is increased while maintaining the same central point. These surveys are called resistivity sounding surveys and they yield information on progressively deeper layers.

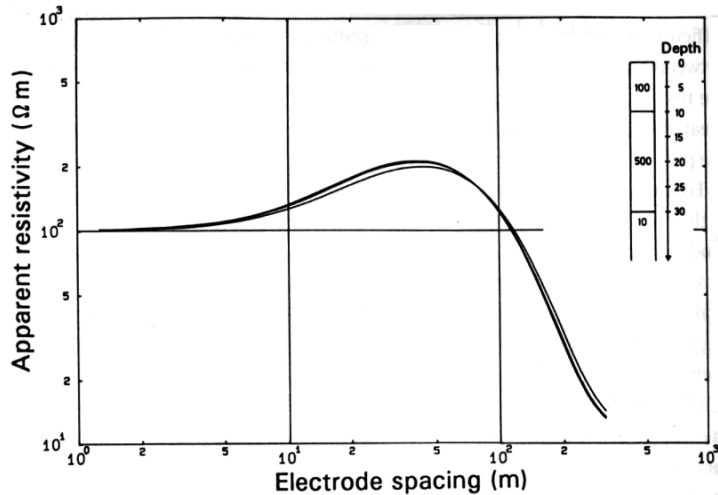


Figure 15.7: Resistivity sounding from a Schlumberger array

The third main electrode array used in resistivity surveying is the dipole-dipole array. For these surveys, the current and potential electrode pairs are the same distance apart, a , and separated by a spacing which is a multiple of a .

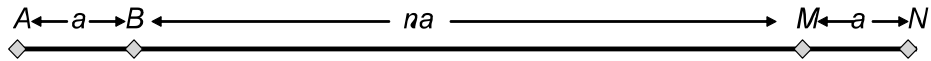


Figure 15.8: Electrode configuration for a dipole-dipole array

$$\rho_a = \pi n(n+1)(n+2)a \frac{\Delta V}{I} \quad (15.11)$$

Results from dipole-dipole surveys are plotted up as shown in figure 15.9 to provide a resistivity pseudo-section.

The idea of a pseudo-section is that it allows an estimate of the lateral and vertical variations in resistivity in the subsurface.

For all of the above resistivity methods, interpretation can be at a qualitative level (spot the anomalies) or through the use of interactive modeling methods.

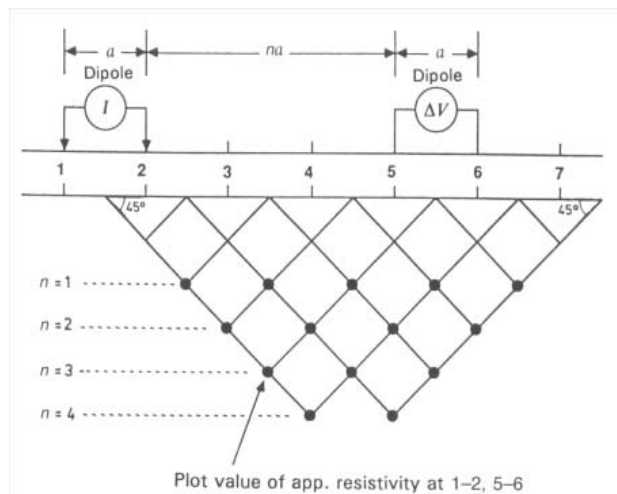


Figure 15.9: Methodology for generating a resistivity pseudo-section from a dipole-dipole array

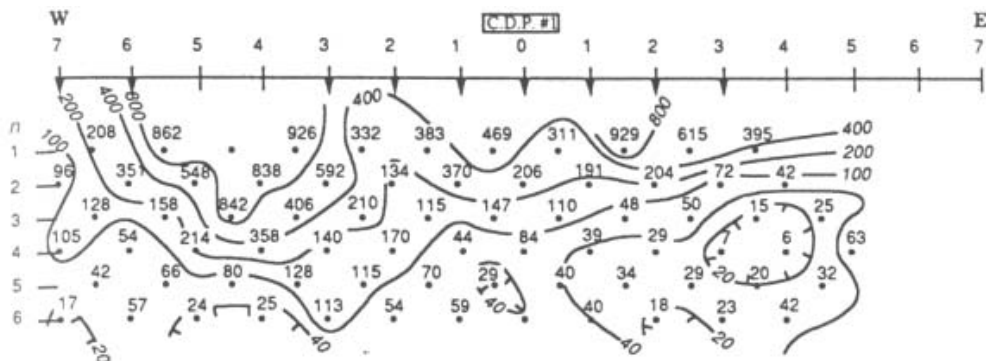
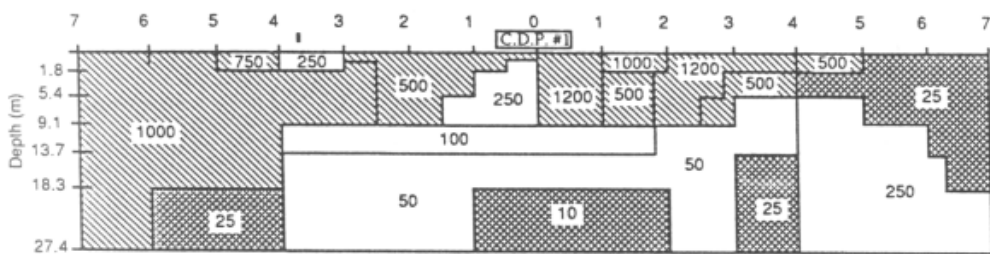


Figure 15.10: Example resistivity pseudo-section from a dipole-dipole array



15.2 The magnetotelluric method (MT)

While not strictly a direct current method, the magnetotelluric method exploits the very low frequency waves of a few cycles per day that are naturally generated in the earth by the interaction between solar radiation and the ionosphere.

The induced currents flow in the more conductive rocks and measures of changes in the potential difference between potential electrodes are indicative of gross changes (basin scale) in the subsurface. Higher frequency magnetotelluric surveys utilising currents generated by distant lightning strikes are known as audio frequency magnetotellurics (AMFT) and it is also possible to introduce a distant low frequency source and conduct a controlled source magnetotelluric survey (CSAMT).

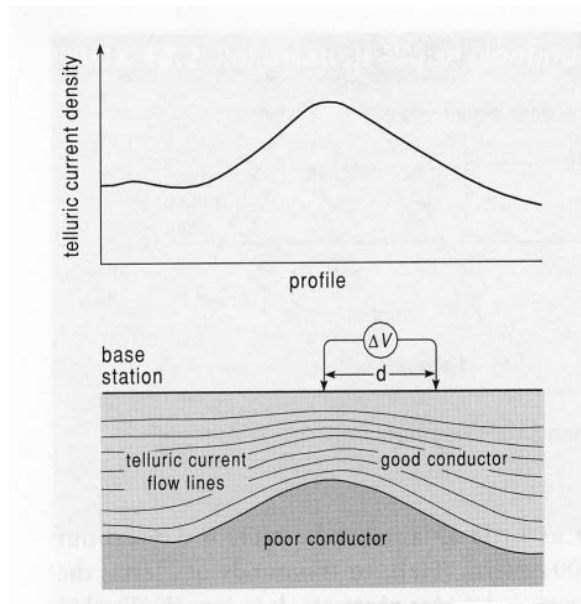


Figure 15.12: The magnetotelluric method

15.3 Self potential surveys

Self potential surveying was introduced earlier in the section on geophysical logging. There are a number of mechanisms involved in the development of natural potentials in the ground. One involves the flow of fluids through porous media in situations where the charge on the ions in the fluid is different to the fixed chemical charges on the surface of the grains. This creates a streaming potential. Self potential can also be generated by temperature gradients and in the vicinity of ground waters with differing ionic concentrations. Self potentials in the millivolt range are readily observable.

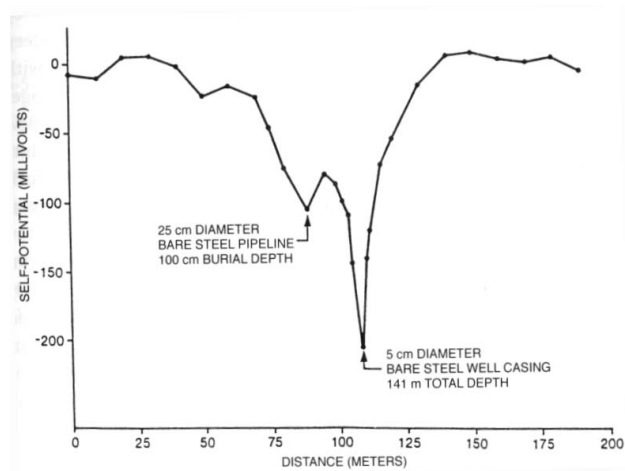


Figure 15.13: SP survey locating a buried pipe

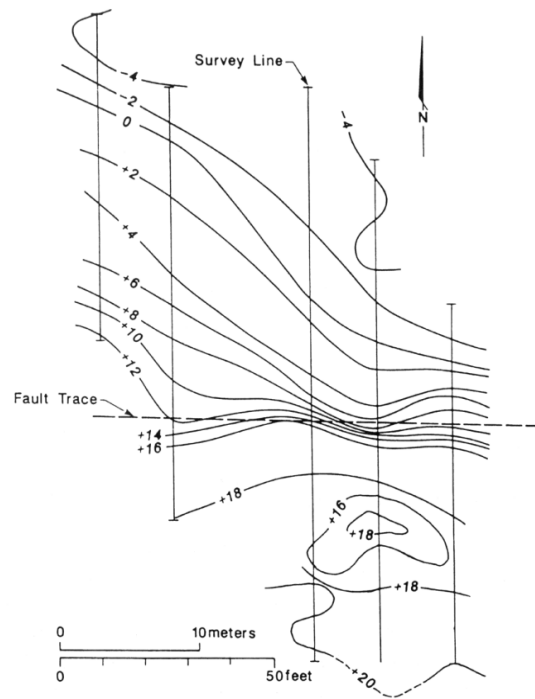


Figure 15.14: SP results locating a change in groundwater flow due to the presence of an impermeable crushed zone

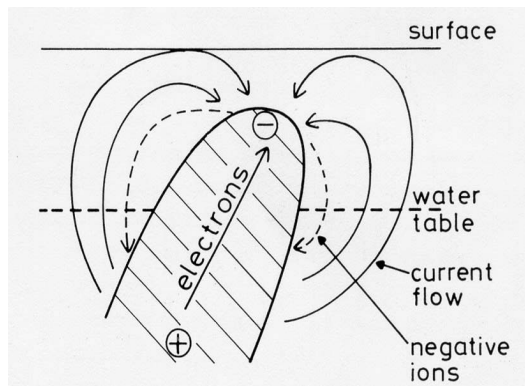


Figure 15.15: Generation of self potential over a conductive mineral deposit.

Self potentials are also observed over conductive mineral deposits where oxidation of that part of the deposit above the water table leads to an electron flow through the deposit and a return flow of negative ions through the ground water.

15.4 Induced polarization surveys (IP)

IP surveys were also introduced in the geophysical logging section. When a current flows through the ground, there is a build-up of ions at the boundary of electrical conductors, and around clay particles which can also carry a net negative charge on their surfaces.

If the applied current is turned off, there is a period of time over which the ions dissipate. While this is happening, there exists an observable potential difference.

These IP effects are observed most significantly with disseminated sulfides (e.g. porphyry copper) and around clays. For investigations into petroleum reservoirs, this allows clays to be distinguished from sands containing saline water.

IP surveys can be undertaken in either the time domain whereby DC pulses are introduced into the ground, or in the frequency domain where low frequency AC currents are utilised. For the time domain surveys, the typical cycle is for the current to be applied for 1 second, then turned off for a second, then applied in the opposite direction for a second, off for a second and then a continuation of the same sequence. Through this arrangement, it is meaningful to measure the polarizability which is 100 times the ratio of the ground voltage at a time, t , after the pulse is switched off, to the ground voltage at the instant the current was switched off. The chargeability is given by the area under the decay curve (obtained by integration) divided by the voltage at the instant the current was switched off.

For the frequency domain surveys, the ground voltages expressed as apparent resistivities at two different frequencies are compared. The two frequencies are typically in the range 0.05 to 0.5 Hz and then 1 to 10 Hz. The overall survey is set up like a resis-

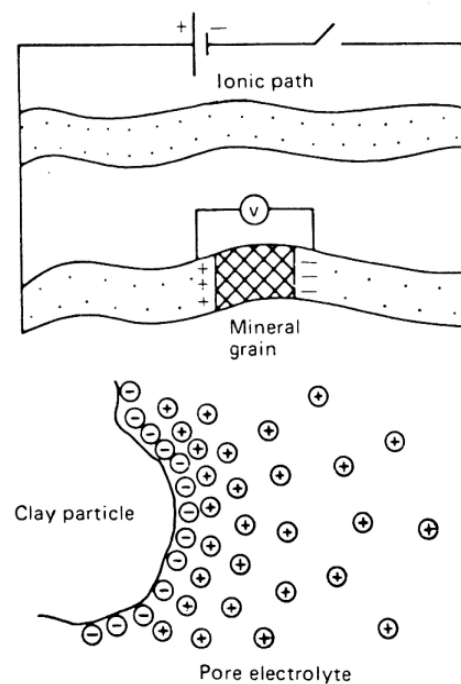


Figure 15.16: Induced polarization surveying - build-up of charge at the boundaries of electrical conductors

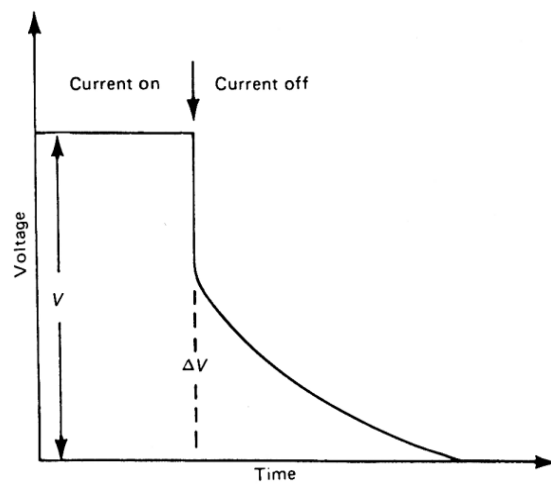


Figure 15.17: Induced polarization surveying - potential difference after applied current is turned off

tivity survey with the current and potential electrodes in a chosen pattern. The percent frequency effect (PFE) at the two frequencies f (lower) and F (higher) is given by:

$$PFE = \frac{100 (\rho_f - \rho_F)}{\rho_F} \quad (15.12)$$

and the metal factor (MF) is given by:

$$MF = \frac{1000 PFE}{\rho_f} \quad (15.13)$$

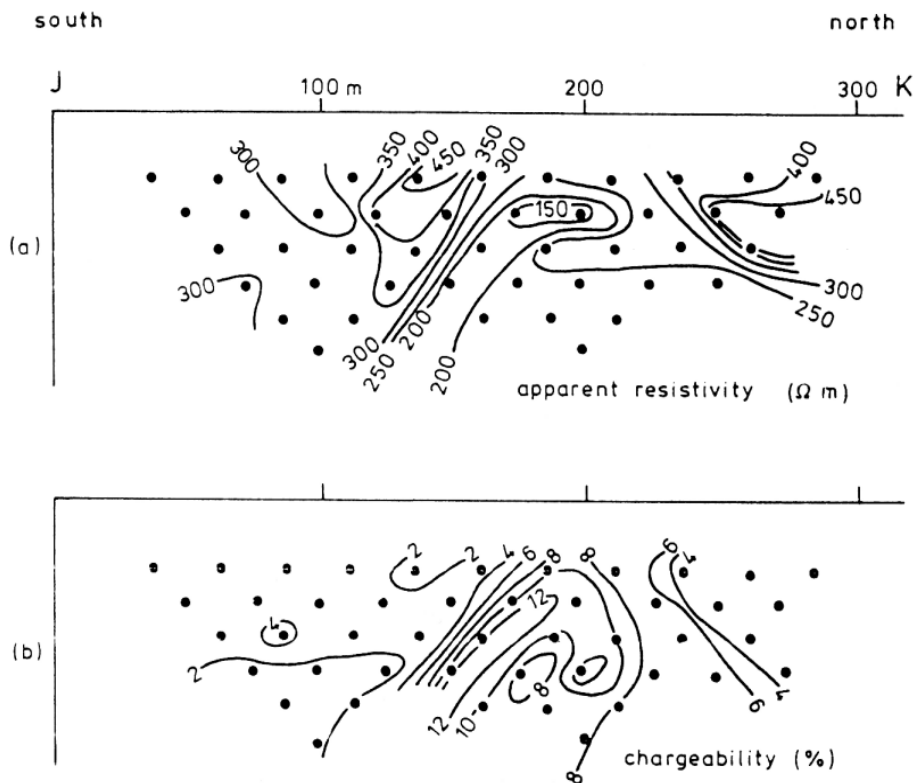


Figure 15.18: Apparent resistivity and chargeability sections from an IP survey

15.5 Electromagnetic Surveys

In a sentence, electromagnetic surveys involve the use of current loops to generate magnetic fields that penetrate the earth, which excite eddy currents in conductive materials which in turn create a secondary magnetic field which can then be detected. The existence and properties of the conductor(s) in the subsurface that generate the secondary

magnetic field can thus be assessed. These conductors might be metallic ore bodies, aquifers and other water charged bodies, or man-made objects – pipes, unexploded munitions, etc. The current loops can be laid out on the ground surface, be installed in portable devices, or installed on aircraft. To sense the secondary magnetic field, another (or the same) current loop can be used, or alternatively, it can be a suitable magnetometer.

The strength of the induced eddy currents will depend on the strength of the primary field, the conductivity of the medium and its orientation with respect to the primary magnetic field. To a first approximation, it is convenient to think of the induced current as following a circular path around the perimeter of the conductive target (i.e. it appears as a ‘coil’ in the ground).

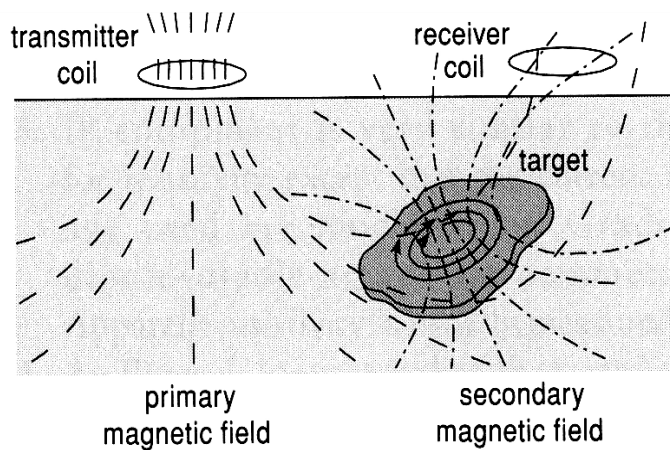


Figure 15.19: Electromagnetic surveying - relationship between transmitter coils, receiver coils and subsurface targets

Electromagnetic surveys can be undertaken using a continuous current source (termed frequency domain electromagnetic surveying - FEM or FDEM) or by undertaking measurements of the decaying secondary field after the primary field has been turned off (termed time domain electromagnetic surveying – TEM or TDEM).

15.5.1 Frequency domain electromagnetic surveying

An important concept, particularly for frequency domain electromagnetic surveying concerns the phase relationships between the primary and secondary fields. There is phase lag of 90 degrees between the primary magnetic field and the induced eddy currents. Then there is an additional lag between the secondary magnetic and the primary field which is also detected at the receiver. This additional lag is a function of the frequency of the wave and the properties of the in-ground conductor. The additional lag φ is given by $\tan^{-1}(\omega L/R)$ where L and R are the inductance and resistivity of the loop that approximates the in-ground conductor.

To measure the received field, it is therefore necessary to consider out-of-phase components. This is effectively a vector problem. The terminology used to express these components can be confusing. The in-phase component is termed the real component and the component that is 90 degrees out of phase is termed the imaginary or the quadrature component. The resultant field that is detected by the receiver can be expressed in terms of the real and imaginary components. For survey design, it can be important to determine whether real or imaginary components are going to be most useful, given the resistivity of the target and the operating frequency. For a good conductor (low resistance) and high frequency, most of the secondary field will be in the real component of the response. For a poorer quality conductor, the imaginary component becomes more important.

Another important concept concerns the skin depth. This is defined as the depth at which the signal strength decreases by $1/e$ (a factor of approximately 37%).

$$\text{skindepth} = 500 \sqrt{\frac{1}{\sigma f}} \text{metres} \quad (15.14)$$

This skin depth equation says the higher the frequency f , the smaller the depth of penetration.

15.5.2 VLF surveys

VLF surveys utilise the very low frequency communication signals transmitted by the world-wide American submarine communication system. (Russia has one too). The VLF waves penetrate about 10 to 20 metres into the ocean, depending on the frequency and conductivity (salinity) of the ocean water. In Australia there is a VLF station at North West Cape. It transmits a continuous signal at 22.3 kHz. There is also a station at Ebino in southern Japan (22.2 kHz).

The VLF signals from these stations also penetrate the earth to depths consistent with skin depth considerations.

To maximize the field generated by the target, the target should have some strike extent in the direction to the chosen VLF transmitter (it therefore helps to have more than one VLF station available to provide signal). The survey traverse then needs to be undertaken in a direction perpendicular to the direction to the transmitter. Lag (phase) information is obtained by noting the tilt required to the receiver antenna to observe a minimum in the signal.

15.5.3 Conductivity surveying

VLF surveying is just one form of frequency domain surveying. More generally, FEM surveying can also be called conductivity surveying. Systems are designed according to the required depths of penetration. Metal detectors represent a form of very shallow conductivity surveying.

The induction number refers to the ratio of the spacing between the transmitter and the receiver and the skin depth. If the operating frequency is very much less than 1,

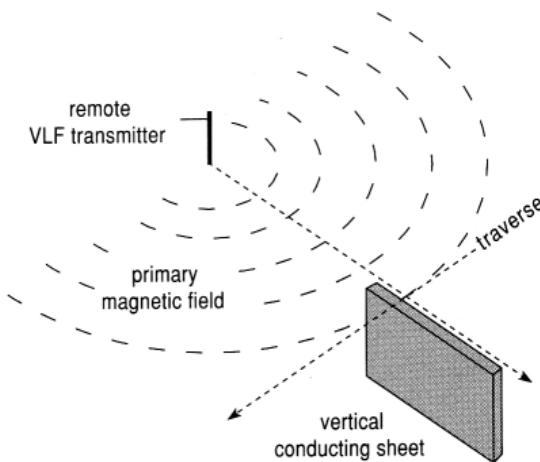


Figure 15.20: VLF surveying

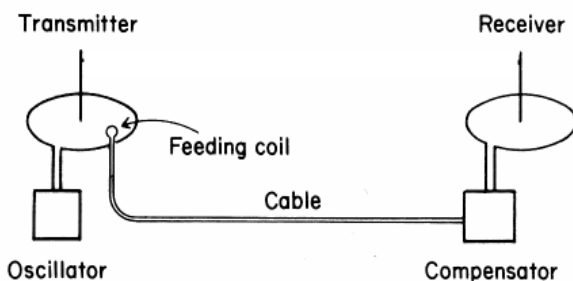


Figure 15.21: Conductivity surveying

then almost all of the ground response is in the quadrature (out-of-phase or imaginary) component. Furthermore, the ratio of the secondary magnetic field strength to the primary magnetic field strength is directly proportional to the conductivity.

For near-surface (to about 60 m) investigations, there is a number of conductivity meters that can be applied, depending on the depth of investigation. Each system has different operating frequencies and sensor spacings.

Applications for these types of surveys include:

- 1.) Mapping groundwater
- 2.) Investigating groundwater pollution
- 3.) Mapping changes to bedrock and bedrock topography
- 4.) Locating karsts and other underground openings

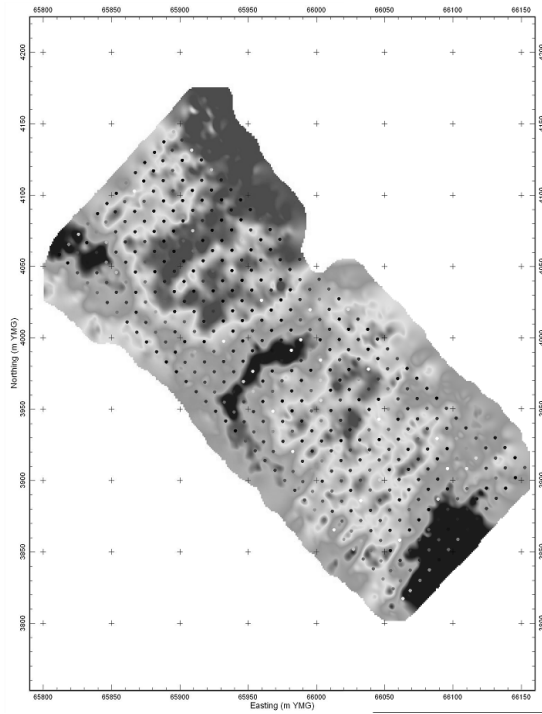


Figure 15.22: A Conductivity Map derived using a Geonics EM31

- 5.) Archeological investigations
- 6.) Location of pipes and other underground metallic conductors.

Results from conductivity surveys are usually presented as maps showing variations in conductivity for the representative depth for the survey frequency.

15.5.4 Time domain EM

Electromagnetic surveys undertaken in the time domain rely upon the switching on an off of a primary magnetic field generated by a current loop. At the time the current is switched off, the decaying time-varying magnetic field induces an electromotive force in subsurface conductors which generates a decaying secondary magnetic field. The secondary magnetic field is sampled over a range of times (typically 0.1 millisecond to 20 milliseconds). The early samples represent the field behaviour due to conducting bodies at shallow depth and over an area not much larger than the transmitting loop. The late samples are from deeper conductors and from a broader region of the subsurface. This behaviour is sometimes said to be analogous to smoke rings.

In practice, the decaying secondary fields can be quite noisy and just as with seismic surveying, stacking can be used to enhance the signal to noise characteristics.

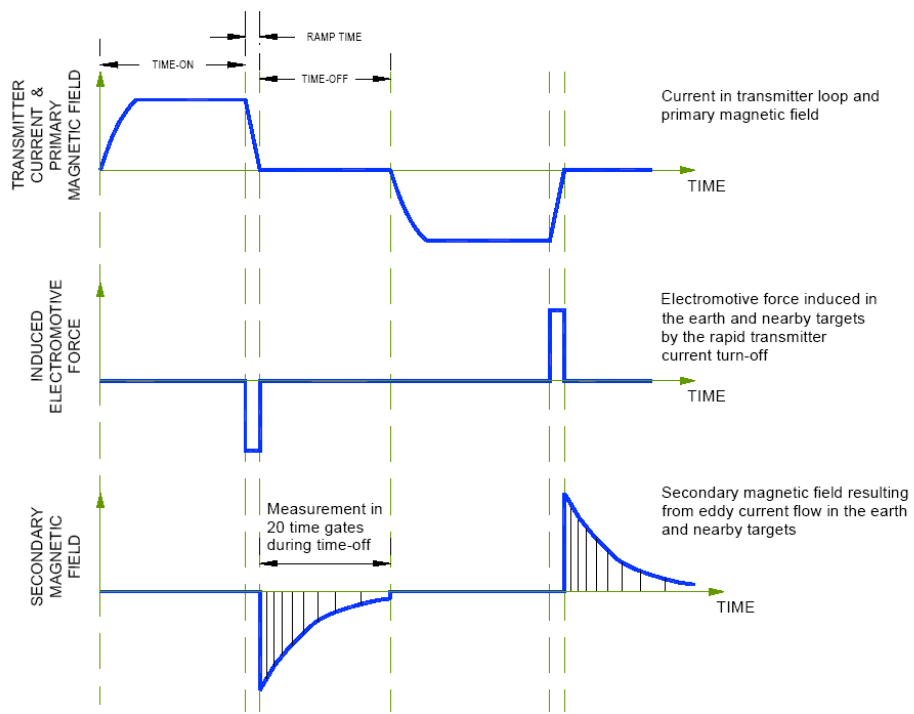


Figure 15.23: TDEM measurement principles, part 1

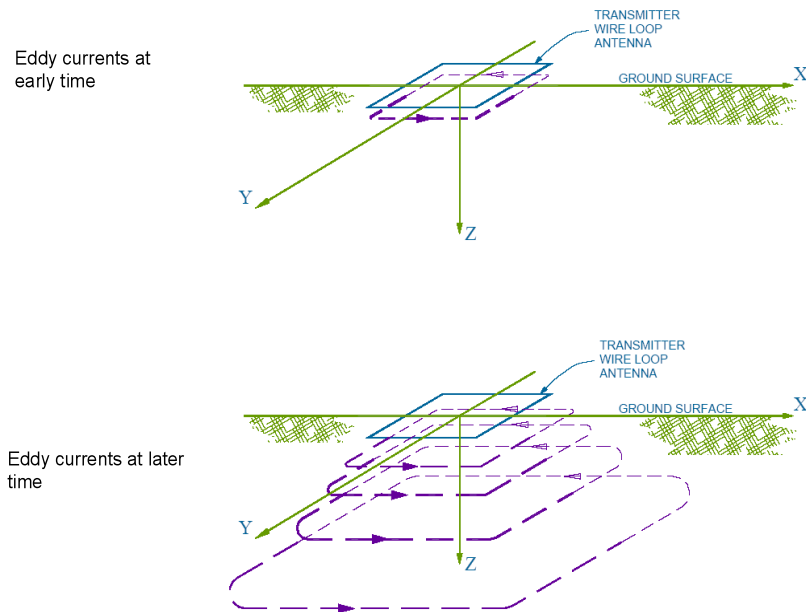


Figure 15.24: TDEM measurement principles, part 2

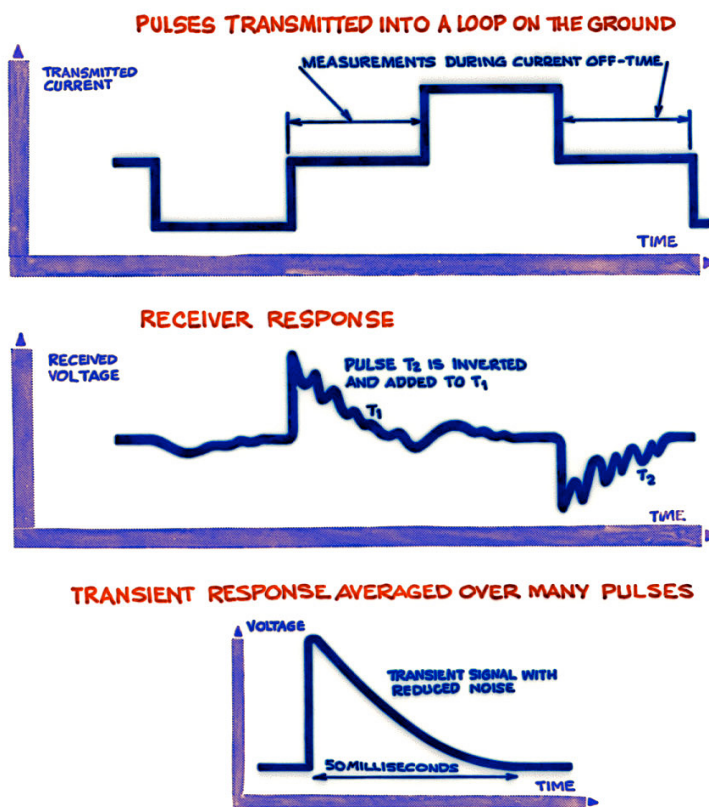


Figure 15.25: TDEM measurement principles - how stacking reduces noise

In general terms the decay curves from poor conductors have high initial amplitudes and decay rapidly. Those from good conductors have lower initial amplitudes but decay more slowly.

Just as with the FEM surveys, TEM surveys can be undertaken from the air, on the ground surface and down boreholes. For the down-hole surveys, the transmitting current loop is on the ground surface and the receiver coil(s) or magnetometer is down the hole.

Ground surveys can be undertaken with a fixed transmitter loop and a series of profile lines perpendicular to the main strike extent of the expected geological conductor.

Results show the received signal strength for each of the time delays recorded. (Early time data is at the top of the stacked profile display.) The anomalies due to the deeper targets will only appear at the late times. Nearby conductors will cause early time anomalies. Computer modelling can be undertaken to investigate what might give rise to the observed behaviour.

Computer modelling can also assist with determining whether the expected geological section will give rise to a TEM anomaly. In a country such as Australia where much

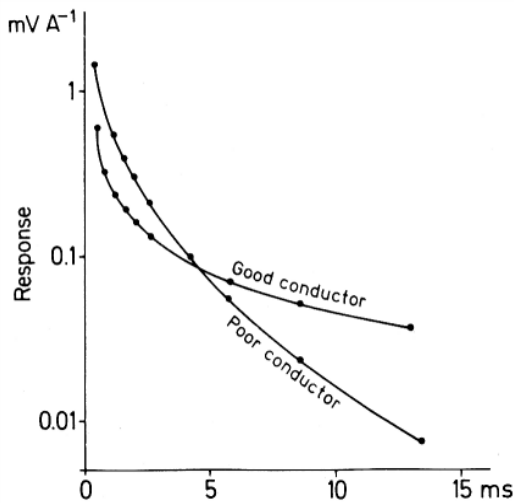


Figure 15.26: TDEM measurement principles - decay curves from good conductors decay more slowly than those from poor conductors

of the inland areas are covered by deep weathered zones (regolith) that are highly conductive, it may not be possible to get sufficient penetration to observe anomalies from the deeper conductive target.

It is also possible to undertake soundings using TEM. The receiver loop is placed inside the transmitter loop.

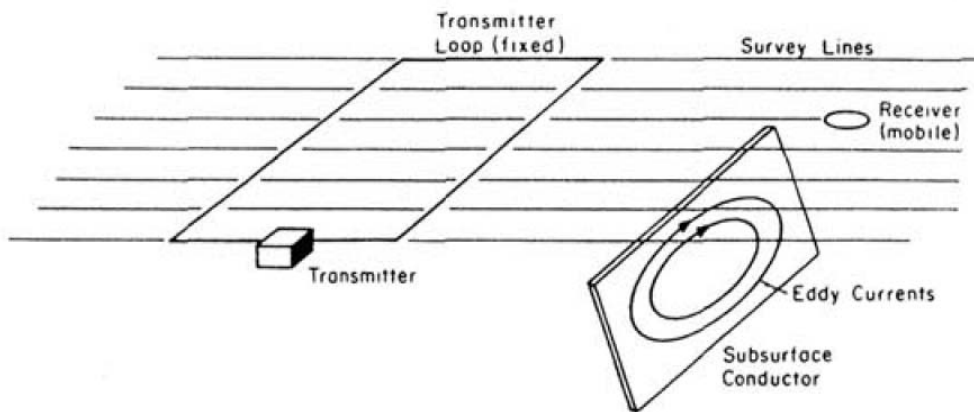


Figure 15.27: TDEM ground surveys

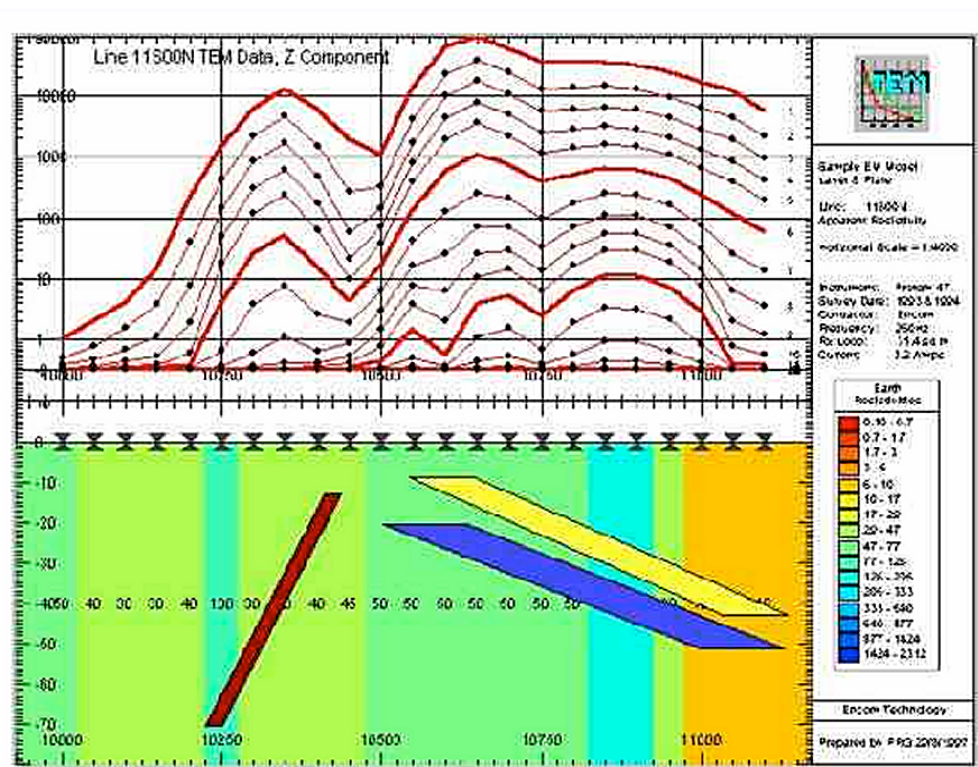


Figure 15.28: Computer modelling of TDEM data

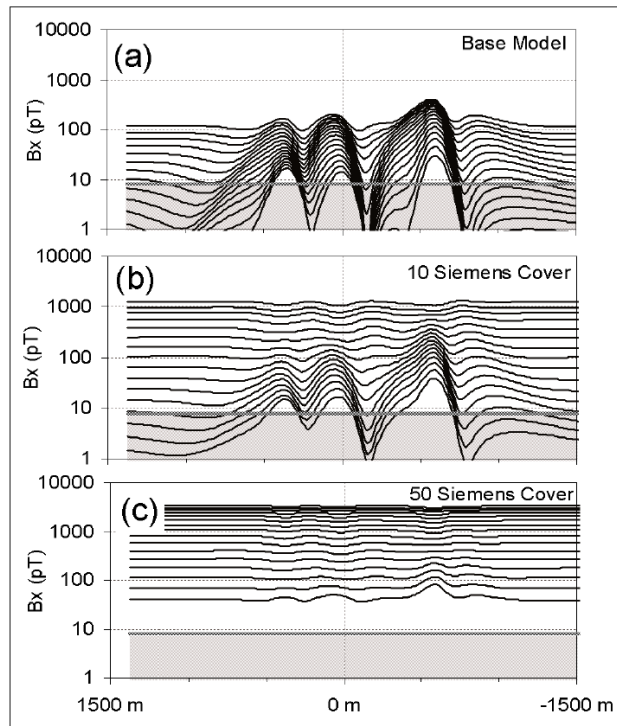


Figure 15.29: A thick, conductive weathered layer can prevent data being obtained from a deeper metallic ore body

Borehole TEM produces results similar to ground profile TEM.

Airborne TEM utilises a current loop can be strung around the wings and fuselage of a fixed wing plane or a loop slung below a helicopter. The receiver, typically a triaxial coil arrangement is towed behind the aircraft.

In addition to applications in the search for conductive ore bodies, airborne TEM surveying has found to be useful for the mapping of shallow ground water and salinity mapping.

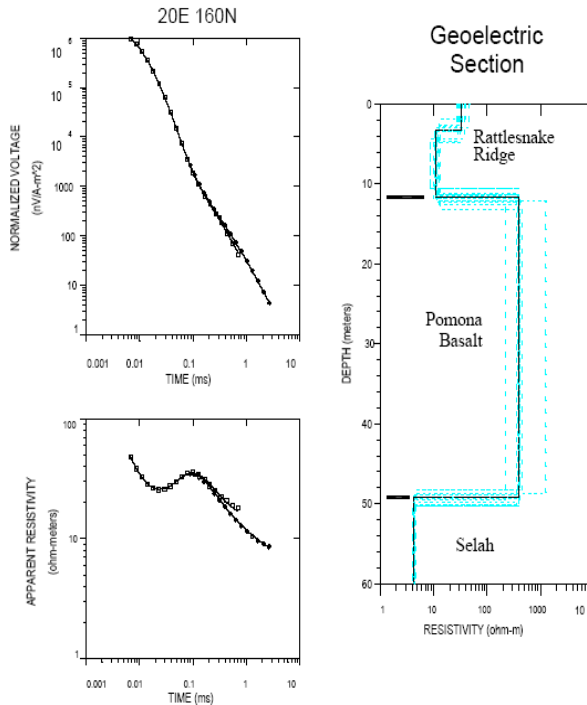


Figure 15.30: TDEM sounding

15.6 Radar and the radio imaging method

Up to this point, we have been considering the situation where a primary magnetic field induces current flow within the earth. However, for situations where the frequency of the magnetic field is much higher and the conductivity of the earth is relatively low, a coupled magnetic and electric field will propagate in the earth. Depending on the conductivity and the dielectric properties of the earth, this electromagnetic wave propagation can occur at frequencies greater than about 1 MHz with mixed current flow and electric field propagation occurring at frequencies in the high kHz range.

There are two electromagnetic methods of geophysics based on electromagnetic wave propagation. In the high kHz range, there is the radio imaging method (RIM). In the MHz range there is ground probing radar (GPR or simply radar).

Because of the lower frequency content, RIM needs to be applied in particularly resistive formations – e.g. coal seams and barren igneous rocks. The wavelengths are large (100's of metres) and so RIM surveys are usually based on tomographic principles and map out areas where differing rates of absorption are observed.

For the radar surveys, the velocity V and reflectivity R of the radar waves are given by:

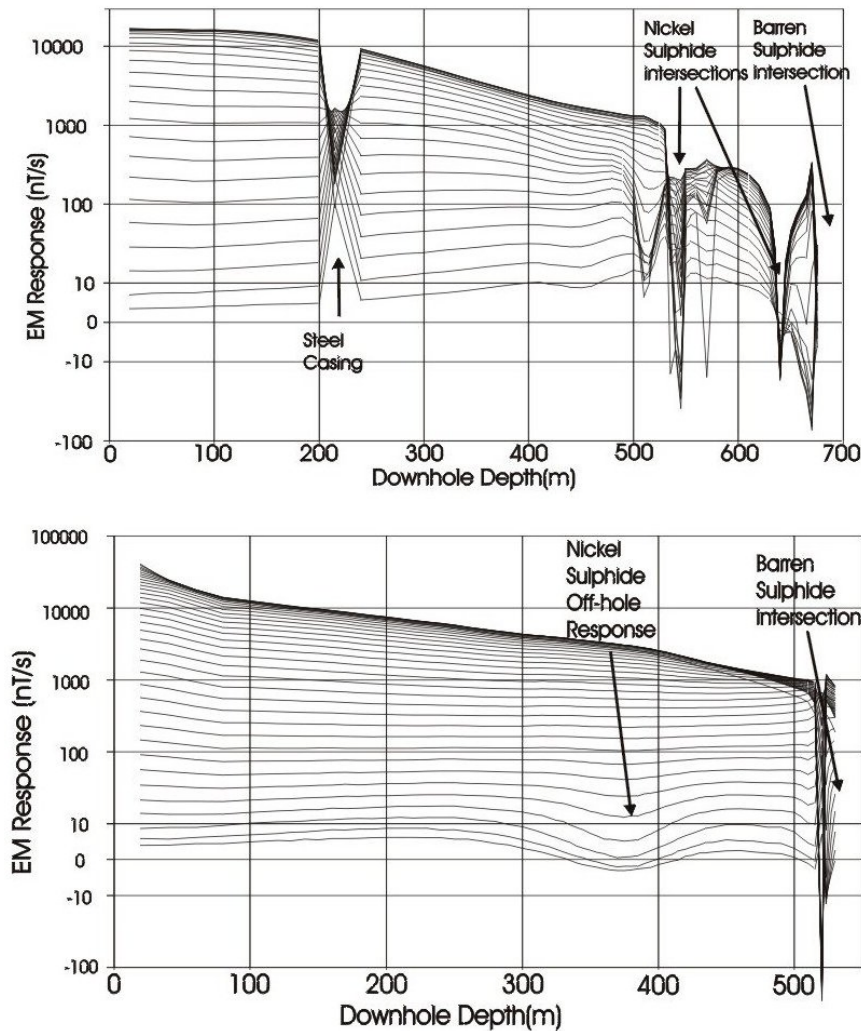


Figure 15.31: An example of TDEM results from a borehole

$$V = \frac{c}{\sqrt{\epsilon_r}}$$

$$R = \frac{V_2 - V_1}{V_2 + V_1} \quad (15.15)$$

where, c is the speed of light in a vacuum, ϵ_r is the relative dielectric constant and μ_r , the relative magnetic permeability is assumed to be 1. For most rocks, the relative dielectric constant is between 3 and 20 (it is 80 in water) and the speed of the radar

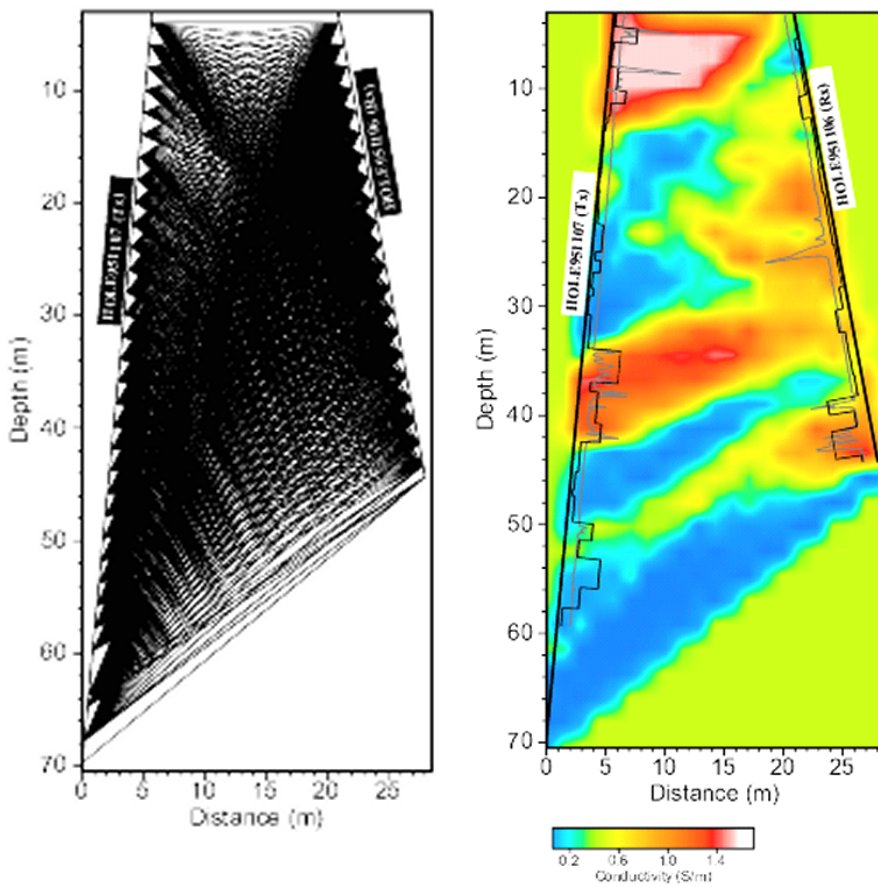


Figure 15.32: Left. Source to receiver raypaths for a cross borehole RIM tomographic survey. Right. tomographic result highlighting areas of strong wave attenuation which coincide with mineralized zones.

wave is therefore about 108 m/s (a third of the speed of light). The wavelengths will depend on frequency but are usually a few metres.

With such relative short wavelengths (a tenth of the seismic wavelengths), radar reflection surveys offer relative precise mapping of reflectors (contrasts in dielectric properties).

The transmitting and receiving antennas for use on surveys along the ground surface are usually bow-tie antennas which can transmit and receive over a relatively broad band of frequencies. For borehole work, the antennas are usually electric dipoles. GPR surveys are usually undertaken for near surface work (including archeology and forensic activities) and also in underground mining, where surveys can be undertaken away from the influence of conducting surface layers.

Figure 15.34 shows an example of a GPR section. Here the topography is not shown

| Material | Relative permittivity, ϵ_r | Conductivity, σ (mS/m) | Velocity (m/ns*) | Wavelength (m) | |
|--------------|-------------------------------------|-------------------------------|------------------|----------------|-------------|
| | | | | at 50 MHz | at 1000 MHz |
| air | 1† | 0 | 0.30 | 6 | 0.3 |
| water, fresh | 81 | 0.5 | 0.033 | 0.66 | 0.033 |
| water, sea | 81 | 3000 | 0.01 | 0.2 | 0.01 |
| ice, pure | 3.2 | 0.01 | 0.16 | 3.2 | 0.16 |
| clay, wet | 25–40 | 50–100 | 0.5–0.6 | 10–12 | 0.5–0.6 |
| granite | 4–6 | 0.01 | 0.1–0.12 | 2–2.4 | 0.1–0.12 |
| limestone | 4–8 | 0.5–2 | 0.1–0.12 | 2–2.4 | 0.1–0.12 |
| sand, dry | 3–6 | 0.01 | 0.15 | 3 | 0.15 |
| sand, wet | 20–30 | 0.1–1 | 0.06 | 1.2 | 0.06 |
| shale | 5–15 | 1–100 | 0.09 | 1.8 | 0.09 |
| silt | 5–30 | 1–100 | 0.07 | 1.4 | 0.07 |

Figure 15.33: Electrical properties of different rocks and other materials in the subsurface

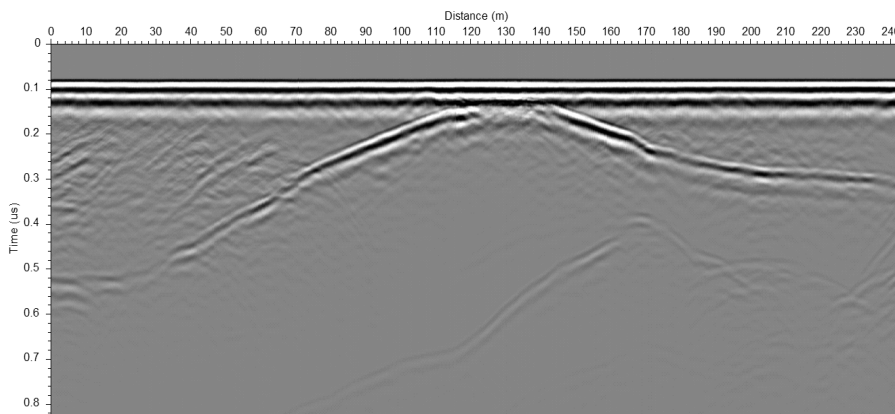


Figure 15.34: An example GPR result

but the survey crosses from the top of one sand dune to another. The reflector is the water table which is close to the surface at the point between the two dunes. The deeper reflectors may be due to reflections off surface features – trees etc. Radar antennas need to be shielded to reduce the occurrence of above ground reflections.

Chapter 16

Radiometric Methods

As we have previously learnt, radioactivity in rocks is due to the natural disintegration of atomic nuclei and the emission of:

- 1.) energy in the form of gamma radiation
- 2.) particles of mass in either the form of alpha particles (Helium nuclei) or beta particles (electrons).

Because the alpha and beta particles are easily stopped by even thin layers of materials (mm thickness), they have limited applications in exploration geophysics. Gamma rays, however, are a form of electromagnetic radiation and can travel a few hundred metres in air. Their frequency is about 10^{20} Hz. X-rays have frequencies of about 10^{18} Hz. Like X-rays, gamma rays can affect photographic emulsions, ionize gas and produce scintillations (phosphorescence) in some minerals and compounds.

Of the approximately 50 naturally occurring radioactive nuclei, the radioactive nuclei of most importance in geophysics are from the Uranium (two series from parents ^{238}U and ^{235}U) and Thorium (parent ^{232}Th). The most significant series is from ^{238}U . ^{238}U has a half life of 4.51×10^9 years and decomposes through a series of 17 unstable daughter products until the stable lead isotope, ^{206}Pb is reached. (Remember, the 238 in ^{238}U refers to the atomic weight – essentially the number of protons and neutrons.)

In addition, there are other naturally occurring isotopes. Of these, ^{40}K which has a half life 1.4×10^9 years is the most important.

Why are these the most important of the naturally occurring isotopes in geophysics? It is because their half-lives are of the same order as the age of the earth. Their emission can therefore be detected using radiometric surveys and ratios between parent and daughter produces form the basis of radiometric dating methods (e.g. K/Ar dating). Other naturally occurring isotopes such as ^{14}C (6 protons and 8 neutrons) which has a half-life of about 5,700 years is very useful for the age dating of 'young' material but of limited use in geological studies.

Radon (an inert gas) is a daughter product of the U and Th series and is soluble in water. Its presence can lead to environmental issues (cancers etc) when significant amounts of ^{238}U are present- e.g. with granitic bedrock.

The gamma rays emitted by radioactive decay are over a range of frequencies (or wavelengths), depending on the radioisotope.

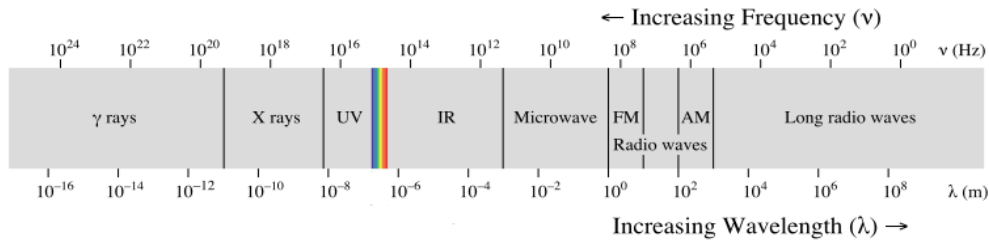


Figure 16.1: The range of frequencies over which gamma radiation is emitted

However, rather than speaking of the frequency or wavelength of the gamma radiation, it is conventional to speak of the energy of the radiation in MeV (Mega electron Volts). The energy is related to the wavelength to the photons of gamma radiation via Planck's constant, h and c , the speed of light = 3×10^8 m/s. (Planck's constant = 1.602×10^{-19} J)

$$E = hc/\lambda \quad (16.1)$$

In other words, the higher the energy, the shorter the wavelength.

The energy associated with our decay series of interest are between 0.1 and 3.0 MeV. Modern geophysical detection of natural gamma emissions records the energies of such a band, conventionally over 256 channels. Within this energy range, there are also windows over which a substantial amount of the radiation will be due to a particular component – Rn, K, U, Th. For geological interpretation, it is conventional to look at the radiation in the K, U and Th windows and interpret the results in terms of the relative abundance of these radioisotopes.

A basic sensor for the detection of gamma radiation is the Geiger counter. It consists of a glass tube containing an ionizing gas (e.g. argon and a pair of electrodes across which a high potential difference is maintained. Gamma rays passing into the tube produce ions which are accelerated by the field to produce a momentary current which is detected and can be shown on a meter or registered by an audible click. A Geiger counter is not able to provide spectral information on the incident gamma radiation.

Scintillation meters (scintillometers) are another form of detector. The basis for these is that they utilise a crystal of material such as sodium iodide which phosphoresces when struck by gamma radiation. A photomultiplier detects the emission of light and hence the gamma radiation. The number of light flashes can be counted over a period of time to give the total counts. In addition spectral measurements are possible because the intensity of the light depends on the energy (frequency) of the gamma radiation.

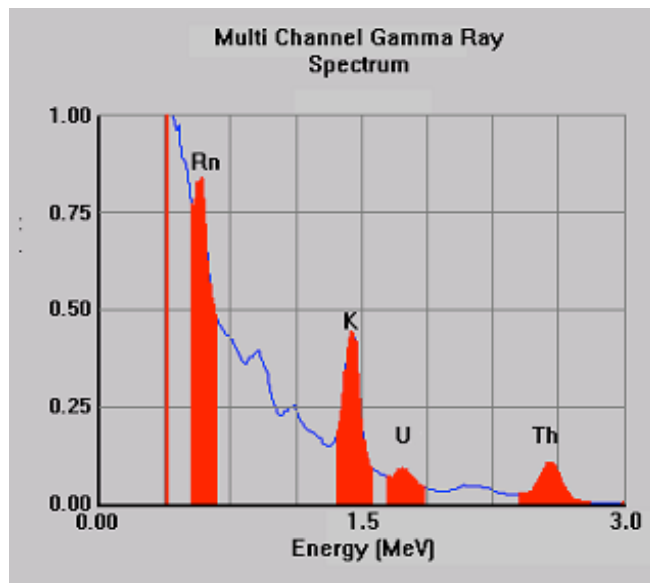


Figure 16.2: Multi Channel Gamma Ray Spectrum

The emission of gamma radiation for any particular rock is not constant and as a result there is statistical noise associated with any measurements. To improve the quality of a result, larger crystals can be used (more gamma rays will be encountered) and measurements can be taken over longer periods of time. NaI crystals are also fragile so instruments have to be treated with care. As an alternative, solid state detectors made of germanium can be used.

For minerals exploration and geological mapping, radiometric surveys are often undertaken as part of an aeromagnetic survey. Radiometric results are usually provided together with magnetic results in the form of maps of the ground surface. Remember, there is little penetration of gamma radiation through earth materials, so the radiometric survey will only be mapping the radiation due to the immediate ground surface.

Processing of radiometric data also needs to be undertaken prior to the provision of radiometric maps. The main processing steps involve noise removal, elevation corrections and the separation (stripping) of the contributions from the different decay series. Normalisation of the results from individual spectral windows against the total counts observed at each survey point also assists with managing elevation effects and the variations in radiation levels due to changes in the surface vegetation.

For interpretation, results are often presented as images of total counts, as images for each of the K, U and Th windows and as false colour images where the three windows are attributed to the red, green and blue channels.

Radiometric surveys are particularly useful for mapping changes in soil type which can be attributed to the properties of the underlying rock units. Transported soils may not provide any indication of the underlying geology. The above example shows

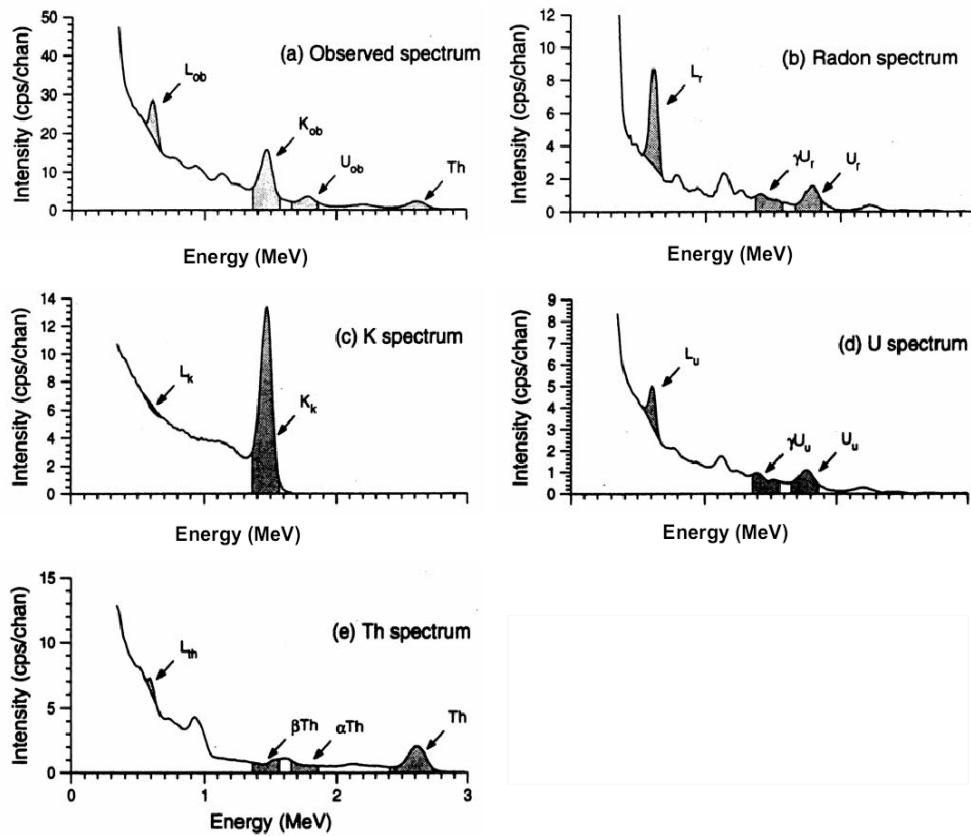


Figure 16.3: Example of processing to strip out the spectra for the different decay series

changes in survey results due to the change in rock type from sandstone to claystone (bottom right corner). The following example is from an arid region and shows how it is possible to resolve quite complex geological conditions.

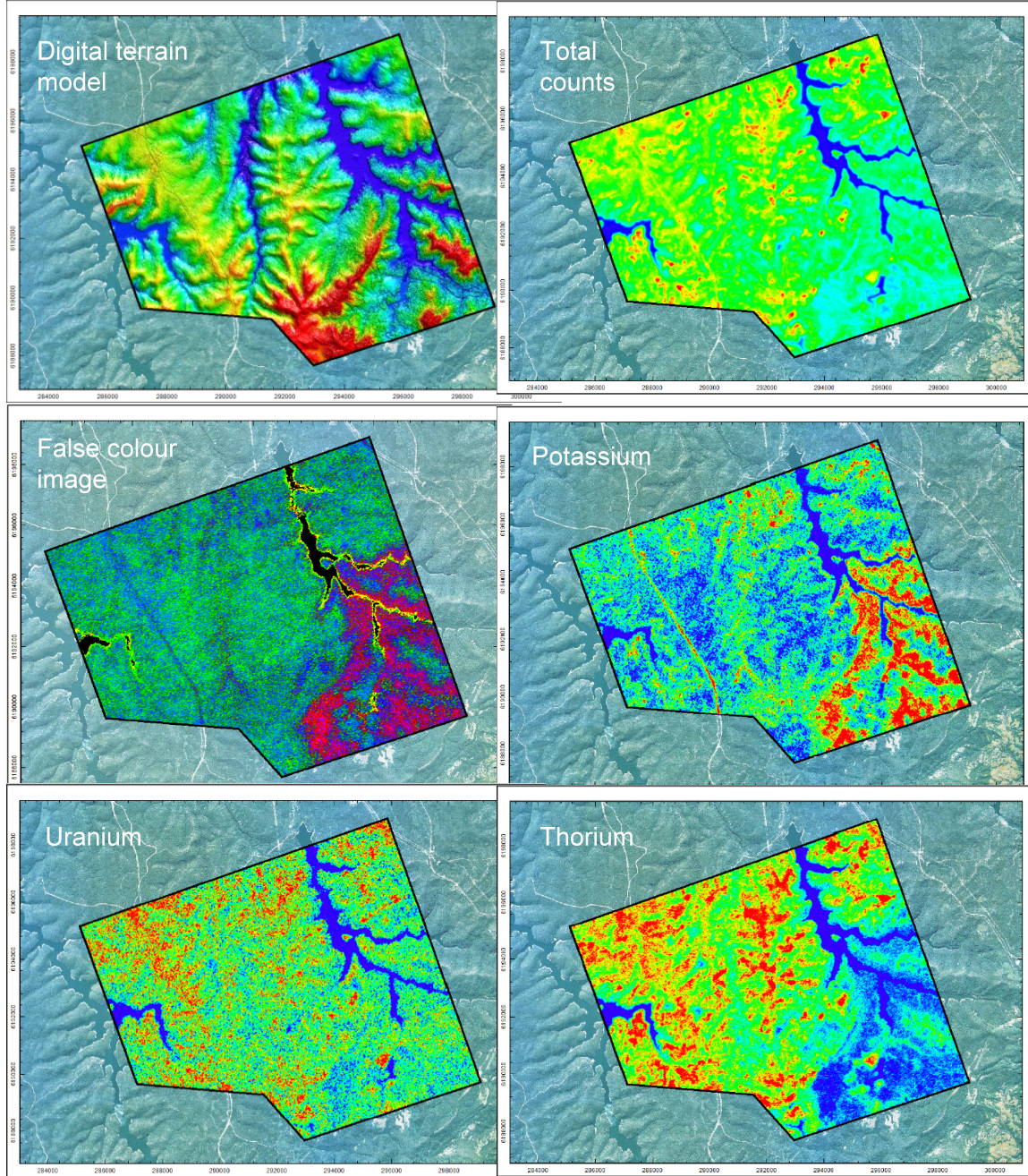


Figure 16.4: Example radiometric survey data

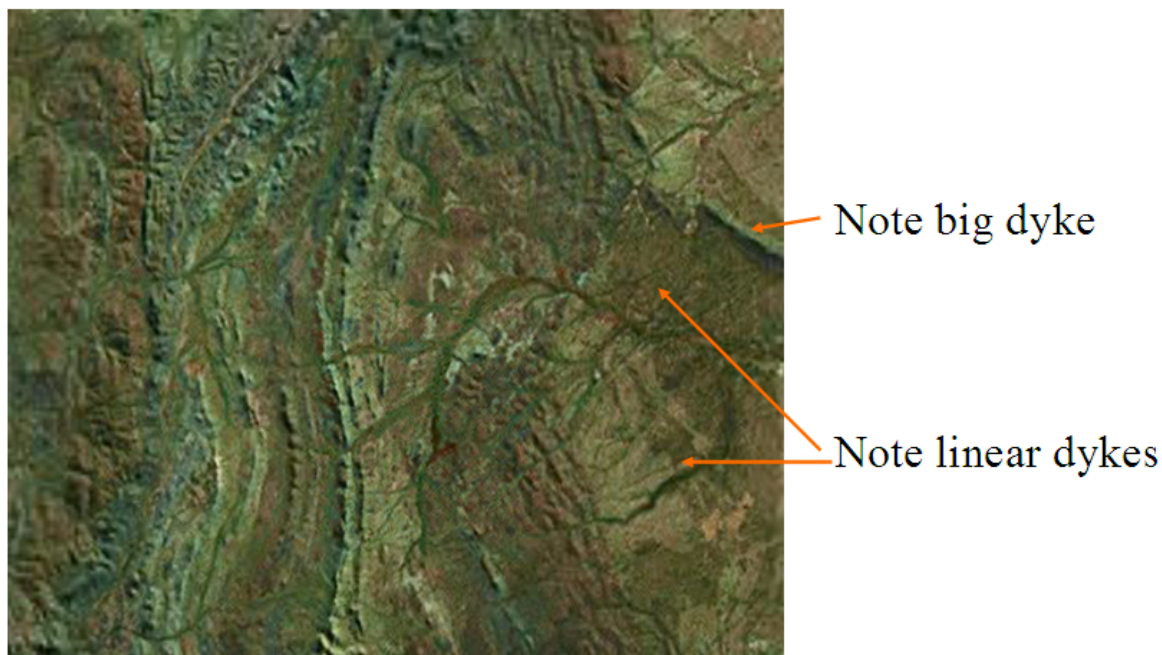


Figure 16.5: Aerial Photograph

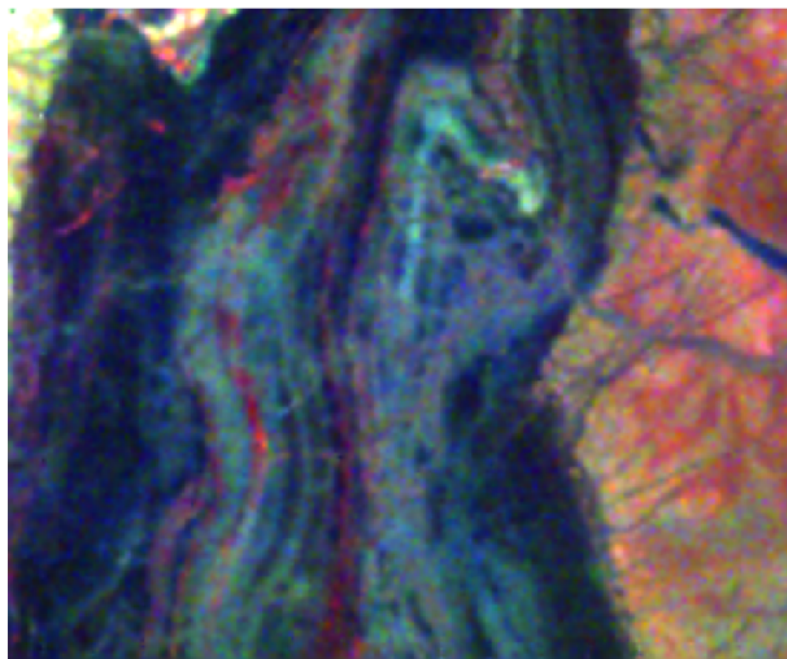


Figure 16.6: Radiometric results (false colour image)

Chapter 17

Seismic Reflection Method

17.1 Introduction

Seismic prospecting is essential for petroleum exploration, as a means to image geological structures by means of elastic waves. The idea involved is to create artificial shock waves and deploy a set of geophones in the best position to record the seismic waves after they have travelled through the a section of the Earth. The aim is to determine the depth and geometry of boundaries, such as interfaces between stratified layers, or edges of bodies such as reefs and salt diapirs, or fault positions or other irregularities, by means of the seismic velocity contrasts and scattering properties.

17.2 Acquisition of marine seismic reflection data

17.2.1 Determining location

The objectives of a seismic survey vary tremendously from surveys having very shallow objectives to those having deep objectives in difficult areas, the scale of seismic equipment varies. Of first importance is determining where data are acquired. To locate the traces to be combined in common-mid point stacking, surveying has to be more accurate than formerly required. Locating positions at sea where there are no landmarks depended mainly on radio-positioning and satellite observations, with reliance on the Global Positioning System.

Marine seismic navigation involves two aspects: (a) placing the ships at a desired position and (b) determining the actual location afterwards so data can be mapped properly. The accuracies obtained in a survey depend upon the system and equipment used, the configuration of reference (shore) stations, the position of the mobile stations with respect to the reference stations, variations in the propagation of radio waves, instrument malfunction, operator error, etc. Navigation systems can be classified according to the way the location are determined:

- piloting – location is determined with respect to known locations;

- dead reckoning – locations are determined with respect to a known starting point and known course;
- celestial measurements based on altitudes of the Sun or stars at known times;
- transit satellite positioning; and
- Global Positioning System (GPS).

Commonly Doppler sonar, gyrocompass and satellite navigation are combined in order to give a more accurate positioning. The satellite gives the periodic updating information needed to maintain Doppler-sonar accuracy, whereas the Doppler-sonar along with the gyrocompass and/or radio systems give the velocity information needed for an accurate satellite fix. Translocation (differential GPS) can be used to improve accuracy of satellite location determination. In differential GPS readings at a fixed second receiver up to 500 km away are utilized can remove short-term satellite perturbations, reaching 2 to 5 m accuracy.

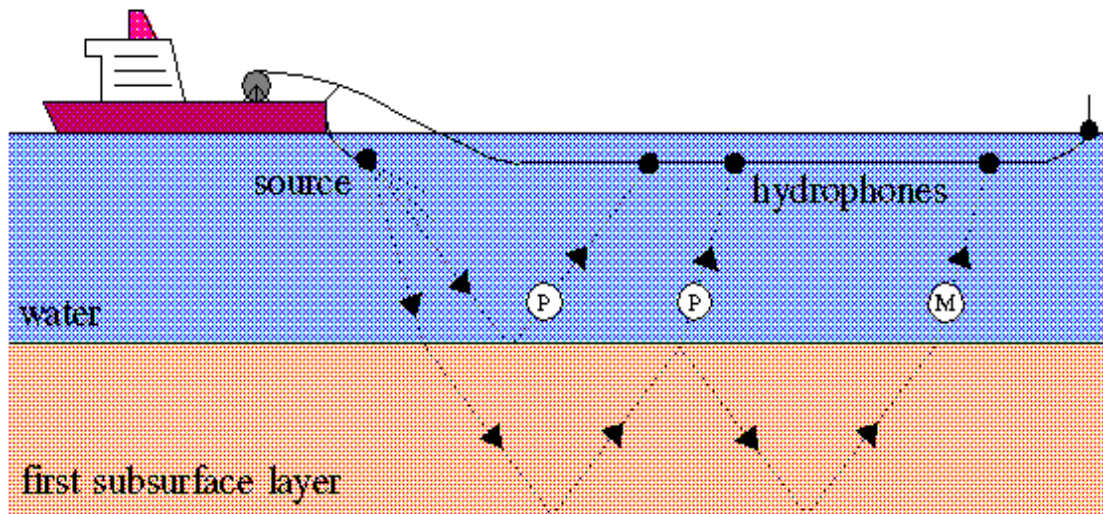


Figure 17.1: Schematic drawing of a marine seismic acquisition.

A seismic ship usually tows one or more long streamers that may extend for 5 km or more behind the ship. Even though the location of the ship is known, the streamer can drift by appreciable amounts.

There is usually a tail buoy (Figure 17.2, the elements labelled 1 to 4) at the end of each streamer on which a GPS receiver is mounted so that its location is known in the GPS system being used to locate the seismic ship.

Magnetic compasses ("birds"), typically 8 to 12 in a 5 km streamer, are included within the streamer. The readings from these are digitised and sent back to the ship.



Figure 17.2: Tail buoys ready to be deployed for a marine seismic reflection survey.

High-frequency pingers (see Fig. 17.3) are incorporated in the system, when more than one source or more than one streamer are employed, to locate the sources and streamers with respect to the ship and to each other, as in 3-D seismic acquisition. High-frequency water-break detectors are also included within the streamer; these measure the channel wave which travels in the water layer at the speed of the sound in water and thus give the distance from the seismic source.



Figure 17.3: Bird (red) and pinger (green) attached to a streamer.

17.3 The reflection method

We follow the assumption that we can image a +/- horizontal “layercake” of sediments or other rock layers by P-waves from a surface energy source, which are nearly normally incident on the interfaces between these layers. The P-waves are reflected at these interfaces, and recorded close to the source by a geophone or hydrophone. Because the rays are very close to normal incidence, virtually no S-waves are generated. The amplitudes of normal incidence reflections are much smaller than those of wide-angle reflections or refractions. Hence the records are obscured by background noise and sophisticated filtering and enhancement techniques have to be used to detect reflecting horizons.

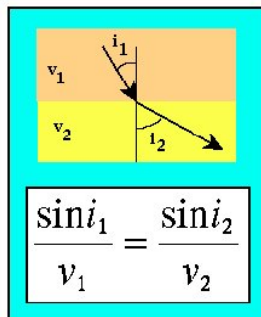
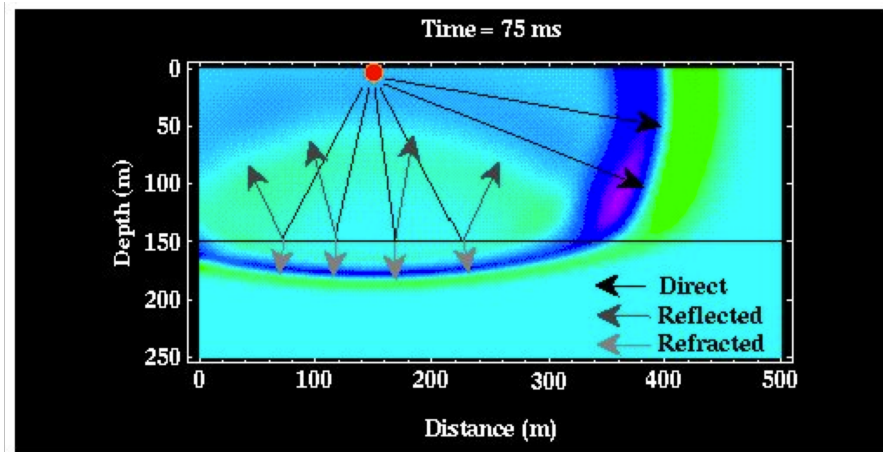


Figure 17.4: Snell’s Law.

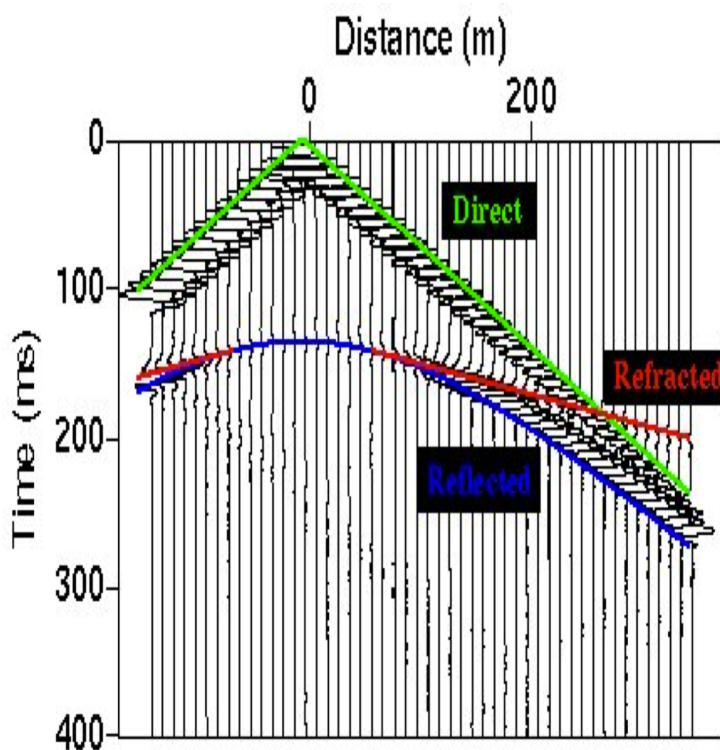
17.3.1 Finite resolution

The resolution of reflection seismology is limited by the physics of the experiment. The *smallest vertical separation between two objects* that can be measured is about *a quarter of a wavelength*. Thus the higher the frequency content of a seismic signal, the greater the vertical resolution. *Vertical resolution decreases with depth* because the *high-frequency component of the seismic signal is preferentially absorbed by frictional energy loss* caused by small-scale motions of grains and crystals as the seismic wave passes through the Earth. The dominant bandwidth of reflections from the middle to lower crust is often decreased to about 20 Hz from an initial 30-40 Hz. Layers thinner than about one-quarter wavelength cannot be individually distinguished.

Horizontal resolution also decreases with depth, but for a different reason. Seismic waves spread in geological structures in three dimensions in much the same way as a ripple spreads in two dimensions from a pebble dropped in a pond. The wavefront is approximately straight within the *Fresnel zone*. The first Fresnel zone is that part of the reflecting interface which returns energy back to the receiver within half a cycle of the first reflection.



(a) Time travel curve 1



(b) Time travel curve 2

Figure 17.5: Travel-Time Curves.

Figure 17.6 shows how a spherical wave from a point source is reflected from a plane interface (from Fowler, 1990). Because the wave must travel from source to interface and back to the receiver, energy from the wavefront one-quarter of a wavelength behind the first wavefront when reflected back to the receiver is delayed by half a cycle (a). The width of the first Fresnel zone can be calculated by applying Pythagoras' theorem to the right triangle SOQ (b); d is the depth of the interface beneath the source, and λ the wavelength of the signal. The upper material is assumed to have constant P-wave velocity a_1 .

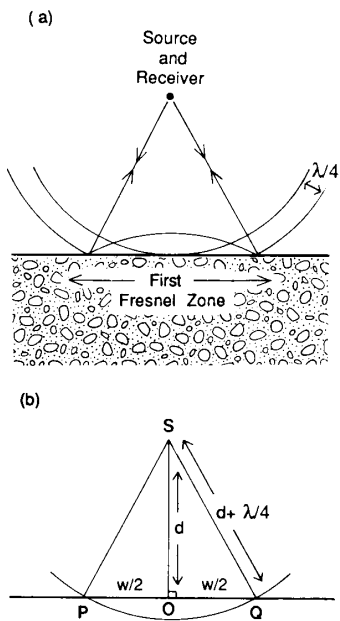


Figure 17.6: Reflection of spherical wave from a point source from a plane interface (from Fowler, 1990).

The first Fresnel zone is circular, the second one is a ring around the first zone from which the reflected energy is delayed by one-half to one cycle. Equivalently, a third, fourth, fifth etc. Fresnel zone exists. The seismic response from the entire area contained within the first Fresnel zone, often referred to as *the* Fresnel zone, adds up to yield a single response; any inhomogeneities within the Fresnel zone are smoothed out.

The Fresnel zone is smallest - hence resolution is best - close to the seismic source, but it increases to a couple of kilometres in the middle crust. Two objects closer than this resolution limit cannot be imaged separately, while an object smaller than this limit cannot be seen clearly and appears on the seismic section as a characteristic *diffraction hyperbola*, a convex-upward hyperbola with its apex at the object.

17.3.2 Recording design

In principle a seismic signal can be produced by a single source, and recorded by a single receiver. However, a single source often limits the depth of penetration and the strengths of the primary recorded signals. The use of multiple sources and multiple receivers overcomes this problem

(Fig. 17.7).

The ships used for marine seismic acquisition are usually large, 30 to >100 m and 5 to 40 m in beam (Fig 17.10). There is usually a platform on which a helicopter can land. It is generally equipped with a number of radio satellite and navigation aids for communication and positioning. The ship's speed while acquiring data is usually 5 to 6 knots (2.5-3 m/s or 9-11 km/hr).

It tows one or several air guns or water guns, which create a water pressure signal which travels through the water and into the sediments and/or crust. A hydrophone streamer is towed which consists of a number of sections. The total number of sections

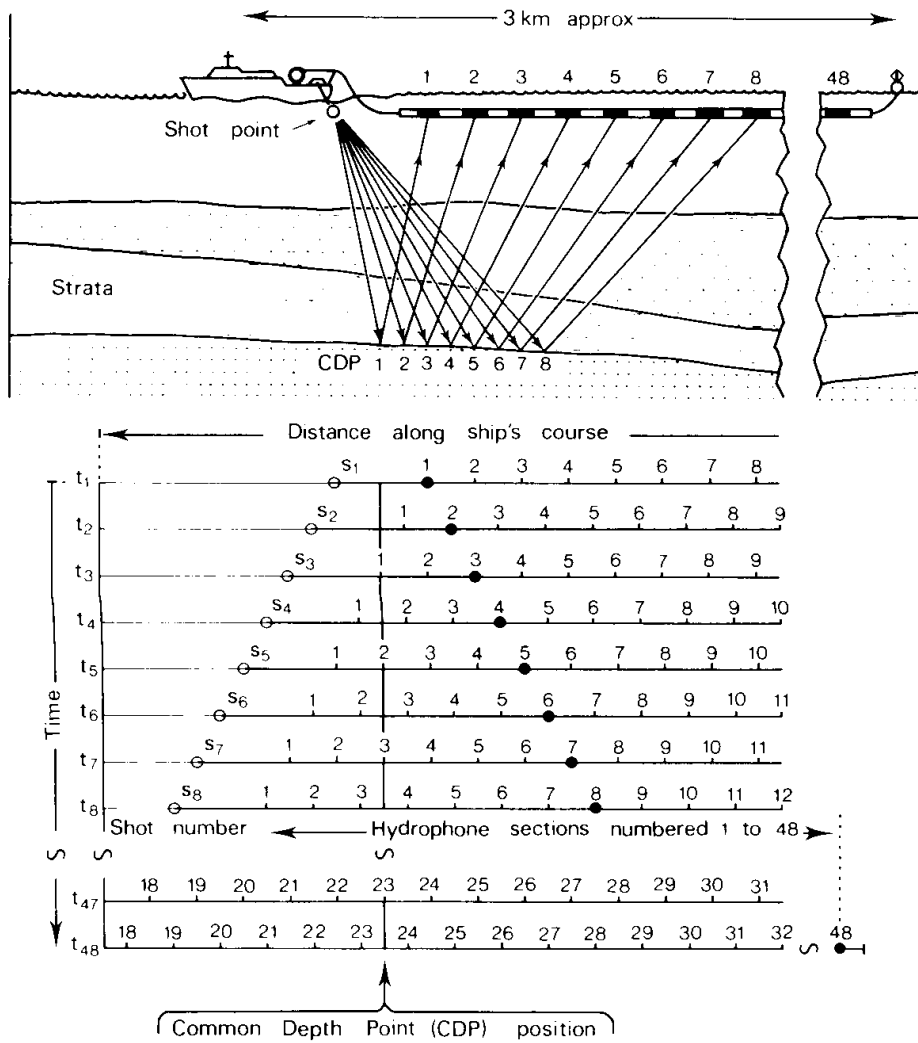


Figure 17.7: A typical layout of marine multichannel acquisition system. From McQuillin, Bacon, and Barclay, 1984

can range between 6 to 96 or even more. Each section includes a group of hydrophones, which are basically water pressure detectors. Signals in each section are summed so that each section can be regarded as an individual signal detector. While the ship is moving and creating sound signals, sound is reflected off identical points and recorded by consecutive sections of the streamer. These so-called common depth points or CDP's are used to stack all data that were reflected off these points to reduce noise.

New methods: the development of the Vertical Cable acquisition system is a joint venture between PGS and Texaco. It was developed for enhanced depth imaging of

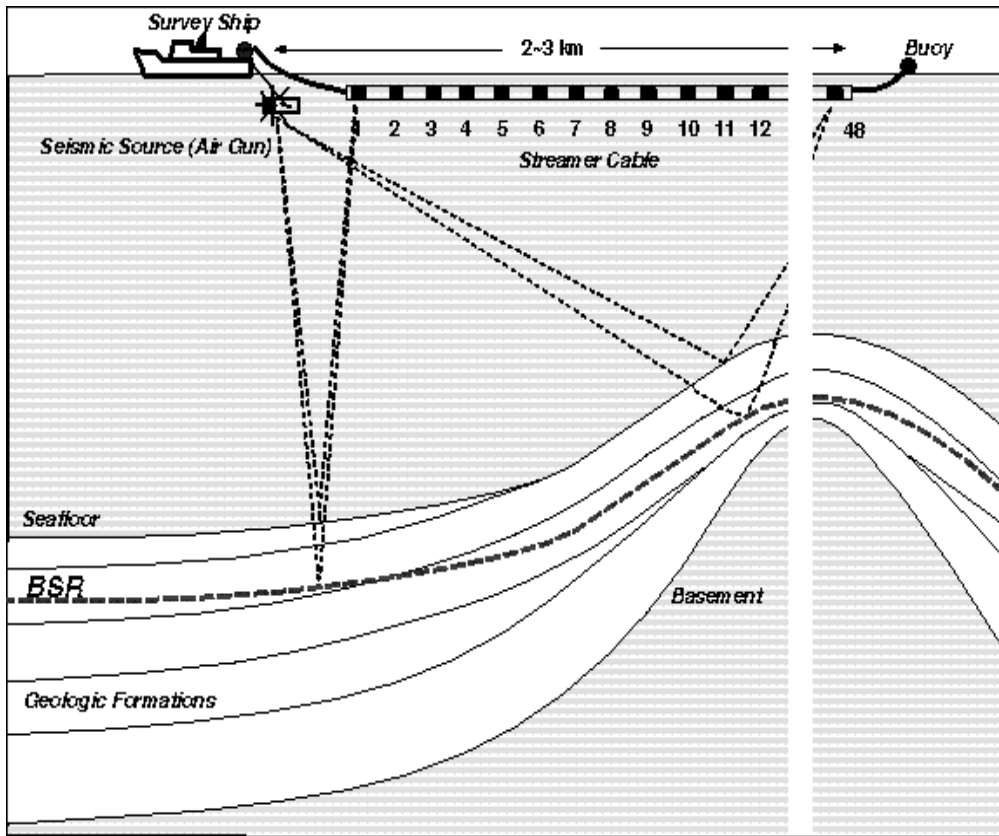


Figure 17.8: Bottom-simulating reflectors (BSRs). Traditional signature for gas hydrates in a seismic profile. The reflecting layer roughly parallels the seafloor and marks a transition in the velocity of reflected sound waves as they pass through icy gas hydrates to sediments below that contain “free” gas

structurally complex areas. The cable design allows complete flexibility in azimuth and offset distribution and with respect to both hydrophone spacing and cable separation.

In this acquisition method, each hydrophone cable, consisting of 16 hydrophones, is suspended in the water column by a floating element at the top and anchored at the sea bottom. The cables are deployed in a grid fashion with a cable separation ranging from 700-1800 meters, depending on water depth and depth to target. A link cable connects each vertical cable to a recording buoy containing the instrumentation for recording the data. The method offers virtually unlimited scope for survey planning in terms of acquisition geometry. The system is designed for smaller 3D surveys and is an attractive high-density acquisition alternative with respect to both cost and data quality. The systems needs a minimum water depth of 70-80 meters, but can go as deep as 1500-2000 meters.

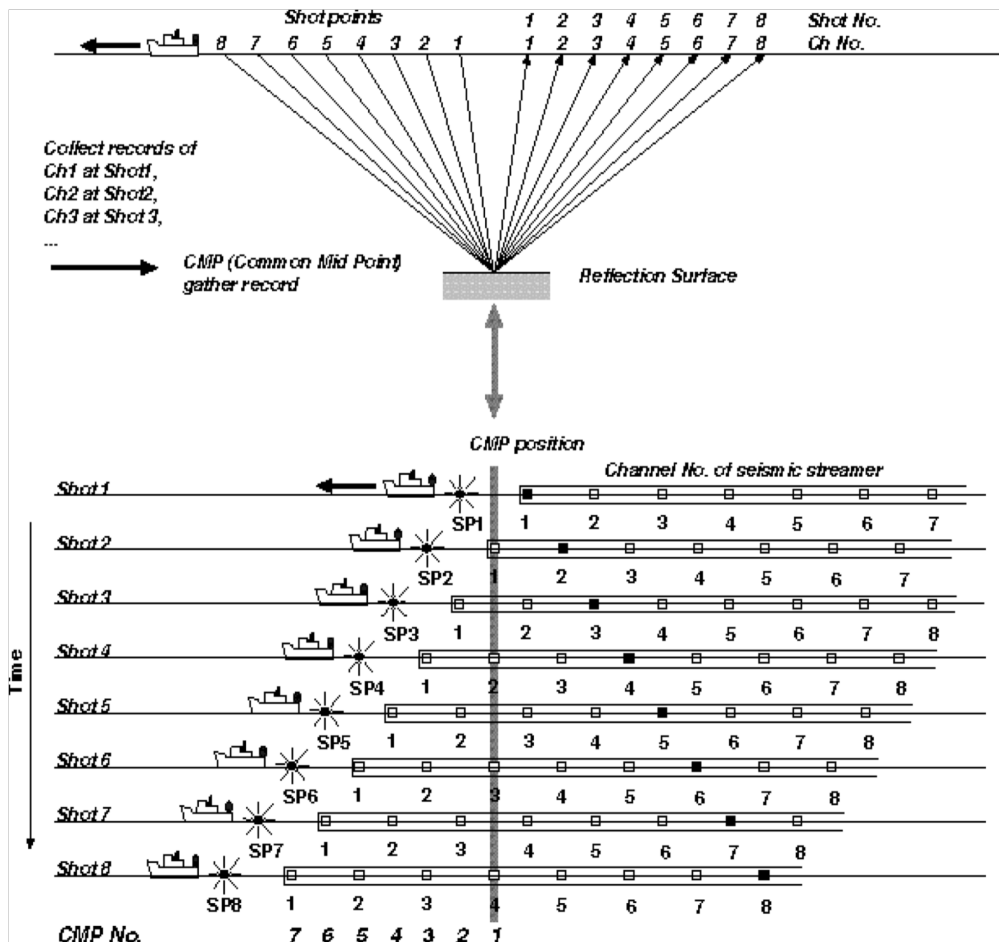


Figure 17.9: Common mid-point concepts

17.3.3 The seismic pulse

An ideal seismic pulse would be represented by a single spike, i.e. an instantaneous, short-period formation of high-frequency energy, decaying rapidly with minimum reverberation or development of source-generated interference. This is of course impossible to achieve in practice. The closer we get to this ideal, the higher is the frequency content of the seismic signal, and the higher the resolution of the recorded signal.

While the seismic pulse travels through the earth, it is attenuated in three ways:

- 1.) by absorption of energy through conversion into heat,
- 2.) by spherical divergence of the wave front, and
- 3.) by reflectivity losses at acoustic interfaces.

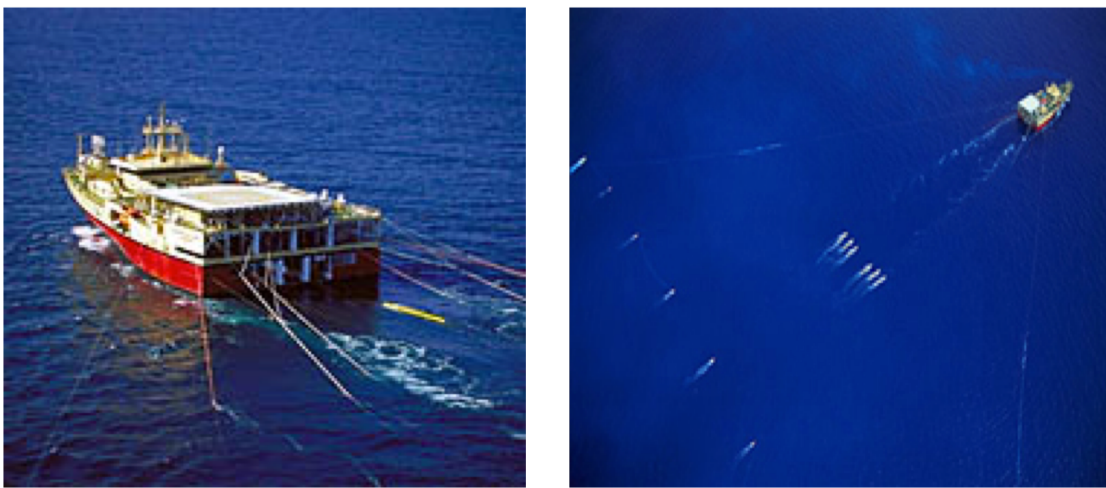


Figure 17.10: Seismic acquisition vessel of the Norwegian-based Petroleum Geo Services (PGS), one of the largest multinational acquisition and processing companies during collection of a marine seismic survey.

By these processes the amplitude is attenuated and the frequency band becomes narrower. Except for surveys of extremely high resolution, the frequency content of seismic signals is usually limited to 5-100 Hz. At depths of 3000 m or deeper, frequencies higher than 40 Hz are rare. Consider a 40 Hz wavelet, and a interval velocity of 3000 m/sec. The resolution is determined by the quarter-wavelength one-way width. In this case, this corresponds to about 19 m. Hence beds smaller than about 19 m would not be resolved at a depth where the frequency of the signal is limited to 40 Hz and lower.

17.3.4 Marine seismic sources

17.3.4.1 Introduction

How do we manage to create a seismic pulse close to a spike in water? It turns out that the main limiting factor for this purpose is the so-called bubble pulse. In water simple explosive sources generate an unwanted train of secondary pulses produced by multiple oscillations of a gaseous bubble. Right after the first pressure pulse is generated the bubble expands, but it implodes under hydrostatic pressure, the bubble compresses, and a new pressure wave is radiated. After multiple periodic oscillations the bubble breaks up due to either condensation or solution of the gases, or instability as it rises to the sea surface. Various schemes have been developed to counteract this phenomenon. The two marine sources most commonly used today are water guns and air guns. For low-energy, but high resolution seismic surveys, sparkers or boomer are also used. These four systems are described below.

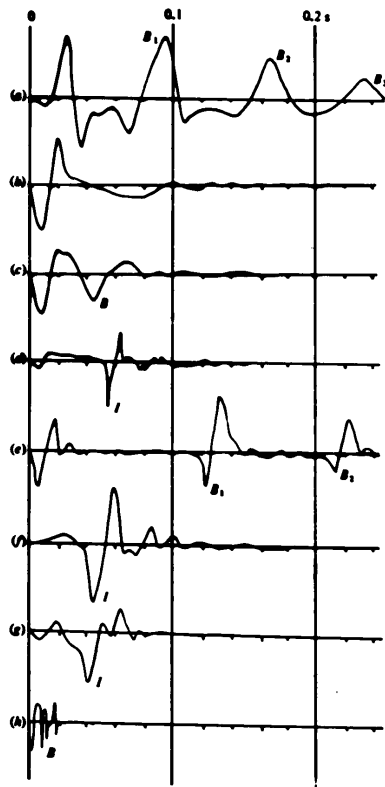


Figure 17.11: Far field wave shapes generated by marine seismic sources. The signals show features of waveshape, not true amplitude relationships. B indicates bubble effects.

- 1.) single 120in^3 airgun
- 2.) array of airguns of different sizes
- 3.) sleeve exploder
- 4.) Vaporchoc
- 5.) Maxipulse
- 6.) Flexichoc
- 7.) watergun
- 8.) 5 kJ sparker

All functions in the figure above represent *impulse response functions*, which depend on the mechanism used to create a pressure signal in water (i.e. injecting a pulse of

water, air, or electrical current into water). Complex mechanisms like the so-called “bubble pulse” result in severely altered signals compared with the initial single “pulse”.

17.3.4.2 Air gun

An air gun is composed of a system of two high-pressure chambers, which are connected and sealed by a double ended piston (Fig. 17.12). During one charging cycle, air is fed at high pressure into the upper chamber and bleeds through the hollow piston into the lower chamber. The piston is held in the closed position due to the air pressure, because the area of the trigger piston (top) is larger than that of the firing piston (bottom). To fire the gun, a solenoid valve is opened and a burst of high pressure air is delivered to the underside of the trigger piston. This produces a force that is large enough to overcome the force holding the piston. The piston shoots upward and releases the high-pressure air from the lower chamber into the water. Pressure in the upper chamber then drives the piston back, and a new cycle starts. Air guns range in size from 10 to about 2000 cubic inches (lower chamber capacity) and operate at pressures of 2000-4000 psi. Often arrays of several air guns are used. Air guns usually produce a bubble pulse, except for the so-called GI air gun, which counteracts the bubble pulse by a secondary explosion. The dominant frequency of the pulse depends on the energy, i.e. the product of the pressure and the volume of air discharged.

17.3.4.3 GI gun

The GI gun was developed to better control the bubble pulse produced by the conventional air gun. It consists of two guns in the same body: a Generator and an Injector. The generator produces the primary pulse, whereas the injector controls the oscillation of the bubble created by the generator. A gun phone triggers the time break and also permanently monitors the shape of the near-field signal. The GI gun can be operated in 3 modes:

- 1.) the “true GI mode” is optimally tuned to suppress the oscillation of the bubble as much as possible;
- 2.) in the harmonic mode the injection is detuned to adjust the oscillation of the gun in a desired manner. For example a reduced injection volume can be used to produce a signature with both a smooth and reduced oscillation with greatly improved primary-to-bubble amplitude ratio.
- 3.) In the third mode, both generator and injector are fired either separately, or simultaneously. In this mode the GI gun is acting just like a normal air gun, and depending on whether the generator and injector are fired together or not the gun volume varies from 45 in³ to 210 in³.

Mode 2 is often used, because even though the gun provides the cleanest pulse in true GI mode, its pulse is also weakest in this mode. Therefore mode provides the

best of both worlds in terms of a high amplitude pulse and a clean signal with reduced bubble pulse.

17.3.4.4 Water Gun

A water gun (Fig. 17.12) is basically a modified air gun in which a volume of compressed air drives a piston, which ejects water instead of air through the gun ports. When the motion of the piston stops, cavitation occurs, and the main acoustic energy is created by implosion of the water body through cavity collapse. No bubble pulse is produced, and the source signature is quite clean.

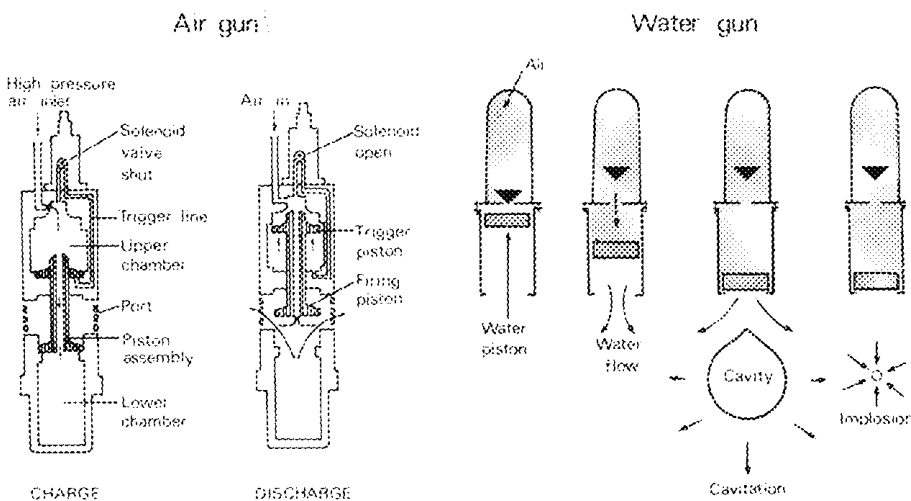


Figure 17.12: Air and Water guns

17.3.4.5 Sparker

In a sparker, acoustic energy is produced by electrical discharges in sea water. Generators are used to charge capacitor banks, which can then be triggered to discharge high voltage (3-10 kV) through spark tip arrays towed in the water. Low energy (100 J-5 kJ) sparkers are widely used in single channel seismic profiling as part of shallow geological and geophysical studies. High energy sparkers (200 kJ) are sometimes used for conventional seismic work.

17.3.4.6 Boomer

In a boomer two plates are forced apart suddenly by a heavy surge of electrical current through a coil on one of the plates that generates eddy currents on the other plate. A

boomer produces relatively little energy, and is only used for shallow, high-resolution seismic exploration.

17.4 Seismic data processing

17.4.1 Introduction

On land, the returning sound wave is recorded, in land experiments, usually by 60 to 240 groups each of 6 to 24 geophones stuck into the ground in a line that may extend between 6 and 20 km from the seismic source. When working at sea, a group of hydrophones is towed behind the ship in a tube or *streamer*. The streamer may contain 50 or 100 groups of hydrophones, and may extend to 3 or 4 km behind the ship.

The signals picked up by each group of seismometers are separately recorded on magnetic tape or in digital form aboard ship or directly at the bottom station. Because the reflected signals may be more than one million times weaker than the initial shock wave, complicated data processing is required to extract these tiny but real reflected signals from all the noise produced by wave action or the ship's propellers etc.

The other reason for applying computer processing is the amount of data recorded. In a typical deep profiling experiment, the airguns may be fired every 50 m along a 250 km profile; each shot is recorded by 60 groups of hydrophones; and the signal at each hydrophone group is recorded on magnetic tape 250 times a second for 15 seconds. These thousand million data samples require a large computer system for data processing.

17.4.2 Basic data processing sequence

Since the introduction of digital recording, a routine sequence in seismic data processing has evolved. There are four primary stages in processing seismic data. In their usual order of application, they are:

- 1.) Pre-processing
- 2.) Deconvolution
- 3.) Stacking
- 4.) Migration

17.4.3 Pre-processing

Field data are recorded in a multiplexed mode using a certain type of format. The data first are demultiplexed. Mathematically, *demultiplexing* is the transposing of a big matrix so that the columns of the resulting matrix can be read as seismic traces recorded at offsets with a common shotpoint. At this stage, the data are converted to a convenient format that is used throughout processing. This format is determined by the type of processing system and the individual company.

Pre-processing also involves *trace editing*. Noisy traces, traces with transient glitches, or monofrequency signals are deleted; polarity reversals are corrected.

A *gain recovery function* is applied on the data to correct for the amplitude effects of wavefront (spherical) divergence. This amounts to applying a geometric spreading function, which depends on travel-time, and an average primary velocity function, which is associated with primary reflections in a particular survey area. Additionally, an exponential gain function may be used to compensate for attenuation losses. As an option, it may be desirable to filter the data with a wide band-pass filter before deconvolution.

Finally, field geometry is incorporated with the seismic data. This may precede any gain correction that is offset dependent. Based on surveying information, *co-ordinates of shot and receiver locations for all traces are stored on trace headers*. Changes in shot and receiver locations are properly handled based on the information available in the observer's log.

17.4.4 Deconvolution

The step that follows pre-processing is *deconvolution*. Typically, *prestack deconvolution* is aimed at improving temporal resolution by *compressing the effective source wavelet contained in the seismic trace to a spike* (spiking deconvolution). *Predictive deconvolution* with a prediction lag (commonly termed gap) that is equal to the *first or second zero crossing of the autocorrelation function* also is commonly used. Deconvolution techniques used in conventional processing are based on optimum Wiener filtering.

Since spiking deconvolution broadens the spectrum of seismic data, traces contain much more high-frequency energy after deconvolution. Because both high-frequency noise and signal are boosted, the data often need *filtering with a wide band-pass filter* after deconvolution. It is important to note that *deconvolution assumes a stationary, vertically incident, minimum-phase source wavelet* and a "white" reflectivity series that is free of noise.

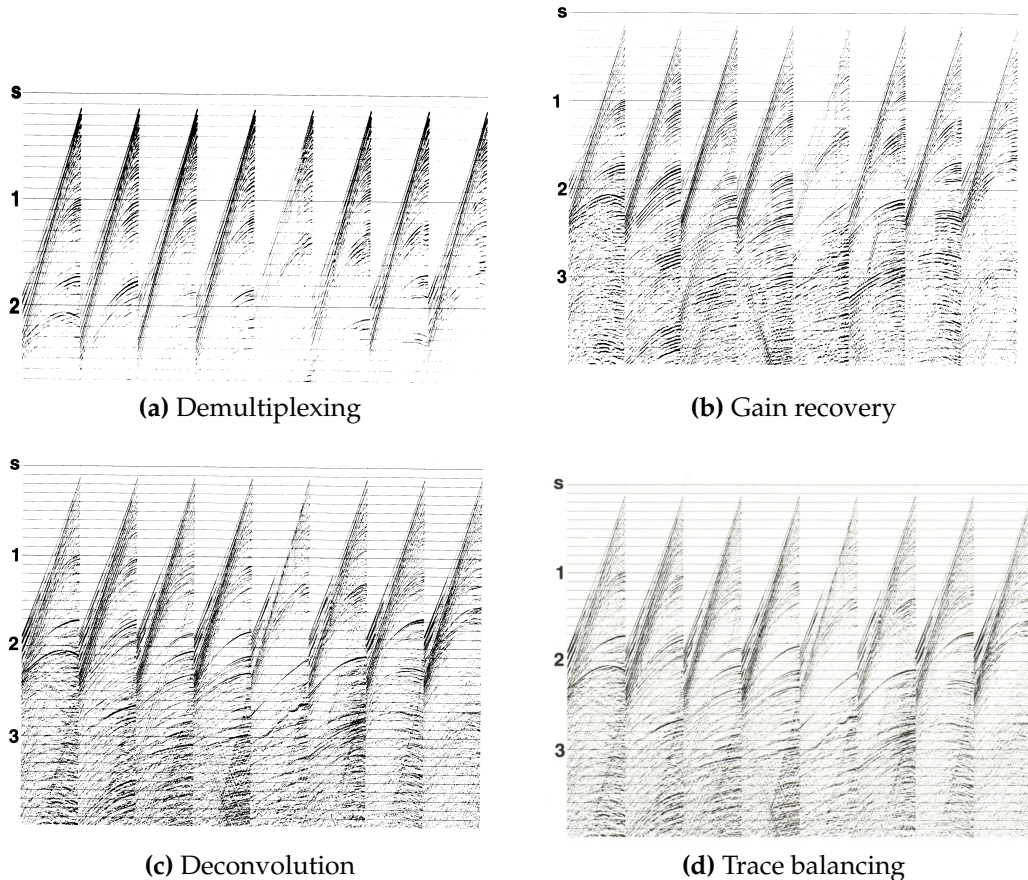


Figure 17.13: Pre-processing steps for seismic reflection data using data from an offshore survey. (17.13a) Common-shot gathers just after demultiplexing – Note the decay in amplitudes due to wavefront divergence. (17.13b) After correcting for the amplitude effects of wavefront divergence. (17.13c) After spiking deconvolution. (17.13d) After trace balancing. Balancing is a time-invariant scaling of amplitudes to a common rms-level for all traces.

17.4.5 CDP Sorting

After the initial signal processing (described above), the data are transformed from shot-receiver to midpoint-offset co-ordinates. This is called *CDP sorting* (the common depth point or CDP), which requires field geometry information. Sometimes this procedure is called Common Midpoint (CMP) sorting.

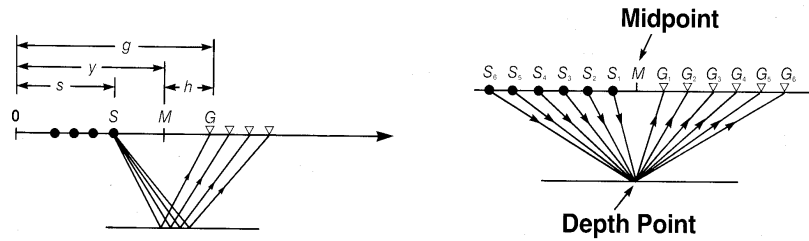


Figure 17.14: Schematic depiction of the recording geometry

In the processing operation, seismic signals recorded from rays incident at different angles upon a particular subsurface are combined to improve the signal-to-noise ratio by summing, and to cancel noise signals by destructive interference. This process is called *CDP stacking*. Though stacking is the single most important step in seismic data processing, many other computer processes are commonly used to remove noise or to increase resolution of the seismic data.

Seismic data acquisition with multifold coverage is done in shot-receiver (s, g) co-ordinates. On the other hand, seismic data processing conventionally is done in midpoint-offset (y, h) co-ordinates. The required coordinate transformation is achieved by *sorting the data into CDP gathers*. Each individual trace is assigned to the midpoint between the shot and receiver locations associated with the trace.

Those *traces with the same midpoint location are grouped together*, making up a CDP gather. The above figure depicts the geometry of a CDP gather. Note that CDP gather is equivalent to a CMP gather only when reflectors are horizontal and velocities do not vary horizontally. However, when there are dipping reflectors in the subsurface, these two gathers are not equivalent and only the term CDP gather should be used.

The CDP recording technique, which was patented in the 1950s, uses redundant recording to improve the signal to noise (S/N) ratio. To achieve redundancy, multiple sources per trace n , multiple receivers per trace n , and multiple offset coverage of the same subsurface point n 1, are used in the field. Given the total number of elements in the recording system, $N = n \cdot n \cdot nf$, the signal amplitude-to-rms noise ratio theoretically is improved by a factor of $N1/7$. This improvement factor is based on the assumptions that the reflection signal on traces of a CDP gather is identical and the random noise is mutually uncorrelated from trace to trace. Because these assumptions do not strictly hold in practice, the S/N ratio improvement gained by stacking is somewhat less than V-N. Common-midpoint stacking also attenuates coherent noise such as

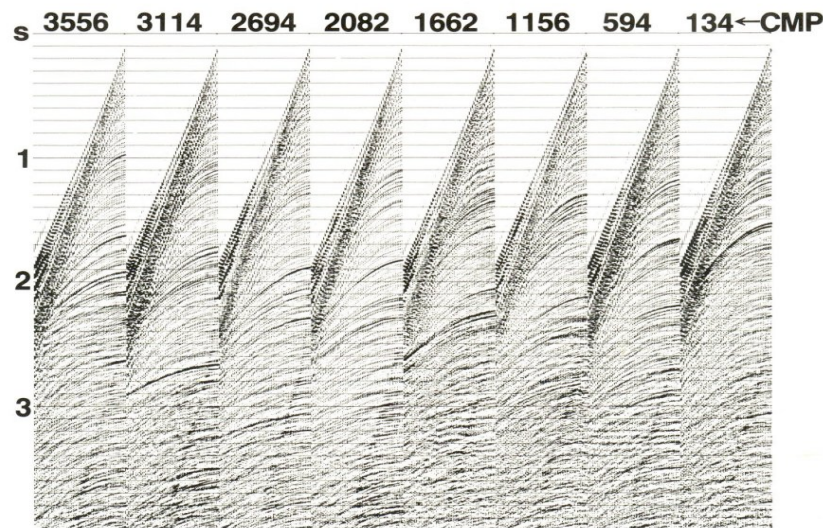


Figure 17.15: CMP gathers

multiples, guided waves, and ground roll. This is because reflected signal and coherent noise usually have different stacking velocities.

17.4.6 Velocity Analysis

In addition to providing an improved S/N ratio, multifold coverage with nonzero-offset recording yields velocity information about the subsurface. Velocity analysis is performed on selected CDP gathers (Fig. 17.16) or groups of gathers.

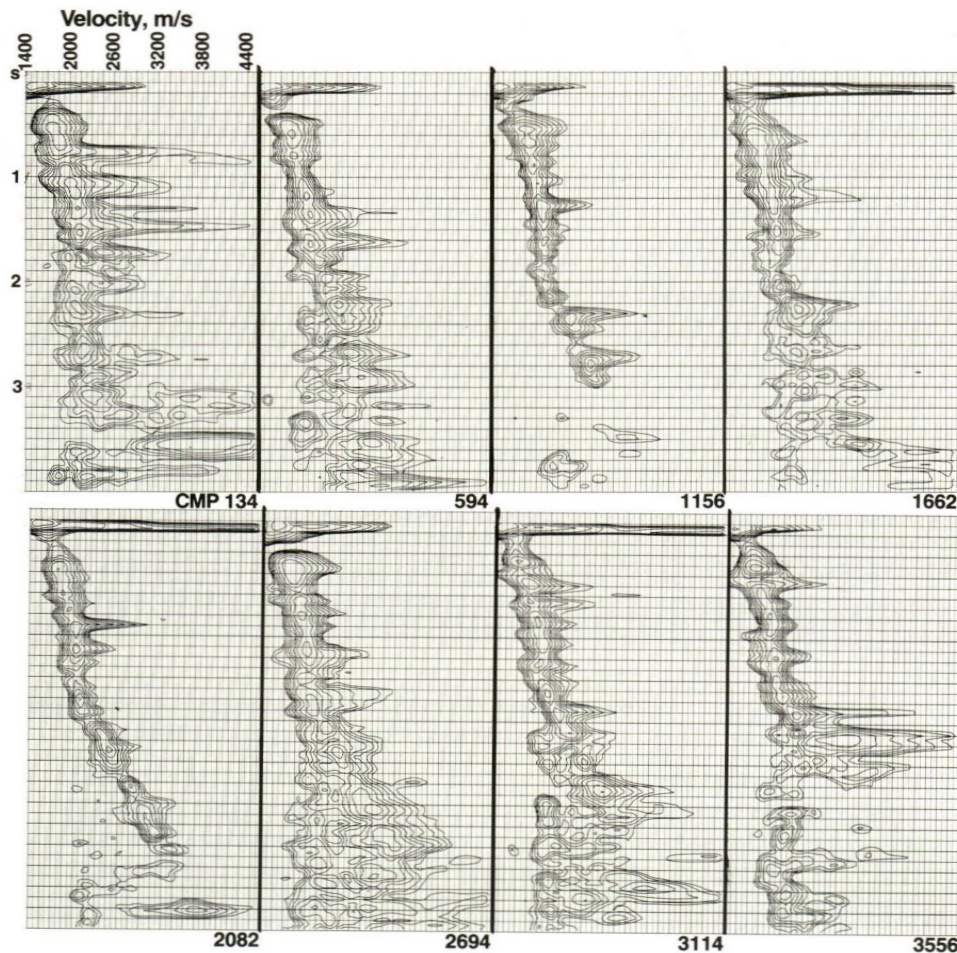


Figure 17.16: Velocity analysis of CDP gathers

The output from one type of velocity analysis is a table of numbers as a function of velocity versus two-way zero-offset time (velocity spectrum). These numbers represent some measure of signal coherency along the hyperbolic trajectories governed by velocity, offset, and traveltime.

In areas with complex structure, velocity spectra often fail to provide sufficient accuracy in velocity picks. When this is the case, the data are stacked with a range of constant velocities, and the constant-velocity stacks themselves are used in picking velocities.

17.4.7 NMO Correction and Stacking

The velocity field is used in **normal moveout** (NMO) correction of CDP gathers. As a result of moveout correction, traces are stretched in a time-varying manner, causing their frequency content to shift toward the low end of the spectrum. Frequency distortion increases at shallow times and large offsets (see below).

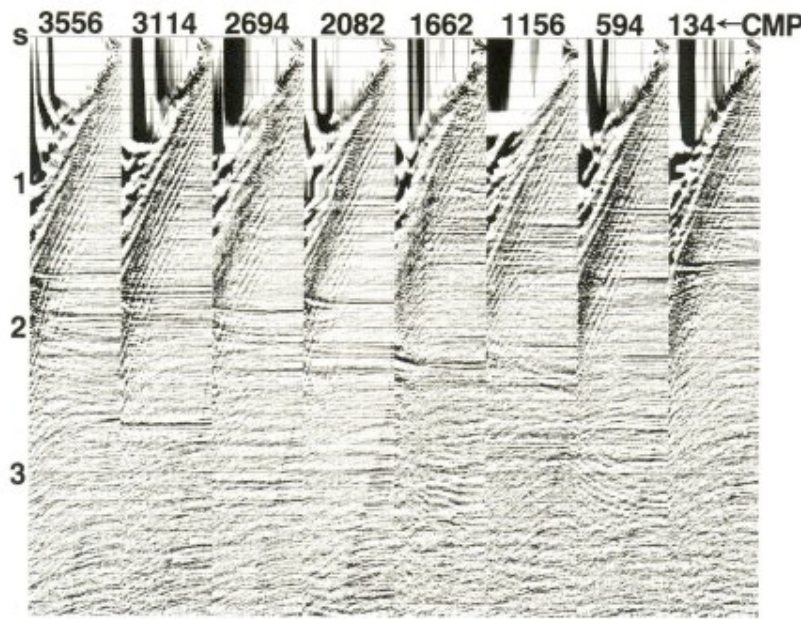


Figure 17.17: Normal moveout correction (NMO)

17.4.8 Residual Statics Corrections

One extra step is needed before stacking for most land and some shallow-water data. The moveout in CDP gathers does not always conform to a perfect hyperbolic trajectory. This often is because of *near-surface velocity irregularities that cause a static or dynamic distortion problem*. Lateral velocity variations due to complex overburden can cause moveouts that could be negative. i.e., a reflection event arrives on long-offset traces before it arrives on short-offset traces.

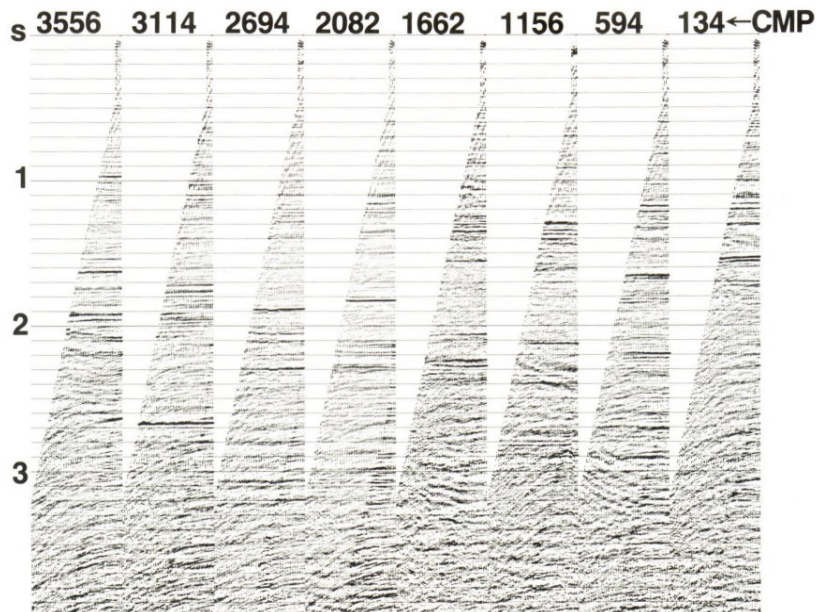


Figure 17.18: CMP gathers after muting of stretched zones

To improve stacking quality, *residual statics corrections* are applied on the moveout-corrected CDP gathers. This is done in a surface-consistent manner; that is, time shifts are dependent only on shot and receiver locations, not on the raypaths from shots to receivers. The estimated residual corrections are applied to the original CDP gathers with no NMO correction. *Velocity analyses* then are often repeated to improve the velocity. With this improved velocity field, the CDP gathers are NMO-corrected. Finally, the *gathers are stacked*.

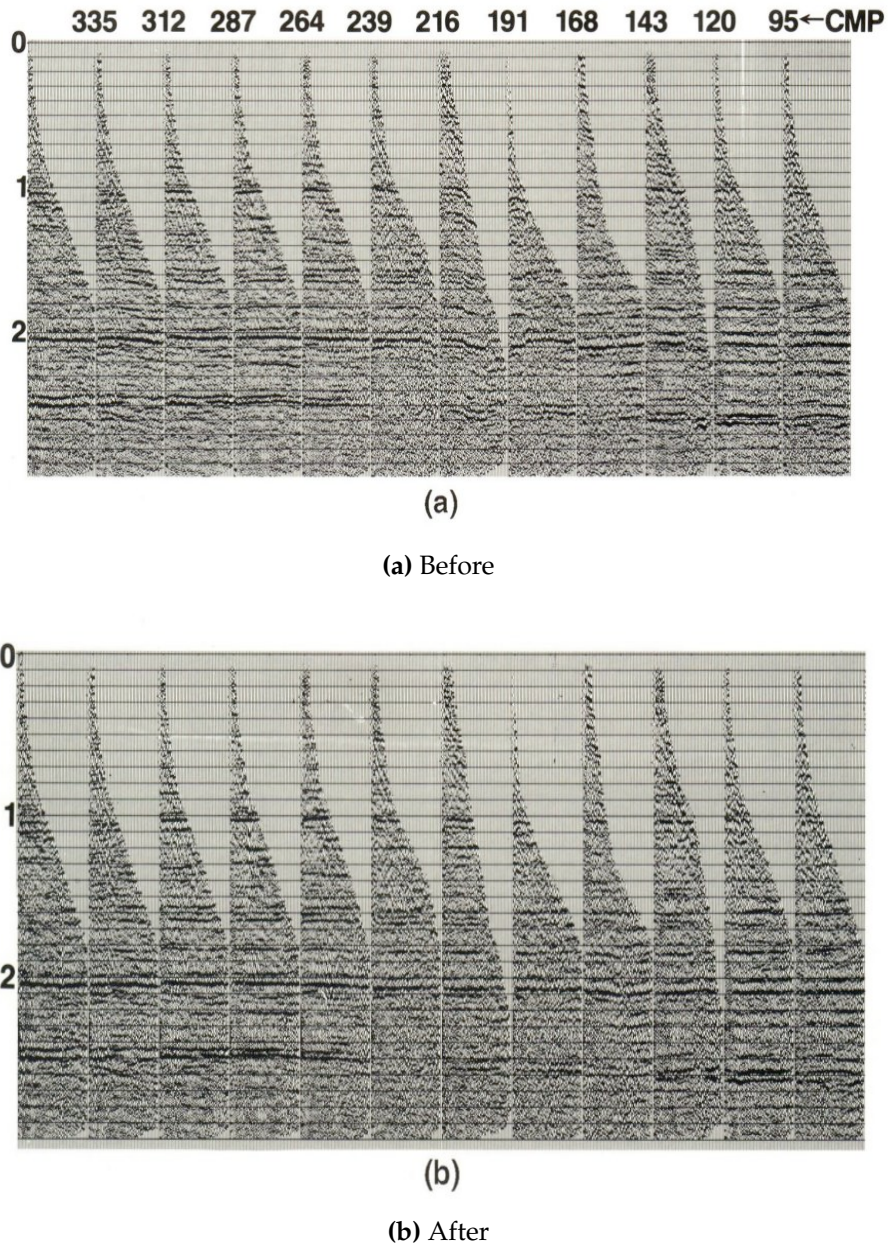


Figure 17.19: NMO-corrected CMP gathers from a land seismic line (a) before and (b) after residual statics corrections. Note that the distorted events (CMP 191, 216) have nearly been flattened.

17.4.9 Poststack Processing

Predictive deconvolution is sometimes effective in suppressing reverberations or short-period multiples and in further whitening the spectrum. Time-variant band-pass filtering is used to suppress noisy frequency bands. Finally, some type of gain is applied to bring up weak reflections. For true amplitude preservation, time-variant scaling of stack amplitudes is avoided; instead, a relative amplitude compensation function that is constant from trace to trace is applied. This is a *time-varying gain function* that amplifies weak late reflections without destroying the amplitude relationships from trace to trace that may be due to subsurface reflectivity.

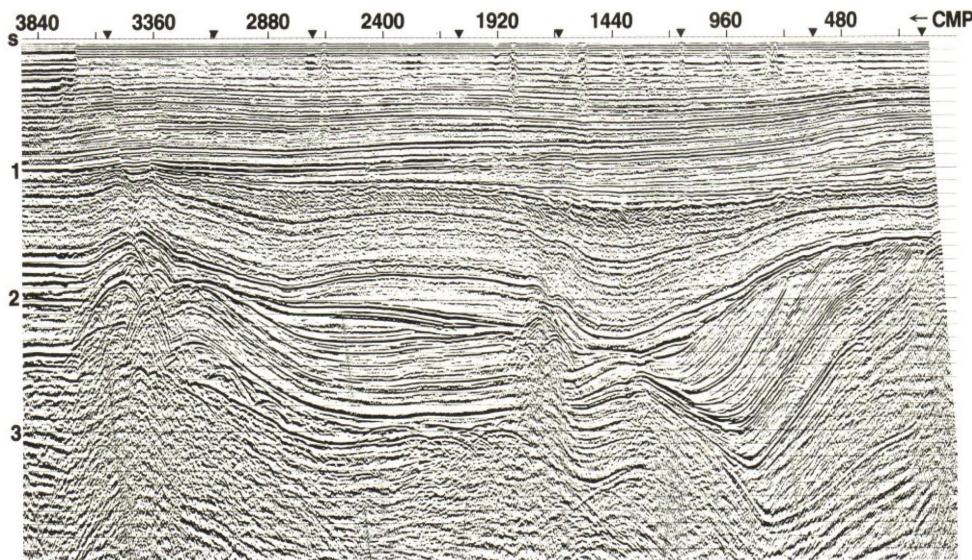


Figure 17.20: CMP stack. A time-variant filter (TVF) applied, followed by an rms gain correction.

17.4.10 Migration

After most of the data processing is completed, the seismic section, known as a stack from the process of CDP stacking, may be passed through another process called migration. *Migration is used to place dipping reflections in their correct spatial location* (Fig. 17.21).



Figure 17.21: Migration is used to diminish dip effects by moving assumed sub-surface data points updip to their true subsurface locations. This process will steepen the dip and shorten the length of the reflection.

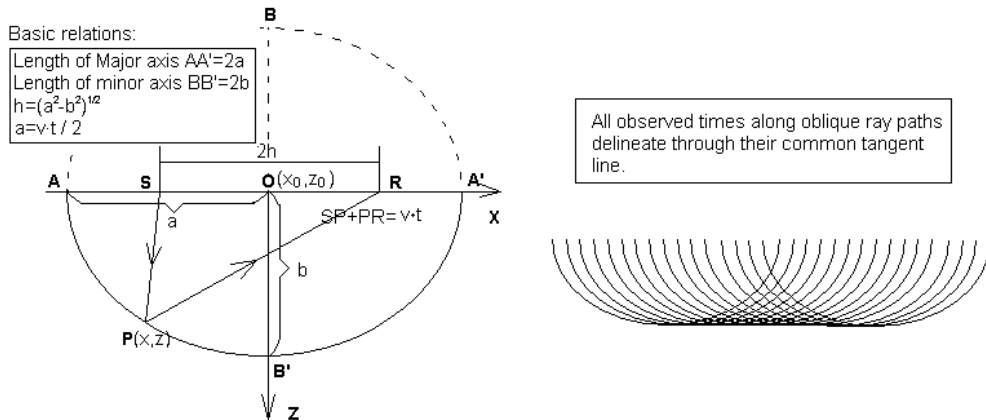


Figure 17.22: The concept of migration.

The traveltime from the source S to the point P , then from P to the receiver R appears the same for a constant velocity, as far as the point P is on the elliptical curve. This ellipse equation can be determined by:

$$\frac{(x - x_0)^2}{\left(\frac{v \cdot t}{2}\right)^2} + \frac{(z - z_0)^2}{\left(\frac{v \cdot t}{2}\right)^2 - h^2} = 1$$

where v is the constant velocity, t is the traveltime and h is the half distance of the source and the receiver. When all ellipses corresponding to various reflection traveltimes are drawn, a common tangent line to those ellipses defines the true position of a reflector. This leads to a general concept of conventional pre-stack migration. When a shot and receiver coincide with each other, the ellipse becomes a circle and the pre-stack migration turns into post-stack migration.

The *Kirchhoff method* migrates the data by searching for diffractions and moving all energy along the diffraction curve to its apex. This works well with steep dips, but not noisy data. The *wave-equation or finite-difference method* uses the wave field observed at the surface to calculate the wave field at various levels. It is adaptable to horizontal velocity gradients, but has difficulty with steeper dips, as can be seen in Figure 17.23b.

Frequency-domain migration transforms the data into a frequency versus wave-number domain. *Anticlines* will appear broader than their true shape, as shown in the figure below. The axis will be in its true position for most cases, but the flanks will appear broader than they really are.

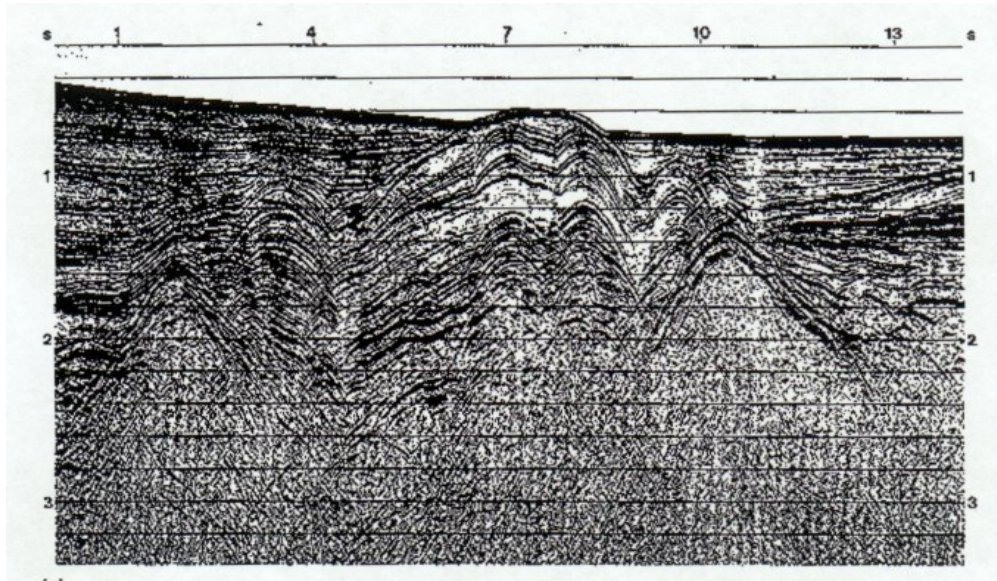
The **focussing or defocusing effect** can also be observed when looking at reflections from a syncline or anticline. Reflection strengths decrease over anticline crests due to a defocusing effect, and they increase over synclinal troughs due to a focusing effect. The axis of some synclines may become too deep for sound waves to penetrate, which brings the reflections together at a point still in the subsurface, as shown in the figure below (a) Figure 17.23a.

Three possible reflection paths are thus produced: one for the axial region and two from the flanks of the syncline. These will produce apparent reflectors which will appear as an anticline, with the approximate axial reflector creating an anticline, which can be seen in figure (b) (above). The resulting seismic output will produce a *bow-tie effect* (Fig 17.25).

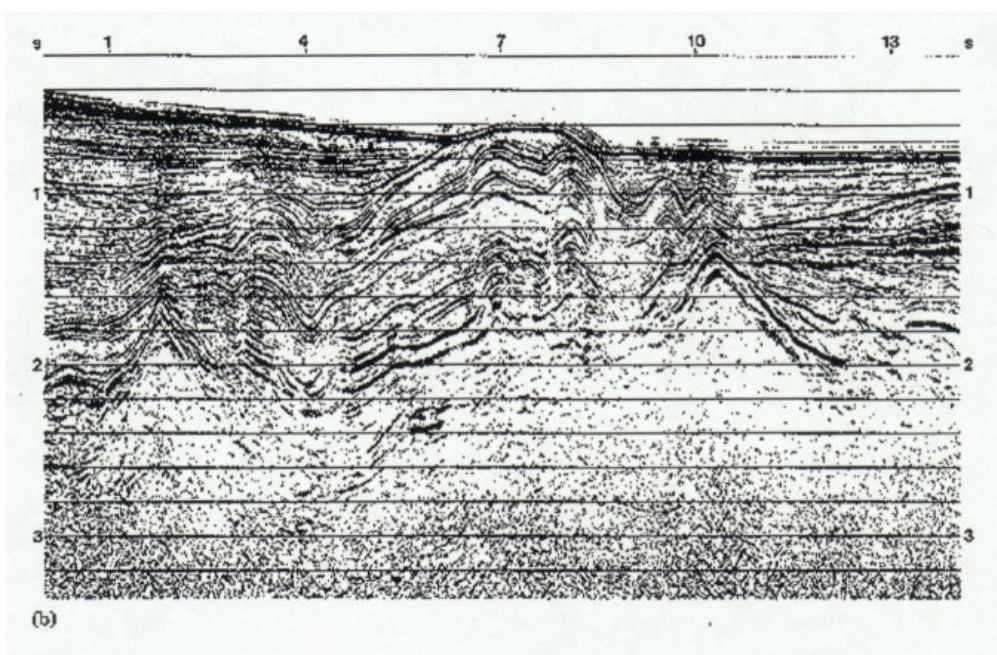
The next figure shows an unmigrated version of a seismic line, two dipping reflections between 1.8 and 2.1s, below B (Fig. 17.26a), could be interpreted to have been overthrust by the flatter overlying reflections to the right.

The following figure shows a cleaned up section after migration techniques had been applied (compare with unmigrated section on previous page).

Dipping planes such as fault planes reflect seismic energy sideways (Fig. 17.26a) rather than vertically, as is the case with flat-lying layers. At any one geophone the interpreter has no way of knowing from which direction each reflection arrives, so all reflections are plotted directly beneath the surface point at which they are recorded (above Fig. b). This results in horizontal layers being plotted in the correct location, but dipping layers being plotted to the side of the correct location. Migration moves the fault-plane reflection (above Fig. b) back to the real location of the fault, and also causes dipping reflections to steepen (above Fig. c). The amount that a reflection must be moved during migration depends on the dip of the reflection and on the seismic velocity above the reflection. Only dipping reflections have been moved on a migrated seismic section - migration has no effect on flat-lying reflections.



(a) Before



(b) After

Figure 17.23: Focussing or defocussing effects after migration. Synclines appear narrower (b) than their true form (a) after frequency migration.

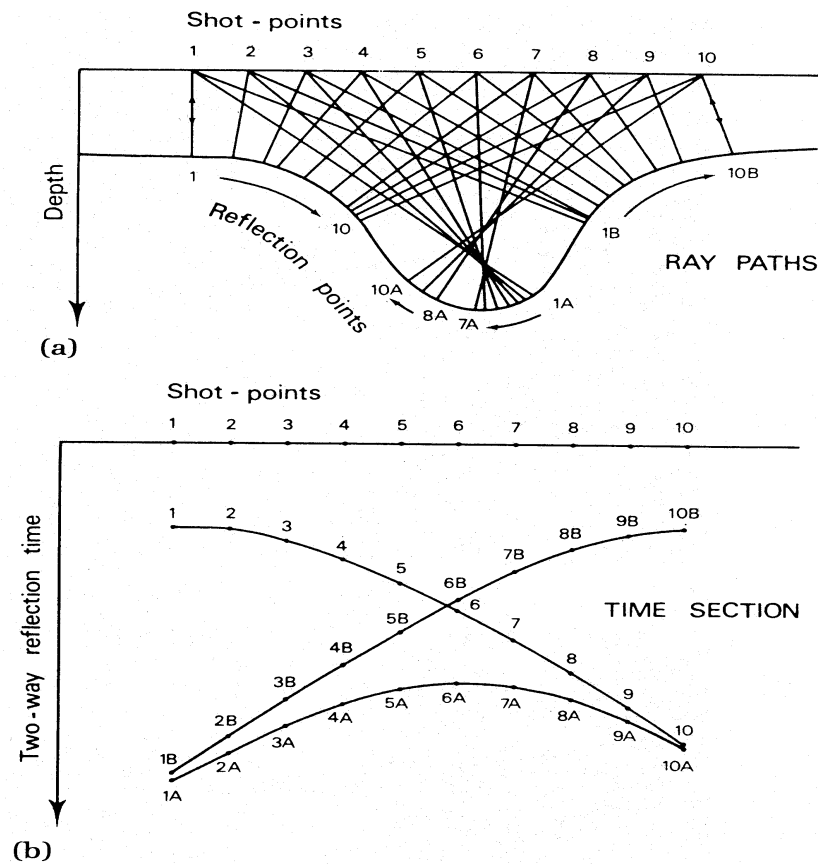


Figure 17.24: Seismic reflection paths over a syncline.

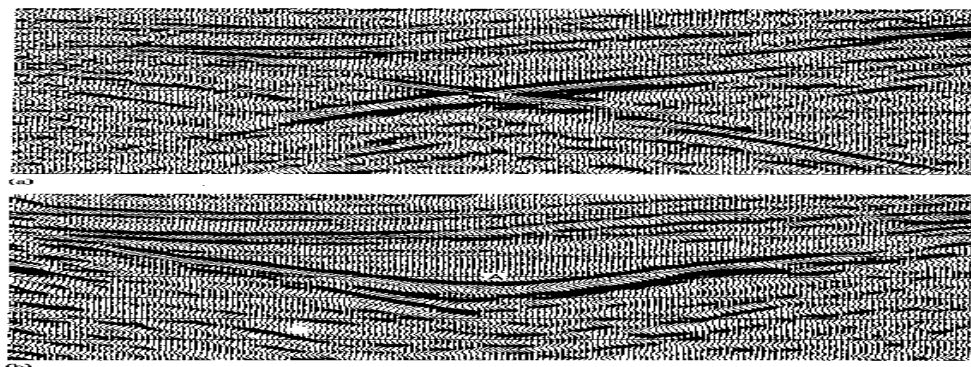


Figure 17.25: Bow tie effect

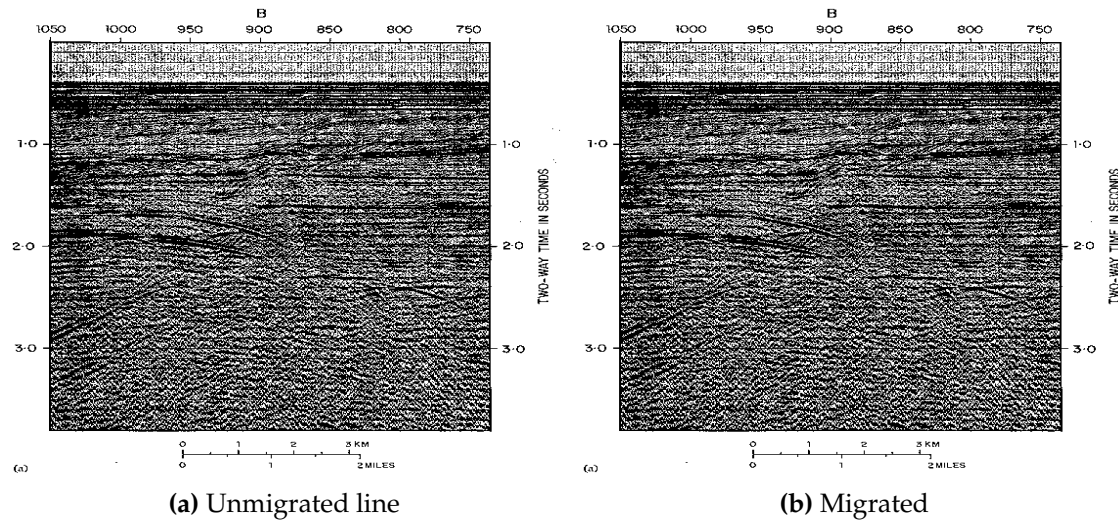


Figure 17.26: (a) unmigrated version of a seismic line, two dipping reflections between 1.8 and 2.1s, below B, could be interpreted to have been overthrust by the flatter overlying reflections to the right. (b) cleaned up section after migration techniques had been applied.

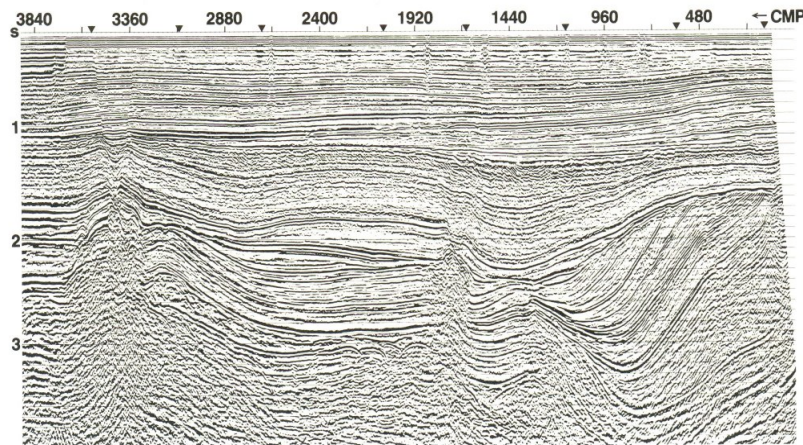


Figure 17.27: Migrated CMP stack

17.4.11 Multiples

Multiples are reflections that have undergone more than one bounce. These appear at a time t below the primary event (Fig. 17.28). *Stacking* or combining the recorded traces after they have been corrected for normal moveout is the best method for attacking long-path multiples. *Deconvolution* is used to eliminate short-path multiples. It is used to sharpen the seismic pulse and attenuate multiples.

- *Water-bottom and base-weathering zone multiples* – In offshore areas both the air/water and water/rock interfaces form reflecting horizons; and energy trapped within the water layer may rebound backward and forward, resulting in a water/bottom multiple or reverberation (Fig. 17.29). The first figure below shows such an example on a seismic line where hard crystalline basement rocks crop out at the sea floor. Multiples also occur due to the opposite polarity phase due to the negative reflection at the air/water interface, which can be seen in the second figure below.
- *Simple multiples* are produced by the reflection bounce of air/sediment or water/sediment contacts.
- *Multiples from dipping reflectors* – When the primary reflector is dipping and the surface layer is flat, the multiple reflection will show twice the angle of dip; since, at any given point, the multiple is twice as deep as the primary event (Fig. 17.30).
- *Pre-leg multiples* are caused by an extra bounce between two reflectors. *Interbed multiples* are found between beds, and are cannot be removed by simple stacking of the CMP gathers.
- *Multiples that come and go* – Figure 17.32 shows multiples in a seismically quiet zone, due to automatic amplification by the automatic gain control (AGC).
- *Ghosts* are short-path multiples, common to both land and marine seismic sections, which develop when part of the seismic pulse that initially traveled upward from the shot is reflected downward from the surface or base of the weathering zone to closely follow the main downgoing seismic pulse (Fig. 17.33).
- *Diffractions* are a common source of noise and can emanate from any abrupt interface in the subsurface, as shown in Fig. 17.34.
- *Reflected refractions* are sound waves that have travelled laterally for some distance in the subsurface before reaching the geophones. For example, as an upgoing ray crosses each acoustic-impedance boundary, it is refracted, the angle of refraction increasing across boundaries with increased acoustic impedance. Above a critical angle, the ray is no longer reflected; instead, it is refracted along the higher-velocity layer, which acts like a leaky waveguide; and, therefore only part of the signal reaches the geophones, as shown below.

htpb

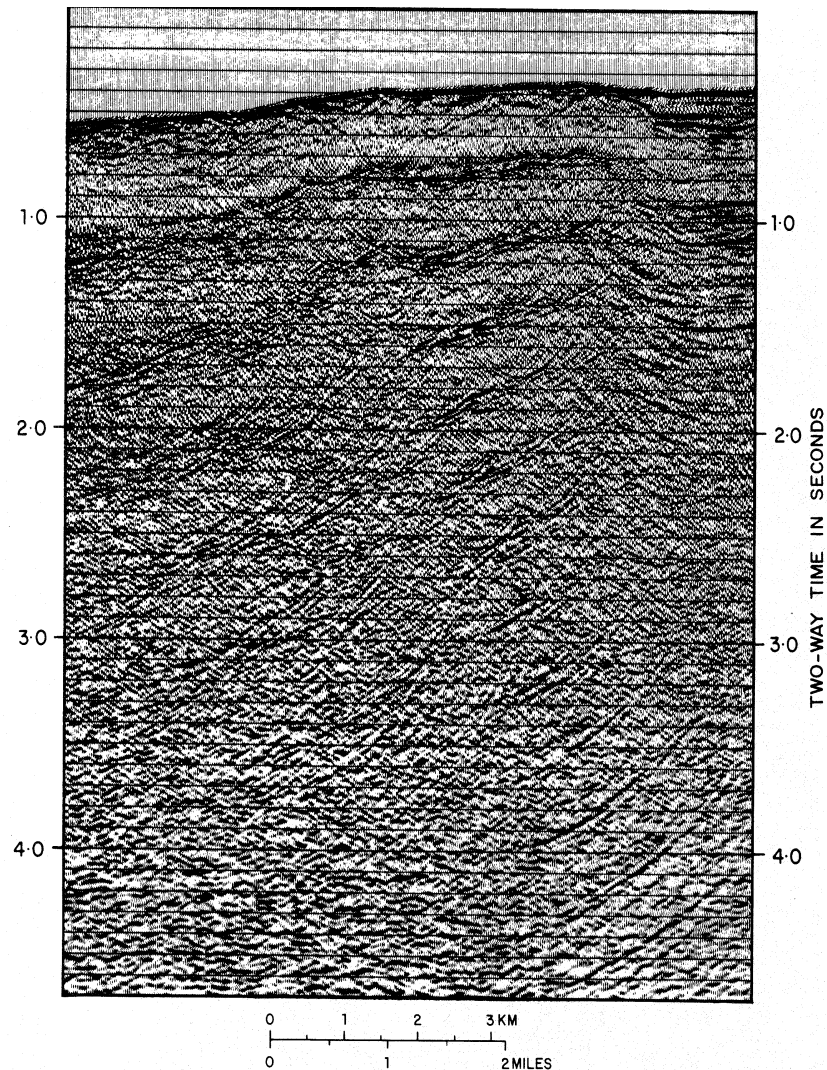


Figure 17.28: Set of multiples within a seismic section. Multiples become weaker due to longer travel paths and consequent transmission losses.

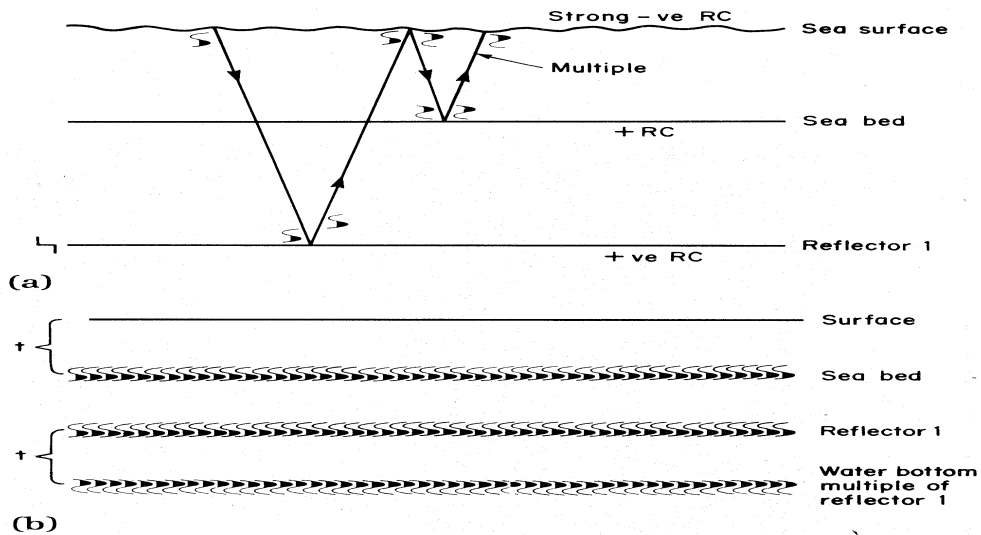


Figure 17.29: Simple multiples

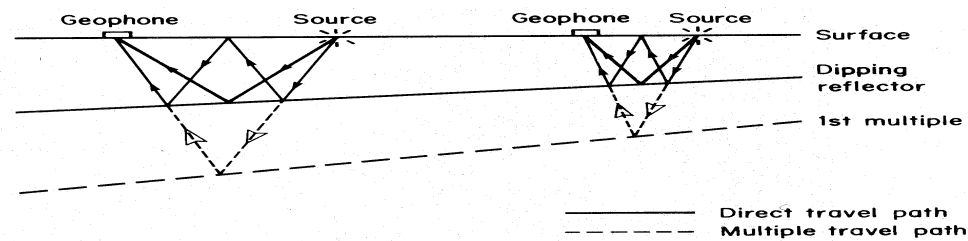


Figure 17.30: Schematic depiction of multiples in dipping layers.

Event A in the figure below is a reflected refraction developed in association with a major fault. Event B is the water-bottom multiple of the reflected refracted A. Dipping Reflectors and Migration.

Normally, for horizontal reflectors, the geophones will record data originating from a point midway between the source and receiver. However, for dipping reflectors, the subsurface data point is not midway between the source and receiver but is offset in an undip direction. On *true-dip lines*, the sample points lie in the plane of the section, as seen in Fig.17.36.

On a *true strike line*, although the reflectors will appear to be horizontal, the actual sampled points are located off-line, as shown below. The amount of distortion increases with dip, depth, and velocity.

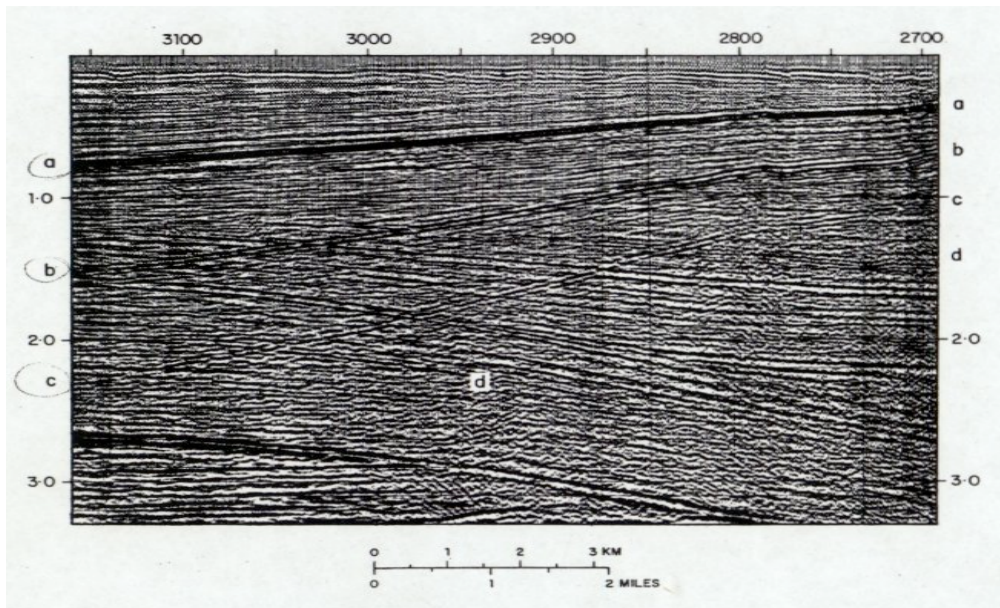


Figure 17.31: The primary reflection (a) The following figure has a positive reflection coefficient and dips from right to left. The first simple multiple (b) has twice the dip and reversed polarity. The third multiple (c) has three times the dip of (a). The reflection quality of the multiple (c) is too poor to demonstrate a polarity reversal. It should have the same polarity as the primary reflection (a). Remnants of a fourth multiple (d) can just be seen.

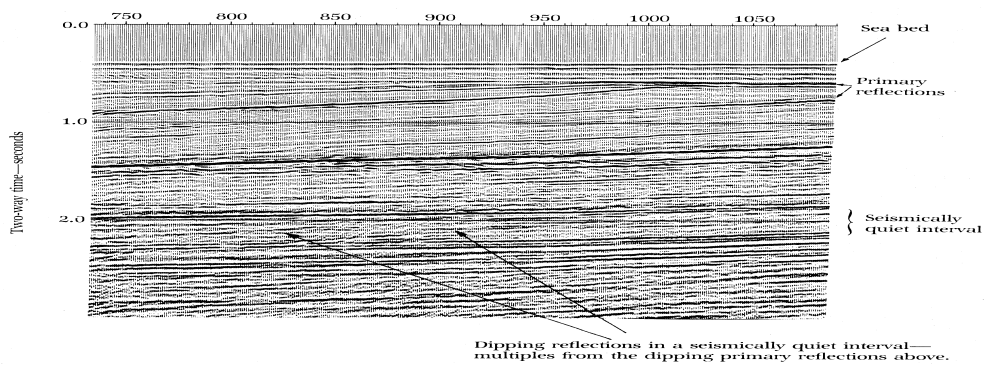


Figure 17.32: Multiples in a seismically quiet zone.

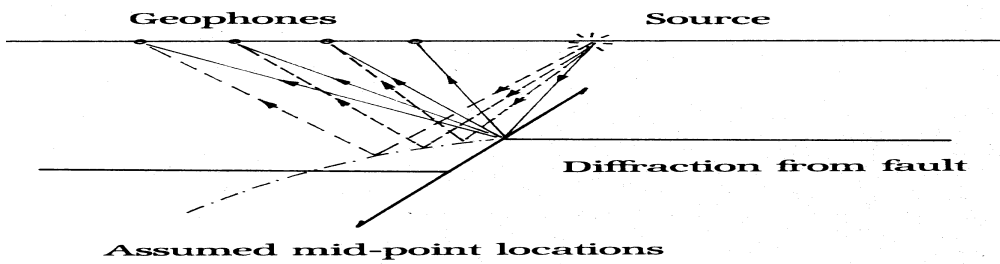


Figure 17.33: Ghosts

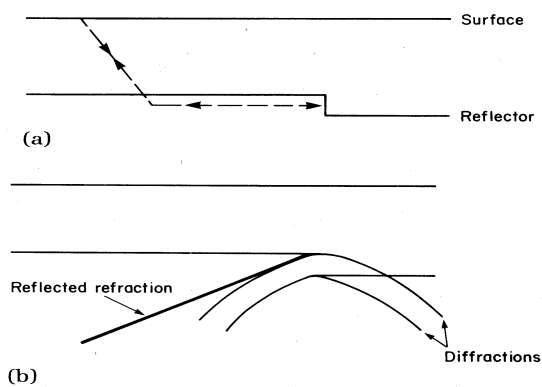


Figure 17.34: Diffraction of seismic waves at abrupt interface changes.

17.4.12 Velocity Distortions

Velocity distortions may also be the result of changes in rock properties, such as: variations in formation thickness and facies change. Such distortions can cause misleading results with regards to depth and thickness. The presence of gas can also cause changes in velocities.

Figure 17.37 shows how **apparent thinning downdip** may occur on seismic, due to a steady increase in interval velocity with depth, when a rock is dipping downward and has in fact a constant thickness in reality.

- *Apparent thinning across faults* occur on the downthrown side of the fault due to increased interval velocity between reflections x and y in the down thrown block (Fig. 17.38).
- *Apparent rollover into faults* can be observed in the upthrown block of a normal fault. These bend towards the fault plane, as portrayed in the below diagram. These bends can be interpreted as being: a true rollover; a portion of a unremoved

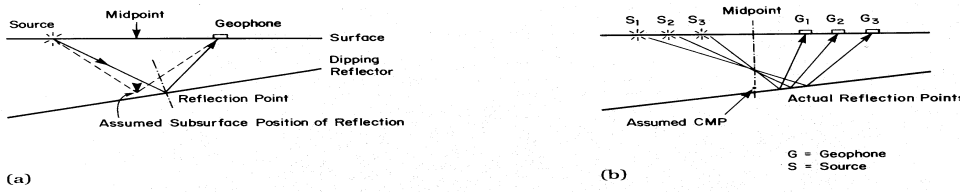


Figure 17.35: reflected refraction

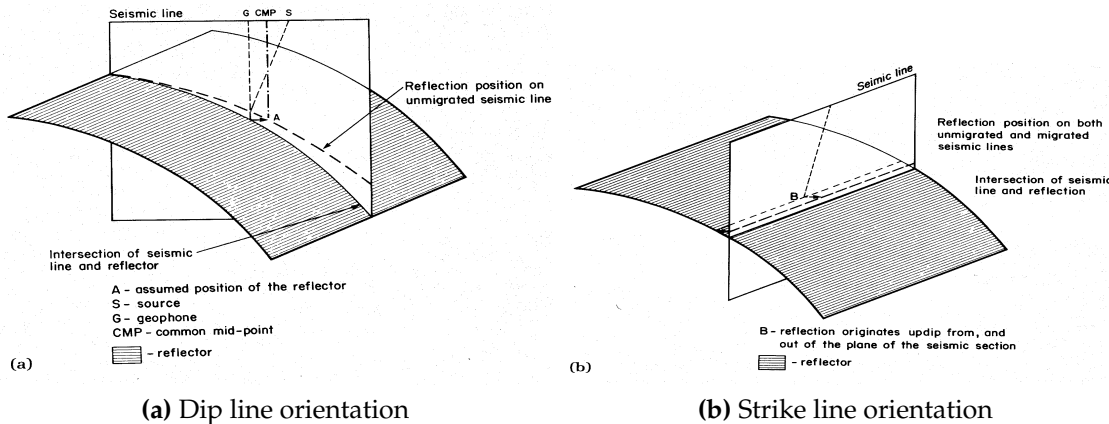


Figure 17.36: Velocity effects when collecting seismic reflection data along dip (a) and strike (b) direction

diffracted curve; or a velocity artefact caused by the wedge of lower-velocity rocks above the fault plane.

- **Velocity anomalies beneath faults** are common. Fig. 17.38b show lateral velocity variations. These are due to the modification of the time structure of deeper reflectors caused by faulting.
- **Velocity anomalies associated with salt** occur because its specific gravity is less than most other sedimentary rocks, and has a tendency to migrate upward. Migration results in changes in lateral salt thickness, which can be observed in Fig. 17.39. Imaging of salt structures and sub-salt structures is the most challenging task for image processing departments in large companies. Due to exploration of plays in large sub-salt areas, like offshore Brazil in the Santos basin or the ultradepth parts of the Gulf of Mexico a lot of money is invested into improving the sub-salt imaging. Salts appear thinner on seismic because soundwaves travel at much faster rates than the surrounding sediment, which is portrayed in Figures 17.39.

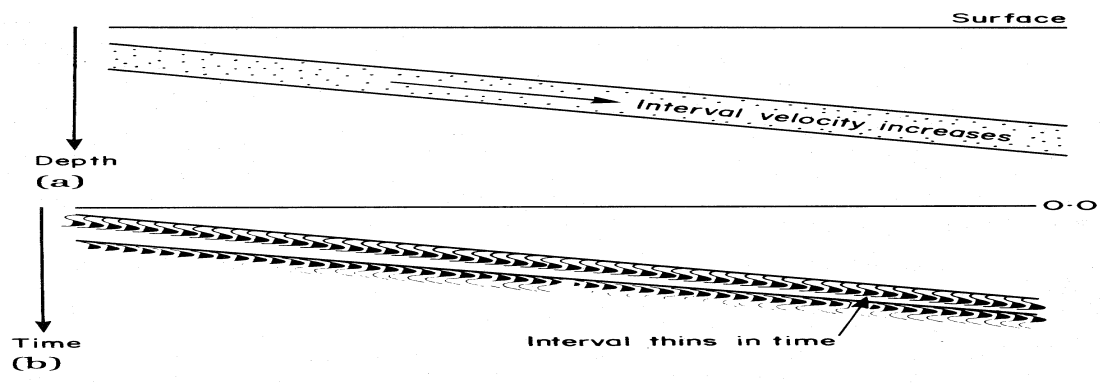
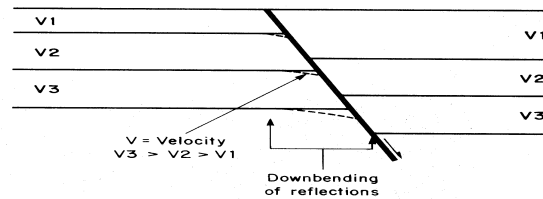
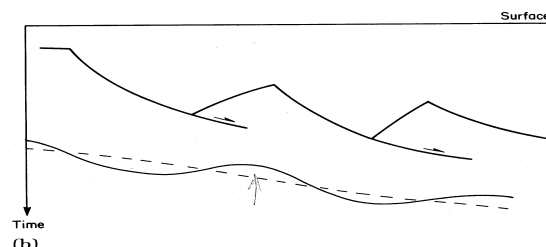
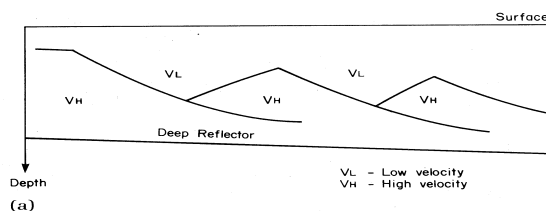


Figure 17.37: Apparent thinning downdip of the structure



(a) Apparent thinning across a fault



(b) Apparent thinning below faults

Figure 17.38: Apparent thinning related to faults

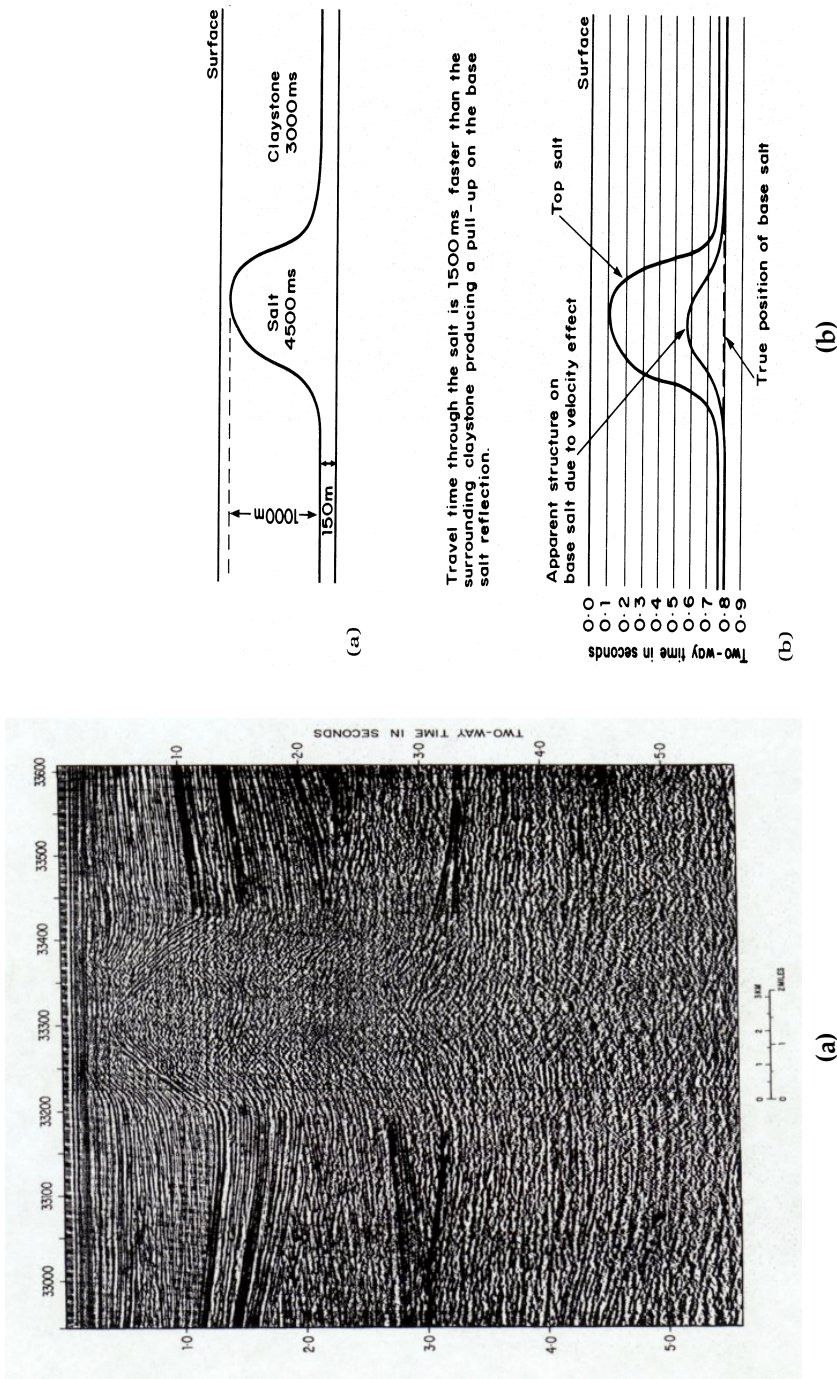


Figure 17.39: Imaging issues related to salt structures: (a) Seismic line across a salt structure; (b) Velocity artefacts related to a salt dome (schematic).

- **Velocity push-down under shale diapirs** – The velocity effects may be the opposite to those of salt, since the shales generally have lower velocity than adjacent sediments. Travel time is lengthened and reflectors are pushed down, as shown in Figure 17.40.

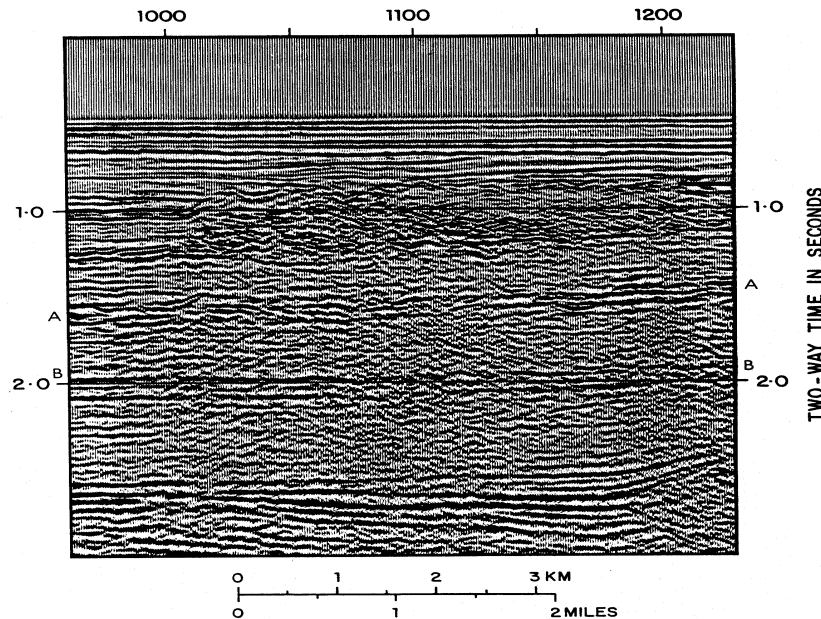


Figure 17.40: Velocity push-down beneath shale diapirs. The seismic velocity of shales is lower than the surrounding rocks.

- **Velocity anomalies beneath reefs** with results similar to salts or shales, depending on their compositions (carbonates or shales), which can be seen in the next figures.
- **High-velocity wedge-focusing effect** may show kinks in the seismic profile (including overlap) because of distortion by the overlying high-velocity wedge (which acts as a distorting lens), as shown below.
- **Velocity anomalies are associated with channels.** Figure 17.42a shows a deep sea-floor canyon system with more than 200 ms (about 100m) of relief that produces undulations in the underlying reflectors (e.g., reflections A and B). Figure 17.42b shows a possible submarine canyon with a compacted sandstone fill, which causes severe disturbances below A. Deeper horizons show a pull-up of 200-300ms.
- **Velocity anomalies caused by varying water depth.** Reflections to the west of the reefoid mass in figure (a) dip to the east and there is no structural closure.

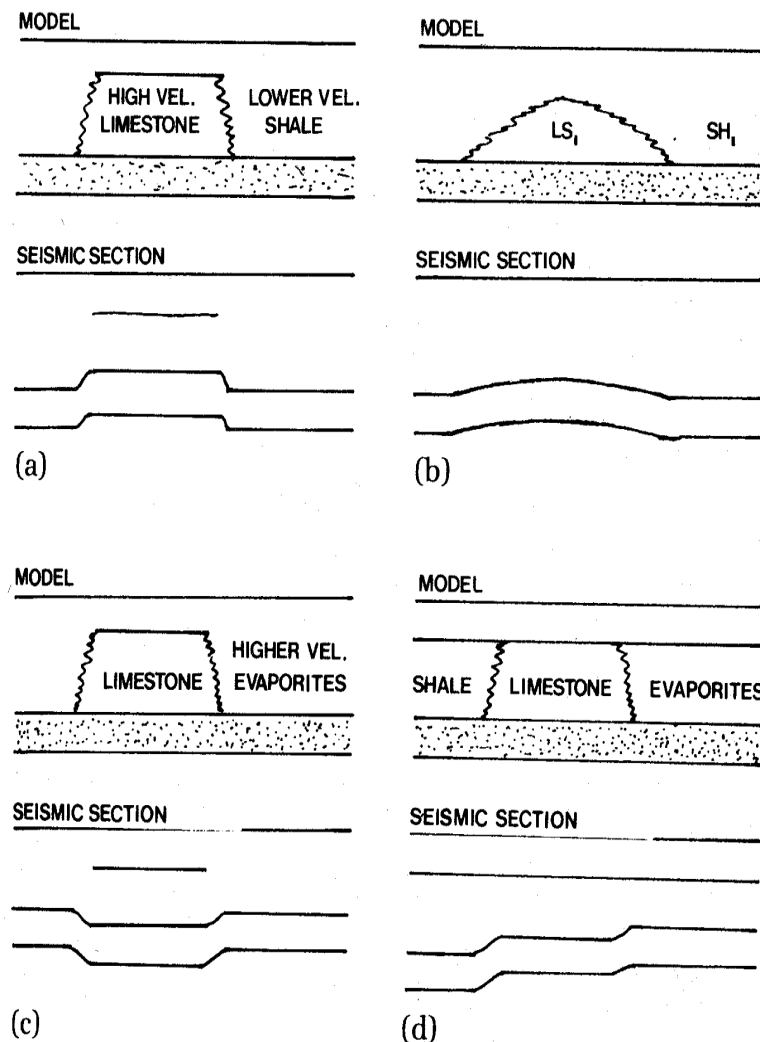


Figure 17.41: Seismic velocity anomalies related to imaging of carbonates.

- **Sideswipes** occur when a seismic line is shot parallel to a fault, which gives a confusing reflector pattern, which may be observed in the following figure. It records data from the upthrown and downthrown sides of the fault. *Poor line orientation* is a variation on the sideswipe theme as shown in Fig. 17.44.

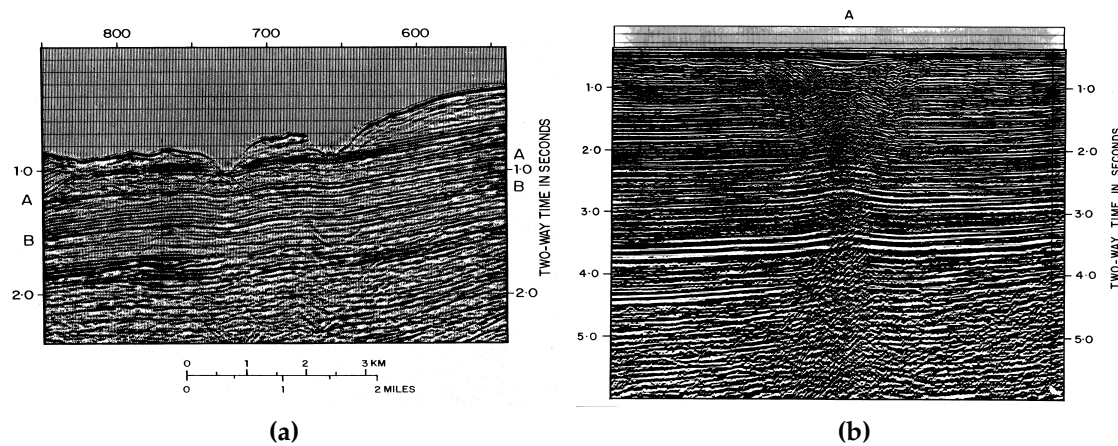


Figure 17.42: Velocity artefacts related to (a) seafloor relief and (b) velocity pull-up beneath an infilled channel

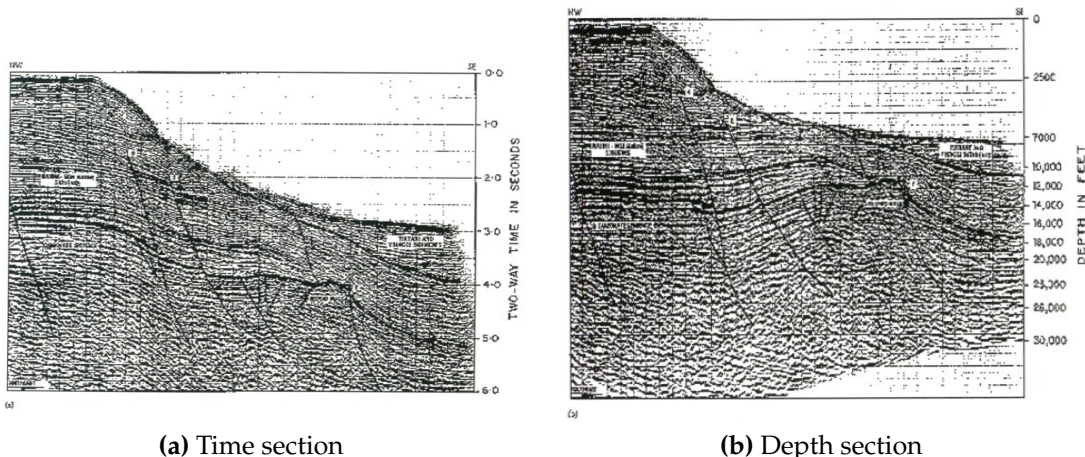
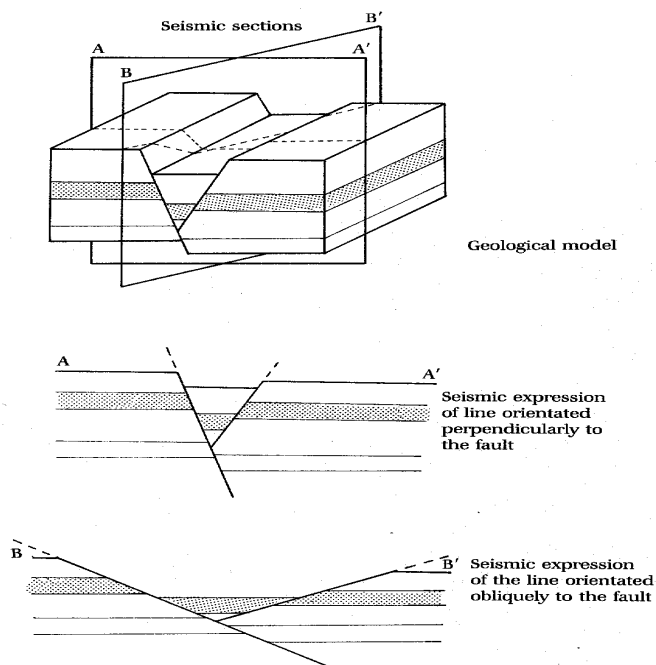
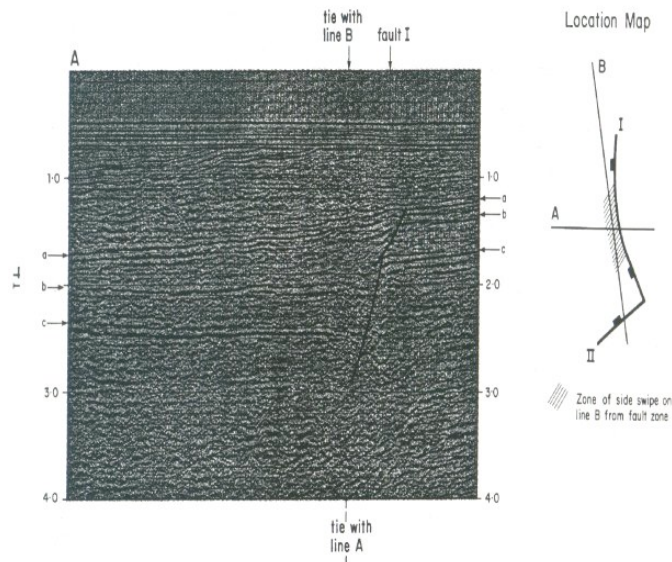


Figure 17.43: Velocity artefacts - Reflections to the west of the reefoid mass in figure (a) dip to the east and there is no structural closure.(b) shows the line after depth conversion.



(a) Line orientation relative to geological structures and seismic imaging



(b) Velocity artefacts through faults

Figure 17.44: Seismic imaging and the effects of geological structures. (a) Imaging of faults depending on seismic line orientation relative to the fault; (b) Velocity artefacts through poor line orientation close to a major fault.

17.4.13 Example: Deep seismic line from Northwest shelf of Australia

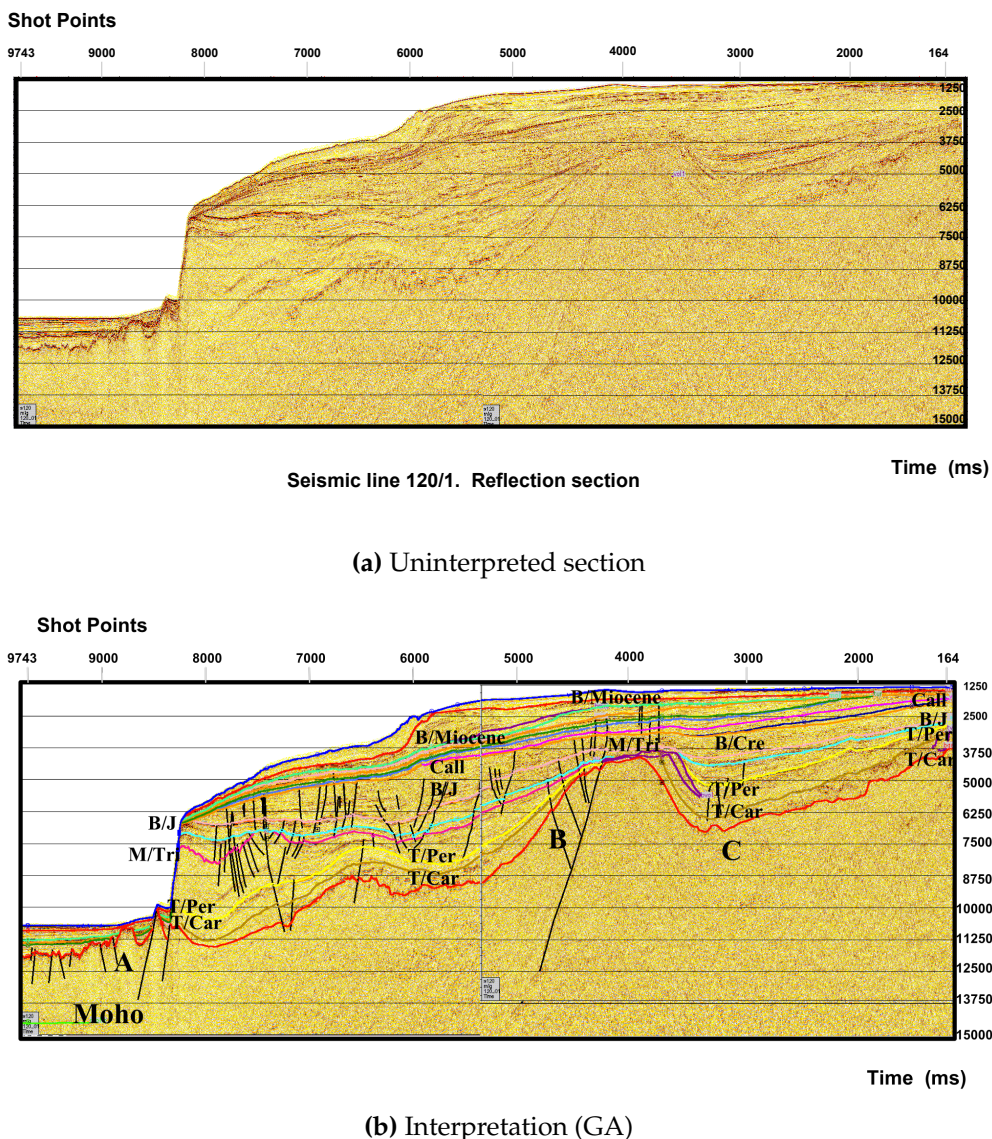


Figure 17.45: Deep seismic reflection transect Geoscience Australia 120/1. Dip line across the North West Shelf into the Argo Abyssal Plain. (a) uninterpreted section; (a) Geological interpretation of the deep seismic reflection transect across the continent-ocean transition (COT) at the Argo Abyssal Plain. T/Car – Carboniferous; T/Per – Top Permian; B/J – Bas, NW Shelf, Australia. Jurassic; M/Tri – Mid Triassic; B/Cre – Base Cretaceous; Call – Callovian; Apt – Aptian; B/Miocene – Base Miocene. Be careful with your interpretation of faults and structures - there is no information on how the section is squashed or stretched horizontally or vertically.

17.5 Wide-angle marine seismic data

Reflection seismology is essential to image the layered structure of the earth. However, the correct reduction of reflection seismic data is dependent on knowledge of the seismic velocities of individual layers. These velocities can be approximated by computing interval velocities from the reflection data themselves, but are dependent on many assumptions. In particular for imaging crustal structures properly, it is extremely helpful, if a combined data set of refraction and reflection data can be obtained. For this reason modern marine deep seismic experiments are sometimes carried out by collecting both types of data simultaneously. In this case, an array of air guns is usually used as source, and a multichannel streamer is towed to record the reflected signals. In other cases refraction data only might be collected. Before the line is shot, Ocean Bottom Seismographs (OBS) (Fig. 17.46) or Hydrophones (OBH's) are deployed, and record refracted signals. Shooting is usually done at a speed of 6 knots. If shooting proceeded continuously for 24 h, a total coverage of 250 km/day could be achieved. The arrival times of these signals reflect the velocities of different layers.

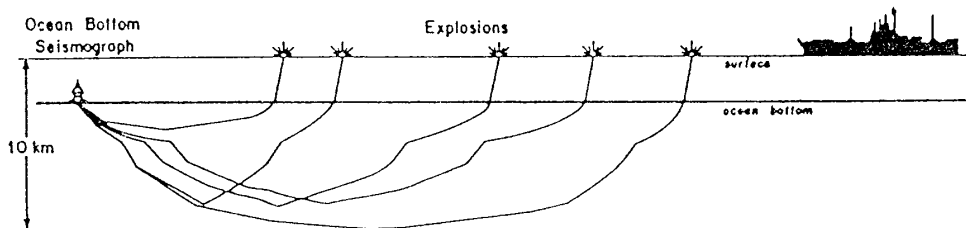


Figure 17.46: OBS seismic acquisition

An extremely cheap way (at loss of resolution) to do marine refraction work are sonobuoys. The sonobuoy is an expendable listening station that radios the information received back to the shooting ship. The sonobuoy is merely thrown overboard. The salt water activates batteries and a radio antenna is extended upward plus one or two hydrophones are suspended beneath the buoy. As the ship travels away from the buoy, shots are fired and the signals received by the hydrophones are radioed back to the ship where they are recorded. The arrival time of the wave that travels directly through the water from the shot point to the hydrophone is used to give the offset distance. Eventually the buoy sinks and is not recovered. Today, sonobuoys are not often used any more.

Ocean bottom seismometers (OBS's; Fig. 17.47), measuring the ground acceleration in 3 directions, are extremely expensive (US \$60000 - 80,000 a piece). OBS's are used for detailed seafloor teleseismic, microseismic and refraction surveys. These instruments are quite complex: their three-component 1-Hz seismometers require a large pressure case, a bulky leveling system, variable gain amplifiers and gain-ranging to maximize

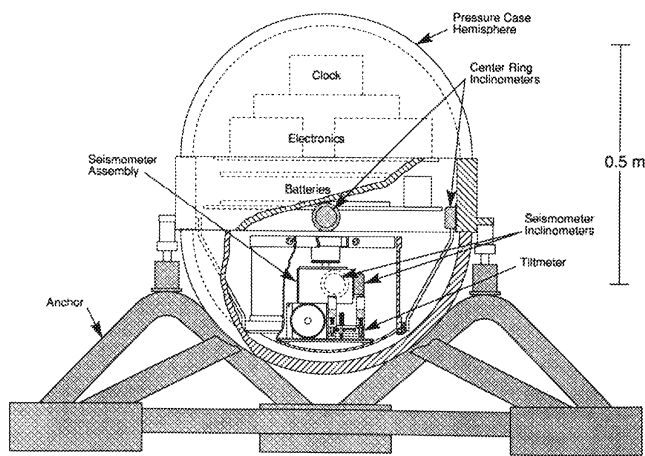


Figure 17.47: Schematic cross section of an ocean bottom seismometer (OBS). Here: Scripps Institution of Oceanography OBS.

their dynamic range add complexity. A broadband pressure sensor further increases their size and requires additional electronics and recently tiltmeters have been added to them, further complicating their electronics and software.

A sample vertical channel record section is plotted in the figure below. The high quality of 'P' and 'S' refraction within oceanic crust, and the 'PmP' reflection from the mantle are clearly observed in this record section.

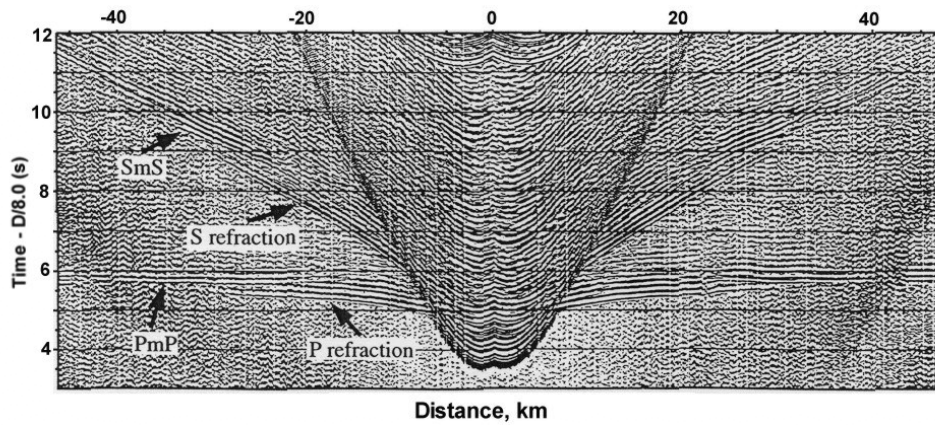


Figure 17.48: Seismic record section from oceanic crust. Vertical channel

The application software *Obstool* from the University of Texas [Christeson, 1995] can be used to correct the recorded data for clock drift, calculate OBS positions, produce

SEG-y format files, and digitise arrivals.

Processing operations for reflection data included applying a correction for clock drift during deployment, inverting the water arrivals for instrument location and orientation, band-pass filtering using a zero phase Butterworth filter with a 5 and 15 Hz passband (48 dB/octave roll-off) before travel time picking and a 5Hz and 20Hz for synthetic seismogram modeling.

First arrival travel times, strong secondary arrivals and normal incidence reflections were interpreted and digitized and then used to model OBS data. Plotted in Fig. 17.49 below is a record section which is located on the strike line. The compressional refrac-tions ('P') within the oceanic crust, and the reflections from the base of the crust ('PmP') are clearly observed in this record section.

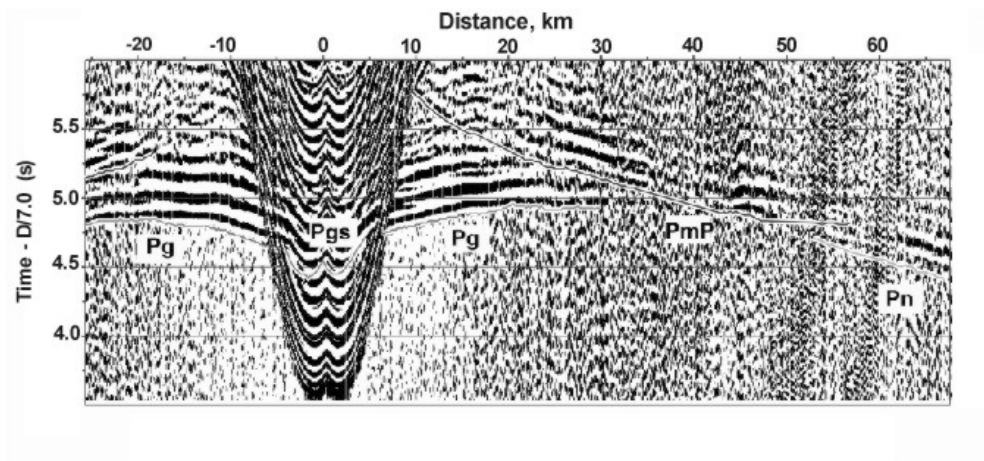


Figure 17.49: Seismic record section with picked 'P' arrivals

Chapter 18

Seismic Refraction Method

The seismic methods are the most widely used and most versatile of the methods of geophysical exploration. They can be used to map rock interfaces at all scales — from investigation of near surface layering, to the detailed mapping of layers down to kilometres of depth — through to the mapping of the structure of the entire earth. Seismic methods can be used on the land and at sea. It is possible to undertake seismic surveys using artificial sources and to use natural sources such as earthquakes of all sizes.

We will be discussing the seismic methods extensively over the next few weeks. By way of introduction to seismic surveying, it is necessary to cover a few of the basics of seismic acquisition.

18.1 Seismic acquisition

Most exploration seismology utilises artificial sources. The detonation of an explosive charge buried in the ground is one obvious way of generating seismic waves. These waves have the desired impulsive behaviour and lead to distinct ‘echoes’ being recorded from the various layers. Another impulsive source is obtained through the dropping of a weight — be it a sledge hammer striking the ground or the dropping of a heavier weight from a purpose built vehicle. At sea, the injection of compressed air into the ocean through an ‘air gun’ is a popular source. For shallow marine work electrical discharges which vaporise water provide another source.

For land surveys, the non-explosive sources utilise some of the important aspects covered in our lecture on signal processing.

First there is a technique known as vibroseis . A purpose built truck is able to jack itself up on a plate beneath the chassis (Fig. 18.1). Over a period of perhaps 10 to 20 seconds, hydraulics on the truck deliver a vibration into the ground sweeping over the seismic frequency range that is effective for the depth of investigation (e.g. 20 to 150 Hz). The sweep is recorded, as is the signal at the seismic sensors (Fig. 18.2). Cross-correlation can transform the echoes from being low amplitude, 20 second long rumbles back to the impulsive events that an explosive source would deliver.



Figure 18.1: A Vibroseis truck in action during a seismic acquisition campaign

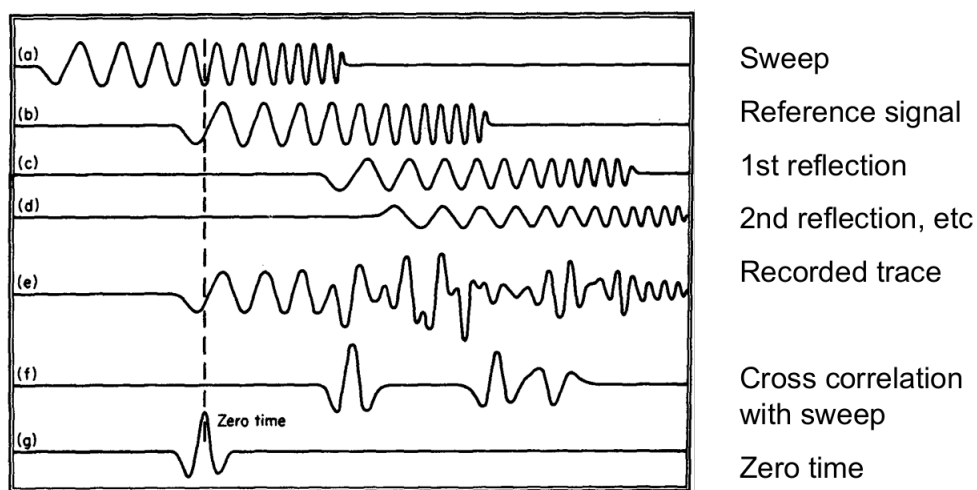


Figure 18.2: Vibroseis sweep signal.

Another technique is known as stacking. The results from repeated impacts on the ground can be added together. With another stacks, the desired signal is enhanced and random background noise is stacked out.

On land, the detection of seismic signals is achieved through the use of low cost sensors known as geophones. A geophone consists of a wire coil mounted on a string which is housed inside a magnet. A 5 cm long spike at the base of the geophone is pushed into the ground. When a seismic wave arrives at the geophone, the housing and the magnet vibrate while the coil remains stationary. Through Faraday's law, an electric current is generated in the coil. Wires connect the geophone to the recording instruments. Surveys can be undertaken with as few as 12 geophones to up to 10,000 geophones all recording the seismic events generated by the seismic source.

At sea, the detectors respond to the pressure pulse associated with the transmission of the P-waves (remember, there are no S-waves travelling in fluids). These instruments are known as hydrophones.

For the recording instruments, the following are important specifications.

- 1.) The sample rate should be at 1 millisecond or better (i.e. recording up to 500 Hz).
- 2.) Shot firing system (and detonators) need to have a timing accuracy better than 1 millisecond.
- 3.) The digitizers and associated amplifiers need to have a large dynamic range, e.g. 24 bit analog to digital conversion preserves signal precision for low amplitude signals.
- 4.) With large numbers of recording channels, the digitization can occur at the geophones using a telemetry system. The signals from each geophone can be returned to the recording system after the detonation of the source and the capture of the signal. These systems make use of wireless and LAN technology.
- 5.) There needs to be a capability to monitor the shot records and to check for system noise and system health.
- 6.) Secure digital recording using discs and DVDs is required.

18.2 Shallow seismic refraction surveying

The ability of a critically refracted wave to return wave energy to the ground surface has been previously explained. The shallow seismic refraction method exploits this behaviour and is widely used for the investigation of near surface layering. In general, the near surface layering contains the weathering profile:

- 1.) The soil layer with a P-wave velocity typically between 300 m/s and 1,000 m/s
- 2.) A layer of weathered rock with a P-wave velocity typically between 1,000 and 3,000 m/s

3.) Fresh bedrock with a P-wave velocity which is typically greater than 3,000 m/s.

If deep alluvium and unconsolidated material is present (i.e. $V_p < 1000$ m/s), once the water table is reached, the V_p will be approximately the speed of sound in water – 1500 m/s.

The shallow seismic refraction method allows the thicknesses and velocities for these layers to be determined. Applications include geotechnical investigations where foundation conditions need to be established, the exploration for deep leads (gold, diamonds etc) and the mapping of buried river valleys for groundwater investigations.

Consider the following example of the ray paths involved in a simple case involving two layers and a horizontal boundary (Fig. 18.3). There are 12 geophones and the source is located at the left of the geophone spread. In this example, the P-waves generated by the source spread out through the surface layer. Some of these waves travel directly to the geophones. Others travel down to the deeper layer where critical refraction can occur. The critically refracted wave travels along the boundary between the two layers and is continuously refracting energy back into the surface layer with the rays departing at the critical angle.

18.3 Travel time curves

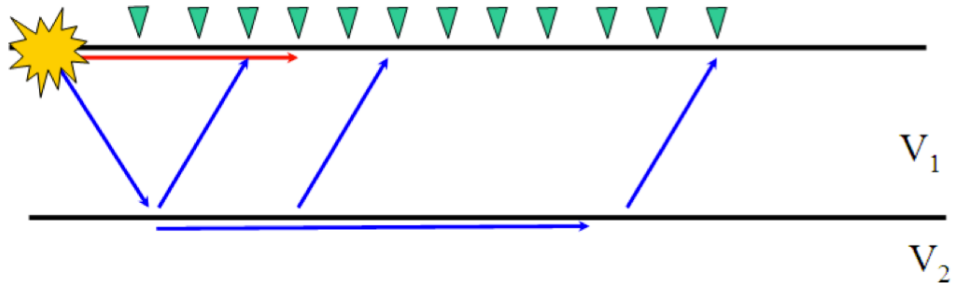


Figure 18.3: Simple survey layout with a source and 12 recording geophones. Seismic wave paths are schematised, $V_1 < V_2$.

The important point about what is going on is that the waves travel faster in the lower layer. Depending on the relative velocities and the thickness of the surface layer, there is certain distance after which the path involving the refraction is quicker than the direct path through the surface layer.

On the seismic recordings, it is easy to identify the time of the onset of the seismic energy at each of the geophones. These times are plotted against the distance from the source point in order to construct a travel time graph (Fig 18.4). If the vertical axis is the travel time, it follows that the inverse slopes of the travel time graphs represent the velocities of the seismic waves. The graph has two segments. The first segment closest to the shot contains the travel time data for the waves travelling directly from the source

to the geophones. The inverse slope of this segment of the travel time graph is the velocity of the direct P-wave. Then, the second part of the graph is for the refracted wave. Its slope gives the velocity of the refracted wave.

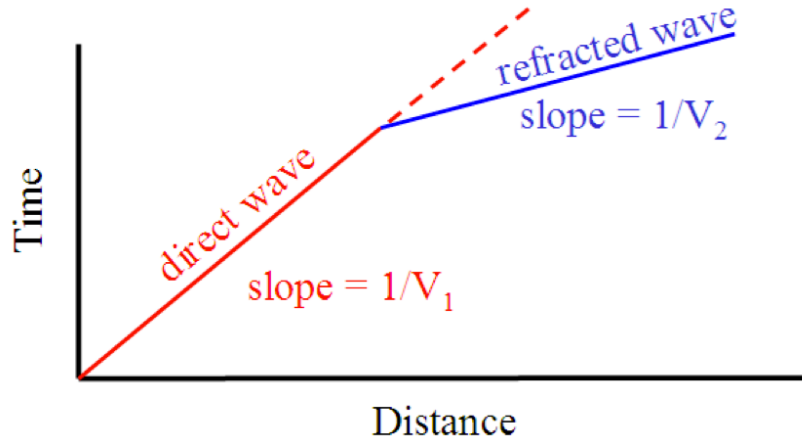


Figure 18.4: Time vs. distance (travel time) plot.

18.4 Simple depth calculation

For the simple example we are discussing, it is possible to determine the thickness of the surface layer. However, we have to first define some terms.

Referring to Figure 18.5 (for a 3 layer case), the intercept time t_i for each layer is given by the intercept of the segment of the travel time curve from that layer back to the source point. The cross-over distance x_c is the distance at which the P-wave arrivals from one layer are overtaken by the P-wave arrivals from the next (faster) layer down.

Using these terms, a configuration like in Fig. 18.6 and remembering that $\sin i_c = \frac{V_1}{V_2}$, the calculation proceeds as follows:

$$\begin{aligned}
 \cos i_c &= \sqrt{1 - \frac{V_1^2}{V_2^2}} \\
 &= \sqrt{\frac{V_2^2 - V_1^2}{V_2^2}} \\
 &= \frac{\sqrt{V_2^2 - V_1^2}}{V_2} \tag{18.1}
 \end{aligned}$$

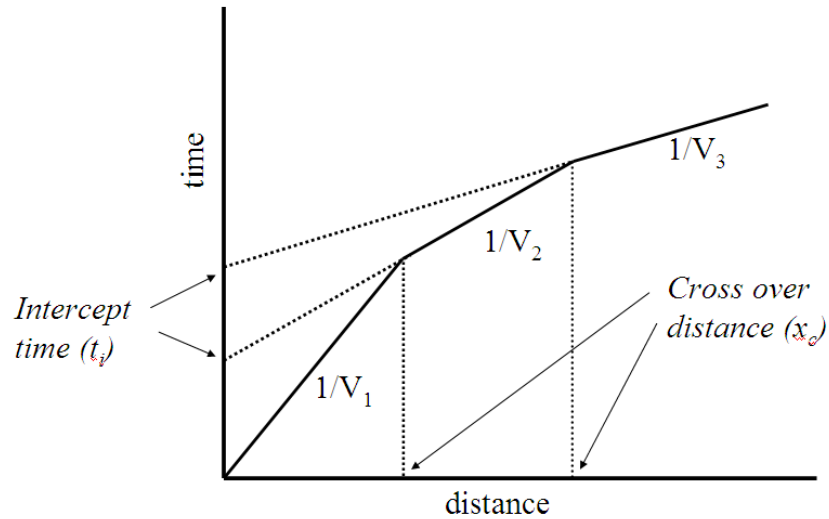


Figure 18.5: Intercept time and cross over distance for a 3-layer case.

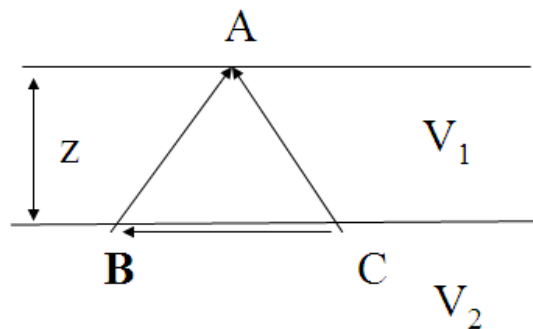


Figure 18.6: Geometric setup for calculation of layer thickness using seismic arrival times.

$$AB = \frac{z}{\cos i_c} \quad (18.2)$$

$$BC = 2AB \sin i_c \quad (18.3)$$

$$\begin{aligned}
T_{AB} &= T_{AC} \\
&= \frac{AB}{V_1} \\
&= \frac{z}{V_1 \cos i_c} \\
&= \frac{z}{V_1} \frac{V_2}{\sqrt{V_2^2 - V_1^2}}
\end{aligned} \tag{18.4}$$

$$\begin{aligned}
T_{BC} &= \frac{BC}{V_2} \\
&= \frac{2z \sin i_c}{\cos i_c V_2} \\
&= \frac{2z V_2}{\sqrt{V_2^2 - V_1^2}} \frac{V_1}{V_2}
\end{aligned} \tag{18.5}$$

$$\begin{aligned}
T_i &= (T_{AB} + T_{AC} - T_{BC}) \\
&= \frac{2z V_2}{V_1 \sqrt{V_2^2 - V_1^2}} - \frac{2z V_1}{V_2 \sqrt{V_2^2 - V_1^2}} \\
&= 2z \left(\frac{V_2}{V_1 \sqrt{V_2^2 - V_1^2}} - \frac{V_1}{V_2 \sqrt{V_2^2 - V_1^2}} \right) \\
&= 2z \left(\frac{V_2^2 - V_1^2}{V_1 V_2 \sqrt{V_2^2 - V_1^2}} \right) \\
&= 2z \left(\frac{\sqrt{V_2^2 - V_1^2}}{V_1 V_2} \right)
\end{aligned} \tag{18.6}$$

So the thickness of the surface layer is given by:

$$z = \frac{t_i}{2} \frac{V_2 V_1}{\sqrt{V_2^2 - V_1^2}} \tag{18.7}$$

Alternatively, it can be shown that the thickness can be expressed in terms of the cross-over distance:

$$z = \frac{x_c}{2} \sqrt{\frac{V_2 - V_1}{V_2 + V_1}} \tag{18.8}$$

18.5 Dipping layers

When layers are dipping, the effect of the dip on the travel time curves is to increase the slope of the arrivals from refracted layer if the direction of propagation is in the down-dip direction (Fig. 18.7). Up-dip, the slope decreases. Expressions can be derived for determining the dip and velocity, provided travel time curves are available in the up-dip and down-dip directions. Once the velocities are known, the layer thickness can be determined using the standard intercept time formula.

At this point, it is also convenient to introduce the concept of the reciprocal time. This is the time that it takes for the P-wave to travel via the refractor from one shot point to another. It is termed the reciprocal time because the same time will be recorded for the P-wave travelling in the opposite direction.

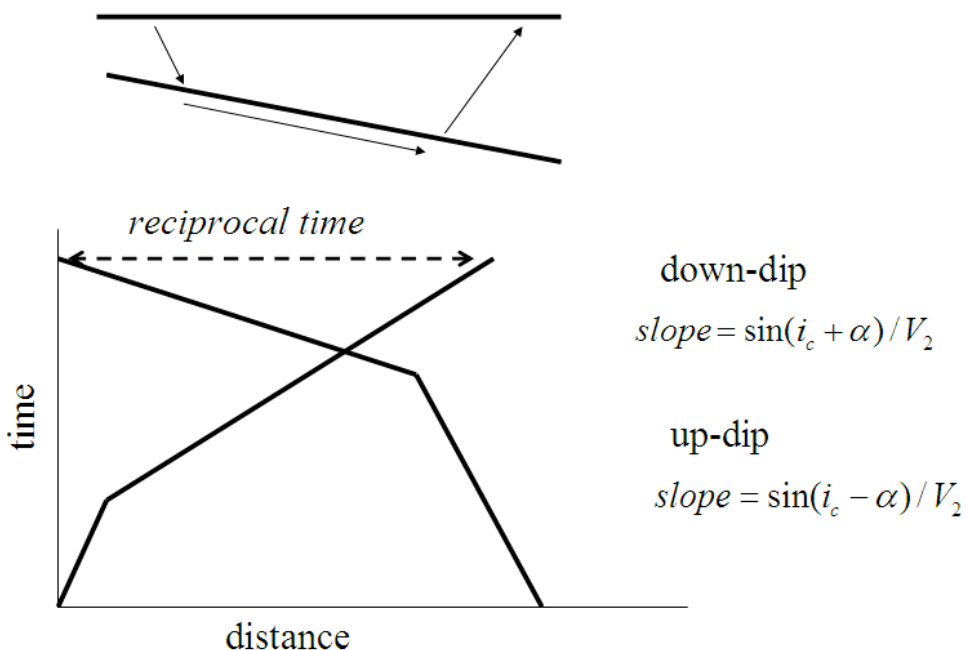


Figure 18.7: Seismic wave paths in dipping layers and reciprocal time.

In real applications, the formulas for the dipping refractors are not often used. It is important to understand the effect of the dip on the travel time curves and to understand the reciprocal time. The concepts of the reciprocal time and the half-intercept times are important in the real applications where methods such as the reciprocal method are applied.

18.6 Practical exercise: The reciprocal method

We will be continuing our instruction in the shallow seismic refraction method through a practical exercise aimed at showing how the analysis of actual seismic refraction data is undertaken.

Chapter 19

Quantitative seismic interpretation

As of today, significant hydrocarbon reservoirs are harder and harder to find and are mostly located in challenging locations which require to undertake large financial and operational risks. Deeper water, more complex reservoirs, smaller and subtle fields as well as sub-salt (Gulf of Mexico or Brazil/Angola) or sub-basalt (e.g. Faroers Basin) plays require sophisticated imaging techniques. This chapter will illustrate the connection between well data, seismic data and rock physics to allow to *quantitatively* describe reservoir parameters.

Aside from the established linking of well data through vertical seismic profiles (VSP) or combining refraction and reflection data, seismic attributes allow through using fundamental rock physics relations to quantify the geophysical signatures of rocks and geologic trends.

19.1 Seismic Sections

Seismic sections show the response of the earth to seismic waves. As Sheriff (1977; p.3) pointed out, as '*... most reflections [in a seismic section] are interference composites, there is no one-to-one correspondence between seismic events and interfaces in the earth*'. Even when it is possible to distinguish between reflections representing a change in acoustic properties, i.e. velocity and density, or impedance and reflections representing interference effects, interpretation ambiguities remain.

First, *changes in acoustic properties can, but need not, represent a lithological change. Only if a lithological change causes changes either in velocity or density, an associated seismic reflection can be expected*. On the other hand, changes in acoustic properties can be caused by diagenetic and/or compaction processes which might not always be visible in the core. Second, the vertical resolution (as the minimum separation between two reflectors needed to define separate interfaces rather than a single interface) is limited by the seismic source.

Generally, resolution is about one eighth to one quarter of a wavelength, depending on the

shape of the wavelet and background noise. Third, the accuracy of relating the position of a seismic reflector in two-way traveltimes to an impedance change in depth represents another uncertainty in seismic stratigraphy. Seismic sections are time-sections and the reflected energy is recorded as a function of two-way traveltimes. For interpretation purposes the reflected energy is displayed against two-way traveltimes. Interpretation of seismic horizons, in the context of identifying lithological boundaries, is based on a time-to-depth interpretation. This is not straightforward because the inversion from time to depth is not unique.

19.1.1 Seismic interpretation techniques and pitfalls

The following sections are based on (Avseth et al., 2010), a highly recommendable book if you are interested in seismic interpretation.

Seismic data records the impedance contrast of different rock layers in the subsurface. Whilst interpreters have long been focussed on qualitative interpretation of seismic data by following horizons of interest to create models of the subsurface, little attention had been paid to the *amplitude variations* in the seismic data. In the early 1970's the so-called *bright-spot* technique gained some interest after a set of discoveries in the Gulf of Mexico - the bright spots on the seismic data coincided with gas-filled sands. However, experience soon showed that this technique would not always work, due to a lack of wavelet phase analysis as hard volcanic intrusions would cause opposite polarity to low-impedance sands. Moreover, experience also showed that gas-filled sands sometimes could cause *dim spots*, not *bright spots* if the sands had high impedance compared to surrounded shales.

19.1.1.1 Wavelet phase and polarity

Determining the wavelet type is one of the first things to do when starting to interpret seismic amplitudes. The essential questions to ask are:

- What is the defined polarity in our case?
- Are we dealing with a zero-phase or a minimum phase wavelet?
- Is there a phase shift in the data?

These questions are not straightforward to resolve as the wavelet phase can change both laterally and vertically. The first thing to do is to define the standard when processing the data - there are two standards:

- 1.) The American standard defines a black peak as a **hard** or **positive** event and a white trough as **negative** or **soft** event. On a near offset stack section a hard event will correspond to an increase in acoustic impedance with depth, whereas a soft event will correspond to a decrease in acoustic impedance with depth.

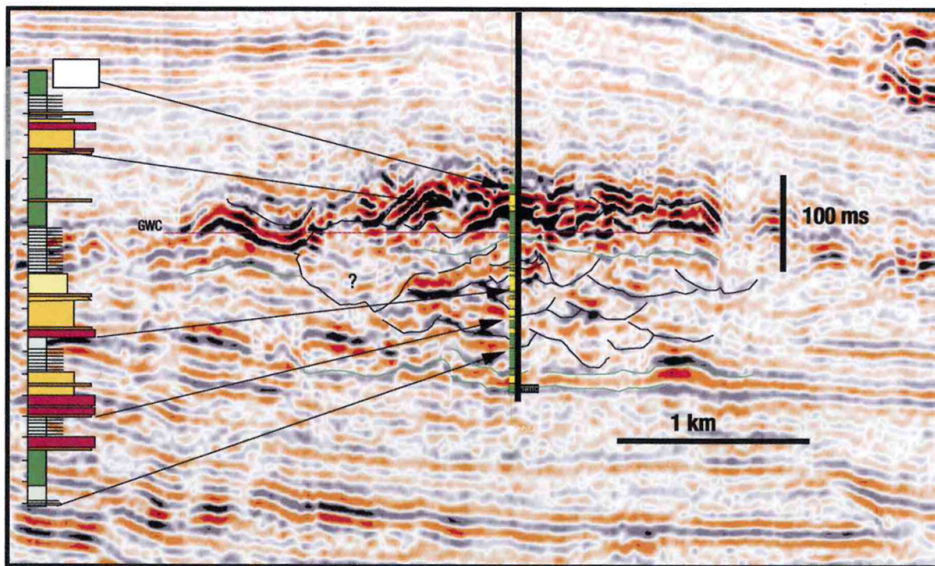


Figure 19.1: Seismic section intersecting a well penetrating a turbiditic gas and oil field, offshore West Africa. Gas was encountered in the upper sandy interval, whereas oil was found in the middle sand interval. Brine was encountered in the lower sandy interval (Avseth et al., 2010).

- 2.) The European or Australian standard defines a black peak as **soft** whereas the white trough is a **hard** event.

Data polarity

- American polarity: An increase in impedance gives positive amplitude, normally displayed as black peak or wiggle (wiggle trace) or red intensity (color display)
- European or Australian polarity: An increase in impedance gives negative amplitudes, normally displayed as white trough (wiggle trace) or blue intensity (color display).

For optimal seismic interpretation you should ensure that the data is a zero-phase. Then, the seismic pick should be on the crest of the waveform corresponding with the peak amplitudes that we desire for quantitative use. Autotracking is one option in the common interpretation packages which ensures that the horizon is always picked at peak amplitude.

19.1.1.2 Hard vs. soft event

Typical hard events

- Very shallow sands at normal pressure embedded in pelagic sands
- Cemented sandstone with brine saturation
- Carbonate rocks embedded in siliciclastics
- Mixed lithologies (heteroliths) likely shaly sands, marls, volcanic ash deposits

Typical soft events

- Pelagic shales
- Shallow, unconsolidated sands (any pore fluid) embedded in normally compacted shales
- Hydrocarbon accumulation in clean, unconsolidated or poorly consolidated sands
- Overpressured zones

Pitfalls in conventional interpretation

- Make sure you always know the polarity of the data. Remember there are two different standards: the American and European which are opposite polarity.
- A hard event can change to a soft event laterallt (ie. lateral phase shifts) if there are lithologic, petrographic or pore-fluid changes. Seismic autotracking will not detect these.
- A dim seismic reflector or interval may be significant, especially in the zone of shale/sand impedance cross-over. AVO analysis should be undertaken to reveal potential hydrocarbon accumulations.

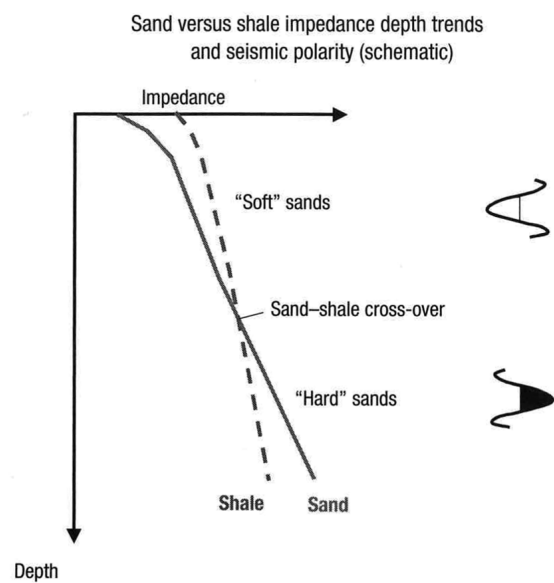


Figure 19.2: Schematic depth trends of sand and shale impedances. The depth trends can vary from basin to basin, and there can be more than one cross-over. Local depth trends should be established for different basins (Avseth et al., 2010).

19.2 Synthetic Seismograms

Velocity and density measurements from drilled sites provide a link between seismic data and the geology of the strata, and those measurements allow depth-to-time conversion and the generation of synthetic seismograms. Comparison of synthetic seismograms and a seismic section provides an excellent tool to constrain the interpretation of seismic horizons. An important requirement for a successful comparison is the similarity of the real wavelet and the one assumed for generating the synthetic seismograms.

Seismic impedance is defined as the product of velocity and density. The impedance contrast between two media of different elastic properties causes the reflections that are recorded along a seismic profile. A measure of the strength of the reflection is the reflection coefficient, which is the ratio of the amplitude of the reflected wave to the amplitude of the incident wave. For normal incidence, or zero offset, the reflection coefficient R , associated with the boundary between two layers 1 and 2, is defined as

$$R = \frac{I_2 - I_1}{I_2 + I_1}$$

where I is the seismic impedance associated with each layer.

Synthetic seismograms for normal incidence can be generated by using a *one-dimensional convolutional model*. This convolutional model does not include multiples, so that reflections can directly be identified in terms of variations in acoustic properties, and in terms of interference effects. In this approach the synthetic seismogram is obtained by convolving two time-series, a wavelet and a reflection coefficient log as functions of two-way traveltime. It is necessary that both time-series be sampled across the same sampling interval. The synthetic seismogram generated is obtained in the time-domain as a function of two-way traveltime, and therefore can directly be compared with the seismic data.

19.3 Synthetic Seismogram Construction

Synthetic seismograms are generated using a convolutional method. Based on velocity and density logs, acoustic impedance logs can be constructed at a given sampling interval (e.g. 15 cm). These logs are depth-to-time converted by using the velocity log and assuming homogenous layers. Given a burrowing mixing depth of about 10 cm to 15 cm in the deep sea it is considered appropriate to assume a linear gradient between calculated impedance samples. After linear interpolation the impedance logs are re-sampled in the time-domain (e.g. 0.0001 s). The reflectivity (or reflection coefficient) is then calculated for all layers to yield two reflection coefficient logs as functions of two-way traveltime (TWT). By convolving the source wavelet with the reflection coefficient logs for each site, synthetic seismograms can be generated.

Figure 19.4 shows the relationship between velocity, density, reflection coefficient, and synthetic seismogram for an ocean drilling site (Site 1137) on the Kerguelen Plateau. The synthetic seismogram is constructed by using a Ricker wavelet of 60 Hz (corre-

sponding to the main, central pulse of a watergun), and by using a watergun source. Comparison between the two allows to distinguish between interference effects and peaks due to a seismic reflector. Comparisons of the synthetic seismograms generated using the Ricker wavelet and the synthetic seismogram generated from the entire source wavelet allows us to distinguish the reflections of the central peak of the source wavelet at an impedance contrast from reflections arising from subsidiary peaks in the source wavelet.

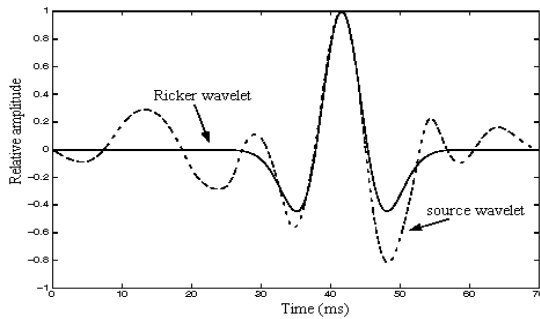


Figure 19.3: Ricker wavelet at 60 Hz centred on the central peak of the watergun wavelet

19.4 Link between Lithology and Seismic Section

In order to constrain seismic stratigraphy one has to determine how closely lithostratigraphy is linked to seismic reflections. It is essential to identify the different causes of reflections seen in the seismic data to know which reflections represent lithological changes and which do not.

First, a comparison of the synthetic seismograms and the seismic data allows the identification of seismic reflections representing noise and multiples. A comparison between the synthetic seismograms and the reflectivity logs makes it possible to determine reflections related to changes in acoustic properties: velocity and density; or impedance — and to distinguish those reflections caused by interference effects. A comparison of velocity and density logs with the lithology based on the visual core descriptions allowed the determination of how changes in the lithology and variations in acoustic properties are linked.

The synthesis of these comparisons defines the uncertainties of seismic stratigraphy concerning vertical resolution and accuracy: the vertical resolution as the minimum separation between two reflectors needed to distinguish separate interfaces rather than a single interface; and the accuracy of relating the position of a seismic reflector in two-way travelttime to an impedance change in depth. The correlation of reflectivity log and synthetic seismogram is not straightforward, because each reflection coefficient (or reflector, respectively) causes the reflection of the whole wave train of the wavelet. Closely spaced reflectors cause each a single reflection which interfere.

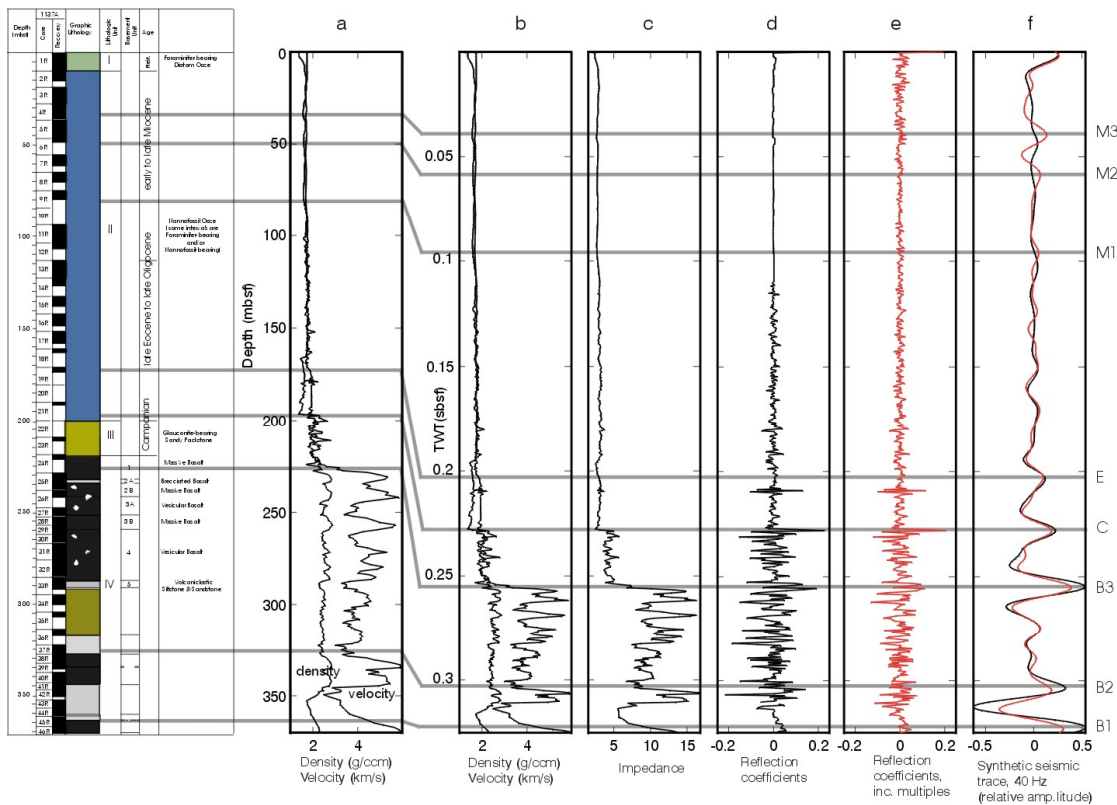


Figure 19.4: Relationship between velocity, density, reflection coefficient, and synthetic seismogram for an ocean drilling site (Site 1137) on the Kerguelen Plateau

Fig. 19.5 shows the seismic reflection data from the Queensland Plateau. For the upper 70 m of the velocity log velocity values are derived from measurements made on core samples (instead of logs) on very soft sediments (porosity >50%). These velocity measurements are quite inaccurate, and explain the discrepancy between synthetic seismogram and observed seismic data.

19.5 Geology and Seismic Sections

Linking well and seismic data helps us to fill in the gap between what can be observed in seismic section and in downhole data. Well information now has to be extrapolated away from where we have “ground truth”. This is done by (a) identifying and eliminating events relating to noise in the seismic data (artifacts), and by (b) using geological skills to translate seismic data into geological reality.

- 1.) *Reflection Continuity* describes the degree of lateral continuations of reflections shown in Fig. 19.6.

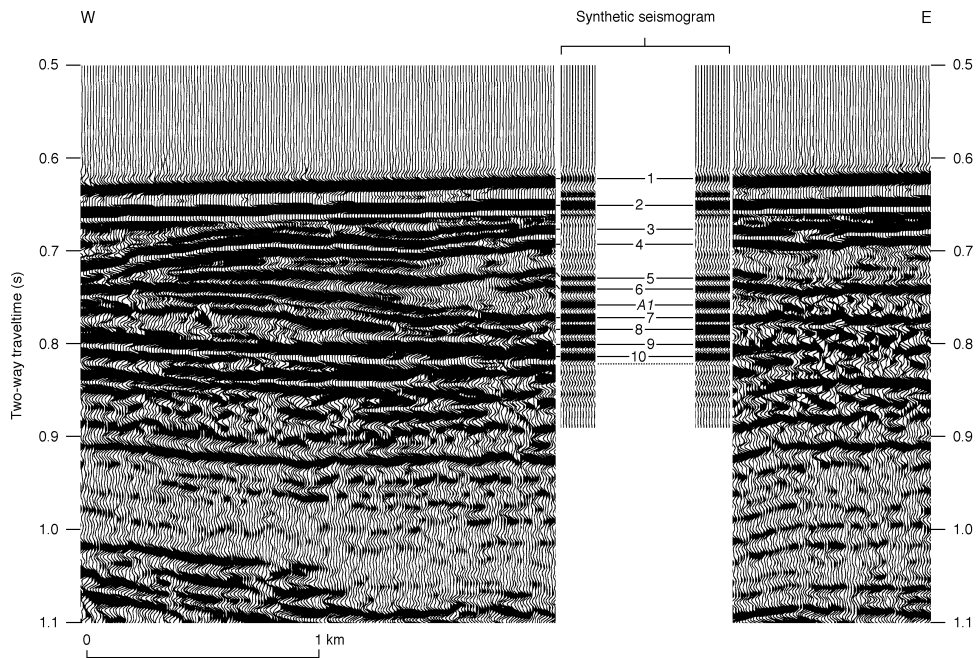


Figure 19.5: Correlation of seismic reflection data from the Queensland Plateau, collected in 1987 by AGSO on the R.V. Rig Seismic, using a water gun source with synthetic seismograms for ODP Site 812 on the Queensland Plateau off northeast Australia.

- 2.) *Reflection Amplitude* – These are thought to be more easily interpretable sections. Figure 19.6 also shows an example of a high and low amplitude section.
- 3.) *Reflection Spacing/Frequency* describes the number of reflections per unit time, also shown in Fig. 19.6 below.
- 4.) *Interval Velocity* – can be calculated to infer lithology if reflectors are spaced more than 100ms apart.
- 5.) Changes in reflections that can be observed in seismic data may suggest also changes in lithology.
- 6.) *Lithologies* are – (a) Sediments deposited mechanically – that is, transported by, and settled out from, a fluid; and (b) Sediments precipitated chemically or biologically.
- 7.) High-energy environments will produce lithologic units containing thick beds of coarse sediment, while still-water environments will take the remainder small particles to form thin deposits, which can be observed in the figure below.

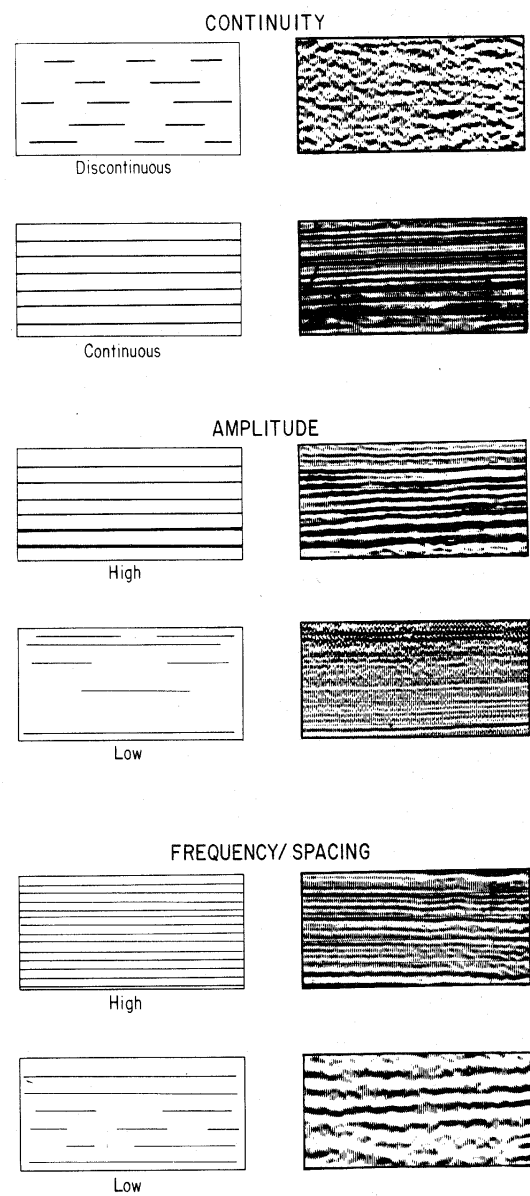


Figure 19.6: Continuity of seismic reflectors

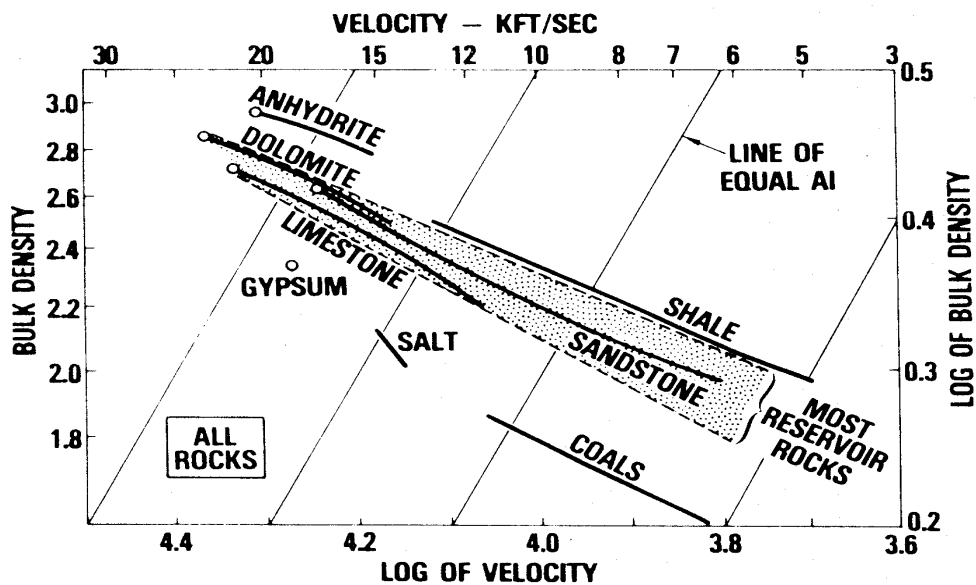


Figure 19.7: Interval velocities, here given in the handy kFt/sec unit, for major sedimentary rocks

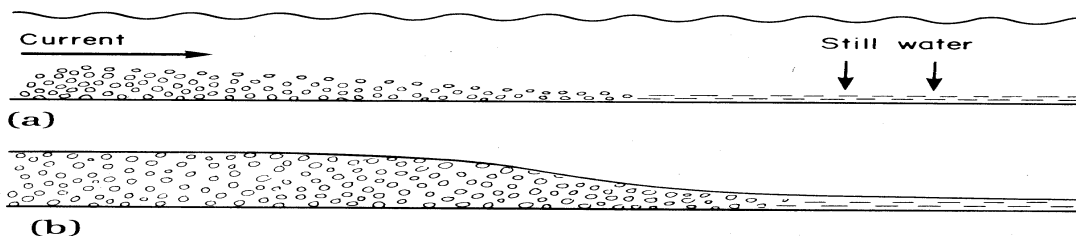


Figure 19.8: Distribution of sediment grain sizes in relation to water currents (a) and expected sequence stratigraphy (b)

- 8.) *Downlap* features may be seen when water levels drop, allowing for clastic sediment to migrate off shore (Fig. 19.9A).
- 9.) *Onlap* features are produced by sea-level rise, allowing for deposits to accumulate on top of previously deposited lithologies (Fig. 19.9 B.).
- 10.) Lithologic (Fig. 19.10) sequences are used to determine the type of event (Fig. A.), as well as the time relationships between different events (Fig. B.). Figure Fig. 19.11 shows potential shape and time relationships when several episodes of clastic deposition have occurred, and the inferred time relationships.
- 11.) Clay sequences, unlike clastic sequences, can thicken laterally due to differential

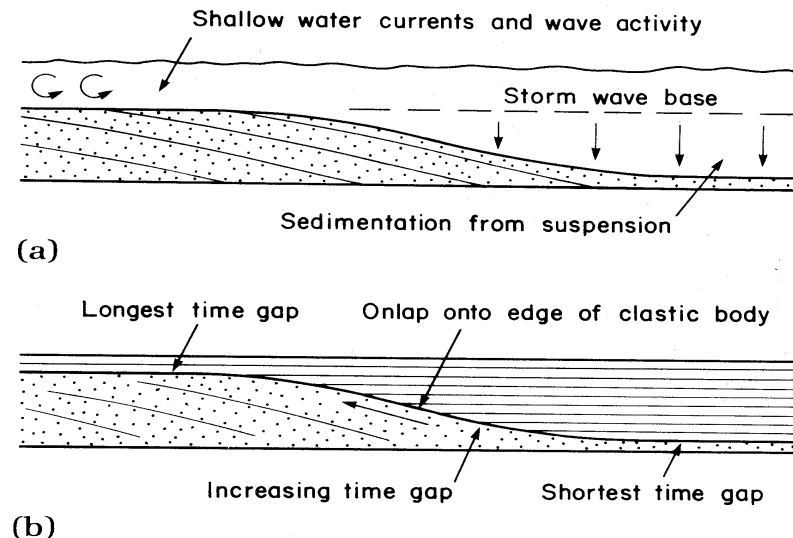


Figure 19.9: Onlap and downlap

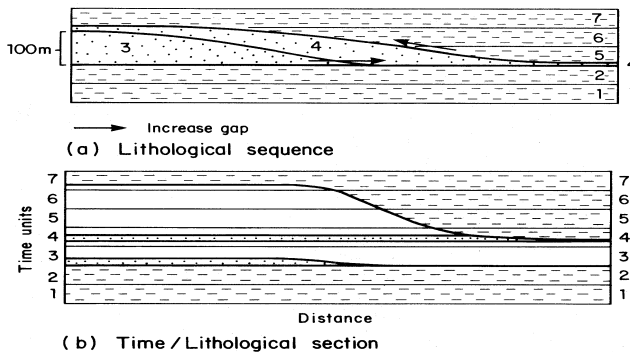


Figure 19.10: Lithologic sequences and seismic imaging

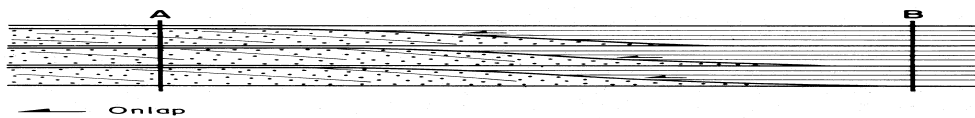


Figure 19.11: Several periods of clastic deposition and their sequence stratigraphic expression.

subsidence without involving major bounding or major internal unconformities, which can be observed in Fig. 19.12.

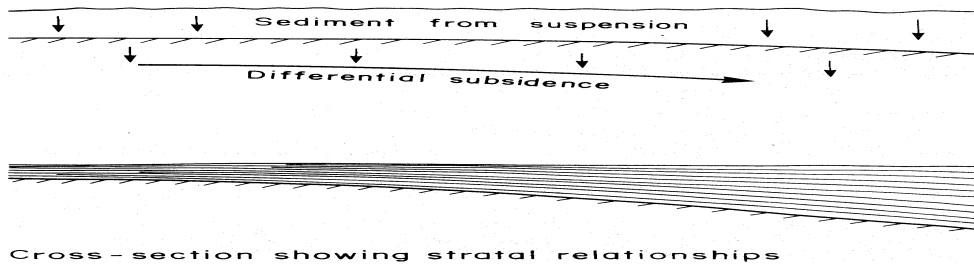


Figure 19.12: Differential compaction in clay sequences

- 12.) In shallow-water clastic environments, most individual units are so thin that they fall between 1/4 the wavelength turning thickness and the limit typically required to produce a reflection (about 1/30 wavelength). Such reflections will only vary in amplitude as thickness changes, as shown in Fig. 19.13.

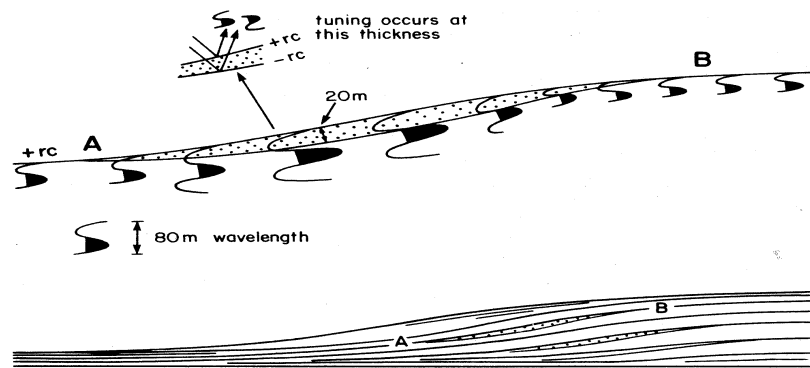


Figure 19.13: Amplitude and thickness changes of localised shallow water depositional units below seismic resolution.

19.6 Recognising Lithology

Recognizing lithology is to recognize fine-grained sediments, clastics, carbonates, salt, basement, and igneous rocks from seismic sections.

- 1.) *Clays and Silt* produce thinly bedded and closely spaced reflections, which may be seen in the figure following.
- 2.) *Clastics* appear at a variety of thicknesses, shape, and lateral extent. They are deposited in all environments. Internal velocity is not a good indicator, as shown in the figures below. It is better to consider the depositional environment.
- 3.) *Carbonates* - Thick sequences may appear thin in time on seismic sections due to high velocity, and the minimum thickness required for adequate vertical resolution can be high. Carbonates may appear as (a) sheet-like deposits, (b) bioclastic deposits, or (c) buildups, reefs, etc, as shown below. Figure 19.14 shows reflection configuration criteria for recognizing carbonate buildup on seismic profiles.

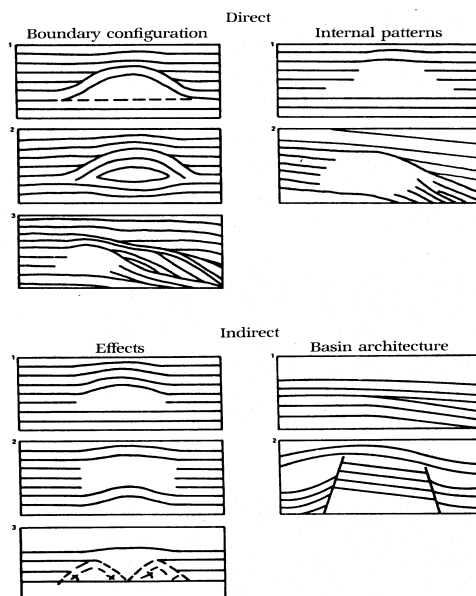


Figure 19.14: Reflection configuration criteria for recognizing carbonate buildup on seismic profiles

- 4.) Salt, shown in Fig. 19.16, may be recognized as pillow, diapir and postdipiric features, in that order, due to its unstable nature when buried (density inversion between the overburden and salt).
- 5.) *Igneous and volcanic rocks* - All of these are characterized by very poor data quality (Fig. 19.17). Gravity and magnetics can be invaluable aids to seismic for such

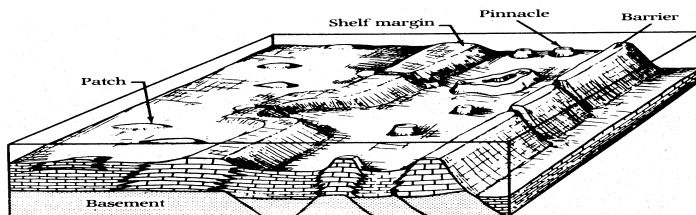


Figure 19.15: Carbonate environments and their spatial configuration

| GROWTH STAGE | UPLIFTED AREA | WITHDRAWAL BASIN |
|--------------|---|--|
| Pillow | <p>Geometry</p> <p>Sediments above pillow are thin over broad, equidimensional to elongate area. Maximum thinning over crest. Area extends 100 to 400 km² (40 to 150 mi²), depending on size of pillow. Percentage thinning, 10 to 100%.</p> <p>Facies</p> <p>Thin, sand-poor, fluvial-deltaic deposits over crest of pillow include interchannel and interdeltaic facies. Erosion common. Carbonate deposits on crest would include reef, reef-associated, and high-energy facies.</p> | <p>Geometry</p> <p>Sediments are overthickened in broad to elongate primary peripheral sink, generally located on up dip side of salt pillow. Axial trace of sink parallels axial trace of elongate uplift, generally separated by 10 to 20 km (6 to 12 mi). Sink attains 300 km² (120 mi²) in extent, depending on size of pillow. Percentage thickening, 10 to 30%. Recognition of primary peripheral sink may be hindered by interference of nearby salt structures.</p> <p>Facies</p> <p>Thick, sand-rich, fluvial-deltaic deposits in primary peripheral sink include channel axes and deltaic depocenters. Aggradation common in topographically low area of sink. Carbonate deposits in sink would include low-energy facies caused by increase in water depth.</p> |
| Diapir | <p>Geometry</p> <p>Strata largely absent above dome. An 8 to 50 km² (3 to 20 mi²) area around diapir is thinned, depending on size and dip on flanks of dome.</p> <p>Facies</p> <p>Facies immediately over dome crest not preserved because of piercing by diapir of all but the youngest strata. Sand bodies commonly pinch out against dome flanks.</p> | <p>Geometry</p> <p>Sediments are thickened up to 215% in secondary peripheral sink. Sinks up to 1,000 km² (390 mi²) in extent are equidimensional to elongate, and they preferentially surround single or multiple domes; several sinks flank domes; percentage thickening ranges from 50 to 215%.</p> <p>Facies</p> <p>Expanded section of marine facies dominates, including limestones, chalks, and mudstones; generally sink is filled with deeper water low-energy facies caused by increased water depth. Elevated saddles between withdrawal basins are favored sites of reef growth and accumulated high-energy carbonate deposits.</p> |
| Postdiapir | <p>Geometry</p> <p>Strata thin or absent in small 10 to 50 km² (4 to 20 mi²) area over crest and adjacent to dome; area depends on size of dome and dip of flanks.</p> <p>Facies</p> <p>Facies and strata over crest of dome not preserved in places of complete piercement. Modern analogs have interchannel and interdeltaic facies in uplifted area. Mounds above dome include thin sands. Carbonate strata would include reef or high-energy deposits; erosion common.</p> | <p>Geometry</p> <p>Sediments within 20 to 200 km² (8 to 80 mi²) tertiary peripheral sink are thickened 0 to 40%, commonly by < 30 m (100 ft). Axial trace of elongate to equidimensional sink surrounds or flanks a single dome, or connects a series of domes.</p> <p>Facies</p> <p>Modern analogs have channel axes in sink. Aggradation of thick sands common in subsiding sink. Carbonate strata would include low-energy facies.</p> |

Figure 19.16: Seismic imaging patterns of salt structures and related salt-tectonics.

interpretations. Sills and dykes are most readily identified in seismic data, as they usually occur together as lateral intrusions (Fig. 19.18). Volcano forms can also be identified in this way (see figure 19.19).

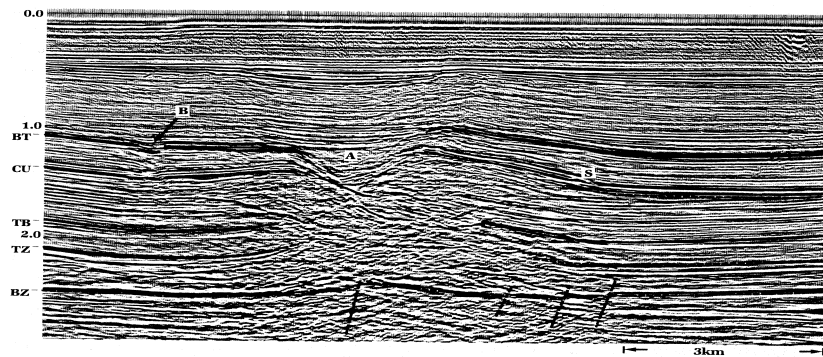


Figure 19.17: Volcanics and igneous rocks on seismic



Figure 19.18: Sills on seismic

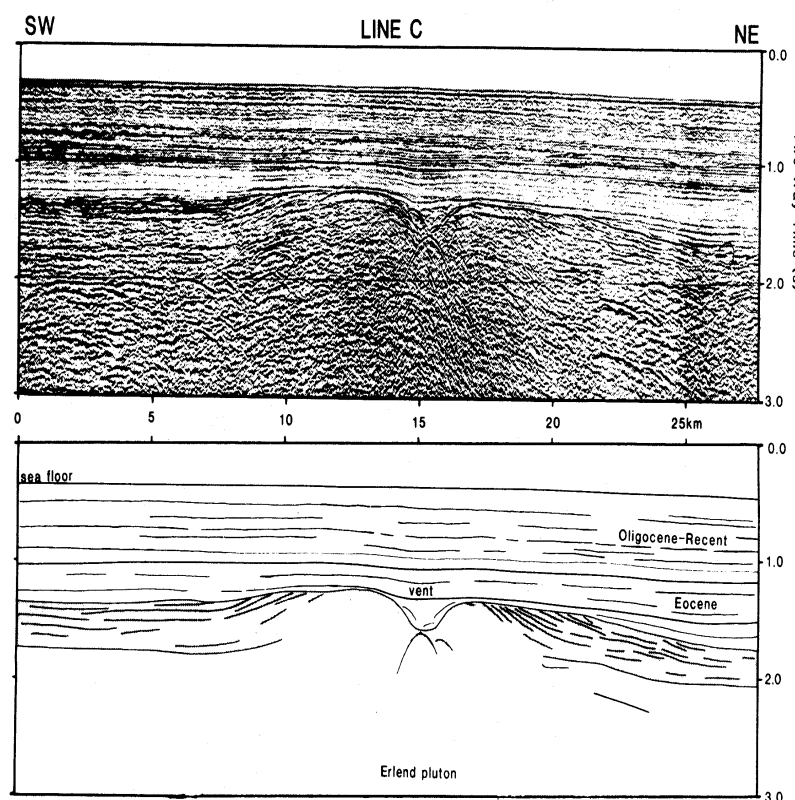


Figure 19.19: Recent volcanics on seismic (top) and interpretation (below)

19.7 Reflections Associated with Hydrocarbon and Diagenetic Effects

- 1.) Hydrocarbons and diagenesis also have visible reflectors on seismic data.
- 2.) Criteria for recognizing GAS in seismic sections include:
- 3.) *Acoustic-Impedance Effects* (Fig. 19.20) - If the gas column is thick enough and there is an acoustic-impedance contrast between the gas-/oil or the gas-/water-filled portions of a reservoir, a reflection commonly called a flat spot will result. Flat spots are likely to be found in porous sandstones or carbonates down to about 2.5 km. *Flat spots* will always have positive reflection coefficients, appearing as a trough on seismic sections, as shown below.

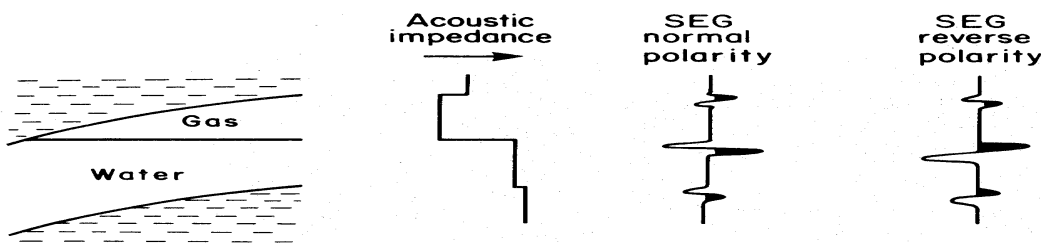


Figure 19.20: Acoustic impedance of a hydrocarbon reservoir

- 4.) *Dim spots* are associated with less-porous or well-compacted sand and carbonate reservoirs. Polarity reversal effects are summed in Fig. 19.21.
- 5.) *Velocity Effects* - If the gas column is sufficiently thick, a push-down effect may be observed on underlying reflectors.
- 6.) *Gas Chimney Effects* - These gas clouds produce poor data zones, as frequency is lost due to defracted reflections (Fig. 19.22).
- 7.) *Pitfalls* - (a) Gas saturation; (b) not all bright spots are caused by gas, shown in the figure below, shows that carbonates, igneous intrusions, thinning beds at tuning thickness, can all produce anomalously high reflection coefficients). Flat spots caused by diagenetic effects.
- 8.) *OIL* cannot be observed at a feature in seismic records, but reflections may be observed at the oil/water contact.
- 9.) *Diagenetic Effects* - The potential of diagenesis effects to produce reflections is observable with oil/water contacts. Also, the diagenesis of fine-grained silica-rich sediments, also, may cause an acoustic-impedance boundary. The figure below shows that the dissolution and precipitation of diatom frustules (the silicous cell

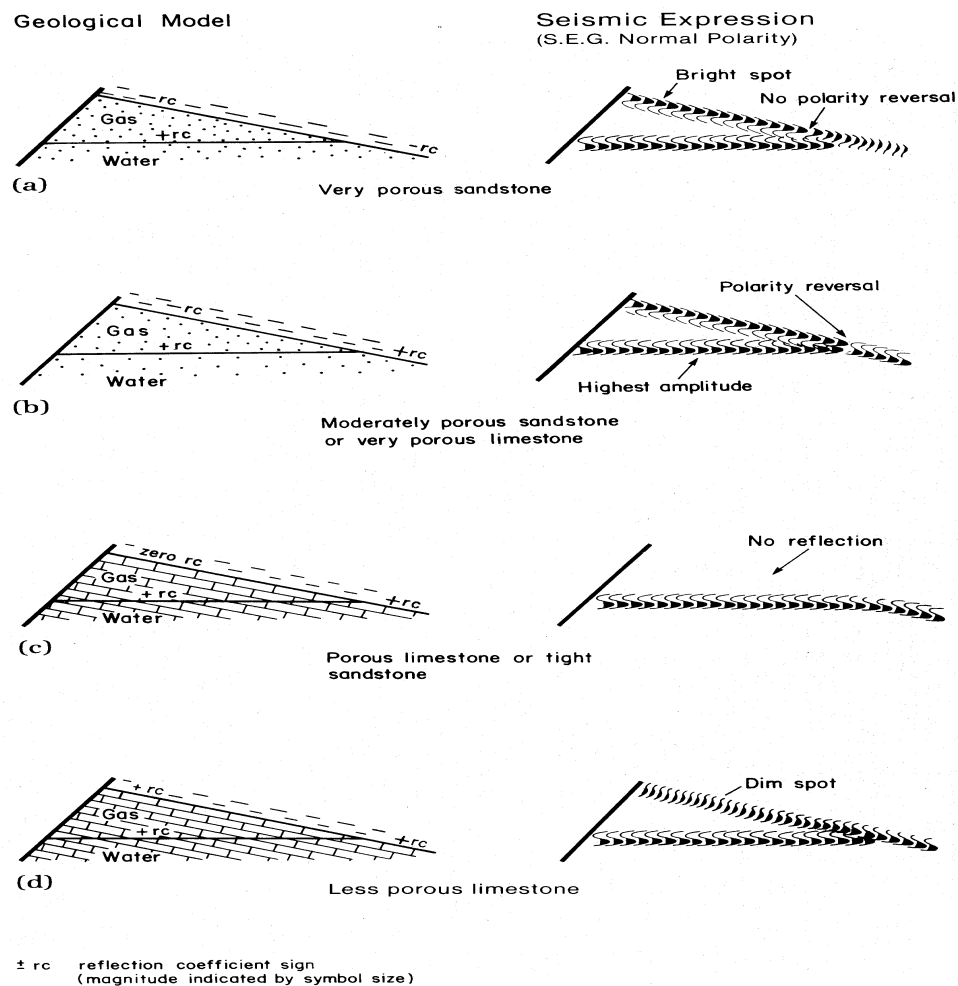


Figure 19.21: Bright and dim spots in seismic data and polarity effects

walls of microscopic single-celled plants) involved a change from opal-A to opal-CT. The change causes a marked porosity reduction, which results in increases in both density and velocity. These increases can produce a detectable acoustic impedance contrast. Since the change from opal-A to opal-CT is dependent on burial depth, the resulting reflection tends to parallel the sea floor. Opal-CT eventually changes to quartz, and the associated diagenesis front may also form a reflection. Opal-A & CT will over time migrate upward through the sequence, and may produce reduced reflection amplitude due to their depth-dependant diagenesis.

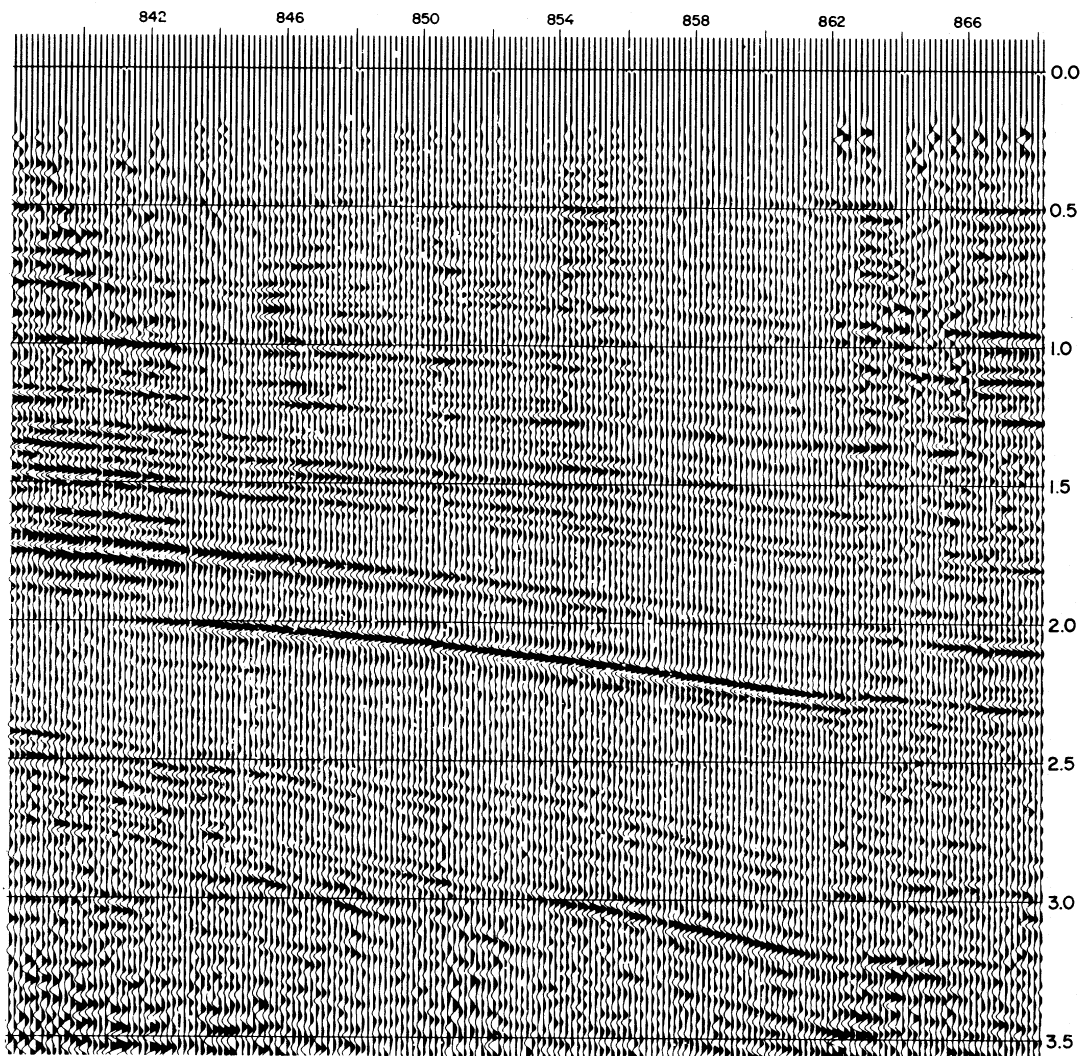


Figure 19.22: Gas chimneys on seismic data

Chapter 20

Borehole logging

20.1 Introduction

Most geophysical exploration techniques involve making measurements from the air or the ground surface. However, there is an additional class of geophysical techniques that involve taking measurements down drill holes. The incentives for this type of measurement are exactly the same as with the others – attempting to infer the properties of a rock mass and locate bodies of interest, but now it is from within a drill hole.

Geophysical downhole logging measures and records data in open or cased boreholes. A sonde, up to 18 m long and 10 cm in diameter is lowered downhole via a wireline connected to surface recorders and computers. The recorded measurements are plotted against depth providing a description of the lithology. The methods were invented by the Schlumberger brothers in France in early 1900's. Schlumberger is still the major logging company in the world.

Drilling is a big business. It is a drill hole that makes a mineral and hydrocarbon discovery and it is drill holes that prove up the resource. Australia's geological exploration expenditure for 2008 will probably be about \$6 billion. Most of this will be spent on drilling, but let us say that \$3 billion is spent on drilling and that drilling costs on average, \$50 per metre. That makes something like 60,000 km of holes drilled per year. Geophysical borehole (drill hole) logging is an important component to this drilling effort.

Drilling techniques could be the subject for another course. Geologists also work closely with drillers because it is geologists who chose the location of drill holes and it is geologists who need to assess the results of the drilling. Furthermore, as it is with most things, there is a trade-off between cost and quality of results. If the best possible drill hole results are required, drill (rock) core need to be recovered. To do this, diamond drilling is needed and costs are high. It is cheaper to drill a hole using rotary and percussion methods. With these methods, rock chips are only recovered. The geological data is compromised but the drilling is much cheaper and so more holes can be drilled.

This is where the geophysical methods fit in. By lowering geophysical tools down

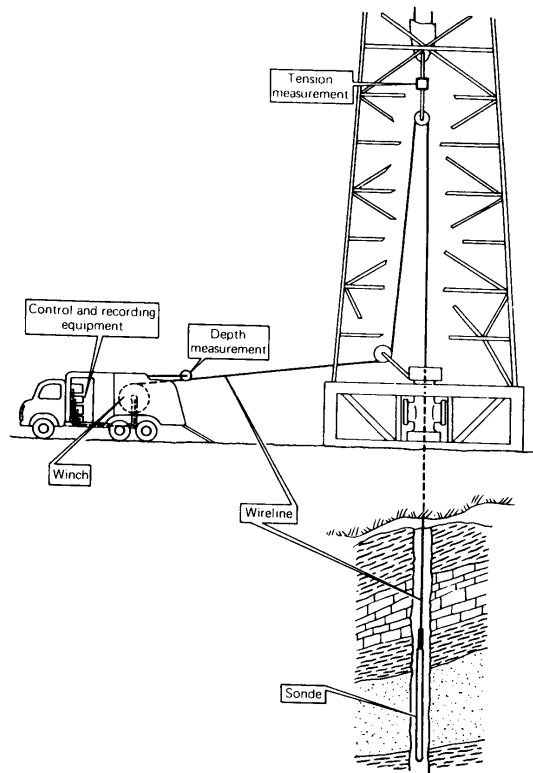


Figure 20.1: Schematic description of geophysical wireline logging. From Desbrandes (1985; Fig 9.2)

a drill hole and then making geophysical measurements along the drill hole wall while extracting the tool, an assessment of the down-hole geology can be obtained which supplements the chip logs. In many circumstances these so-called geophysical logs can provide adequate information – particularly given that most of a drill hole passes through the unproductive cover and host rocks prior to reaching the target.

It turns out that most of the surface and airborne geophysical methods that we are learning about can also be applied down drill holes. There are also some geophysical logging techniques that don't have an analogue outside of the drill hole. The main geophysical drill hole logging techniques are:

1.) Radiometric logs

- natural gamma
- density (gamma-gamma)
- neutron (neutron-neutron)
- spectrometric logging

2.) Sonic logs

3.) 'Electric' logs

- resistivity
- conductivity
- dip meter
- self potential
- magnetic susceptibility
- induced polarisation

4.) Imaging tools

- acoustic scanner
- electrical imaging

5.) Drill hole survey tools (magnetic and non-magnetic)

6.) Temperature

7.) Caliper (borehole diameter)

Externally, geophysical logging tools all look much the same. They are encased in steel cylinders designed to fit within the drill holes and to withstand the pressures that might exist from a head of water that can be hundreds, if not thousands of metres. A cable is attached to the tool and connects the tool to control and recording apparatus in a truck at the ground surface. There may be a bow spring or caliper arms to push the tool against the borehole wall.

The tool is moved up and down the hole using a winch which measures the position of the tool with cm accuracy, even at great depth. If the depth control is not accurate, then the benefits of the logging are lost. Survey is also important and there is a class of geophysical logging tools designed to accurately determine where the hole has gone. Again, the value of the hole can only be properly realised if we know the position of the hole.

In general terms, the holes drilled in petroleum exploration are wider (e.g. 30 cm diameter) and deeper (kilometers), compared to the holes drilled for coal exploration (10 cm diameter, 100's of metres depth), and compared to the holes drilled for minerals exploration (3-6 cm diameter and up to several hundred metres depth). The additional size afforded by a petroleum well has advantages for the development of geophysical logging instrumentation (more room for instrumentation). A petroleum well can also cost millions of dollars to drill and so the incentives to maximize the amount of geophysical information that can be obtained from the well are considerable.

The use of geophysical logging is deeply entrenched in petroleum exploration and also in coal exploration. In minerals exploration, geophysical logs are still often run

but the diameter of the drill holes can restrict the number of tools that can be run. The remote locations of many drilling sites can also provide problems for the mobilization of a geophysical logging crew.

TRADE NAMES OF MAIN LOGGING TOOLS

| | HALLIBURTON | | SCHLUMBERGER | | ATLAS WIRELINE SERVICES | |
|--------------------------|--|---------------|--|---------------------------------|--|-------------------|
| Induction | Induction Electrolog Dual Induction Laterolog | IEL DIL | Induction Electrical Logging Ind. Spherically Focused Dual Induction Log Dual Induction SFL Array Induction Tool | IEL ISF DIL DIS AIT | Induction Electrolog Dual Ind. Focused | IEL DIFL |
| Resistivity | Dual Laterolog | DLL | Dual Laterolog | DLL | Dual Laterolog | DLL |
| Micro-resistivity | Microlaterolog Micro Spherically Focused | MLL MSF | Microlaterolog Micro Spherically Foc. Log Proximity log | MLL MSFL PL | Microlaterolog Proximity Log | MLL PL |
| Neutron | Sidewall Neutron Compensated Neutron Log | SNT CNS | Sidewall Neutron Compensated Neutron Log | SNP CNL | Sidewall Neutron Compensated Neutron Log | SWN CNS |
| Density | Compensated Density Log | CDL | Formation Density Litho Density Log | FDC LDL | Compensated Density Log | CDL Z.Densilog |
| Acoustic | Borehole Compensated sonic Long Spacing sonic | BCT BCT-EA | Sonic Log Sonic Long Spacing Sonic Digital Tool Dipole Sonic Imaging Tool | BHC SLS SDT DSI | Normal Space Acoustilog Long Spacing Acoustilog | AC ACL |
| Gamma ray | Gamma Ray Spectral Gamma Ray | UGR SGR | Gamma Ray Gamma Ray Spectroscopy | GR NGS | Gamma Ray Spectralog | GR SPL |
| Dipmeter | Four Electrode Dipmeter Omnigraphic Dip. Tool Six Arm Dipmeter | FED SED | High Resolution Dipmeter Tool Stratigraphic Dip. Tool Formation Micro Scanner | HDT SHDT FMS | Four-arm Dipmeter | DIP |

- The above list is not exhaustive and the abbreviations given may be subject to slight modifications.
- Other contractors offer comparable services under different trade names.
- Most of the commercial logging tools mentioned here can be used in combination with each other, under names and conditions given by the manufacturer (see catalogues for more details).

Figure 20.2: Trade Names of Main Logging Tools. The list is not exhaustive and the abbreviations may be subject to slight modifications. Other contractors offer comparable services under different trade names. Most of the commercial logging tools mentioned here can be used in combination with each other, under names and conditions given by the manufacturer (From Boyer & Mari 1997).

20.2 Radiometric tools

The radiometric tools can be passive or active. The passive tools detect the natural gamma radiation for the rocks in the borehole wall (Fig. 20.3). Just as with airborne and ground surface radiometric surveys, the radiation can be measured as total counts (most commonly) and/or as a spectrum (K, U and Th channels).

20.2.0.3 Natural gamma logging

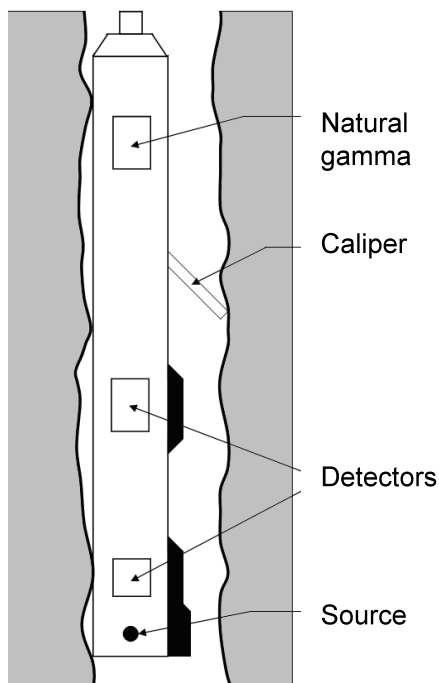


Figure 20.3: Gamma ray log tool

tive material. The advantage of the API is that provides for the calibration of natural gamma logs.

For the simple case of a borehole passing through a sequence of clean sandstones and clays, the clay content at any particular point can be scaled using this formula:

$$C \approx \frac{\gamma - \gamma_{\min}}{\gamma_{\max} - \gamma_{\min}}$$

Where the maximum and minimum values are those for the ‘pure’ clay and the clean sands respectively.

The natural gamma log is often used to indicate the presence of shale and clay layers within a borehole because most common clay minerals contain potassium and so there is an increase in the natural gamma radiation. (An exception occurs with the clay mineral kaolinite. Kaolinite does not contain any K and so there is no increase in gamma radiation due to the absence of K in kaolinitic clays. Shales and other lithic material also tend to have greater concentrations of Th and U which are also important for the generation of natural gamma rays.

At the other extreme, the clean sands that make for good petroleum reservoirs contain little clay and so the gamma radiation from a clean sand is low.

Natural gamma logs can be recorded in total counts per second, or alternatively in API units (American Petroleum Institute). The API is an arbitrary unit devised on the basis of a world-wide system of test beds where concrete blocks are seeded with known amounts of radioactive material.

20.2.0.4 Density logging

The density log also measures gamma radiation but there is a source of gamma radiation – usually ^{60}Co or ^{137}Cs , at the base of the tool. This source emits much stronger radiation than the natural gamma radiation and detectors located close to the source detect gamma radiation back-scattered from the electrons on the atoms in the rocks around the borehole wall. The greater the electron density, the greater the amount of back-scattered gamma radiation. Electron density is approximately related to the atomic density, and so to the mineral density and therefore the rock density. With the use of two detectors, compensation can be made for variations in the diameter of the borehole and a calibrated density measurement can be made,

In minerals exploration, density measurements may tell you about the presence of metallic ores in the borehole. In clastic rocks – i.e. petroleum reservoir rocks, the density is related to both the mineral density and the porosity. The following simple formula relates porosity, ϕ , to the measured density, ρ , the density of the dominant mineral, ρ_{ma} , and the density of the fluid in the pore spaces, ρ_f .

$$\phi \approx \frac{\rho_{ma} - \rho}{\rho_{ma} - \rho_f}$$

It is essential for a petroleum reservoir to have adequate porosity.

20.2.0.5 Neutron logging

The neutron tool utilises a source (either PuBe or AmBe) that emits neutrons that bombard the borehole wall. The neutrons interact with the atoms in the rocks in the borehole wall. When the atoms have a similar atomic weight to a neutron, the neutrons collide, like billiard balls and loose energy. When they have lost enough energy they can be captured by a detector which is container filled ^3He gas and a detectable charge is generated. The atoms that have similar mass to neutrons are hydrogen atoms (1 neutron and 1 proton). In rocks, hydrogen is present mainly in water (and hydrocarbons – coal, petroleum) and so the neutron log is able to detect the presence of water. The neutron log therefore supplements the porosity information available from a density log. Integrated analysis of these two logs permits inference of the nature of the fluids filling the pores – water, hydrocarbons and gas. If calibrated, neutron logging data can be provided in terms of porosity.

In sedimentary rocks, water can be present in two modes. It can be present as free water within the pores of the rocks. It can also be bound within the crystal lattice of clay minerals. Clays have a sheet-like atomic structure and the bound water occurs between the layers. The clay content can be determined using the following formula.

$$C = \frac{\phi_N - \phi_D}{\phi_{NSh} - \phi_{DSh}} \quad (20.1)$$

where C is the clay content, φ_N is the porosity from the neutron log, φ_D is the porosity determined from the density log, φ_{Nsh} is the observed neutron porosity in a shale (clay), and φ_{Dsh} is the shale porosity indicated by the density log.

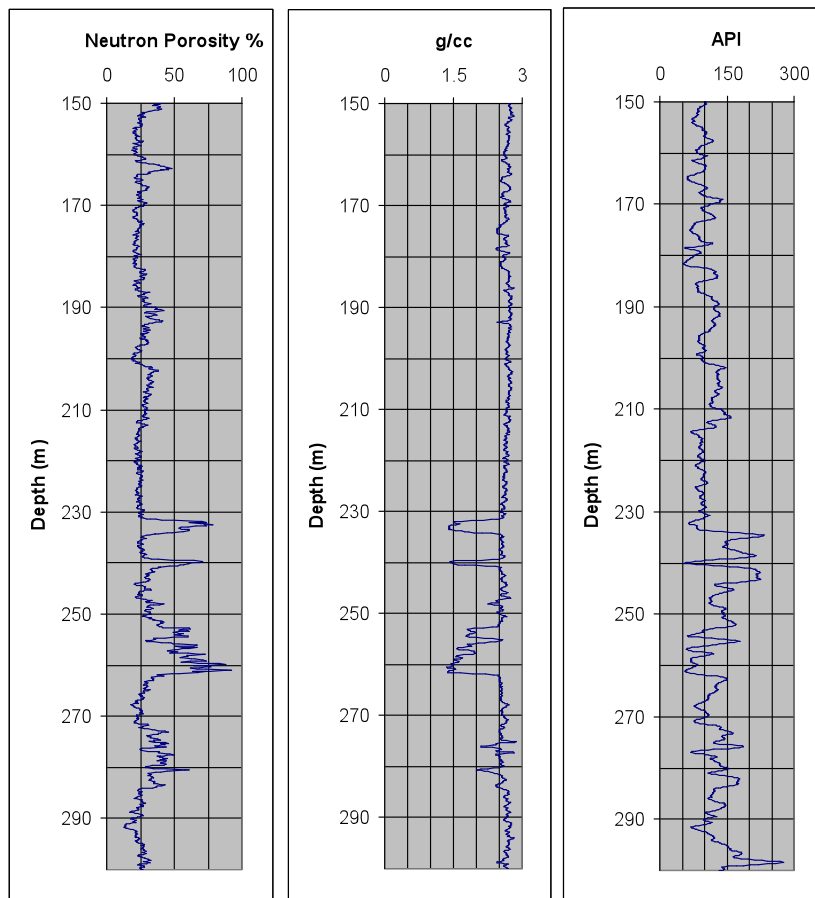


Figure 20.4: Radiometric log data (neutron, density and natural gamma) through a sequence of sandstones, shales and coal

20.2.0.6 Sonic logging

Sonic logging¹ is effectively a seismic refraction survey undertaken up the borehole wall. At the base of the tool there is a source of acoustic energy emitting pulses with a frequency content of about 15-20 kHz. These pulses are transmitted through the fluid (water) within the borehole and to the borehole wall. Here the energy can be reflected, transmitted and mode converted, just as with a seismic survey. Critically refracted P-

¹Sonic logging is the conventional name for this type of logging technique. The term sonic refers to the fact that acoustic waves (i.e. sonic, or P-waves) are the main type of wave that is measured.

and S-waves can propagate up the borehole wall, refracting P-wave energy (remember, there are no S-waves in water) back into fluid column in the borehole. An array of receivers mounted near the top of the tool detects the arrival of the P-waves. Given the simple geometry of this experiment, the difference in the arrival times to the receivers (transit times) can be used to determine the speed of either the P-wave, or the S-wave travelling in the borehole wall (Fig. 20.5).

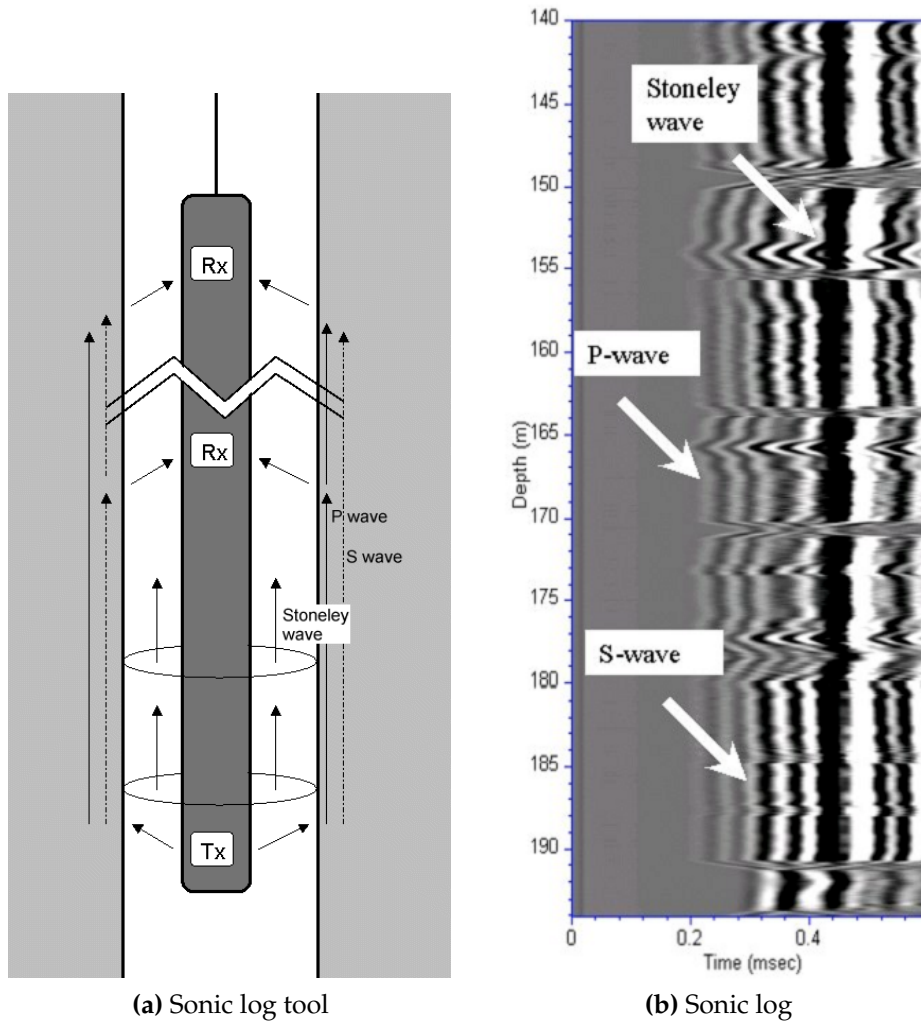


Figure 20.5: Sonic log tool (a) and annotated sonic log (b)

Some sonic logging detects just the first onset of the seismic energy. The P-wave velocity is therefore the only measurement possible. If the full waveform of the seismic signals arriving at the receivers is recorded – full waveform sonic logging, then later arrivals can be identified – the S-wave and a surface wave known as a tube or Stoneley

wave which travels up through the fluid column and borehole wall (Fig.??).

$$V_{St} = \left[\rho_f \left(\frac{1}{K_f} + \frac{1}{\mu} \right) \right]^{-\frac{1}{2}} \quad (20.2)$$

With a knowledge of P- and S-wave velocities, as well as density, it is possible to determine dynamic elastic moduli. You will sometimes see sonic logging data given in terms of microseconds per foot. Conversion to km/s is straightforward.

20.2.0.7 Resistivity logging

There are many types of resistivity logging tools. The earliest and simplest tool involved passing a current between two electrodes and recording potential differences between another two (Fig. 20.6). More modern tools, utilise guard electrodes which maintain a desired balance between multiple current electrodes and force the current to flow away from the borehole in the direction perpendicular to the wall. Generally known as the laterologs, these types of resistivity logs provide much better bed resolution. Resistivity logs can also be run off the pads of a multi-armed caliper log which measures the borehole diameter. The resistivity measurement is known as microresistivity logging or as a dipmeter because the dips on beds can be determined.

We have already been introduced to Archie's Law which relates resistivity to porosity and the fluid resistivity. The application of Archie's Law is very important in assessing hydrocarbon reservoirs because, the resistivity of a formation will vary depending on the type of pore fluid – liquid hydrocarbon versus water versus gas.

Another use for resistivity logs is in estimating clay content. Unlike most rocks which are resistors, clay will allow some electric current flow. Extending Archie's Law to include parallel resistors – one for the flow through the pore waters and one for the flow through the clay, we get:

$$\frac{1}{\rho_{total}} = \frac{V_{shale}}{\rho_{shale}} + \frac{1}{\rho_{DueToFluid}} \quad (20.3)$$

The resistivity due to the fluid is given by Archie's Law and thus it possible to determine V_{shale} .

20.2.0.8 Some additional logs

Logs often run in conjunction with the above tools are a survey tool and a temperature tool. The survey tool needs to determine both the orientation and the dip of the hole. This is achieved using a combination of accelerometers which determine the dip and orientation devices – either magnetic or non magnetic for use in magnetic rock types (e.g. gyroscopes and ring lasers).

The temperature log determines the formation temperature. This relatively simple log can be useful for determining unusual heat flows – e.g. the cooling effect of a nearby mine entry or a heating due to radioactively 'hot' materials such as granite.

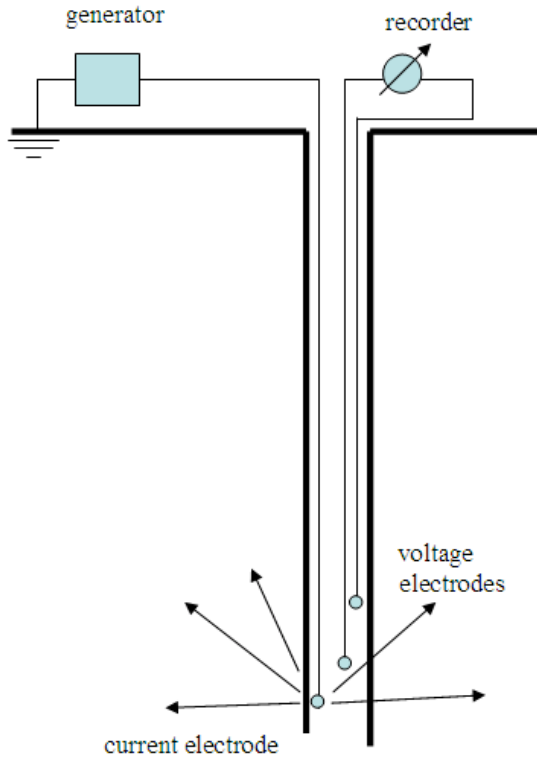


Figure 20.6: Resistivity logging (schematic)

The caliper is another useful log. It can be as simple as a single spring loaded arm which is kept in contact with the borehole wall while the log is being drawn up a borehole. Multiple arm calipers are also available. The caliper log provides some degree of quality control on down-hole conditions. If the holes are caving (opening up) due to the degradation of weak rock in the borehole wall, this is potentially useful information in its own right and it can also point to the possibility of data quality issues with the other logs. Breakout is special form of borehole collapse. This occurs when the horizontal stress field is sufficiently strong to cause failure in the borehole wall in the direction perpendicular to the dominant horizontal stress. The directions of the major and minor horizontal stresses can thus be obtained from a knowledge of the orientation of the breakout. Figure 20.7 gives an overview.

20.3 Acoustic and optical scanners

Acoustic scanners (or telev viewers) utilise a high frequency sonic beam which rotates around the borehole to produce what is effectively a seismic reflection image of the borehole wall. The frequency content of an acoustic scanning signal is centred at about 1

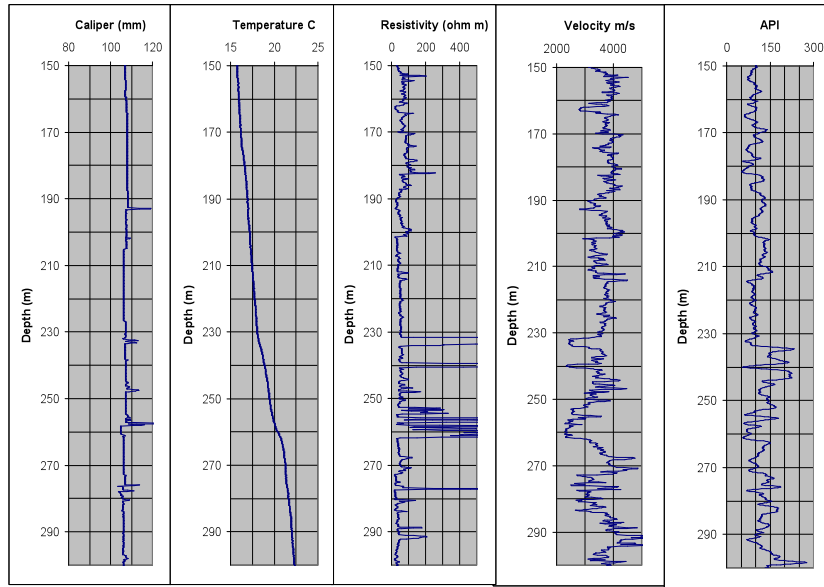


Figure 20.7: Caliper, temperature, focused resistivity, velocity and natural gamma logs for the previous example.

MHz and the tool produces images at vertical spacings of just a few mm up the borehole wall. By recording the reflection time for each pulse it is also possible to get an accurate 360° measure of the shape of the borehole. Combined with an accurate determination of the orientation of the tool, accurate breakout measurements are thus possible.

The image of the wall shows the differences in the acoustic impedance contrast between the different rock types and the borehole water (i.e. it is responding to the same reflection coefficients utilised in seismic reflection surveying). Fractures in the borehole wall also produce changes in reflection amplitude. The fractures appear as sinusoidal patterns with peaks and troughs appearing at the directions corresponding respectively to the highest and lowest point of the fracture plane in the borehole. Fracture directions and dips are thus obtained.

Acoustic televiewers must operate in water. Optical scanners allow measurements out of water and in water (if the water is clear).

20.4 Self potential logging

Self potential (SP) logging is a simple logging procedure with a complicated explanation. All that is involved is a measurement of potential difference between a down-hole electrode and an electrode at the surface. It is found that the potential difference changes at the boundaries of beds e.g. sandstone to shale to coal because of differences in the salinity between the borehole fluid and the fluids in the formation and differences

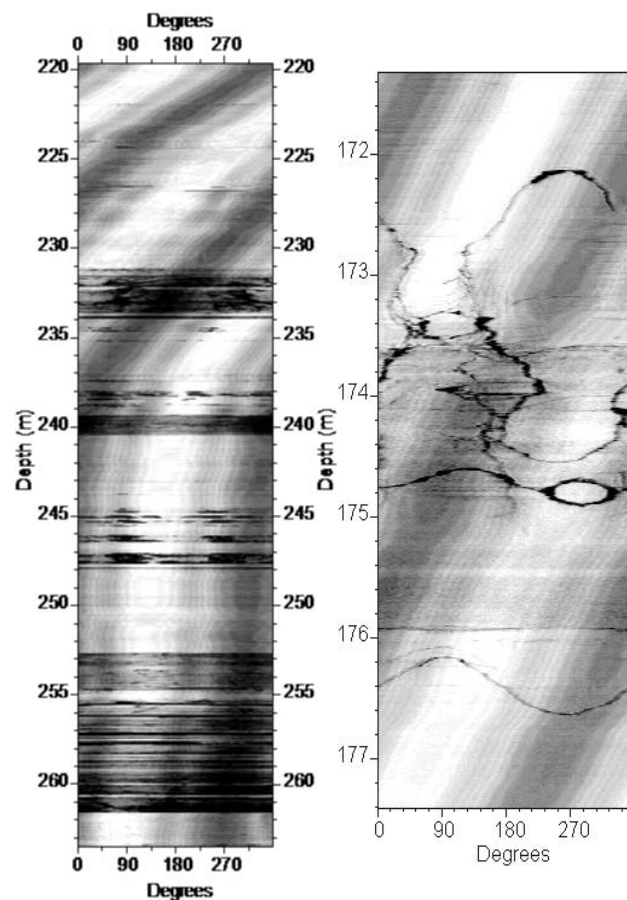


Figure 20.8: Acoustic scanner data. Left - changes in acoustic impedance indicates changes in rock type. Right – dipping fractures and breakout evident in detailed section of scanner log. Diagonal banding is due to tool being off the centre of the borehole.

in the porosity and permeability in the rock units. Similar electrochemical processes can also be at play when boreholes intersect sulfide orebodies and there are differences in the mineralization caused by oxidation above the water table.

20.5 Logging methods for hard rock/mineral targets

In addition to the logging methods that we have been discussing there are a few additional logging techniques that are applied in minerals exploration and mining.

20.5.1 Conductivity logging

In minerals exploration and mining, the target ore bodies are often electrically conductive. Boreholes can also be drilled in environments where there is no water in the boreholes. In both of these cases, conductive logging can replace resistivity logging and the presence of the ore body can be detected.

The source for the conductivity log is a wire coil inside the probe through which an alternating electric current is passed. By Ampere's law this generates a magnetic field which passes into the body of rock surrounding the hole. By Faraday's law the alternating magnetic field induces an electric current in any geological conductors present. In turn, the induced electric current generates a magnetic field and that magnetic field will generate an electric current in a receiving coil in the conductivity probe.

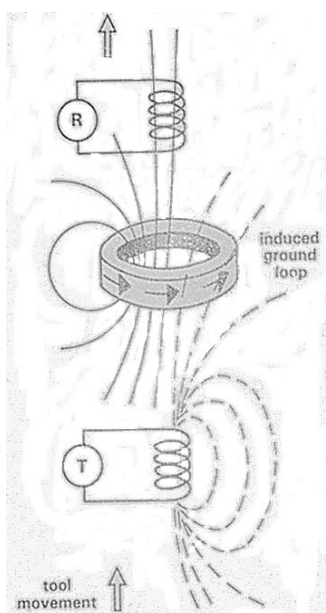


Figure 20.9: Conductivity Logging

The strength of the electric current in the receiver depends on the strength of the current in the ground – i.e. the conductivity of the geological target. Note that the conductivity tool does not require direct contact between the probe and the borehole wall.

20.5.2 Magnetic susceptibility logging

Magnetic susceptibility logging utilises the same principals as conductivity logging. If magnetically susceptible material is present, the current induced in the ground has different properties that can be detected and assigned to variations in magnetic susceptibility.

20.5.3 Induced polarization logging

The IP tool utilises the fact that current flow through disseminated ore bodies is a mixture of ionic flow through pore waters and electron flow through the metallic ores. If a down-hole current source is

switched on, current flow will commence. As the result of the ionic flow through the pore ware, ions will build up at the metallic contacts where electron flow then occurs. It takes time for ionic flow to occur. (Much longer than electron flow!) If the current is switched off, the rock material will return to equilibrium and so the ionic flow will re-

verse. Potential electrodes located on the IP logging tool detect the current flow during the on and off period to assess the polarisability (chargeability) of the rock mass.

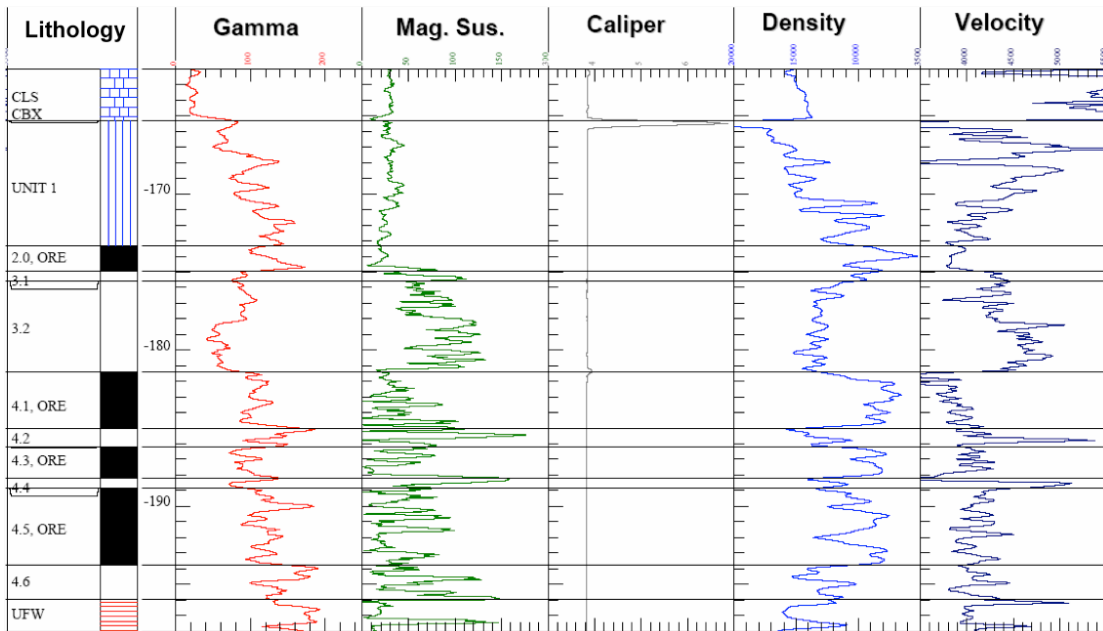


Figure 20.10: Example of geophysical log results in sphalerite (Zn) ore from Century Mine

20.5.4 Out-of-hole detection and imaging

Boreholes also provide the opportunity for other types of geophysical exploration. These include:

- 1.) Cross-hole seismic imaging. The sources and geophones are in separate holes. Tomographic analysis which is similar to some types of medical imaging, can be undertaken of the waves propagated between the holes.
- 2.) Borehole vertical seismic profiling. VSP surveys usually involve a repeatable seismic source at the surface and geophone(s) moving down the hole. Reflections are obtained from reflectors intersecting the hole and from below the hole. VSP surveys assist with the characterisation of the wave propagation and the identification of seismic reflectors on seismic reflection surveys.
- 3.) Down-hole gravity and magnetic surveys for locating off-hole targets.
- 4.) Down-hole em surveys for locating conductive targets off-hole (discussed later).
- 5.) Down-hole radar surveys for imaging reflecting boundaries (discussed later).

Chapter 21

Sedimentary Basins and margins

21.1 Introduction

21.1.1 Overview

Approximately 70% of the continental crust is covered by more than 2 km of sediment (see Fig. 21.1). The major accumulations occur in sedimentary basins and on continental shelves. Basins host enormous quantities of natural resources, including coal, oil and gas, as well as various mineral deposits. Sediments in basins also record relative sea level and climate change through time. Because of the importance of basins in understanding Earth history, we devote a separate portion of this class to understanding the mechanisms how basins form and evolve.

In many cases the areas of large subsidence are underlain by thinned crust, showing clear evidence for extension. However, some basins lack such evidence and seem to have formed by a period of thermal heating, uplift, erosion, and subsequent subsidence. However, these cases are rare. Another widespread origin for basin subsidence is flexure due to loading of the lithosphere, e.g. by a mountain belt.

21.1.2 Basin classification

The gradual exploration of continental margins since the 1970's, mainly driven by the search for hydrocarbons, has resulted in the formulation of various models for basin formation and evolution. The physical mechanisms that form sedimentary basins can be divided in 3 categories:

- 1.) Extension and faulting
- 2.) Flexure of the lithosphere
- 3.) Dynamic topography

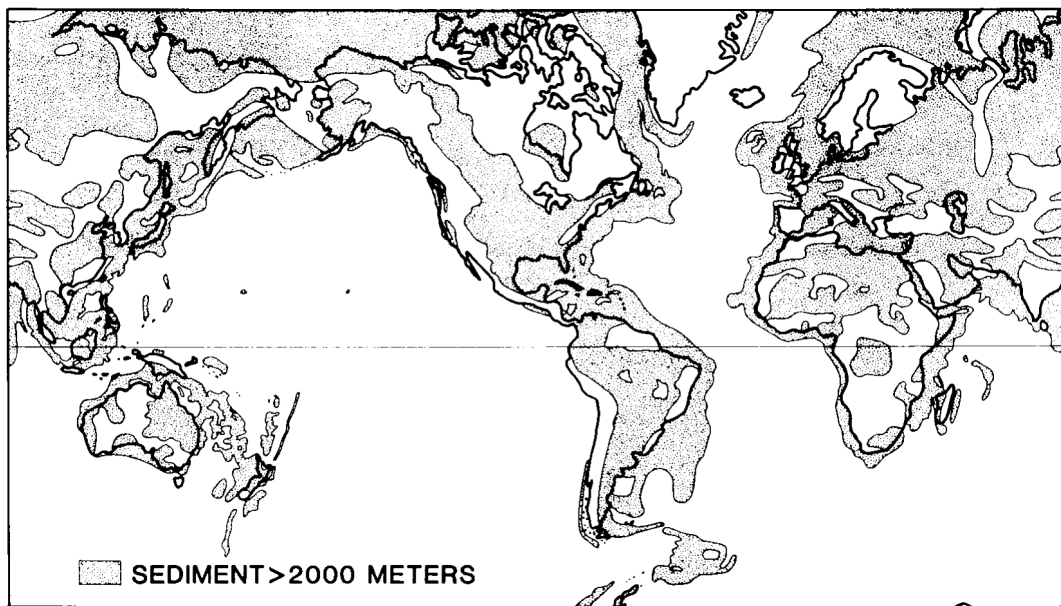


Figure 21.1: Global distribution of sediment thickness > 2km from Sclater and Célérier (1989).

When extensional basin formation results in breakup between two plates, two passive margins are formed. Preceding rifting is often stretched out over many tens of millions of years, sometimes over 100 million years, expressed by a number of consecutive rift phases. When the lithosphere eventually breaks, seafloor spreading starts, and the two conjugate margins are assumed to become tectonically passive. The continental shelves formed by this process may be symmetric or asymmetric, narrow or wide, and accompanied by volcanism or non-volcanic. Passive margins are classified into

- 1.) Non-volcanic
- 2.) Volcanic margins

depending on whether or not their formation is accompanied by substantial volcanic and magmatic activity. These margins are tectonically passive because those extensional stresses that result in lithospheric stretching and basin formation before breakup, are taken up by seafloor spreading along the newly formed mid-ocean ridge. The sedimentary sequence deposited on passive margins is divided by a *breakup unconformity* that separates the *syn-rift* from the *post-rift* sedimentary sequence.

Cross-section of a typical volcanic margin. Volcanic margins are identified from seismic reflection data by the presence of seaward dipping reflector sequences (SDRS) near the continent-ocean transition, as well as a number of other seismic characteristics related to extensive breakup volcanism.

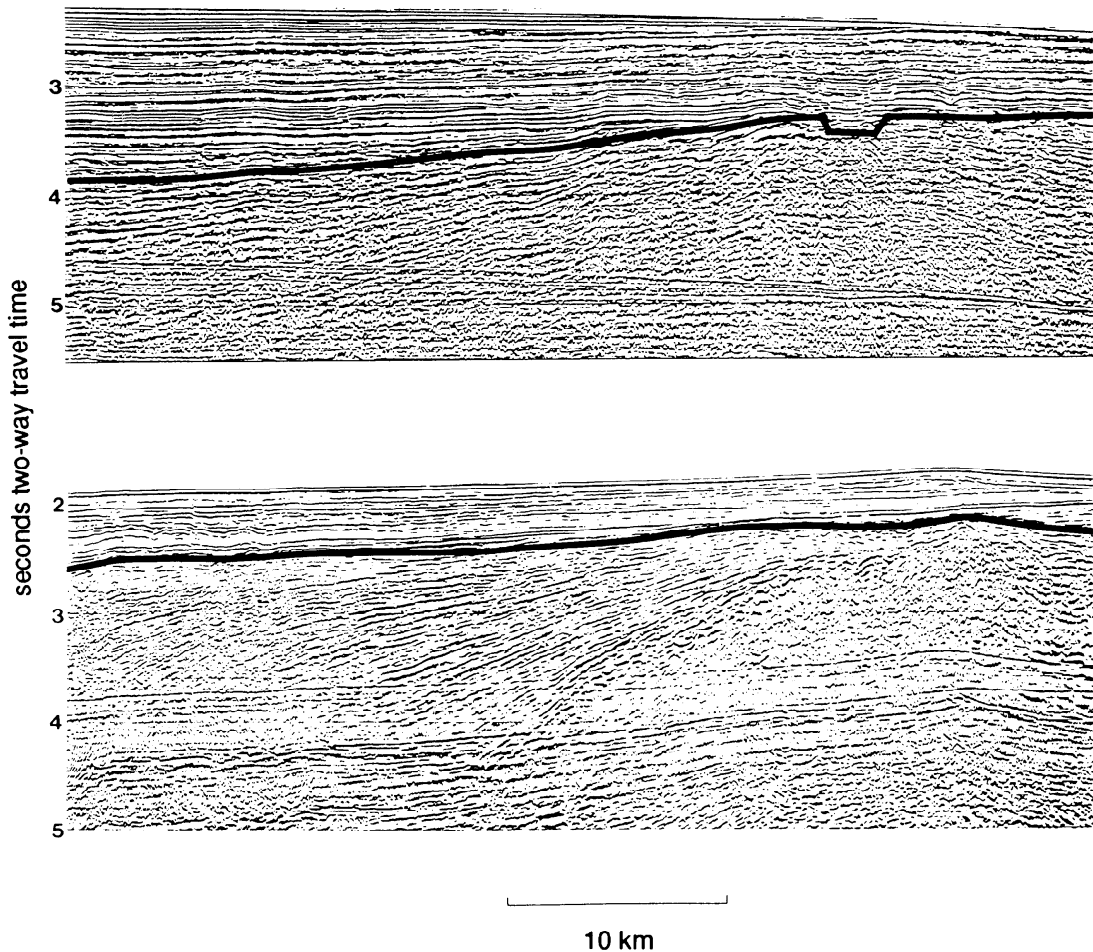


Figure 21.2: Dipping reflector sequences (below thick black lines) consisting primarily of basalt flows on (top) the Kerguelen oceanic plateau and (bottom) the Norwegian volcanic passive margin. The dipping wedge of Norway was sampled at Ocean Drilling Project site 642; no dipping reflectors were drilled on Kerguelen. Taken from Coffin and Eldholm (1994)

Such magmatism may have significant influence on the regional, and possibly global, environment, and plays an important role in generation of continental crust by magmatic underplating and emplacement of extrusives and intrusives (e.g. Coffin and Eldholm, 1994). There is good evidence of a connection between hotspot activity related to mantle plumes and formation of volcanic margins e.g. the Iceland hotspot and the north-east Atlantic volcanic margins and the Tristan da Cunha hotspot and the south Atlantic volcanic margins (White and McKenzie, 1989).

The lithosphere-scale evolution of non-volcanic (or magma-poor) margins is conceptualised by Whitmarsh et al. (2001) based on extensive data collection and scientific

drilling of the conjugate Iberia-Newfoundland margin system in the southern North Atlantic.

In the following, we will focus mostly on basins and margins caused by extension of the lithosphere and on flexural basins.

21.2 Extensional Basins

21.2.1 Lithospheric stretching and thinning

21.2.1.1 Development of the concept

It was first suggested by Hsü (1965) and Vogt and Ostenso (1967) that the subsidence of continental shelves could be related to thermal contraction beneath the crust. Sleep (1971) was the first one to observe correctly that the east coast of the USA and other continental basins subsided exponentially to a constant value with a time constant similar to ocean floor. Fig. 21.4 shows the basement subsidence averaged from seventeen wells on the east coast margin of the USA.

Sleep (1971) suggested that the subsidence was caused by a thermal perturbation resulting in doming, uplift, erosion, subsidence, and sediment deposition. Falvey (1974) modified this model by suggesting that deep crustal metamorphism increases the crustal density and thus contributes to subsidence. However, the problem with these models is that the massive eroded dome necessary to provide space for the sediments is not observed. Therefore it was realised that the observed passive margin subsidence requires another mechanism.

The first suggestion that extension and thinning of the continental crust may be responsible for the upwelling of hot upper mantle material was brought forward by Artemyev and Atushkov (1971) to explain the high heat flow in Lake Baikal. Salveson (1978) extended this model to continental shelves by interpreting shelves as rift basins that had extended so far that pure oceanic crust had formed.

McKenzie (1978), independently of Salveson (1978), developed a quantitative model for lithospheric stretching and thinning based on the concept of uniform extension of the lithosphere. In this model the brittle upper lithosphere is extended by pure shear.

Today there are three conventional kinematic models for lithospheric extension: The *finite uniform extension model* (Jarvis and McKenzie, 1980) and *depth dependent extension model* (Royden and Keen, 1980) are so-called *pure-shear* models, as in these models large-scale lithospheric extension is symmetric and does not involve rotation. The *simple shear* extension model by Wernicke (1985) involves a *low-angle shear zone* which extends through the entire lithosphere. In the Wernicke (1985) model, faulting occurs along a detachment surface that extends through the entire lithosphere. This results in differential stretching in the upper and lower lithosphere to form a plate detachment, resulting in a “lower plate” and “upper plate” margin. Both models are shown in Fig. 21.5.

In contrast, observations of large-scale homogeneous extension and symmetrical detachment on the Iberian/Newfoundland margin in the North Atlantic have led to the advancement of pure shear lithospheric stretching models (left figure). Various au-

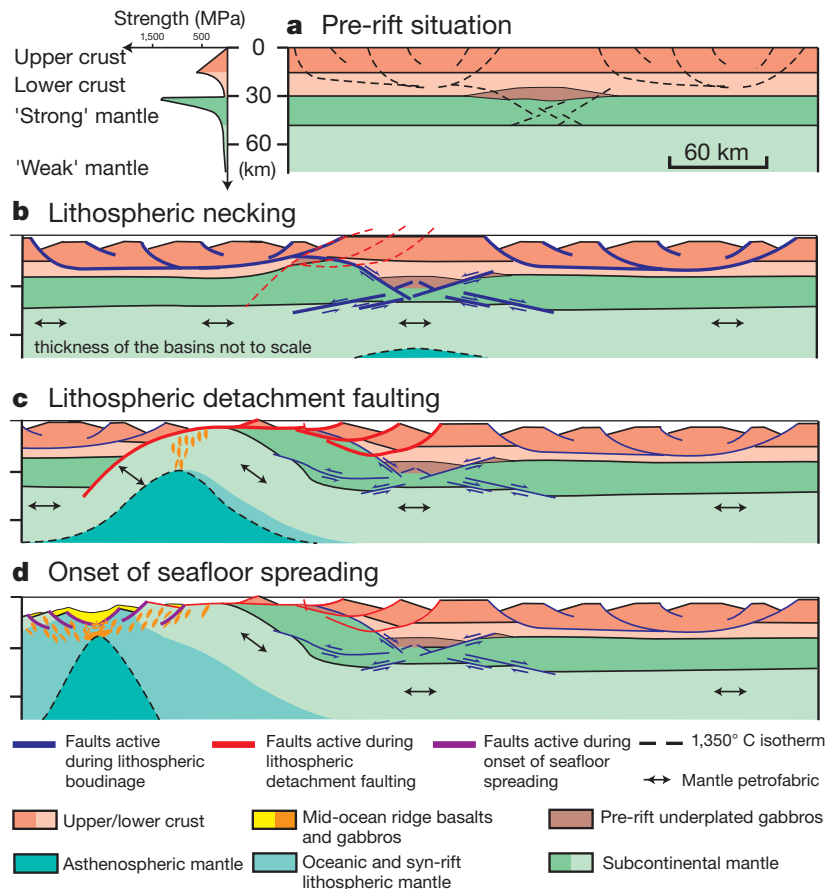


Figure 21.3: Conceptual lithosphere-scale model of development of a rifted magma-poor margin relative to a fixed right-hand edge. **a**, Initial situation with four-layer rheology (justified because the pre-rift lower crust often contains quartz-rich horizons) and crust locally thickened by pre-rift underplated gabbro. **b**, Initially the upper mantle, the strongest part of the lithosphere, necked beneath the gabbros where it was weakest, allowing the asthenosphere to rise. Elsewhere, ductile flow of the lower crust determined where rift basins formed at the surface. Relatively little crustal thinning and subsidence occurred above the necked region, whereas the adjacent areas were strongly thinned. Arrows indicate a hypothetical, initially sub-horizontal, petrofabric. **c**, Later, the thermal structure and gravitational response associated with the rising asthenosphere started to influence the rifting. Then, rifting was localized at the margin of the relatively weak unextended, or only slightly extended, crust. This allows the important initial thinning of the lower crust and its observed abrupt transition to weakly thinned crust to be explained. The change in extensional geometry from listric to one or more concave-downward faults reflected a change in the distribution of weak layers. Whereas listric faults sole out in horizontal weak layers, concave-downward faults might be favoured by sub-vertical weak zones, possibly resulting from rising magma and higher thermal gradients above the rising and narrowing asthenosphere. **d**, The asthenosphere ascended close to the surface and mid-ocean-ridge basalt melts were intruded into, and even extruded onto, sub-continental mantle. Deeper mantle layers were exhumed oceanward. Eventually, increasing melt production led to the creation of 'continuous' oceanic crust and the asthenosphere spawned oceanic upper mantle. Seafloor spreading had begun. Taken from Whitmarsh et al. (2001).

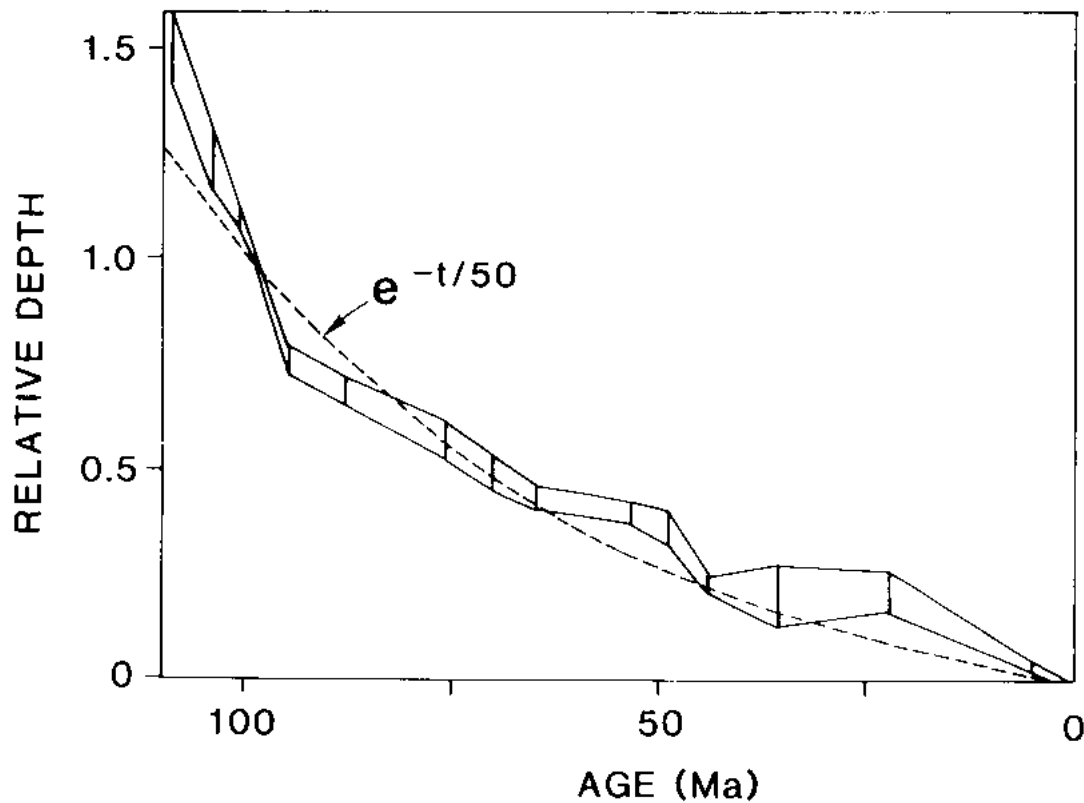


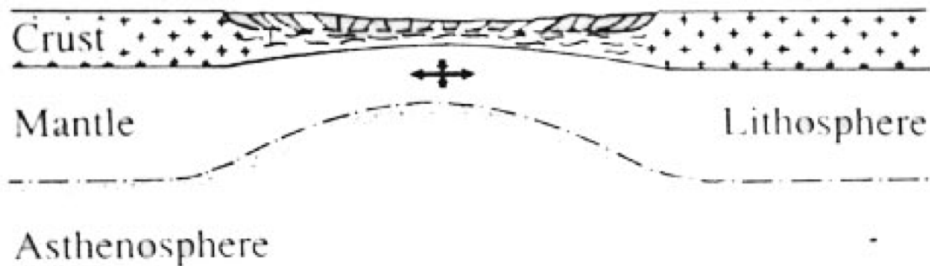
Figure 21.4: Basement subsidence averaged from seventeen wells on the US East Coast margin (Sleep, 1971).

thors have argued for pure-shear models based on laboratory experiments, in which relative movement between upper crustal layers is accommodated by layer parallel shear in lower ductile layers, with increased stretching this becomes a decollement between upper crust and the mantle, resulting in mantle exhumation. The pure shear model by Brun and Beslier (1996, Fig. 21.6) has been used as an analogue for the south western Australian passive margin, and as an alternative for Lister et al. (1991) simple shear model.

21.2.1.2 Uniform extension model

During extension, both the crust and the mantle part of the lithosphere are stretched and extended by means of normal faulting and ductile flow and hot mantle rises to the base of the thinned lithosphere. The resultant thermal perturbation decays exponentially, producing subsidence due to thermal contraction of the lithosphere. The tectonic subsidence is dependent on the degree of the crustal extension, which is defined by a

Pure Shear



Simple Shear

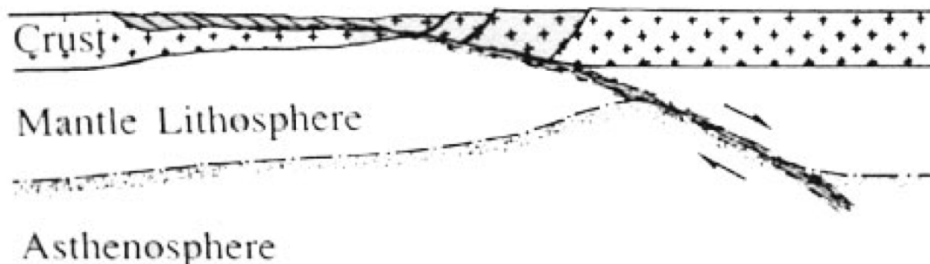


Figure 21.5: Pure shear (top) and simple shear (bottom) extension model

stretching factor, β (McKenzie, 1978). This model is illustrated in the figure below.

Bulk pure shear (i.e. no solid body rotation) is accommodated by brittle faulting in the upper crust and by plastic flow in the lower crust and mantle lithosphere. The whole lithosphere is thinned by a factor, β , which induces passive upwelling of the asthenosphere in order to maintain isostatic equilibrium. The thermal perturbation caused by this resultant asthenospheric upwelling raises the geothermal gradient. The stretching factor β is defined as the ratio of the original crustal thickness, to the thickness after extension. Extension occurs instantaneously and uniformly at time $t = 0$ at all depths within the crust and mantle lithosphere. The crust is permanently thinned but the lithosphere is restored to its original equilibrium thickness at time $t = \infty$ by heat conduction away from the thermal anomaly since the lithosphere is simply defined by an isothermal boundary.

The cooling and resultant increased density of the hotter asthenosphere produces subsidence as the temperature perturbation decays. Initial syn-rift subsidence, S_i occurs if the initial crustal thickness, t_c , greater ≥ 18 km. For instantaneous extension this initial water-loaded syn-rift subsidence is related to the stretching factor, β by the term:

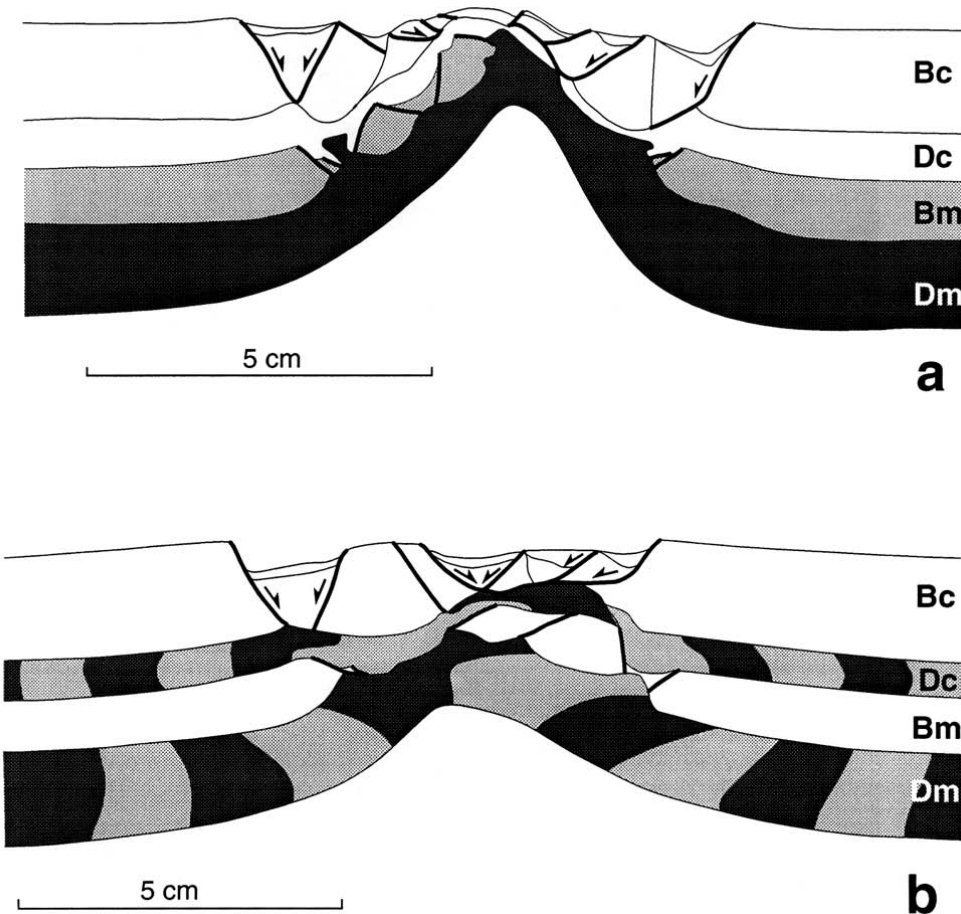


Figure 21.6: Analogue crustal extension model (Brun and Beslier, 1996)

$$S = \frac{a \left[(\rho_m - \rho_c) \frac{t_c}{a} \left(1 - \alpha T_1 \frac{t_c}{2a} \right) - \alpha T_1 \frac{\rho_m}{2} \right] \left(1 - \frac{1}{\beta} \right)}{\rho_m (1 - \alpha T_1) - \rho_w} \quad (21.1)$$

Depending on the thicknesses and densities involved, either initial subsidence or uplift occurs as a result of isostatic re-equilibration. The initial subsidence S_i can be determined by *balancing the before and after columns of lithosphere and asthenosphere*, given that both are in Airy-isostatic equilibrium. This assumption is a good approximation for those rift basins, which have an elastic plate thickness of only 5 km.

For the McKenzie (1978) instantaneous model, the initial thermal anomaly is produced by heat advection but the effects of heat diffusion during initial subsidence are not included. The resultant subsidence as a function of time is described by a one-dimensional heatflow equation. However, for the finite-duration stretching model de-

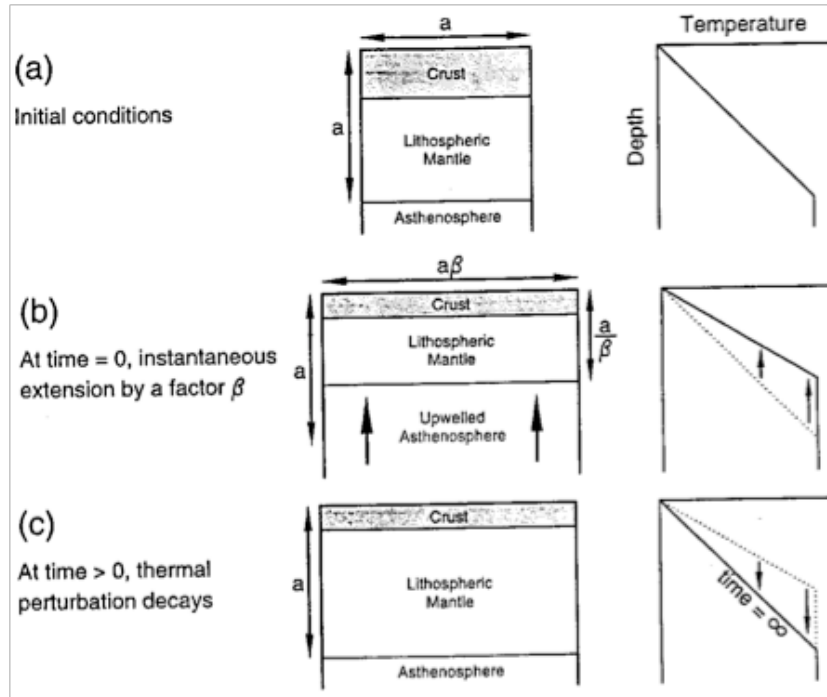


Figure 21.7: Schematic representation of the lithospheric stretching model (?). a) Shows the initial unextended crust. b) At time = 0 the initial piece of thermally equilibrated continental lithosphere is extended by a factor β . Isostatic compensation causes upwelling of hot asthenosphere and the geothermal gradient increases. c) Cooling of the lithosphere produces subsidence as the thermal perturbation decays, and at $time = \infty$ the lithosphere returns to its original steady state thickness although the crust is permanently thinned.

veloped by Jarvis and McKenzie (1980) both advective and diffusive heat transfer occur during stretching. Therefore, to solve for the thermal evolution of the lithosphere during and after stretching, the 1-D heat flow equation is used, as for the instantaneous case, with an additional advective term:

$$\frac{\partial T}{\partial t} = G(a - z) \frac{\partial T}{\partial z} = \kappa \frac{\partial^2 T}{\partial z^2} \quad (21.2)$$

where t is the time, T is the temperature, a is the lithospheric thickness with a temperature of 0° C at the surface and z is the distance measured from the base of the lithosphere at $z = a$, maintained at constant temperature. G is the strain rate and can be defined as $G = \frac{\partial u}{\partial x} = -\frac{\partial v}{\partial z}$ therefore $v(z) = G(a-z)$; where $v(z)$ is the vertical velocity and $u(x)$ is the horizontal velocity. The strain rate is equal vertically and horizontally to conserve area. The relationship between the parameters is shown below:

For rift periods less than ≈ 20 Ma, the instantaneous stretching model adequately describes the subsidence. For basins stretching over longer periods, finite-duration

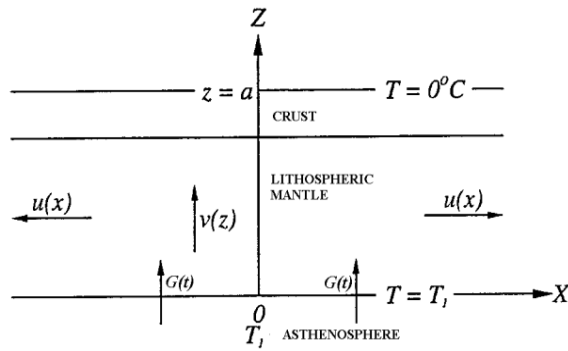


Figure 21.8: Relationship between vertical and horizontal strain rate described by a physical model for time-dependent stretching (White, 1994). The vertical and horizontal strain rate are assumed to be equal. a = lithospheric thickness; T_1 = temperature of the asthenosphere; $G(t)$ = vertical strain rate as a function of time, t ; $u(x)$ = horizontal velocity; $v(z)$ = vertical velocity. z is measured from the base of undeformed lithosphere.

stretching is a better description of the subsidence through time as the effect of lithospheric cooling during stretching becomes pronounced enough to change the proportions of syn-rift and thermal subsidence. The total subsidence is equal for both instantaneous and finite stretching cases.

The total subsidence of a sedimentary basin consists of two components; initial fault controlled subsidence, dependent upon the initial thickness of the crust and the amount of crustal and lithospheric mantle stretching, and secondly, a slower phase of thermal subsidence which decays exponentially with time as a result of the decrease in heat flow with time. Approximately 60 Ma after active extension has ceased the lithosphere is close to thermal re-equilibration. This time period is determined by thermal decay constant of the lithosphere, described by the following expression (Parsons and Sclater, 1977):

$$\tau \cong \frac{a^2}{\pi^2 \kappa} \quad (21.3)$$

The total tectonic subsidence attained at the time of the thermal re-equilibration of the lithosphere is dependent on the initial crustal thickness and the total amount of crustal stretching, β . Maximum tectonic subsidence is approached when the value of β is large (Fig. 21.9).

In real life, the basement subsidence is amplified by the loading effect of sediments which result in additional subsidence due to isostatic compensation of the load. Depending on the sedimentation rate, it can result in more than twice the subsidence of the water loaded basement alone. Note that extension by more than a factor of about four results in break-up of the continental crust and sea-floor spreading.

The densities involved are given as follows: ρ_{m0} and ρ_{c0} are the mantle density and the crustal density given at 0° C. In order to determine the effective average densities,

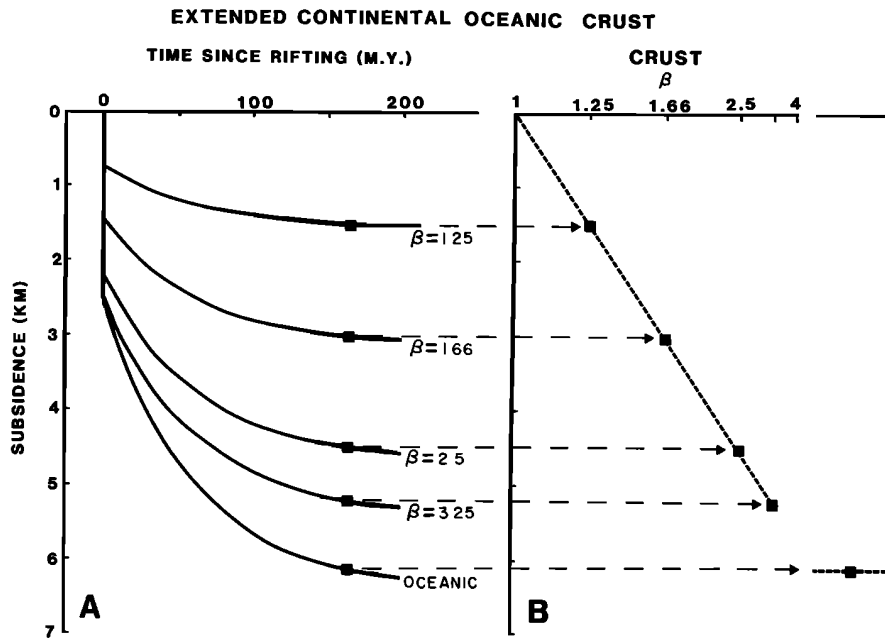


Figure 21.9: Water-loaded basement subsidence as a function of time for various values of the extension factor β , as well as the resulting total subsidence (Sawyer, 1985). It illustrates the initial subsidence due to crustal thinning, followed by exponential thermal subsidence due to decay of the thermal anomaly and contraction of the lithosphere.

we have to take into account the thermal expansion coefficient α and the thicknesses of the layers. The temperature at the midpoint in the crust is located at $z = h_c/2$. the temperature at any depth in the crust is given by

$$T = \frac{T_m}{h_l} z \quad (21.4)$$

assuming that the temperature gradient in the crust is linear, and that the asthenospheric temperature is constant. The temperature at $z = \frac{h_c}{2}$ is

$$T = \frac{T_m}{h_l} \frac{h_c}{2} \quad (21.5)$$

and the effective density of the crust is given by

$$\rho_c = \rho_{c0} \left(1 - \frac{\alpha T_m h_c}{2 h_l} \right) \quad (21.6)$$

The average density of the lithosphere is given by:

$$\rho_l = \rho_{m0} \left(1 - \frac{\alpha T_m}{2} \frac{\alpha T_m h_c}{2 h_l} \right) \quad (21.7)$$

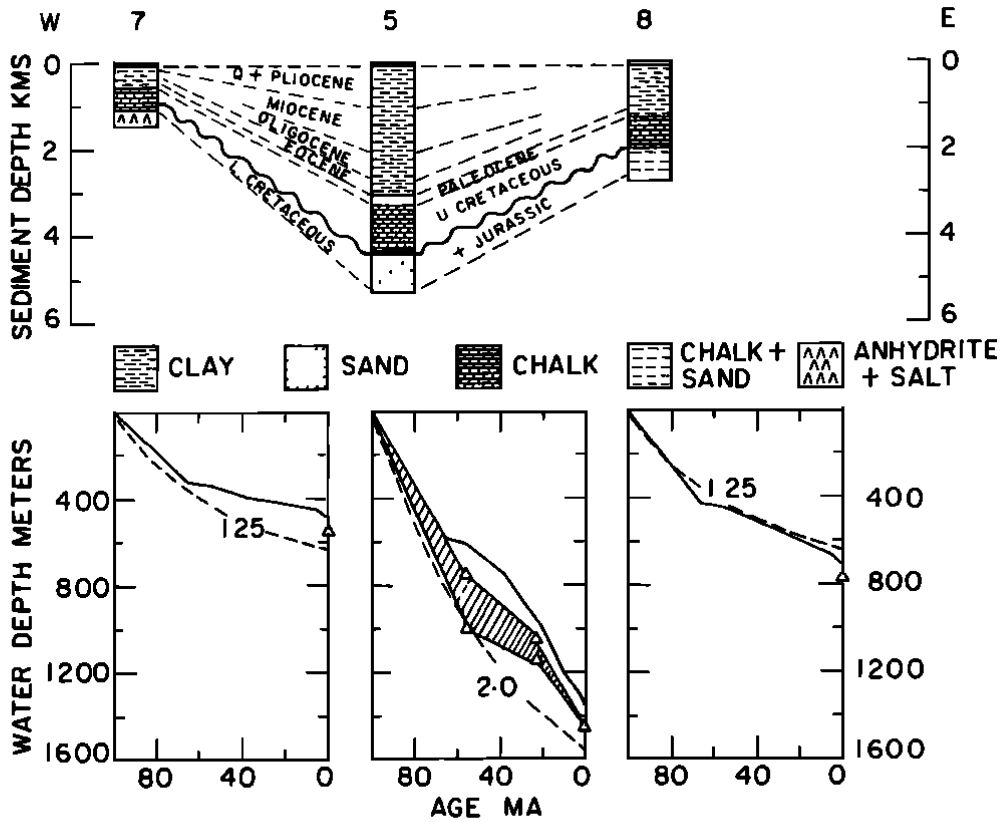


Figure 21.10: Lithospheric thinning and total subsidence may vary significantly across a sedimentary basin. An example from three wells in the Central Graben in the North Sea (Sclater and Christie, 1980) illustrates that here the extension factor b varies from 1.25 to 2 from the basin flanks to the basin center, equivalent to stretching by 25% and 100%, respectively.

The average density of the asthenosphere ρ_m is only dependent on the temperature T_m and α :

$$\rho_m = \rho_{m0}(1 - \alpha T_m) \quad (21.8)$$

Isostatically balancing the *before* and *after* lithospheric columns and re-arranging the equation yields the initial subsidence S_i :

$$S_i = \left[\frac{h_l(\rho_m - \rho_l) + h_c(\rho_l - \rho_c)}{\rho_m - \rho_w} \right] \left(1 - \frac{1}{\beta} \right) \quad (21.9)$$

The surface of the continent is taken to be at or below sea level, and continental crust is assumed to be preserved. The sign of the initial subsidence S_i depends on the initial crustal thickness h_c and is independent on the stretching factor β . Initial subsidence will occur (i.e. $S_i = \text{positive}$) if $h_c > 18 \text{ km}$. If $h_c < 18 \text{ km}$, initial uplift will occur (under

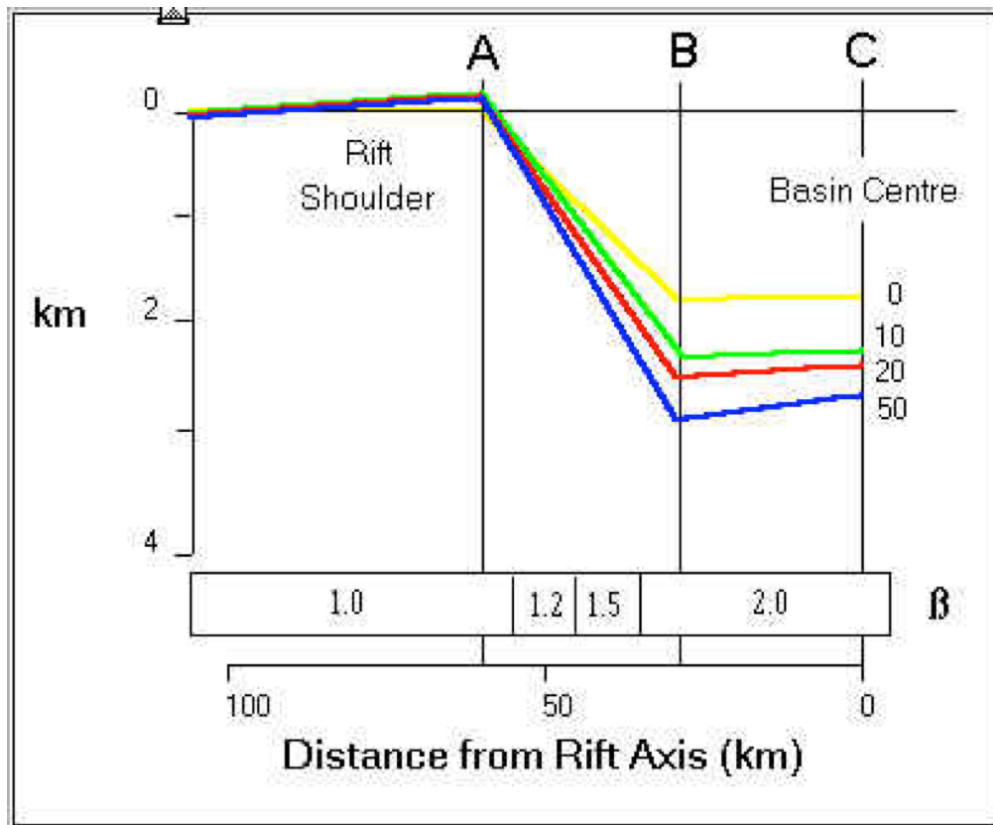


Figure 21.11: Profile of lithospheric thinning across a typical continental margin

water, though). The crustal thickness must be at least 27.6 km for the crustal surface to be at sea level, or above. Hence it is impossible that *initial subaerial uplift* would occur.

After the initial subsidence a phase of thermal subsidence from lithospheric cooling and contraction starts. It can be modelled by solving the one-dimensional heat-flow equation:

$$\frac{\partial T}{\partial t} = \frac{\kappa}{\rho c_p} \frac{\partial^2 T}{\partial z^2} \quad (21.10)$$

by using the following boundary conditions: $z = 0 \quad T = 0$ at all times, $z = h_l T = T_m$ at all times. $T_m = 1350^\circ \text{C}$

$$t=0$$

Here z is measured downward from the surface. This problem can be solved by using a Fourier expansion, and the eager reader is referred to Carslaw and Jaeger (1959) for details of such methods. McKenzie (1978) solution for the temperature structure is

$$\frac{T}{T_m} = 1 - \frac{z}{h_l} + \frac{2}{\pi} \sum_{n=1}^{\infty} \frac{(-1)^{n+1}}{n} \left[\frac{\beta}{n^\pi} \right] e^{-\frac{n^2 t}{\tau}} \sin \frac{n\pi z}{h_c} \quad (21.11)$$

where

$$\tau = \frac{h_c^2}{\pi^2 \kappa} \quad (21.12)$$

As $\beta \rightarrow \infty$ the term in square brackets $\rightarrow 1$ for all n and the solution is that for an oceanic ridge model when all the heat is conducted vertically. The elevation $E(t)$ above the final depth to which the upper surface of the lithosphere sinks is given by

$$E(t) = \frac{h_l \rho_m \alpha T_l}{\rho_m - \rho_w} \left\{ \frac{4}{\pi^2} \sum_{m=0}^{\infty} \frac{1}{(2m+1)^2} \left[\frac{\beta}{(2m+1)^\pi} \sin \frac{(2m+1)^\pi}{\beta} \right] e^{-(2m+1)^2 \frac{t}{\tau}} \right\} \quad (21.13)$$

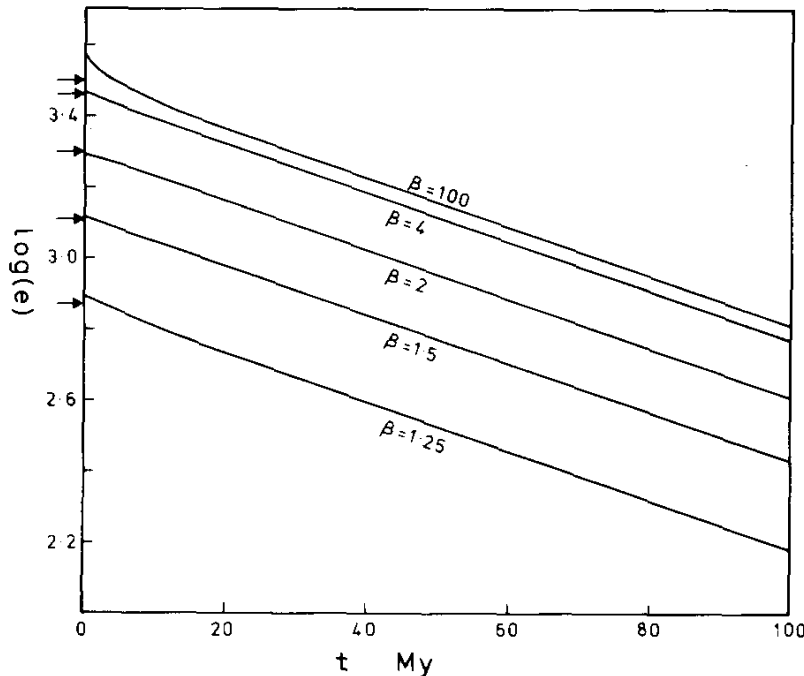


Figure 21.12: From ?: the elevation plotted as $\log 10[e^t]$ versus time for different extension factors β . The curves are almost straight lines when $\beta < 4$ for all times.

The total amount of thermal subsidence is the difference between the total subsidence S_t and the initial subsidence S_i is $S_t = S - S_i$.

The total final amount of subaqueous subsidence S by assuming Airy isostasy is

$$S = \frac{h_l(\rho'_l - \rho_l) + h_c \left(\rho_l - \frac{\rho'_l}{\beta} + \frac{\rho'_c}{\beta} - \rho_c \right)}{\rho'_l - \rho_w} \quad (21.14)$$

So far we have discussed the subsidence of an empty basin only. In reality basins of course contain sediments, and it is the sediment thickness, rather than the subsidence

that we actually observe. To obtain the subsidence the sediment load must be removed using either an Airy isostasy or a flexural model for the isostatic compensation. For this varying sediment densities and compaction must be taken into account. This procedure is referred to as *backstripping* (Fig. 21.13).

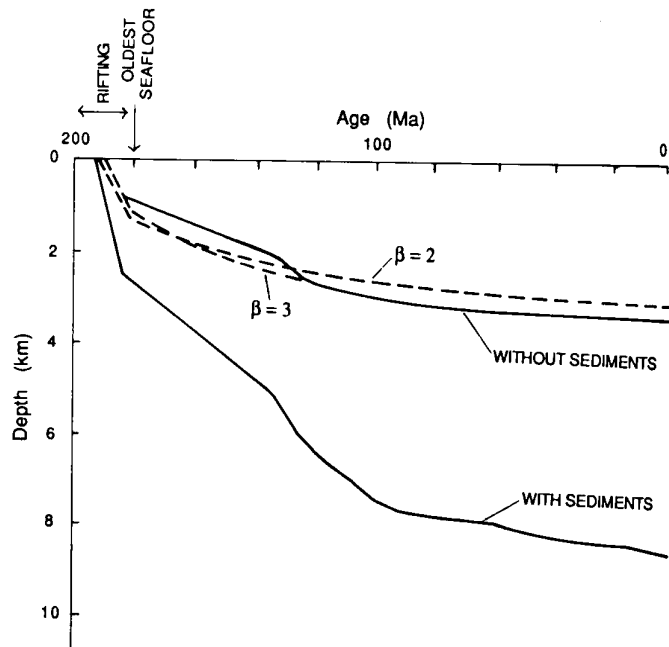


Figure 21.13: Observed and computed subsidence for a well on the Nova Scotia continental margin off eastern Canada. To obtain the subsidence curve without sediments (i.e. tectonic subsidence), the sediments are “backstripped” in order to isolate the loading effect of the sediments from tectonic subsidence. The dashed lines shows two subsidence models for stretching factors $\beta = 2$ and $\beta = 3$.

The best method to estimate crustal extension is from measuring the crustal thickness from seismic refraction data. Any volcanic additions to the continental crust during extension cause a decrease in the estimate of β , unless recognised properly. Another method for estimating the amount of initial extension is measuring the heaves of normal faults in the basement surface. Basement faults in extensional basins often have steep dips at the surface, with the dip decreasing with increasing depth. These faults are called rotational, or listric faults.

In the very basic model for crustal extension discussed above, we have also neglected the lateral conduction of heat, radioactive production of heat in the crust, and the time over which initial extension takes place (it was assumed to be instantaneous). However, Jarvis and McKenzie (1980) showed that unless the time period of extension is longer than 20 m.y., the influence of time is negligible.

The average depth of mid-ocean ridges gives another clue to the understanding of continental stretching and breakup of continents. The average water depth of a mid-ocean ridge is about 2.5 km. This depth reflects the isostatic equilibrium of the asthenosphere, i.e. the surface of the asthenosphere's geoid. If extension leads to submergence of continental crust of more than 2.5 km, volcanism, rupture of the lithosphere, and eventually seafloor spreading will occur. Thus the boundary between oceanic and continental crust should occur at a depth of 2.5 km.

21.2.1.3 Refined models

Sclater *et al.* (1980) and Royden and Keen (1980) have found in several regions that the crustal extension and initial subsidence are much less than that predicted by the model of McKenzie (1978). Equivalently, the thermal subsidence is much greater than that predicted from the observed crustal extension. In their applications of this concept Some other continental margins have been found to be characterised by no initial subsidence, but some uplift of doming. In the simple model discussed above this is only possible when the pre-rift crustal thickness is less than 18 km. Initial doming in crust with thickness greater than 18 km calls for an explanation different from McKenzie's (1978) stretching model.

To account for these observations, Royden and Keen (1980) proposed to increase the heat input during extension by thinning the lower crust and subcrustal lithosphere more than the upper crust. Their extensional model had much in common with that proposed originally by Salveson (1978). Sclater and Christie (1980) and Royden and Keen (1980) placed the brittle-ductile transition at the base of the continental crust. An important feature of this model is that it allows crustal thinning to be significantly less than subcrustal thinning within the region of extension. The extension in the crust is denoted by the parameter β , and the extension in the mantle by γ .

Where differential stretching between ductile and brittle crust occurs, the initial subsidence is drastically reduced compared to that which would be observed if the crustal thinning were the same as the subcrustal thinning. However, the thermal subsidence, which is strongly dependent on the subcrustal thinning, would in contrast change far less from what would be observed if crustal thinning were the same as subcrustal thinning. If mass were conserved during the extensional process, that is, if none of the lithosphere that underwent extension were removed from the region of extension, then there would also be places within the region of extension where crustal thinning is greater than subcrustal thinning. In such areas, the initial subsidence could be quite large.

All models discussed so far assume a pure shear mechanism for extension. This reflects the fact that in case of simple shear, it is not trivial to estimate β and γ across the basin, because the two parameters would vary continuously. The three models, i.e. uniform extension by pure shear, depth-dependent extension by pure shear, and extension by simple shear, are illustrated in Figure 21.14, .

Another refinement of McKenzie (1978) original model was presented in a paper by Jarvis and McKenzie (1980), in which the modified the original model to account for

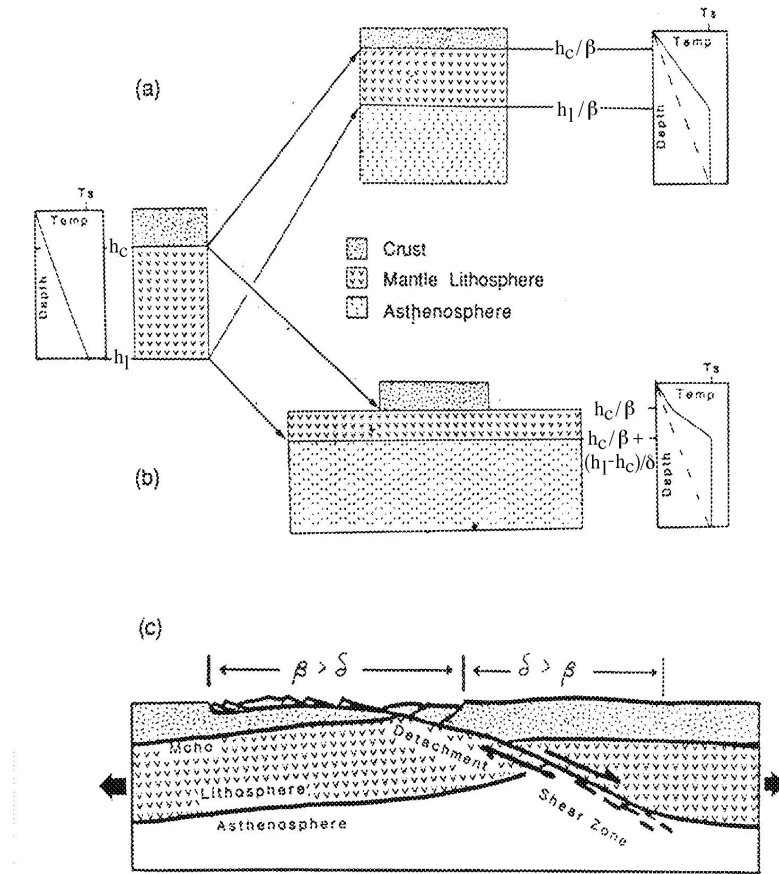


Figure 21.14: Figure (a) corresponds to McKenzie (1978) uniform extension model; (b) illustrates Royden and Keen (1980) depth-dependent model, in which the crust is extended by factor b , and the mantle by a factor d ($d > b$). In both figures the solid line shows the temperature profile immediately after extension; the dashed line shows the final equilibrium profile. (c) shows Wernicke (1985) simple shear extension model with faulting along a detachment surface, which extends through the entire lithosphere. Here b and d vary continuously across the structure. Modified from Fowler (1990)

the impact of time-dependent stretching on subsidence (Fig. 21.15). When stretching occurs over a period comparable to the diffusion time scale some of the heat diffuses away before stretching is completed. The resultant thermal anomaly and subsequent contraction is thus reduced. Their analysis showed that if the time period of extension by a factor b is less than $60/b^2$ m.y., the resulting subsidence differs little from an instantaneous stretching model for $\beta < 2$. For $\beta > 2$, the time period of stretching must be shorter than $60(1 - 1/\beta)^2$.

Le Pichon and Sibuet (1981) and Hellinger and Sclater (1983) pointed out that it is useful

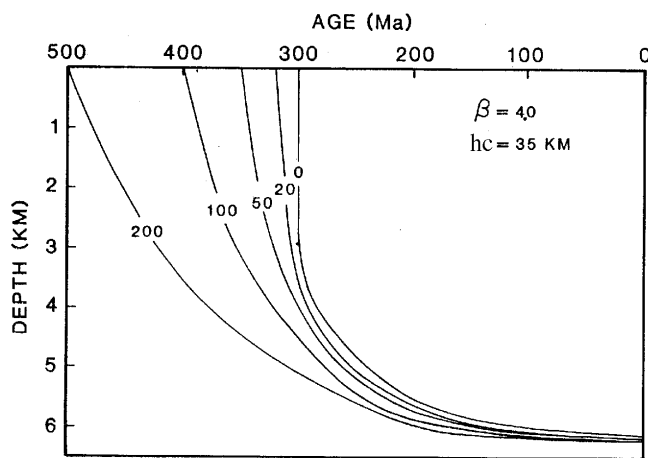
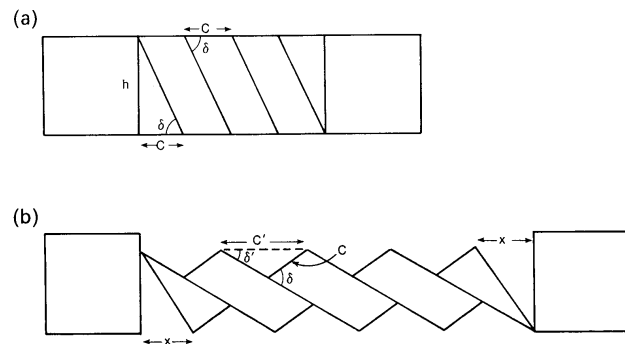


Figure 21.15: Total subsidence S_t for five different time intervals of extension for $\beta = 4.0$ and $h_c = 35 \text{ km}$ (Slater et al., 1986). The numbers on the curves indicate the time interval of extension in m.y.

to evaluate the initial subsidence S_i and the total subsidence S in relation to the variable $\gamma = (1 - 1/\beta)$. g represents the reduction in the thickness of the lithosphere measured as a percentage of the original lithospheric thickness.

21.2.2 Estimating extension from faults

In regions of extensional tectonics, a knowledge of the geometry and kinematics of large-scale faults is of crucial importance to understand the nature and amount of extension involved. Extension of brittle crust involves the rotation of planar fault blocks. *Jackson and White (1989)*, show that large seismogenic normal faults on continents appear to be restricted to a dip range of 30° - 60° , and that fault dips of $<20^\circ$ have not been observed in fault plane solutions of large earthquakes. Large seismogenic normal faults, therefore, are approximately planar in cross-section and rotate about a horizontal axis as they move. However, movement along both planar and some curved (listric) faults must also be considered when estimating extension from fault heaves (*Sclater and Shorey, 1989*, see Fig. 21.16).



Block model showing the termination of the dominos before extension. h is the height of the blocks, C the horizontal distances between the faults and δ the original angle of dip of the faults. (b) Block model after extension. C' is the final horizontal distance between the faults, δ' the final angle of dip of the faults after extension and x is the horizontal distance of the base of the end half blocks from the undisturbed regions.

Figure 21.16: Domino model of upper crustal brittle faulting under extension

The faults can be traced deep into the crust and are not bounded by a detachment surface. At the time when these faults formed they reached a depth at which the crust was hot enough to deform by ductile flow, causing sub-horizontal reflections in the lower crust.

Difficulties with the domino model:

- 1.) How to accommodate the differential rotation about a horizontal axis between a tilted terrain and its stable margin
- 2.) The model requires all faults to be active at the same time with the same dip, whereas in reality the timing of extension and tilting often varies across a basin.

internal deformation of blocks through time must be accounted for, as shown in Fig. 21.18:

Sclater and Shorey (1989), suggest that in the absence of other information, summing the fault heaves provides a useful ‘first approximation’ estimate of extension in the

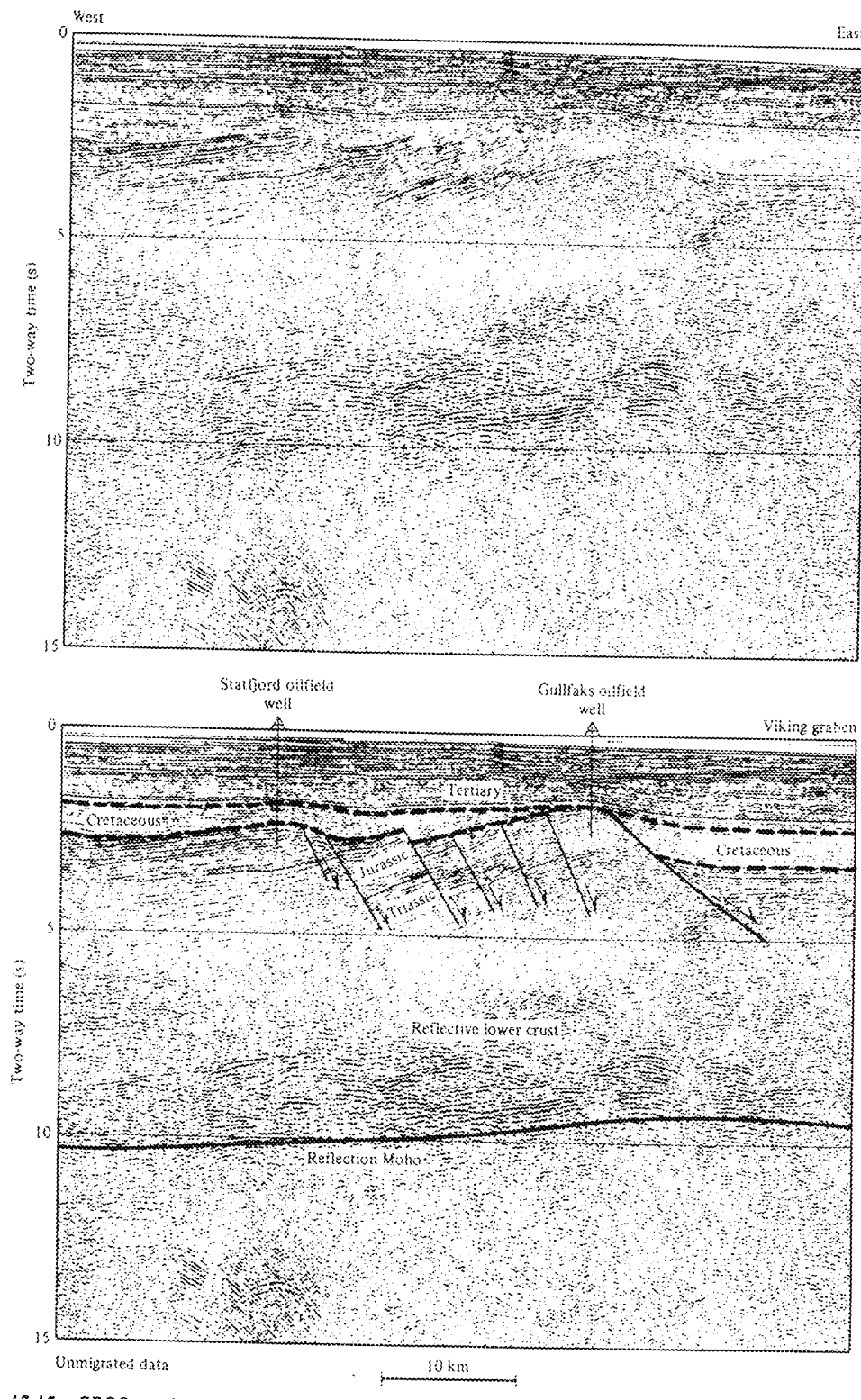


Figure 21.17: Classical example: Viking Graben in the North Sea where Triassic and Jurassic sedimentary strata have been rotated between subparallel high-angle listric faults.

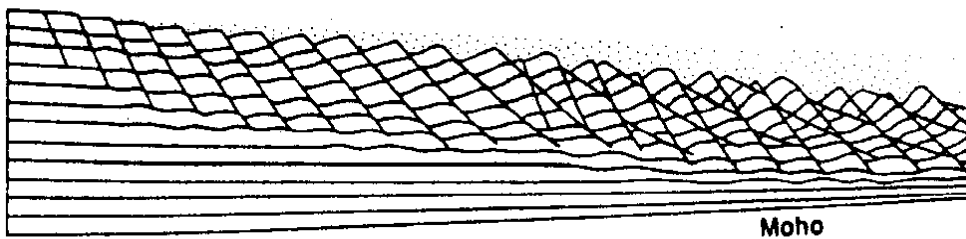


Figure 21.18: So-called “listric” faults form due to formation of several generations of faults. Once the initial fault has rotated substantially it becomes easier to form a new fault than continue

motion on the same fault surface.

case of domino-type planar faulting. For curved ‘listric’ faults, the heave is only a true measure of elongation if the antithetic faulting which removes the voids is vertical.

21.2.3 Factors Limiting Extension

England [1983], first investigated factors that limit the amount of extension. He defines strength of the lithosphere as the force per unit length required to maintain the deformation. Stretching weakens the lithosphere and cooling strengthens it, however only a small amount of cooling is necessary to require a large increase in the magnitude of the force per unit length to maintain the deformation. Several factors may be responsible for limiting extension; (i) cessation of ascent of the asthenosphere, (ii) decrease or removal of the initiating stress, (iii) change in the mechanical properties of the lithosphere such that the stresses which were sufficient to initiate the rifting are no longer great enough to deform the lithosphere [England, 1983; Newman & White, 1997; 1999]. Recent analyses of a global dataset show that it is most likely the final factor, change in mechanical properties, which limits lithospheric extension. The change is induced simply by cooling, which causes the lithosphere to strengthen, and is recorded by a characteristic change in strain rate with time [Newman & White, 1997; 1999].

The relative strengths of the crust and lithosphere also effect the cessation of extension [Newman & White, 1997]. Since extension is limited by cooling, if the crust is initially stronger than the lithospheric mantle, a large drop in the Moho temperature is required before the crust and lithospheric mantle have the same strength. This results in higher β values.

21.3 References

Badley M.E., 1985, Practical Seismic Interpretation, 266pp, Prentice Hall, New Jersey

- Bally, A.W., 1983, Seismic Expression of Structural Styles, Am. Ass. Petrol. Geol. (publ.) Studies in Geology Series 15
- Barton P. & Wood R., 1984, Tectonic evolution of the North Sea basin: crustal stretching and subsidence, *Geophys. J. R. Astr. Soc.* **79**; 987-1022
- Bassi, G., *Factors controlling the style of continental rifting: insights from numerical modelling*. Earth & Planetary Science Letters, 1991. **105**: p. 430-452.
- Baxter K., 1998, The role of small-scale extensional faulting in the evolution of basin geometries. An example from the late Palaeozoic Petrel Sub-basin northwest Australia, *Tectonophysics* **287**, 21-41
- Baxter K., Buddin T., Corcoran D. & Smith S., 1999, Structural modelling of the south Porcupine Basin, offshore Ireland: implications for the timing, magnitude and style of crustal extension, (*extended abstr.*), in Proceedings of "Petroleum Exploration of Ireland's Offshore Basins"
- Bond G.C. & Kominz M.A., 1984, Construction of tectonic subsidence curves for the early Paleozoic miogeocline, southern Canadian Rocky Mountains: implications for subsidence mechanisms, age of breakup, and crustal thinning, *Geol. Soc. Am. Bull.* **95**, 155-173
- Bond G.C., Nickeson P.A. & Kominz M.A., 1984, Break-up of a supercontinent between 625Ma and 555Ma: new evidence and implications for continental histories, *Earth Planet. Sci. Lett.* **70**; 325-345
- Brodie J. & White N., 1994, Sedimentary basin inversion caused by igneous underplating - northwest European continental-shelf, *Geology* **22**(??), 147-150
- Brun, J.P. & M.O. Beslier, *Mantle Exhumation At Passive Margins*. Earth & Planetary Science Letters, 1996. **142**(1-2): p. 161-173.
- Buck, W.R., *et al.*, *Thermal Consequences of Lithospheric Extension : Pure and Simple*. Tectonics, 1988. **7**(??): p. 213-234.
- Burov E.B. & Diament M., 1995, The effective elastic thickness (Te) of continental lithosphere: What does it really mean?, *J. GEOPHYS. RES.* **100**; 3905-3927
- Carlson R.L. & Herrick C.N., 1990, Densities and porosities in the oceanic crust and their variations with depth and age, *J. Geophys. Res.* **95(B6)**, 9153-9170
- Christie-Blick N. & Biddle K.T., 1985, Deformation and basin formation along strike-slip faults, in Biddle K.T. & Christie-Blick N. (eds.), "Strike-slip Deformation, Basin Formation and Sedimentation", *Spec. Publ. Soc. Econ. Paleont. & Mineral.* **37**, 1-34
- Cloetingh S., Stein C., Reemst P., Gradstein F., Williamson P., Exon N. & von Rad U., 1992, Continental margin stratigraphy, deformation and intraplate stresses for the Indo-Australian region, in Gradstein F.M. *et al.* (eds.), "Proceedings of the ocean Drilling Program, Scientific Results", **123**; 671-713
- Cochran J.R., 1980, Some remarks on isostasy and the long-term behaviour of the continental lithosphere, *Earth Planet. Sci. Lett.* **46**; 266-274
- Coward M., 1990, Inversion Tectonics, in Hancock P. (ed.) "Continental Deformation" chapter 14, 289-304
- Cowie P.A. & Scholz C.H., 1992a, physical explanation for the displacement-length relationship of faults using a post-yield fracture mechanics model, *J. Struct. Geol.* **14**,

1133-1148

Dunbar J.A. & Sawyer D.S., 1989, How preexisting weaknesses control the style of continental breakup, *J. Geophys. Res. Solid Earth and Planets* **94(B6)**, 7278-7292

England P., 1983, Constraints on extension of continental lithosphere, *J. GEOPHYS. RES.* **88**; 1145-1152

Forsyth D.W., 1985, Subsurface loading and estimates of the flexural rigidity of continental lithosphere, *J. Geophys. Res.* **90**, 12623-12632

Galloway W.E., 1989, genetic stratigraphic sequences in basin analysis I: architecture and genesis of flooding-surface bounded depositional units, *AAPG Bull.* **73**; 125-142

Haq B.U., Hardenbol J., & Vail P.R., 1987, Chronology of fluctuating sea levels since the Triassic, *Science* **235**; 1156-1167

Harland W.B., Armstrong R.L., Cox A.V., Smith A.G. & Smith D.G., 1990, A geological time scale, Cambridge University Press, Cambridge; 263pp

Houseman G., & England P., 1986, A dynamical model of lithosphere extension and sedimentary basin formation, *J. Geophys. Res.* **91(B1)**, 719-729

Jarvis G.T. & McKenzie D.P., 1980, Sedimentary basin formation with finite extension rates, *Earth Planet. Sci. Lett.* **48**; 42-52

Klemperer S.L. & White N., 1989, Coaxial stretching of lithospheric simple shear in the North Sea? Evidence from deep seismic profiling and subsidence, *AAPG Mem.* **46**; 511-522

Kusznir N.J. & Ziegler P.A., 1992, The mechanics of continental extension and sedimentary basin formation: A simple shear/pure shear flexural cantilever model, *Tectonophysics* **215**; 117-131

Le Pichon X. & Sibuet J-C., 1981, Passive margins: a model of formation, *J. Geophys. Res.* **86**; 3708-3720

Lister G.S., Etheridge M.A & Symonds P.A., 1986, Detachment faulting and the evolution of passive continental margins, *Geology* **14**; 246-250

McKenzie D.P., 1967, Some remarks on heat flow and gravity anomalies, *J. Geophys. Res.* **72**, 6261-6273

McKenzie D. & Bowin C., 1976, The relationship between bathymetry and gravity in the Atlantic Ocean, *J. Geophys. Res.* **81**, 1903-1915

McKenzie D., 1978, Some remarks on the development of sedimentary basins, *Earth Planet. Sci. Lett.* **40**, 25-32

McKenzie D. & Bickle M.J., 1988, The volume and composition of melt generated by extension of the lithosphere, *J. Petrol.* **29(??)**, 625-679

McKenzie D. & Fairhead D., 1997, Estimates of the effective elastic thickness of the continental lithosphere from Bouguer and free air gravity anomalies, *J. Geophys. Res.* **102**; 27523-27552

McNutt M., 1990, Flexure reveals great depth, *Nature* **343**; 596-597

Muller R.D., Mihut D. & Baldwin S.J, 1998, A new kinematic model for the formation and evolution of the West Australian margin, in Purcell P.G. & Purcell R.R. (eds.), 1998, "The Sedimentary Basins of Western Australia: Part II", Proceedings West Australian Basins Symposium, Perth, W.A.

- Negredo, A.M., M. Fernandez, & H. Zeyen, *Thermo-Mechanical Constraints On Kinematic Models of Lithospheric Extension*. Earth & Planetary Science Letters, 1995. **134**(1-2): p. 87-98.
- Newman R. & White N., 1997, Rheology of the continental lithosphere inferred from sedimentary basins, *Nature* **385**, 621-624
- Newman R. & White N., 1999, The dynamics of extensional sedimentary basins: constraints from subsidence inversion, *Phil. Trans. R. Soc. Lond.* **357**, 805-834
- Parsons B. & Sclater J.G., 1977, An analysis of the variation of ocean floor bathymetry and heat flow with age, *J. Geophys. Res.* **82**, 803-827
- Parsons B. & McKenzie D.P., 1978, Mantle convection and the thermal structure of the plates, *J. Geophys. Res.* **83**, 4485-4496
- Price N.J. & Cosgrove J.W., 1990, Analysis of geological structures, Cambridge University Press (publ.)
- Rowley D.B. & Sahagian D., 1986, Depth-dependent stretching: a different approach, *Geology* **14**, 32-35
- Royden L. & Keen C.E., 1980, Rifting processes and thermal evolution of the continental margin of eastern Canada determined from subsidence curves, *Earth Planet. Sci. Lett.* **51**, 343-361
- Sandwell D.T. & Smith W.H.F., 1997, Marine gravity anomaly from Geosat and ERS 1 satellite altimetry, *J. Geophys. Res. Solid Earth* **102(B5)**, 10039-10054
- Sclater J.G. & Christie P.A.F., 1980, Continental stretching: an explanation of the post mid Cretaceous subsidence of the central North Sea Basin, *J. Geophys. Res.* **85**, 3711-3739
- Sclater J.G. & CÃ'lÃ'rier B., 1989, Errors in extension measurements from planar faults observed on seismic reflection lines, *Basin Res.* **1**, 217-221
- Sleep N.H., 1971, Thermal effects of the formation of Atlantic continental margins by continental break up, *Geophys. J. R. Astr. Soc.* **24**; 325-350
- Steckler M.S. & Watts A.B., 1978, Subsidence of the Atlantic-type continental margin off New York, *Earth Planet. Sci. Lett.* **41**, 1-13
- Steckler M.S. & Watts A.B., 1981, Thermal and mechanical evolution of united-states Atlantic continental-margin, *Am. Ass. Petrol. Geol. Bull.* **65**(??)1671-
- Vail P.R., Mitchum R.M. Jr & Thompson S. III, 1977, Seismic stratigraphy and global changes of sea level, part 4: global cycles of relative changes of sea level, in Payton, C.E. (ed.), 1977, "Seismic Stratigraphy - Applications to Hydrocarbon Exploration", AAPG Mem. **26**; 83-97
- Veevers J.J., 1984, Phanerozoic earth history of Australia, Clarendon Press, Oxford, 418pp
- Walcott R.I., 1972, Gravity, flexure and the growth of sedimentary basins at a continental edge, *Geol. Soc. Am. Bull.* **83**; 1845-1848
- Watts A.B. & Ryan W.B.F., 1976, Flexure of the lithosphere and continental margin basins, *Tectonophysics* **36**; 25-44
- Watts A.B., Karner G.D. & Steckler M.S., 1982, Lithospheric flexure and the evolution of sedimentary basins, *Phil. Trans. R. Soc. Lond.* **305**; 249-281

- Watts A.B. & Marr C., 1995, Gravity anomalies and the thermal and mechanical structure of rifted continental margins, in Banda E. et al. (eds.), "Rifted Ocean-Continent Boundaries", Kluwer (publ.), 65-94
- Wernicke B. & Burchfiel B.C., 1982, Modes of extensional tectonics, *J. Struct. Geol.* **4**(??), 105-115
- Wernicke B. & Tilke P.G., 1990, Extensional tectonic framework of the U.S. Central Atlantic passive margin, *AAPG Mem.* **46**; 7-21
- Wernicke B., 1981, Low-angle normal faults in the Basin and Range Province: nappe tectonics in an extending orogen, *Nature* **291**; 645-648
- Wernicke B., 1985, uniform-sense normal simple shear of the continental lithosphere, *Can. J. Earth Sci.* **22**(??), 108- 125
- White N. & Latin D., 1993, Subsidence analyses from the north-sea triple-junction, *J. Geol. Soc.* **150**(??), 473-488
- White N. & McKenzie D., 1988, Formation of the "steer's head" geometry of sedimentary basins by differential stretching of the crust and mantle, *Geology* **16**; 250-253
- White N. & Yielding G., 1991, Calculating normal fault geometries at depth: theory and examples, in Roberts A.M., Yielding G. & Freeman B. (eds.), 1991, "The Geometry of Normal Faults", *Geol. Soc. Spec. Publ.* **56**; 251-260
- White N., 1989, Nature of lithospheric extension in the North Sea, *Geology* **17**; 111-114
- White N., 1993, Recovery of strain rate variation from inversion of subsidence data, *Nature* **366**, 449-452
- Zienkiewicz, O.C. & P.N. Godbole, *Finite Elements in Fluids*. Vol. 1. 1975, New York: John Wiley.
- Zuber M.T., Bechtel T.D. & Forsyth D.W., 1989, Effective elastic thickness of the lithosphere and mechanisms of isostatic compensation in Australia, *J. Geophys. Res.* **94**; 9353-9367

21.4 Flexural basins

21.4.1 Mechanism of formation

Foreland basins are associated with major zones of compression and are defined as those sedimentary basins that form between an orogenic belt and the adjacent craton. It is widely accepted that unlike extensional basins, the processes that form and modify foreland basins are mechanical rather than thermal in nature (Watts, 1992b). Thus, downward flexure of the lithosphere as a result of progressive loading of the craton by an encroaching thrust mass forms the depocentre. The depocentre migrates toward the craton as the orogenic belt develops (Dickinson, 1974; Beaumont, 1981; Allen et al, 1986).

Current models of the lithosphere suggest that foreland basins develop on former passive margins i.e. on already thinned continental lithosphere, and the characteristic underfilling of the early stages of development may be a consequence of this (Allen et

al, 1986; *Watts*, 1992b). However, foreland basins vary greatly, particularly with respect to the state of the supporting lithosphere (*Allen et al*, 1986).

Two mechanical models have been developed to explain the response of the lithosphere to loading - the elastic and viscoelastic models. *Flemings and Jordan* (1989) and *Sinclair et al* (1991) compare the two and conclude that despite the presence of unconformities in foreland basins associated with apparent tectonic quiescence and deepening of the depocentre close to the thrust front, the elastic model of the lithosphere is more appropriate, as the existence of ancient foreland basins is evidence that the lithosphere can maintain flexural strength over long periods of time. Furthermore, *Sinclair et al* (1991) state that simple spatial redistribution of the load can produce the same stratigraphic effects that have been attributed to a viscoelastic model. According to *Watts* (1992), the elastic thickness of the continental lithosphere is characterised by its bimodality (elastic plate thicknesses of 10-20 km and 80-90 km). Foreland basins are either narrow and deep if flexural rigidity of the lithosphere is low or are wide and shallow if the flexural rigidity is high. He points out that it is not load shape that controls the width and depth of a basin, but rather the effective elastic thickness of the lithosphere, which does not change markedly through time once thrust loading has commenced (*Kominz and Bond*, 1986).

Foreland basins produce patterns of subsidence that are the inverse of those typically displayed by extensional basins. Whereas extensional basins formed by rifting tend to exhibit an exponential decrease of the rate of subsidence with time (*McKenzie*, 1978), initial foreland subsidence is generally slow but the rate progressively increases with time as the thrust mass continues to load the supporting lithosphere (*Watts*, 1992). Additionally, foreland basins exhibit an asymmetry of subsidence magnitude, decreasing with distance from the orogenic belt.

21.4.2 Subsidence of flexural basins

The existence of foreland basins is a piece of evidence by itself that the lithosphere does act as an elastic sheet. In case of Airy isostasy, no load at the surface would ever produce a basin, because the crust underneath the load would simply locally isostatically compensate for the load. The width of a basin that is caused by a given surface load is a function of the elastic thickness of the plate. Intuitively one would expect that the thicker an elastic sheet the wider the diameter of the depression and the shallower the depression caused by any given load. This is indeed the case, and shown in Figure 21.19.

If we model the lithosphere as a viscoelastic sheet the initial flexure is the same as for an elastic lithosphere, but the lithosphere relaxes with time. The viscoelastic relaxation time t , the time taken for any stress to relax to $1/e$ of its original value, is defined by $t = 2h/E$, where E = Young's modulus, and h the dynamic viscosity. This means that the basin becomes deeper and narrower with time, evolving towards local isostatic equilibrium.

An example for a well-studied foreland basin is the Canadian basin, formed by eastward thrusting in the Rocky Mountains from about 140-35 Ma. After 35 Ma massive

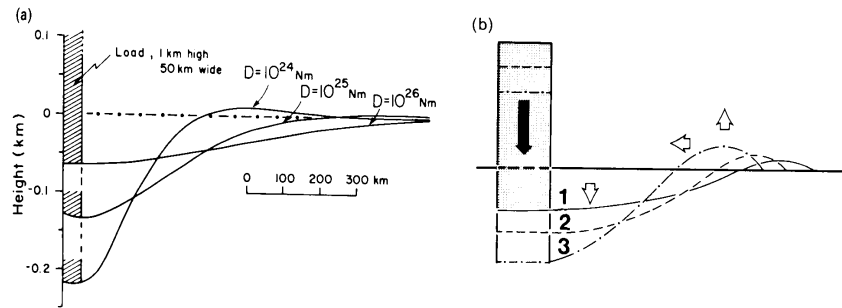


Figure 21.19: The isostatic balance requires the mass of the mantle displaced to be the same as the mass of the surface load. Alternatively, we can model the lithosphere as a viscoelastic sheet, behaving elastically on a short time scale, and viscously on a long time scale (from Beaumont, 1981).

erosion of almost 10 km of material and resulting isostatic uplift took place. Another example is the Appalachian Basin, formed by westward thrusting of the Appalachian mountain system from about 470 Ma–200 Ma. The modelled elastic thickness of the lithosphere is 80–90 km. A third well studied example is the northern Alpine molasse basins. Figure 21.20 shows a cross section through the Swiss molasse basin (from Ziegler, 1988) and Fi. 21.21 a profile through the northern Austrian Alps.

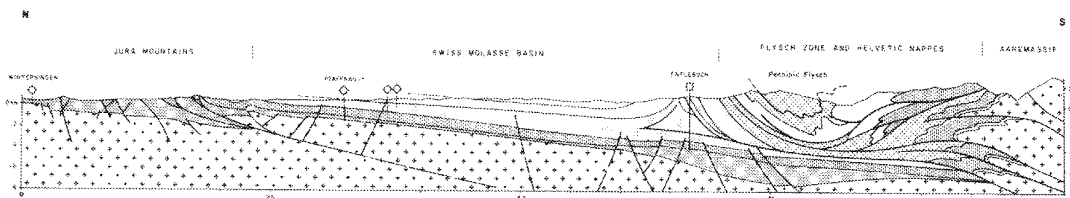


Figure 21.20: Here Eocene-early Miocene obduction of the Austro-Alpine and Penninic nappes onto the margin of the North European craton was accompanied by the development of the Alpine foredeep, which is called the Molasse basin. The axis of the basin migrated cratonward through time in response to the advancing nappe systems.

21.5 Inversion and basin uplift

21.5.1 Overview

The term “inversion” (Glennie and Boegner, 1981) refers to the fact that an initial structural low is subsequently uplifted or inverted to form a structural high. Positive inversion structures form by the compressional reactivation of pre-existing extensional

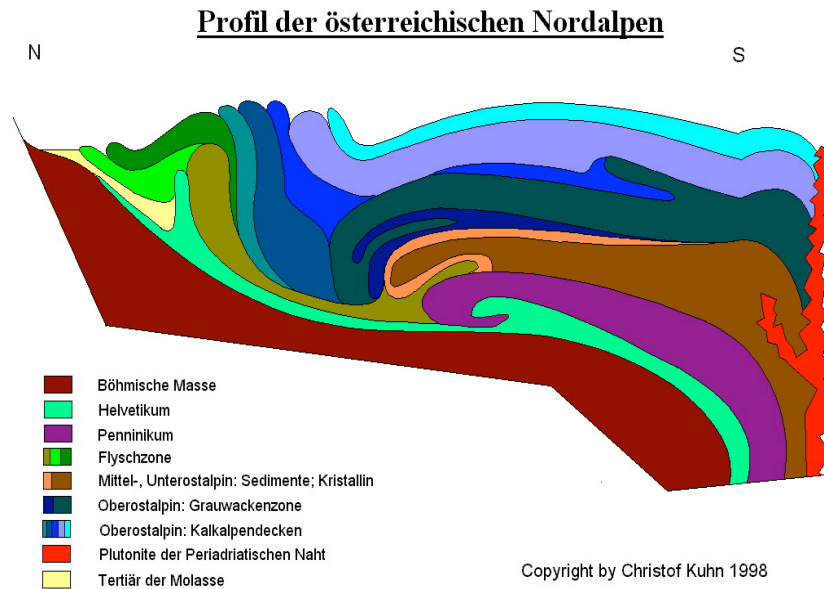


Figure 21.21: Profile of the foreland basin in northern Alps, Austria. Kuhn, 1998.

structures. The converse is also possible so that inversion can be considered in both positive (uplift), and negative (subsidence) senses relative to the immediately preceding history (Mitra, 1993; Williams et al., 1989). Basin inversion is not only the result of fault related structural reactivation and compression, it can also occur as a result of diapirism (both locally and regionally), and by isostatic, thermal and flexural processes affecting the lithosphere, usually of a significantly larger wavelength than the fault-related structuring (Cooper et al., 1989).

Several authors have developed methods for recognising and quantifying inversion structures. Mitra (1993) used experimental models and observations of natural structures to develop quantitative models for the geometry and kinematic evolution of inversion structures. Analysis of two main formation mechanisms of inversion structures, fault-propagation folding on planar faults and fault-bend folding on listric faults, allowed recognition of the characteristic variations in bed geometry and thickness, which led to the development of a predictive model for interpreting the subsurface geometries of these two classes of inversion structures, in particular in areas with poor seismic data.

Williams et al. (1989), quantified the relative magnitude of continental and extensional movement measured in the plane of section using the position of the null point (the point of change from net extension to net contraction) in a syn-rift sequence. The resulting ‘inversion ratio’ is defined as the ratio of contractional to extensional displacement. White et al.’s (1986) method relating the geometry of normal faults and that of

sedimentary layers in their hanging walls is equally valid and applicable to inversion and thrust faults.

21.5.2 Case history: Inversion in the Canning Basin/NW shelf of Australia

The *Canning Basin* is the largest sedimentary basin in Western Australia, covering an area of around 640,000 square kilometres. Current models of the basin indicate four main tectonic events have taken place since the initiation of subsidence in the Ordovician. The Fitzroy Trough was the most tectonically active region in the Canning Basin during these tectonic events.

The Fitzroy Trough is currently modelled as a series of half-graben bounded by transfer faults. A section covering the north-east margin of the Fitzroy Trough has been interpreted and a geodynamic model of movement on the Pinnacle Fault developed. This has allowed interpretation of the timing of extension and crustal shortening/inversion within the Canning Basin (Fig. 21.22).

Subsidence in the Canning Basin initiated in the Ordovician. Major extension and subsidence did not begin until the Mid-Devonian. Extensional movement on the Pinnacle Fault took place syn-depositionally with the Famennian sedimentary sequence. Extension continued in the Fitzroy Trough through the Devonian and into the Carboniferous, ceasing in the Late Carboniferous. Erosion in the Late Carboniferous produced an unconformity between the Early Carboniferous and Early Permian sedimentary sequences.

Crustal shortening and inversion took place in the Canning Basin from the Middle Triassic until the Early Jurassic. This shortening folded and faulted the sequences producing uplift and erosion. The crustal shortening reactivated the previously extensional Pinnacle Fault as a thrust fault producing an inversion structure (see Fig. 21.22).

Extension in the Canning Basin occurred from the Mid-Devonian to the Late Carboniferous. Crustal shortening in central Australia was at a peak around 400 Ma. The timing of these two events is similar, indicating a possible link between the two tectonic events. Precise timings of the amount of extension in the Canning Basin will provide information about the tectonic similarity between these regions.

21.6 References

Beaumont, C., 1978, The Evolution of Sedimentary Basins on a Viscoelastic Lithosphere: Theory and Examples: Geophysical Journal of the Royal Astronomical Society, v. 55, p. 471-497.

Beaumont, C., Ellis, S., Hamilton, J., and Fullsack, P., 1996, Mechanical model for subduction-collision tectonics of Alpine-type compressional orogens: Geology, v. 24, p. 675-678.

Beaumont, C., Kamp, P.J.J., Hamilton, J., and Fullsack, P., 1996, The continental collision zone, South Island, New Zealand: Comparison of geodynamical models and observations: Journal of Geophysical Research - Solid Earth, v. 101, p. 3333-3359.

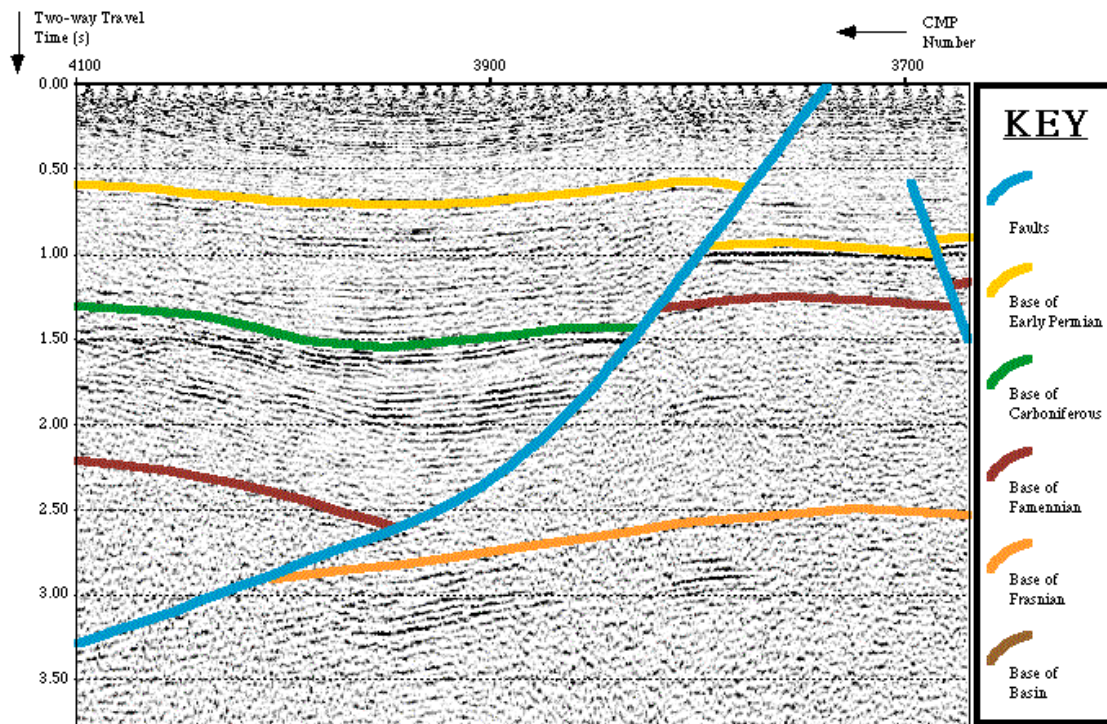


Figure 21.22: Interpreted seismic section showing movement on the Pinnacle Fault, Canning Basin

Beaumont, C., and Quinlan, G., 1994, A geodynamic framework for interpreting crustal-scale seismic-reflectivity patterns in compressional orogens: Geophys. J. Int., v. 116, p. 754-783.

Haddad, D., and Watts, A.B., 1998, Subsidence history, gravity anomalies and flexure of the northeast Australian margin in Papua New Guinea.

Holt, W.E., and Stern, T.A., 1994, Subduction, platform subsidence, and foreland thrust loading: the late Tertiary development of the Taranaki Basin, New Zealand: Tectonics, v. 13, p. 1,068-1,092.

Karner, G.D., and Watts, A.B., 1983, Gravity Anomalies and Flexure of the Lithosphere at Mountain Ranges: Journal of Geophysical Research, v. 88, p. 10,449-10,477.

Lorenzo, J.M., Obrien, G.W., Stewart, J., and Tandon, K., 1998, Inelastic Yielding and Forebulge Shape Across a Modern Foreland Basin - North West Shelf of Australia, Timor Sea: Geophysical Research Letters, v. 25, p. 1455-1458. Ziegler, P.A., van Wees, J.D., and Cloetingh, S., 1998, Mechanical controls on collision-related compressional intraplate deformation: Tectonophysics, v. 300, p. 103-129.

21.7 Extensional basin modelling

21.7.1 Introduction

The way in which the lithosphere deforms during extension is an important mechanism in the dynamics of the Earth. The problem of modelling lithospheric extension has been attacked from many different angles. Some have constructed analogue models in tanks using various fluids to represent the crust and mantle, others have used computer simulations of varying complexity. Analogue models have lent insight but are difficult to set up, only a limited number of parameters can be controlled, and the results are still somewhat empirical. Numerical solutions break free of these constraints, allowing more flexibility in the design of the model and the way in which results are analysed.

Even since their early years, computers have been used in various fields of science to solve problems too complex or tedious to be solved by hand. The problems in geodynamics are no different. While the equations governing the dynamics of such a system have been known and well understood for some time, solving them has never been easy. This is largely due to the sheer magnitude of the system being modelled. The huge number of particles that need to be tracked and the different physical effects being observed translate to requiring vast amounts of computing power. Fortunately, the exponential growth of computing speed and their increasing accessibility have put such problems within reach. Their continued growth will ensure that solving such problems will only get easier in the future, from a computational standpoint.

Mathematical modelling in its various guises has been an established scientific method in many disciplines for some time, even before the advent of computers. Even though results can be calculated with great accuracy, the overall complexity of models are still very simple compared to actual systems - there are simply too many things going on in even the simplest interactions to keep track of, so at best such simulations are just approximations of actual processes. Part of the design of a mathematical model is to weigh up the importance of certain effects and see whether they influence the final outcome enough to be worth including into the model. Despite this, mathematical modelling has been successful in predicting the behaviour of numerous systems across a wide range of systems from the most minute subatomic particle interactions to predicting orbits of planets and their satellites.

Methods of basin analysis can be divided into forward and reverse modeling. *Forward modeling* utilises analytical or numerical implementations of simple basin models to calculate the subsidence of a basin through time, given a certain model and certain starting conditions. Then the result is compared with a given data set. *Reverse or inverse modeling* uses the data directly to invert for a particular best fit model, using some kind of least-squares minimisation technique. The fit of certain model parameters with respect to the data is minimised to obtain the best-fit model. Both modeling approaches only work if we are certain that we understand which model applies to a given basin. Figure 21.23 gives an overview about the input and output of basin modelling exercises.

21.7.2 Backstripping

21.7.2.1 Introduction

Sedimentation in basins significantly modifies the magnitude of subsidence due to sediment loading. The sediment record can be utilised to determine the subsidence history of the underlying basement had it occurred in the absence of sedimentation. The latter is referred to as “tectonic subsidence”, as opposed to the subsidence caused by sediment loading. To obtain subsidence of a basin floor loaded only with water, the sediment load must be removed using either an Airy model or a flexure model for the isostatic compensation. Backstripping therefore, is a technique used to recover the tectonic component of subsidence.

The backstripping procedure starts with restoring the lowest unit in a stratigraphic section to its initial thickness and bulk density and placing its top at a depth below sea level corresponding to the average water depth in which the unit was deposited. The isostatic subsidence of the basement caused by the weight of the sediment in the unit is then removed, and the depth to the surface on which the unit was deposited is recalculated with only the weight of the water as the basement loading factor. This procedure continues for all the sedimentary units in the section placing each successively younger unit on top of the previous unit. Palaeowater depth variation and changing sea levels during deposition must be included in these calculations.

Consider a basin of depth z_w , filled with water of density ρ_w . Let's assume that we completely fill this depression with sediments, and that Airy isostatic equilibrium is maintained.

Now we can calculate the total sediment thickness z_{sd} by equating the mass of water in the depression plus the mass of depressed asthenospheric mantle to the mass of sediments:

$$z_w \rho_w + (z_{sd} - z_w) \rho_m = z_{sd} \rho_{sd} \quad (21.15)$$

Here ρ_{sd} is the decompacted sediment density, and z_{sd} is the decompacted sediment thickness. By solving for the sediment thickness z_s , we obtain:

$$z_{sd} = z_w \left(\frac{\rho_m - \rho_w}{\rho_m - \rho_{sd}} \right) \quad (21.16)$$

If we use $\rho_m = 3300 \text{ kgm}^{-3}$, $\rho_{sd} = 2500 \text{ kgm}^{-3}$ and $\rho_w = 1000 \text{ kgm}^{-3}$, the presence of sediments amplifies the original depression in water by a factor of z_{sd}/z_w of 2.9. The infilling of a water-filled depression 1.5-2 km deep by sediment would produce a basin about 5 km thick. The exact relationship depends on the densities of the infilling sediments. If we know the decompacted sediment thickness z_s then we can rearrange the above formula to calculate the subsidence in water in the absence of sediments:

$$z_w = z_{sd} \left(\frac{\rho_m - \rho_{sd}}{\rho_m - \rho_w} \right) \quad (21.17)$$

We use z_{sd} , the decompacted sediment thickness, instead of z_s , the observed sediment thickness, because except for the top-most sediment layer deposited recently in geological time, z_s will have undergone compaction. As a result we can write:

$$z_s < z_{sd} \quad \rho_{sd} < \rho_s \quad (21.18)$$

Therefore $\rho_m - rs < (\rho_m - \rho_{sd})$. Without decompaction, the tectonic subsidence, i.e. the subsidence of the basement in the absence of a sediment load, eustatic sea-level changes, etc., would always be underestimated.

21.7.2.2 Decompression

The first step in the backstripping process involves removing the effect of burial compaction by restoring each sedimentary layer to its original surface porosity and thickness at the time of deposition. The porosity-depth relationship of the compacted lithologies in the sedimentary basin must be determined (e.g. Fig. 21.26), and the lithologies returned to their pre-compaction state. Densities of decompacted sediments must be used otherwise the tectonic subsidence will always be underestimated. Usually, the porosity-depth relationship for a given lithology is assumed to be an exponential function:

$$\phi = \phi_0 e^{-z/D} \quad (21.19)$$

where ϕ is the porosity at depth z , ϕ_0 is the porosity at the surface during deposition, and D is the decay constant, which gives the porosity at a depth of ϕ_0/e , and is defined as

$$\phi(z) = \frac{\phi_0}{e} \quad \text{when } z = D \quad (21.20)$$

as shown in Fig. 21.25. Petrophysical parameters of eight typical lithologies found in sedimentary basins are listed in Tab. 21.1

It is important to note that compaction is not the only process which reduces porosity. Addition of precipitated cement from an external source can occlude porosity at any stage of burial. Since a wide variety of carbonate lithologies are identified from well logs and outcrop in the Bonaparte Basin, porosity reduction by cementation as well as mechanical compaction must be considered. The best approach is to estimate minimum and maximum thicknesses for an original carbonate layer. A maximum original thickness is obtained if it is assumed that limit the burial thicknesses and densities are purely the result of compaction. Conversely, a minimum limit is obtained if porosity reduction solely by precipitation of cement is assumed [Schmoker & Halley, 1982; Bond & Kominz, 1984].

Consider a sequence of n sediment units. Then the decompacted sediment thickness at the time of final deposition of the n th unit is the sediment thickness with the porosity that it had at the time of deposition of the n th unit. If we are backstripping sediments

| Lithology | Sediment Grain Density | Initial Porosity | Compaction Decay Length |
|--------------------------------|---------------------------------|------------------|-------------------------|
| | $\rho_s g$ (kgm ⁻³) | ϕ_0 | D (m) |
| Shale | 2700 | 0.6 | 2000 |
| Micrite (fine gr. 'limestone') | 2700 | 0.65 | 1000 |
| Grainstone (compactable) | 2700 | 0.48 | 3500 |
| Reef (early cementation) | 2700 | 0.1 | 3500 |
| Sandstone | 2650 | 0.5 | 2500 |
| Basalt | 3000 | 0.1 | 2500 |
| Anhydrite | 2960 | 0.4 | 500 |
| Salt | 2160 | 0.2 | 750 |

Table 21.1: Lithologies and decompaction parameters of eight typical lithologies found in sedimentary basins

from a well so that we know the actual porosity variation with depth, we would of course use those porosities instead of the simple relationship shown above.

Example: Let the top 500 m of sediment of a sediment sequence be Pliocene to Holocene sediments. If we want to decompact the Miocene and older sediments, we have to calculate z_{sd} for 5 Ma. Then we remove the top 500 m of sediment, moving the older units up, with the youngest Miocene at the surface. But at 5 Ma the youngest Miocene sediments had a porosity of ϕ_0 . That is, all porosities (bold curve in the figure below) are now too low. The original porosities (finer curve) must be restored to the section (Fig. 21.27).

If the Miocene section is currently 1000 m thick then we can calculate its present average porosity as follows:

$$\hat{\phi}_{\text{Mio}/0\text{Ma}} = \frac{\int_{500}^{1500} \phi dz}{1000} \quad (21.21)$$

Here the average value is indicated by a "hat" sign, and the index "Mio/OMa" indicates that this is the average porosity for the time interval between 5 Ma (Miocene) and the present. When we remove 500 m of Pliocene to recent sediments, the average porosity becomes:

$$\hat{\phi}_{\text{Mio}/5\text{Ma}} = \frac{\int_{500}^{1500} \phi dz}{1000} \quad (21.22)$$

or an increase in porosity of

$$\Delta\hat{\phi} = \hat{\phi}_{\text{Mio}/5\text{Ma}} - \hat{\phi}_{\text{Mio}/0\text{Ma}} \quad (21.23)$$

How is the average porosity $\hat{\phi}$ of the decompacted section related to the thicknesses of the fully lithified section z_s and the decompacted sections z_{sd} ? z_s and z_{sd} are related to each other by the unknown thickness z_w :

$$z_{sd} = z_w + z_s\phi = \frac{z_w}{z_w + z_s} \quad (21.24)$$

The above equation simply expresses that porosity is defined as the percentage of water with respect to the total thickness of sediment (including water).

$$\phi(z_w + z_s) = z_w \quad (21.25)$$

$$\phi z_w + \phi z_s - zw = 0 \quad (21.26)$$

$$zw(1 - \phi) = \phi z_s \quad (21.27)$$

$$\frac{zw}{z_s} = \frac{\phi}{1 - \phi} \quad (21.28)$$

$$z_{sd} = zw + z \quad (21.29)$$

$$z_{sd} = z_s \left(\frac{zw}{z_s} \right) + z_s = z_s + z_s \left(\frac{\phi}{1 - \phi} \right) \quad (21.30)$$

$$z_{sd} = z_s \left(1 + \frac{\phi}{1 - \phi} \right) \quad (21.31)$$

The expression in brackets corresponds to a factor that we have to multiply z_s by to obtain the uncompacted sediment thickness. Figure 21.28 shows $\frac{\phi}{1 - \phi}$ plotted versus the porosity of the decompacted section.

Therefore, the thickness of our Miocene section becomes

$$z_{\text{Mio}/5\text{Ma}} = z_{\text{Mio}/0\text{Ma}} \left(1 + \frac{\hat{\phi}}{1 - \hat{\phi}} \right) \quad (21.32)$$

and the now the average porosity is

$$\hat{\phi}_{\text{Mio}/5\text{Ma}} = \frac{\int_0^{z_{\text{Mio}/5\text{Ma}}} \phi dz}{z_{\text{Mio}/5\text{Ma}}} \quad (21.33)$$

which is less than $\hat{\phi}_{\text{Mio}/5\text{Ma}}$ because $z_{\text{Mio}/5\text{Ma}}$ is greater than 1000m. This example exemplifies that calculating porosity and decompacted sediment thicknesses requires iteration, but it does converge.

21.7.2.3 Backstripping a stratigraphic section

We will now go through an example of backstripping a stratigraphic section of Miocene age, with a compacted thickness of 800 m.

z_{Mio} = thickness of fully lithified Miocene sediments = 800 m

When the top of this section was at the surface, i.e. had just been deposited (top = 0 Ma), what was the thickness of the section? The first step in this iteration is to calculate the thickness of the water present in the pores in the Miocene section with its top at the surface:

$$z_{\phi\text{Mio1}} = z_{\text{Mio}/0\text{Ma}} \left(\frac{\phi}{1 - \phi} \right) \quad (21.34)$$

where

$$\bar{\phi} = \int_0^{800} \frac{\phi}{800} dz \quad (21.35)$$

This means that the total thickness of the fully compacted sediment and water is

$$z_{\text{Mio}} + z_{\phi\text{Mio1}} \quad (21.36)$$

However, the result of this first iteration is that we have overestimated the thickness of the decompacted section, because we have overestimated its porosity. Now we use the decompacted thickness from iteration 1 to calculate a new, more realistic porosity, as follows:

$$\bar{\phi}_{\text{Mio2}} = \int_0^{800+z_{\phi\text{Mio1}}} \frac{\phi}{800 + z_{\phi\text{Mio1}}} dz \quad (21.37)$$

and the related depth would be

$$z_{\phi\text{Mio2}} = z_{\text{Mio}/0\text{Ma}} \left(\frac{\bar{\phi}_{\text{Mio2}}}{1 - \bar{\phi}_{\text{Mio2}}} \right) \quad (21.38)$$

This thickness is smaller than the decompacted thickness from iteration 1. While we continue iterating, the section shrinks towards its correct length. We continue to iterate:

$$\bar{\phi}_{\text{Mio3}} = \int_0^{800+z_{\phi\text{Mio2}}} \frac{\phi}{800 + z_{\phi\text{Mio2}}} dz \quad (21.39)$$

$$z_{\phi\text{Mio3}} = z_{\text{Mio}/0\text{Ma}} \left(\frac{\bar{\phi}_{\text{Mio3}}}{1 - \bar{\phi}_{\text{Mio3}}} \right) \quad (21.40)$$

Because porosity decreases with depth, this procedure converges, and a stop point to the iteration can be specified, e.g. stop when

$$\frac{z_{\phi\text{Mion}-1} - z_{\phi\text{Mion}}}{z_{\phi\text{Mion}-1}} < \text{small \#}$$

z_{sd} is not only the decompacted thickness of the Miocene section, but that unit plus all strata below it down to basement. After decompacting the whole section, z_{sd} is the sum of all z_i 's and $z_{\phi i}$'s, summed over the entire section:

$$z_{sd} = \sum_{j=1}^n z_i + z_{\phi} \text{ for } n \text{ units in the section}$$

The density of the decompacted section is

$$\rho_{sd} = \rho_s(1 - \phi) + \rho_w\phi \quad (21.41)$$

where ρ_s is the grain density of the sediment, i.e. the fully compacted sediment density. But, we don't really have to calculate the decompacted sediment density ρ_{sd} .

Tectonic subsidence is defined as the subsidence of the basement in the absence of sediments, but covered with water. Thus, the water depth of the backstripped basin does not have to be removed to calculate tectonic subsidence. Now, all we have to do is replace the uncompacted sediment thickness of each unit by water, and add it to the original water depth, which is the water depth in which each sedimentary unit was deposited.

Now we replace the fully compacted sediment column z_i with water and obtain z_{wi} , which is the subsidence in water, that remains after isostatically compensating for the removal of the sediment.

$$z_{wi} = \frac{\rho_m - \rho_{si}}{\rho_m - \rho_w} z_{si} \quad (21.42)$$

Here z_i is the fully compacted sediment thickness of the i -th unit as before, and ρ_{Si} is the fully compacted density of the i -th unit (i.e. its grain density). The tectonic subsidence S_{tec} recorded by that unit is equivalent to the sum of the subsidence that is due to

- 1.) the water column left after replacing the fully compacted sediment with water and isostatically uplifting the section accordingly (z_{wi}): $S_{tec} = z_{wi} + z_{\phi i}$
- 2.) and the thickness of the water column zfl that is proportional to the average porosity in the sediments, i.e. equal to the average porosity multiplied by the total thickness of the sediment column.

Hence the backstripping procedure is a process of calculating the pore water volume in each unit at each time and adding its thickness to the equivalent subsidence in water of the compacted sediment column (c.f. Fig. 21.29). This gives us the tectonic subsidence of the basin in water in the absence of sediments. Remember that our objective here is to utilise the sediment record to distinguish between the subsidence caused by the sediment load itself and the tectonic subsidence of the basin floor.

21.7.2.4 Summary of backstripping procedure:

- 1.) Begin with a geologic section with thicknesses $z'_i, i = 1, 2, 3, \dots, n$ where $i = 1$ is the oldest unit and n the youngest.
- 2.) Fully lithify the section to calculate values z_i , the compacted solid sediment thicknesses.
- 3.) Decompact z_1 . Calculate tectonic subsidence from pore water volume and equivalent subsidence under water z_{w1} —NOT solid sediment load, z_1 .
- 4.) Decompact z_2 , putting it at the surface. Calculate its contribution to tectonic subsidence from pore water volume and equivalent subsidence under water z_{w2} as opposed to solid sediment load, z_2 . Then decompact z_1 by putting it just below the depth of $z_2 + z_{\phi 2}$. Calculate its contribution to tectonic subsidence from pore water volume and equivalent subsidence under water. Calculate total tectonic subsidence for time interval 1 + 2.
- 5.) Repeat steps outlines in 4 for z_3 to z_n .
- 6.) If top of section was deposited recently, then it is possible to check the decompressed thicknesses to see that they agree with the calculated $z_i + z_{\phi i}$ for all sediment units.

21.7.2.5 Water depths

If sediments do not accumulate exactly to sea level (which they usually do not) then there is more water in the basin than just the water in the pores. Because the water was there at the time of sediment deposition it must be included in the calculation of tectonic subsidence. In general, then, at the time of deposition of the j 'th unit ($i < j < n$) the tectonic subsidence S_{tec} is given by

$$S_{tec_j} = \sum_{i=1}^j \left[z_i \frac{\rho_m - \rho_{Si}}{\rho_m - \rho_w} + z_{\phi i} \right] + z_w \quad (21.43)$$

where S_{tec_j} = sum of tectonic subsidence including all units from 1 to j ; and z_w = water depth.

Adding water depths to the subsidence model is not straightforward, because the inaccuracies involved in the determination of *paleo-water depths* from microfossils (see Fig. 21.30) are often larger than the water depth. Because of that it is often ignored in tectonic subsidence analyses (VERY dangerous, since this can introduce large errors).

21.7.2.6 Sea level

We know that *sea level does not remain fixed while a basin subsides*.

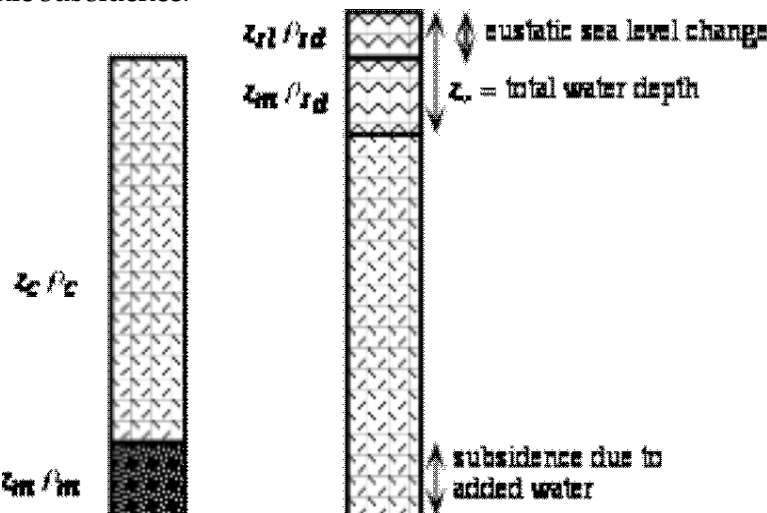
Main reasons for changing eustatic (i.e. global) sea level changes:

- 1.) *Waxing and waning ice sheets* (short term, i.e. hundred thousands - millions of years)
- 2.) *Changes in the volume of ocean basins* (i.e. age-area distribution of ocean crust) - tens of millions of years

In other words the base level to which the calculation of tectonic subsidence is related, is not fixed. For example an increase in relative sea level will result in an increase in the relative accommodation space for accumulating sediments and water depths, and an overestimate of tectonic subsidence. Additionally, a rise in sea level, relative to land, depresses the basin beneath the rise of sea level. Thus, the accommodation space is increased by more than the apparent sea level rise.

It is important that error bars be attached to fossil assemblages in sediments which are used to estimate sea level, since *uncertainties in water depth estimates can be quite large and must be taken into account*. This information is also important so that the weight of the water mass above the sediments at the time of their deposition can be included in the subsidence calculations.

One way to get around this problem is to "plug in" a published sea level curve into the model, e.g. Haq *et al.*'s (1989) curve. The benefit of doing so however is questionable, because published eustatic sea level curves cannot be taken at face value. If one decides to do so, then the sea level change must be removed from calculations of tectonic subsidence.



Isostatically balancing the two above columns gives:

$$z_{sl}\rho_w + z_m\rho_w = z_m\rho_l \quad (21.44)$$

$$z_{sl} = z_m(\rho_m - \rho_w) \quad (21.45)$$

$$z_{sl} = z_m \frac{(\rho_m - \rho_w)}{\rho_w} \quad (21.46)$$

$$z_m = z_{sl} \frac{\rho_w}{\rho_m - \rho_w} \quad (21.47)$$

z_m is the subsidence caused by a sea level rise of z_{sl} . The space available for the sediments is

$$z_m + z_s \quad (21.48)$$

$$z_m + z_{sl} = z_{sl} \frac{\rho_w}{\rho_m - \rho_w} + z_{sl} \quad (21.49)$$

$$z_m + z_{sl} = z_{sl} \frac{\rho_w + (rho_m - rho_w)}{\rho_m - \rho_w} = z_{sl} \frac{\rho_m}{(\rho_m - \rho_w)} \quad (21.50)$$

As a result the tectonic subsidence becomes

$$S_{tecj} = \sum_{i=1}^j \left[z_i \frac{\rho_m - \rho_{si}}{\rho_m - \rho_w} + z_{\phi_i} \right] - z_{sl} \frac{\rho_m}{(\rho_m - \rho_w)} + z_{wl} \quad (21.51)$$

where, for the i^{th} sediment layer of a total of j layers, S_{tecj} is the water loaded (tectonic) basement subsidence, z_i is the decompacted sediment thickness, ρ_{si} is the mean density of the decompacted sedimentary column, ρ_m is the density of the lithospheric mantle, ρ_w is the density of sea water, z_{sl} is the difference between palaeo- and present sea level, and z_{wl} is the water depth. Here a positive z_{sl} is equivalent to a sea level rise, and therefore must be removed from the calculated tectonic subsidence.

The pressure at the base of the unloaded column must be equated to the pressure at the base of an equivalent isostatically balanced mid ocean ridge column to ensure that isostatic equilibrium is maintained.

21.7.2.7 Hiatuses

What if some time period is not represented in our sediment column due to erosion? The presence of a hiatus implies that time is missing in the section. One assumption we can follow is that the entire duration of the hiatus is represented only by non-deposition (lower left figure). If there was non-deposition, then we only had to specify zero sediment thickness for the time period of the hiatus. This is, the basement is neither uplifted nor does it subside (Fig. 21.31).

The more reasonable scenario is to assume that there was *additional deposition during that time, and that subsequently the sediments were removed by erosion*. Evidence of erosion beneath a hiatus may come from an *angular unconformity* or an *abrupt change in porosity within a single type of lithology* above and below an unconformity. This implies that tectonic subsidence continued beyond the observed sediments beneath the hiatus, and the subsequent erosion corresponds to uplift of the basement. Two possibilities are shown in the right figure. This assumption of course includes an inherent non-uniqueness. Basically, there is no record to tell us what exactly happened during this time.

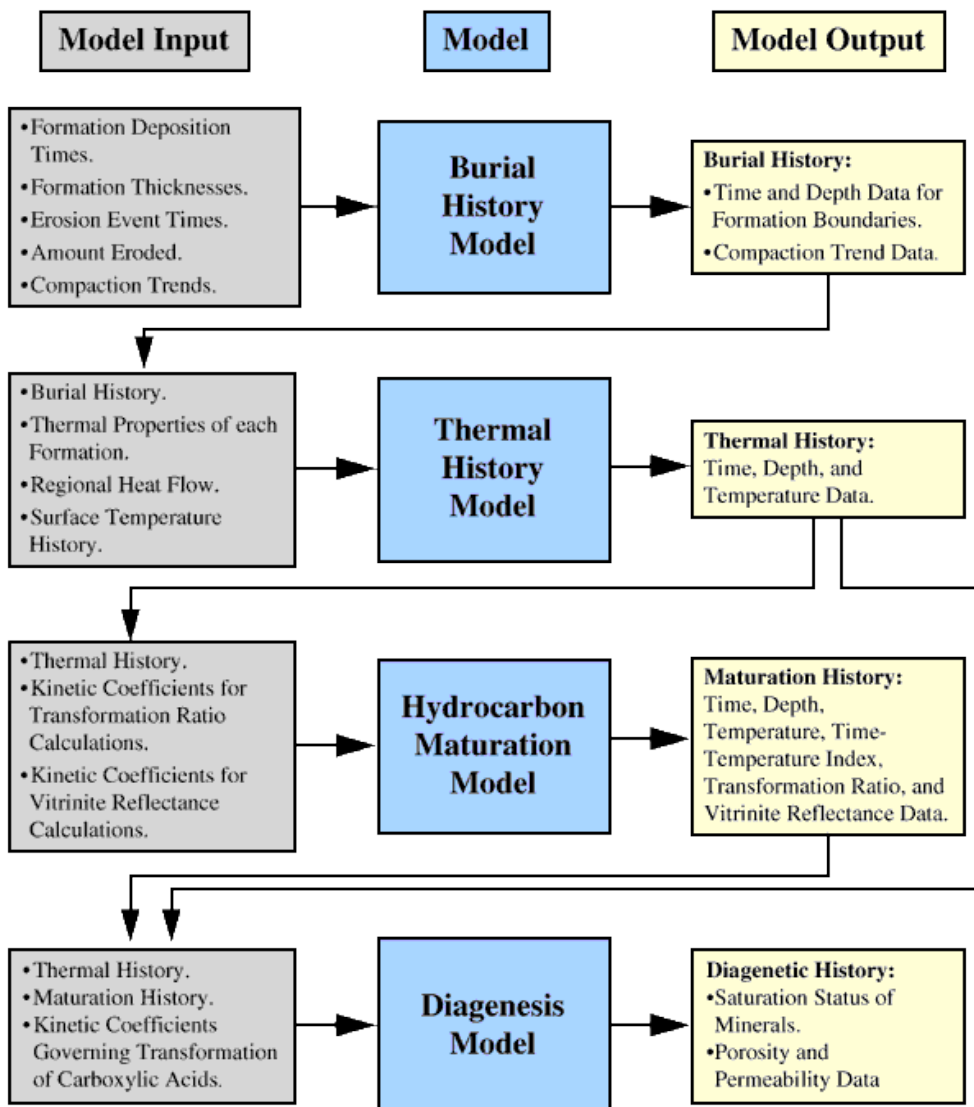


Figure 21.23: Inputs and outputs of basin models.

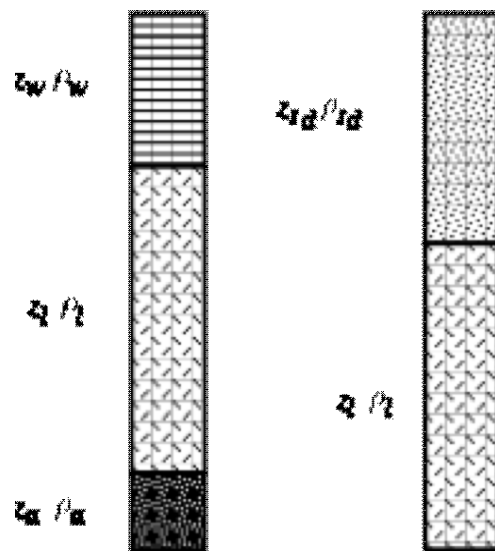


Figure 21.24: Decomposition of a sediment column by backstripping.

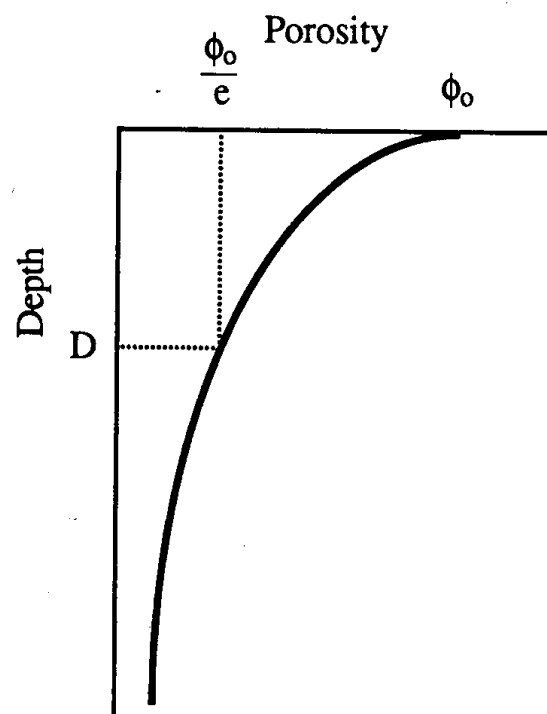


Figure 21.25: Compaction decay of the porosity

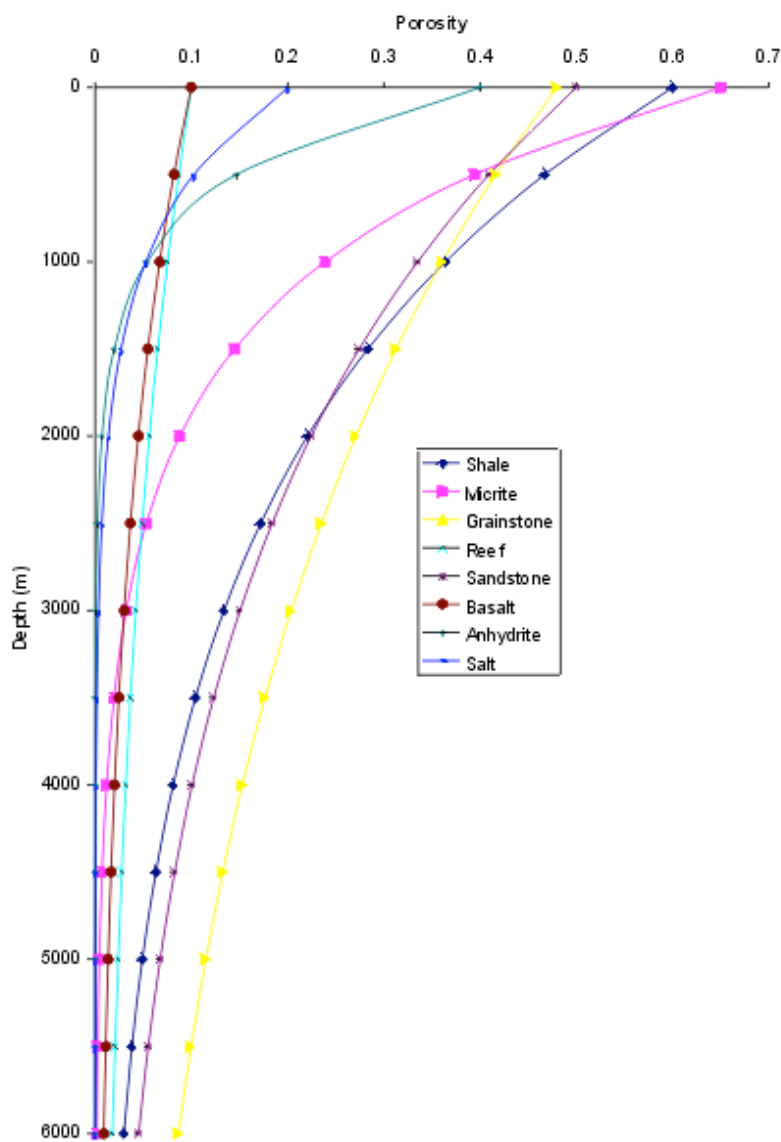


Figure 21.26: Porosity-depth curves for 8 typical lithologies

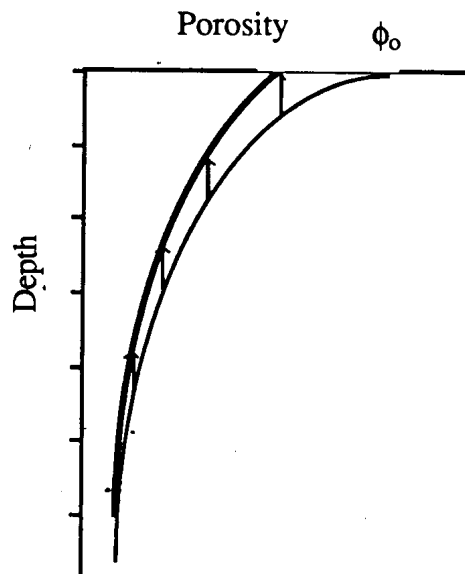


Figure 21.27: Porosities (bold curve) are too low after backstripping the top 500 m of a sedimentary sequence. The original porosities (finer curve) must be restored to the section.

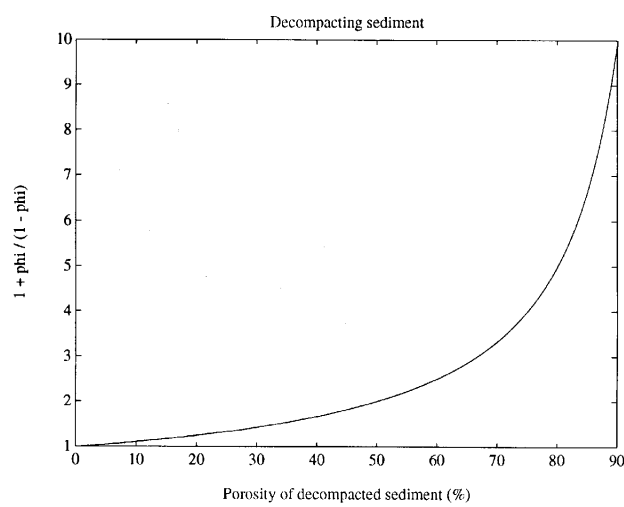


Figure 21.28: $\frac{\phi}{1-\phi}$ plotted versus the porosity of the decompacted section

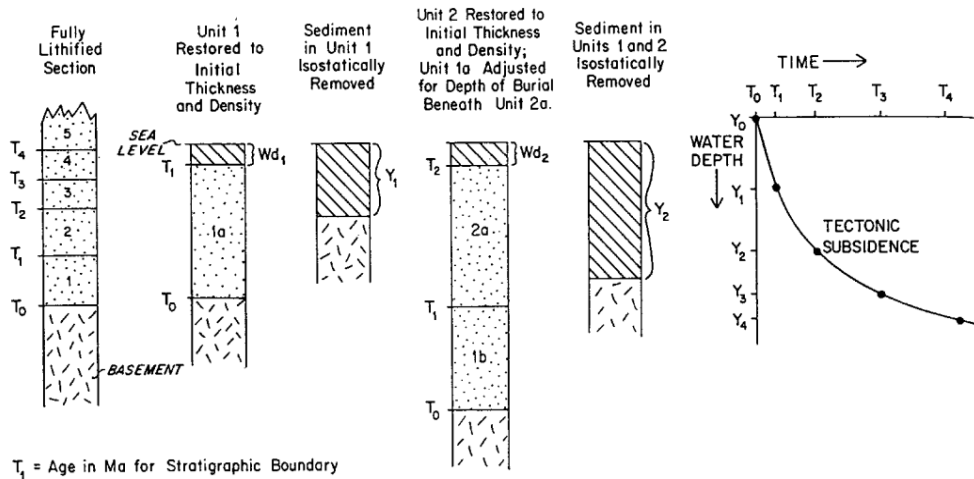


Figure 21.29: Diagram showing the procedure for iteratively backstripping a fully compacted sedimentary column. The entire sedimentary sequence is removed and the initial unit is replaced with its original depositional density and thickness. The volume of this initial unit is then replaced with an equivalent volume of water ($\rho \approx 1$). The amount of basement subsidence that this water load causes is the tectonic basement subsidence. This procedure is repeated for every compacted unit in the entire column (from Bond & Kominz, 1984).

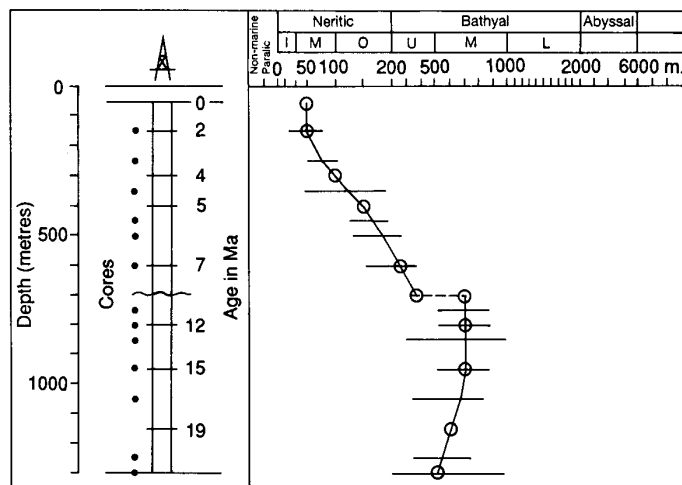


Figure 21.30: Paleo-waterdepth determination from a well based on micropaleontology

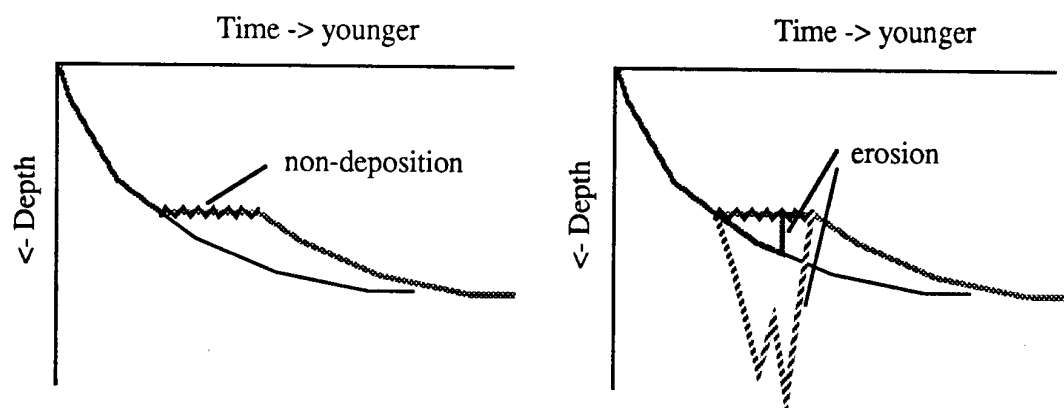


Figure 21.31: Different scenarios for the presence of a hiatus.

Appendix A

MATLAB manual

A.1 Introduction: What is MATLABTM?

MATLAB is a high-performance language for technical computing. After mastering the basics, you will see amazing power that combines computational capabilities with graphics capabilities. MATLAB stands for *matrix laboratory*, which reflects its original application to matrix applications. With MATLAB, you have the following capabilities:

- 1.) math and computation
- 2.) algorithm development
- 3.) modeling, simulation, and prototyping
- 4.) data analysis, exploration, and visualization
- 5.) scientific and engineering graphics
- 6.) application development, including Graphical User Interface (GUI) building

A.2 Getting started

Simply type `matlab &` in a terminal window and hit RETURN. When MATLAB starts you will notice the main window contains three separate windows, the *Command*, *Command History* and *Workspace* windows. The *Command* window is where you type instructions to MATLAB. The *Command History* window shows you the previous commands given to MATLAB (note: you can highlight the commands and press ENTER to run them again). The *Workspace* window shows the variables currently being stored by MATLAB. You can change the configuration of these windows – for further instruction go to the Help menu and select Demos, then select the Desktop Environment Demo. You will also notice that the *Command History* and *Workspace* windows have Tabs to display other windows. The *Workspace* window has a Tab to display the *Launch*

Pad window which is a quick access to the various Help and demo materials for MATLAB and it's modules. The *Command History* window has a tab to display the *Current Directory* window, which can be used to graphically navigate through your file system.

A.3 Getting help

Your first resource should be the `help` function that is part of the MATLAB program. There is a “Help” icon which will bring up a searchable help data base. It contains tutorials for basic MATLAB functions.

If you are not familiar with MATLAB we strongly recommend to go through the help pages on all basic MATLAB functions.

Another nice tool is the `lookfor <keyword>` command. (type `help help` for information on this). It will look through all the help pages and give you back the commands that have the *keyword* in the first line of its help page. For example, what would we do to learn of all the commands that relate to “meshes” in MATLAB? Type:

```
lookfor mesh
```

You can then follow this up by doing a `help` on any of these programs/tools.

A.4 Introductory tutorials

The following subsections give a very short introduction into the MATLAB basics you will need during the course. This is by far not an extensive tutorial and you should by any chance have a look at online resources.

A.4.1 Vectors

Let’s start off by creating something simple, like a vector. Enter each element of the vector (separated by a space) between brackets, and set it equal to a variable. For example, to create the vector `a`, enter into the Matlab command window (you can “copy” and “paste” from your browser into Matlab to make it easy):

```
a = [1 2 3 4 5 6 9 8 7]
```

Matlab should return:

```
1 a =
2     1 2 3 4 5 6 9 8 7
```

Let’s say you want to create a vector with elements between 0 and 20 evenly spaced in increments of 2 (this method is frequently used to create a time vector):

```

3 t = 0:2:20
4 t =
5     0 2 4 6 8 10 12 14 16 18 20

```

Manipulating vectors is almost as easy as creating them. First, suppose you would like to add 2 to each of the elements in vector a. The equation for that looks like:

```

6 b = a + 2
7 b =
8     3 4 5 6 7 8 11 10 9

```

Now suppose, you would like to add two vectors together. If the two vectors are the same length, it is easy. Simply add the two as shown below:

```

9 c = a + b
10 c =
11     4 6 8 10 12 14 20 18 16

```

Subtraction of vectors of the same length works exactly the same way.

A.4.2 Functions

To make life easier, MATLAB includes many standard functions. Each function is a block of code that accomplishes a specific task. MATLAB contains all of the standard functions such as sin, cos, log, exp, sqrt, as well as many others. Commonly used constants such as π , and i or j for the square root of -1, are also incorporated into MATLAB.

```

12 sin(pi/4)
13 ans =
14     0.7071

```

To determine the usage of any function, type `help [function name]` at the MATLAB command window.

A.4.3 Plotting

It is also easy to create plots in Matlab. Suppose you wanted to plot a sine wave as a function of time. First make a time vector (the semicolon after each statement tells Matlab we don't want to see all the values) and then compute the sin value at each time.

```

15 t=0:0.25:7;
16 y = sin(t);
17 plot(t,y)

```

The plot contains approximately one period of a sine wave. Basic plotting is very easy in Matlab, and the plot command has extensive add-on capabilities.

A.4.4 Matrices and Arrays

Entering arrays into Matlab is the same as entering a vector, except each row of elements is separated by a semicolon (;) or a return:

```

18 B = [1 2 3 4;5 6 7 8;9 10 11 12]
19 B =
20     1   2   3   4
21     5   6   7   8
22     9   10  11  12

```

```

23 B = [ 1 2 3 4
24 5 6 7 8
25 9 10 11 12 ]
26 B =
27     1   2   3   4
28     5   6   7   8
29     9   10  11  12

```

Arrays in Matlab can be manipulated in many ways. For one, you can find the transpose of an array using the apostrophe key:

```

30 C = B'
31 C=
32     1   5   9
33     2   6   10
34     3   7   11
35     4   8   12

```

It should be noted that if C had been complex, the apostrophe would have actually given the complex conjugate transpose. To get the transpose, use .' (the two commands are the same if the matrix is not complex). Now you can multiply the two matrices B and C together. Remember that order matters when multiplying matrices.

```

36 D = B * C
37 D=
38    30   70   110
39    70   174  278
40   110   278  446
41 D = C * B
42 D=
43   107  122  137  152
44   122  140  158  176
45   137  158  179  200
46   152  176  200  224

```

However, in all our pracs we will actually just work with data arrays, not matrices in a mathematical sense. Usually we have to sets of numbers, and all we want is to carry out an “element-wise” operation. **We can multiply the corresponding elements of two arrays by using the .*** operator (the data arrays must be the same size to do this).

```

47 E = [1 2;3 4]
48 F = [2 3;4 5]
49 G = E .* F
50 E = 1 2 3 4
51 F = 2 3 4 5
52 G = 2 6 12 20

```

A.5 Colons and brackets

The colon operator is very useful and important for array definitions, and number increment size. For instance, type the expression: 20 : 30 and you’ll get a row vector with the integers:

```

53 ans =
54      20 21 22 23 24 25 26 27 28 29 30

```

You can easily change the default increment, in this case “1”, to anything else, if you simply add the incrementation size between the end values. For example, type: `20:2:30` and you’ll get a row vector with the integers:

```
55 ans =
56     20 22 24 26 28 30
```

Using the left and right brackets “[” and “]”, you can define matrices, where the rows are separated by a semicolon “;”. For example, to define a 3 by 3 matrix with the numbers 1 through 9, type: `[1 2 3; 4 5 6; 7 8 9]`. You’ll get a matrix back as:

```
57 ans =
58     1 2 3
59     4 5 6
60     7 8 9
```

To give this matrix a name in MATLAB’s memory, such as `Ed`, then type:
`Ed = [1 2 3; 4 5 6; 7 8 9]`. You’ll get a matrix back as:

```
61 Ed =
62     1 2 3
63     4 5 6
64     7 8 9
```

If you don’t give such things a name, the default name “`ans`”, which stands for *answer* is the variable name. Let’s use the colon and brackets to define a 5×5 matrix:
`junk = [1:5; 10:10:50; 5:9; 1000: -100:600; 3 5 2 9 44]`. You’ll get a matrix back as:

```
65 junk =
66     1    2    3    4    5
67     10   20   30   40   50
68     5    6    7    8    9
69    1000  900  800  700  600
70     3    5    2    9    44
```

A.6 Command line tricks

Arrow keys on the keyboard repeat previous commands. By typing a letter, and then using the arrow keys, the last used command starting with that letter is shown. Also **CTRL-A** jumps to the beginning of a line, and **CTRL-E** to the end. To erase a line, simply press escape twice (**ESC** **ESC**). You can also navigate through your directories and file system as you would do in a linux terminal window by using the commands **pwd**, **cd** and **ls**.

A.7 M-FILES

When you want to write a program or set of instructions for MATLAB to carry out, you can save them as an m file. Go to the File menu and select **New -> M-file**. This brings up a new window into which you can write your MATLAB commands, but unlike the in command window, you can save the scripts. This is very important if you want to run a script numerous times. Once you have saved the script, you simply need to type the script's name (without the .m file extension) into the command window and the script will run. Using M-files saves a lot of time, and is very useful for debugging as well. ALL exercises will be submitted as an M-file.

A.8 Conditionals and Loops

Conditionals and loops are a very necessary part of any programming. These allow you to make decisions in your code as to what will happen to a variable, how many times it will happen and how it will happen depending on the variable.

A.8.1 The If Statement

Matlab has a standard if-elseif-else conditional; for example:

```

71  >> t = rand(1);
72  >> if t > 0.75
73      s = 0;
74  elseif t < 0.25
75      s = 1;
76  else
77      s = 1-2*(t-0.25);
78  end
79  >> s
80
81      0

```

```

82 >> t
83 t =
84 0.7622

```

Thus the general form of the if statement is

```

85 if expr1
86     statements
87 elseif expr2
88     statements
89 ...
90 else
91     statements
92 end

```

The first block of statements following a nonzero expression executes.

A.8.2 MATLAB operators

The logical operators in Matlab are $<$, $>$, \leq , \geq , == (logical equals), and ~= (not equal). These are binary operators which return the values 0 and 1 (for scalar arguments):

```

93 >> 5 > 3
94 ans =
95 1
96 >> 5 < 3
97 ans =
98 0
99 >> 5 == 3
100 ans =
101 0

```

A.8.3 For and While Loops

Matlab provides two types of loops, a for-loop (comparable to a Fortran do-loop or a C for-loop) and a while-loop. A for-loop repeats the statements in the loop as the loop index takes on the values in a given row vector:

```

102 >> for i=[1,2,3,4]
103     disp(i^2)
104 end
105     1
106     4
107     9
108     16

```

Note the use of the built-in function `disp`, which simply displays its argument! The loop, like an if-block, must be terminated by `end`. This loop would more commonly be written as

```

109 >> for i=1:4
110     disp(i^2)
111 end
112     1
113     4
114     9
115     16

```

Recall that `1:4` is the same as `[1,2,3,4]`.

The while-loop repeats as long as the given expression is true (nonzero):

```

116 >> x=1;
117 >> while 1+x > 1
118     x = x/2;
119 end
120 >> x
121 x =
122     1.1102e-16

```

A.9 Plotting/Graphs

Let's go through some online resources to learn some graphics and plotting basics. Where indicated, cut and paste the text from the resource page into your window that is running MATLAB, to try the example. The following web site has an in depth tutorial on plotting data using MATLAB. Spend some time working through it and doing the examples. http://www.mathworks.com/access/helpdesk/help/techdoc/learn_matlab/learn_matlab.shtml

One at a time, let's go through some other online resources – various tutorial pages people have set up, to learn some graphics and plotting basics. Where indicated, cut

and paste the text from the resource page into your window that is running MATLAB, to try the example.

- Online Reference MATLAB manual, and a very nice Frequently Asked Questions page (Univ. Texas, Austin): <http://www-math.cc.utexas.edu/math/Matlab/Manual/ReferenceTOC.html>
- Let's look at an example from the above site. Here's a "plotting lines in 3D" page - *Do the example*: <http://www-math.cc.utexas.edu/math/Matlab/Manual/plot3.html>
- Here's another example – animating your graph: <http://www-math.cc.utexas.edu/math/Matlab/Manual/comet3.html> *Do the example*
- Meshes for surfaces: <http://www-math.cc.utexas.edu/math/Matlab/Manual/mesh.html> *Do the example*
- Surfaces where meshes are filled: <http://www-math.cc.utexas.edu/math/Matlab/Manual/surf.html> *Do the example*
- Colormaps: <http://www-math.cc.utexas.edu/math/Matlab/Manual/colormap.html>
- Some prefab shapes – cylinder: <http://www-math.cc.utexas.edu/math/Matlab/Manual/cylinder.html> *Do the example*
- Prefab shapes – sphere: <http://www-math.cc.utexas.edu/math/Matlab/Manual/sphere.html> *Do the example* – and launch the MATLAB window, go to the 3D shapes page in Visualizations, and experiment with changing *Operators and special characters*: <http://www-math.cc.utexas.edu/math/Matlab/Manual/Operators.html>
- A UTAH PAGE: (nice tutorial) note, an important point about array math: http://www.mines.utah.edu/gg_computer_seminar/matlab/tut3.html
- General intro plotting info from the above UTAH site: http://www.mines.utah.edu/gg_computer_seminar/matlab/tut18.html *Do the examples*
- More good graphics basics: <http://www-math.bgsu.edu/~gwade/matlabprimer/graphics.html> *Do the examples*

A.9.1 Important steps for making 2D Graphs

One of the books that comes with MATLAB is primarily focused on graphics. It has some nice tables on building 2 and 3D graphs. I reproduce them below to emphasise what is the proper train of thought in organizing your information so that you can produce a graphic most efficiently. Figure A.1 shows the most important functions when

dealing with 2D graphs. The table below shows seven essential steps. The examples in the right column are simply just that – examples (more info on any of these is available with MATLAB's help function).

| Step | Typical Code |
|---|--|
| 1 Prepare your data | <pre>x = 0:.2:12; y1 = bessel(1,x); y2 = bessel(2,x); y3 = bessel(3,x);</pre> |
| 2 Select window and position plot region within window | <pre>figure(1) subplot(2,2,1)</pre> |
| 3 Call elementary plotting function | <pre>h = plot(x,y1,x,y2,x,y3);</pre> |
| 4 Select line and marker characteristics | <pre>set(h,'LineWidth',2,{'LineStyle'},{'--';':';'-'}) set(h,{'Color'},{'r';'g';'b'})</pre> |
| 5 Set axis limits, tick marks, and grid lines | <pre>axis([0 12 -0.5 1]) grid on</pre> |
| 6 Annotate the graph with axis labels, legend, and text | <pre>xlabel('Time') ylabel('Amplitude') legend(h,'First','Second','Third') title('Bessel Functions') [y,ix] = min(y1); text(x(ix),y,'First Min \rightarrow',... 'HorizontalAlignment','right')</pre> |
| 7 Print graph | <pre>print -dps2</pre> |

Figure A.1: Matlab workflow for generating 2D graphs.

A.9.2 Important steps for making 3D Graphs

The typical steps in making a 3D graph are similar to the 2D case, except now we call a 3D graphing function, which typically has far more options, such as lighting and viewpoint, etc. These are really just attributes to the projection and how we “beef” it up. They are important functions to know about if you are going to continue on in MATLAB. Figure A.2 shows the most important functions when dealing with 3D graphs.

A.9.3 Functions that create and plot continuous surfaces

MATLAB defines a surface by the z-coordinates of points above a rectangular grid in the x-y plane. The plot is formed by joining adjacent points with straight lines. Surface

| Step | Typical Code |
|---|--|
| 1 Prepare your data | <code>Z = peaks(20);</code> |
| 2 Select window and position plot region within window | <code>figure(1) subplot(2,1,2)</code> |
| 3 Call 3-D graphing function | <code>h = surf(Z);</code> |
| 4a Set colormap and shading algorithm | <code>colormap hot shading interp set(h,'EdgeColor','k')</code> |
| 4b Add lighting | <code>light('Position',[-2,2,20]) lighting phong material([0.4,0.6,0.5,30]) set(h,'FaceColor',[0.7 0.7 0],... 'BackFaceLighting','lit')</code> |
| 5 Set viewpoint | <code>view([30,25]) set(gca,'CameraViewAngleMode','Manual')</code> |
| 6 Set axis limits and tick marks | <code>axis([5 15 5 15 -8 8]) set(gca,'ZTickLabel','Negative Positive')</code> |
| 7 Set aspect ratio | <code>set(gca,'PlotBoxAspectRatio',[2.5 2.5 1])</code> |
| 8 Annotate the graph with axis labels, legend, and text | <code>xlabel('X Axis') ylabel('Y Axis') zlabel('Function Value') title('Peaks')</code> |
| 9 Print graph | <code>set(gcf,'PaperPositionMode','auto') print -dps2</code> |

Figure A.2: Matlab workflow for generating 3D graphs.

plots are useful for visualizing matrices that are too large to display in numerical form, and for graphing functions of two variables.

For us in the Earth sciences, the importance of plotting surfaces is obvious: so much of our data is spatially oriented, such as topography, gravity, heat, magnetism, etc. Figure A.3 lists functions that make surfaces from your input matrices. And all of our spatial data sets can be made into matrices (since we have $x=longitude$, $y=latitude$, and $z=measurement$).

A.9.4 Figure windows

MATLAB directs its graphics output to a window called the *figure window*. If no figure window is currently open, MATLAB will create one. If a figure window exists, MATLAB uses that one. If multiple figure windows are open, MATLAB uses the most

| Function | Used to Create |
|---------------------------|--|
| <code>mesh, surf</code> | Surface plot |
| <code>meshc, surfc</code> | Surface plot with contour plot beneath it |
| <code>meshz</code> | Surface plot with curtain plot (reference plane) |
| <code>pcolor</code> | Flat surface plot (value is proportional only to color) |
| <code>surfl</code> | Surface plot illuminated from specified direction |
| <code>surface</code> | Low-level function (on which high-level functions are based) for creating Surface graphics objects |

Figure A.3: Some important graph features

recently used/created figure window. The `figure` function creates figure windows. For example, `figure` creates a new window and makes it the current destination for graphics output. You can make any figure window the current/active one by clicking it with the mouse, or look at the title bar of your figure windows – they are numbered. To make the *n*th window active, just type: `figure(n)`

A.9.5 Subplots

You can display multiple plots in the same figure window. The function `subplot(m,n,i)` breaks the figure window into an m-by-n matrix of small subplots (m rows and n columns), and selects the *i*th subplot for the current plot. For example, if m=3 and n=4, then we are dividing the figure window into 12 subplots: 3 rows and 4 columns. Let's do one with 2 rows and 2 columns. Then we have “`subplot(2,2,i)`”. We would designate *i*=1 for the 1st plot – they are ordered from left to right in row one, then row two, and so on. Here's our example... let's plot a bunch of relationships between the sine and cosine function, all on the same page:

```

123 t=0:pi/20:2*pi
124 [x,y]=meshgrid(t);
125 subplot(2,2,1)
126 plot(sin(t),cos(t))
127 axis equal
128 subplot(2,2,2)
129 z = sin(x) + cos(y)
130 plot(t,z)
131 axis([0 2*pi -2 2])

```

```
132 subplot(2,2,3)
133 z = sin(x).*cos(y);
134 plot(t,z)
135 axis([0 2*pi -1 1])
136 subplot(2,2,4)
137 z = (sin(x).^{}2)-(cos(y).^{}2);
138 plot(t,z)
139 axis([0 2*pi -1 1])
```

A.10 Formats, Saving and Loading files

A.10.1 Formats

MATLAB has different formating options for how we view the variables in the workspace. Common formats are listed below (do a help on these to learn more): format short format short eformat long format long eformat bankThese produce the following for a vector $x = [4/3 \ 1.2345e-6]$:

```
140 x = [4/3 1.2345e-6]
141 x =
142     1.3333 0.0000
143 format short
144 x
145 x =
146     1.3333 0.0000
147 format short e
148 x
149 x =
150 1.3333e+00 1.2345e-06
151 format long
152 x
153 x =
154     1.33333333333333 0.00000123450000
155 format long e
156 x
157 x =
158     1.33333333333333e+00 1.23450000000000e-06
159 format bank
160 x
161 x =
```

162

```
1.33 0.00
```

Suppressing output: By default, MATLAB always displays the results of a command you type onto the screen. This is not always optimal, especially if you define a rather large array of numbers. However, to suppress the output from being displayed on the screen, simply, put a semi-colon at the end of the line “;”.

A.10.2 Saving and loading the workspace

A nice feature of MATLAB is that you can save everything in your workspace (which contains all the variables). Simply typing:

```
save
```

will create a file called **matlab.mat** in your present working directory. To access this file during another MATLAB session, just type:

```
load
```

which load’s the matlab.mat file. You can give the file it’s own name with:

```
save <filename>
```

then to load it into memory at a later time (as you might imagine), type: `load <filename>`

If you are only interested in saving a particular variable, no problem: let’s say we want to just save our `A`, and want to put it into a file called `A_nov21.mat`. Then type:

```
save A_nov21
```

The syntax in general for this is: `save {filename var1 var2 var3 ...}`

A.10.3 Loading Plain Text Data Files

Arrays of numbers can be stored in files on disk. For instance, open an **Editor** (gvim) and create a file that has an array of numbers:

163

```
1 3
```

164

```
2 2
```

165

```
3 4
```

166

```
4 1
```

167

```
5 8
```

168

```
6 2
```

Then save your file. Ideally, save it as `filename.dat`, then you will know it is a data file that you use with MATLAB (however, the “.dat” extension is not necessary). If I called my file “`crap.dat`”, then to load it into MATLAB, I type `load crap.dat`. Now, the variable “`crap`” (without the “.dat”) is assigned to the data that was in that file. To be sure it is properly loaded, in MATLAB, simply type the variable name and hit return.

A.11 Debugging

Programs can run very quickly, and examining variables as they fly by during real-time execution can be difficult. A more sophisticated way of examining variables during execution is to set “breakpoints” in a program. The computer will pause at these breakpoints during execution of the code to allow you to inspect the values of variables.

It is important when debugging that you have an understanding of what you want the code to do and have some preconceived notion of how the variables will change and how the code will work. Obviously there is no point just copying down a whole bunch of code, say from a 3rd year geophysics tutorial handout, and having absolutely no idea of what the code is doing.

Debugging is the process by which you isolate and fix problems with your code. Debugging helps to correct two kinds of errors:

- 1.) **Syntax errors:** such as misspelling a function name or omitting a parenthesis. MATLAB detects most syntax errors and displays a message describing the error and showing its line number in the M-file.
- 2.) **Runtime errors:** These errors are usually algorithmic in nature; for example, you might modify the wrong variable or perform a calculation incorrectly. Runtime errors are apparent when an M-file produces unexpected results.

MATLAB’s editor allows you to set breakpoints by clicking the right mouse button to the left of the line of interest. They are indicated by a red dot at the left side of the window. The next time you run the m-file, the program will stop at the breakpoint and allow you to step through the code one line at a time.

For a debugging tutorial, go to the following website: http://www.glue.umd.edu/~nsw/matlab.doc/techdoc/using_m1/ch3_debu.html

Appendix B

SI Units and other useful tables

B.1 Basic Units for the SI System as Used in Geophysics

| Quantity | Unit | Abbrev. | Other |
|--------------|--------------|---------|-------|
| Mass | kilogram | kg | |
| Length | metre | m | |
| Time | second | s | |
| Acceleration | metre/second | m/s^2 | |

B.1.1 SI units

In this course almost all calculations and data will adhere to the SI standard units. Table B.1 will give you an overview

B.2 Greek alphabet

Letters of the greek alphabet are traditionally used as names in mathematics, physics and sciences and, along with latin characters, usually denote certain parameters. For

| Prefix | Symbol | Factor | Numerically | Name |
|--------|--------|-----------|---------------|------------|
| giga | G | 10^9 | 1 000 000 000 | Billion |
| mega | M | 10^6 | 1 000 000 | Million |
| kilo | k | 10^3 | 1 000 | thousand |
| centi | c | 10^{-2} | 0.01 | hundredth |
| milli | m | 10^{-3} | 0.001 | thousandth |
| micro | μ | 10^{-6} | 0.000 001 | millionth |
| nano | n | 10^{-9} | 0.000 000 001 | billionth |

Table B.1: Common prefixes for use with SI units

| | | | | | |
|------------|-----------|---------|----------|------------|---------|
| α | A | alpha | ν | N | nu |
| β | B | beta | ξ | Ξ | xi |
| γ | Γ | gamma | o | O | omicron |
| δ | Δ | delta | π | P | pi |
| ϵ | E | epsilon | ρ | R | rho |
| ζ | Z | zeta | σ | Σ | sigma |
| η | H | eta | τ | T | tau |
| θ | Θ | theta | v | Υ | upsilon |
| ι | I | iota | ϕ | Φ | phi |
| κ | K | kappa | χ | X | chi |
| λ | Λ | lambda | ψ | Ψ | psi |
| μ | M | mu | ω | Ω | omega |

Table B.2: The Greek Alphabet

more info see (Wikipedia) (http://en.wikipedia.org/wiki/Greek_Alphabet). See Table B.2 for a list of characters of the Greek alphabet.

Bibliography

- F. Albarede and R. van der Hilst. New mantle convection model may reconcile conflicting evidence. *EOS Transactions American Geophysical Union*, 80(45):535–539, 1999.
- R. Albert, R. Phillips, A. Dombard, and C. Brown. A test of the validity of yield strength envelopes with an elastoviscoplastic finite element model. *Geophysical Journal International*, 140(2):399–409, 2000.
- D. Anderson. Hotspots, polar wander, mesozoic convection and the geoid. *Nature*, 297 (5865):391–393, 1982.
- D. Anderson. Lithosphere, asthenosphere, and perisphere. *Rev. Geophys*, 33(1):125–149, 1995.
- D. Anderson. Top-down tectonics? *Science*, 293(5537):2016, 2001.
- D. Anderson and J. Bass. Mineralogy and composition of the upper mantle. *Geophysical Research Letters*, 11(7):637–640, 1984.
- D. Anderson and J. Bass. Transition region of the earth’s upper mantle. *Nature*, 320 (6060):321–328, 1986.
- N. Arndt, C. Ginibre, C. Chauvel, F. Albarede, M. Cheadle, C. Herzberg, G. Jenner, and Y. Lahaye. Were komatiites wet? *Geology*, 26(8):739, 1998.
- M. Artemyev and Y. Atushkov. Structure and isotasy of the baikal rift and the mechanism of rifting. *Journal Geophysical Research*, 76:1197–1211, 1971.
- Y. Asahara, E. Ohtani, and A. Suzuki. Melting relations of hydrous and dry mantle compositions and the genesis of komatiites. *Geophysical research letters*, 25:2201–2204, 1998.
- L. Ashwal, P. Morgan, S. Kelley, and J. Percival. Heat production in an archean crustal profile and implications for heat flow and mobilization of heat-producing elements. *Earth and planetary science letters*, 85(4):439–450, 1987.

- M. Audley-Charles, P. Ballantyne, and R. Hall. Mesozoic-cenozoic rift-drift sequence of asian fragments from gondwanaland. *Tectonophysics*, 155(1-4):317–330, 1988.
- P. Avseth, T. Mukerji, and G. Mavko. *Quantitative Seismic interpretation: Applying Rock Physics Tools to Reduce Interpretation Risk*. Cambridge University Press, 2010. URL <http://www.cambridge.org/9780521151351>.
- S. Ballard and H. Pollack. Modern and ancient geotherms beneath southern africa. *Earth and Planetary Science Letters*, 88(1-2):132–142, 1988.
- W. Baragar and A. Goodwin. Andesites and archean volcanism of the canadian shield. In *Proceedings of the Andésite Conference: Oregon Dept. Geology and Mineral Industries Bull*, volume 65, pages 121–142, 1969.
- J. Barrell. The strength of the earth’s crust. *The Journal of Geology*, 22(7):655–683, 1914.
- H. Benioff. Seismic evidence for the fault origin of oceanic deeps. *Bulletin of the Geological Society of America*, 60(12):1837, 1949.
- D. Bercovici, G. Schubert, and G. Glatzmaier. Three-dimensional spherical models of convection in the earth’s mantle. *Science*, 244(4907):950, 1989a.
- D. Bercovici, G. Schubert, and G. Glatzmaier. Influence of heating mode on three-dimensional mantle convection. *Geophysical Research Letters*, 16(7):617–620, 1989b.
- M. Bickle, E. Nisbet, and A. Martin. Archean greenstone belts are not oceanic crust. *The Journal of Geology*, 102(2):121–137, 1994.
- F. Birch, R. Roy, and E. Decker. Heat flow and thermal history in new york and new england, 1968.
- B. Blankenbach, F. Busse, U. Christensen, L. Cserepes, D. Gunkel, U. Hansen, H. Harder, G. Jarvis, M. Koch, G. Marquart, et al. A benchmark comparison for mantle convection codes. *Geophysical Journal International*, 98(1):23–38, 1989.
- J. Boak and R. Dymek. Metamorphism of the ca. 3800 ma supracrustal rocks at isua, west greenland: implications for early archaean crustal evolution. *Earth and Planetary Science Letters*, 59(1):155–176, 1982.
- J. Bodine, M. Steckler, and A. Watts. Observations of flexure and the rheology of the oceanic lithosphere. *Journal of geophysical research*, 86(B5):3695–3707, 1981.
- B. Bodri and A. Jessop. Geothermal model of the continental margins of eastern canada. *Tectonophysics*, 164(2-4):139–150, 1989.
- M. Bott. Solution of the linear inverse problem in magnetic interpretation with application to oceanic magnetic anomalies. *Geophysical Journal of the Royal Astronomical Society*, 13(1-3):313–323, 1967.

- M. Bott. The mechanism of continental splitting. *Tectonophysics*, 81(3-4):301–309, 1982.
- F. Boyd, J. Gurney, and S. Richardson. Evidence for a 150–200-km thick archaean lithosphere from diamond inclusion thermobarometry. *Nature*, 315(6018):387–389, 1985.
- R. Bracewell. *The Fourier Transform and Its Applications*. McGraw-Hill, New York, 3rd edition, 1999.
- E. Bullard. The time necessary for a bore hole to attain temperature equilibrium. *Geophysical Journal International*, 5:127–130, 1947.
- E. Bullard. Heat flow through the deep sea floor. *Advances in geophysics*, 3:153, 1956.
- K. Burke and W. Kidd. Were archean continental geothermal gradients much steeper than those of today? *Nature*, 272:240–241, 1978.
- K. Burke, J. Dewey, and W. Kidd. Dominance of horizontal movements, arc and microcontinental collisions during the later permobile regime. *The Early History of the Earth*, pages 113–130, 1976.
- J. Byerlee and W. Brace. Stick slip, stable sliding, and earthquakes—effect of rock type, pressure, strain rate, and stiffness. *Journal of Geophysical Research*, 73(18):6031–6037, 1968.
- A. Calvert, E. Sawyer, W. Davis, and J. Ludden. Archean subduction inferred from seismic images of a mantle suture in the superior province. *Nature*, 375(6533):670–674, 1995.
- T. Campbell McCuaig, R. Kerrich, et al. Phosphorus and high field strength element anomalies in archean high-magnesian magmas as possible indicators of source mineralogy and depth. *Earth and planetary science letters*, 124(1-4):221–239, 1994.
- S. Cande and D. Kent. A new geomagnetic polarity time scale. *Journal of geophysical research*, 97(B10):13–917, 1992.
- S. Cande and D. Kent. Revised calibration of the geomagnetic polarity timescale for the late cretaceous and cenozoic: *Journal of geophysical research. B, Solid Earth and Planets*, 100(4):6093–6095, 1995.
- S. C. Cande, C. A. Raymond, J. Stock, and W. F. Haxby. Geophysics of the Pitman Fracture Zone and Pacific-Antarctic Plate Motions During the Cenozoic. *Science*, 270: 5238, 1995.
- R. Carlson. Models for convergence, subduction and back-arc development: Plate motions, boundary forces, and horizontal temperature gradients: Implications for the driving mechanism. *Tectonophysics*, 99(2-4):149–164, 1983.

- R. Carlson, F. Boyd, S. Shirey, P. Janney, T. Grove, S. Bowring, M. Schmitz, J. Dann, D. Bell, J. Gurney, et al. Continental growth, preservation, and modification in southern africa. *GSA Today*, 10(2):1–7, 2000.
- A. Cazenave, A. Souriau, and K. Dominh. Global coupling of earth surface topography with hotspots, geoid and mantle heterogeneities. *Nature*, 340(6228):54–57, 1989.
- D. Chapman and H. Pollack. Regional geotherms and lithospheric thickness. *Geology*, 5(5):265, 1977.
- U. Christensen. Convection with pressure-and temperature-dependent non-newtonian rheology. *Geophysical Journal Of the Royal Astronomical Society*, 77(2):343–384, 1984.
- S. Cloetingh and R. Wortel. Stress in the indo-australian plate. *Tectonophysics*, 132(1-3):49–67, 1986.
- S. Cloetingh, R. Wortel, and N. Vlaar. On the initiation of subduction zones. *Pure and Applied Geophysics*, 129(1):7–25, 1989.
- D. Coblenz, M. Sandiford, R. Richardson, S. Zhou, and R. Hillis. The origins of the intraplate stress field in continental australia. *Earth and Planetary Science Letters*, 133 (3-4):299–309, 1995.
- J. Cochran and M. Talwani. Gravity anomalies, regional elevation, and the deep structure of the north atlantic. *Journal of Geophysical Research*, 83(B10):4907–4924, 1978.
- M. Coffin and O. Eldholm. Volcanism and continental break-up: a global compilation of large igneous provinces. *Geological Society, London, Special Publications*, 68(1):17, 1992.
- M. F. Coffin and O. Eldholm. Large igneous provinces: crustal strucure, dimensions, and external consequences. *Rev. Geophys.*, 32(1):1–36, February 1994.
- W. Collins. Slab pull, mantle convection, and pangaean assembly and dispersal. *Earth and Planetary Science Letters*, 205(3-4):225–237, 2003.
- C. Conrad and B. Hager. Effects of plate bending and fault strength at subduction zones on plate dynamics. *Journal of geophysical research*, 104:17, 1999.
- C. Conrad and B. Hager. The thermal evolution of an earth with strong. *Geophysical research letters*, 26(19):3041–3044, 1999.
- C. Conrad and C. Lithgow-Bertelloni. How mantle slabs drive plate tectonics. *Science*, 298(5591):207, 2002.
- C. Conrad and C. Lithgow-Bertelloni. The temporal evolution of plate driving forces: Importance of “slab suction”versus “slab pull”during the cenozoic. *Journal of Geophysical Research*, 109(B10):B10407, 2004.

- V. Courtillot and J. Besse. Magnetic field reversals, polar wander, and core-mantle coupling. *Science*, 237(4819):1140, 1987.
- A. Cox and R. Hart. *Plate tectonics: How it works*. Wiley-Blackwell, 1986.
- S. Crough. Thermal origin of mid-plate hot-spot swells. *Geophysical Journal of the Royal Astronomical Society*, 55(2):451–469, 1978.
- S. T. Crough. Rifts and swells: Geophysical constraints on causality. *Tectonophysics*, 94(1-4):23–37, 1983.
- S. T. Crough and D. M. Jurdy. Subducted Lithosphere, Hotspots, and the Geoid. *Earth Planet. Sci. Lett.*, 48:15–22, 1980.
- I. Dalziel, S. Mosher, and L. Gahagan. Laurentia-kalahari collision and the assembly of rodinia. *The Journal of Geology*, pages 499–513, 2000.
- G. Davies. Thickness and thermal history of continental crust and root zones. *Earth and Planetary Science Letters*, 44(2):231–238, 1979.
- G. Davies. Role of the lithosphere in mantle convection. *Journal of Geophysical Research*, 93(B9):10451–10, 1988.
- G. Davies. Conjectures on the thermal and tectonic evolution of the earth. *Lithos*, 30(3-4):281–289, 1993.
- J. De Smet, A. Van den Berg, and N. Vlaar. Early formation and long-term stability of continents resulting from decompression melting in a convecting mantle. *Tectonophysics*, 322(1-2):19–33, 2000.
- M. de Wit. On archean granites, greenstones, cratons and tectonics: does the evidence demand a verdict? *Precambrian Research*, 91(1-2):181–226, 1998.
- C. DeMets, R. G. Gordon, F. Argus, and S. Stein. Current plate motions. *Geophys. J. Int.*, 101:425–478, 1992.
- C. DeMets, R. Gordon, D. Argus, and S. Stein. Effect of recent revisions to the geomagnetic reversal time scale on estimates of current plate motions. *Geophysical Research Letters*, 21:2191–2194, 1994.
- R. Desbrandes. *Encyclopedia of well logging*. Editions Technip, 1985.
- R. Dietz. Continent and ocean basin evolution by spreading of the sea floor. *Nature*, 190(4779):854–857, 1961.
- M. Doin, L. Fleitout, and D. McKenzie. Geoid anomalies and the structure of continental and oceanic lithospheres. *Journal of geophysical research*, 101(B7):16119–16, 1996.

- M. Doin, L. Fleitout, and U. Christensen. Mantle convection and stability of depleted and undepleted continental lithosphere. *Journal of geophysical research*, 102(B2):2771–2787, 1997.
- S. Dyksterhuis and R. Müller. Modelling the contemporary and palaeo stress field of australia using finite-element modelling with automatic optimisation. *Exploration Geophysics*, 35(4):236–241, 2004.
- S. Dyksterhuis, R. Albert, and R. Müller. Finite-element modelling of contemporary and palaeo-intraplate stress using abaqus (tm). *Computers & geosciences*, 31(3):297–307, 2005a.
- S. Dyksterhuis, R. Müller, and R. Albert. Paleostress field evolution of the australian continent since the eocene. *Journal of geophysical research*, 110(B5):B05102, 2005b.
- C. Ebinger and N. Sleep. Cenozoic magmatism throughout east africa resulting from impact of a single plume. *Nature*, 395(6704):788–791, 1998.
- W. Elsasser. Sea-floor spreading as thermal convection. *Journal of Geophysical Research*, 76(5):1101–1112, 1971.
- P. England. Continental geotherms during the archaean. *Nature*, 277:556–558, 1979.
- P. England and M. Bickle. Continental thermal and tectonic regimes during the ar-chaean. *The Journal of Geology*, 92(4):353–367, 1984.
- D. A. Falvey. The development of continental margins in plate tectonic theory. *Astr. Petro. Explor. Assoc. Jour.*, 14:95–106, 1974.
- K. Feigl, D. Agnew, Y. Bock, D. Dong, A. Donnellan, B. Hager, T. Herring, D. Jackson, T. Jordan, R. King, et al. Space geodetic measurement of crustal deformation in cen-tral and southern california, 1984–1992. *J. geophys. Res*, 98(B12):1677–712, 1993.
- A. Finnerty and F. Boyd. Thermobarometry for garnet peridotites: basis for the determi-nation of thermal and compositional structure of the upper mantle. *Mantle xenoliths*, pages 381–402, 1987.
- R. Folinsbee, H. Baadsgaard, G. Cumming, and D. Green. A very ancient island arc. *The crust and upper mantle of the Pacific area. Am. Geophys. Union Geophys. Monogr*, 12: 441–448, 1968.
- D. Forsyth and S. Uyeda. On the relative importance of the driving forces of plate motions. *Geophysical Journal of the Royal Astronomical Society*, 43(1):163–200, 1975.
- A. Fowler. Fast thermoviscous convection. *Studies in applied mathematics*, 72(3):189–219, 1985.
- D. Frank-Kamene "etiskiae. Diffusion and heat transfer in chemical kinetics. 1969.

- L. Franz, G. Brey, and M. Okrusch. Reequilibration of ultramafic xenoliths from namibia by metasomatic processes at the mantle boundary. *The Journal of Geology*, 104(5):599–615, 1996.
- Y. Fukao, S. Widjiantoro, and M. Obayashi. Stagnant slabs in the upper and lower mantle transition region. *Reviews of Geophysics*, 39(3):291–323, 2001.
- P. Gegout and A. Cazenave. Temporal variations of the earth gravity field for 1985–1989 derived from lageos. *Geophysical Journal International*, 114(2):347–359, 1993.
- R. Gordon and S. Stein. Global tectonics and space geodesy. *Science*, 256(5055):333, 1992.
- J. Grambling. Pressures and temperatures in precambrian metamorphic rocks. *Earth and Planetary Science Letters*, 53(1):63–68, 1981.
- W. Griffin, F. Kaminsky, C. Ryan, S. O'Reilly, T. Win, and I. Ilupin. Thermal state and composition of the lithospheric mantle beneath the daldyn kimberlite field, yakutia. *Tectonophysics*, 262(1-4):19–33, 1996.
- W. Griffin, A. Zhang, S. O'reilly, and C. Ryan. Phanerozoic evolution of the lithosphere beneath the sino-korean craton. *Mantle dynamics and plate interactions in East Asia*, 27: 107–126, 1998.
- W. Griffin, B. Doyle, C. Ryan, N. Pearson, Y. Suzanne, R. Davies, K. Kivi, E. Van Achterbergh, and L. Natapov. Layered mantle lithosphere in the lac de gras area, slave craton: composition, structure and origin. *Journal of Petrology*, 40(5):705, 1999.
- M. Gurnis and R. D. Müller. Origin of the Australian-Antarctic Discordance from an ancient slab and mantle wedge. In R. R. Hillis and R. D. Müller, editors, *Evolution and Dynamics of the Australian Plate*, Geol. Soc. Aust. Spec. Publ. 22 and Spec. Paper Geol. Soc. Am. 372, pages 417—429, 2003.
- B. Hager and R. O'Connell. A simple global model of plate dynamics and mantle convection. *Journal of Geophysical Research*, 86(B6):4843–4867, 1981.
- W. Hamilton. Archean magmatism and deformation were not products of plate tectonics. *Precambrian Research*, 91(1-2):143–179, 1998.
- R. Heestand and S. Crough. The effect of hot spots on the oceanic age-depth relation. *Journal of Geophysical Research*, 86(B7):6107–6114, 1981.
- J. Heirtzler, G. Dickson, E. Herron, W. Pitman III, and X. Le Pichon. Marine magnetic anomalies, geomagnetic field reversals, and motions of the ocean floor and continents. *Journal of Geophysical Research*, 73(6):2119–2136, 1968.
- H. Hess. History of ocean basins. *Petrologic studies*, pages 599–620, 1962.

- K. J. Hsü. Collapsing Continental Rises: An Actualistic Concept of Geosynclines and Mountain-Building: A Discussion. *The Journal of Geology*, 73(6):897–900, 1965.
- B. Isacks, J. Oliver, and L. Sykes. Seismology and the new global tectonics. *Journal of Geophysical Research*, 73(18):5855–5899, 1968.
- G. T. Jarvis and D. P. McKenzie. Sedimentary basin formation with finite extension rates. *Earth Planet. Sci. Lett.*, 48(1):42–52, June 1980.
- C. Jaupart, J. Sclater, and G. Simmons. Heat flow studies: constraints on the distribution of uranium, thorium and potassium in the continental crust. *Earth and Planetary Science Letters*, 52(2):328–344, 1981.
- A. Jessop and L. Trevor. Heat flow and heat generation in the superior province of the canadian shield. *Tectonophysics*, 50(1):55–77, 1978.
- E. J. W. Jones. *Marine geophysics*. Wiley, Chichester; New York, 1999. ISBN 0471986933.
- T. Jordan. The continental tectosphere. *Reviews of Geophysics*, 13(3):1–12, 1975.
- T. Jordan. Composition and development of the continental tectosphere. *Nature*, 274 (5671):544–548, 1978.
- T. Jordan. Continents as a chemical boundary layer. *Philosophical Transactions of the Royal Society of London. Series A, Mathematical and Physical Sciences*, 301(1461):359, 1981.
- S. Karato and H. Jung. Water, partial melting and the origin of the seismic low velocity and high attenuation zone in the upper mantle. *Earth and Planetary Science Letters*, 157(3-4):193–207, 1998.
- S. Karato and P. Wu. Rheology of the upper mantle: a synthesis. *Science*, 260(5109):771, 1993.
- H. Kawakatsu and F. Niu. Seismic evidence for a 920-km discontinuity in the mantle. *Nature*, 371(6495):301–305, 1994.
- D. Kemp and D. Stevenson. A tensile, flexural model for the initiation of subduction. *Geophysical Journal International*, 125(1):73–93, 1996.
- M. Kikuchi and H. Kanamori. The mechanism of the deep bolivia earthquake of june 9, 1994. *Geophysical Research Letters*, 21(22):2341–2344, 1994.
- C. Kincaid and P. Olson. An experimental study of subduction and slab migration. *Journal of Geophysical Research*, 92(B13):13832–13, 1987.
- E. Klein and C. Langmuir. Local versus global variations in ocean ridge basalt composition: A reply. *Journal of Geophysical Research*, 94(B4):4241–4252, 1989.

- A. Kr
"oner. Precambrian plate tectonics. *Developments in Precambrian Geology*, 4:57–90, 1981.
- T. Kusky and W. Kidd. Remnants of an archean oceanic plateau, belingwe greenstone belt, zimbabwe. *Geology*, 20(1):43, 1992.
- A. Lachenbruch. Crustal temperature and heat production: implications of the linear heat-flow relation. *Journal of Geophysical Research*, 75(17):3291–3300, 1970.
- Y. Lagabrielle, J. Goslin, H. Martin, J. Thirot, and J. Auzende. Multiple active spreading centres in the hot north fiji basin (southwest pacific): a possible model for archaean seafloor dynamics? *Earth and Planetary Science Letters*, 149(1-4):1–13, 1997.
- I. Lambert and K. Heier. The vertical distribution of uranium, thorium, and potassium in the continental crust. *Geochimica et Cosmochimica Acta*, 31(3):377–390, 1967.
- R. Lambert. Archean thermal regimes, crustal and upper mantle temperatures, and a progressive evolutionary model for the earth. In *The Early History of the Earth*, volume 1, pages 363–373, 1976.
- R. Lambert. Earth tectonics and thermal history: review and a hot-spot model for the archean. *Precambrian Plate Tectonics*, pages 57–90, 1981.
- A. Lenardic. On the heat flow variation from archean cratons to proterozoic mobile belts. *Journal of geophysical research*, 102(B1):709–721, 1997.
- A. Lenardic. On the partitioning of mantle heat loss below oceans and continents over time and its relationship to the archaean paradox. *Geophysical Journal International*, 134(3):706–720, 1998.
- A. Lenardic and W. Kaula. Mantle dynamics and the heat flow into the earth's continents. *Nature*, 378(6558):709–711, 1995.
- A. Lenardic, L. Guillou-Frottier, J. Mareschal, C. Jaupart, L. Moresi, and W. Kaula. What the mantle sees: the effects of continents on mantle heat flow. *Geophysical monograph*, 121:95–112, 2000a.
- A. Lenardic, L. Moresi, and H. M "uhlhaus. The role of mobile belts for the longevity of deep cratonic lithosphere: The crumple zone model. *Geophysical research letters*, 27(8):1235–1238, 2000b.
- M. Lisowski. Recent plate motions and crustal deformation. *Reviews of Geophysics Supplement*, 29:162–171, 1991.
- G. S. Lister, M. A. Etheridge, and P. A. Symonds. Detachment models for the formation of passive continental margins. *Tectonics*, 10:1038–1064, 1991.

- C. Lithgow-Bertelloni and M. Richards. The dynamics of cenozoic and mesozoic plate motions. *Reviews of Geophysics*, 36(1):27–78, 1998.
- Maddox. ? ?, 1998.
- G. Masters, G. Laske, H. Bolton, and A. Dziewonski. The Relative Behavior of Shear Velocity, Bulk Sound Speed, and Compressional Velocity in the Mantle: Implications for Chemical and Thermal Structure. In S.-I. Karato, A. M. Forte, R. C. Liebermann, G. Masters, and L. Stixrude, editors, *Earth's Deep Interior: Mineral Physics and Tomography From the Atomic to the Global Scale*, volume 117 of *Geophys. Monogr. Ser.*, pages 63–87. American Geophysical Union, Washington D.C., 2000.
- S. Maus, F. Yin, H. Lühr, C. Manoj, M. Rother, J. Rauberg, I. Michaelis, C. Stolle, and R. Müller. Resolution of direction of oceanic magnetic lineations by the sixth-generation lithospheric magnetic field model from champ satellite magnetic measurements. *Geochemistry, Geophysics, Geosystems*, 9:07021, 2008.
- D. McKenzie. Speculations on the consequences and causes of plate motions*. *Geophysical Journal of the Royal Astronomical Society*, 18(1):1–32, 1969a.
- D. McKenzie. Evolution of triple junctions. *Nature*, 224:125–133, 1969b.
- D. McKenzie. Temperature and potential temperature beneath island arcs. *Tectonophysics*, 10(1-3):357–366, 1970.
- D. McKenzie and M. J. Bickle. The Volume and Composition of Melt Generated by Extension of the Lithosphere. *J. Petrology*, 29(3):625–679, 1988.
- D. Mckenzie and R. Parker. The north pacific: an example of tectonics on a sphere. *Nature*, 216:1276–1280, 1967.
- D. McKenzie and N. Weiss. Speculations on the thermal and tectonic history of the earth. *Geophysical Journal of the Royal Astronomical Society*, 42(1):131–174, 1975.
- D. McKenzie, J. Roberts, and N. Weiss. Numerical models of convection in the earth's mantle. *Tectonophysics*, 19(2):89–103, 1973.
- D. P. McKenzie. Some Remarks on the Development of Sedimentary Basins. *Earth Planet. Sci. Lett.*, 40:25–32, 1978.
- M. McNutt and A. Judge. The superswell and mantle dynamics beneath the south pacific. *Science*, 248(4958):969, 1990.
- C. Mégnin and B. Romanowicz. The three-dimensional shear velocity structure of the mantle from the inversion of body, surface and higher-mode waveforms. *Geophysical Journal International*, 143(3):709–728, 2000.
- P. Meijer and M. Wortel. The dynamics of motion of the south american plate. *Journal of Geophysical Research*, 97(B8):11915–11, 1992.

- I. Metcalfe. *Gondwana dispersion and Asian accretion*. Balkema, 1999.
- P. Molnar. Continental tectonics in the aftermath of plate tectonics. *Nature*, 335(6186):131–137, 1988.
- J. Montagner and D. Anderson. Constrained reference mantle model. *Physics of the earth and planetary interiors*, 58(2-3):205–227, 1989.
- L. Moresi. Short course on numerical modeling in solid earth dynamics, 1999.
- L. Moresi and V. Solomatov. Numerical investigation of 2d convection with extremely large viscosity variations. *Physics of Fluids*, 7(9):2154, 1995.
- L. Moresi, M. Gurnis, and S. Zhong. Plate tectonics and convection in the earth's mantle: Toward a numerical simulation. *Computing in Science & Engineering*, 2(3):22–33, 2000.
- L. N. Moresi and V. Solomatov. Mantle convection with a brittle lithosphere: thoughts on the global tectonic styles of the Earth and Venus. *Geophys. J. Int.*, 133:669–682, 1998.
- J. MORGAN and W. SMITH. Flattening of the sea-floor depth-age curve as a response to asthenospheric flow. *Nature*, 359(6395):524–527, 1992.
- J. Morgan, W. Morgan, Y. Zhang, and W. Smith. Observational hints for a plume-fed, suboceanic asthenosphere and its role in mantle convection. *Journal of geophysical research*, 100(B7):12753–12, 1995.
- W. Morgan. Rises, trenches, great faults, and crustal blocks. *J. geophys. Res.*, 73(6):1959–1982, 1968.
- W. Morgan. Convection plumes in the lower mantle. *Nature*, 230:42–43, 1971.
- S. Mueller and R. PHILLIPS. On the initiation of subduction. *Journal of Geophysical Research*, 96(B1):651–665, 1991.
- R. D. Müller, J.-Y. Royer, and L. A. Lawver. Revised plate motions relative to the hotspots from combined Atlantic and Indian Ocean hotspot tracks. *Geology*, 21(3):275–278, 1993.
- R. D. Müller, W. R. Roest, J.-Y. Royer, L. M. Gahagan, and J. G. Sclater. Digital isochrons of the world's ocean floor. *J. Geophys. Res.*, 102(B2):3211–3214, 1997.
- S. Nagihara, C. Lister, and J. Sclater. Reheating of old oceanic lithosphere: Deductions from observations. *Earth and planetary science letters*, 139(1-2):91–104, 1996.
- E. Nisbet. The tectonic setting and petrogenesis of komatiites. *Komatiites*. London: George Allen & Unwin, pages 501–520, 1982.
- E. Nisbet and C. Fowler. Model for archean plate tectonics. *Geology*, 11(7):376, 1983.

- A. Nyblade and H. Pollack. A global analysis of heat flow from precambrian terrains: implications for the thermal structure of archean and proterozoic lithosphere. *Journal of Geophysical Research*, 98(B7):12207–12, 1993.
- H. Ohta, S. Maruyama, E. Takahashi, Y. Watanabe, and Y. Kato. Field occurrence, geochemistry and petrogenesis of the archean mid-oceanic ridge basalts (amorbs) of the cleaverville area, pilbara craton, western australia. *Lithos*, 37(2-3):199–221, 1996.
- S. Y. O'Reilly. Indian & Pacific MORB-type mantle beneath Australia: Relevance to large-scale convection. In J. J. Vevers, editor, *Billion-year earth history of Australia and neighbours in Gondwanaland*, chapter 13, page 81. GEMOC Press, Sydney, Australia, 2001.
- D. Parasnis. *Principles of Applied Geophysics*. Chapman and Hall, London ; New York, 4th ed. edition, 1986. ISBN 0412283204.
- S. Parman, J. Dann, T. Grove, and M. De Wit. Emplacement conditions of komatiite magmas from the 3.49 ga komati formation, barberton greenstone belt, south africa. *Earth and Planetary Science Letters*, 150(3-4):303–323, 1997.
- B. Parsons and D. McKenzie. Mantle convection and the thermal structure of the plates. *J. geophys. Res.*, 83:4485–4496, 1978.
- B. Parsons and J. G. Sclater. An analysis of the variation of ocean floor bathymetry and heat flow with age. *J. Geophys. Res.*, 82(5):803–827, 1977.
- D. Perkins and R. Newton. Charnockite geobarometers based on coexisting garnet-pyroxene-plagioclase-quartz. *Nature*, 292:144–146, 1981.
- A. Poliakov and H. Herrmann. Self-organized criticality of plastic shear bands in rocks. *Geophysical research letters*, 21(19):2143–2146, 1994.
- H. Pollack and D. Chapman. Mantle heat flow. *Earth and Planetary Science Letters*, 34(2):174–184, 1977a.
- H. Pollack and D. Chapman. On the regional variation of heat flow, geotherms, and lithospheric thickness. *Tectonophysics*, 38(3-4):279–296, 1977b.
- H. Pollack, S. Hurter, and J. Johnson. Heat flow from the earth's interior: analysis of the global data set. *Reviews of Geophysics*, 31(3):267–280, 1993.
- Y. Popov, S. Pevzner, V. Pimenov, and R. Romushkevich. New geothermal data from the kola superdeep well sg-3. *Tectonophysics*, 306(3-4):345–366, 1999.
- D. Pyle, D. Christie, J. Mahoney, and R. Duncan. Geochemistry and geochronology of ancient southeast indian and southwest pacific seafloor. *Journal of Geophysical Research*, 100(B11):22261–22, 1995.

- R. Pysklywec and J. Mitrovica. Mantle flow mechanisms for the large-scale subsidence of continental interiors. *Geology*, 26(8):687, 1998.
- C. Reeves, T. S. Ltd, B. G. S. Dept, and C. I. D. Agency. *Reconnaissance Aeromagnetic Survey of Botswana, 1975-1977: Final Interpretation Report*. Geological Survey Dept. with the authority of the Ministry of Mineral Resources and Water Affairs, 1978.
- J. Regan and D. Anderson. Anisotropic models of the upper mantle. *Physics of the earth and planetary interiors*, 35(4):227–263, 1984.
- A. Reymer and G. Schubert. Phanerozoic addition rates to the continental crust and crustal growth. *Tectonics*, 3(1):63–77, 1984.
- R. Richardson. Ridge forces, absolute plate motions, and the intraplate stress field. *Journal of Geophysical Research*, 97(B8):11739–11, 1992.
- S. Richardson, J. Gurney, A. Erlank, and J. Harris. Origin of diamonds in old enriched mantle. *Nature*, 310:198–202, 1984.
- F. Richter. Regionalized models for the thermal evolution of the earth. *Earth and planetary science letters*, 68(3):471–484, 1984.
- F. Richter. Models for the archean thermal regime. *Earth and planetary science letters*, 73 (2-4):350–360, 1985.
- L. Ricou. Tethys and transit plate patterns viewed against long-term periodicity of magnetic field reversals. *Physics of the Earth and Planetary Interiors*, 87(3-4):255–265, 1995.
- A. Ringwood. *Composition and Petrology of the Earth's Mantle*, volume 618. McGraw-Hill New York, 1975.
- A. Ringwood. *Origin of the Earth and Moon*, volume 1. New York, Springer-Verlag New York, Inc., 1979. 307 p., 1979.
- J. Ritsema, H. J. van Heijst, and J. H. Woodhouse. Complex shear wave velocity structure imaged beneath Africa and Iceland. *Science*, 286:1925–1928, 1999.
- L. Royden and C. E. Keen. Rifting Process and Thermal Evolution of the Continental Margin of Eastern Canada determined from Subsidence. *Earth Planet. Sci. Lett.*, 51: 343–361, 1980.
- R. Rudnick, W. McDonough, and R. O'Connell. Thermal structure, thickness and composition of continental lithosphere. *Chemical Geology*, 145(3-4):395–411, 1998.
- A. Salem, S. Williams, J. Fairhead, D. Ravat, and R. Smith. Tilt-depth method: A simple depth estimation method using first-order magnetic derivatives. *The Leading Edge*, 26 (12):1502, 2007.

- A. Salem, S. Williams, D. Fairhead, R. Smith, and D. Ravat. Interpretation of magnetic data using tilt-angle derivatives. *Geophysics*, 73(1):L1, 2008.
- J. Salveson. Variations in the geology of rift basin-a tectonic model. In *Rio Grande Rift Symposium*, volume LA-7487-C, pages 82–86, Santa Fe, New Mexico, Oct 1978, 1978. Los Alamos Scientific Laboratory.
- M. Sandiford, D. Coblenz, and R. Richardson. Ridge torques and continental collision in the indian-australian plate. *Geology*, 23(7):653, 1995.
- D. Sandwell and W. H. F. Smith. Marine gravity anomaly from GEOSAT and ERS-1 satellite altimetry. *J. Geophys. Res.*, 102:10039 – 10054, 1997.
- D. S. Sawyer. Total Tectonic Subsidence: A Parameter for Distinguishing Crust Type at the U.S. Atlantic Continental Margin. *J. Geophys. Res.*, 90(B9):7751–7769, 1985.
- J. Schatz and G. Simmons. Thermal conductivity of earth materials at high temperatures. *Journal of Geophysical Research*, 77(35):6966–6983, 1972.
- W. Schellart. Kinematics of subduction and subduction-induced flow in the upper mantle. *Journal of Geophysical Research*, 109(B7):B07401, 2004.
- H. Schouten and K. McCamy. Filtering marine magnetic anomalies. *Journal of Geophysical Research*, 77(35):7089–7099, 1972.
- J. Schouten. A fundamental analysis of magnetic anomalies over oceanic ridges. *Marine Geophysical Researches*, 1(2):111–144, 1971.
- J. Sclater and J. Francheteau. The implications of terrestrial heat flow observations on current tectonic and geochemical models of the crust and upper mantle of the earth. *Geophysical Journal of the Royal Astronomical Society*, 20(5):509–542, 1970.
- J. Sclater and L. Wixon. The relationship between depth and age and heat flow and age in the western north atlantic. *The Geology of North America*, 1000:257–270, 1986.
- J. Sclater, R. Anderson, and M. Bell. Elevation of ridges and evolution of the central eastern pacific. *J. geophys. Res.*, 76(32):7888–7915, 1971.
- J. Sclater, C. Jaupart, and D. Galson. The heat flow through oceanic and continental crust. *Rev. Geophys. Space Phys.*, 18:269–311, 1980.
- J. Sclater, B. Parsons, and C. Jaupart. Oceans and continents: similarities and differences in the mechanisms of heat loss. *Journal of Geophysical Research*, 86(B12):11535–11, 1981.
- J. G. Sclater and B. Célérier. Errors in extension measurements from planar faults observed on seismic reflection lines. *Basin Research*, 1:217–221, 1989.

- J. G. Sclater and P. A. F. Christie. Continental Stretching: An Explanation of the Post-Mid-Cretaceous Subsidence of the Central North Sea Basin. *J. Geophys. Res.*, 85(B7):3711–3739, July 1980.
- R. Sheriff. Limitations on resolution of seismic reflections and geologic detail derivable from them. *AAPG Memoir*, 26:3–14, 1977.
- R. Sheriff. Sheriff and geldart (1995) exploration seismology, 1995.
- M. Shore and A. Fowler. The origin of spinifex texture in komatiites. *Nature*, 397(6721):691–694, 1999.
- N. H. Sleep. Thermal Effects of the Formation of Atlantic Continental Margins by Continental Breakup. *Geophysical Journal of the Royal Astronomical Society*, 24:325–350, 1971.
- V. Solomatov. Scaling of temperature-and stress-dependent viscosity convection. *Physics of Fluids*, 7:266, 1995.
- V. Solomatov and L. Moresi. Stagnant lid convection on venus. *Journal of geophysical research*, 101(2):4737–4753, 1996.
- V. Solomatov and L. Moresi. Three regimes of mantle convection with non-newtonian viscosity and stagnant lid convection on the terrestrial planets. *Geophysical research letters*, 24(15):1907–1910, 1997.
- D. Spence, P. Sharp, and D. Turcotte. Buoyancy-driven crack propagation: a mechanism for magma migration. *Journal of Fluid Mechanics*, 174(-1):135–153, 1987.
- C. Stein and S. Stein. A model for the global variation in oceanic depth and heat flow with lithospheric age. *Nature*, 359(6391):123–129, 1992.
- D. Stevenson and J. Turner. Angle of subduction. *Nature*, 270:334–336, 1977.
- P. Stoddard and D. Abbott. Influence of the tectosphere upon plate motion. *Journal of geophysical research*, 101(B3):5425–5433, 1996.
- B. Storey. The role of mantle plumes in continental breakup: case histories from gondwanaland. *Nature*, 377(6547):301–308, 1995.
- W. Su and A. Dziewonski. On the scale of mantle heterogeneity. *Physics of the earth and planetary interiors*, 74(1-2):29–54, 1992.
- W. Su, C. Mutter, J. Mutter, and W. Buck. Some theoretical predictions on the relationships among spreading rate, mantle temperature, and crustal thickness. *Journal of geophysical research*, 99(B2):3215–3227, 1994a.
- W. Su, R. Woodward, and A. Dziewonski. Degree 12 model of shear velocity heterogeneity in the mantle. *Journal of Geophysical Research*, 99(B4):6945–6980, 1994b.

- C. Swain. Reduction-to-the-pole of regional magnetic data with variable field direction, and its stabilisation at low inclinations. *Exploration Geophysics*, 31(2):78–83, 2000.
- C. Swanberg, M. Chessman, G. Simmons, S. Smithson, G. Grønlie, and K. Heier. Heat-flow–heat-generation studies in norway. *Tectonophysics*, 23(1-2):31–48, 1974.
- L. Sykes. Mechanism of earthquakes and nature of faulting on the mid-oceanic ridges. *Journal of Geophysical Research*, 72(8):2131–2153, 1967.
- P. Tackley. Self-consistent generation of tectonic plates in three-dimensional mantle convection. *Earth and planetary science letters*, 157(1-2):9–22, 1998.
- W. Telford, L. Geldhart, and R. Sheriff. *Applied Geophysics*. Cambridge University Press, Cambridge [England]; New York, 2nd edition, 1990. ISBN 0521326931.
- D. Tozer. The present thermal state of the terrestrial planets. *Physics of the Earth and Planetary Interiors*, 6(1-3):182–197, 1972.
- D. Turcotte and E. Oxburgh. Finite amplitude convective cells and continental drift. *Journal of Fluid Mechanics*, 28(01):29–42, 1967.
- D. Turcotte and G. Schubert. Geodynamics applications of continuum physics to geological problems. 1982.
- V. Vacquier. The origin of terrestrial heat flow. *Geophysical Journal International*, 106(1):199–202, 1991.
- V. Vacquier. Corrigendum to ‘origin of terrestrial heat flow’. *Geophysical Journal International*, 111(3):637–638, 1992.
- R. Van der Hilst, E. Engdahl, W. Spakman, and G. Nolet. Tomographic imaging of subducted lithosphere below northwest pacific island arcs. *Nature*, 353:37–42, 1991.
- B. Verduzco, J. Fairhead, C. Green, and C. MacKenzie. New insights into magnetic derivatives for structural mapping. *The Leading Edge*, 23(2):116, 2004.
- F. Vine and D. Matthews. Magnetic anomalies over oceanic ridges. *Nature*, 199:947–949, 1963.
- P. R. Vogt and N. A. Ostenso. Steady State Crustal Spreading. *Nature*, 215(5103):810–817, 1967.
- R. Von Herzen, M. Cordery, R. Detrick, and C. Fang. Heat flow and the thermal origin of hot spot swells: the hawaiian swell revisited. *Journal of Geophysical Research*, 94(B10):13783–13, 1989.
- G. Wasserburg, G. MacDonald, F. Hoyle, and W. Fowler. Relative contributions of uranium, thorium, and potassium to heat production in the earth. *Science*, 143(3605):465, 1964.

- J. Watson. Precambrian thermal regimes. *Philosophical Transactions of the Royal Society of London. Series A, Mathematical and Physical Sciences*, 288(1355):431, 1978.
- A. Watts. The effective elastic thickness of the lithosphere and the evolution of foreland basins. *Basin research*, 4(3-4):169–178, 1992.
- A. Wegener. Origin of continents and oceans, translated by john biram in 1966, 1929.
- L. Wen and D. L. Anderson. The fate of slabs inferred from seismic tomography and 130 million years of subduction. *Earth Planet. Sci. Lett.*, 133:185–198, 1995.
- B. Wernicke. Uniform-sense normal simple shear of the continental lithosphere. *Canad. J. Earth Sci.*, 22:108–125, 1985.
- N. White. An inverse method for determining lithospheric strain rate variation on geological timescales. *Earth and Planetary Science Letters*, 122(3-4):351–371, 1994.
- R. White. The earth's crust and lithosphere. *Journal of Petrology*, (1):1, 1988.
- R. White and D. McKenzie. Magmatism at rift zones: the generation of volcanic continental margins and flood basalts. *Journal of Geophysical Research*, 94(B6):7685–7729, 1989.
- R. B. Whitmarsh, G. Manatschal, and T. A. Minshull. Evolution of magma-poor continental margins from rifting to seafloor spreading. *Nature*, 413:150–154, 2001.
- Wikipedia. Greek alphabet.
- J. Wilson. A possible origin of the hawaiian islands. *Canadian Journal of Physics*, 41(6):863–870, 1963.
- J. Wilson. A new class of faults and their bearing on continental drift. *Nature*, 207:343–347, 1965.
- M. Wilson. Plate-moving mechanisms: constraints and controversies. *Journal of the Geological Society*, 150(5):923, 1993.
- J. Woodhouse and A. Dziewonski. Mapping the upper mantle: three-dimensional modeling of earth structure by inversion of seismic waveforms. *Journal of Geophysical Research*, 89(B7):5953–5986, 1984.
- J. H. Woodhouse and A. M. Dziewonski. Seismic modelling of the earth's large-scale three-dimensional structure. *Philosophical Transactions of the Royal Society of London. Series A, Mathematical and Physical Sciences*, 328(1599):291–308, 1989.
- O. Yilmaz. Seismic data processing: Soc. Expl. Geophys, 252, 1987.
- S. Zhong, M. Gurnis, and L. Moresi. Role of faults, nonlinear rheology, and viscosity structure in generating plates from instantaneous mantle flow models. *Journal of geophysical research*, 103(B7):15255–15268, 1998.

P. Ziegler. Plate-moving mechanisms: their relative importance. *Journal of the Geological Society*, 150(5):927, 1993.

M. Zoback. First-and second-order patterns of stress in the lithosphere-the world stress map project. *Journal of Geophysical Research*, 97:11703, 1992.

Index

intercept time, 318
Seismic impedance, 328
VibroSeis, 314

